PROCEEDINGS OF THE SECOND CONFERENCE ON THE CLIMATIC IMPACT ASSESSMENT PROGRAM

NOVEMBER 14-17, 1972

ANTHONY J. BRODERICK, EDITOR

SPONSORED BY THE
U.S. DEPARTMENT OF TRANSPORTATION

DOT-TSC-OST-73-4

This document is available to the public through the National Technical Information Service, Springfield, Virginia 22151

HELD AT THE
TRANSPORTATION SYSTEMS CENTER
KENDALL SQUARE
CAMBRIDGE, MASSACHUSETTS 02142

TECHNICAL REPORT STANDARD TITLE PAGE

1. Report No.	2. Government Accession No.	3. Recipient's Catalog No.
DOT-TSC-OST-73-4		

4. Title and Subtitle	5. Report Date
Proceedings of the Second Conference on the Climatic Impact Assessment Program	April 1973
	6. Performing Organization Code
7. Author(s)	8. Performing Organization Report No.
Anthony J. Broderick, Editor	DOT-TSC-OST-73-4
9. Performing Organization Name and Address DOT Transportation Systems Center Kendall Square Cambridge, MA 02142	10. Work Unit No. R3537
	11. Contract or Grant No. PPA OS 320
	13. Type of Report and Period Covered Conference Proceedings November 14-17, 1972
12. Sponsoring Agency Name and Address Office of the Secretary Department of Transportation 400 Seventh Street, S.W. Washington, D.C. 20590	14. Sponsoring Agency Code

15. Supplementary Notes

16. Abstract

This volume contains the proceedings of the Second Conference on the Climatic Impact Assessment Program (CIAP), held at the DOT Transportation Systems Center on November 14-17, 1972. It includes 37 invited papers, four unscheduled presentations, three edited panel discussions, and edited question-and-answer sessions following some of the papers. The conference was essentially a progress report on CIAP. Therefore, some of the papers contain new data not yet published elsewhere, others describe detailed experiment plans or hardware for use in the near future, and a few deal with proposed investigations which may be directly relevant to CIAP. The subjects covered include aircraft-engine emissions, the nature of the "undisturbed" stratosphere of 1974, the nature of the "perturbed" stratosphere of 1990-2025, the possible resulting tropospheric perturbations, and the biological and economic effects of such perturbations.

17. Key Words			18. Distribution Statement
ozone	atmospheric transport	NO_x	Document is available to the public through the National Technical Information Service, Springfield, Virginia 22151
emissions	atmospheric modeling	climate	
stratosphere	atmospheric dynamics		
SST's	chemical kinetics		
aerosols	ultraviolet radiation	sampling	
	photochemistry	pollutants	

19. Security Classif. (of this report)	20. Security Classif. (of this page)	21. No. of Pages	22. Price
Unclassified	Unclassified	437	

Form DOT F 1700.7 (8-69)

EDITOR'S PREFACE

The Second Conference on the Climatic Impact Assessment Program was held at the DOT Transportation Systems Center, November 14-17, 1972. This volume documents the proceedings of that conference. Some 41 papers were presented, including four unscheduled contributions. Also included are edited transcripts of three panel discussions and the informal discussions which followed many of the presentations.

This conference was, in essence, a progress report. Many of the papers contain new data which will eventually find its way into the open literature, while others describe detailed experiment plans or hardware designs to be used in the near future on a project directly related to CIAP. A few of the presentations concentrate on proposed investigations which were felt to be directly relevant to CIAP. A mixture of exactly this kind was sought for this conference, the third major public reporting milestone of the Climatic Impact Assessment Program.

The nature of our editing deserves a few specific comments. The major constraint was time; we feel that the utility of such works decays exponentially from the date of the conference adjournment. All of the authors were given an opportunity to review galley proofs of the edited versions of their papers. This was not true, however, for the panel discussions or the question-and-answer sessions which followed many of the presentations. We have tried to maintain both the flavor and the accuracy of these informal exchanges; we apologize in advance for any errors which have crept in.

The authors devoted considerable time to their papers, and most were quite cooperative in meeting our deadlines. We acknowledge their efforts with thanks. Dr. Thomas Hard of TSC contributed many hours of technical review and criticism, for which we are most grateful. We owe our deepest debt, however, to Ms. Ellen Rice of Raytheon Service Company, who has borne most of the responsibility in this effort. Without her incisive editing, thoughtful revision, and persevering attention to detail, we could never have produced a book of such high quality in the time available.

Anthony J. Broderick, Editor
DOT Transportation Systems Center
March 20, 1973

NOTICE

The views expressed in these papers are the authors' personal opinions, and do not necessarily reflect those of any organization of which they may be members. The Department of Transportation is distributing this document in the interest of information exchange, and assumes no liability for its contents.

PROCEEDINGS OF THE SECOND CONFERENCE ON THE CLIMATIC IMPACT ASSESSMENT PROGRAM

U.S. DEPARTMENT OF TRANSPORTATION NOVEMBER 1972

CONTENTS

Introduction . . . . . *William C. Steber, Jr.* 1

Chairman's Address . . . . . *Alan J. Grobecker* 2

SESSION I: THE NATURAL STRATOSPHERE
Chairman: Ernest Bauer
Institute for Defense Analyses

Atmospheric Monitoring and Experiments: A Summary of Ongoing Projects
Samuel C. Coroniti and Anthony J. Broderick 13

Evaluation of Several Sensors for Measuring Low Concentrations of Water Vapor
Arnold Wexler, Saburo Hasegawa, and Lewis Greenspan 22

Global Measurements of Stratospheric Aerosol, Ozone, and Water Vapor by Balloon-Borne Sensors
D.J. Hofmann, J.M. Rosen, T.J. Pepin and J.L. Kroening 23

Recent Measurements of the Injection of Water Vapor and Ozone into the Stratosphere by Thunderstorms . . . . . *E.W. Barrett, P.M. Kuhn, and A. Shlanta* 34

Examples of Stratospheric Transport . . . . . *L. Machta and K. Telegadas* 47

SESSION II: THE NATURAL STRATOSPHERE
Chairman: Marcel Ackerman
Institut d'Aéronomie Spatiale de Belgique

Panel Discussion: The Physics and Chemistry of Stratospheric Aerosols
Chairman, James P. Friend 57

Near-Infrared Interferometric Measurements of Stratospheric Composition to be Made from the Concorde . . . . . *Crofton B. Farmer, Robert A. Toth, Rudolph A. Schindler, and Odell F. Raper* 65

Measurements of Some Hydrogen-Oxygen-Nitrogen Compounds in the Stratosphere, From Concorde 002 . . . . . *J.E. Harries and N.W.B. Stone* 78

Vertical Distribution of Minor Atmospheric Constituents as Derived from Air-Borne Measurements of Atmospheric Emission and Absorption Infrared Spectra
D.G. Murcray, A. Goldman, F.H. Murcray, W.J. Williams, J.N. Brooks and D.B. Barker 86

High-Resolution Spectra of the Stratosphere Between 30 and 200 cm^{-1}
J.P. Baluteau, E. Bussoletti, P. Léna, and A. Marten 99

SESSION III: THE NATURAL STRATOSPHERE – TRACE GASES

Chairman: Milton Scheer
National Bureau of Standards

The Present Status of Ozone Research: Photochemistry and Observations . . . . . *H.U. Dütsch* 106

Evaluated Rate and Photochemical Data for Modeling of the Stratosphere
David Garvin and Robert F. Hampson 114

Recent Kinetic Measurements on the Reactions of $O(^3P)$, H and HO_2
D.D. Davis, W.W. Wong, S.D. Fischer, R.L. Schiff, J.O. Lephardt, J. E. Prusaczyk, W.A. Payne, L.J. Stief, R.E. Huie, J.T. Herron 126

Investigation of the Rate Coefficient for $O(^3P) + NO_2 \rightarrow NO + O_2$
Tom G. Slanger, Bernard J. Wood, and Graham Black 144

Instrumentation for NO Measurement in the Stratosphere
B.A. Ridley, K.H. Welge, H.I. Schiff, L.R. Megill and A.W. Shaw 146

Panel Discussion: Stratospheric Aeronomy . . . . . *Chairman, Marcel Nicolet* 154

SESSION IV: ENGINE EMISSIONS

Chairman: Robert Oliver
Institute for Defense Analyses

Engine Exhaust Emissions Subprogram . . . . . *A.K. Forney* 169

Emission Levels of the Olympus 593 Engine at the Supersonic Cruise Conditions of the Concorde Aircraft . . . . . *M.R. Williams* 173

Emission Level of the YJ93-GE-3 Engine, an SST-Like Engine
James Neely and Donald L. Davidson 180

Trace Components of Aviation Turbine Fuels and Exhausts
R.W. Hurn, J.W. Vogh, F.W. Cox, and D.E. Seizinger 194

Emissions Measurement System for Jet Engines in Altitude Test Cells . . . . . *J. Lloyd Grissom* 199

Concentration of OH and NO in YJ93-GE-3 Engine Exhausts Measured in Situ by Narrow-Line UV Absorption . . . . . *W.K. McGregor, B.L. Seiber, and J.D. Few* 214

SESSION V: THE PERTURBED ATMOSPHERE

Chairman: Robert L. Underwood
Department of Transportation

The Perturbed Atmosphere: A Review of CIAP Activities . . . . . *Robert L. Underwood* 230

The Design of Chemical-Release Experiments in the Stratosphere . . . . . *Frank Hudson* 237

Transport Measurements in the Stratosphere . . *N.W. Rosenberg, R.E. Good, and S.P. Zimmerman* 247

Dispersion of Tracers in the Stratosphere . . . . . *Ernest Bauer* 254

High-Altitude Aircraft Wake Dynamics . . . . . *H. Hoshizaki, L.B. Anderson, and R.J. Conti* 263

Comments on Photochemical Modeling . . . . . *Eigil Hesstvedt* 285

SESSION VI: THE PERTURBED ATMOSPHERE – MODELING

Chairman: Robert L. Underwood
Department of Transportation

Time-Dependent Two-Dimensional Parameterized Model . . . . . *T. Shimazaki and D.J. Wuebbles* 291

Zonal Atmospheric Model ZAM2 . . . . . *Michael C. MacCracken* 298

Preliminary Results from a Three-Dimensional, General-Circulation/Tracer Model . . *J.D. Mahlman* 321

Comments on the Possible Effect of NO_x Injection into the Stratosphere by Atmospheric Nuclear Weapons Tests . . . . . *Julius S. Chang* 338

The Effect of Nuclear Explosions on Stratospheric Nitric Oxide and Ozone
Harold Johnston, Garry Whitten, and John Birks 340

Solutions of the Chemical Kinetic Equations for Initially Inhomogeneous Mixtures
Glenn R. Hilst 351

Development of a Three-Dimensional Stratospheric Global Circulation Model at the National Center for Atmospheric Research . . . . . *Warren M. Washington* 358

The Sensitivity and Comparison of General Atmospheric Circulation Models . . . *Michael Warshaw* 363

SESSION VII: BIOLOGICAL IMPACT

Chairman: Alan J. Grobecker
Department of Transportation

Status of the CIAP Biological Impact Project . . . . . *Donald R. Sheldon* 369

Ultraviolet Radiation of Sunlight and Skin Cancer . . . . . *Harold F. Blum* 373

Ultraviolet Radiation and Photosynthesis . . . . . *Edward B. Knipling* 379

Ecologic Considerations of Solar Radiation Change . . . . . *Martyn M. Caldwell* 388

Agronomic Effects of Climatic Change . . . . . *R.H. Biggs and J.F. Bartholic* 394

Remarks on Determining Social and Cost Measures of Climatic Changes . . . . . *Henry M. Peskin* 404

SESSION VIII: SUMMARY

Chairman: Alan J. Grobecker
Department of Transportation

Panel Discussion: The Climatic Impact of Pollutants Injected into the Stratosphere
Chairman, Alan J. Grobecker 407

Conference Summary . . . . . *Alan J. Grobecker* 416

List of Participants 419

The cover photograph was taken by the 58th Weather Reconnaissance Squadron, U.S. Air Force.

INTRODUCTION

WILLIAM C. STEBER
Deputy Assistant Secretary for Systems Development and Technology
United States Department of Transportation
Washington, D.C.

The U.S. Department of Transportation's business is the improvement of the modes of transportation presently available to Americans, and the projection of the country's future transportation needs. This projection has two faces: first, the development of new or improved modes of travel, and second, the assessment of the social impacts of the various kinds of transportation – including, of course, the environmental effects.

The Department of Transportation is seriously concerned with the ecological consequences of both existing and future modes of travel, as witness our activities in automotive-emissions reduction and aircraft-noise abatement. Now that our subsonic aircraft are flying in the lower stratosphere all around the globe, the environmental effects of air transportation have become a matter of world-wide interest. The possible introduction of supersonic aircraft, which fly higher in the stratosphere, makes the importance of this issue even more evident.

The Climatic Impact Assessment Program was organized in 1971 to assess the possible environmental effects of the fleet of aircraft which will be in service in 1990. It has the support of both the Administration and Congress; Congressional appropriations so far have been more than $12 million, and the total cost is expected to be over $20 million.

The target date for CIAP's summary assessment is the end of 1974. The task is a monumental one, embracing scientific disciplines from basic physics and chemistry to weather forecasting to medical and agricultural sciences. Obviously we cannot achieve total understanding of every possibly contributing phenomenon by then. Nonetheless, we feel that it will be possible to assess the probable importance of these factors and investigate those which merit the most attention within the time available.

The Climatic Impact Assessment Program represents the first effort which has been made to gather all the significant factors together for a study of their separate and collective impacts. We are fortunate to be able to draw on the work of other U.S. agencies, industry, and academia, and on a significant amount of research abroad. We hope that wide dissemination of CIAP data will encourage international assessment of the results and contribution to the conclusions.

We will be pressed many times in the next two years to provide "partial" answers. We hope you share our conviction that the entire task outlined must be completed before we can venture to draw conclusions as to the environmental impact of a large fleet of high-flying aircraft. We welcome your participation in this conference. Be productive, and enjoy yourselves!

CHAIRMAN'S ADDRESS

ALAN J. GROBECKER
Department of Transportation
Washington, D.C.

INTRODUCTION

The Climatic Impact Assessment Program is designed to provide an assessment, by 1974, of the climatic effects of perturbations of the upper atmosphere, caused by the propulsion effluents of a world high-altitude aircraft fleet as projected to 1990. Its final report will provide answers to environmental questions which may relate to the operation of supersonic transports, and for which federal decisions must be made in or before 1974.

The CIAP effort in 1972 has been primarily one of initiating projects. We now have more than 56 contract participants, with funding about equally divided among government activities, universities, profit-making organizations, and nonprofit organizations. In addition, a similar number of institutions and government agencies, both in this country and abroad, are making contributions from their own research. The government agencies include NOAA, NASA, AEC, DOD, HEW, NSF, NBS, EPA, and the Department of the Interior. Among the participants abroad are the British Meteorological Office, Aérospatiale and the University of Paris in France, the Institute of Aeronomy in Belgium, the Japan Meteorological Agency, and the Commonwealth Scientific and Industrial Research Organization (CSIRO) in Australia.

In calendar year 1973, the primary focus will be on the assimilation of results of experiments and the development of computational models for the projection of future changes in the stratosphere. Figure 1 shows how the various steps in the program tie into each other.

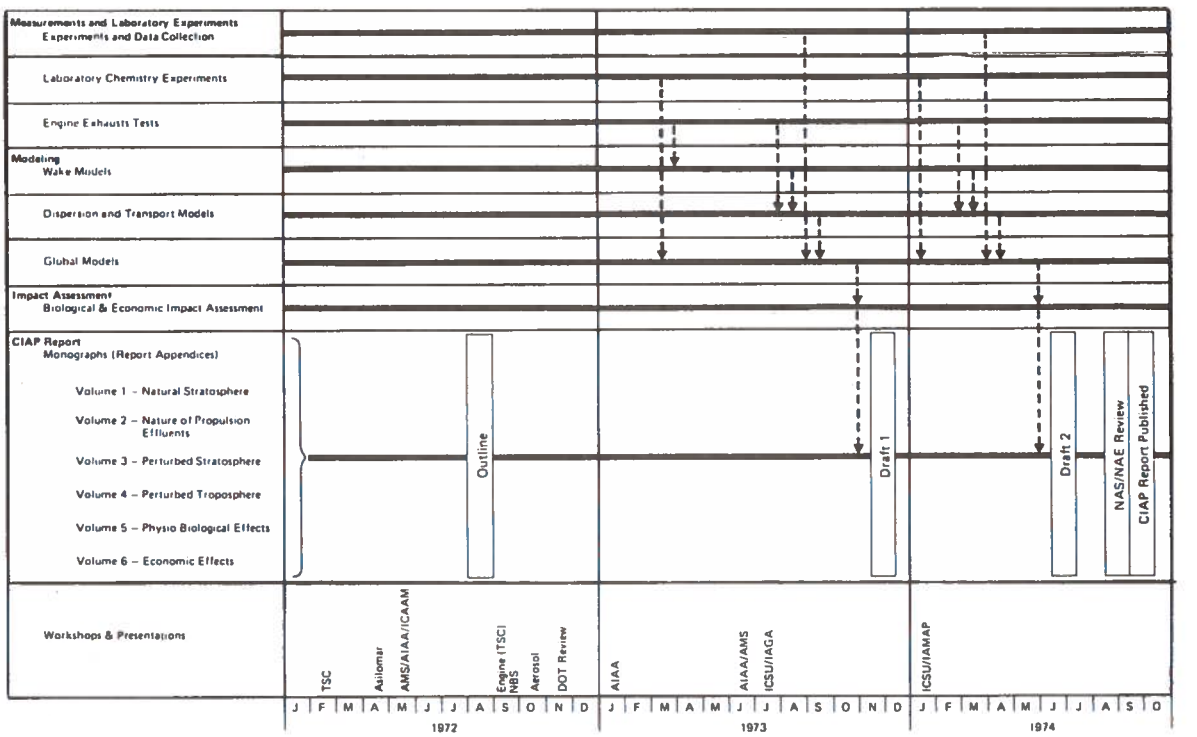

Figure 1. CIAP data flow.

MONOGRAPHS

A principal effort this year is the organization and preparation of the six reporting monographs. The first versions will be available worldwide in early 1974, for a variety of uses:

1. They will be utilized by CIAP investigators as the basis for further analysis, leading to the final Report of Findings.
2. They will become a data base for the NAS/NAE summer study in July of 1974.
3. They will be reviewed for technical completeness by professional societies.
4. They will be disseminated abroad so that similar analyses may be performed in other countries.

The Natural Stratosphere of 1974

The first of the monographs, dealing with the natural stratosphere of 1974, its structure, gaseous and aerosol chemistry, photochemistry, radiation, and motions is the scientific foundation of the study. Its principal subjects will be the density distributions of the chemical species and aerosols found in the stratosphere; the chemical and aerosol reactions which affect the gaseous and heterogeneous chemistry; the absorption cross-sections, chemical rate constants, and quantum yields of the principal reactants; the insolation at the tropopause; and the diffusion coefficients and mean motions that define the rates of transport of the chemical constituents and aerosols from the sources to the sinks. The initial compilation of the first monograph is to be accomplished in December 1972. The volume will be revised as CIAP continues to derive new data on the stratosphere.

To a considerable extent this data base already exists in the current literature. However, the references have not been collected, collated, and updated recently. In addition, one of the principal functions of the CIAP study is to augment the knowledge described in the present literature with results of meaningful physical experiments, measuring in situ the stratospheric constituents and radiation flux, and determining with suitably precise laboratory measurements the rates of chemical and photochemical reactions. (The chemistry of the stratosphere is of course different from that of the laboratory, especially as a consequence of the low atmospheric temperatures and large and variable winds.) The subsequent paragraphs review a few of the more important topics covered by the Monograph 1 investigation.

The meridional cross-section of temperature as a function of altitude and latitude is given in Figure 2, derived from work by R.E. Newell in 1969. In the troposphere, temperatures at the pole are low with respect to the higher temperatures at the equator. In contrast, in the stratosphere above 20 km, the high temperatures are at the poles and the low temperatures are near the Equator.

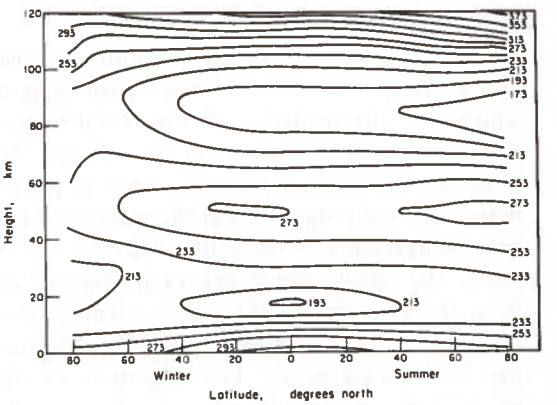

Figure 2. Meridional cross-section of temperature (after Newell, 1969 [1]).

In Figure 3, Newell shows the meridional cross-section of mean zonal winds. The tropospheric cross-section illustrates the Hadley-cell circulation with hemispheric motions directed by three meridional circulations. By contrast, in the stratosphere, there is a single cell in each of the two hemispheres and the effects of meridional circulation move the heat as in a refrigerator, from a region of low temperature near the Equator to one of high temperature at the poles.

Meridional and vertical transport in the stratosphere are accomplished mainly by variable motions. The vertical winds, greatest at about latitude 30 in the troposphere, are approximately 10 times as intense in the stratosphere.

Figure 4 shows a spectrum of wind speed as measured at an altitude of about 100 m at Caribou, Maine. In this spectrum, which shows

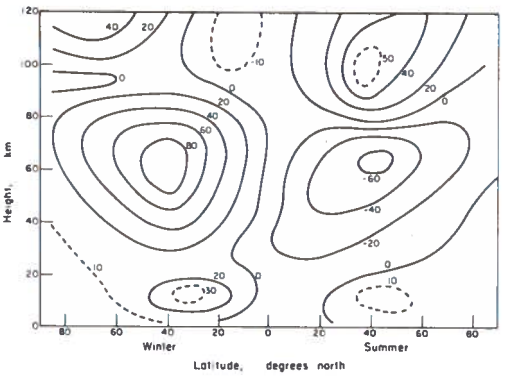

Figure 3. Meridional cross-section of mean zonal wind (m/sec) (after Newell, 1969 [1]).

the square of wind speed as a function of wave period from 1 minute to 1 year, peaks appear which are characteristic of the Brunt-Väisala period of about 2 minutes, of the 12- and 24-hour tidal motions, of planetary waves of period between 3 and 6 days, and of the rotation of the sun (30 days) and of the earth about the sun (1 year). The long-period waves are propagated up from the troposphere through the temperature minimum at the tropopause more strongly than the short-period waves. The magnitude of the stratospheric motions shows similar features. At 20 km the large-scale geostrophic motions of horizontal scale about 5,000 km have a horizontal value of about 10 m/sec in periods of about 30 days, as estimated by Newell in 1969 [1]. Thermal tidal motions having a horizontal scale of about 1,000 km have horizontal motion of about 0.3 m/sec in period of about 12 hr. The internal gravity waves at 20 km, having a horizontal scale of about 100 km, have a horizontal velocity of about 5 m/sec in a period of half an hour.

The chemistry of the stratosphere is a complicated mix. Both species density and variability are important for consideration. Some of the important constituents are shown for the daylight atmosphere in Figure 5, the work of Bortner and Kummler, 1969 [3]. The constituents shown represent only two-thirds the number of stratospheric constituents which we would like to consider in CIAP. Of particular interest in Figure 4 is the region between 10 and 50 km. As may be seen, the constituents vary in mixing ratio from one part in 10 to one part in 10^{16} in a mix which is of the order of 10^{18} particles/cm^3. For the chemical reactions, it is necessary to consider uncertainties associated with rate constants and photochemical absorption cross-sections. Of the more than 200 such reactions, 63 seem to be important in the stratosphere.

The concentrations of the constituents listed in Figure 5 may vary greatly over the globe of the earth, as indicated for ozone, for example, in Figure 6. This figure shows the total ozone content in a column above the surface of the earth, as measured by satellite, expressed in units of 0.001 cm at standard temperature and pressure. On one day the total ozone varies over the

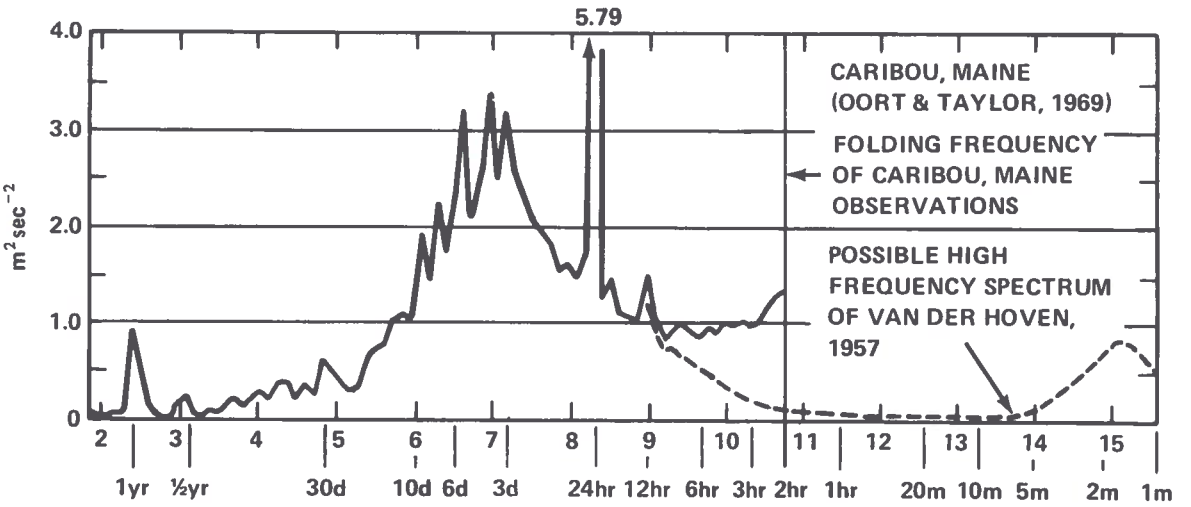

Figure 4. Horizontal wind-speed spectrum at Caribou, Maine (after Oort and Taylor, 1969 [2]).

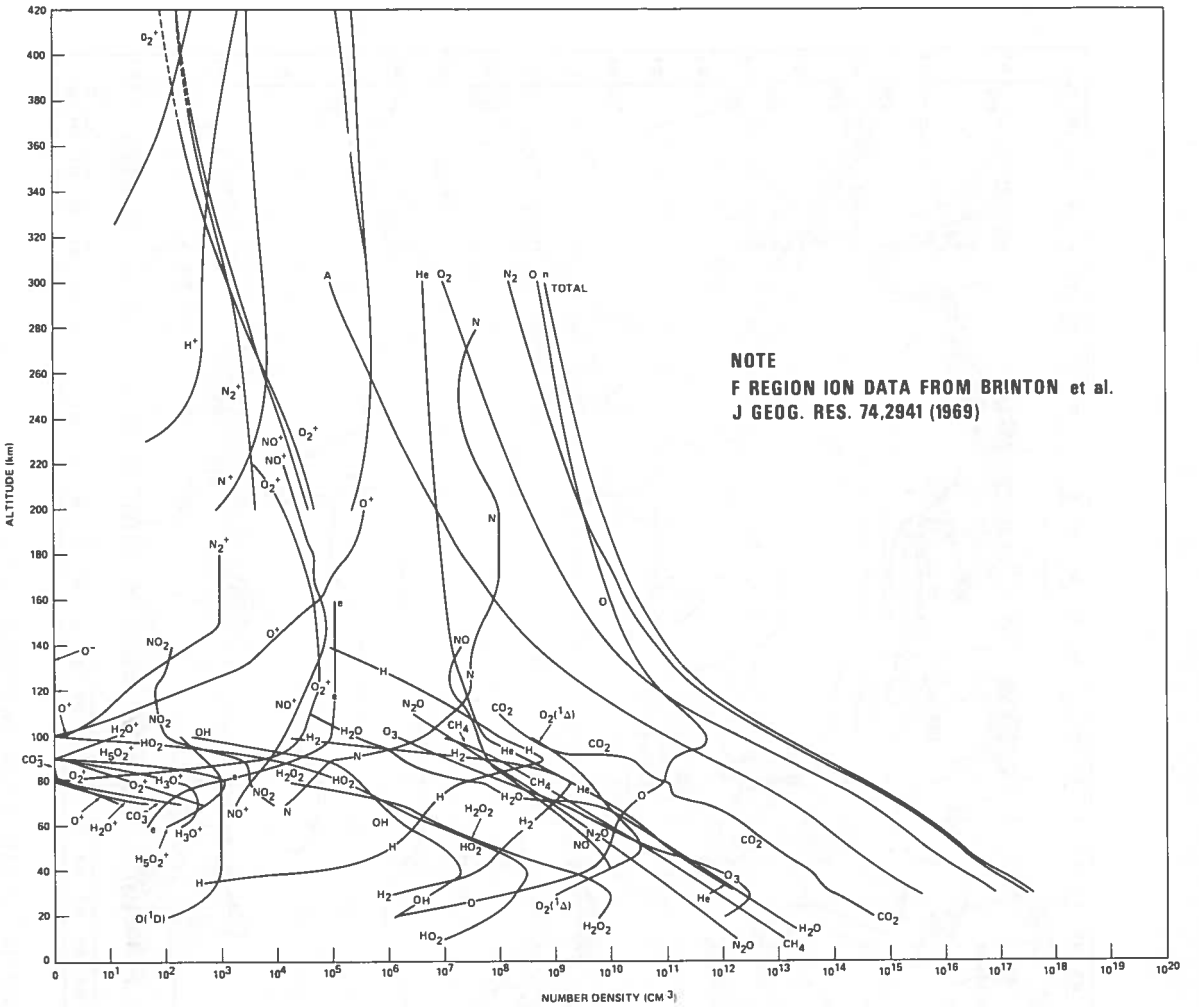

Figure 5. The daylight atmosphere 1969 (after Bortner and Kummler, 1968 [3]).

earth from about 2 mm to more than 6 mm. Since the radiative flux in the ultraviolet part of the spectrum, which drives important photochemical reactions, is very sensitive to the vertical column of ozone, this particular variation may be very important.

The story of the natural stratosphere of 1974 is incomplete. Filling in some of the more important gaps is a major part of the CIAP effort, involving a number of experiments intended to determine the densities of species, ultraviolet radiation flux, and temperature in the stratosphere. Measurements of ultraviolet flux are being made not for monitoring purposes, but to determine specific levels to aid us in understanding the local photochemistry. These experiments, as illustrated in Figure 7, include measurements made from the ground as well as in situ, and remote measurements made from many vehicles, such as low-flying aircraft, stratospheric vehicles, balloons, and satellites.

In addition to the in-situ measurements of the stratosphere, extensive laboratory experiments at the National Bureau of Standards, the University of Maryland, and the University of California at Berkeley will determine with suitable precision the chemical parameters required for solution of the CIAP problem.

Engine Emissions in the 1990 Stratosphere

A second monograph is concerned with the emissions of both existing engines and engines in development as projected to 1990, routes, and frequency of 1990 travel. This monograph, which is essential to subsequent stages of the

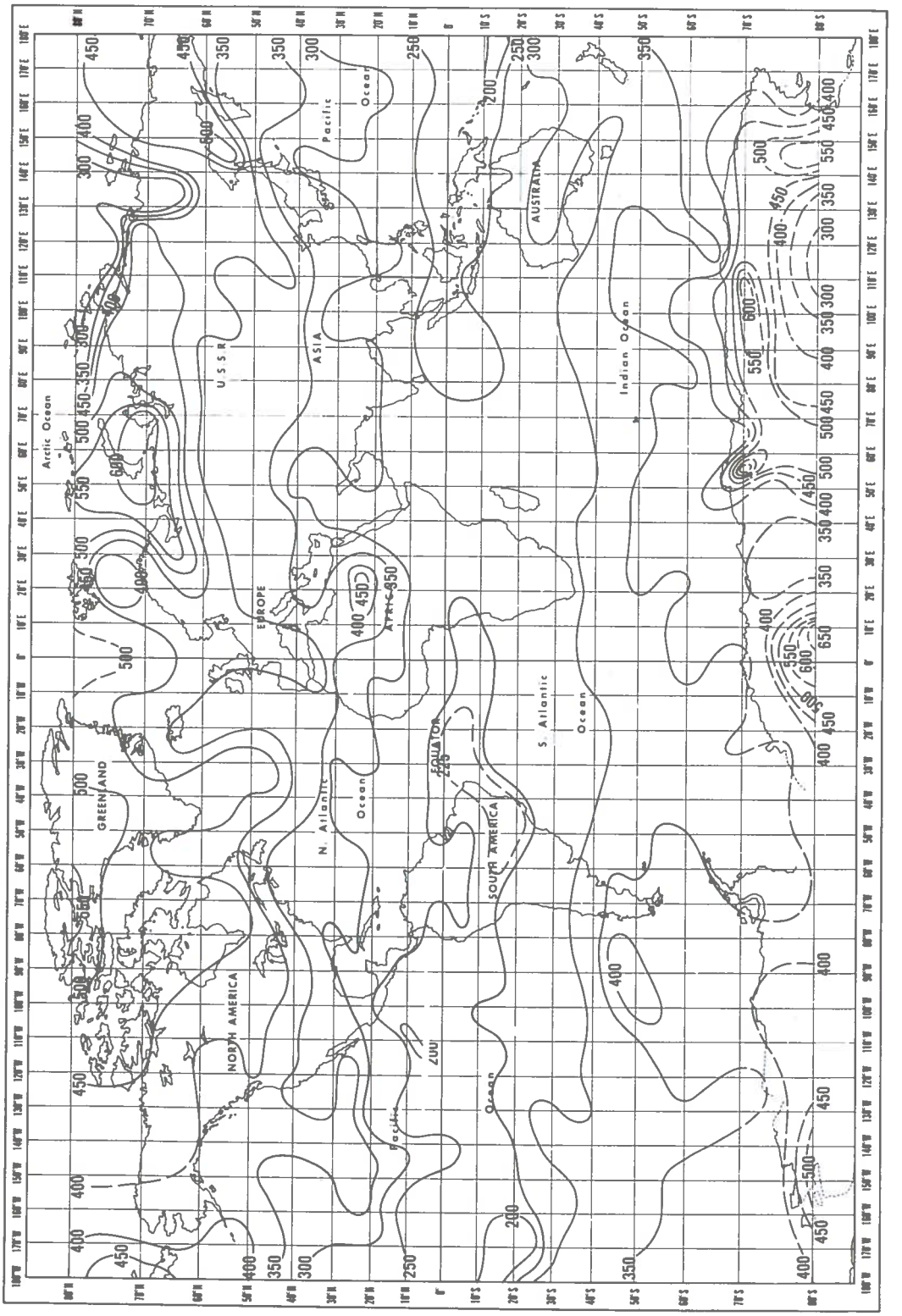

Figure 6. Total ozone content (10^{-3} cm STP) on April 28, 1969 (after C. Prabhakara, 1971 [4]).

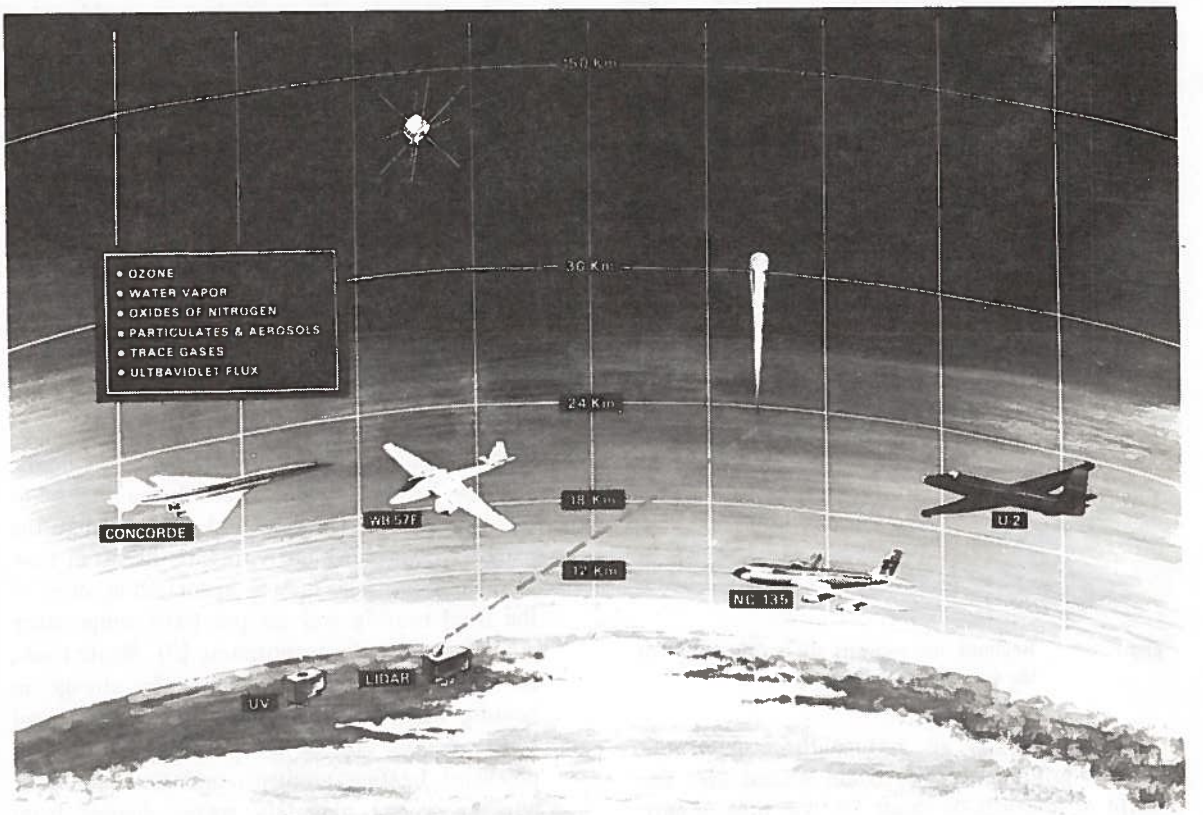

Figure 7. CIAP in-situ stratospheric measurements.

study, includes a determination (as a function of latitude, longitude, and altitude) of the rate of introduction of engine effluents into the stratosphere for a variety of vehicles. These include, in addition to supersonic transports, subsonic aircraft, hypersonic vehicles, and rockets passing through the stratosphere.

The Perturbed Stratosphere of 1990

The third monograph will provide a basis for modeling changes in the vehicle wake, dispersion of effluents from the flight trajectory, and transport by global circulation. These models will take into account sources, sinks, density distributions, and the radiation which initiates photochemical reactions. This monograph will include new values of the solar insolation at the tropopause and the distribution of densities of species.

Figure 8 shows the four regimes considered for analysis of perturbations of the stratosphere. Regime I involves the wake immediately behind the nozzle of the aircraft. This regime is characterized by a temperature much greater than that of the ambient stratosphere, and the motions are induced primarily as a result of the propulsion system. This regime continues for perhaps 10 sec. In Regime II, the dominant effects are due to the vortex motion induced by the passage of the aircraft. The temperature is essentially that of the ambient stratosphere. In general, the horizontal and vertical scales are of the order of 100 m, and the important chemical reactions have a reaction time less than about 120 sec. Regime III is dominated by small-scale structure of the stratosphere, which produces anisotropic diffusion from the line in which the wake is laid down. Both the temperatures and velocities are those characteristic of the stratosphere.

Individual wakes occur separately in both time and space along the travel routes over all the world, and are anisotropically diffused at rates which vary with direction, latitude, longitude, altitude, and season. In Regime III, they must be

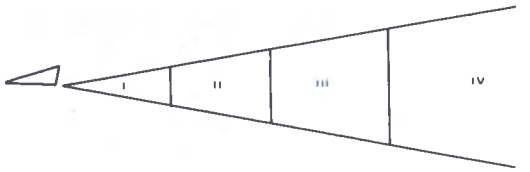

Investigators	LMSC ARAP Aerospace	LMSC ARAP Aerospace	ARAP LMSC LLL	LLL NCAR UCLA GFDL
τ_F	(0)	(sec)	(120 sec)	(days, weeks)
τ_w	$\tau_w > \tau_s$	$\tau_w = \tau_s$	$\tau_w = \tau_s$	$\tau_w = \tau_s$
V_w	$V_w > V_s$ (Jet)	$V_w > V_s$ (Vortices)	$V_w = V_s$	$V_w = V_s$
U (Scales)	m	10^2m	$4(10)^4$m	
W	m	10^2m	$5(10)^3$m	
Key Chemical Reaction*	$\tau_{chem} <$ sec	$\tau_{chem} <$ 120 sec	$\tau_{chem} =$ days	
Diffusion Rate*	$\tau_{diff} <$ sec	$\tau_{diff} <$ 120 sec	$\tau_{diff} =$ days	

*It is important to find for each regime whether the chemical-reaction rate or the diffusion rate is dominant.

Figure 8. Regimes for analysis of perturbations of the stratosphere.

combined to give an average for each of the model's grid points, which are spaced over the world at intervals of about 500 km horizontally and 3 km vertically. This regime is terminated when the perturbations become greater than about 400 km horizontally and 5 km vertically, which is the grid size of the global-circulation models. Regime IV involves the mean motions of the global models. There the important chemical reaction times are on the order of days.

The DOT-CIAP modeling plan includes a number of investigators involved in the data collection, the modeling of the jet and wake regimes, the modeling of the diffusive transport regime, and the modeling of mean winds on a global scale. Their models work in sequence to provide estimates of the equilibrium distribution of species in the perturbed stratosphere. Since many of these models are being developed for the first time, parallel effort by several investigators in each of the areas has been invited, and the Program Office encourages frequent exchanges of technical information.

The Perturbed Troposphere of 1990 and 2020

Monograph 4 describes simulation of the circulation of the 1990 and 2020 tropospheres under the assumption that the radiation will be as described for the perturbed stratosphere of 1990. Consideration of two different dates within the perturbed troposphere is necessary to distinguish the immediate effect of changes in heating from the longer-term effect of a progressive cooling of the oceans, which is a slowly felt effect of heating reduction. This cooling of the oceans may take 30 years or more under 1990 stratospheric conditions before its effect on tropospheric climate can be felt. This monograph will provide estimates of mean values and standard deviations of temperatures, winds, precipitation, and sea-level ultraviolet flux.

The information in this monograph can be used to estimate the implications of climatic changes. In 1961 Y. Mintz described a method of computing such changes and showed that the planetary waves which represent the mean flow in the mid-latitudes may be estimated in terms of the total heating and the poleward temperature gradient within the troposphere [5]. Mintz finds, as indicated in Figure 9, that the change in heating which occurs between the summer and winter causes change by a factor of four in poleward heating gradient, and that the wave number of the planetary waves changes from seven or eight in the summer to five or six in the winter. The mean square velocity of the winds in the winter is about twice that of the mean square velocity of the summer. The sketch suggests some implications: W indicates the schematic trajectory of winds in the troposphere near the polar front in the winter, under the assumption that the shape is dominantly positioned by the persistent high-pressure region of continental Siberia. S indicates the summer wind trajectory; a slight shift of phase within the continental United States is apparent. Both the summer and winter winds, from the standpoint of the United States, seem to originate in Alberta, bringing dry polar air down through the west to a southern extreme at about Oklahoma. The zonal trajectory there turns north, carrying with it masses of moist tropical air dragged out of the Gulfstream area, alternating with masses of dry polar air. A consequence of this process is that the United States west of the Mississippi is generally dry in contrast with the United States east of the Mississippi.

Marked cooling of the troposphere might result from changes in the stratosphere. As inferred from Mintz' study, the winds may be

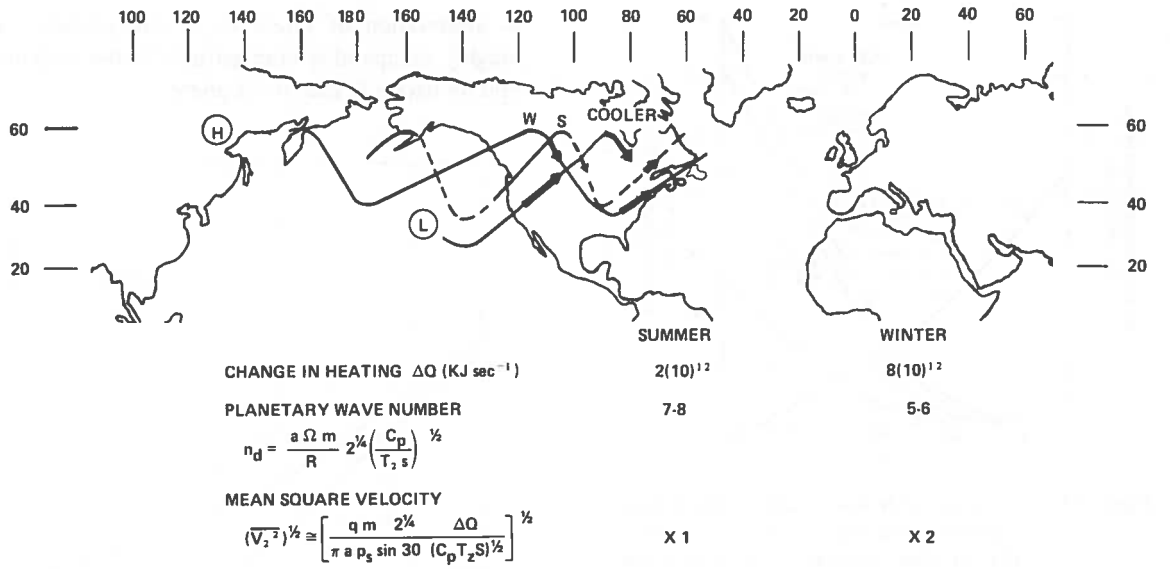

Figure 9. Implications of climatic change (after Mintz, 1961 [5]).

weaker or stronger, depending on whether the combined effects of pollution in the stratosphere weaken or strengthen the poleward temperature gradient. There may even be a phase shift of the polar front. This may bring, as this sketch suggests, warm humid air onto the shores of the Pacific Northwest, with polar dry air coming down into the eastern part of the United States. Such an effect, if realized, could strongly affect the U.S. climate. Such speculations can be tested by climatological simulation.

Another climatological variable, one not often treated by meteorologists and climatologists, is the intensity of solar ultraviolet radiation experienced at ground level. The direct uv intensity in the waveband between 260 and 330 nm is sensitive to the amount of ozone in the total column along the line to the sun, as shown by the coefficient of Figure 10. The curves show both experimental data and an approximate analytic representation which fits well in the 280-320 nm region. This ozone coefficient, multiplied by the ozone thickness, yields the optical thickness for direct ultraviolet. The variation from equator to pole of ozone thickness described by Prabhakara's measurements (given earlier) implies a possible spatial variation of radiation at 290 nm of four orders of magnitude, and at 300 nm of two orders of magnitude.

Green et al. [6] have shown (Figure 11) the variation with uv wavelength of direct solar

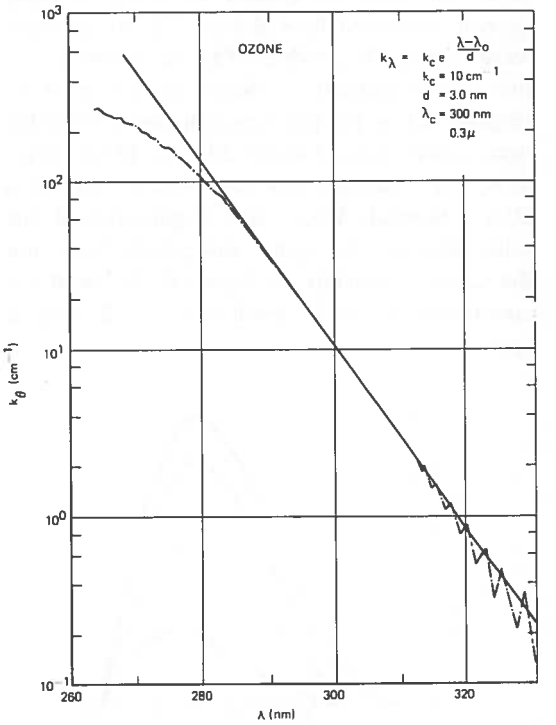

Figure 10. Ozone absorption coefficient (Green et al., 1972 [6]).

radiation at the ground, with computed effects of ozone, Rayleigh scattering, and aerosol scattering for various solar zenith angles corresponding to various times of day, near the autumnal equinox, in Gainesville, Florida. Green

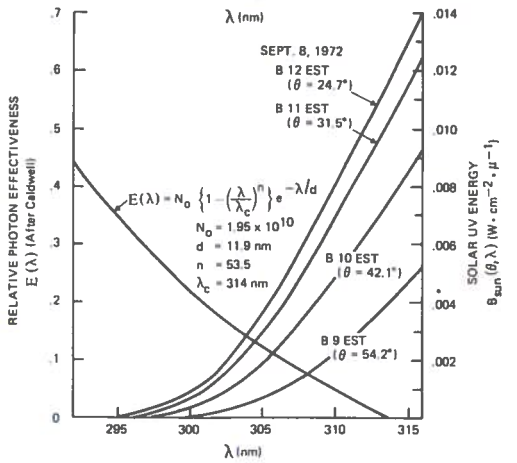

Figure 11. Variation with wavelength of direct solar radiation at the ground and relative sensitivity of plant growth to uv wavelength (Green et al., 1972 [6]).

et al. also show the relative sensitivity of plant growth, described by Caldwell [7], to the same wavelengths. The product of the solar energy and the plant sensitivity is shown by Green et al. (Figure 12) as the plant-growth-inhibiting radiation, which peaks at about 307 nm. These curves show the radiation variations which occur in a 20-nm interval. When the irregularities in the solar radiance, the ozone absorption curve, and the action spectrum are included, the need for measurements with resolution to 2 nm is apparent.

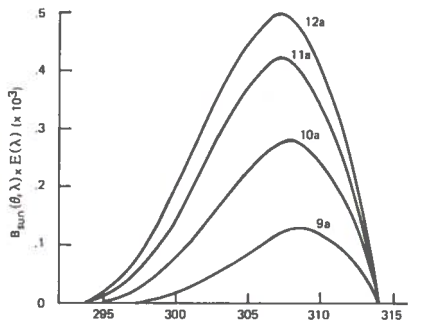

Figure 12. Relative response of plant growth to solar radiation (Green et al., 1972 [6]).

Attenuation of direct uv at low altitudes has been estimated by Green et al. [6] (Figure 13) in terms of optical depths as functions of wavelengths in the 300-nm region. The relative contribution of tropospheric aerosols and air molecules to attenuation of direct uv at low altitudes is roughly comparable in magnitude to the attenuation by ozone in the stratosphere.

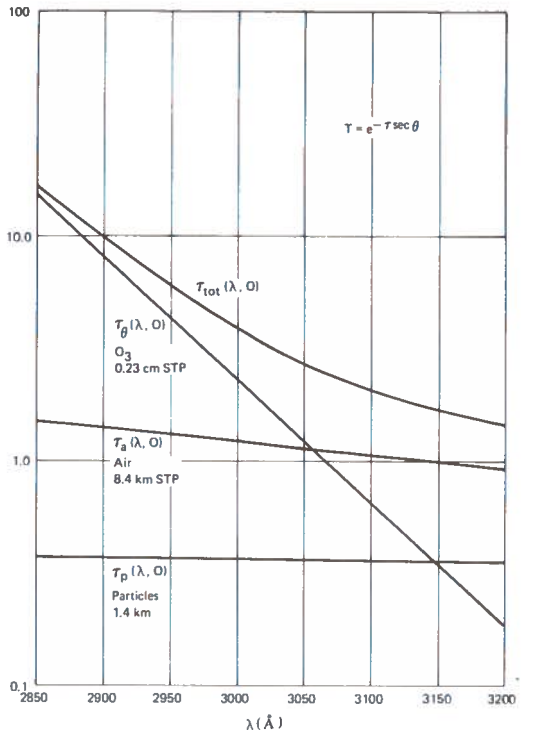

Figure 13. Computed optical depths of ozone, air, and particulates, at Gainesville, Florida (Green et al., 1972 [6]).

The uv radiation felt by plants and animals at the earth's surface includes scattered radiation as well as the direct. Green et al. [6] have made sample calculations (Figure 14) which show that at a zenith angle of 24.7°, the scattered component of uv radiation at 305 nm is about 2/3 the direct component. Moreover, due to the strong forward component of aerosol scattering, the contribution of tropospheric aerosols to the diffuse component is even more important than the Rayleigh scattering by the air molecules.

The Biological Effects of the Tropospheric Changes

So much, then, for the projections of the engine effluents of 1990 as they may affect the

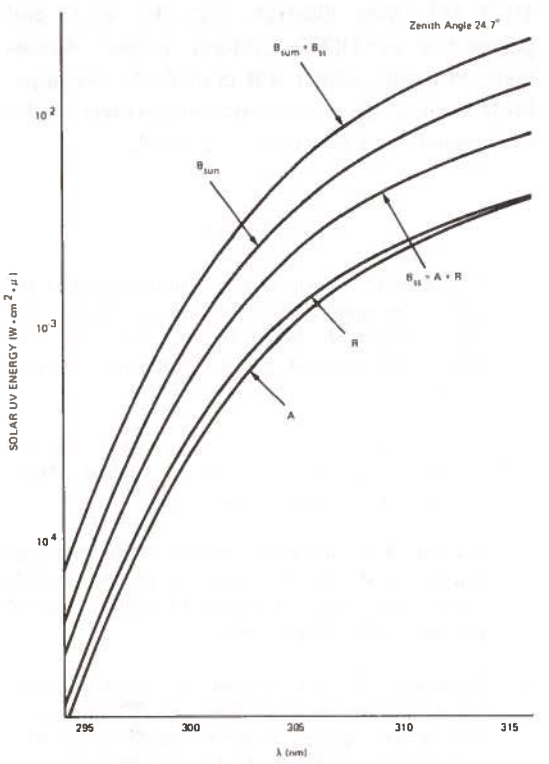

Figure 14. Computed effective solar energy at the earth's surface (Green et al., 1972 [6]).

NOTE: Solar uv energy at 12:00 EST, September 8, 1972 at Gainesville, Florida. The sun's azimuth angle θ is 24.7°. The curves labeled B_{sun}, R and A are respectively the direct solar energy, single Rayleigh scattering, and single aerosol scattering components, computed by using the optical depths shown in Figure 13. In computing R and A, the sky radiance for all directions is assumed to be equal to the spectral sweep at $\phi=\theta$ (horizontal scan). For the aerosols the index of refraction used is 1.47, and the cumulative size distribution is assumed to be of the regularized power law (RPL) $[1 + (r/a)^{\nu}]^{-1}$ with $\nu=3$ and a=100 nm. Multiple scattering would be expected to approximately double the single-scattering contributions, although the exact extent depends on the aerosol size-altitude distribution.

geophysics of the stratosphere and the troposphere. What would be the impact of these climatological changes on the biosphere in 1990? Monograph 5 will describe the effects of increased uv radiation on man, animals, and plants (such as skin cancer, genetic alteration, and reduced photosynthesis), the biological effects of other changes in solar radiation, and the effects of various climatic changes on agriculture. The biological studies of flora are expected to include both laboratory and field studies of growth of corn, trees, tomatoes, and other crops under changed climatic conditions. Since the estimates of climatological change are not yet available, the biologists are beginning studies of the effect of a range of variables, which represent extreme limits of the changes which may be imagined. These limits are to be regarded as the basis for parametric considerations from which one may infer the sensitivity of the biosphere to changes in climatic variables. The range of variables to be initially considered is: surface temperature from a 2°C cooling to a 0.2°C warming, wind speed and precipitation from a 12% weakening to a 6% increase, and erythemal uv radiation (flux at 307 nm) from an increase of 7% to an increase of 300%.

The biological studies of fauna include epidemiological studies of the incidence of skin cancer in six United States cities, for which the hourly variation of the erythemally sensitive ultraviolet solar flux is to be also determined over a one-year period. The studies may also include investigations of uv-induced carcinogenesis in mice, and of effects of uv on habits of insects whose vision is sensitive in this range, and on shallow-water-breeding fish whose spawn may be affected.

The Social and Cost Measures of the Biological Changes

Monograph 6 will apply social-cost indices to the biological effects described in monograph 5. Such an effort is a necessary and logical part of CIAP. It provides an opportunity to describe the projected changes in terms meaningful to the majority of those concerned.

SCIENTIFIC OBJECTIVITY

I should now like to address a rather ticklish question. The possible climatic effects of increased stratospheric flight have been the subject of a good deal of recent controversy. We have tried, in the following ways, to ensure that our

findings are not influenced by any non-technical factors.

First, we have invited the participation of the world's best-qualified scientists.

Second, they have defined specific problems in such a way as to provide bases for technical solutions.

Third, their careful technical investigation is expected to justify their conclusions to the most critical eye.

Fourth, we are disseminating the details of the studies to scientific communities around the world for their consideration and comment.

The Department of Transportation wants CIAP to be regarded as "good science and engineering." Embroilment in political controversy, based on premature, incomplete, or partial answers to the CIAP questions, can only hurt, not help, the scientific objectives. On the other hand, good science and engineering can in the end decrease the judgmental degrees of freedom, and thereby make it possible for related political decisions to be made more easily, with a lessened possibility of error.

An important function of conferences such as this one is to solicit suggestions for improvement of the study, which is by no means frozen in its present form. Of the questions for CIAP which I posed at last February's conference, a few will remain unanswered by the study as it is presently outlined. Expansion of the study to provide the needed answers is a matter of urgency. The Department of Transportation welcomes your suggestions and participation, so that our best-effort report in 1974 may have findings which are complete, comprehensive, and convincing to the scientific community.

The papers which follow in this book examine a number of aspects of the CIAP study. In certain respects, they represent a report of progress. As additions to the papers presented in the CIAP Survey Conference of February 15-16, 1972 [8], they illustrate also the scope and perspective of DOT's Climatic Impact Assessment Program, which will contribute, we hope, both to wise decisions concerning travel in the stratosphere and to science in general.

REFERENCES

1. Newell, R.E., "Radio active contamination of the upper atmosphere," in *Progress in Nuclear Energy – Series XII, Health Physics*, Vol. 2, ed. A.M. Francis Duhamel, pp. 535-550, Pergamon, Oxford, 1969.

2. Oort, Abraham H., and Albion Taylor, "On the kinetic energy spectrum near the ground," Mon. Wea. Rev. *97*, 623-636, 1969.

3. Bortner, M.H., and R.H. Kummler, "The Chemical Kinetics and the Composition of the Earth's Atmosphere," Rept. GE-9500-ECS-SR-1, General Electric, Valley Forge, 1968.

4. Prabhakara, C., B.J. Conrad, L.J. Allison, and J. Steranka, "Seasonal and Geographic Variation of Atmospheric Ozone Derived from Nimbus III," NASA-TN-D-6443, Goddard Space Flight Center, Greenbelt, Md., 1971.

5. Mintz, Y., "Appendix 8 – The general circulation of planetary atmospheres," in *The Atmospheres of Mars and Venus*, ed. W.W. Kellogg and C. Sagan, pp. 107-146, Publ. 944, National Academy of Sciences and National Research Council, Washington, D.C., 1961.

6. Green, A.E.S., T. Sawolda, and E.P. Shettle, unpublished manuscript, 1972.

7. Caldwell, M.M., "Solar ultraviolet radiation and the growth and development of higher plants," in *Photophysiology*, Vol. 6, ed. A.C. Giese, pp. 131-177, Academic Press, New York, 1971.

8. Barrington, A.E., editor, *Proceedings of the Survey Conference*, February 15-16, 1972, Climatic Impact Assessment Program, Dept. of Transportation, DOT-TSC-OST-72-13, 1972.

ATMOSPHERIC MONITORING AND EXPERIMENTS: A SUMMARY OF ONGOING PROJECTS

SAMUEL C. CORONITI
Department of Transportation
Washington, D.C.
and
ANTHONY J. BRODERICK
Department of Transportation
Transportation Systems Center
Cambridge, Massachusetts

ABSTRACT: The measurements and experiments which constitute the Atmospheric Monitoring and Experiments Subprogram of CIAP are briefly described. Experiment platforms and geographic coverage are discussed and individual instruments catalogued. A brief description of the Stratospheric Aitken Nuclei Detection Systems (SANDS) is included.

INTRODUCTION

The principal purpose of the CIAP Atmospheric Monitoring and Experiments Subprogram is to fill critical gaps in our understanding of the natural stratosphere. Of primary interest are species concentrations as a function of altitude, and sources and sinks of minor stratospheric constituents. These data are needed for analysis of perturbations of the stratosphere, which will be done by modeling. To provide the required information, we have organized a complex series of measurements and experiments.

EXPERIMENT PLATFORMS AND GEOGRAPHIC COVERAGE

One major reason for the present dearth of knowledge of the stratosphere is the difficulty encountered in making in-situ measurements. Conventional subsonic jet aircraft, such as the CV990 and NC-135, are limited to altitude ceilings of about 15 km (45,000 ft), and maintain this ceiling for only a short time under typical conditions. Subsonic aircraft originally built for military reconnaissance purposes, such as the WB-57F and the U-2 [1], are easily able to operate above 20 km (60,000 ft), and have altitude ceilings in the vicinity of 23 km (70,000 ft). Equipment installed on these aircraft must be completely automated, however, and operate in an unpressurized, unheated environment. Such restrictions, along with the costs incurred in aircraft modifications, add significantly to the cost of experiments, especially because of the resultant requirements for specialized hardware.

Supersonic aircraft such as the Concorde and YF-12 are just now becoming available for experiments on a limited basis. Prototype versions of the Concorde have been used for some optical measurements [2], but availability of the airplane is understandably restricted during its current flight-test program. To our knowledge, the YF-12 and similar aircraft have not yet been used for any stratospheric measurements other than those made with standard avionics equipment. All supersonic aircraft, of course, present considerable difficulty to the experimenter who seeks direct sampling of the stratosphere. Careful analysis of any sampler design will have to be performed to ensure that samples are not seriously affected by the shock system in and around the probe.

Balloon soundings of the atmosphere can provide data up to altitudes in the vicinity of 45 km (140,000 ft). The experimental difficulties here are well-known; the hardware must be completely self-contained and special attention must be paid to thermal control problems. The expense of balloon launches increases with both increasing payload and increasing altitude ceiling. However, balloons do provide some of the most

valuable data, in the form of in-situ altitude profiles of constituent concentration.

Sounding rockets and satellites are valuable tools in atmospheric research [3], but their use in this program is minimal for a number of reasons. In general, satellite experiments take several years to go from the stage of conception to that of operation. Most rocket experiments are designed for studies of altitudes above the stratopause. The time and financial constraints of our program thus eliminated consideration of all but a few experiments in these categories. We are, however, making extensive use of existing operational satellite experiments, such as the BUV and other experiments on the Nimbus satellites.

Ground-based measurements also play an important part in the CIAP effort. Most notable are the lidar experiments, which attempt to derive altitude profiles of atmospheric particulates, and UV-monitoring stations, whose data will be correlated with epidemiological studies carried out in neighboring regions.

The CIAP experiments will cover altitude regions roughly between 0-40 km (130,000 ft) within an area bounded by 80°N latitude (Ice Island T-3) and the South Pole, from Europe west around the globe to Japan. A very general summary of this plan is presented below.

Aircraft

NC-135 Series

A prime use of the NC-135 aircraft (USAF-flown, dedicated to LASL/AEC missions) in CIAP is to carry the NCAR dye lidar above the low atmosphere (at about 10 km) while mapping stratospheric particulates. Current plans are to complete two north-south traverses at approximately constant longitude, three months apart, during the first half of 1973. The NOAA infrared radiometric water-vapor measurement instrument will also be flown, for correlation with the lidar and for integrated water-vapor mapping as a function of latitude. Other experiments may be flown if available.

WB-57F Series

These aircraft are provided and flown by the USAF Military Airlift Command, Air Weather Service, 58th Weather Reconnaissance Squadron, Kirtland Air Force Base, Albuquerque, New Mexico. Aircraft modifications and operations are coordinated by Los Alamos Scientific Laboratories (LASL) of the AEC. One aircraft (#13298) is being modified to be the "prime" CIAP aircraft.

Sources and sinks. The sources and levels of water vapor, ozone, and trace gases in the stratosphere will be explored and better quantified by means of a series of background measurements, using many instruments and specific tests designed to explain the phenomena of thunderstorms and tropical upwelling. All instruments being designed to fly on the WB-57F that are of a synoptic data-gathering nature, and are currently at a sufficiently high state of development (low risk) to be included in CIAP planning, are programmed to be flown on both shakedown flights and background-data-gathering flights. The exact complement of experiments on the aircraft at any time will depend on many factors, including available flight time, development status, and detailed flight plan.

Thunderstorm flights, designed to investigate the transport of water vapor into the stratosphere through the thunderstorm process, and also the changing ozone and particulate concentration and electric-field strength around and above thunderstorms that penetrate the tropopause, will be flown from Albuquerque during August 1972 and the summer of 1973, and possibly from Panama during the fall Airstream series. The tropical upwelling, presumed to be another major source of water vapor in the stratosphere, will be investigated with the same instrumentation during the fall of 1972 and spring of 1973.

Two wind-profile experiments, designed for better understanding of those portions of the physical-transport phenomena in the lower stratosphere that can be attributed to winds, are planned. AFCRL has developed techniques for photographically analyzing the movement of smoke trails with time [4] that will be used to develop wind profiles. A grid of three vertical smoke trails of $TiCl_4$ dispensed from rockets and two horizontal trails dispensed from a specially modified WB-57F will be photographed at White Sands Missile Range. The rocket payloads are being arranged by AFCRL directly with WSMR; the aircraft dispenser is being designed by LASL.

Second, an inertial data system will be installed on the WB-57F for positional and dynamic reference by all experimenters. This system is also important to a data-reduction experiment by NCAR, which will deduce lower stratospheric winds by analyzing aircraft motion.

Airstream cooperative. A great deal of CIAP-related data will be obtained by flying the instrumented aircraft (#13298) as part of the AEC's Project Airstream. These flights will add latitudinal and seasonal variations to the background data discussed above. They will also perform tropical upwelling flights (CIAP-dedicated, from Panama), and may add to the thunderstorm data. Airstream flights will be flown to South America in October and April and to Alaska in January and July. The instrumentation will vary during the program.

Comparative experiment series. These tests are intended to gather near-simultaneous stratospheric particulate data from both lidars and aircraft (and in the case of Laramie, from balloons) that can be compared and interrelated. The first series was successfully completed in June 1972. A second was completed in September. A third flight will be scheduled over the NASA-ARC/SRI lidar at Menlo Park as soon as the lidar is ready in winter 1972-1973. Comparative data was also taken by the NCAR lidar (ground-based at Boulder) and the aircraft sampler in July 1972. Additional data will be obtained when the lidar is operational in the NC-135.

Japan series. This test series is intended to add longitudinal variation, maritime data, and a latitudinal traverse in the Eastern Hemisphere to the background data. It will use the dedicated WB-57F aircraft and as many of the background-data-gathering instruments as can be accommodated.

Dedicated WB-57F experiment series. These tests, which are to be flown from Kirtland AFB, are of a rather specialized nature. A cryogenic sampling experiment, designed to capture trace gases and analyze them in the laboratory (and, we hope, observe some of the more active radicals), will require only short flights.

A question exists regarding the validity of stratospheric water-vapor measurements from the different instruments to be used on CIAP. At some point in the program, the three instruments will be flown simultaneously (with the tritium device believed to be the "truth" instrument) and cross-calibrated. It may be instructive to simultaneously fly the two ozone monitors for model verification.

The WB-57F will be flown with the SANDS instrument (described in more detail in the next section) to measure the total number of condensation nuclei from the tropopause to 22 km (65,000 ft) in the southwestern U.S. If space is available on the aircraft, this experiment package will also be incorporated into other flights to assess spatial variations.

Concorde Series

CIAP expects to gain considerable data in the altitude regime of interest through the cooperation of the Anglo-French management of the Concorde program. Specifically, NO and ultraviolet data will be made available from the instruments of J. Blamont. Provisions are also being made to fly the JPL infrared interferometer in early 1973 on board the Concorde.

U-2 Series

This series involves regular flights by a NASA-Ames U-2 aircraft carrying a set of instruments provided by Ames (CO, CO_2, O_3, and NO) and the NOAA infrared water-vapor radiometer. It will obtain high-altitude (18 to 25 km; 55,000 to 75,000 ft) east-west background data, including trace-gas concentrations over the U.S.

Balloons

The University of Wyoming is performing a seasonal/geographic matrix of balloon flights to measure background level of and changes in particulates, ozone, and water vapor. The University of Denver will also extend its balloon-borne infrared measurement experiments, using hardware specially fabricated for CIAP. They will include high-resolution atmospheric-transmission measurements, moderate-resolution atmospheric-radiance measurements, and, with the cooperation of a U.S. Army project, high-resolution atmospheric-radiance measurements.

Satellite

A University of Wyoming-developed sensor will be launched on an Air Force satellite in the fall of 1973 to measure stratospheric aerosols by observing solar extinction.

Ground Monitoring

NOAA is monitoring the total ultraviolet radiation reaching the earth's surface, ozone, and turbidity at two latitudes in the U.S. for a period of one year. In addition, six U.S. cities where extensive epidemiological studies have been carried out will have UV monitors for a one-year period.

INSTRUMENTATION AND MEASUREMENTS

Table 1 lists the major pieces of equipment employed in CIAP, giving a brief designation of the hardware, the principal platform from which it will gather data, the measurements to be made, and a few remarks about each, followed by the responsible agency and its principal contact for the project.

Due to time limitations at this conference, we were not able to include a description of the condensation nuclei counter being fabricated for CIAP experiments. What follows is a brief discussion of that instrument and its operating principles. Other papers in this volume individually treat the remainder of most of the major CIAP experiments.

The stratospheric Aitken-nuclei detection system (SANDS) is composed of an automatic cycling Aitken-nuclei counter and a pressurization unit. The Aitken-nuclei counter is functionally similar to that described by Skala [5]. Humidified sample air is adiabatically expanded within a few milliseconds to create a supersaturation of several hundred percent. All nuclei present which are large enough to initiate condensation of water vapor will form droplets which will grow to visible size, given sufficient growth time and water vapor. The minimum size of nuclei which will condense water vapor under the planned conditions is on the order of 10^{-7} cm radius. In Skala's instrument, growth is allowed to proceed for 25 ms, resulting in water droplets of about 2.5×10^{-4} cm radius; in the SANDS instrument growth will be allowed for a period of about 80 to 100 ms to gain increased droplet size (and thus sensitivity). The nuclei concentration is obtained by measurement of light scattered by the droplets, in a manner similar to that described by Skala. Such a measurement is indicative of total nuclei concentration only; no size information is provided.

It can be seen that this type of instrument is affected by several key parameters: to be accurate, the instrument must maintain both the illumination and droplet size constant at the time of measurement, as well as maintaining constant amplification in the photodetector and electronics system.

The stabilization of illumination and electronic characteristics is reasonably straightforward. However, droplet growth is significantly influenced by the pressure and temperature of the sample. Thus the system incorporates a pressurization unit which serves to acquire sample air from the ambient atmosphere and raise the temperature and pressure to standard (sea-level pressure, 298°K) conditions. The change in specific volume is measured to allow for correction of the measured nuclei concentration to ambient conditions. The pressurization unit has several stringent limitations: the nuclei count must not be significantly altered either by the addition of particles or loss of particles; the sample pressure must be increased by a factor as large as 18 to 1; and temperature must be regulated to room conditions from ambient values in the range of 190°K and up.

The design approach uses two alternating compression chambers, each containing a metallized Mylar bag shaped to conform snugly to the interior surfaces of the chamber. A hydraulic fluid is pumped into and out of the inside of the bag. The volume between the outside of the bag and the chamber interior then forms an isolated pressurization cavity which can be operated with inherently high volumetric efficiency, no rubbing friction, and good heat-transfer characteristics. The chambers alternate, one supplying sample air to the Aitken-nuclei counter while the other one intakes and compresses a new charge. Final pressure is controlled by a combination of absolute-pressure regulator and active sensing and control elements which determine the intake volume. Temperature regulation is obtained by a large thermal mass (the hydraulic fluid and metal portions of the compression chambers).

Table 1. CIAP Atmospheric Monitoring and Experiment Instrument Descriptions

Brief Designation	Platform	Measures	Remarks	Agency	Principal Contact
Aerosol Detector	Balloons	Number of particles in two ranges: >0.25μ and >0.5μ diameter	Light-scattering techniques. Ground level to 30 km with ≈0.1 km resolution.	ONR/U. Wyo.	Rosen
Cloud Camera 415P	WB-57F	Photographic record of cloud overflights	Standard camera, provides down-looking horizon-to-horizon photos of clouds required for data correlation in thunderstorm and tropical upwelling flights.	LASL/USAF	Guthals
CO Detector	U-2	CO concentration, 10 ppb	Hot mercuric-oxide technique	NASA-ARC	Poppoff
CO_2 Detector	U-2	CO_2 concentration, 5 ppb	NDIR technique	NASA-ARC	Poppoff
Cryogenic Sampler	WB-57F	NO, NO_2, N_2O_2, H_2O, H_2O_2, HNO_3, OH, HO_2, CO, CH_4, 10^7-10^8 molecules/cc	Freezes air sample for laboratory analysis by electron spin resonance.	IITRI	Snelson
Electric Field Mill	WB-57F	Voltage fields in vicinity of thunderstorms	Data to be correlated with ozone data to investigate effect of electric fields on transport processes.	NMIMT/ NOAA	Moore/ Shlanta
Gas Phase Sampler	WB-57F	Ice concentration among aerosols	While using filter-paper samples, a sample of air is captured in evacuated bottles to determine water content.	LASL	Sedlacek
Inertial Data System	WB-57F	Winds	Wind data inferred from aircraft position, rate data measured with IDS.	NCAR	Danielson
Ion Density	WB-57F	Aerosols down to 10 mμ	Modified Gerdien tube detects charged particles.	NOAA	Shlanta
IR Extinction	Balloon	Extinction of solar radiation 2.7μ H_2O band to derive H_2O concentration profiles	Measures extinction of solar radiation during sunrise from 30 km with 0.5 km resolution.	ONR/U. Wyo.	Pepin
IR Interferometer	Concorde	Trace constituents (CH_4, CO_2, N_2O, CO, NO, NO_2, O_3, C_2H_2, C_2H_4, H_2CO_2 and others)	Fourier spectrometer, resolution ≈0.25 cm^{-1}, 1.2 to 7.4 μ range, solar absorption.	JPL	Schaper
IR Spectrometer	WB-57F	Trace constituents (CH_4, CO_2, N_2O, CO, NO, NO_2, O_3, etc.)	LHe-cooled Czerny-Turner with warm window; 3-30μ range depending on grating employed; resolution ≈0.5 cm^{-1} at 10μ.	U. Denver	Murcray

Table 1. CIAP Atmospheric Monitoring and Experiment Instrument Descriptions (Cont.)

Brief Designation	Platform	Measures	Remarks	Agency	Principal Contact
Lidar	Ground	Aerosols	Uses a tunable dye laser and a pulsed ruby laser. Night measurements of aerosols, including pre-dawn and post-sunset to determine effects of sunlight on the concentration and vertical distribution of aerosols.	NASA-ARC/SRI	Collis
Airborne Lidar	NC-135	Aerosols	Maps stratospheric aerosols to determine background levels and spatial/temporal variations. Tunable dye lidar.	NCAR	Schuster
Lidar	Ground	Aerosol concentration, composition	48-in. dia. telescope. Ruby laser at 6943 and 3472 Å. Neodymium laser at 1.06μ and 5300 Å. Also measures N_2 in lower atmosphere by Raman N_2 scattering.	NASA-LRC	Melfi
NO Detector	Balloon	NO concentration	UV resonant scattering	ONR	Blamont
NO Detector	U-2	NO concentration	Chemiluminescence technique	NASA-ARC	Poppoff
NO Detector	WB-57F, Balloon	NO concentration	NO/O_3 chemiluminescence, 3×10^7 mol/cc sensitivity.	Utah State/ York	Megill/ Schiff
Stratospheric Aitken Nuclei Detection (SAND) System	WB-57F	Aitken nuclei size and mobility spectrum	Sensitivity limit, 1 CN/cc	GE/UMR	Podzimek (UMR)
Ozone Detector	Balloon	Ozone concentration	Chemiluminescent. Partial ozone pressure by Rhodamine B excitation. Time constant $<<1$ sec.	ONR/ U. Minn	Kroenig
Ozone Detector	Balloon	Ozone concentration	Electro-chemical type by Scientific Pump Co. Partial ozone pressure by KI oxidation. Time constant $\approx$90 sec.	ONR/ U. Minn	Kroenig
Ozone Monitor	WB-57F	Ozone concentration	Aircraft-powered "automatic" Komhyr cell	NOAA	Shlanta
Ozone Detector	U-2	Ozone concentration, 10 ppb	KI oxidant meter	NASA-ARC	Poppoff
Ozone Monitor	WB-57F	Ozone concentration	Regener (chemiluminescence) instrument. O_3-specific. Fast response (<1 sec)	NOAA	Shlanta

Table 1. CIAP Atmospheric Monitoring and Experiment Instrument Descriptions (Cont.)

Brief Designation	Platform	Measures	Remarks	Agency	Principal Contact
Ozone Monitor	WB-57F	Ozone concentration	Battery-operated Komhyr (KI) cell. Uses a Mk III probe air intake.	NCAR	Danielson
Aerosol Monitor	Satellite	Particulate concentration	Solar extinction at satellite sunset/sunrise; measures total average scattering coeff. at 4000 and 9100 A with 1-2 km resolution.	U. Wyo.	Pepin
Particulate Sampler	WB-57F	Particle concentrations, size, and composition	Uses impact filters. Collects particles down to 0.1μ. Analysis includes gamma irradiation and X-ray fluorescence, down to about sodium. Also uses scanning electron microscope.	LASL	Sedlacek
Particulate Sampler	WB-57F	Particle concentrations, size, and composition	Uses impact filters. Analysis techniques include colorometric, X-ray, neutron-activation. Especially looking for silicates, alkali metals, halogens, and metals found in engine exhaust. Also sulfates, and cations of sodium, potassium, calcium and magnesium.	NCAR	Shedlovsky
Temperature Monitor	Balloon	Temperature fine structure	0.2 mm spherical bead thermistor. 0.2°C resolution. <1m vertical resolution.	ONR/ U. Wyo.	Pepin
$TiCl_4$ Smoke	WB-57F/ Rocket	Wind measurements	Smoke canisters in conjunction with photographic techniques. Produce vertical and horizontal smoke trails in the 15-25 km altitude region, which together with ground photographic techniques will be used to measure atmospheric transport properties.	AFCRL	Good
UV Monochromator	WB-57F	UV flux vs wavelength (2300–4000 A in 10 A bands)	Engineering model of BUV instrument adapted to aircraft use. Double monochromator, scans zenith to horizon ±23° from aircraft heading.	NASA-GSFC	Heath

Table 1. CIAP Atmospheric Monitoring and Experiment Instrument Descriptions (Cont.)

Brief Designation	Platform	Measures	Remarks	Agency	Principal Contact
UV Flux Instrument	WB-57F	UV solar irradiance at 2150 Å and several wavelengths 2800–3200 Å	Measured over upper hemisphere from aircraft	ONR/ Parametrics	Sellers
Ground UV	Ground sites (Bismarck, N.D. & Tallahassee, Fla.)	Ozone, UV flux, turbidity (dust)	Modified Dobson spectrophotometers, one for each parameter at each of two locations.	NOAA	Machta
Al_2O_3Water vapor	WB-57F, Balloon	Water-vapor concentration	Al_2O_3 hygrometer; samples through a Rosemont total-temperature probe.	NASA-GSFC	Hilsenrath
Water Vapor Detector	Balloon	Water-vapor concentration	Aluminum-oxide hygrometer. Dew point from water-absorptive reactive element. Time constant about 30 sec.	ONR/ Parametrics	Goodman
Water Vapor Detector	U-2	Water-vapor concentration, 1 ppm	LiCl crystal oscillator	NASA-ARC	Poppoff
Water Vapor Radiometer	NC-135, WB-57F, U-2	Total mass of water vapor above instrument	Integrates 18-28μ. Pyroelectric detector for early flights, cooled detector for later flights. Ultimate sensitivity 0.1×10^{-4} gr/cm^2 or 0.1×10^{-6} gr/gr.	NOAA	Kuhn
Tritium Water Vapor	WB-57F	Water-vapor concentration	Uses activated tritium in the substrate of a column; exchanges hydrogen ions	ONR/ Parametrics	Goodman

To obtain size (mobility) data, a "drift tube" is provided between the pressurization unit and the Aitken-nuclei counter. Selective precipitation of charged Aitken particles using preprogrammed voltages will cause changes in total particle concentration which can be used to deduce the size characteristics of the nuclei.

The more significant system characteristics are approximately as follows:

Sample Flow Rate	200 cc per second (STP)
Sample Cycling Rate	2.45 times per second
Measurement Range	About one particle per cc (ambient) to about 10^4 particles per cc (ambient)
Pressurizer Cycle Rate	One per second
Particle Sizes Detected	10^{-7} centimeters radius and larger
Output Signal	Continuous analog voltage, updated for each sample

CONCLUDING REMARKS

The Atmospheric Monitoring and Experiments Subprogram of CIAP was designed to utilize, as far as possible, the existing capabilities and ongoing research of various organizations throughout the world. This approach avoids costly duplication of previously funded development work, though it also requires nearly unprecedented cooperation among dozens of widely scattered investigators.

Despite our limited budget, we have been able to make a great deal of progress in getting the various projects under way. Most of the major ones are described in the papers which follow. Many of them are able to report initial results; others can only give design details for hardware and experiments yet to be flown. Although the most difficult part of the job – data validation and reduction – lies ahead, we are confident of the value of the results.

REFERENCES

1. Poppoff, I.G., "The measurement of minor stratospheric constituents using high-altitude aircraft," in *Proceedings of the Survey Conference*, February 15-16, 1972, Climatic Impact Assessment Program, Department of Transportation, DOT-TSC-OST-72-13, 217 (1972).

2. Harries, J.E., and N.W.B. Stone, "Measurements of some hydrogen-oxygen-nitrogen compounds in the stratosphere, from Concorde 002," in this volume.

3. Heath, Donald F., "Some experimental techniques and problems associated with stratospheric measurements," in *Proceedings of the Survey Conference*, February 15-16, 1972, Climatic Impact Assessment Program, Department of Transportation, DOT-TSC-OST-72-13, 226 (1972).

4. Rosenberg, N.W., R.E. Good, and S.P. Zimmerman, "Transport measurements in the stratosphere," in this volume.

5. Skala, George F., "A new instrument for the continuous measurement of condensation nuclei," Anal. Chem. *35*, 702 (1963).

EVALUATION OF SEVERAL SENSORS FOR MEASURING LOW CONCENTRATIONS OF WATER VAPOR

ARNOLD WEXLER, SABURO HASEGAWA, AND LEWIS GREENSPAN
National Bureau of Standards
Washington, D.C.

A laboratory investigation of the performance characteristics of several humidity sensors is in progress at the National Bureau of Standards. This study is intended to indicate which sensor, if any, has the best promise of providing meaningful measurements of stratospheric moisture content from instrumented balloons. Included in this study are an aluminum-oxide element, a miniature crystal-array element, an expendable dew-point hygrometer, and a piezoelectric quartz crystal. Tests have been designed to yield information on sensitivity, range, hysteresis, temperature effect, pressure-altitude effect, and repeatability. The following ranges of parameters are covered in the tests: ambient temperatures from 20 to -60°C, ambient humidities corresponding to dew/frost points from 20 to -100°C, and ambient pressure-altitudes corresponding to sea level and 20 km.

Equipment used to perform these tests includes the NBS two-pressure humidity generator and the NBS low-frost-point humidity generator. These devices produce atmospheres of known humidity under controlled conditions of temperature, pressure, and flow rate. The maximum uncertainty in frost-point of the test air, over most of the operating range, does not exceed 0.2°C.

Data have been obtained thus far on two types of aluminum-oxide sensors and on the miniature crystal array. The aluminum-oxide sensor consists of an aluminum base with an anodized surface on top of which is a thin porous film of gold. The gold and aluminum act as electrodes. When the oxide surface sorbs water vapor, the change in its impedance is measured with appropriate ac circuitry to yield a variable low-frequency output signal. The crystal-array sensor is a semiconductor device 10 mils in diameter and 100 mils in length, and is mounted in a transistor case. It consists of an alignment of crystals and interstitial spaces. Presumably water-vapor molecules drift or diffuse into the interstitial spaces and change the bulk resistivity of the material. The sensor is excited by a 5-V 100-Hz ac source, and through appropriate circuitry, yields a 0 to 5 Vdc output.

Preliminary results indicate that the aluminum-oxide sensor is capable of operating at ambient temperatures as low as -60°C and of detecting frost points as low as -100°C. The miniature crystal array loses sensitivity at an ambient temperature of -40°C. Each sensor has a characteristic family of temperature-dependent curves. The calibration curves of individual elements within a class vary substantially, indicating that every element must be calibrated.

Tests are continuing on these two types of sensors. One important characteristic that will be studied is long-term stability. Another is the effect of saturation or near-saturation. The highest relative humidity, at each ambient test temperature, to which the sensors have been subjected so far is 90 percent. This upper limit was set to preclude the possibility that humidities close to saturation might adversely affect the performance of the sensors. One vital characteristic which should be studied, but which is not included in the present program, is the response time.

GLOBAL MEASUREMENTS OF STRATOSPHERIC AEROSOL, OZONE, AND WATER VAPOR BY BALLOON-BORNE SENSORS

D.J. HOFMANN, J.M. ROSEN, T.J. PEPIN
Department of Physics and Astronomy
University of Wyoming
Laramie, Wyoming
and
J.L. KROENING
Department of Physics
University of Minnesota at Duluth
Duluth, Minnesota

ABSTRACT: To date, the University of Wyoming CIAP program has conducted 44 balloon soundings from nine stations situated in latitude from 84°N to 90°S. Aerosol, ozone, and water vapor were measured, the latter two simultaneously and the aerosol nearly simultaneously. Upon one occasion when near-simultaneity was obtained, apparently correlated layers of all three were observed, suggesting that these layers were probably a product of laminar transport rather than a local chemical process.

In June 1972, a tropospheric layer of submicron dust, presumably due to the volcanic eruption of Alaid (51°N, 156°E), was detected by our northerly stations and tracked as a function of time from Laramie. Dissipation was rapid, as expected, and no significant stratospheric aerosol injection has been apparent in our observable size range ($> 0.3\mu$ diameter).

Aerosol measurements at the poles suggest stratospheric concentrations which are similar to those observed presently at northern hemisphere midlatitudes ($\approx$ 1 particle/cc $> 0.3\mu$ diameter). The general form of the size distribution also appears to be similar. The stratospheric aerosol thus does not appear to be affected by local habitation, but is truly a global phenomenon.

The improved time resolution of the aerosol measurements at Laramie (approximately one sounding per month) has revealed an increase by a factor of at least two in the concentration of stratospheric aerosol $> 0.3\mu$ diameter during late 1971, followed by a subsequent decay with a time constant on the order of 7 months. The cause of this increase has not been determined.

INTRODUCTION

In early 1971 the University of Wyoming's Atmospheric Physics group began a program aimed at measuring the stratospheric aerosol by balloon sounding from the Arctic, the Antarctic, and Australia on a yearly basis and from Laramie, Wyoming, on a bi-monthly basis. Measurements dating back to 1963 with the light-scattering dustsonde developed by Rosen [1] had given us a solid background of experience with the detector and calibration of its response. We planned to use a detector which was essentially the same, so that the new data could be compared with some 20 soundings made between 1963 and 1970 at mid-northerly latitudes.

The program had hardly gotten started when it was expanded significantly in both geographic and scientific scope. Under sponsorship of the Climatic Impact Assessment Program and the Office of Naval Research, and in conjunction with the University of Minnesota at Duluth, this expansion included bi-monthly flights from eight stations in addition to the polar stations, measuring the vertical distribution of aerosol, ozone, and water vapor. The stations are shown in Figure 1. All but the Australian and Duluth stations are operated by University of Wyoming personnel. The stations at Mildura and Longreach are operated by the University of Melbourne under Dr. Jean Laby.

Since its conception, the program has remained more or less on its proposed course, and to date more than 40 soundings from nine stations ranging in latitude from 85°N to 90°S have been carried out successfully. The results obtained to date, especially as concerns the stratospheric aerosol with diameters $> 0.3\mu$, appear to be particularly noteworthy in view of the paucity of such data in the past. These results

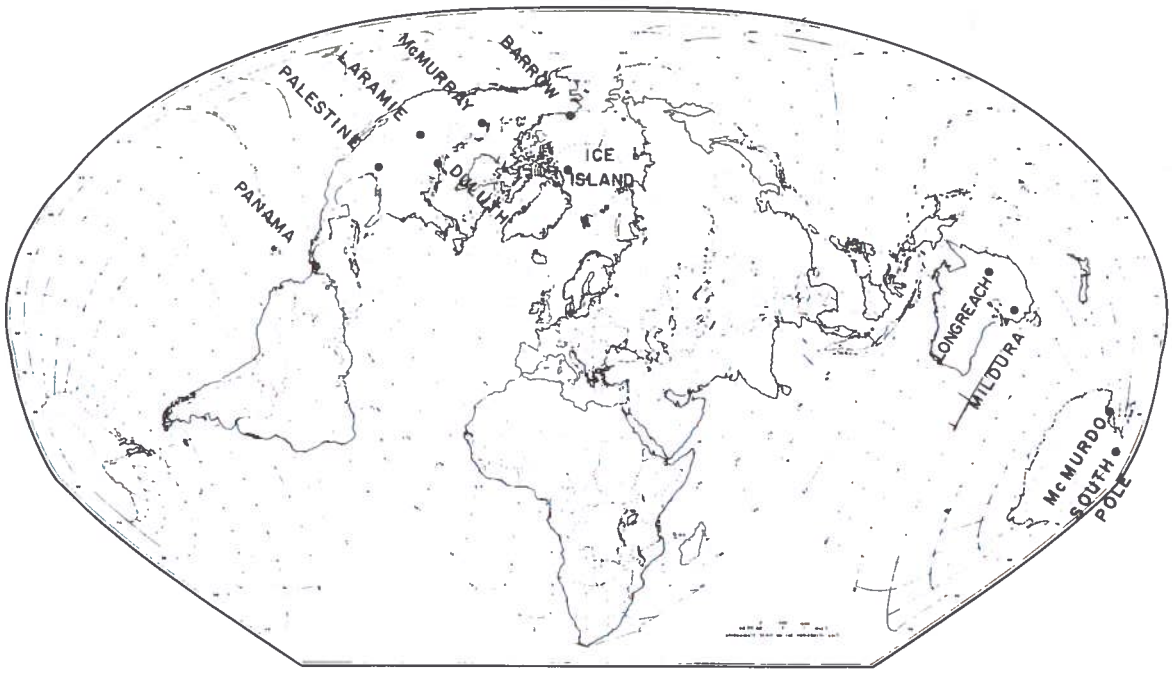

Figure 1. University of Wyoming stratospheric monitoring stations.

may be conveniently separated into four categories:

1. Simultaneous observations of stratospheric aerosol, ozone, and water vapor.
2. Polar observations of stratospheric aerosol.
3. The detection of an extensive dust layer in the northern hemisphere.
4. Measurement of the time variation of the stratospheric aerosol at midlatitude.

DESCRIPTION OF THE INSTRUMENTATION AND BALLOON CONFIGURATION

Table 1 lists the methods of measurement generally employed for each of the constituents. Detector characteristics are also included. The standard detector complement generally includes the aluminum-oxide water-vapor sensor constructed and calibrated by Panametrics, Inc.; the electrochemical ozone detector constructed by Scientific Pump Corp. and calibrated at the University of Minnesota (Duluth); and the light-scattering dustsonde constructed and calibrated by the University of Wyoming. Calibration of the latter instrument involves the generation of spherical monodisperse aerosol of known indexes of refraction. For nonabsorbing aerosol over a large range of index (1.33 to 1.60), this calibration indicates that the two channel discriminator levels correspond to particle diameters of 0.30 and 0.50 microns. If the aerosol is of an absorbing nature, the smaller-size channel remains the same while the larger-size channel edge increases to about 0.75μ diameter. The response of the detector to slightly nonspherical particles has been shown to be approximately the same as it is to spherical particles of the same volume and refractive index.

The ozone detectors are recalibrated upon receipt at the University of Minnesota (Duluth), where the ozone sensitivity is measured and the pump speed is determined. Operation of the KI electrochemical detectors has been satisfactory. Discrepancies between ascent and descent profiles have been traced to a difference in the balloon ascent and parachute descent rates and the long response time (about 90 seconds) of the sensor.

The water-vapor sensors, which are calibrated by Panametrics, Inc., are currently under study by the National Bureau of Standards along with other types of sensors. Until these tests are

Table 1. Instrumentation Characteristics

AEROSOL:

Detector Type:	Light Scattering
Detector Mfgr:	University of Wyoming
Detector Calib:	University of Wyoming
Characteristics:	Concentrations > 0.30μ diameter and > 0.50μ diameter from ground level to 30 km with ≈ 0.1 km resolution. Weight, 20-30 lb. depending on battery supply.

OZONE:

Detector Type:	Electrochemical
Detector Mfgr:	Scientific Pump Corp.
Detector Calib:	University of Minnesota at Duluth (J.L. Kroening)
Characteristics:	Partial ozone pressure by oxidation. Time constant ≈ 90 seconds. Weight ≈ 2 lb.

H_2O:

Detector Type:	Aluminum Oxide
Detector Mfgr:	Panametrics, Inc.
Detector Calib:	Panametrics, Inc. (P. Goodman) and the National Bureau of Standards.
Characteristics:	Dew point from water-absorptive reactive element. Time constant ≈ 30 seconds. Weight < 1 lb.

completed, the authors prefer not to discuss absolute data obtained with these sensors but will interpret observed variations in sensor response as being due to variations in the ambient water-vapor content. Preliminary results of the NBS tests indicate that the detector is sensitive to changes in the frost point at frost points as low as -100°C [4].

Figure 2 depicts the types of balloon flight components employed. The "standard" flight train incorporates a 70,000-ft^3 (50 ft inflated diameter) 0.50-mil plastic balloon; all constituents are measured during a single sounding. The "lightweight" flight trains utilize rubber balloons and require two separate soundings, aerosol being measured on one and ozone and water vapor on the other. This separation is necessitated by the limited load capability of the rubber-balloon systems. However, since rubber balloons are not constant-volume devices, as are plastic balloons, they are considerably smaller in size at time of launch, yet have similar sounding altitude capabilities with sufficiently light loads. Thus the rubber-balloon systems are advantageous for launching from remote stations, such as the South Pole, where shelter from wind is not available.

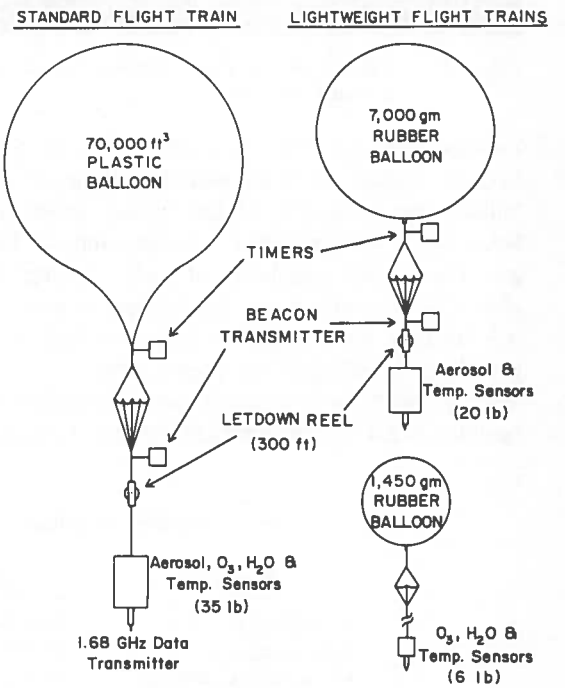

Figure 2. University of Wyoming balloon flight trains.

Figure 3 is a photo of the launching of one of the plastic balloon systems by University of Wyoming personnel from the Balloon Launch

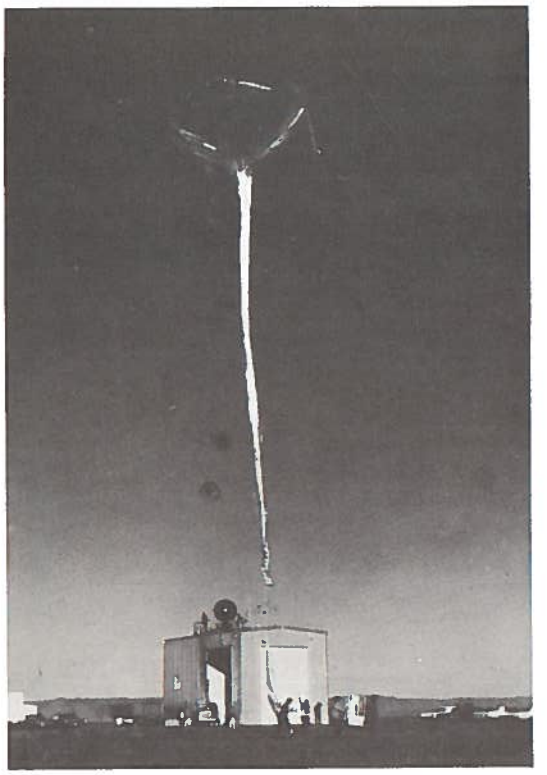

Figure 3. Launch of the plastic balloon system at Laramie, Wyoming.

Facility near Laramie. Less than 10% of the balloon volume is filled with helium prior to launch, the remainder of the balloon envelope being filled during ascent by expansion of the gas. The altitude capability of such a system is about 30 km, with a rise rate of approximately 0.3 km/min. Upon reaching ceiling altitude the parachute is released by preset timers and it descends with the payload at approximately 0.5 km/min, again sampling the atmosphere. Data on descent are important for at least two reasons. First, on descent the water-vapor sensor is the first element to penetrate the atmosphere and thus avoids contamination by the balloon system. Second, comparison of the aerosol data on ascent and descent allows one to verify unusual observations. The aerosol-measuring device is not contaminated by the balloon during ascent, because the instrument package is lowered following balloon launch by a reel device to a position 90 meters below the balloon. All data are telemetered via 1680-MHz standard U.S.-Weather-Bureau-type transmitters, so that soundings can be made from any U.S. weather station equipped for radiosonde flights. In addition, a portable receiving system has been developed which can easily be utilized at such remote stations as the ice island T-3.

Table 2 lists the number of soundings made at various stations during the period December 1971 to November 1972. Some of the measurements, but not all, are simultaneous or nearly so, the latter qualification generally meaning a few hours' separation between soundings of different constituents.

SIMULTANEOUS OBSERVATIONS OF AEROSOL, OZONE, AND WATER VAPOR

In order to study the ozone:water-vapor relationship, we felt it imperative to make these measurements simultaneously if at all possible. To study the ozone:water-vapor problem, one should ideally have a very large body of data so that the study will be statistically significant. Lacking this, one can still obtain significant

Table 2. Summary of Balloon Soundings, December 1971 - November 1972

Station	Latitude	Aerosol	Ozone	Water Vapor
Ice Island T-3	84.6°N	1	1	2
Barrow, Alaska	71.3°N	1	2	3
Ft. McMurray, Alberta	57.4°N	2	2	2
Duluth, Minnesota	46.7°N	2	3	3
Laramie, Wyoming	41.2°N	13	5	6
Palestine, Texas	31.8°N	2	1	1
Panama	9°N	2	2	2
Longreach, Australia	23.5°S	1	–	–
Mildura, Australia	34.2°S	1	–	–
McMurdo, Antarctica	77.2°S	–	–	–
South Pole, Antarctica	90°S	1	1	1

results by carefully analyzing individual soundings and noting correlations or anticorrelations, as the case may be. This requires the presence of some definite, prominent features in the data. Ozone profiles generally have such features, at least in the region between the local tropopause and the ozone maximum. These features appear as ozone-rich layers; or, conversely, the spaces between them can be interpreted as lacking in ozone. In contrast, water-vapor soundings appear generally to be more featureless, at least insofar as layered structure is concerned. We have, however, found exceptions, as shown in Figure 4. This was a simultaneous measurement of ozone and water vapor during parachute descent at Laramie on March 27, 1972. There is some suggestion of a positive correlation of variations between 10 and 20 km.

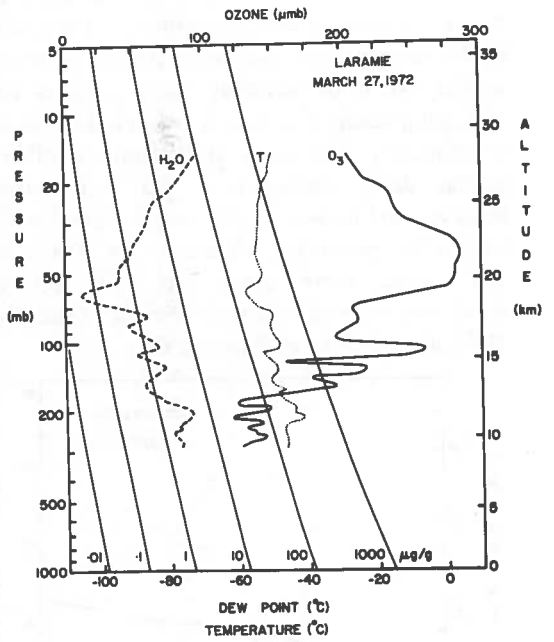

Figure 4. A simultaneous measurement of the vertical distribution of ozone (O_3), water vapor (H_2O), and temperature (T). The smooth curves are lines of constant water-vapor mixing ratio.

On May 16, 1972, ozone and water vapor were measured simultaneously about 5 hours after an aerosol sounding at Laramie. The results of these measurements are shown in Figure 5. The aerosol- and ozone-rich layers in the 15-km region are observed to be highly correlated. Such highly correlated aerosol and ozone layers have been observed previously by Rosen [2]. In addition, the water-vapor mixing ratio is also seen to increase in layers at about 15 and 20 km. Since there is presumably no chemical link in the production of aerosol and the production of either water vapor or ozone that could occur during the lifetime of such layers, this observation must be viewed as due to a transport property, i.e., a dynamic rather than a chemical effect. These layers apparently originated in a region richer in these constituents than the new surrounding air. Thus an increase in one constituent with a corresponding increase *or decrease* in another need not necessarily imply a chemical relation between the two. The apparent inconsistency of correlations between water vapor and ozone on other occasions suggests to us that dynamic effects are far more important in determining the relative profiles of these constituents than any chemical effects. It should be pointed out that any efforts to measure chemically related constituents should be accompanied by a measurement of a non-related constituent so as to sort out the dynamic effects.

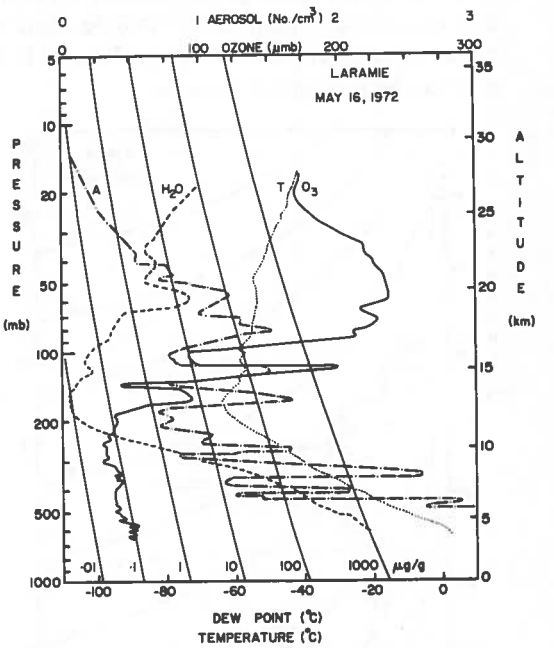

Figure 5. A simultaneous measurement of the vertical distribution of ozone (O_3), water vapor (H_2O), and temperature (T). The aerosol (A) sounding was made about 5 hours before the ozone : water-vapor sounding. The smooth curves are lines of constant water-vapor mixing ratio.

POLAR OBSERVATIONS OF THE STRATOSPHERIC AEROSOL

During December 1971 and January 1972, the stratospheric aerosol was measured at the ice island T-3 (84°37′N) and the South Pole (90°S). In addition, ozone was measured, though not on the same soundings.

Figure 6 shows the aerosol results from the two polar stations. The tropopause occurred at about 300 mb pressure at both stations. Although these are the first such measurements from such remote locations, and thus should obviously be interpreted cautiously, a few comments are warranted. Except for a region between 10 and 15 km, where the T-3 concentration is higher, the aerosol concentration above the tropopause is remarkably similar in the two polar regions. This is in spite of the fact that the northerly measurement was in mid-winter and the southerly in mid-summer, and also in spite of the large inhabitation difference between the two hemispheres. In addition, preliminary results from the first Australian flight on October 13, 1972, suggest a stratospheric aerosol concentration of around 1 particle/cm^3 $> 0.3\mu$ diameter, similar to what is presently being observed in the northern hemisphere at Laramie.

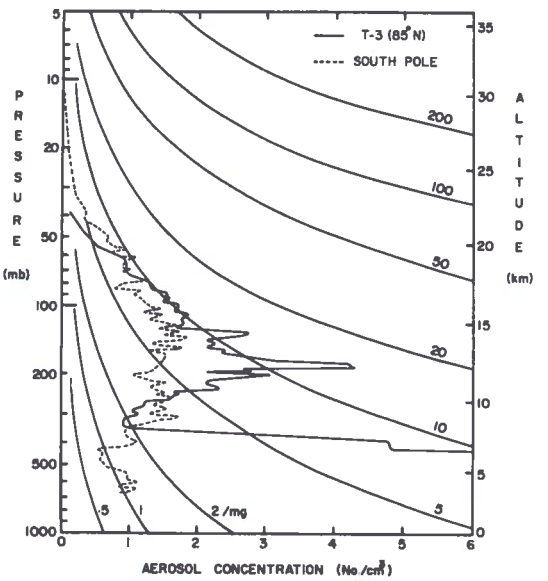

Figure 6. Aerosol concentrations ($> 0.3\mu$ diameter) over ice island T-3 on December 3, 1971, and over the South Pole on January 24, 1972. The Arctic tropopause was observed at 310 mb and the Antarctic tropopause at 320 mb. The smooth curves are lines of constant mixing ratio.

A remarkable feature of the size distribution of aerosol in the lower stratosphere, in this size range, is its apparent lack of appreciable variation. From numerous soundings at midlatitudes the ratio of the concentration of particles $> 0.3\mu$ to that of particles $> 0.5\mu$ appears to remain steadfastly in the range 4 ± 1. In contrast, tropospheric, and occasionally upper-stratospheric (> 25 km), aerosols at times display a ratio as high as 100, suggesting the presence of a preponderance of small particles. This ratio is shown for the polar flights in Figure 7. We see here the typical stratospheric ratio of around 4 except for the region just above 10 km in the T-3 sounding, the same region which displayed a higher concentration. Thus the excess concentration observed in the north polar region appears to be made up of particles constituting a size distribution which is steeper than that normally encountered in the lower stratosphere. A sounding at Laramie about this same period showed a similar excess of relatively small particles that was not present two months earlier. This excess subsequently died away at Laramie. Whether a similar decay occurred at T-3 is unknown; however, the answer to this may be found in T-3 soundings presently scheduled for December 1972, since there appears to have been no significant stratospheric injection since December 1971, according to midlatitude data.

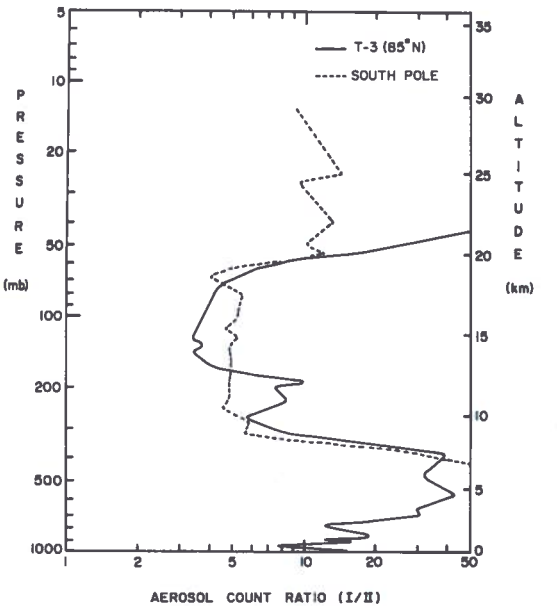

Figure 7. Ratio of aerosol concentrations (I = $> 0.3\mu$ diameter, II = $> 0.5\mu$ diameter) observed over ice island T-3 and the South Pole.

Data from a Rhodamine B chemiluminescent ozone sensor, launched 7.5 hours before the aerosol sounding at T-3, are shown in Figure 8 with the aerosol data for comparison. Although the measurements were not strictly synoptic, the observation of a possible correlated layer at about 14 km suggests laminar transport in this region, and warrants further investigation during the 1972 T-3 program.

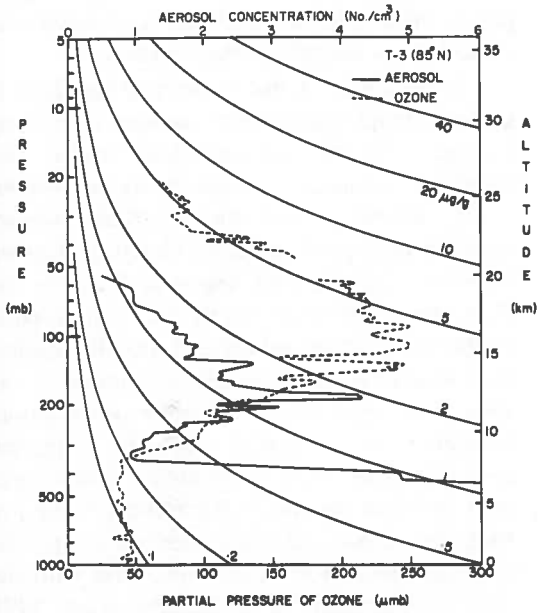

Figure 8. Aerosol (> 0.3μ diameter) and ozone concentrations over ice island T-3 on December 3, 1971. The smooth curves are lines of constant mixing ratio.

AN EXTENSIVE DUST LAYER IN THE NORTHERN HEMISPHERE

Following the recent, relatively small volcanic eruption of Alaid (50°51′N latitude, 155°34′E longitude) on June 19, 1972, in which the ash cloud was reported to reach 8 km (350 mb pressure), a series of soundings was attempted approximately 4000 miles downwind. Balloon measurements at Ft. McMurray (Canada), Duluth, Laramie, and Palestine (Texas) showed a dust layer present in the 300-350 mb pressure region. Due to its persistence and extent, this layer has been tentatively identified as a volcanic-ash injection by Alaid. A sounding at Panama did not detect the layer.

Figure 9 is a comparison of the soundings made at Laramie (41°N latitude, 106°W longitude) and Ft. McMurray (57°N latitude, 112°W longitude). Both profiles show a layer in the 300 to 350 mb region (the maximum reported altitude of the volcanic ash cloud). The concentration of particles was largest at Ft. McMurray, which was most nearly at the same latitude as the eruption.

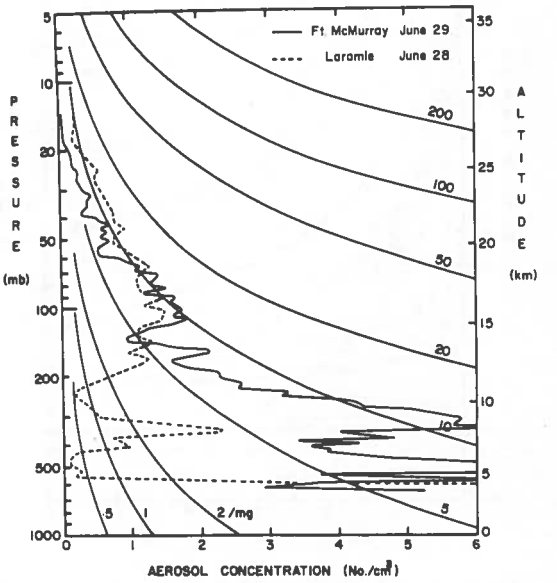

Figure 9. A comparison of the aerosol (> 0.3μ diameter) soundings made at Laramie, June 28, 1972, and at Ft. McMurray, June 29, 1972. The smooth curves are lines of constant mixing ratio.

The presence of tropospheric layers of submicron aerosol in a single sounding is not unusual, but the correspondence in altitude of these layers at four stations over a wide range in latitude (32°N – 57°N) strongly suggests that they are associated with a single event, which could be the eruption of Alaid. Further evidence of this is provided by the time development of the layer as observed at Laramie during the month following the eruption, which is shown in Figure 10. We see a persistent layer, over a 24-day period, in the 300-370 mb region. The profiles also suggest the presence of other layers, but these are not persistent. In addition, the particle size ratio of the persistent tropospheric layers is consistent with that of stratospheric

aerosols; ordinary tropospheric layers usually have a higher ratio, corresponding to a smaller average particle size. The persistent layers thus probably consist of particles larger than those of tropospheric features such as cirrus clouds. There is some evidence for a gradual settling of the layer from the data at Laramie.

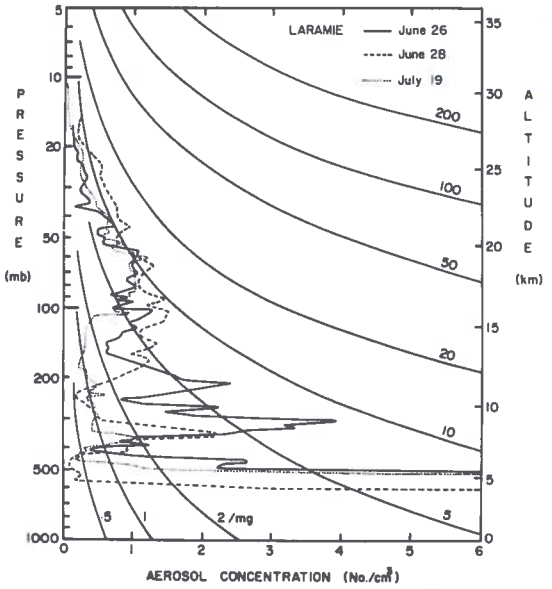

Figure 10. A comparison of three aerosol ($> 0.3\mu$ diameter) soundings made at Laramie in June and July, 1972. The smooth curves are lines of constant mixing ratio.

The short-term dispersion was observed to occur along lines of constant pressure and to spread out at least one degree of latitude per day. Long-term dispersion of radioactive debris, observed extensively in the past, shows that the movement tends to be along lines of constant potential temperature averaged over a month.

Although a small increase in the integrated stratospheric aerosol was observed in the June soundings at Laramie, it does not appear to be statistically significant. Subsequent flights at Laramie in July, August, and September have indicated the lowest stratospheric aerosol concentrations ever recorded by the aerosol counter.

TIME VARIATIONS OF THE STRATOSPHERIC AEROSOL AT MIDLATITUDE

Figure 11 shows the time variation of the integrated stratospheric aerosol at midlatitude over a period of about 10 years. All data were obtained utilizing the same technique, viz., the light-scattering dustsonde. No data were obtained before the volcanic injection of Mt. Agung in 1963, so it is difficult to determine a "natural stratospheric background." The gross feature of a general decrease in the integrated stratospheric aerosol since 1963 is apparent. This may be contrasted with the typical concentration of aerosol at the minimum just below the tropopause, which has remained relatively constant at about 0.5 particles/cm^3 over the years.

Since late 1971, the number of soundings at Laramie under this program has been stepped up to once a month, with gratifying results. This increased frequency immediately makes obvious that a relatively small but significant aerosol injection took place in late 1971. One is then led to believe that the large degree of scatter in the data prior to 1971 is probably due to incomplete resolution of additional finite stratospheric injections which have taken place, for example, in late 1964, late 1965, and late 1968. In addition, measurements of the atmospheric extinction coefficient due to aerosols in the 26-km layer from balloons by one of the authors (T.J.P.) in 1966 also show a definite increase during the latter part of that year. Coupling these with the definite observation of an increase in late 1971 leads one to connect the increases with phenomena that occur late in the year. The hurricane season, which peaks around October, immediately comes to mind as a possibility. It is notable that the current year has been the lowest in hurricane occurrences for the past 30 years and that the stratospheric aerosol level is presently at its lowest in at least the past 10 years.

Figure 12 is a closeup of the data obtained at Laramie to date. The first sounding in October 1971 indicated a very low integrated stratospheric loading; an increase by more than a factor of two was observed on the next sounding in late December. A flight at the ice island T-3 on December 3, 1971, gave an integrated loading of about 1.7×10^6 particles/cm^2-column, suggesting that the injection probably took place prior to December 1971. However, the relation between the midlatitude and polar stratosphere in terms of aerosol distribution and dissipation has not as yet been established. Stratospheric turbidity at Bedford, Massachusetts, as measured utilizing twilight photometry [3], exhibited the increase; however, these data suggest that the

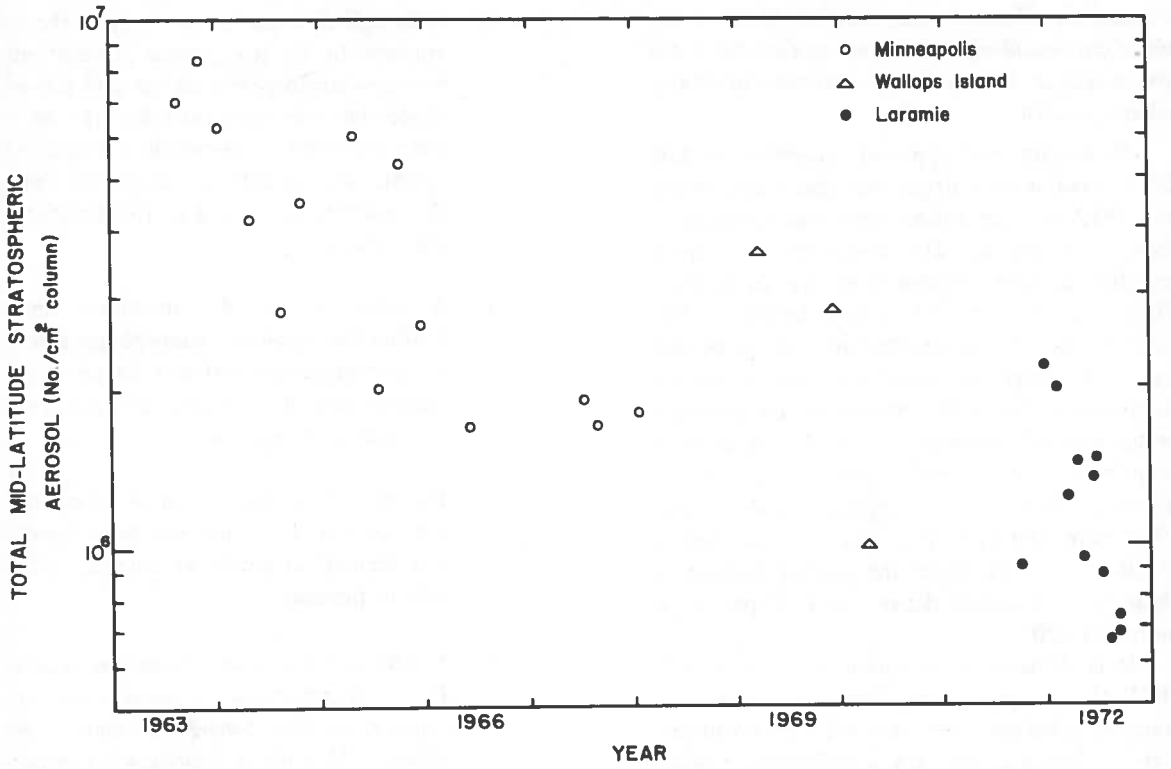

Figure 11. Time development of the total stratospheric aerosol > 0.3μ diameter integrated in a cm^2 column above the tropopause at northern hemisphere midlatitude since 1963.

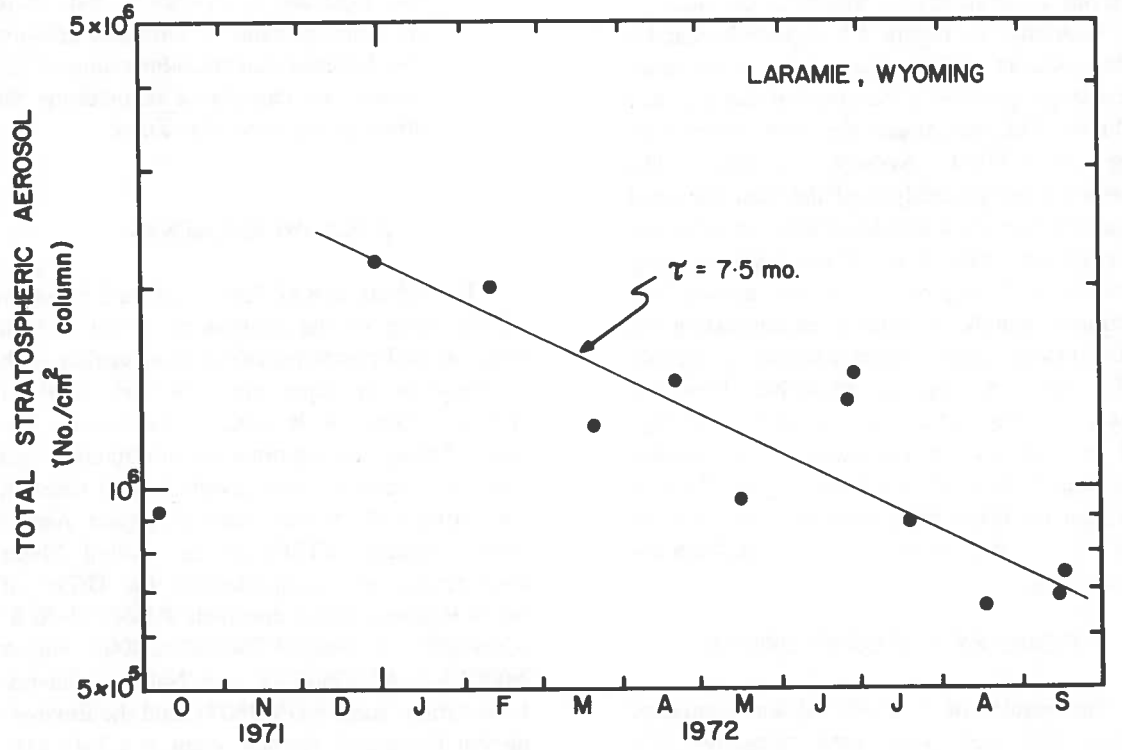

Figure 12. Time development of the total stratospheric aerosol > 0.3μ diameter integrated in a cm^2 column above the tropopause at Laramie during the past year.

increase was already present on October 1, 1971, while our sounding at Laramie on October 6 did not detect an enhanced concentration of stratospheric aerosol.

Following the apparent injection in late 1971, a subsequent decay was observed throughout 1972 with an exponential time constant of about 7.5 months. The possibility of a small injection in June, alluded to earlier, seems from Figure 12 not to be statistically significant. The difficulty lies in the fact that to date we do not know how large the uncertainty due to natural fluctuations should be. We feel we are getting a better idea of this with increased frequency of soundings. For example, the closely spaced points in late June 1972 and mid-September 1972 were two days apart and show differences of about 10%. However, the general fluctuation about the 7.5-month decay line in Figure 12 is more like ±20%.

It is difficult to assign the increase in late 1971 to any particular occurrence such as a volcanic injection. One can find minor volcanic activity during almost any 2-to-3-month period, but the observations are usually not good enough to determine the importance of a particular event in terms of stratospheric injection. On most of the soundings in Figure 12, a particle sampler which collects aerosol on a number of electron-microscope grids as a function of altitude was included. This instrument was provided by E.K. Bigg of CSIRO, Sydney, Australia. The Australian group's analysis of the data suggested a concentration and size distribution more or less in agreement with those of our light-scattering detector, and suggested that the aerosol was composed mainly of substances containing the sulfate radical. Thus a volcanic source for the late 1971 injection appears attractive. However, injection during hurricanes remains a possibility, and is currently being studied by attempting soundings in or near a hurricane region. To date this year no major hurricanes have occurred, so that no data on this aspect of the problem are yet available.

SUMMARY AND CONCLUSIONS

The results of over 40 balloon soundings during the past year have suggested the following:

1. Although data are as yet limited, there appears to be no general correlation between stratospheric ozone and water vapor. On one occasion when the two were observed to correlate, the stratospheric aerosol did also, suggesting that the correlation was due to transport phenomena.

2. A similarity in the northern- and southern-hemisphere stratospheric aerosol concentration and size distribution suggests that the source is independent of human inhabitation.

3. The short-term dissipation of an apparent volcanic ash cloud was very rapid, and seemed to spread at constant altitude or pressure.

4. A stratospheric aerosol injection in late 1971 was observed to decay with an exponential time constant of about 7.5 months. This decay is somewhat more rapid than that suggested by the decay of radioactive debris. The source of the injection is unknown but could be either volcanic or hurricane activity. It is believed that small injections of this variety are capable of maintaining the stratospheric aerosol reservoir.

ACKNOWLEDGMENTS

The efforts of R.G. Pinnick of the University of Wyoming in the calibration of the aerosol detector and computer calculations dealing with its response are appreciated. The field work of the University of Wyoming Atmospheric Research Group was instrumental in obtaining data from the many stations involved. This research was supported by the Climatic Impact Assessment Program (CIAP) of the United States Department of Transportation; the Office of Naval Research under contracts # N00014-70-A-0266-0002, # N00014-70-A-0266-0003, and # N00014-70-A-0266-0005; the National Science Foundation, grant # GV-28077; and the Environmental Protection Agency, grant # 1 R01 APO 1289-01.

REFERENCES

1. Rosen, J.M., "The vertical distribution of dust to 30 kilometers," J. Geophys. Res. *64*, 4673, 1964.

2. Rosen, J.M., "Correlation of dust and ozone in the stratosphere," Nature *209*, 1342, 1966.

3. Volz, F.E., "Return of normal stratospheric turbidity and a new short dust event during October, 1971," paper presented at International Radiation Symposium, Sendai, Japan, May/June, 1972.

4. Wexler, A., S. Hasegawa, and L. Greenspan, "Evaluation of several sensors for measuring low concentrations of water vapor," in this volume.

DISCUSSION

(UNIDENTIFIED): What is the layer of aerosol integration?

HOFMANN: From the tropopause to the top of the atmosphere. If you lay an aerosol distribution curve on its side, the layer is the area under the curve from the tropopause to zero atmospheric depth.

(UNIDENTIFIED): Do you take some mean tropopause value?

HOFMANN: The aerosol concentration at the tropopause is extremely low in all the data; it has been less than about half a particle per cubic centimeter. This makes it a good place to start integrating from.

(UNIDENTIFIED): Is the integration always done over the same altitude range?

HOFMANN: Not necessarily. Since the concentration decreases in the upper atmosphere, the contribution is extremely small once you get above about 30 km. The major portion of the contribution to the integral is in the region from the tropopause to 25 km or so. Most soundings go to 30 or 35 km.

SCHAINKER: I have two questions on the aerosol-measurement curves. First, how are the water-vapor results interpreted in the light of Dr. Wexler's comments on the uncertainties in that type of measurement? Second, what are the error bars of the measurements?

HOFMANN: We began flying these water-vapor sensors because they were available and they met criteria set for the program. The sensors which we flew were not calibrated as a function of temperature. Also, they had been calibrated by the manufacturer, and although agreement is not bad, the manufacturer's calibration tends to suggest a dryer region. The ones we have flown to date have not been calibrated by NBS. We were hoping that eventually these sensors could be calibrated by a standard technique, as a function of temperature and frost point, so that we could pin down the water-vapor concentrations more accurately. So far, however, we have been flying manufacturer-calibrated sensors and looking at relative data rather than absolute values. Since the sensor apparently responds to changes in water vapor at frost points as low as -100°C, and since the temperature remains relatively constant while the sensor shows variations, we'd like to think that the sensor is responding to water vapor.

As for the errors, the aerosol concentration is perhaps the most accurate of the measurements. The aerosol curves are based on a large number of particles, so their accuracy is quite good. The averaging is done over a certain region of height, something like 0.1 km, however, so this averaging interval could be used to put an error bar on the data. The ozone-sensor error is probably similar, with an averaging interval of a few tenths of a kilometer or so. The water-vapor error is dominated by other uncertainties in calibration.

SISSENWINE: Even given the possibility that the water-vapor sensor might have been temperature-sensitive, I was struck by the extremely high mixing ratio at the top of your soundings and the very rapid decrease during descent. Is it possible that your sensors were contaminated at the start of the down flight, and it took a while before the readings represented uncontaminated air?

HOFMANN: Yes, this is the general interpretation of such profiles. The ascent generally looks completely different from the descent. When descent begins, and the sensor is the first thing penetrating the sampling region, a finite decontamination period can be expected.

SISSENWINE: Could the lack of detail in the data you mentioned have been due to the rapid descent rates of your parachute? How fast does it fall at, say, 50 millibars?

HOFMANN: The average is about 60 minutes for 100,000 feet. It descends somewhat faster at the top, so I'd guess it's on the order of 3000 feet a minute in that region, decreasing to perhaps 1500 feet a minute at lower altitudes

McCORMAC: A number of the Chinese and French nuclear tests have penetrated the stratosphere. It would be interesting to see how they would correlate with your data.

HOFMANN: Unfortunately, the only tests made since we started taking data on this program did not penetrate the stratosphere, and we have only a few earlier data points for comparison.

RECENT MEASUREMENTS OF THE INJECTION OF WATER VAPOR AND OZONE INTO THE STRATOSPHERE BY THUNDERSTORMS

E.W. BARRETT, P.M. KUHN, AND A. SHLANTA
Atmospheric Physics and Chemistry Laboratory
NOAA Environmental Research Laboratories
Boulder, Colorado

ABSTRACT: During August and September 1972, water vapor and ozone in the stratosphere were measured in the vicinity of thunderstorms which reached or penetrated the tropopause. Water-vapor overburden (precipitable water) above flight level was measured by the infrared radiometric technique devised by Dr. Kuhn; ozone at flight level was measured by a Komhyr-type KI-cell instrument constructed by Dr. Shlanta. All instrumentation was modified for unattended operation on the aircraft; data were recorded on the aircraft analog magnetic-tape logging system. Two storms were studied extensively: one which penetrated 3000 feet above the tropopause, and another which just reached to the tropopause level. In both cases, water-vapor overburdens above and downwind averaged some 40 percent higher than those upwind of the storms. Ozone concentrations above the deeper storm were about 35 percent higher than those away from the storm, while those above the weaker storm were 10 to 20 percent less than those in undisturbed air. It thus appears that thunderstorms do inject substantial amounts of water vapor into the stratosphere, and that growing, electrically-active storms also generate ozone at their tops.

INTRODUCTION

In support of the basic objectives of CIAP, we are conducting a number of airborne surveys directed toward determining the strengths of various natural sources and sinks of stratospheric trace constituents whose abundances might be affected by SST operations. Our total program is designed to study the transports of water vapor, ozone, and (indirectly through small-ion measurements) aerosols into the stratosphere by mesoscale convective circulations, and to observe the global-scale variations in these constituents on long meridional and zonal flights above the tropopause. In this paper we will restrict ourselves to a discussion of the techniques of measurement and of the data obtained in August and September 1972 from isolated thunderstorms which penetrated or reached the tropopause in the southwestern United States. Discussion will be limited to water vapor and ozone, because the ion counter had not yet been installed on the aircraft at the time of these missions.

The two kinds of measurements we have made are: (a) determination of the total mass per unit area of water vapor above the aircraft (water-vapor overburden, or "precipitable water") by the infrared radiometric technique and (b) measurements of the in-situ ozone mixing ratio by the potassium-iodide/iodine electrochemical concentration cell. The instrumentation for these measurements was constructed or modified for unattended operation on board the aircraft for periods of 6 hours or more. These instruments were carried aloft by a WB-57F aircraft of the 58th Weather Reconnaissance Squadron, U. S. Air Force; for the past several years this squadron has conducted numerous atmospheric probing missions under a contractual arrangement with the Los Alamos Scientific Laboratory, U. S. Atomic Energy Commission. This latter organization has handled the arrangements for installation of our instrumentation and initial data retrieval, and has worked closely with us in planning our missions.

Since the introduction of microwave radar as a meteorological tool, many instances of thunderstorm echoes reaching to heights of 50 to 70 thousand feet above mean sea level (MSL) have been reported. Thunderstorms which produce tornadoes and severe flash floods almost always reach to such heights. Since the tropopause in summer in the south central U.S. averages around 48,000 ft, it is clear that many thunderstorm tops, containing liquid and solid water, extend

well into the stratosphere. It is well known that the relative humidity, on the average, drops rapidly above the tropopause; therefore a rapid evaporation from the cloud top should take place and the mixing ratio of the stratospheric air should be raised. Wind shear and eddy diffusion will then ensure that some of this vapor will be transported away from the immediate neighborhood of the cloud and thus be retained in the stratosphere. If enough clouds contribute to this source, it might well be comparable in strength to the upward transport by the Hadley circulation, which is limited by the "cold trap" at the tropical tropopause.

The effect of a penetrating convective updraft on the ozone concentration is more complex. Since the air injected by the cloud comes from all levels of the troposphere, one would expect a reduction in the amount of this gas by dilution of the ozone-rich stratospheric air. On the other hand, the upward-moving bubble at the cloud top may cause a smoke-ring type of circulation in the circumambient air. Since the vertical gradient of ozone is very large at the heights involved here (this will be shown in a subsequent figure), downward transport in this vortex-ring would produce at least transient elevations of ozone mixing ratio at some distance away from the cloud axis. There is a third possibility, namely, that the cloud top may act as an ozone source by virtue of its electrical properties. The cloud top contains a large number of ice crystals with sharp points or corners. If the electric field is sufficiently strong, corona discharges will take place from the particles; the ultraviolet emission by the excited air molecules will produce ozone photochemically in the cloud top, and this will be mixed into the surrounding air by eddy diffusion. It has already been shown by one of us [1] that this does, in fact, happen in the lower levels of thunderstorm clouds.

Heretofore, almost no data have been obtained on the concentrations of either water vapor or ozone in the air around the tops of thunderstorms. This is due mainly to the fact that balloon soundings are the only inexpensive means of collecting free-atmospheric data. It is nearly impossible to control the launch of a free balloon so that it will arrive (with its instrument package still functional) in the air above the storm top. Furthermore, the usual water-vapor sensor (carbon humidity element) of the radiosonde is far too sluggish and insensitive to give meaningful water-vapor data, although ozonesondes using the same principle as our sensor are available at a reasonable cost. A dirigible instrument carrier is therefore essential; only military aircraft have the required high service ceiling of 60,000 ft or more. These aircraft have not been available in the past for meteorological measurements; we are therefore grateful that the present collaboration of the three agencies (APCL, LASL, USAF) has been achieved so as to make these measurements feasible.

The flights reported in this paper were conducted out of Kirtland AFB, Albuquerque, New Mexico. On receipt of a report of favorable aircraft status, one or more of us would proceed to the base on the day prior to a mission. Forecasts of target areas were made that afternoon with the very able assistance of the National Weather Service forecast center at Albuquerque. If good storms were forecast within operating range of the aircraft, the mission was scheduled for the following afternoon. Preflight checks of instruments and aircraft were carried out during the morning, with the final decision to go or abort reserved until 1300 hours. On conclusion of a successful flight, crew debriefing and electronic transcription of data for a "quick look" were conducted.

Completely satisfactory data were collected on two storms. The first of these was located 65 miles west of Amarillo, Texas on the afternoon of 3 August 1972. This very active storm attained a peak altitude of about 51,000 ft, some 3000 ft above the reported tropopause height of 48,500 ft. Four overflights and five boxes (circumnavigations) were carried out.

Figures 1 and 2 show the appearance of the storm as seen from the aircraft at 55,000 ft. The cirrus sheet is the anvil top and is located at the tropopause; the penetration by the rising bubble or turret is clearly visible.

The second storm, located near Tucson, Arizona on 7 September 1972, was less massive and did not reach to such a great height as the first. There has been some slight disagreement among us as to whether the storm did penetrate the tropopause. The latter was rather diffuse, and could be placed anywhere between 40 and 45 thousand feet, while the peak height reached by

Figure 1. Downward-sweep aerial-camera view of top (51.5 kft) of storm cell near Amarillo, 3 August 1972.

the cloud was 42,500 ft. We therefore classify this storm as *weakly penetrating* in comparison with the first.

Two overflights and two boxes were flown. The storm reached peak height during the second overflight and was declining noticeably during the boxes.

MEASUREMENT TECHNIQUES

We now give a short discussion of the theory of the measurements and the instruments employed.

Figure 2. Forward-sweep aerial-camera view of storm cell shown in Figure 1.

Water Vapor

The water-vapor overburden is computed from primary measurements of the infrared radiation emitted in a downward direction from the entire column of air above the upward-looking instrument. Emission in the 18- to 23-μm band is due almost entirely to water vapor; hence, the received power is proportional to the vapor density in each slab of air in the viewing cone of the radiometer, multiplied by a weighting factor depending on the temperature and pressure of the slab and the wavelength. The power is thus the weighted mean, or integral, of a function of pressure, temperature, vapor density, and wavelength. The explicit form of the integral is

$$N\downarrow_c(\text{w cm}^{-2}\text{sr}^{-1}) = \int_{\nu_1}^{\nu_2} \int_{p}^{p=0.1} \phi(\nu)\, B(\nu, T(p))\, \frac{d}{dp}\tau(\nu, p, H_2O)\, dp\, d\nu \qquad (1)$$

where $B(\nu, T(p))$ is the Planck function (w cm^{-2}sr^{-1} cm);

$T(p)$ is temperature (°K) at pressure p (mb);
$\phi(\nu)$ is the spectral sensitivity of the radiometer;
$\tau(\nu, p, H_2O)$ is the transmission of the atmosphere along a path from p_1 to p_2 and is a function of the pressure, temperature, and water-vapor mass, and the spectroscopic data for the 18.0 to 23.0μm band.

Of these quantities the only unknown is the water-vapor mass, so, in principle, it can be determined. This assumes the existence of water-vapor transmissivity tables or functions versus water-vapor optical mass.

Since the water-vapor concentration, H_2O, is inside the integral, no unique description of the variation of vapor density with height can be extracted from the power measurement. However, the calculation is not over-sensitive to the form of the vertical distribution unless rather strange distributions (i.e., all the water in one slab) are encountered. A smooth and not physically-unreasonable distribution is that of a constant water-vapor mixing ratio (g g^{-1}), which leads to a calculable steady decrease in vapor density (g cm^{-3}) with decreasing pressure. Evaluation of the integral then gives a unique value of the overburden (g cm^{-2}).

To invert the integral one assumes a mixing ratio, computes $N\downarrow_c$, and compares this with the observed $N\downarrow_o$. The difference is used to adjust the mixing ratio in the right direction so as to reduce the difference to a small value ϵ, i.e.,

$$|N\downarrow_c - N\downarrow_o| \leqslant \epsilon, (5.0 \times 10^{-7} \text{ w cm}^{-2}\text{sr}^{-1}), \quad (2)$$

where ϵ is the noise-equivalent radiance (NEN) of the radiometer. In practice, this is done using an iterative scheme on an electronic computer. Convergence is rapid for reasonable first guesses based on experience.

It is clear that the actual water-vapor profile could be obtained from data taken at a number of different altitudes (by numerical differentiation). However, the error band for such differentiated data will be determined by the value of the radiometer noise-equivalent radiance, so that this method requires a radiometer of exceedingly low noise level.

Figure 3 summarizes the method of calculation and assumptions. To illustrate the actual computations of the program, a sample input and output is montaged as Figure 4. This figure illustrates a calculation of downward radiance at 100 millibars (53,000 feet) against a downward radiance observation at this level for the 3 August 1972 storm cell. Note that eight iterations were required to achieve convergence of $N\downarrow_o$ and $N\downarrow_c$. The series of "circled" quantities indicates the progression from observed radiance 1.115×10^{-4} w $cm^{-2}sr^{-1}$ and initial-guess mixing ratio 3.5×10^{-3} g kg^{-1} (3.5×10^{-6} g g^{-1}) to the final radiance convergence of 1.114964×10^{-4} w cm^{-2} and the corresponding final inferred water-vapor burden, 2.429×10^{-4} g cm^{-2}.

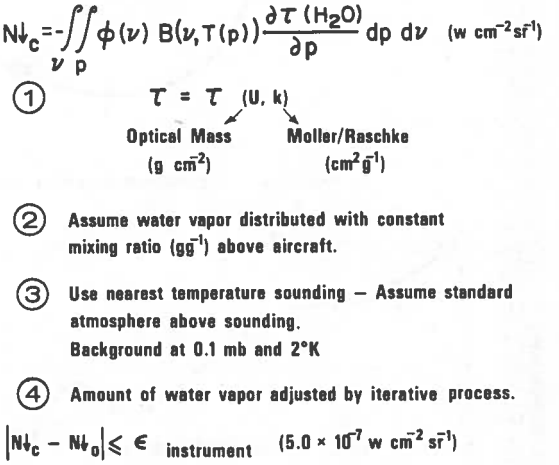

Figure 3. Method of calculation of water vapor from downward IR signal with assumptions.

The radiometer used in our work is a prototype water-vapor bolometer with an NEN of 5×10^{-7} w $cm^{-2}sr^{-1}$, which corresponds to a maximum water-vapor resolution of $\pm 0.7 \times 10^{-6}$ g g^{-1} or $\pm 0.7 \times 10^{-4}$ g cm^{-2} of water-vapor burden. The filter spectral sensitivity of the radiometer with a pyroelectric (triglycine sulfate) detector covers the band 18.0 to 23.0μm (555 to 435 cm^{-1}) with an average relative response of 0.55. The response function of the radiometer appears in Figure 5.

It is evident that, if emitting substances other than water vapor (such as aerosols or cloud particles) that are optically active in the spectral band of the instrument come within the instrument's view, errors will result. To guard against

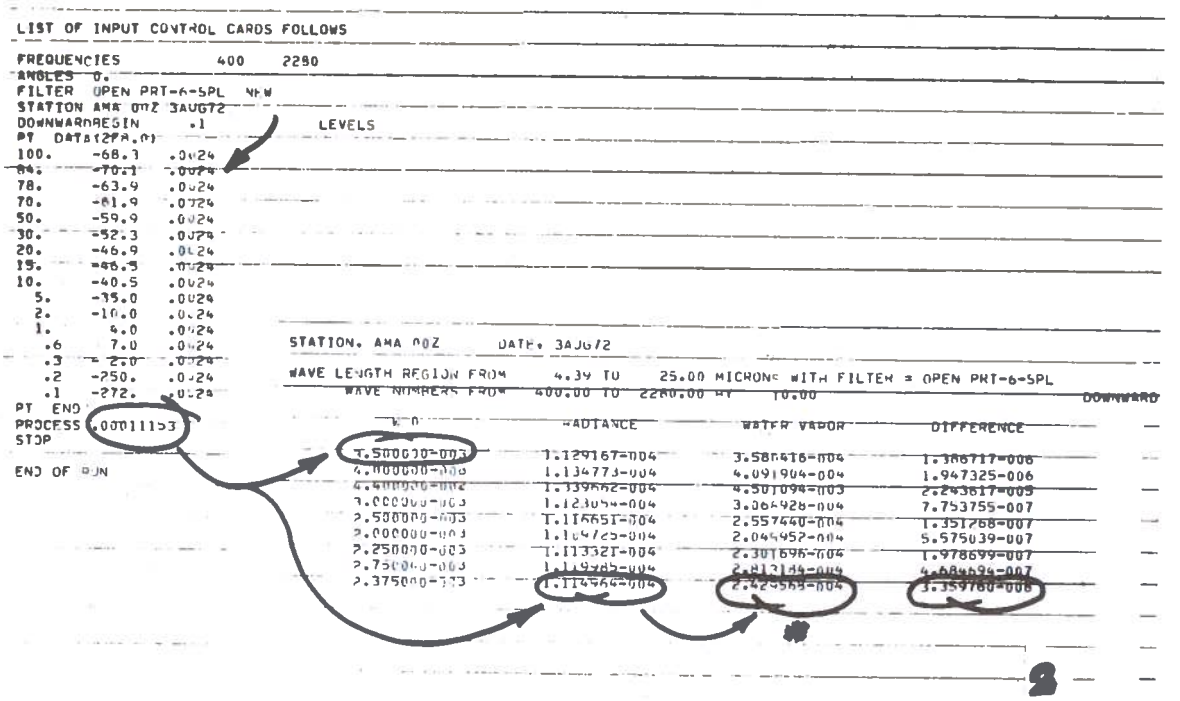

Figure 4. Sample computer input and output: complete solution in eight steps.

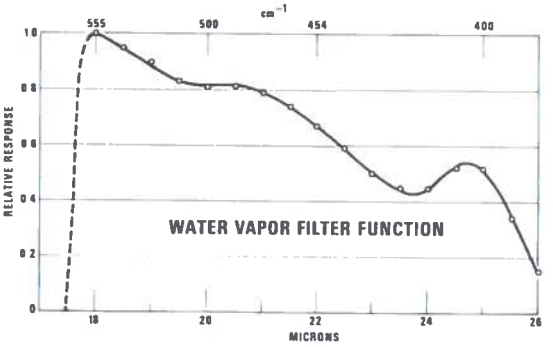

Figure 5. Response function of radiometer.

this, the radiometer also has a second channel from 10 to 12μm (a band in which water-vapor emission is negligibly small). Data from the water-vapor channel are not used if the guard channel shows abnormally-high received power.

The sampling rate of the radiometer is 10 sec^{-1}; these samples are averaged electronically over one-second intervals. The values of water vapor upwind and downwind of the storms (shown in later figures) are thus averages of some 350 observations.

Additional discussions of the radiometric technique of water-vapor measurement from aircraft may be found in references [3] and [4].

Ozone

For measurements of ozone concentration in the atmosphere, several units of pressure, density, and mixing ratio have been used in the literature. For a comprehensive discussion of these various ozone units see Sticksel [2].

To normalize the effects of the wide range of atmospheric pressures encountered in the studies described here, the concentration units used for ozone are those of a volume mixing ratio, i.e., the number of ozone molecules per hundred million air molecules. An ozone-air mixing ratio of 1 pphmv is equivalent at standard conditions to an ozone concentration of 2.69 X 10^{17} ozone molecules m^{-3}, or 21.4 micrograms of ozone per cubic meter of air. During the summer months, the usual atmospheric pressure at the ground at Albuquerque is about 835 mb, and the air temperature about 305°K. Accordingly, an ozone concentration of 2.69 X 10^{17} ozone molecules m^{-3} is equivalent to a mixing ratio of 1.35 ozone molecules per hundred million air molecules at Albuquerque.

The measuring instrument used for this work is the electrochemical concentration-cell device developed by Komhyr [6] and modified by Dr. Shlanta for unattended operation aboard the

WB-57F aircraft. When this instrument is in operation, ambient air together with any ozone present is drawn through a stainless steel probe, located outside the skin of the aircraft, by a constant-volume Teflon gas-sampling pump and then forced into the monitor's sensing chamber. When air containing ozone is bubbled through the electrolyte in this meter's sensing chamber, I_2 is formed according to the reaction

$$2KI + H_2O + O_3 \rightarrow 2KOH + O_2 + I_2 \qquad (3)$$

Iodine is then converted to iodide in the sensing chamber, with the net result of the chemical reactions being the transfer of two electrons through the ozone meter's measuring circuit for each ozone molecule reacting in the sensing chamber. Consequently, the current flow in the instrument's output circuit as a result of the ozone reactions is directly proportional to the ozone flux in the sensing chamber. The ratio of ozone flux to air flux then gives a linear function of the mean effective concentration of ozone in the incoming air. The ozone mixing ratio in the sampled air can then be calculated from the equation

$$\text{pphmv}\,(O_3) = \frac{43.07}{F}\left(\frac{T}{P}\right)(i - i_0) \qquad (4)$$

where i = current flow as a result of ozone reacting in the sensing chamber

i_0 = background current when ozone-free air is bubbled through the sensing chamber

F = flow rate of the sampled air in milliliters sec^{-1}

T = outside air temperature in °K

P = pressure in millibars.

By means of a current-to-voltage transducer, i is converted to a voltage and recorded on the WB-57F's magnetic tape recording system.

It should be kept in mind that the Komhyr-type ozone monitor, like the one used in these studies, measures *local* values of the ozone concentration, while the water-vapor radiometer measures the *overburden* of water vapor, i.e., the water vapor for the entire atmosphere above flight level. The ozone monitor used in these studies also has a response time constant of about 20 sec to a sudden change in local ozone concentration, as compared to the water-vapor radiometer, which has a response time constant of about 1 sec to a sudden change in overhead water-vapor.

RESULTS OF MEASUREMENTS

Water Vapor

Water-vapor overburdens, calculated by the method discussed earlier in this paper, are given for the storms of 3 August and 7 September, respectively, in Figures 6 and 7. In these figures, flight tracks for the circumnavigations are shown in perspective and with approximately-correct compass headings; no accurate distance scale is given because the aircraft had not been equipped with an inertial navigation system at that time. The downwind crossings are, however, at about 10 nautical miles from the cloud. Altitudes appear at the left, and water-vapor overburdens (in g $cm^{-2} \times 10^4$) are plotted on the upwind and downwind crosstracks. Tropopause heights are also shown.

Referring to Figure 6, it is clear that the values observed downwind exceed those upwind except at the highest levels (53 and 55 kft). However, on the *overflights* at these heights, anomalously high values do appear. The mean excess of water vapor in the layer between 45,000 and 50,000 ft on the downwind side over that on the upwind side is 27 percent of the upwind value for this storm.

For the second storm (Figure 7) the downwind water-vapor values again exceed those upwind at all flight levels, even at 2000 ft above the cloud top. The mean excess of downwind water-vapor overburden in the layer 41,000-46,000 ft is 109 percent, a much larger figure than that for the earlier storm. If we accept the possibility of some data contamination at 45,000 ft on the downwind side, and eliminate some high readings on this basis, the 45×10^{-4} g cm^{-2} overburden is reduced to 16×10^{-4} g cm^{-2} and the excess becomes 53 percent. We then arrive at the result that the two storms studied exhibited a *mean excess of 40 percent in water-vapor overburden on the downwind side* of the storm, above the tropopause, with respect to that on the upwind side.

If we assume a constant mixing ratio with height in the expression

$$q = (gu)/p \qquad (5)$$

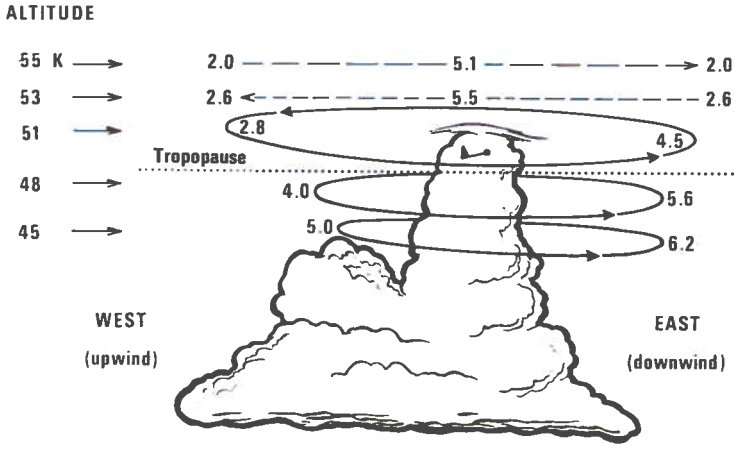

Figure 6. Thunderstorm cell near Amarillo, 3 August 1972. Altitudes in kft, water-vapor burden in gm cm^{-2} X 10^{4}.

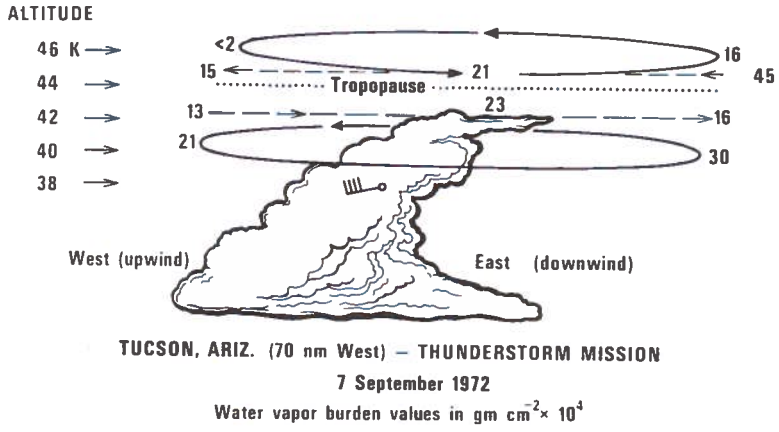

Figure 7. Thunderstorm cell, Tucson area, 7 September 1972. Altitudes and water-vapor burden as in Figure 6.

where g is acceleration due to gravity, q is mixing ratio (g g^{-1}), u is water-vapor burden (g cm^{-2}), and p is pressure, we obtain the results of Figure 8. Clearly the water-vapor mixing ratio is greater downstream than upstream. Here, of course, we assume a uniform mixing ratio to the top of the atmosphere.

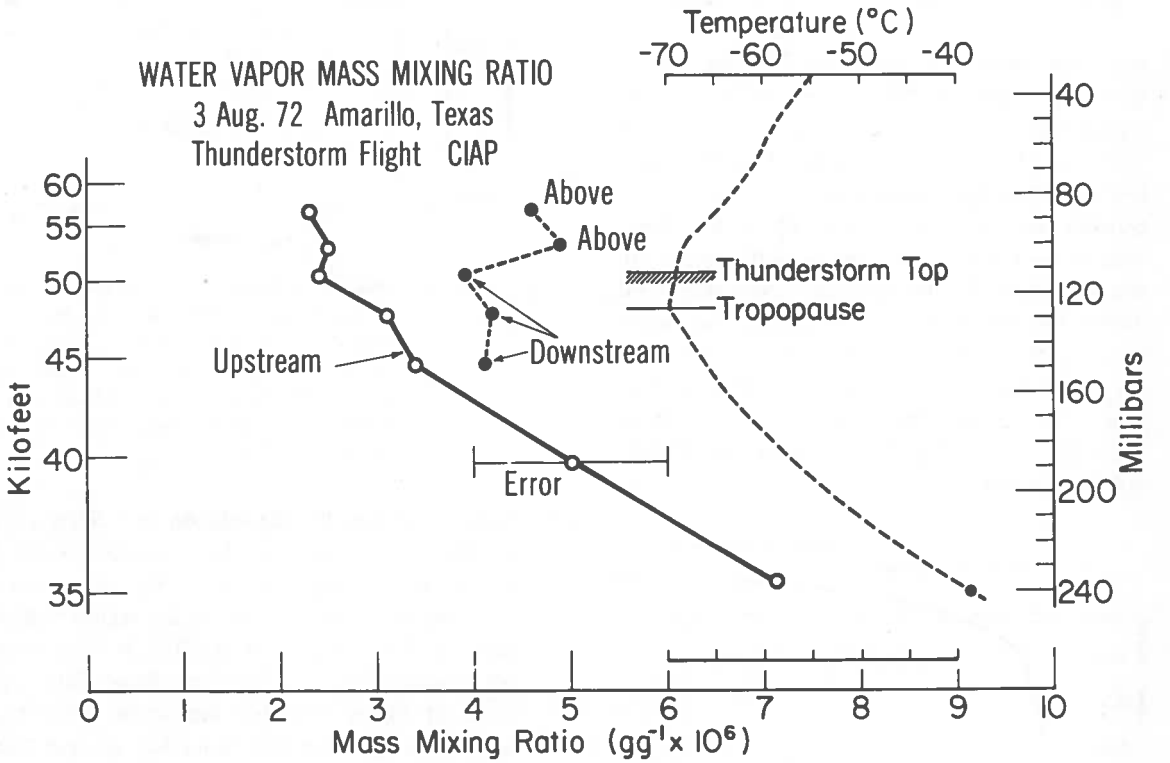

Figure 8. Water-vapor mass mixing ratio, 3 August 1972, upstream, above, and downstream of cell.

If we employ radiance observations at different aircraft altitudes, and the corresponding water-vapor burden changes, we can calculate the mean layer mixing ratios between flight levels from the expression

$$\bar{q} = g\,\Delta u/\Delta p \qquad (6)$$

where the symbols are as in Eq. (5). The results appear in Table 1 for the mission of 3 August 1972.

In Table 2 we compare water-vapor mixing ratios derived from averages of H.J. Mastenbrook's direct frost-point hygrometer measurements in the mid-latitude stratosphere during the six years 1964-1969 [7] with the mean mixing ratios we have measured upwind of thunderstorms. The differences between the two types of observations, however small, can be explained in at least two ways. First, the radiometer optimum resolution is $\pm 0.70 \times 10^{-6}$ g g^{-1}, whereas Mastenbrook's optimum resolution is approximately $\pm 0.20 \times 10^{-6}$ g g^{-1}. Second, Mastenbrook's observations are over the Washington, D.C. area, while the observations reported here are over the southwest U.S.A., which could result in some differences due to dissimilar high-level flow patterns.

Table 1. Water-Vapor Measurements, 3 August 1972

Layer (kft)	Mean Mixing Ratio Upwind of Cell (g $g^{-1} \times 10^{-6}$)	Mean Mixing Ratio Downwind of Cell (g $g^{-1} \times 10^{-6}$)
51 – 53	2.4	18.6
48 – 51	2.7	7.2
45 – 48	3.1	2.9

Ozone

The ozone data from the mission of 3 August are displayed in Figure 9 as a function of altitude alone. This has been done to call attention to the strong vertical gradient of ozone

Table 2. Water-Vapor Mixing Ratio Comparison

Level (ft)	Mixing Ratio $g\,g^{-1}$ ($\times 10^{-6}$) Mastenbrook [7]	Mixing Ratio $g\,g^{-1}$ ($\times 10^{-6}$) This Study
55,000	2.40	2.20 ± 0.60
53,000	2.45	2.40 ± 0.60
49,000	2.5	2.70 ± 0.60
46,000	2.6	3.1 ± 0.60

near and above the cloud top. The solid curve gives the vertical profile of ozone away from the storm; the crosses and circles give values above and around the storm as detailed in the figure legend. These data show that the ozone concentrations are *higher* above the top of the storm than at the same height away from the storm. On the other hand, the average values measured during the boxes of the cloud below the tropopause were *lower* than those in undisturbed air at the same levels. This is shown more clearly in Figure 10, where deviations of ozone mixing ratio from the background sounding are plotted against altitude.

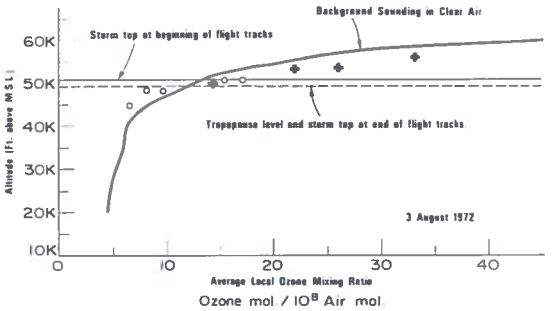

Figure 9. The ozone concentration measured in the vicinity of a thunderstorm located near Amarillo, Texas. The continuous line from 20 to 60 kft is the background sounding made away from the storm in clear air. The plus signs are ozone concentrations measured directly over the top of the storm during aircraft overflights. The zeros are the mean ozone concentrations measured during circumnavigations of the thunderstorm.

Figure 11 gives the spatial distribution of ozone mixing ratio around the storm. The distribution is quite similar to that of water vapor (Figure 6); downstream concentrations exceed those upstream at all levels.

The distribution of ozone concentration with altitude, and the background sounding away

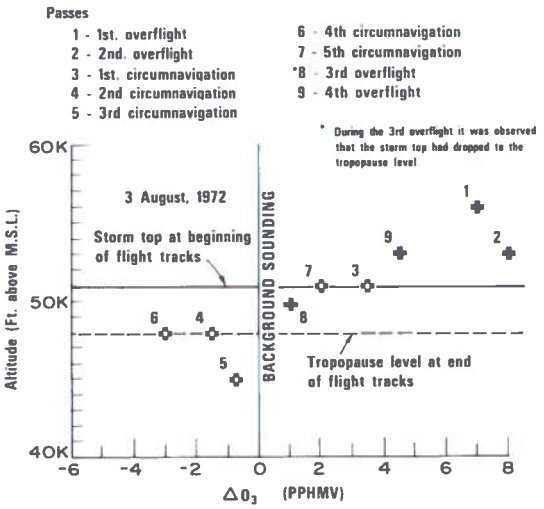

Figure 10. Average differences in ozone mixing ratios in the vicinity of a thunderstorm from the background sounding made away from the storm in clear air. The ozone-concentration measurements were made in the vicinity of a thunderstorm located near Amarillo, Texas.

from the storm, for the mission of 7 September are shown in Figure 12. The tropopause level as plotted is the height of the minimum temperature, but, as mentioned earlier, the region of high static stability began at 41,000 ft. The most significant difference between these data and those of Figure 9 is that the ozone concentrations directly above the cloud top are *less* than the fair-weather values at the same height; the concentrations measured during the boxes above the storm-top level are, however, *higher* than the fair-weather values (as for the storm of 3 August).

The perspective display of the ozone data in Figure 13 shows that, once again, the downstream concentrations of ozone exceed those upstream.

Correlation between Ozone and Water Vapor

It is evident from the preceding discussion that, with the exception of the region directly above the second storm top, excesses of ozone and water-vapor overburden occur in the same regions. This implies a positive correlation between deviations (from the background values) of ozone and water vapor. In order to test this

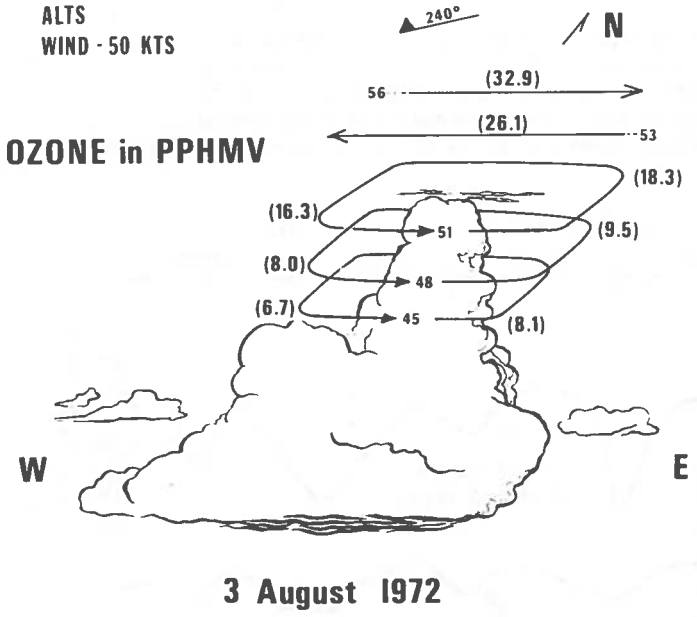

Figure 11. The flight tracks made at descending altitudes in the vicinity of a thunderstorm located near Amarillo, Texas that penetrated into the stratosphere. The numbers in parentheses are the ozone mixing ratios, in ozone molecules per 10^8 air molecules, measured along the flight tracks.

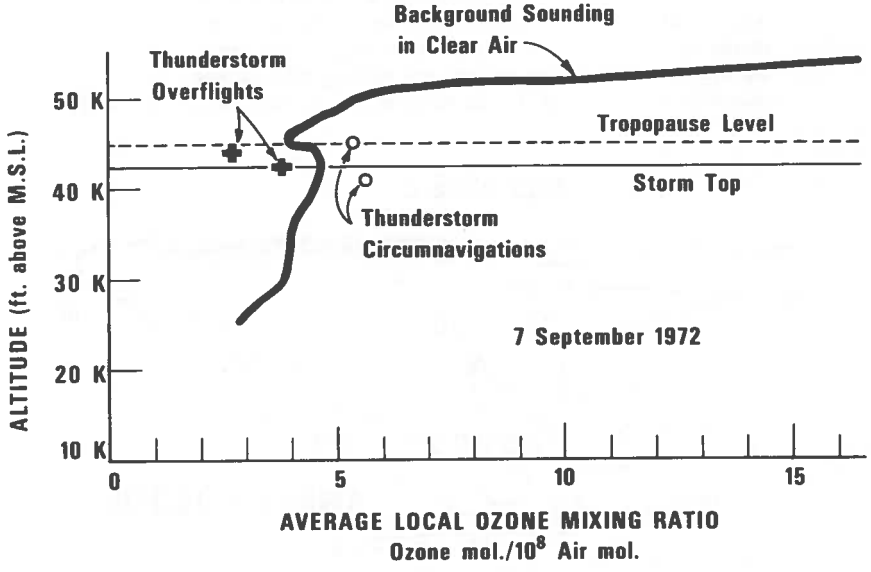

Figure 12. The ozone concentrations measured in the vicinity of a thunderstorm located near Tucson, Arizona.

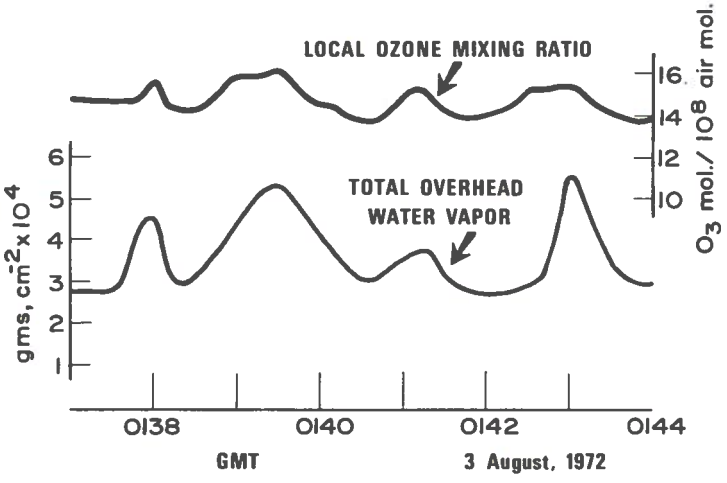

Figure 14. Total overhead water-vapor and local ozone concentration measurements made while circumnavigating at an altitude of 51 kft above the top of a thunderstorm located near Amarillo, Texas. The storm top at the time of this circumnavigation was at the tropopause level of 48.5 kft.

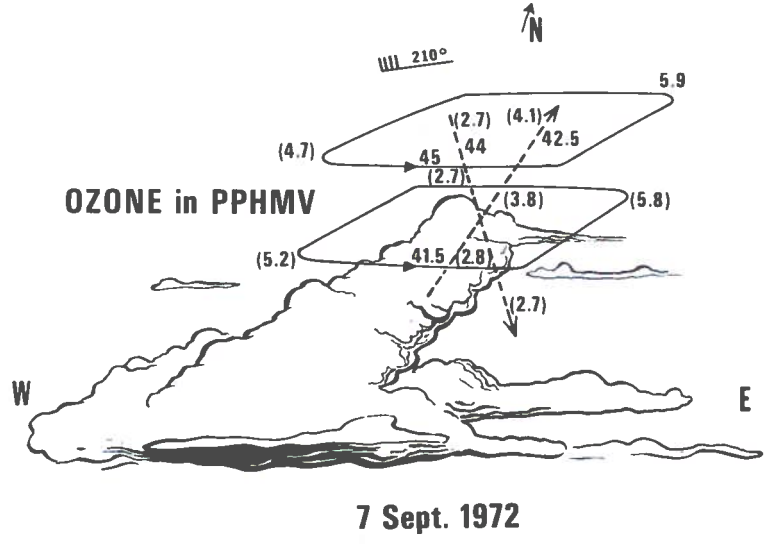

Figure 13. The flight tracks made in the vicinity of a thunderstorm located near Tucson, Arizona that did not penetrate into the stratosphere. The numbers in parentheses are the ozone mixing ratios, in ozone molecules per 10^8 air molecules, measured along the flight tracks.

hypothesis on a shorter-term basis, a section of one pass (at 3500 ft above the cloud top) from the mission of 3 August was subjected to statistical analysis. The result, shown in Figure 14 as a pair of time series, yields a zero-lag correlation coefficient of 0.67.

DISCUSSION

From these measurements (admittedly few in number) and from others made in 1971 [5], we conclude that a significant fraction of thunderstorms in the plains and southwest of the U.S. do penetrate the tropopause and deposit significant amounts of water vapor in the stratosphere near and downwind of their tops. This effect can be explained quite straightforwardly on the basis of evaporation and eddy transport processes.

The perturbations of the ozone distribution by storms is clearly a more complex matter (as was mentioned in the introduction); the data sample is as yet too small to permit a choice of one model over another. The first storm, which penetrated strongly into the stratosphere, exhibited an ozone excess directly over the top, while the second (weakly- or non-penetrating) showed a deficit there. On the other hand, boxes around both storms above cloud-top heights gave ozone excesses. In the case of the strongly-penetrating storm, ozone deficits were found on boxes below the tropopause (no such boxes were made for the second storm).

In attempting to reconcile these facts, one must consider the fact that the first storm was still in a vigorously-growing stage at the beginning of the measurements, and was therefore probably characterized by a great deal of electrical-charge production and a strong electric field. The second storm, on the other hand, had reached its peak of maturity and had begun to decay; it probably possessed a much weaker electric field.

Taking this into account, together with the positive correlation between water vapor and ozone above the first storm, we may draw the tentative conclusion that the ozone excess above the top of the first storm was generated by the cloud itself. In the case of the second storm, the deficit above the top and the excess at the same level around the storm lend some support to the hypothesis of a vortex-ring circulation bringing ozone-poor air upward above the cloud top and ozone-rich air downward at some radial distance from the cloud axis. Dr. Barrett has observed just this type of circulation (at a lower altitude) when a growing cumulus turret penetrated a stable layer of thin altocumulus; a cap formed above the cloud top, while a clear ring appeared in the altocumulus deck around the rising turret.

While the data we have gathered show that thunderstorms definitely contribute positively to the stratospheric water budget, and probably to the ozone budget as well, they do not yet permit us to answer the quantitative question: how much do they contribute? In order to answer this, one must be able to compute (or at least estimate) the flux through a closed surface around the storm and above the tropopause. This requires that we know not only the concentrations, but also the deviations of the wind from the mean wind around a box. This was not possible on these missions because the aircraft had neither a Doppler nor an inertial navigation system; the aircraft position as a function of time is known only from occasional voice records made by the navigator. Such information is much too imprecise to permit even accurate reconstruction of the aircraft's position as a function of time, to say nothing of computing the wind deviations (which are the second derivatives with respect to space and time of the position).

Fortunately, the aircraft has now been equipped with an inertial navigation system; we therefore expect that we will be able to give some more quantitative answers at the end of the summer 1973 thunderstorm season.

The flux calculations mentioned above are especially applicable to ozone, since we measure the local in-situ concentrations, which may then be correlated with the computed winds. In the case of the water-vapor measurement, we know the total overhead mass per unit area but have the wind only at flight level. To compute flux in this case, we must take the difference between vapor overburdens at two levels and correlate this with the mean of the winds at the two levels. There is, however, another way in which the amount of water vapor supplied by the storm may be estimated, which does not require taking so many small differences between large numbers. If boxes can be made until the storm has decayed well below the tropopause, the total

mass of water above the tropopause can be computed as a function of time. This will permit us to estimate a "residence fraction", i.e., what percentage of the water which is delivered to the region above the tropopause by the storm remains there after the storm has subsided. An advantage of this approach is that only the aircraft *position* is needed for the computation; it need not be differentiated to compute a wind. In order to carry out this approach, however, it will be necessary for the aircraft to remain on station for up to 3 hours; this reduces considerably the radius of action within which the storms must be located.

We are hopeful that the data from the 1973 season will enable us to present some quantitative figures on the water-vapor flux to the stratosphere by thunderstorms, and to clarify the role of thunderstorms in modifying the ozone distribution.

ACKNOWLEDGMENTS

The work reported in this paper has been supported by the Climatic Impact Assessment Program, Department of Transportation, under Contract DOT-AS-20038. The flight and logistic support provided by the Los Alamos Scientific Laboratory and the 58th Weather Reconnaissance Squadron, U.S. Air Force, are gratefully acknowledged.

REFERENCES

1. Shlanta, A., and C.B. Moore (1972), "Ozone and point discharge measurements under thunder clouds," J. Geophys. Res. *77*, 4500-4510.

2. Sticksel, P.R. (1966), "The Vertical Distribution of Ozone Over Tallahassee, Florida," Ph. D. Dissertation, Florida State University, Tallahassee, Florida (see Appendix A, pp. 120-126).

3. McKinnon, D., and H.W. Morewood (1970), "Water vapor distribution in the lower stratosphere over North and South America." J. Atmos. Sci. *27*, 483-493.

4. Kuhn, P.M., M.S. Lojko, and E.V. Petersen (1969), "Infrared measurements of variations in stratospheric water vapor," Nature, *223*, 462-464.

5. Kuhn, P.M., M.S. Lojko, and E.V. Petersen (1971), "Water vapor stratospheric injection by thunderstorms," Science *174*, 1319-1321.

6. Komhyr, W.D. (1969), "Electrochemical concentration cells for gas analysis," Ann. Geophys. *25* (1), 203-210.

7. Mastenbrook, H.J. (1971), "The variability of water vapor in the stratosphere," J. Atmos. Sci. *28*, 1495-1501.

DISCUSSION

KIRCHHOFF: When you say the thunderstorm puts some water up there "temporarily", what do you mean?

BARRETT: With the doughnut toroidal circulation the turret might punch upward, and there would be evaporation from the cloud top because of the low relative humidity at those levels; if the cloud collapses, however, the turret might go right back down.

(UNIDENTIFIED): It seems to me that it would be useful to go further downwind, perhaps 40 or 50 nautical miles. To answer the question of how much thunderstorms contribute to the overall water vapor in the stratosphere, we need to find out how much of the water remains there over a long period of time.

BARRETT: The best way to do this would be to compute fluxes, which we cannot do without better wind data. We plan to try next year.

HOFMANN: I thought you said that you approximated a constant mixing ratio, yet you say the integrated water vapor varies by a factor of two.

BARRETT: That was the *horizontal* variation in the water vapor, both upwind and downwind of the storm. The variation in the computed background mixing ratio, compared with Mastenbrook's data, was only 1.3 or so. The observed water-vapor emission is temperature-dependent, which introduces additional uncertainty into the computation.

EXAMPLES OF STRATOSPHERIC TRANSPORT

L. MACHTA AND K. TELEGADAS
Air Resources Laboratories
National Oceanic and Atmospheric Administration
Silver Spring, Maryland

ABSTRACT: Radioactivity concentrations and ratios in stratospheric air sampled to 30 km describe the latitudinal and vertical spread of stratospheric debris from a stratospheric source. On September 29, 1969, China detonated a 3-MT high-yield device at 40°N. The spread of this debris, which could be followed for about a year, and its stratospheric depletion are discussed and compared with patterns from other nuclear tests. The residence halftime of debris injected into the stratosphere at 40°N between 15 and 20 km appears to be from 6 to 10 months, depending on the season of injection.

INTRODUCTION

There is renewed interest in the meteorological community, particularly among those engaged in developing numerical models of global circulation, in stratospheric distribution of radioactivity from nuclear events, since it can be followed for many months to verify the transport and diffusion simulated by their models.

The three Chinese high-yield nuclear tests of June 17, 1967, December 28, 1968, and September 29, 1969, presented such opportunities. Each had a total yield of about 3 megatons (MT), was detonated as an air burst at 40°N, and initially injected most of its debris into an altitude range of 15 to 20 km, the SST cruise range. The debris from these events has been injected into an atmosphere relatively free of debris from earlier Northern-Hemisphere nuclear tests. To distinguish the radioactivity from the Chinese events not only amongst themselves, but also from debris injected into the Southern Hemisphere at 22°S by the French, concentrations and ratios of short-lived isotopes were used. The age of the debris, and hence its source, can be found from the ratio of Zr-95 (65-day half-life) to Ce-144 (285-day half-life).

The stratospheric distribution of debris from the first Chinese event (June 17, 1967) could be followed for about a year [1] and the second test (December 28, 1969) for about 7 months [2]. This study reports on the distribution of debris from the third event (September 29, 1969), which could be followed for about a year. An effort was made to reconstruct the initial source distribution from all three Chinese events and to report on the depletion of their stratospheric burdens. A comparison of the stratospheric distribution from these events and data concerning events prior to the nuclear-test moratorium of 1963 [1] reveals certain common features.

TRACER DATA

The pertinent information for both French and Chinese nuclear tests is given in Table 1. A test can be classified as injecting its debris primarily into either the troposphere or the stratosphere [3,4], depending on its total yield. The theoretical activity ratio of Zr-95 to Ce-144 at time of production for debris is 4.74 [5] unless there is a separation of isotopes called "fractionation". Table 1 shows the Zr-95 to Ce-144 ratios for the individual high-yield tests corrected for radioactive decay to September 29, 1969, the date of the third Chinese high-yield test. Each of the tests in Table 1 should inject part or all of its debris into the lower stratosphere. Several of the French detonations in 1968 and 1970, classified as low-yield (<20 kilotons) or medium-yield (20-200 kT) tests, should have injected debris up to 17 km at most, with the bulk of the debris remaining in the tropical troposphere, and can be ruled out as significant contributors to the stratospheric radioactivity concentrations.

Table 1. French and Chinese High-Yield Nuclear Tests (1968 to mid-1970)

Date	Approximate Total Yield	Zr-95/Ce-144 Activity Ratio* Calculated	Observed
	French, 22°S		
Aug. 24, 1968	2 MT	0.14	0.12-0.22
Sept. 8, 1968	<2 MT	0.15	0.12-0.22
May 31, 1970	High	40	20-70
July 4, 1970	High	53	20-70
	Chinese, 40°N		
Dec. 27, 1968	3 MT	0.46	0.39-0.54
Sept. 29, 1969	3 MT	4.7	3.9-7.0

*Decay-corrected to September 29, 1969

The radioactive decay and growth of the Zr-95/Ce-144 values for the high-yield Chinese and French tests listed in Table 1 are shown graphically in Figure 1. All devices are assumed to produce an activity ratio of 4.74 at detonation. It can be seen that by normalizing the data to the fiducial date of September 29, 1969, the French high-yield tests of August 24 and September 9, 1968, would by radioactive decay have a ratio of 0.14 and 0.15 on September 29, 1969, whereas the high-yield Chinese test of December 28, 1968 would have a ratio of 0.46. The hatched areas about the decay curves of these tests are the assumed ranges associated with these events; they are based on unambiguous samples containing high concentrations. These limits are also shown in Table 1. Samples containing a Zr-95 to Ce-144 ratio outside these ranges are classified as "mixtures". For example, Mixture A is a mixture of the high-yield Chinese test of December 1968 and the two French high-yield tests of 1968. The Zr-95 to Ce-144 ratio of the September 29, 1969 Chinese test with its range (3.9-7.0) is shown similarly in Figure 1. Samples with a ratio between the limits of the December 28, 1968 and the September 29, 1969 high-yield Chinese tests are classified as Mixture B. It can be seen that debris from the high-yield French tests of May 31 and July 4, 1970, would have a ratio of 40 and 53 by correcting for radioactive decay back in time to September 29, 1969. The assumed range is about 20 to 70. Samples with a

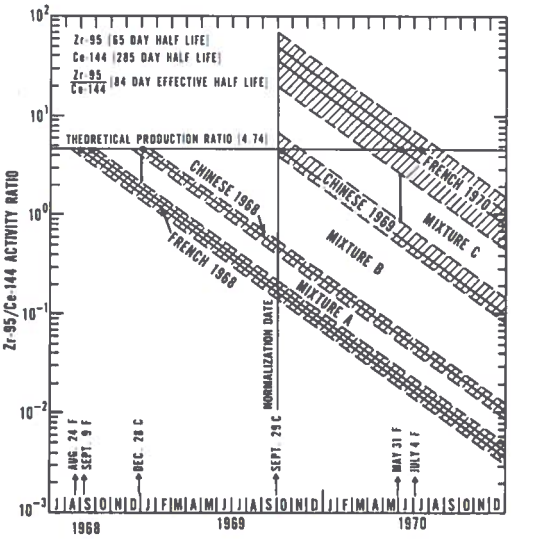

Figure 1. Schematic presentation of the decay rate of Zr-95 to Ce-144 activity ratio for the high-yield Chinese (C) and French (F) nuclear tests of 1968 to mid-1970.

decay-corrected ratio of Zr-95 to Ce-144 falling between the limits of the Chinese 1969 high-yield test and the two high-yield French tests of 1970 are classified as Mixture C.

The French and Chinese test debris can, of course, also be separated because their source latitudes were 62° apart.

DISCUSSION

Latitudinal Distributions

The September 29, 1969 test of the 3-MT nuclear device at 40°N by China occurred when the atmosphere contained relatively small amounts of short-lived fission products, and no injections of debris into the Northern Hemisphere atmosphere had occurred for more than a year. A 3-MT low air burst should result in a cloud top in the vicinity of 21 to 24 km [4] and maximum radioactivity between 15 and 20 km when the debris cloud stabilizes [3,4].

Four successive stratospheric distributions of radioactivity from this event at one-half month, 3 1/2 months, 7 1/2 months, and 11 1/2 months after input show the actual radioactivity distribution based on the U. S. Atomic Energy Commission's quarterly aircraft sampling program to about 20 km [6], and distribution at higher altitudes from the AEC balloon

sampling [7]. Certain cautions must be noted. First, the true altitude and distribution of the debris with height are unknown. Second, aircraft sampling was performed for only a limited number of days along a single corridor extending southward from Alaska over the western North and South American continents to the tip of South America, so that the results may not be representative of the mean latitudinal distribution. Third, the balloon data are limited to only 4 or 5 sites.

The last series of aircraft and balloon data taken before the September 29, 1969 test (July 14-29, 1969) are shown in Figure 2. For this and subsequent figures the isolines are concentrations of Zr-95; the numbers denote the ratio of Zr-95 to Ce-144. All numbers have been adjusted for radioactive decay to September 29, 1969. The letter A following the ratio signifies that the counting error expressed as one standard deviation is between 20 and 50%; B indicates the counting error to be 51-100%; if no letter is listed the counting error is less than 20% and usually less than 10%; an asterisk means that activity is not detectable. The thin dashed line represents the average observed tropopause along the flight path of the aircraft. The observed maximum concentrations of Zr-95 in the Northern Hemisphere were about 7 picocuries per standard cubic meter of air at STP, while those in the Southern Hemisphere were about 3 pCi/SCM. The observed ratio in the equatorial stratosphere had a range of 0.39 to 0.54, which is indicative of the high-yield Chinese nuclear test of December 28, 1968. The heavy lines show the southerly limits of predominantly 1968 Chinese debris and the northerly limits of the French 1968 high-yield tests, which have a ratio lying between 0.18 and 0.22. Between the boundaries of the regions containing Chinese or French debris lies a mixture of the two.

During October 13-17, 1969, approximately two weeks after the Chinese 1969 event, stratospheric samples were again collected. The analysis of these data is shown in Figure 3. It can be seen that the maximum concentrations in the Northern Hemisphere have increased from a low pre-test background of 7 pCi/SCM to 5000 pCi/SCM, with the highest concentrations from 17 to 19 km between 40° and 65°N. The regions containing debris predominantly from earlier tests are delineated by the heavy lines. There is

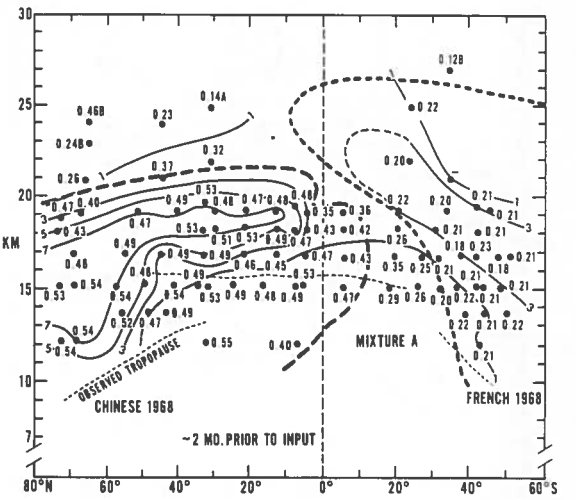

Figure 2. Distribution of Zr-95 and Zr-95/Ce-144 for July 14-29, 1969. Solid lines are isopleths of average Zr-95 concentrations (pCi/m^3 STP) corrected for radioactive decay to September 29, 1969. The numbers represent the activity ratio of Zr-95 and Ce-144. The thin dashed lines represent the mean tropopause along the aircraft sampling corridor.

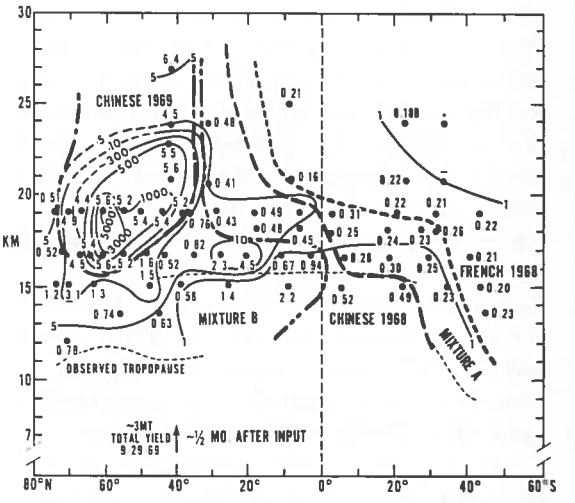

Figure 3. Distribution of Zr-95 and Zr-95/Ce-144 for October 13-17, 1969 (see Figure 2 for nomenclature).

less confidence in this pattern than in subsequent ones because the nuclear cloud is likely to have been more inhomogeneous.

Three months later (January 5-20, 1970) debris was again collected; the analysis of this debris is shown in Figure 4. The 1969 Chinese test, which was originally contained mainly in a

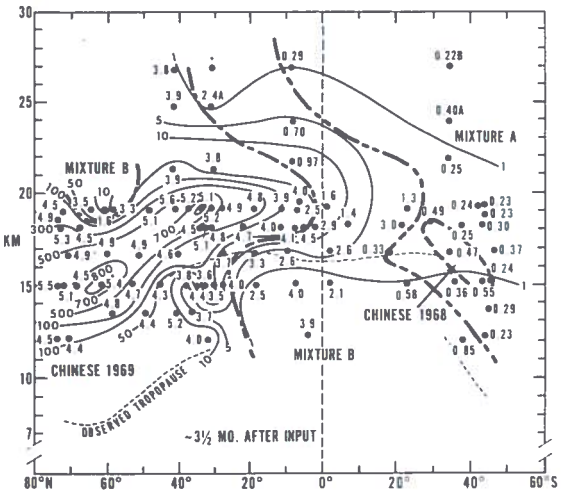

Figure 4. Distribution of Zr-95 and Zr-95/Ce-144 for January 5-20, 1970 (see Figure 2 for nomenclature).

latitude band of about 25° (40-65°N), has now spread to encompass virtually the whole Northern-Hemisphere lower stratosphere, with the isolines of highest concentration sloping from higher altitudes in the equatorial region to lower altitudes in the polar region. The radioactivity-concentration data indicate that during the winter the quasi-horizontal eddy mixing was sufficiently intense to produce a very small north-south gradient along the line of maximum concentration. Again on the basis of ratios, regions containing similar characteristics are separated by the heavy lines. In the Southern-Hemisphere temperate stratosphere, although the concentrations are low, a region whose Zr-95/Ce-144 values would be classified as Chinese 1968 debris appears to be surrounded by a mixture of French and Chinese 1968 debris.

In early May 1970, radioactivity samples were again collected; an analysis of these data is shown in Figure 5. The regions containing similar ratios are separated by the appropriate heavy lines. The Chinese 1969 test dominates the Northern-Hemisphere lower stratosphere and the equatorial region of the Southern-Hemisphere lower stratosphere. The orientation of the isolines is similar to that in Figure 4, sloping from higher altitudes over the equator to lower altitudes over the northern polar region. At 22 km in Figure 4 a mixture of Chinese 1968 and 1969 debris was indicated over the balloon station at Panama (9°N), while in Figure 5 not only has the concentration increased by over an order of magnitude (the reported concentrations increased from 15 pCi/SCM to 230 pCi/SCM) but the ratio has increased by a factor of 5, indicating this to be Chinese 1969 debris. This is the highest concentration observed above about 15 km; if the data are indeed representative, it is difficult to visualize simple turbulent mixing producing this. Remnants of the mixture of the 1968 and 1969 Chinese debris (Mixture B) are still evident. Low concentrations, together with large counting errors, preclude the classification of the debris in the Southern-Hemisphere temperate stratosphere with any degree of confidence.

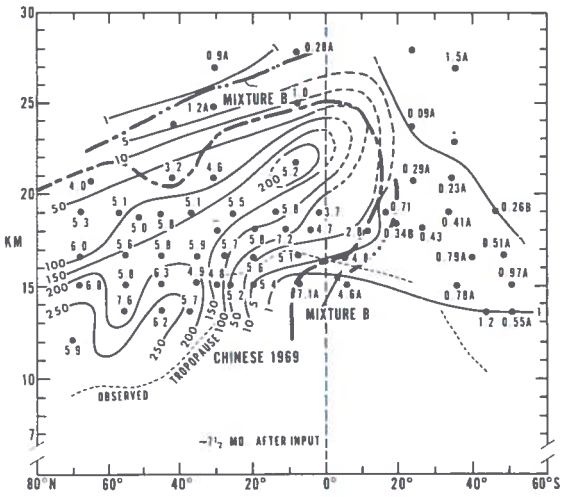

Figure 5. Distribution of Zr-95 and Zr-95/Ce-144 for May 6-11, 1970 (see Figure 2 for nomenclature).

The French conducted high-yield nuclear tests at 22°S on May 31 and July 4, 1970. The input of debris from these tests is quite evident in the samples collected in August 1970 (Figure 6). The heavy line indicates the northerly limit of French debris containing ratios equal to or greater than 20. The Chinese 1969 debris is still very much evident in the Northern Hemisphere, even though the equatorial lower-stratospheric region it once occupied was overwhelmed by French debris. A mixture of Chinese 1969 and French 1970, classified as Mixture C, is also evident in Figure 6. The concentration found in the balloon flights over Panama (9°N) has remained almost constant (230 pCi/SCM at 22 km

in May and 260 pCi/SCM at 21 km in August). The ratio increased from 5.2 to 12.4, indicating that Chinese debris was replaced by a mixture of French and Chinese debris. At 25 km over Panama the concentration has increased by an order of magnitude, and the ratio indicates that the debris, which was previously a mixture of Chinese 1968 and 1969, is now Chinese 1969 debris. At 27 km over Mildura, Australia (34° S) the concentration was essentially zero in Figure 5, while in Figure 6 it is 11 pCi/SCM with a ratio 0f 7.6, indicative of Chinese 1969 debris. Unfortunately, the balloon station at 23° S (Longreach, Australia) was not operating at this time, so it is not confirmed that this one sample taken over Mildura was Chinese 1969 debris penetrating deeply into the Southern Hemisphere. A similar change exists over Mildura at 21 km. Here the concentration increased between May (Figure 5) and August (Figure 6) from essentially zero to 15 pCi/SCM, with a ratio of 3.4 in August, indicating this to be a mixture of Chinese 1968 and 1969 debris.

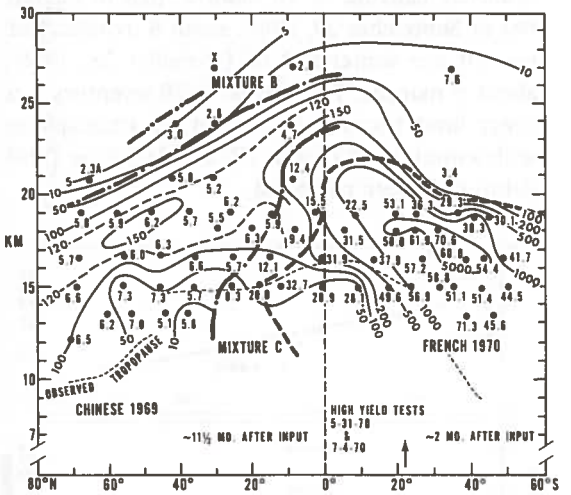

Figure 6. Distribution of Zr-95 and Zr-95/Ce-144 for August 17-22, 1970 (see Figure 2 for nomenclature).

The Chinese conducted a high-yield nuclear test at 40°N on October 14, 1970, preventing a continuation of the history of the Chinese 1969 stratospheric debris.

Estimate of the Initial Vertical Activity Distribution

If the radioactivity from high-yield detonations is used for general-circulation modeling or verification, its changes in space and time must be known. The initial vertical distribution of radioactivity within a nuclear cloud as a function of yield has been estimated by Ferber [3]. Although the total amount of radioactivity produced by high-yield tests may be known, its distribution in the vertical is based on very limited data observed in the equatorial regions of the Pacific. The initial vertical distribution for a 3-MT air burst in temperate latitudes, shown by the dotted curve in Figure 7, is our modification of Ferber's [3] and Peterson's [4] estimates. The bulk of activity is between 14 to 20 km, with the maximum at about 16 km.

An educated guess as to the initial distribution of the Chinese September 29, 1969, 3-MT test can be made from the previous events and the early distribution of radioactivity. Figure 3 (October 1969) shows the latitudinal distribution of Zr-95 concentrations from this test about 2 weeks after input. Integration of the ratio patterns characteristic of predominantly Chinese-1969 radioactivity reveals the stratospheric burden to be about 45,000 kCi of Zr-95, equivalent to a fission yield of about 2 MT. Integration of the Chinese 1969 radioactivity patterns shown in Figure 4 (January 1970) indicates that the burden remains about 45,000 kCi, which suggests that little or no debris has left the stratosphere. This is verified by surface-air measurements, which show little Chinese 1969 debris at surface stations until late winter or early spring, 1970 [8]. The radioactivity distribution in Figure 3 therefore might be used to estimate the vertical distribution, exercising certain cautions. First, it is assumed that the distribution observed along the American meridians about 2 weeks after input is representative of the average concentration in the nuclear cloud; that is, it is zonally well-mixed. This assumption is unlikely to be valid. Second, within this time period vertical transport of the debris by air movement is insignificant and the radioactive particle size of the debris is small enough for gravitational settling in the lower stratosphere (up to about 25 km) to be negligible. The bulk of the activity 2 weeks after the September 1969 test was between 15 and 22 km, with the maximum at about 18 km (Figure 7). Also shown in Figure 7 are the distributions for the June 17, 1967, 3-MT

test about 16 weeks after input and the December 28, 1968, 3-MT test about 6 weeks after input. The general features of the initial vertical distribution for the Chinese 3-MT tests are that the bulk of the activity is located between 15 and 20 km, and it is centered at about 18 km. These features are in general agreement with the distribution assumed a priori.

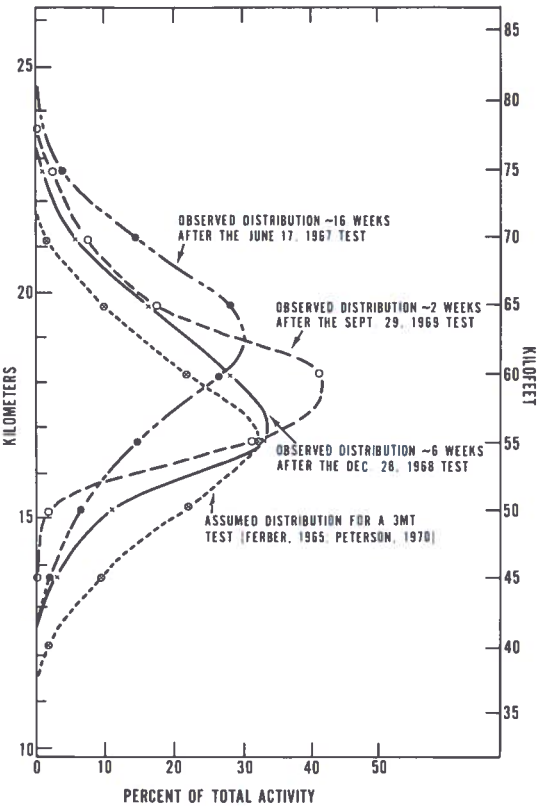

Figure 7. Observed vertical Zr-95 activity distribution for the 3-MT total-yield Chinese nuclear tests of 1967, 1968, and 1969.

Stratospheric Burdens

The modelers of stratospheric tracers must know not only the initial source distribution and its change in time and space, but also the depletion rate from the stratosphere. The residence halftime in the stratosphere has been used to denote the rate of transfer from the stratosphere to the troposphere; particulate radioactivity is subsequently removed from the troposphere primarily by precipitation scavenging. The residence halftime is that time required for material in a reservoir to decrease to one-half of its initial amount, as shown in Figures 3-6; corrections for radioactive decay are applied before computing the residence halftime. The assumptions inherent in this definition are that the fractional removal is constant with time and that fast mixing within the reservoir preserves the uniformity of concentration in the reservoir. These assumptions are less valid for the stratosphere than the troposphere. An examination of Figures 3-6 indicates that the stratosphere is not well mixed, even though its radioactivity burden is decreasing. This non-uniformity, which suggests slow mixing on a time scale of many months, is characteristic of all past debris distributions.

Accepting these limitations, the residence halftimes of the Zr-95 burden for the Chinese 3-MT tests of 1967, 1968, and 1969 are shown in Figure 8. The vertical arrow points to the inferred fission yield for each event; note that this fission yield, based on the production of Zr-95, does not exceed the total yield of 3 MT. It can be seen from Figure 8 that the residence halftime depends on the timing of the test. The summer test of June 17, 1967, had an estimated residence halftime of 10 months; that of the fall test of September 29, 1969, about 8 months; and that of the winter test of December 28, 1968, about 6 months. The August 1970 inventory is a lower limit because volumes of the stratosphere with a mixture of French 1970 and Chinese 1969 debris have been neglected.

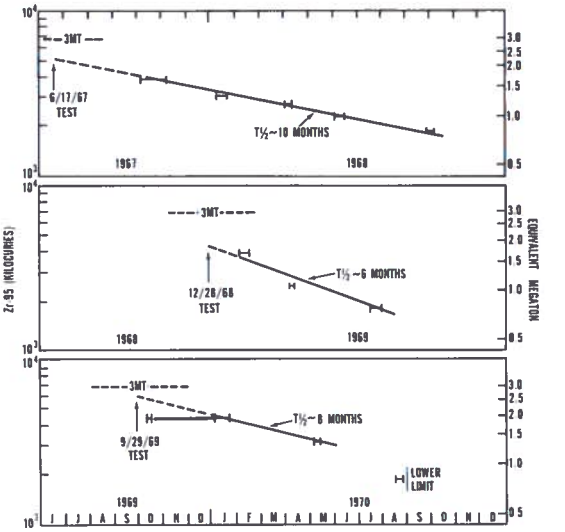

Figure 8. Stratospheric residence halftime of the Zr-95 burden for the 3-MT total-yield Chinese nuclear tests. Observed burdens are indicated by the short horizontal lines.

It has been noted from earlier nuclear-test data that the annual fallout in the Northern Hemisphere would be approximately the same as the amount of debris found in the volume of the stratosphere bounded by the tropopause and 17 km and lying between 30°N and the North Pole [9]. Telegadas [10] reported that the stratospheric burden of debris in this compartment had a cyclical behavior such that the burden had a maximum in the winter and spring seasons and a minimum in the summer and fall seasons. This suggested an influx of debris during fall and winter. In the late winter and spring, about a month or so before the period of maximum deposition on the ground, the debris is transferred to the troposphere. A composite picture for the three Chinese events reveals that the residence halftime in the fall-to-winter period is 16 months; winter-to-spring, 7 months; spring-to-summer, 9 months; and summer-to-fall, 11 months. These average residence halftimes are consistent with Telegadas' findings [10].

It can be seen in Figure 8 that the stratospheric Zr-95 burden for the September 29, 1969 test observed in October 1969 and January 1970 remained almost constant, and was not observed to decrease until the next observation time of May 1970. An extrapolation of the stratospheric burdens back to time of injection in Figure 8 might be in error, insofar as a finite time elapsed before the debris from the summer and fall tests was redistributed and made available for exchange with the troposphere. If this is so, the concept of residence halftime is totally unacceptable for the first few months following an injection.

Common Features

Machta et al. [1] summarized the data from several tracers having individual sources and measurable distributions in the stratosphere many months after input. The tracers examined were: (1) tungsten-185 (W-185) a year after its input into the equatorial lower stratosphere in the summer of 1958; (2) the short-lived fission product strontium-89 (Sr-89) from the nuclear tests in polar latitudes in the fall of 1961 for about 6 months; (3) cadmium-109 (Cd-109) 42 months after input into the equatorial thermosphere (about 400 km) in the summer of 1962; (4) the plutonium-238 (Pu-238) resulting from a satellite reentry and burn-up in the mesosphere (40 to 60 km) at 11°S in April 1964; and (5) the short-lived nuclide Sr-89 from the Chinese 3-MT nuclear detonation at 40°N in June 1967.

Figure 9 shows the observed levels of maximum concentration of these tracers, and also a tracer injected into a stratospheric model by the NOAA Geophysical Fluid Dynamics Laboratory. A feature common to all these tracers is the slope of the level of maximum concentration from higher altitudes over the equator to lower altitudes over the polar region. The three tracers introduced into the lower stratosphere at different seasons and latitudes of injection (75°N, 40°N, and 11°N) had almost identical slopes after 6 to 12 months despite the probable differences in initial altitude and vertical distribution of debris. We conclude that the explanation for the phenomenon is meteorological.

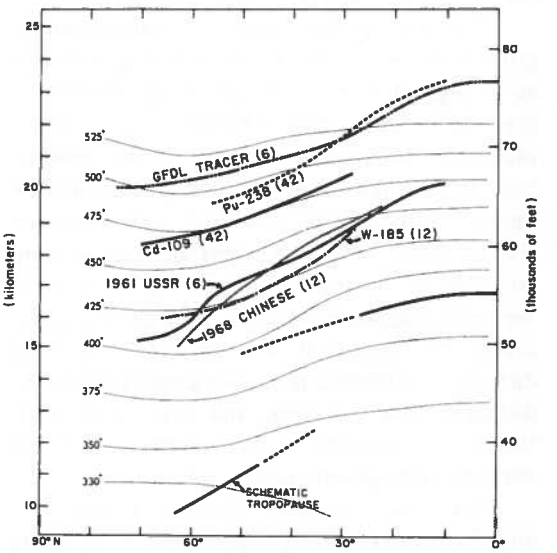

Figure 9. Observed levels of maximum concentration and mean annual isentropes. Numbers in parentheses are months from injection into the stratosphere to observation. (After Machta et al. [1].)

The stratospheric distribution of radioactivity based on the last observed data after the Chinese 1967, 1968, and 1969

high-yield tests is shown, in part, in Figure 10. The isolines are Zr-95 concentrations (pCi/SCM) decay-corrected to the date of the individual test; the dashed line is the level of maximum concentration. An estimate of the slope of the line of maximum concentration is also given. Although the time after the events varied from 7 to 16 months, the Zr-95 stratospheric burden for all three cases is almost the same, about 19,000 kCi. Remember that the sources (the fission yields) were also quite similar. The most striking feature of Figure 10 is the almost identical slopes of the lines of maximum concentration (about 0.1 kilometer of altitude per degree of latitude, making an angle of less than 0.1° with the horizontal), sloping from higher altitudes over the equator to lower altitudes over the northern polar regions, similar to the results shown in Figure 9. Figure 11 displays the same pictures for the three Chinese nuclear tests about 7 months following the detonations. The slopes found in all three figures, 9, 10, and 11, are remarkably similar considering the natural atmospheric and sampling variability.

The vertical distributions of concentrations around the line of maximum concentration such as in Figures 4, 5 and 6, and in similar pictures for the earlier two Chinese tests, exhibit relatively small vertical spread. If one assumes that the vertical transfer takes place solely by mixing away from the level of maximum concentration, the coefficient of mixing turns out to be of the order of 1 to 5 x 10^3 cm^2 sec^{-1}. We must emphasize, however, that the characterization of transfer in the vertical by a single diffusion coefficient is an oversimplification; the diffusion varies in time and space, and other transfer processes, particularly organized motions, may play important roles.

The same transfer process involving a quasi-horizontal mixing coefficient can be found from the north-south concentration pattern along, say, the lines of maximum concentration. Here the composite picture of the three events 7 months after input suggests that the quasi-horizontal diffusion or mixing coefficient along the surface of maximum concentrations is 5 x 10^9 cm^2 sec^{-1} (with a very large variability amongst these three cases), if all transport is assumed to take place by a flux-gradient process. Again, the reservations noted at the end of the previous paragraph apply.

SUMMARY

The three high-yield Chinese nuclear tests of June 17, 1967, December 28, 1968, and September 29, 1969 provided tracer material to illustrate transport and dispersion in the lower stratosphere. The inputs took place at 40°N, mainly in the range of 15-20 km, the SST operating range.

Four successive pictures of the distribution of the radioactivity from the event on September 29, 1968, at one-half month to about 12 months after input depict the actual concentration distribution along the U.S. Atomic Energy Commission's aircraft and balloon network. To distinguish the radioactivity from this event from preexisting radioactivity, a short-lived isotope, Zr-95, and the ratio of Zr-95 to Ce-144, have been employed.

The integrals of stratospheric content from the three Chinese nuclear tests show a decrease with time which suggests residence halftimes of between 6 and 10 months, or mean residence times of between 9 and 14 months. Although it is believed that loss of radioactivity in the lower stratosphere (below 20 km) is very small because of the sedimentation of particles, this sedimentation may produce a smaller residence halftime than would be the case if the substance were gaseous.

Perhaps the most common feature of the radioactivity patterns of the three Chinese tests, as well as many other stratospheric tracers, is the slope of the line (or surface) of maximum concentration, downward towards the poles and in excess of the slope of the isentropic surfaces. This is found at virtually all times after the injections. The gradient of concentration along this line of maximum concentration suggests a coefficient of lateral mixing of 5 x 10^9 cm^2 sec^{-1}, and for the gradients normal to it, a vertical mixing coefficient of 1 to 5 x 10^3 cm^2 sec^{-1}.

ACKNOWLEDGMENT

The support of this work by the Division of Biomedical and Environmental Research, U.S. Atomic Energy Commission, is gratefully acknowledged.

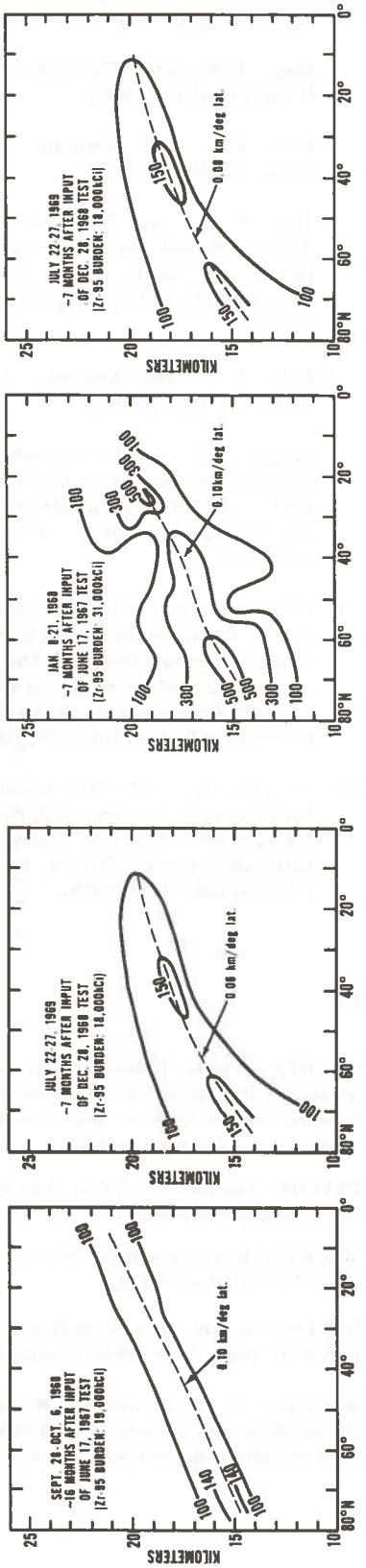

Figure 10. Observed levels of maximum concentration for the three high-yield Chinese nuclear tests of 1967, 1968 and 1969. Solid lines are isopleths of average Zr-95 concentrations (pCi/m^3 STP) corrected for radioactive decay to date of test. Dashed lines are the levels of maximum concentrations, with an estimate of the slope.

Figure 11. Observed levels of maximum concentration for the three high-yield Chinese nuclear tests of 1967, 1968, and 1969 about 7 months after input. (See Figure 10 for line designations.)

REFERENCES

1. Machta, L., Telegadas, K., and List, R. J., 1970: "The slope of surfaces of maximum concentration in the lower stratosphere", J. Geophys. Res. *75*, 2279-2289.

2. Telegadas, K., 1971: "The upper portion of the Hadley cell circulation as deduced from 1968 French and Chinese nuclear tests", J. Geophys. Res. *76*, 5018-5024.

3. Ferber, G., 1965: "Distribution of radioactivity with height in nuclear clouds", in *Radioactivity Fallout from Nuclear Weapons Tests*, U.S. Atomic Energy Commission Publ. 5, Symposium Series, 629-645 (available from NTIS, Springfield, Va. 22151).

4. Peterson, K. R., 1970: "An empirical model for estimating world-wide deposition from atmospheric nuclear detonations", Health Physics *18*, 357-378.

5. Harley, N., Fisenne, I., Ong, L. D. Y., and Harley, J., 1965: "Fission Yield and Fission Product Decay", U.S. AEC Health and Safety Lab. Quarterly Summary Report. HASL-165, 251-260 (available from NTIS).

6*a*. Krey, P. W., and Kleinman, M., 1970: "Project Airstream", U.S. AEC Health and Safety Lab. Quarterly Summary Report, HASL-224, II-9, to II-34 (available from NTIS).

b. Krey, P. W., and Kleinman, M., 1971: *ibid*, HASL-239, II-10 to II-73.

c. Krey, P. W., and Kleinman, M., 1971: *ibid*, HASL-242, II-10 to II-51.

d. Krey, P. W., and Kleinman, M., 1971: *ibid*, HASL-243, II-10 to II-37.

7*a*. Krey, P. W., and Kleinman, M., 1971: "High Altitude Balloon Sampling Program", U.S. AEC Health and Safety Lab. Quarterly Summary Report, HASL-239, II-75 to II-129 (available from NTIS).

b. Krey, P. W., and Kleinman, M., 1971: *ibid*, HASL-245, II-37 to II-93.

8. Telegadas, K., 1972: "Atmospheric radioactivity along the HASL ground level sampling network, 1968 to mid-1970, as an indicator of tropospheric and stratospheric sources", J. Geophys. Res. *77*, 1004-1011.

9. U.S. Government, 1963: "Estimates and Evaluation of Fallout in the United States from Nuclear Weapons Testing Conducted Through 1962", Report of the Federal Radiation Council, F.R.C. 4 (available from Superintendent of Documents, U.S. Government Printing Office, Washington, D.C.).

10. Telegadas, K., 1968: "The Seasonal Stratospheric Distribution of Cadmium-109, Plutonium-238 and Strontium-90", U.S. AEC Health and Safety Lab. Quarterly Summary Report, HASL-184, I-53 to I-118 (available from NTIS).

DISCUSSION

ELLSAESSER: I have seen a paper on the Mt. Agung cloud which shows contour heights and isochrones over Australia. On the basis of measurements of the wind profiles at levels corresponding to the apparent movement of the cloud, the paper concluded that as the cloud moves poleward it is ascending.

MACHTA: I am sceptical of its validity, since evidence in both hemispheres shows that everything else slopes downward toward the pole.

BARRETT: It seems to me that you cannot really talk about a residence time until the injected material is more or less evenly distributed longitudinally. Before then, it is following the global general-circulation pattern, rather than an eddy-diffusion mechanism.

MACHTA: I agree; I would prefer not to deal with residence time at all, but just derive the exchange between the stratosphere and troposphere from the physics of atmospheric transport.

TAYLOR: You mentioned that there was a variation in fallout time with latitude. What was it based on?

MACHTA: It was a sort of average, integrating from about 20°N to about 80°N.

BAUER: Did you feel you could specify vertical eddy diffusivity better than within a factor of two or three?

MACHTA: We can describe the standard deviation of the variation with altitude; it is up to you whether you want to convert that to eddy diffusivity.

THE PHYSICS AND CHEMISTRY OF STRATOSPHERIC AEROSOLS

PANEL DISCUSSION

JAMES P. FRIEND
New York University
Chairman

RICHARD CADLE	*National Center for Atmospheric Research*
MYRON CORRIN	*Colorado State University*
ROCCO NARCISI	*Air Force Cambridge Research Laboratories*
E.T. PIERCE	*Stanford Research Institute*

FRIEND: The panel members have been asked to make preliminary remarks on the state of current knowledge in the following fields: temporal and spatial distribution of concentrations; sources (which includes mechanisms of aerosol formation); size distribution and composition, which also relate to optical properties; use of aerosols as tracers for stratospheric air masses, and the chemical and physical aspects thereof; and models of aerosol formation and dispersal.

CADLE: This morning's talks have covered a good deal of the temporal-distribution question, particularly the University of Wyoming paper. The latter showed that there has been a general decrease in the concentration of the so-called sulfate layer, at least since the 1963 Agung eruption. Some of our work at NCAR has also shown this.

Some of the particulate material can be traced to volcanoes, but some cannot. Brookhaven's HASP project is doing some interesting work along this line. They have taken filter samples collected by the AEC over many years and analyzed their sulfur-32/sulfur-34 ratio. They have found that every time the concentration increases, the delta value of these isotopes decreases sharply. This suggests a volcanic origin for the particles.

As far as spatial distributions of concentration are concerned, we at NCAR have been making studies in connection with the AEC's Project Airstream. We are taking samples at four altitudes over a meridional range of something like 65°N to 65°S; the results show variations with latitude very similar to those Lester Machta discussed this morning in connection with radioactive debris. The total integrated amounts of particulate material in the stratosphere above various points were roughly the same, but the altitude at which the maximum occurred varied markedly with latitude. Like Machta, we found that it was highest in the equatorial regions and lowest near the poles.

One interesting aspect of this – and there are several – is that there is reason to believe that the sources of the materials we are looking at are very different. For example, sometimes the amount of silicate present, which may be either volcanic ash or soil, is almost as great as the amount of sulfate, yet silicates and sulfates normally show the same altitude distribution as a function of latitude. Nitric-acid vapor seems to follow a very similar pattern.

As far as sources are concerned, there have been two major theories as to how the "sulfate layer" is formed. One is that it is the result of oxidation of sulfur dioxide. I think that if this is the major source, the oxidizing agent is atomic oxygen, and the formation of sulfate takes place in the stratosphere. The other theory is that the layer isn't really a sulfate layer *per se*, but just a layer of large particles produced by the agglomeration of sulfate particles in the form of Aitken nuclei which somehow got into the stratosphere. (Of course, there are many other substances in that layer, such as silicates.) I think most people feel that the major sources of the sulfate are the reactions that lead to the oxidation of sulfur dioxide to sulfur trioxide, SO_3, which reacts immediately with water vapor to form droplets of sulfuric acid.

There is one other possible source of sulfate. Volcanic eruptions not only put large amounts of sulfur dioxide into the atmosphere, but also inject large amounts of sulfate. Apparently considerable oxidation of SO_2 occurs in the eruption cloud, while the hot gases are being injected into the stratosphere.

With regard to size distributions, we are collecting particulate material on filters flown on a B-57F aircraft, which are very efficient far down into the Aitken size range. It is interesting that as the particulate concentrations decrease the lidar measurements drop to zero. The lidar does not show Aitken particles, because of their poor scattering efficiency, so the discrepancy suggests that the decrease in concentration occurs in this size range, 0.1 to 1 μm radius.

Going back to spatial distributions, I think one is almost forced to assume that stratospheric air motions are responsible for the aerosol distribution along the meridian and the variation in altitude of the maximum concentration as a function of latitude. Stratospheric aerosols serve as a means for studying the mixing in the stratosphere and the exchange between the stratosphere and troposphere. Sulfate particles, like ozone and radioactive material, have been used quite successfully to demonstrate that upward motion or mixing of tropospheric air into the stratosphere on the anticyclonic side of the jetstream occurs at the same time that stratospheric air is brought down into the troposphere by the so-called "tropopause folding".

FRIEND: What do you think of the quality of the present data and the extent of our knowledge of the temporal and spatial distributions of the concentrations? The University of Wyoming has done a number of vertical soundings recently. We have a great deal of lidar data, but it was taken rather sporadically. The last direct sampling that gave us size distributions was done quite a while ago. Do you feel that it would be useful to have more knowledge in this area?

CADLE: Well, I have a few ideas, of course. One thing we know almost nothing about is the organic composition of stratospheric particles, if in fact there are organic particles. I think this could be very important, since a lot of the particulate material in aircraft exhaust will presumably be organic. It is very difficult to study, however.

Another thing we are doing at NCAR is collecting particles along a meridian at various altitudes during different meteorological conditions. We hope to get more information on the role that stratospheric air motions play in determining the distribution of particulate material in the stratosphere.

Efforts are also being made to model the processes which result in the particle size distributions we observe.

You might also be interested, in connection with particle concentrations, in one of our recent studies. During the last few months we have been comparing the relative efficiencies of our current filters and the impactors originally used in collecting aerosol particles in the stratosphere. The five flights made so far show that the relative efficiency of the impactors is between 13 and 18% of the filters' efficiency, so to compare early results with recent ones you would have to multiply them by a factor of six or seven. Of course, this difference in efficiencies does not account for the differences in stratospheric particle concentrations before and after the Agung eruption of 1963, which were a factor of 50 or so.

FRIEND: I'd like to add a few of my own opinions. It seems to me that sampling over a single point on the earth does not give you enough information about the distribution of concentrations. The results of stratospheric sampling for radioactive material suggest that a reasonable amount of spatial and temporal coverage is required, and that the sampling must be continuous so that there will be no large gaps in the data. Of course, time and space smoothing will be done on the results to obtain an integral or average, so that large-scale features of these distributions can be determined. However, if there are large variations which are not taken into account because of inadequate sampling, the results may be seriously wrong.

There is one question I should like to see addressed, and answered through more comprehensive sampling and analysis. In the early 1960's, Stan Mossop and I both found, using

electron microscopy, that most of the particles collected on impactors were ammonium sulfate. More recent findings show that present-day aerosols contain very small amounts of ammonium relative to sulfate, implying that it is mostly sulfuric acid that exists in the stratosphere. I think ammonia gas mixes into the stratosphere from the troposphere, subsequently reacting with the sulfuric acid, and that the process is probably highly variable in both space and time. I should like to see further study done on the matter, however.

CORRIN: I would like to raise a different issue: the role of particulates in the chemistry of the stratosphere. The importance of the interaction between particulates and the gases surrounding them can be illustrated by an admittedly extreme example: the introduction of 5 to 10 silver-iodide particles per liter into a cloud has a marked effect on what goes on inside that cloud.

I think we need to know more about the composition of the chemical species present in the stratosphere. We already know the elements and the ions. The University of Wyoming presentation this morning reinforces my belief that particulates play an important role in terms of a surface process which enables them to combine chemically with gases, or to act as catalysts for heterogeneous gas-phase reactions. Since I suspect that a process involving physical adsorption is likely to be insignificant, I think that it is catalysis that we should look at.

CADLE: I once made a back-of-the-envelope calculation, using ordinary gas-kinetics theory, of the rate at which ozone molecules would hit stratospheric particles. Assuming that the particles had a 0.5-μm radius and a concentration of about 0.3 $\mu g\ m^{-3}$, and that every molecule of ozone would decompose in a unimolecular reaction when it collided with a particle, the rate of decomposition would be orders of magnitude faster than the air exchange rate. If ozone were decomposed this efficiently, the rate of collision would certainly be fast enough for decomposition to be important.

As far as the catalytic action of the particles on two reacting gases is concerned, the situation is quite different. One of the gases would have to be greatly in excess over the other, and would have to be very strongly adsorbed on the surface to give enough coverage to make it likely that the collision with the other species would be sufficiently rapid to lead to a reaction.

So for one type of chemical reaction, such as ozone decomposition, the particles *could* play a role. It is improbable, though, that at these extremely low concentrations there would be enough physical adsorption of one species on a particle that the other species would be likely to hit the covered surface and react.

FRIEND: If the decomposition mechanism were actually at work there would be a strong negative correlation between the ozone and the particles. Presumably it would be possible to measure it, if it were fast enough in comparison to the time required for exchange of stratospheric air.

CADLE: That's true, provided nothing else interferes. If there were a great deal of mixing the correlation would be lost in the process; we are talking about long periods of time.

(UNIDENTIFIED): It should be pointed out that the two principal constituents of stratospheric aerosols, sulfuric acid and silica, are non-catalytic to ozone in the laboratory.

CADLE: Yes, that's so. I started out to show that ozone destruction could not be significant, just on the basis of lifetimes in the atmosphere and particle concentrations, but my quick calculation showed that it could not be ruled out.

CORRIN: I think it quite possible that the particulates found in jet-engine exhaust may be much more effective catalysts for ozone decomposition than silica or sulfuric acid.

NARCISI: I should like to address the question of aerosols from the point of view of CIAP. It seems to me that CIAP should be most concerned with defining the perturbations caused by aircraft, by making in-situ measurements of the spatial and temporal variation of the particles in the exhaust trail – their concentrations, their sizes, and their composition. I also think that whole-air sampling and other techniques should be used to measure the spatial and temporal distribution of NO, SO_2, and other gases at the same time.

I did some back-of-the-envelope calculations too, and came up with some rather ridiculous possibilities. I found I could manipulate the numbers to show that 100% of the engine pollutants, like water vapor, NO_x, SO_2, hydrocarbons, and particulates, could form aerosols, settle out of the stratosphere into the troposphere, and eventually wash out. We certainly need some serious and detailed calculations.

As for the possible formation of aerosols: There are particulates in the exhaust trail, as was mentioned earlier. There are neutral gases – specifically, polar molecules – which are possible condensation nuclei. There are ions; a measurement of ion concentration (both positive and negative) at the exit plane of a small jet engine showed about 10^7 ions cm^{-3} with essentially no electrons, since three-body attachment to O_2 is very fast. The particulates, gases, and ions can all serve as centers for possible condensation.

GOLDBURG: Would it be possible to see the exhaust trail if all the exhaust constituents were converted to particulates?

NARCISI: The probability of visible exhaust trails' occurring at 20 km is very low, but they have been seen on a very few occasions. It depends on the number of condensation centers available, and whether the particles grow to visible sizes. About 3-μm particles are needed for the sedimentation velocities which remove particles from the stratosphere at a rate of about 10 km a month. Not much is known about the rate of gas-to-particle conversion; experimental evidence shows that it can be very fast in adiabatic free jet expansions, UV photolysis of water vapor, and the like. After initial expansion, the exhaust trail remains fairly constrained for a long time, allowing particle growth.

GOLDBURG: Nonetheless, experimental evidence indicates that exhaust trails are not visible in the stratosphere.

VOLZ: I have seen photographs of primary contrails from rocket launchings on the Pacific Coast, but I have never seen anything like an aerosol contrail from an ordinary jet aircraft after sunset in the bright twilight arch where you would be most likely to see it. That includes high-altitude aircraft contrails.

GELINAS: We could clearly see the shadows of the contrails on the cloud layer below us at 37,000 feet from the plane yesterday.

ROSENBERG: RB-57 pilots say that on occasion the planes lay contrails at 50,000 or 60,000 feet, so apparently there are visible particulates on occasions when the climatic conditions are right.

VOLZ: The RB-57 pilots probably view along the trail of carbon particulates which do not scatter enough light to be visible from the ground.

NARCISI: Also, there is experimental evidence that a lot of the particulates formed are stable under extreme conditions of temperature and pressure. I just point this out as a possibility. We don't really know how many molecular clusters are being formed, and, once the gases have formed some sort of small particle, how they react chemically in the atmosphere. The situation is very complex, and I suggest it be given serious study. In any case, what I should like to stress is that the measurements should be made in situ, in the exhaust of an aircraft, where the conditions for particle formation exist. This is my main point: define the perturbation, in terms of particle composition, size distribution, and so on.

FRIEND: I neglected to mention earlier that many of these issues were discussed last month at a meeting in San Coroniti's office, chaired by Christian Junge. One of the questions that wasn't resolved was precisely this matter of looking at the perturbed stratosphere. One point of view is that we must study the significant aspects of the natural stratosphere before we can understand the perturbed stratosphere. Dr. Narcisi's point is that much of this slow, costly detailed work could be bypassed in favor of experiments and measurements on systems directly related to the perturbed stratosphere. Myself, I favor doing some of each.

PIERCE: My basic interest is in the electrification of the atmosphere, from the stable situations to the ultimate transients of the lightning discharge. If we consider the stable situation, our primary interest is the ionic concentrations, and the nature and characteristics of the ions. The people who study the subject have traditionally

been divided into the atmospheric electricians like Siksna, who work in the troposphere, and the D-region people like Narcisi, who work up around 70 km. Thanks to CIAP, they have finally gotten together in the stratosphere.

Now, what do the ions of the atmosphere have to do with aerosols? We have long known that the electrical and ionic state of the troposphere is very sensitive to the pollutant and particulate content. Small or cluster ions, which consist of a few molecules, attach themselves to the aerosols, and thus change their electrical characteristics completely. We believe that this sensitivity to particulate content increases as we go up into the stratosphere. Unfortunately, the experimental evidence on the electrical characteristics of the stratosphere is not very complete; measurements have been made over the last 12 or 15 years, but only spasmodically. However, I do have confidence in the early work of Kroening in the USA, of Paltridge in Australia, of Mühleisen, Fischer, and some others in Germany, and of certain active groups in Japan – including Drs. Ogawa and Ishikawa, whom I see in the audience.

Let me mention one of the salient results of the better data. A profile of the small-ion content against height shows a great deal of fine structure; there are variations of about 10% to 20% in a height range of a few hundred meters. (This is just what Dr. Hofmann's profiles showed this morning for particulates, water vapor, and ozone.) We feel that the most plausible theoretical interpretation of this small-ion fine structure is that it is associated with the fine-particulate structure: many of the small ions attach themselves to particulates, become large ions, and are lost as far as electrical conductivity goes.

Now to put some numbers into this, let us say we have a 10% variation in small-ion concentration at 15 km. According to our theory, this could be produced by one 1-μm particle or six 0.3-μm particles per cubic centimeter. Dr. Hofmann's profiles showed concentration variations over a few hundred meters at 15 km of about two particles greater than 0.3 μm per cubic centimeter, which is pretty good agreement with theory.

As an experimentalist, I enjoy tests of theory. I should like to see simultaneous measurements of electrical profiles and aerosol profiles, so that we could tell whether there really is a connection between the two. If so, we could then confidently use electrical measurements – which are fairly easy to make – as indicators of particulate content.

FRIEND: Do you think that the formation of ions can lead to the formation of large particles in the stratosphere?

PIERCE: I feel this is an unresolved but important question. It would establish another connection between ion content and particulate concentration.

ELLSAESSER: At the meeting in Washington last month, Dr. Junge suggested that there were two distributions of particulates – large ones, which were sulfates, and small Aitken nuclei, of essentially unknown composition. Do we know anything more about the latter's composition, or whether there is a continuous distribution in the size range between the two?

CADLE: The work done over the last decade tends to give one the impression that there is a change in size distribution with time. Dr. Junge's impressive early work involved measurements with an Aitken-nuclei counter. He got concentration profiles, and then made particle collections using impactor surfaces whose collection efficiency was good down to about one-tenth micrometer densities. He obtained much higher mass concentrations for the 0.1 to 1 μm particles, which indicated that most of the particles were much larger than Aitken nuclei. Our more recent particle-collection data, interpreted in the light of the absence of lidar returns, suggest that the particle size distribution has changed, with Aitken particles now predominating. This is speculative, however, since our filters' collection efficiency has not been calibrated in the Aitken size range.

FRIEND: We have been studying in my own laboratory the mechanism of the formation of stratospheric aerosols. We think the two size distributions are real, and have an educated guess as to how they come about. The formation of Aitken nuclei can be accounted for by the following process: SO_2 is oxidized by O-atoms in a three-body reaction – and also, as Doug Davis

pointed out, by HO_2 – to give SO_3. This then forms H_2SO_4, which can rapidly collect water molecules to form a hydrated embryonic nucleus of sulfuric acid. In our laboratory tests, larger particles have been formed by the coagulation of these nuclei. If ammonia gas is added to this mixture of air, water vapor, sulfur dioxide, and sulfuric acid nuclei, a population of large particles of ammonium sulfate is very rapidly formed.

Thus, from a population of Aitken nuclei, which might be in a quasi-steady state of coagulation like that given by Friedlander's theory, a population of large ammonium-sulfate particles can be grown. If ammonia is in limited supply, further coagulation and mixing will give intermediate compositions. We hope, of course, that this laboratory experimentation has some bearing on what is actually going on in the stratosphere; we can produce results consistent with various observations of the behavior of stratospheric particles, but we may not have the whole picture.

CADLE: I should like to add that if what we are collecting now are primarily Aitken particles, they must be very similar in composition to the larger ones collected previously. There is very little difference in composition between particles from recent collections and those collected two or three years ago, when the concentrations were much higher.

ROSENBERG: I would like the panel to address the problem of vertical fluctuations of aerosol content. Such fluctuations in the ionosphere have been ascribed to the interactions of electric fields, wind shears, and ionized particles. I don't think that particles of the size we are discussing have significant mobility in magnetic fields or under the wind shears involved, however, and photochemically it is difficult to account for more than a single layer. What sort of mechanism can explain the multiple layers present over thousand-kilometer separations reported by the Wyoming group?

FRIEND: In terms of the mechanism we have been studying, ammonia is very critical as a participant in the catalytic oxidation of SO_2. This oxidation of embryonic nuclei of sulfuric acid and water proceeds very rapidly when ammonia is present. If little patches of ammonia are being mixed into the stratosphere, thin laminae of large particles would be formed. This would account for the Wyoming observations. Also, some of the layer-like characteristics might be due to sporadic, fairly large-scale injections of SO_2, either from volcanoes or from convective processes in the equatorial regions.

PIERCE: Some of the fluctuations in these profiles seem to be associated with minor temperature inversions – a kind of stable trapping of various constituents, but in small stratified layers.

OLIVER: Could the panel discuss the possible role of sulfuric-acid aerosols in NO_x chemistry – that is, the aerosol chemistry of nitrates as a possible sink?

FRIEND: I think that NO_2 would be a good source of O atoms for oxidizing SO_2. If the mixing ratio of NO_x is on the order of 10^{-8}, however, there probably won't be enough SO_2 to have a significant effect on the NO_x chemistry with regard to ozone.

CADLE: In our very first experiments at these altitudes using the so-called IPC filter paper, which is a cellulose paper impregnated with an organic oil, we found that we were getting large amounts of nitrate, but no nitrite at all. We thought of a variety of reasons to account for this. For example, we did not find the ammonium ion we expected. We thought that perhaps the ammonium was being oxidized during or after collection, which would account for both the presence of nitrates and the absence of the ammonium ion. We also thought that perhaps oxides of nitrogen were somehow associated with the sulfuric acid, either chemically or as a solution of nitric-acid vapor in the droplets. After further experiments, however, we concluded that essentially no nitrate or nitrite was associated with the particles we were collecting, that the nitric-acid vapor was in the gaseous form, and that no NO or NO_2 was associated with the particulate material either.

NARCISI: When Joe Calo of AFCRL was discussing his microscopic-scale laboratory work at that meeting in Washington, he mentioned that he had found varying quantities of small molecular clusters of H_2O, SO_2, and NO resulting from free jet expansion of mixtures of those compounds. Of course, we don't know whether these clusters are stable in the long term.

DAVIS: As a chemist, I am a little confused by your claiming that sulfuric acid formed in the stratosphere reacts with ammonia, while nitric acid just sits there. Can you explain this?

FRIEND: I think we could certainly use some calculations on this. We need to consider, though, what the vapor pressure of ammonium nitrate is over a solid in the stratosphere. Perhaps molecular ammonium nitrate exists there.

CADLE: The amount of ammonium ion we collect is about 1%, far less than the amount of sulfate and nitrate. On the basis of this, I think most of the nitrates must exist as nitric-acid vapor, and most of the sulfates as sulfuric-acid droplets. The same inequality holds for many of the cations other than hydrogen.

ZIMMERMAN: Did you say that particulate matter could reduce ozone in the stratosphere?

CADLE: No, indeed. I merely made the unlikely assumption that every collision of an ozone molecule with a particle would result in decomposition, in an attempt to show that the theory of gas kinetics alone might rule out the possibility of particulate material's having a catalytic effect on the gas-phase reactions. If that assumption were correct – which I doubt – the reaction rate would be orders-of-magnitude faster than the exchange times in the stratosphere, and an inverse correlation between ozone concentration and particulate concentration should be apparent. I doubt that you could see any diurnal effect on composition, since photochemical recovery times in this region are about a year, but this inverse correlation has indeed been pointed out by some experimenters.

ZIMMERMAN: Some of this morning's data seems to contradict that; one paper showed that particle distributions follow the water-vapor distribution fluctuations, and another said that the ozone distributions did the same to some degree.

CORRIN: It is not the number of particles that is important to the catalytic process, but the surface area involved, which is not the same thing at all.

LAZRUS: Do you think that an SST fleet would increase aerosol concentrations so much that the stratosphere's electrical properties would be affected enough to alter the environment?

PIERCE: Well, Dr. Grobecker said at the meeting in Washington that he felt that by 1990 the increased particulate content might be detectable over the whole stratosphere. I think an SST would produce quite a long, traceable path of electrical perturbation.

HINKLEY: Have we any evidence as to what happens in the stratosphere to hydrocarbons such as those which might be emitted by a high-flying jet? Do they tend to go to one particular hydrocarbon? Do they form particulates or aerosols?

FRIEND: The natural stratosphere has methane; some of the chemistry of the oxidation of methane has been worked out by McElroy, McConnell, Levy, and others. The oxidation of methane could lead to the formation of formaldehyde, which might associate with a condensed phase in the stratosphere. I couldn't tell you at the moment how the more complex compounds would affect aerosol formation. I suspect that oxidation mechanisms will be available, such as O_3, HO, and HO_2 radicals in the lower stratosphere, but what role they would play in the formation of particulates I am not prepared to say.

CADLE: In principle, the same reactions that lead to the particles in photochemical smog could occur in the stratosphere. However, the types of organic compounds emitted by jet engines burning jet fuel will be quite different from those emitted by automobiles burning gasoline. Difficult though it would be, we really ought to find out whether smog-type reactions

occur under stratospheric conditions for jet-engine effluents.

VOLZ: I have my doubts about limiting consideration of aircraft emissions to just NO and the like. I made experiments with my oil burner at home, with the AFCRL heating plant, and with a small jet engine. In each case I filled a plastic bag with emissions, added some water, let it sit for a few hours, and extracted the water by evaporation. The resulting brownish residues did not look at all like what photochemists lead us to expect. Part of the material was liquid, which can never be completely dried out, and had very fancy infrared absorption bands. I have rarely found those bands in precipitation residues – more often from snow than from rain – and I am at a loss as to what they are.

I also separated the alcohol-soluble substances from the water-soluble ones. The water-soluble substances constitute about 50% and, when analyzed by normal procedures, appear to be mainly sulfates. Of the alcohol-soluble fraction, only about 20% are the familiar inorganic constituents, mostly nitrates.

I am no chemist, and it is difficult to identify these things. However, I have seen the spectrum of substances which appear in the lead-chamber process, and they seem to be unstable when heated, whereas atmospheric combustion residues are stable to at least 120°C or so.

BARRETT: We at NOAA started to investigate this problem of aerosols and ozone about two years ago, thinking that if existing aircraft were depositing particles into the stratosphere, some sort of effect might already be evident. We examined ozone trends at stations on the NOAA Dobson network and eventually all over the world, and we found to our surprise that ozone had risen, as I recall, by about 6% at nearly all stations, including all the European and American ones. This suggests, if anything, a correlation in the opposite direction. However, we think that factors such as circulation changes and wave patterns are probably more significant.

We have also investigated the apparent trend of aerosol pollution over the North Atlantic for the last 50 years, keeping in mind this inverse correlation between ions and aerosols. When we put together data from expeditions going from 1967 all the way back to Challenger, we found a steady downward trend, while in the South Pacific there is a straight line with no apparent trend.

BENSON: What is known about the contribution of meteorites to aerosols in the upper atmosphere?

CADLE: Several attempts have been made to determine this; they have only been able to set an upper limit on the amounts that could be found up to about 60,000 feet. Generally they say that the concentrations of meteoritic material must be less than 10% of the total particulate material. Of course, meteoritic contributions are sporadic – they come in bits and pieces.

NEAR-INFRARED INTERFEROMETRIC MEASUREMENTS OF STRATOSPHERIC COMPOSITION TO BE MADE FROM THE CONCORDE

CROFTON B. FARMER, ROBERT A. TOTH,
RUDOLPH A. SCHINDLER, AND ODELL F. RAPER
Jet Propulsion Laboratory
California Institute of Technology
Pasadena, California

ABSTRACT: A high-speed stepping Fourier spectrometer will be flown during the coming months on board the French prototype Concorde 001, as part of the current series of flights which uses both the French and British aircraft as platforms for stratospheric observational studies. The instrument covers the wavelength range from 1 to 8 microns (1200 to 8000 cm^{-1}) and has a spectral resolution of 0.25 cm^{-1}; spectra covering the entire range at maximum resolution can be recorded in approximately two to three minutes. The interferometer will view the sun close to the limb. The errors associated with limb observations, and the extent to which these will be minimized by the choice of aircraft flight path, are briefly discussed.

The main purposes of the present observations are to obtain an inventory of stratospheric neutral trace species, to determine accurate abundance values for each, and, within the constraints of the available flight altitudes and geometries, to investigate their vertical distributions. Diurnal variations in composition may be detectable from comparison of the results of observations made at sunrise and sunset.

The spectral range of the instrument is such that adequately low levels of CO_2, CO, N_2O, NO, NO_2, SO_2, O_3, H_2O, and the lower hydrocarbons will be observable. In general, minimum detectable concentrations lie within the range of 10^{-8} - 10^{-10} for observations made at aircraft altitudes of 15 to 20 km. The instrument's detection capability should thus allow the spatial and temporal variations of many of these species to be determined. In addition, it should be possible to set new upper limits for several of the neutral species which have not yet been detected. These minimum detectable concentration levels and accuracies are consistent with the performance achieved in previous observations.

INTRODUCTION

This paper describes a series of stratospheric observations to be made from the Anglo-French SST Concorde prototype (001) during early 1973. The observations will be made in absorption, by tracking the central portion of the sun's disk at zenith distances close to 90°, with a Michelson interferometer-spectrometer covering the 1200 to 8000 cm^{-1} range at a resolution of 0.25 cm^{-1}. We shall briefly describe the background of the present instrument in order to explain how it was adapted to the Concorde stratospheric observations.

Remote-sensing spectroscopic observations (as opposed to the use of in-situ techniques) are generally made by observing either the sun, at fairly low elevation angles, or the earth's limb. The spectrum is observed in absorption in the former case and emission in the latter. In both cases the large advantage in terms of the gain in effective optical depth at large zenith angles is exploited, to maximize the spectral contrasts to be measured. Each of the respective techniques has its own advantages and disadvantages, however, and it is perhaps worth commenting briefly on these; by exploiting the best features of each we can make a more comprehensive attack on the problem of understanding the composition of the stratosphere and its spatial and temporal variations.

Observations made in transmission (absorption) suffer from the major disadvantage that some form of solar tracking device is required, and the measurements must be made fairly rapidly to minimize the errors introduced by the changing optical path which results from the relative motion of the sun. At zenith angles close

to 90° this effect can be as large as an order of magnitude in the effective optical path over periods of a few minutes. Against this is the advantage that, for a given path, the abundance of a detected molecular species can be determined from the observed spectrum to relatively high accuracy (usually limited by knowledge of the transition strengths) and, for most of the bands of interest here, is not dependent on the detailed physical conditions over the atmospheric path. In particular, the determination of molecular concentrations from the observed spectrum does not require an accurate knowledge of the atmospheric temperature structure along the observation path. Observations by solar transmission are generally easier to perform because there are generally no problems with available energy – but, against this, molecular transition strengths are weaker in the overtone and combination bands which occur at wavelengths where the energy is greatest.

Measurements made in emission, on the other hand, do not require any special tracking device and can, in principle, be made over any atmospheric path, which furthermore can be kept constant during the time of the observation. However, because the spectral lines are formed such that their continua and centers arise from different regions of the atmospheric path, the spectral contrast for a given gas abundance is dependent on the detailed thermal profile along the path, and this must be known to an accuracy dictated by the accuracy required of the final abundance determination. This so-called "thermal anomaly" becomes particularly serious when the atmospheric path over the region of line formation approaches an isothermal condition, when the spectral-line contrast disappears. The problem can be surmounted in the case of a gas which is known to be uniformly mixed by comparing its intensity with that of a known permanent constituent, for those cases in which there is an adequate lapse rate over the observed optical path.

In the initial design of the instrument to be described here, the important requirement was to make as complete an inventory of the minor and trace species in the atmosphere as possible, under conditions at which their abundance or mixing ratios could be determined with sufficient accuracy to enable their spatial and temporal variations to be discerned. These accuracies implied also that the minimum detectable mixing ratios for each should be at least compatible with the known or expected natural background levels. For these reasons we chose to work in the range from approximately 1 to 8 microns (1200 to 8000 cm^{-1}). As can be readily shown, and is borne out by previous measurements of this sort, a spectral resolution of at least a few tenths of a wavenumber is necessary to achieve the required detection levels, and the signal-to-noise ratios in the final spectra must exceed 100:1. An additional factor which increases the requirement for a very high information-rate system is the need to complete each observation rapidly, in order to maintain spatial resolution in global and regional surveys. In the present application of the instrument to the Concorde flights, this same requirement arises because of the rapid changes in air mass which occur in solar observations at large zenith distances; details of the uncertainties due to this source during the flights are discussed later. We gain a large advantage, however, from the fact that the instrument was designed to enable us to achieve this performance in *downlooking* observations from a satellite platform; hence, when using the sun directly as a source, rather than its diffuse reflection from the surface of the earth, we can work very rapidly and achieve S/N ratios which approach 10^3:1 in the final spectra.

INSTRUMENT

The instrument is a modification of Connes' version of the Michelson interferometer [1]; its principal characteristics are the use of a double-passed (cat's-eye) optical system and a high-speed stepping motion of the moving retroreflector arm. The double-passed system (see Figure 1) makes the instrument relatively insensitive to mechanical distortions, which renders it particularly well suited to airborne applications; this scheme also provides, of course, a factor-of-two increase in the total optical-path difference in the interferometer, and hence in its spectral resolution. The fixed and moving arms are Cassegrain retroreflectors with about 8 cm apertures; the optical-path difference between the two arms is incrementally stepped at high speed by controlling the position of the lightweight secondary

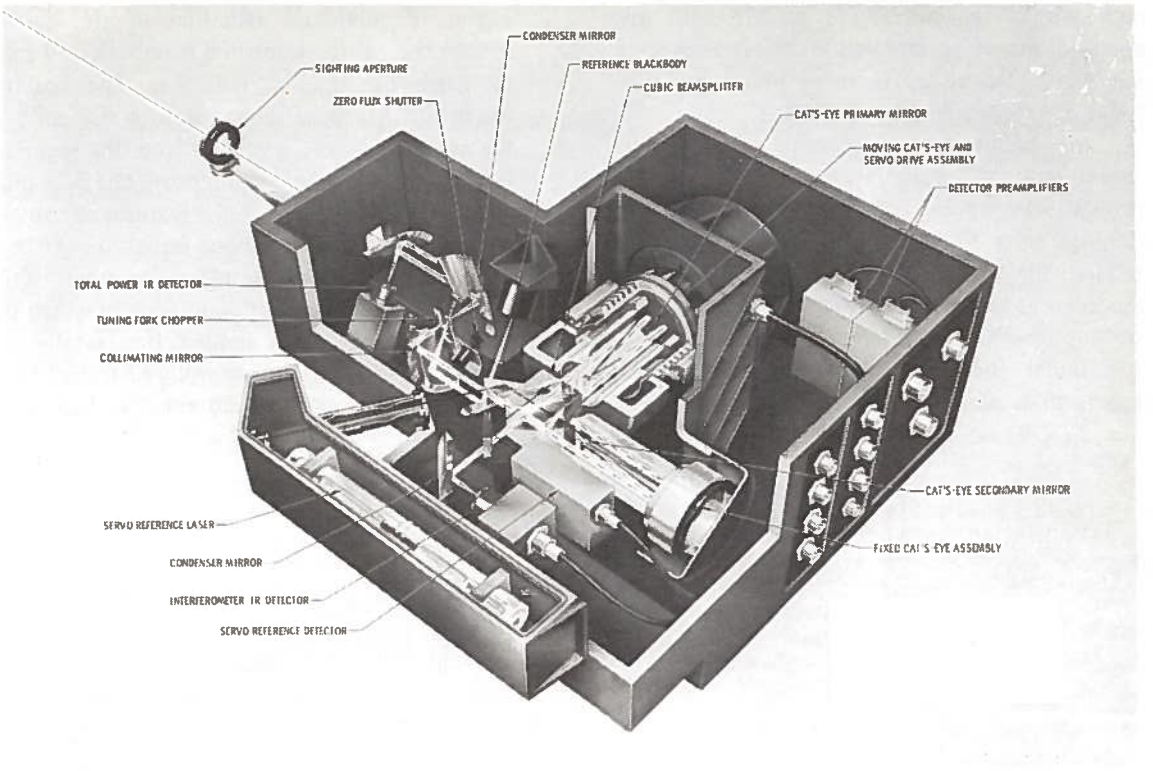

Figure 1. Optical and mechanical configuration of the interferometer.

mirror in the moving arm. This element is mounted on a piezoelectric stack, forming part of a servo loop which controls the element's position with reference to the interference fringes of a He-Ne laser. The fringes are formed through the optical system in the plane normal to the signal path. By this means the more massive primary and housing of the retroreflector can be driven at constant speed (with either a solenoid arrangement or a linear motor) and the positional changes at high rates need be applied only to the low-inertia secondary. In the present instrument the moving arm can be stepped at rates up to 500 times per second. While the digitally-stepped system provides a marginal advantage over continuous motion, in terms of signal integration, its greatest benefit is the fact that the instrument becomes very much more efficient and flexible in its operation. The conditions under which the interferogram is recorded can be very simply commanded to suit the spectral region and resolution required, through the appropriate choice of the number of control fringes per integration step and the total number of steps (path difference) to be covered, respectively. In certain applications, where only a limited spectral range at a particular resolution is required to be covered (as, for example, in monitoring a particular molecular band), this flexibility is reflected in the economics of the subsequent data-handling requirements. This aspect, of course, is of considerable importance in easing some of the data-management problems associated with an instrument covering a large spectral range when it is used in an automated mode over long periods of time.

For the Concorde observations, the interferometer will be used in conjunction with a solar tracker built by ONERA for other measurement programs (principally that of Girard, using the grille spectrometer). This shared use of the ONERA tracker has considerably reduced the problems of interfacing the interferometer to the aircraft. The instrument will look out through a 3-cm-thick CaF_2 window, and will track the center 1/4° of the solar disk. The entire optical

path within the aircraft is purged with dry nitrogen. For solar observations, spectra covering the whole frequency range at maximum resolution are recorded in 100 to 200 sec.

An example of a segment of the solar spectrum in the region of the 1-0 CO bands is shown in Figure 2a. This result, which shows the familiar solar CO lines in addition to several telluric CO_2, N_2O, H_2O, and O_3 bands, was recorded at sea level in a few seconds. A portion of the spectrum of a laboratory sample of CO run under the same conditions as the solar spectrum is included (Figure 2b) for reference.

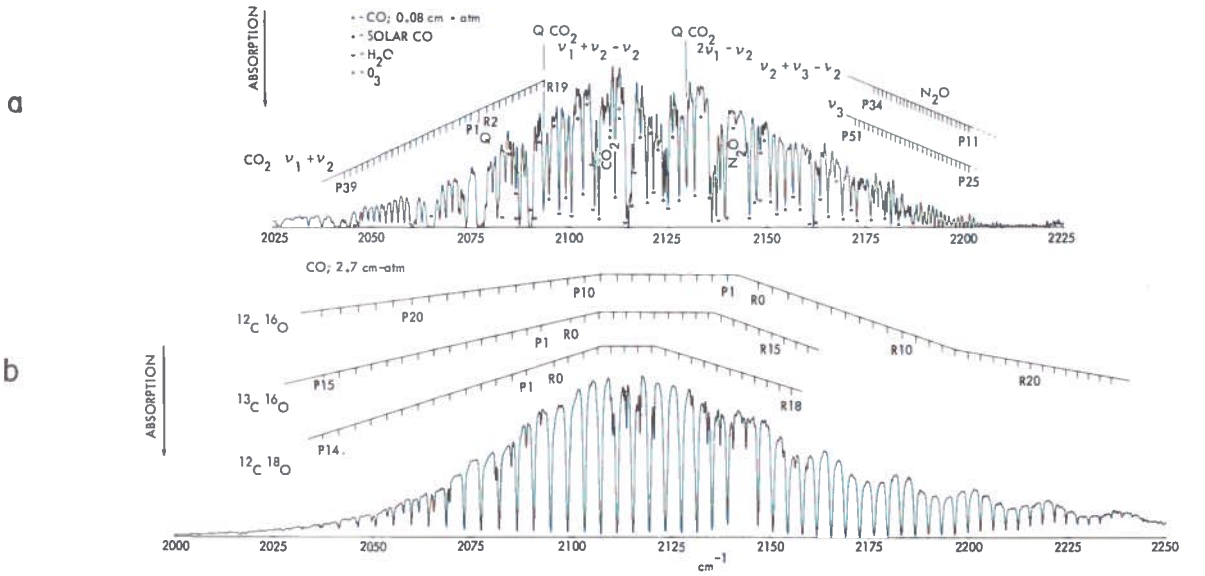

Figure 2. a. Segment of solar spectrum obtained with the instrument.
b. Spectrum of a laboratory sample of CO run under the same conditions as a.

The signal-to-noise ratio in solar runs of this sort is most usefully judged in terms of repeatability, for the purpose of assigning confidence to spectral features in quantitative analyses. The rms deviation of the transformed spectral samples, in repeated recordings made under the same conditions, is 3×10^{-3} at maximum intensity.

A perhaps more interesting result is the spectrum shown in Figure 3, taken from an airborne platform looking vertically down over Los Angeles from a height of about 1 km. The segments of the spectrum shown in the figure – the P branch of ν_3 CH_4 at 3.3μ, the 1-0 CO band at 4.7μ, and the H_2O vapor region encompassing the R branch of NO at 5.3μ – are close to the region of minimum radiation of the earth's surface, i.e., at the transition from reflected solar to thermally emitted radiation. The spectral resolution has been degraded to ≈ 0.5 cm^{-1} in the recovery of the spectrum from the recorded interferogram, to further improve the S/N ratio in an attempt to identify the features due to NO and the lower hydrocarbons (apart from CH_4). This result is a good example of the power of the Fourier technique under conditions in which the available energy is very limited. Incidentally, the hydrocarbons were not positively identified from these down-looking measurements, but were easily seen over very much shorter horizontal paths at the surface, giving a strong indication of their inhibited vertical mixing.

OBSERVATION GEOMETRY AND AIR-MASS ACCURACY

In addition to attempting to determine concentrations or setting upper limits for as many of the neutral stratospheric species as possible, it is the intent of the projected Concorde observations to derive quantitative results of sufficient accuracy to allow three-dimensional inhomogeneities and temporal (for example, diurnal) variations to be studied. Two principal factors affect the accuracy of the derived total

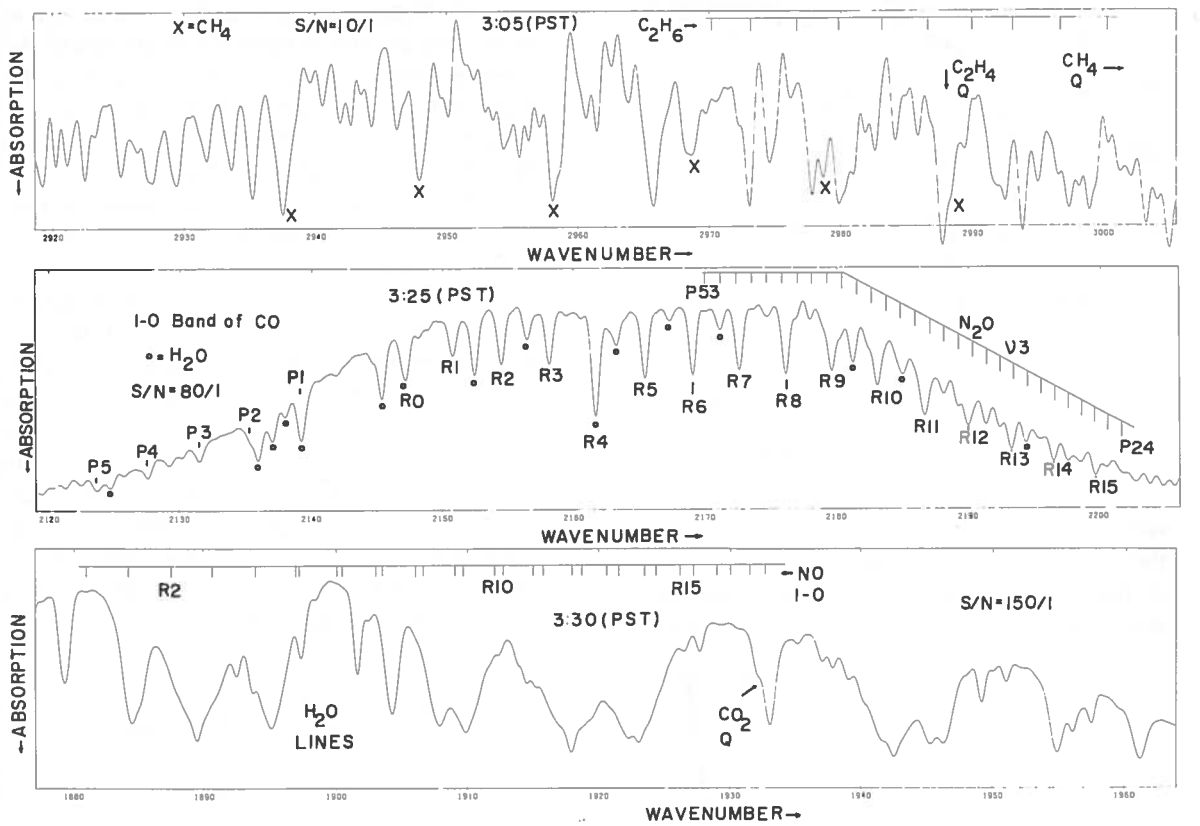

Figure 3. Spectra taken from an airborne platform looking vertically down over Los Angeles from a height of 1 km.

abundance of a given observed species and its density distribution over the sampled atmospheric paths. These are the variation of the air mass during each observation, caused by the angular motion of the sun, and the distortion of the shape of the spectral lines, resulting from the fact that all of the lines are formed throughout the time interval of the recording. By contrast, with the grating spectrometer the air mass increases or decreases progressively as the wavelength interval is scanned, so that the effects of air-mass variations during the course of the recording can be fairly easily corrected. In the case of the interferometric method, the error can be reduced by keeping to a minimum the total observation time or (in the high-speed-aircraft case) by choosing a flight trajectory which minimizes the apparent motion of the sun. The conditions relevant to the Concorde flights are illustrated in Figures 4 through 7. Figure 4 shows the fractional contribution to the total integrated optical path as a function of height above the observation point, for zenith angles of 82, 90, and 92°. For the 90° case, 90% of the total occurs within an 8-km-thick layer above the base altitude. For paths below horizontal, the range of contributing altitudes is smaller. In Figure 5, the total optical path, or air-mass factor, is shown (normalized to the 90° case) as a function of zenith angle. The lower limit of about 84° for the Concorde 001 arrangement is set by the observation window and the solar tracker; the upper limit of 93° to 94° is set by the earth's limb at flight altitudes of about 15-18 km. We thus have a range of two orders of magnitude in accessible air masses for the measurements.

Superimposed on Figure 5 is a time scale for a stationary equatorial observer at the equinox, and below it the time interval required for recording the full spectrum at maximum resolution. Hence, in the worst case (maximum solar rate, maximum zenith distance) we have a

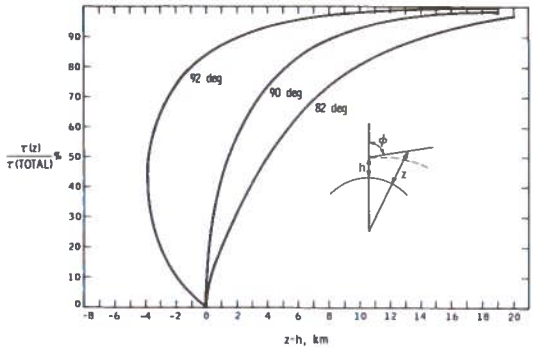

Figure 4. Fractional contribution to the total integrated optical path as a function of height above the observation point, for zenith angles (ϕ) of 82, 90, and 92°.

variation of a factor of 2 in the air mass during the period of recording each interferogram. This is directly the error in the derived atmospheric abundance, provided of course the observed spectral features are not at the noise-detection limit. The situation is improved in the case of the moving observation platform by choosing the flight paths appropriately. Figure 6 illustrates the variation in the effective optical path as a function of time, again normalized to the 90° case, for three values of the flight-path azimuth, corresponding to sunset observations over the Atlantic north of Spain in February. In the case of 310° flight azimuth, the Concorde is capable of providing a sensibly constant air mass, and such observations could be extended over periods in excess of a half-hour. (These data are based on analyses of the possible flight trajectories provided by Dr. Ackerman's group at the Institut d'Aéronomie Spatiale.) Figure 7 shows the limiting observation geometry for a typical 20-minute interval, chosen in this case to give a moderate range of air-mass factor (4:1) with a maximum uncertainty of ± 30%.

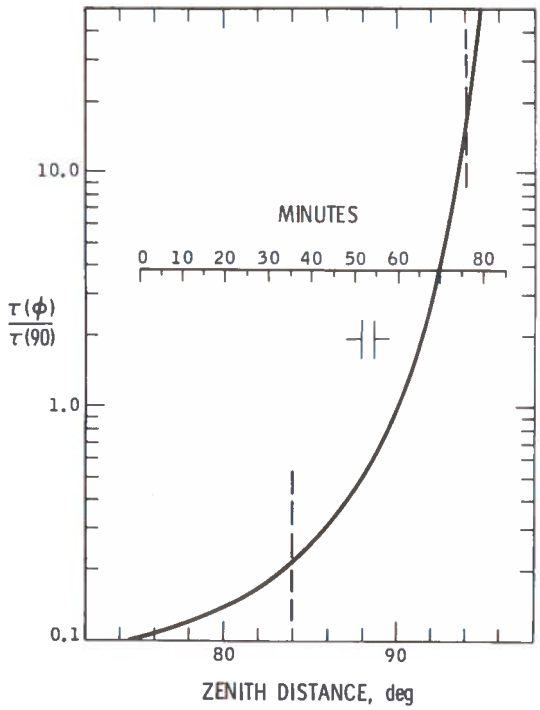

Figure 5. Total optical path, or air-mass factor, normalized to the 90° case as a function of zenith angle. Superimposed on the figure is a time scale for a stationary equatorial observer at the equinox, and below it is the time interval for recording the full spectrum at maximum resolution.

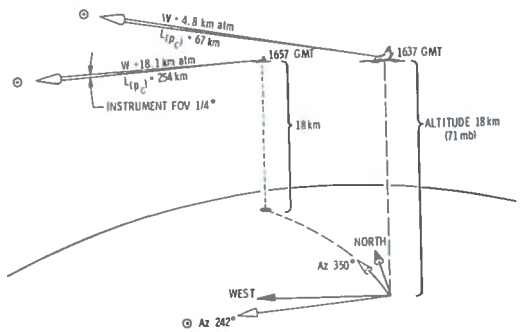

Figure 7. Limiting observation geometry for a typical 20-minute interval.

MINIMUM DETECTABLE DENSITIES AND EXPECTED RESULTS

Table 1 lists the more important of the neutral molecular species to be studied during the course of the observations. In the first four columns the present understanding of the mixing ratios of each of these is summarized, with references to relevant investigations where fairly recent determinations have been made. Allowance should be made for the fact that the table was compiled prior to the November CIAP conference; the results presented during the meeting suggest that the table can be improved.

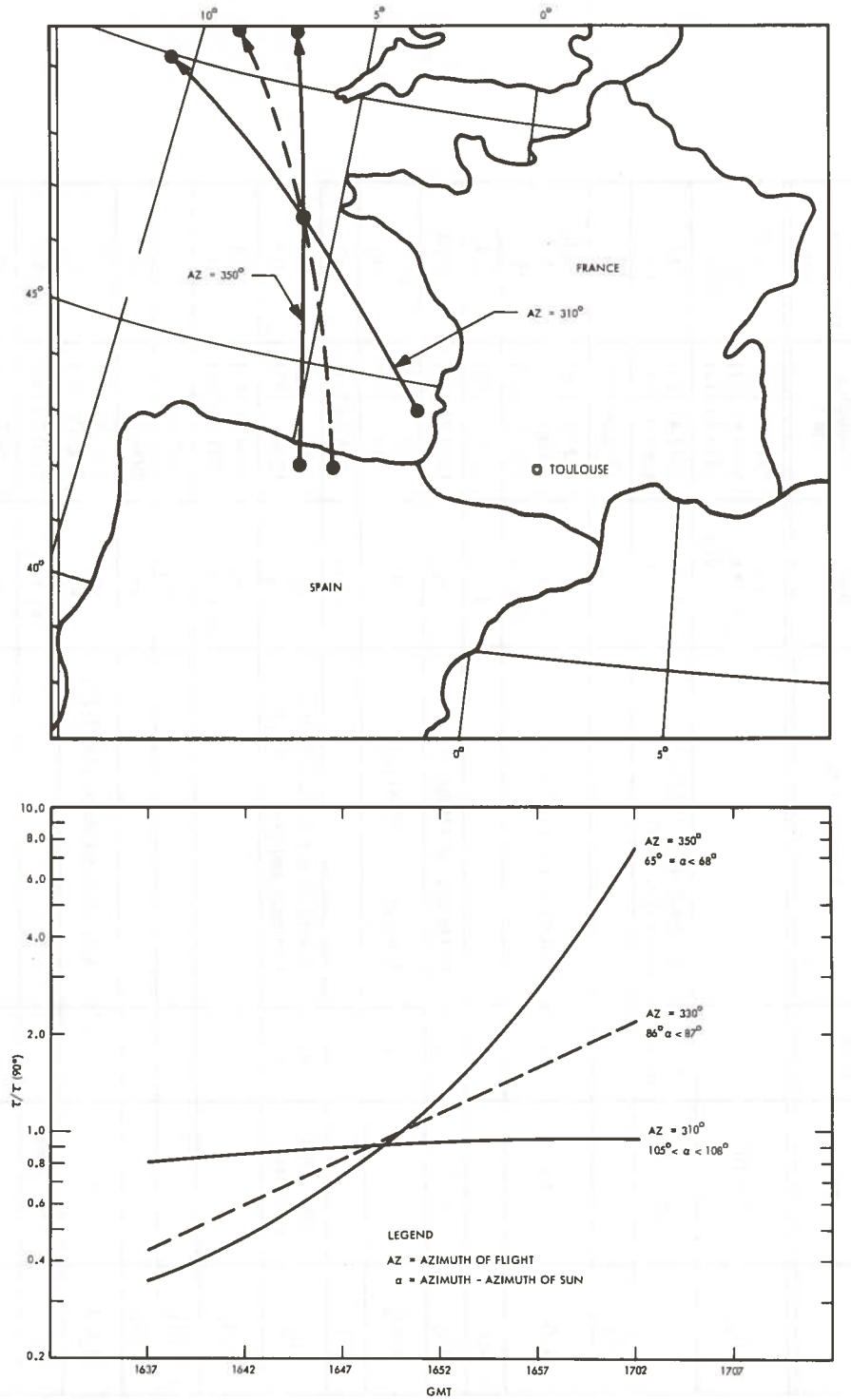

Figure 6. Illustrations of the variation of the effective optical path as a function of time, normalized to the 90° case, for three values of the flight-path azimuth, corresponding to sunset observations over the Atlantic north of Spain in February.

Table 1. Summary of Stratospheric Molecular Concentrations and Expected Detection Levels

Molecule	Previous Stratospheric Measurements			Concorde Experiment (15 km altitude, 30 km-atm)		
	Concentration ppb	Band	Recent Investigations	Band	Center Frequency cm^{-1}	Minimum Detectable Concentration ppb
CO_2	3.2×10^5			ν_3 $2\nu_1 + \nu_3$ $\nu_1 + 3\nu_2$	2349.16 [10] 5099.63 [11] 3339.34 [12]	0.02 40 5000
CO	40 - 80	1 - 0 In situ	Goldman et al. (1972) [2] Seiler (1972) [3]	1 - 0 2 - 0	2143.47 [13] 4260.07 [14]	0.1 13
SO_2				ν_3	1362.00 [15]	0.3
N_2O	110	ν_3	Goldman et al. (1970) [4]	ν_3 $\nu_1 + \nu_3$ $2\nu_2 + \nu_3$	2223.76 [16] 3480.82 [17] 3363.97 [17]	0.04 2 25
NO				1 - 0	1876 [18]	0.4
NO_2	$5^{(?)}$	ν_3	Goldman et al. (1970) [5]	ν_3	1617.75 [19]	0.04
HNO_3	?	ν_4	Murcray et al. (1968) [6]	ν_4 ν_2	1322 [20] 1710 [20]	<0.5 <0.5
HCl				1 - 0	2885.98 [21]	0.1
CH_4	750 - 2200 830 - 1009	ν_3 ν_3	Ackerman and Muller (1972) [7] Cumming and Lowe (1972) [8]	ν_3 ν_4	3018 [22] 1306 [22]	0.2 0.2
C_2H_2				ν_3 $\nu_2 + \nu_4 + \nu_5$	3294.85 [12] 3281.92 [12]	0.3 0.3
C_2H_4				ν_{11}	2988.65 [12]	3
C_2H_6				ν_7	2986.73 [12]	0.2
H_2CO	<10	ν_1, ν_5	Ackerman and Muller (1972) [7]	ν_1 ν_5	2782.40 [12] 2843.24 [12]	~0.1 ~0.1
O_3	100 - 3000			$\nu_1 + \nu_3$	2110.79 [23]	5
H_2O	3200	Rotation	Mastenbrook (1968) [9]	ν_2 ν_3 ν_1 $2\nu_2$	1594.73 [24] 3755.92 [12] 3657.08 [12] 3151.60 [12]	0.1 0.2 2 16

It nevertheless serves as a background and guide to the contribution which the Concorde interferometer observations are expected to make to the natural stratospheric data to be acquired under the CIAP program. The right-hand portion of the table lists the bands accessible to the instrument and the corresponding minimum detectable concentration for each, in parts per billion by volume, assuming constant mixing. The minimum concentration levels, given here for the 15-km altitude, 90° zenith distance case, are defined as the molecular concentrations which, under these observation conditions, give a peak absorption equal to an rms noise level of 1% of the continuum intensity. This criterion is conservative in the sense that the noise level in the solar observations will be considerably less than 1%. In each case the band or line strengths used in the analyses have been corrected to an assumed mean molecular temperature of 220°K; in most cases the departure of actual temperatures from this mean value will not introduce errors comparable to the uncertainty in the measured air-mass factor discussed in the previous section. The references listed in the column of band center frequencies give the sources of intrinsic line-intensity data used in computing the detection limits for each species. In the interest of consistency, the strongest accessible region of each band has been used.

For the more abundant species it is evident that some of the bands listed are far too intense to be of any practical value for deriving concentration levels; their inclusion in the table implies that, in practice, either the very weakest lines of the band could be used (to provide additional temperature information) or that their principal value lies in the determination of relative isotopic abundances.

It should also be pointed out that in making any comparison between the presently understood stratospheric abundances (Column 2) and the minimum detectable concentration levels listed for the Concorde observations (Column 7) we do not intend to imply a major improvement in our detection capability over that of the previous observers of specific molecules. In the case of the already detected molecules, the principal benefit from the Concorde observations should be a refinement of the mixing-ratio values and the possible elucidation of the effects of spatial and diurnal variations.

For the remaining (as yet undetected) molecules, the feasibility of detection and the computed detection levels have been verified in part by the synthesis of spectra, including the known telluric transitions over the appropriate spectral intervals, and also by measurement of representative laboratory samples. Some examples of the results of these computations are shown in Figures 8, 9, and 10, for SO_2, NO, and NO_2 respectively. The spectra were synthesized by the now-familiar techniques, using a layered model atmosphere, mixed Doppler-Lorentz line profiles, and an apodized instrumental half-width of 0.3 cm^{-1}. In each case the abundances of those molecules which might cause interference (for example, H_2O vapor and CH_4) have been somewhat exaggerated in order to ensure a conservative estimation of the ability to discriminate the species in question in the presence of severe blending.

The low hydrocarbons acetylene, ethylene and ethane are not expected to be found as stratospheric trace constituents. They are included here, however, because they have been detected in the urban atmosphere and have thus provided a useful verification of the computations of minimum detectable concentration levels.

Finally, the list of molecules included in the table is by no means exhaustive; other constituents may well be detected. Among such possibilities are two candidate stratospheric gases of particular interest, NH_3 and H_2O_2. NH_3 can best be detected with the present instrumentation from the ν_1 and ν_3 bands at 3336 and 3414 cm^{-1} respectively, for which the concentration limit will be of the order of 0.1 ppb. H_2O_2 has strong bands at 1370 and 3417 cm^{-1} (ν_6 and ν_5, respectively) and a band of medium strength, ν_1, at 2869 cm^{-1}. The latter occurs in a clear region of the background telluric spectrum and is thus a good means by which to search for this molecule. The stronger band at 3417 cm^{-1}, while located within the complex of water-vapor bands centered at 2.7 microns, should nevertheless be clear even under relatively wet stratospheric conditions. Unfortunately, no laboratory data for the strengths of these bands are available as yet, and the necessary experimental work is difficult to perform. However, estimates of the transition strengths can be made by analogy with molecules of similar structure, from which a conservative

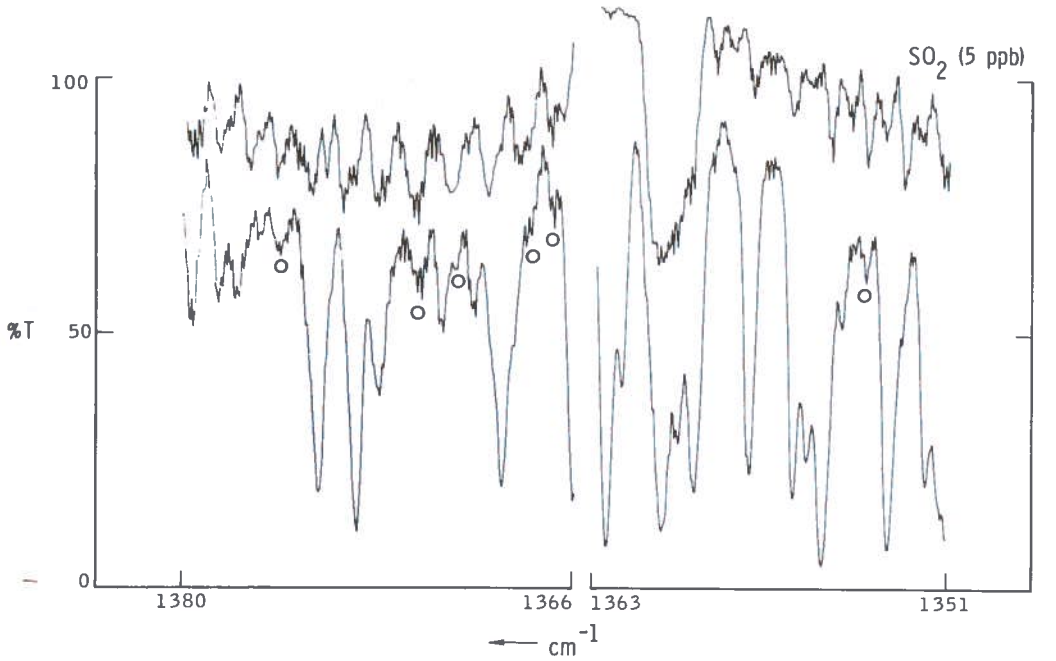

Figure 8. Computed spectra for the observing conditions of an altitude of 15 km and a zenith angle of 90° with an instrumental resolution of 0.3 cm^{-1}. The upper spectrum is of SO_2 for a mixing ratio of 5 ppb. The lower spectrum contains spectral features of H_2O (5 ppm), CH_4 (1.5 ppm), and the resultant detectable SO_2 features (circles).

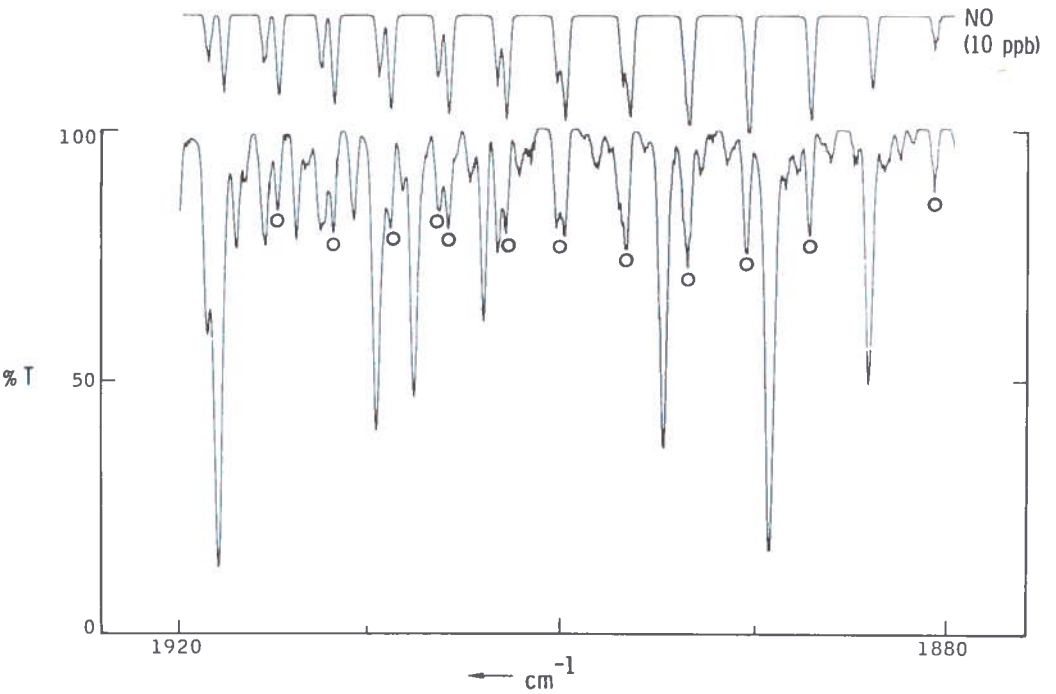

Figure 9. Computed spectra for the observing conditions of an altitude of 15 km and a zenith angle of 90° with an instrumental resolution of 0.3 cm^{-1}. The upper spectrum is of NO for a mixing ratio of 10 ppb. The lower spectrum includes spectral features of H_2O, CO_2, solar CO, and the resultant detectable NO features (circles).

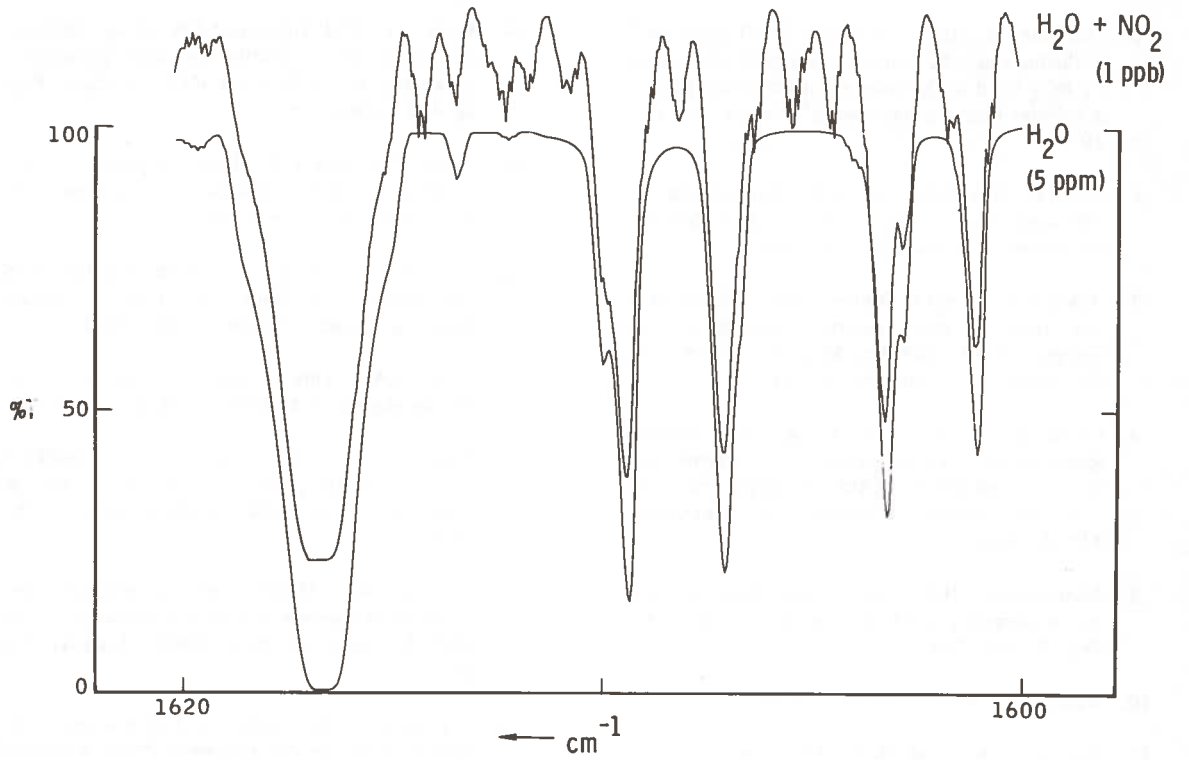

Figure 10. Computed spectra for the observing conditions of an altitude of 15 km, zenith angle of 90°, and an instrumental resolution of 0.3 cm^{-1}. The lower spectrum is of H_2O and the upper spectrum shows the features of H_2O and NO_2 (1 ppb).

estimate of the attainable minimum concentration would be 1 ppb. It should therefore be possible to set useful new upper limits for species such as these if they are not detected in the course of the observations.

ACKNOWLEDGMENT

The instrumentation described in this paper was developed at the Jet Propulsion Laboratory, California Institute of Technology, under Contract Number NAS 7-100, sponsored by the National Aeronautics and Space Administration. The work associated with the adaption of the instrument to the Concorde, and the stratospheric observations themselves, is supported by the Climatic Impact Assessment Program of the Department of Transportation, under Contract Number DOT-AS-20094.

REFERENCES

1. Schindler, R.A., "A small interferometer for aircraft, balloon and spacecraft applications," Applied Optics *9*, 301, 1970.

2. Goldman, A., D.G. Murcray, F.H. Murcray, W.J. Williams, J.N. Brooks, and C.M. Bradford, "Vertical distribution of CO in the atmosphere," Meeting of Am. Geophys. Union and Am. Meteorological Society, St. Petersburg, Florida, August 1972.

3. Seiler, W., "Carbon monoxide in the atmosphere," Meeting of Am. Geophys. Union and Am. Meteorological Society, St. Petersburg, Florida, August 1972.

4. Goldman, A., D.G. Murcray, F.H. Murcray, W.J. Williams, T.G. Kyle, and J.N. Brooks, "Abundance of N_2O in the atmosphere between 4.5 and 13.5 km," JOSA *60*, 1466, 1970.

5. Goldman, A., D.C. Murcray, F.H. Murcray, W.J. Williams, and F.S. Bonomo, "Identification of the ν_3 NO_2 band in the solar spectrum observed from a balloon borne spectrometer," Nature *225*, 443, 1970.

6. Murcray, D.G., T.G. Kyle, F.H. Murcray, and W.J. Williams, "Nitric acid and nitric oxide in the lower stratosphere," Nature *218*, 78, 1968.

7. Ackerman, M. and C. Muller, "Stratospheric methane from infrared spectra," Meeting of Am. Geophys. Union and Am. Meteorological Society, St. Petersburg, Florida, August 1972.

8. Cumming, C. and R.P. Lowe, "Balloon-borne spectroscopic measurements of stratospheric methane," Meeting of Am. Geophys. Union and Am. Meteorological Society, St. Petersburg, Florida, August 1972.

9. Mastenbrook, H.J., "Water vapor distribution in the stratosphere and high troposphere," J. Atmos. Sci. *25*, 299, 1968.

10. Williams, D., private communication.

11. Downing, H. and R.H. Hunt, private communication.

12. A number of subsidiary laboratory measurements of line and band strengths have been made by the authors in the course of this work, for those cases for which no suitable data are available in the literature.

13. Penner, S.S. and D. Weber, "Quantitative infrared intensity measurements. I: Carbon monoxide pressurized with infrared inactive gases," J. Chem. Phys. *19*, 807, 1951.

14. Korb, C.L., R.H. Hunt, and E.K. Plyler, "Measurement of line strengths at low pressures – application to the 2-0 band of CO," J. Chem. Phys. *48*, 4252, 1968.

15. Chan, S.H. and C.L. Tien, "Infrared radiation properties of sulfur dioxide," Transactions of the ASME WA/HT-4, 172, 1971.

16. Lowder, J.E., "Band intensity and line half-width measurements in N_2O near 4.5μ," J. Quant. Spectrosc. Radiat. Transfer *12*, 873, 1972.

17. Toth, R.A., "Line strengths of N_2O in the 2.9 micron region," J. Mol. Spect. *40*, 588, 1971.

18. James, T.C., "Intensity of the forbidden $X^2\Pi_{3/2} - X^2\Pi_{1/2}$ satellite bands in the infrared spectrum of nitric oxide," J. Chem. Phys. *40*, 762, 1964.

19. Guttman, A., "Absolute infrared intensity measurements of nitrogen dioxide and dinitrogen tetroxide," J. Quant. Spectrosc. Radiat. Transfer *2*, 1, 1962.

20. Goldman, A., T.G. Kyle, and F.S. Bonomo, "Statistical band model parameters and integrated intensities for the 5.9μ, 7.5μ, and 11.3μ bands of HNO_3 vapor," Appl. Opt. *10*, 65, 1971.

21. Toth, R.A., R.H. Hunt and E.K. Plyler, "Line strengths, line widths, and dipole moment function for HCl," J. Mol. Spec. *35*, 110, 1970.

22. Kyle, T.G., "Line parameters of the infrared methane bands," AF 19(628)-5706 Scientific Report No. 1, October 1968.

23. McCaa, D.J. and J.H. Shaw, "The infrared spectrum of ozone," J. Mol. Spec. *25*, 374, 1968.

DISCUSSION

SNELSON: How do you do the transform for your spectrum?

FARMER: It is the standard Fourier transform with fast algorithms, and the apodization is standard also. In the present system, in order to use an existing laboratory instrument in the aircraft, we have not attempted to do things like putting in real-time transformations. The interferogram is recorded on tape in the aircraft; the instrumentation includes units for formatting, error diagnosis, and so on, since there are some 10^5 elements per spectrum and we must make sure that the data are usable. The tapes are processed after each flight, so we do not see the spectra until a few hours later.

(UNIDENTIFIED): How long does it take to do the transformation?

FARMER: Well, it takes $20 per spectrum in computer time.

WIJNTJES: What resolution can you get in your spectrum? Also, are your spectra apodized?

FARMER: 0.2 cm^{-1} is the best we can achieve. All of the spectra that you saw here are apodized.

(UNIDENTIFIED): What effects do you expect from aircraft-induced turbulence?

FARMER: I suspect that there are several problems from that; one of them, that perhaps you are referring to, is the question of the fluctuation of the apparent path. I think it is not serious; the instrument has a total-power detector with a very fast response, which takes out errors that might creep in from variations in the total incident power of the source.

SNELSON: How do you consider the problem of naturally-occurring radical species' interfering with the measurements? For example, you didn't have OH or HO_2 in your list. These are going to probably overlap some of the regions of interest for H_2O or O_2, for example, and then there is the possibility of methyl radicals. All of these, it seems to me, are possible interferences. I would also like to know the absolute detection limit of the system. In other words, what is the minimum *absolute* number of molecules of something like water you can then detect?

FARMER: The detection limit for water is very small. To answer the first part of your question: You are quite right about the radicals. If we see radical species' transitions there is very little at present that we can do about it, because of our lack of knowledge of their frequencies, let alone strengths.

MEASUREMENTS OF SOME HYDROGEN-OXYGEN-NITROGEN COMPOUNDS IN THE STRATOSPHERE, FROM CONCORDE 002

J.E. HARRIES AND N.W.B. STONE*
Division of Electrical Science
National Physical Laboratory
Teddington, Middlesex, England

ABSTRACT: Measurements of the sub-millimeter wavelength far-infrared emission spectrum of the stratosphere were made from Concorde 002 during its tour of the Far East in June 1972. The spectra have been analyzed to provide concentration data for H_2O, O_3, HNO_3, N_2O, and NO_2.

INTRODUCTION

Previous high-resolution measurements [1,2] of the submillimeter infrared emission spectrum of the stratosphere have shown that, in addition to lines of H_2O, O_2, and O_3, other lines may be observed; these are due to species such as HNO_3, NO_2, N_2O, and SO_2, particularly at large zenith angles. These observations are clearly very important in view of the current scientific debate on the physics and chemistry of the stratosphere, and the possible effects of high-flying aircraft. The work reported here is the first of a series of measurements being made to determine the concentrations of several species of interest, using the far-infrared spectrum.

DESCRIPTION OF THE EQUIPMENT

The basic technique, which has been described in detail in the past [1,3], uses a Michelson interferometer together with a helium-cooled Rollin bolometer; the whole system has a spectral response in the 300-μm to 3000-μm range. The advantages of this system over others for making atmospheric observations have been previously identified [1,3,4].

The apparatus was a modified version of that previously flown in a Comet 2 [1]; it was installed in Concorde 002 in April 1972. Particular modifications which had to be made included (a) the manufacture of a special polypropylene window to be fitted into the fuselage in one of the passenger-window apertures; (b) the design and construction of a new data-logging and control system, to permit faster scanning of the interferometer; and (c) change of the viewing angle to 90° from the zenith, in order to increase the air mass viewed by the apparatus. The use of a cassegrain telescope was abandoned in favor of a radiation collecting horn, with a 5° (total) field of view.

Data was recorded on paper tape which was stored for processing in the laboratory. The resolution of the interferometer was 0.067 cm^{-1} (unapodized [5]) and a single interferogram was recorded in 11 min. The equipment, once started, operated automatically, with the scanning motion of the interferometer mirror being reversed by micro-switches.

During the Far East tour, interferograms were recorded wherever the following two criteria were met: the aircraft was flying at sufficiently high altitude to yield stratospheric data; and liquid helium was available.† Some 55 interferograms were recorded, of which 30 were finally used to provide data; the others were rejected because of unsuitable atmospheric conditions, excessive aircraft maneuvering, or serious noise interference (from a number of sources).

The tour went through Iran to India, Singapore, and Japan; then on to Australia (most of the time being spent in S. Australia); and returned via Singapore, India, and Saudi Arabia. It started on June 2, and the last set of observations was made on June 28. (Details of the experiment dates and locations may be found below in Table 2.) Some data for the U.K. were recorded prior to the tour, on shakedown flights.

*This paper was presented at the conference by P. Graystone of the Meteorological Office, Bracknell, England.

†Liquid helium was supplied by associate companies of the British Oxygen Company Ltd., and by Air Products Ltd.

RESULTS

Figure 1 shows a sample spectrum (20/6.3 + 4 in Table 2) which is the average of two 11-minute runs recorded over the Sydney (Australia) area on 20 June 1972. The spectrum has been labeled with assignment numbers, and a partial list of assignments is given in Table 1 for the species HNO_3, N_2O, NO, NO_2, and SO_2. The complete list, including H_2O, O_2, and O_3, may be found in Reference 6. The lines of HNO_3 and NO_x used for concentration determination are marked in Figure 1 by an asterisk and listed in Table 1.

The spectral lines were identified, using the compiled data [6], and the equivalent widths of the lines of interest were measured manually and tabulated. For H_2O and O_3 a previously described technique [3,7] of deriving the mixing ratio relative to O_2 emission lines was used. For the other species, which are in the weak region of the curve of growth and thus cannot simply be compared with strong O_2 emission lines, laboratory measurements [8,9,10,11] and calculations [12,13] were used to compute the equivalent path length of the species above the aircraft. A correction for the temperature of the stratosphere (assumed to be 225 K) was made, and the equivalent path expressed in units of atm-cm. The data were then treated in two ways. First, the concentrations were converted to units of column density, cm^{-2} (i.e., the total number of molecules above the flight level in a column of 1 cm^2 cross-section). Second, it was assumed that the mixing ratio was constant with height*, and a standard curved-atmosphere model [14,15] was used to derive the total air mass (in atm-cm) with which to produce the volume mixing ratio, V, for each species. This mixing ratio, therefore, is an effective mean value (averaged over height) for each species. For the gases emitting in the weak region of the curve of growth (HNO_3, NO_x, weak O_3 lines) the scale height is the atmospheric scale height. For H_2O and strong O_3 lines the scale height is smaller ($\approx$ 2 km in the vertical for H_2O). Both column density and average mixing ratio are listed in Table 3.

*This is, of course, certainly not true for several of the species; however, vertical distributions of mixing ratio were not the prime concern of this work, and will be considered later.

Individual values of volume mixing ratios derived in this way for H_2O, HNO_3, N_2O, NO_2, and O_3 are given in Table 2; also entered in the table are details of the flight level, tropopause level, and approximate geographical location.

Table 3 gives the global averages for the data, with an estimate for the spread in values obtained. The errors involved in this spread will include (a) random errors in equivalent width measurement (including the effect of noise in the spectrum), (b) fluctuations in air mass due to aircraft roll and maneuvering, and (c) real variations due to height h, tropopause height h_t, or latitude change. It also includes a contribution due to systematic errors in source spectroscopic data [8-13], which have been considered elsewhere [6]. The systematic errors are due to poor signal-to-noise ratios in the laboratory spectra, incorrect estimates of transmission coefficients, and lack of theoretical data on line strengths and half-widths. For NO_2 the quoted errors show a larger lower error limit because of the possible effects of blended lines.

For the purposes of the present paper we wish to report only on measured total concentrations and mean mixing ratios, as the first stage in this program of work. However, it should be noted that in several cases the behaviour of volume mixing ratio as a function of height indicates variations which may be significant. Figure 2 shows examples, for H_2O, N_2O, and HNO_3, of data taken from Table 2. The lines have been hand-drawn through the points. These trends are being considered and, along with further measurements at several zenith angles, it is hoped that vertical distribution profiles will be evaluated. These will be reported in due course.

DISCUSSION

We will now summarize the results obtained to date, with a brief species-by-species discussion, and compare these with measurements and calculations by other investigators.

For HNO_3, values fairly closely grouped around a mean mixing ratio of 3×10^{-9} are obtained. No significant latitudinal variation is observed (Table 2), but some evidence of a non-linear vertical distribution may be derived from the behaviour with height above the tropopause (Figure 2). HNO_3 has previously been

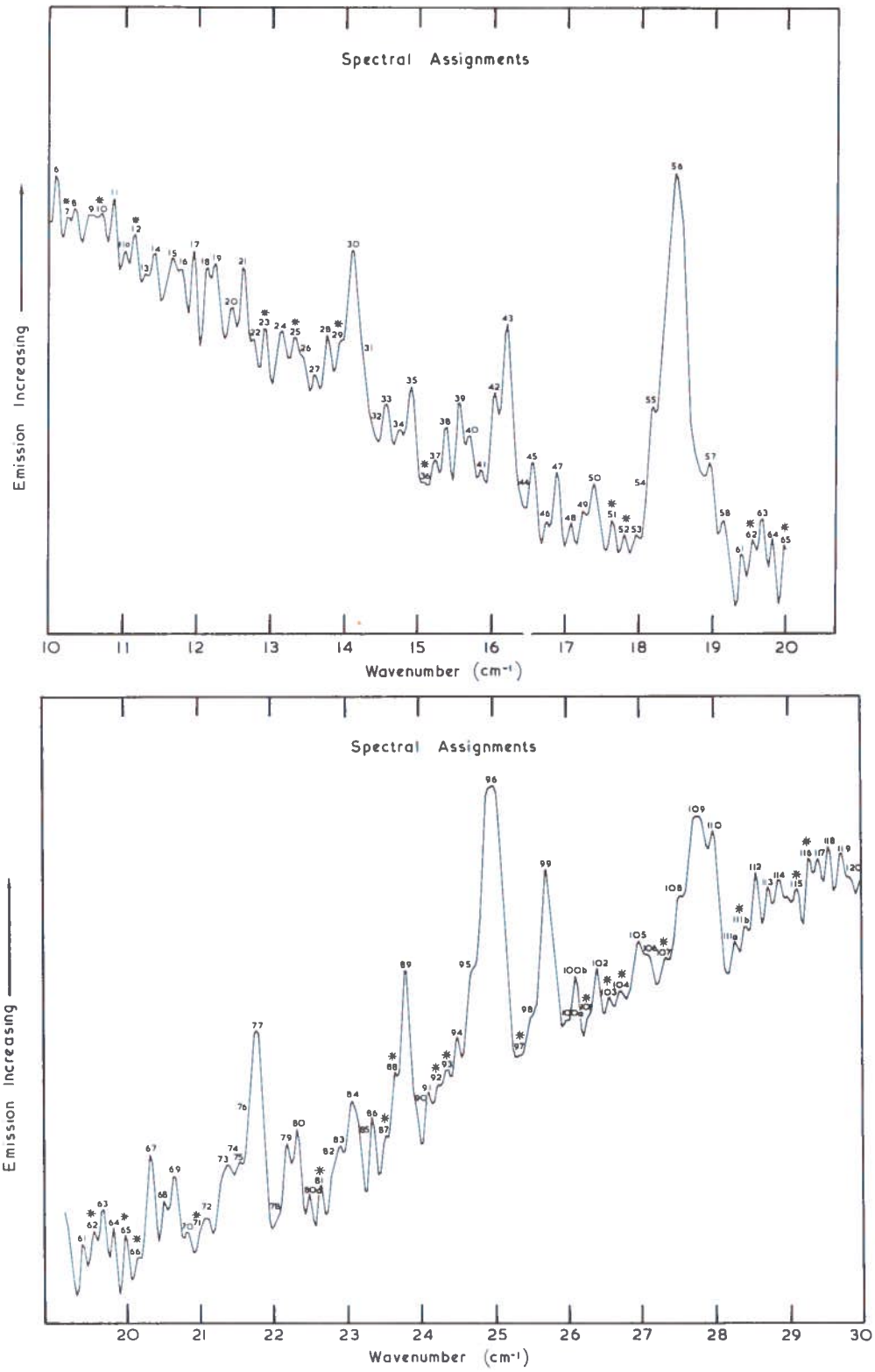

Figure 1. The average of two spectra at a resolution of 0.067 cm^{-2}. The numbers refer to the full assignment table to be found in Reference 6; a partial list is given in Table 1 for the asterisked lines, which are those due to HNO_3, N_2O, NO_2, and SO_2. (a) 10-20 cm^{-1}, (b) 20-30 cm^{-1}.

Table 1. Partial List of Spectral Line Assignments*

Line Number	Measured Wavenumber (cm^{-1})	Predicted Wavenumber (cm^{-1})	Species
7	10.181	10.25	HNO_3
10	10.650	10.65	HNO_3
		10.72	N_2O
12	11.064	11.08	HNO_3
23	12.963	12.96	HNO_3
25	13.200	13.14	HNO_3
29	14.10 (s)	13.94	HNO_3
36	15.094	15.06	N_2O
51	17.593	17.58	N_2O
52	17.70 (s)	17.75	HNO_3
62	19.566	19.566	SO_2
65	19.988	20.09	N_2O
66	20.172	20.26	NO_2
		20.26	HNO_3
71	20.944	21.01	NO_2
81	22.578	22.59	N_2O
		22.62	HNO_3
83	22.96 (s)	22.89	NO_2
87	23.59 (s)	23.45	N_2O
88	23.71 (s)	23.67	HNO_3
92	24.262	24.18	NO_2
		24.26	N_2O
93	24.375	24.45	HNO_3
97	25.381	25.45	NO_2
		25.48	SO_2
101	26.287	26.14	HNO_3
103	26.609	26.54	HNO_3
104	26.766	26.73	NO_2
		26.76	N_2O
107	27.325	27.39	HNO_3
		27.339	O_3 (weak)
111b	28.47	28.44	NO
		28.50	SO_2
115	29.119	29.05	HNO_3
116	29.280	29.28	N_2O
		29.29	NO_2

*Full list of assignments given in Reference 6.
s = Shoulder

Table 2. Experimentally Measured Volume Mixing Ratios (assumed constant with height)

Run Identifier (Date/number)	V_{HNO_3}	V_{H_2O}	V_{N_2O}	V_{NO_2}	V_{O_3}	Flight Altitude (h)		Tropopause Altitude (h_t)		$h - h_t$	Approximate Latitude and Longitude	
	$\times 10^9$	$\times 10^6$	$\times 10^9$	$\times 10^9$	$\times 10^6$	(kft)	(mb)	(kft)	(mb)	(kft)		
30/5.1	2.0	3.93	240	23	4.9	48	140	38	230	10	48N	08W
9/6.2+3	3.1	5.50	300	21	4.6	50	120	52	105	-2	01N	104E
11/6.1+2	3.4	6.60	275	22	4.6	48	125	50	115	-2	05N	110E
11/6.3+4	2.8	6.22	270	20	4.8	51.5	110	50	115	1.5	10N	115E
14/6.1+2	3.2	6.55	325	28	4.6	47	145	52 to 55	85 to 105	-5 to -8	35N	140E
15/6.2	2.9	5.70	270	26	5.5	44.5	155	52.5	100	-8	30N	135E
15/6.5	2.7	6.80	365	23	5.1	48	130	53	95	-5	18N	121E
20/6.1+2	3.7	5.90	265	24	4.8	45	150	37.5	230	7.5	35S	151E
20/6.3+4	3.0	3.60	190	23	3.7	49	120	37.5	230	11.5	35S	151E
20/6.6+7	1.9	2.85	215	18	4.8	47.5	130	37	235	10.5	37S	149E
20/6.8	2.7	3.60	215	16	3.7	40	195	37	235	3	40S	145E
22/6.2	2.1	3.15	210	18	4.9	49	125	39.5	200	9.5	40S	145E
22/6.3	3.0	5.62	350	22	5.4	40	195	39.5	200	0.5	40S	145E
23/6.1+2	2.5	2.49	240	23	4.0	52	105	37	235	15	30S	140E
23/6.3+8	2.7	10.2	390	–(a)	5.9	40	190	52.5	100	-12.5	20S	133E
23/6.12+13	2.5	9.21	250	24	3.9	47	145	54	90	-7	12S	125E
23/6.14+15	3.2	8.75	245	25	4.9	52	105	52.5	100	-0.5	05S	115E
24/6.3	1.9	12.9	270	30	3.7	44	155	–(b)	–	–	01N	104E
28/6.1+2	3.5	16.1	250	22	3.4	35	260	52.5	100	-17.5	20N	70E

Notes: (a) Tropopause too high
(b) No meteorological data available

Table 3. Experimentally Derived Global-Average Stratospheric Mixing Ratios

Species	Column Density (mols cm^{-2})	Average Volume Mixing Ratio	Comments
H_2O	7.7×10^{18}	$(3.0 \pm 0.3) \times 10^{-6}$	Rapid increase below tropopause. Constant up to 60 km.
O_3	1.2×10^{19}	$(4.8 \pm 1.0) \times 10^{-6}$	Naturally variable.
HNO_3	7.2×10^{15}	$(2.8 \pm 0.7) \times 10^{-9}$	
N_2O	5.4×10^{17}	$(210 \pm 50) \times 10^{-9}$	Measured 3 km above tropopause.
	7.0×10^{17}	$(270 \pm 60) \times 10^{-9}$	Measured at the tropopause.
NO_2	5.7×10^{16}	$(22 + 8) \times 10^{-9}$ $- 12)$	Systematic error problem due to poor source data. Could range from 10 to 30×10^{-9} in absolute value.

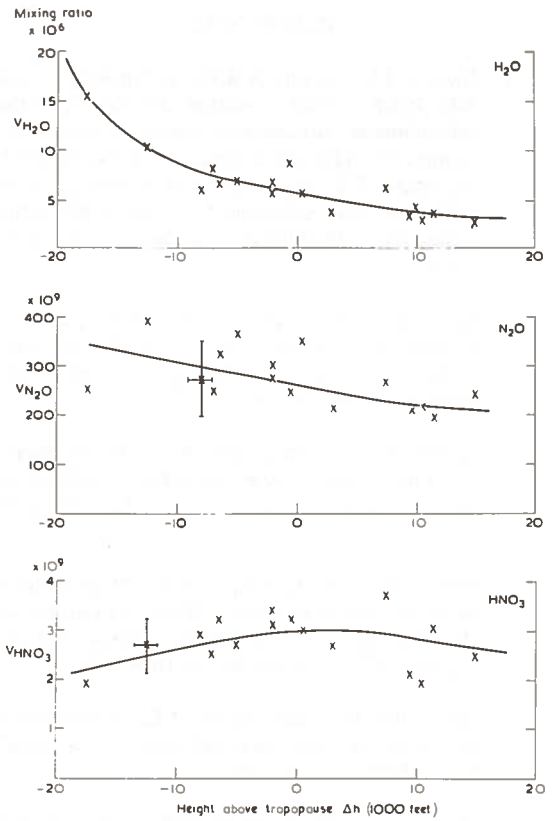

Figure 2. A compound diagram showing the variation of V_{H_2O}, V_{N_2O}, and V_{HNO_3} with height above the tropopause. The curves are hand-drawn through the data points and the significance of the variations is discussed in the text.

observed by Murcray and his co-workers [15], and Rhine et al. [16] have interpreted their results to be equal to an average mixing ratio of about 3.2 ± 30% x 10^{-9}, with an "ozone-like" distribution. Lazrus et al. [29] obtained values between 2 and 4 x 10^{-9} at 20 km. Recently Murcray has obtained values of 4.5 x 10^{-9} by volume at about 23 km, with about 1 x 10^{-9} at 15 km [30].

N_2O has been measured in the troposphere and the stratosphere by a number of people, on account of its importance in the nitrogen cycle. Schutz et al. [18] obtain results very similar to our own (cf. Table 3), 250 x 10^{-9} at the tropopause and 220 x 10^{-9} at about 15 km. Goldman et al. [19] obtain a distribution of similar shape, but with lower absolute values, reporting 150 x 10^{-9} at the tropopause. Bates and Hays [20] have considered the factors affecting the concentration of N_2O in the stratosphere, and present a number of profiles depending on the value of the vertical exchange coefficient K_z (cm^2 s^{-1}) adopted. Our results indicate (using Figure 3 of Bates and Hay's paper) a best fit with K_z equal to 1 x 10^3 cm^2 s^{-1} (details to be published).

In the case of NO_2 our results give about 20 x 10^{-9} by volume. As mentioned above, however, the accuracy of this measurement is severely limited by poor source spectroscopic data (which are currently being improved) and blending of lines. Table 3 indicates the confidence limits. The only other estimate is one by Ackerman and Muller [22], who have used data obtained by Murcray and his co-workers, from a balloon at 32 km, as well as their own data, to produce a profile of NO_2 which varies between 10^{-9} and a maximum of about 10 x 10^{-9} centered at about 28 km. This estimate is considerably lower than our own. However, until the accuracy of source spectroscopic data has been established in both the spectral bands (particularly our own – see above) it is probably more meaningful to comment on the similarity of the results. The column density of NO_2 we calculated approximately from Ackerman and Muller's data is 6.5 x 10^{15} cm^{-2}; our result was about 5 x 10^{16} cm^{-2}. The latter figure will be revised as soon as improved source data is available.

For water vapor our group has made a large number of observations over several years [3,4, 28] which agree well with the present result of 3 x 10^{-6} by volume in the stratosphere, constant with height up to about 60 km [28]. Houghton et al. [23] have obtained results around 5 x 10^{-6}, and Mastenbrook [24] quotes values of 3-4 x 10^{-6}. Note that our own estimates for H_2O should be accurate to better than ± 10% [3,4]. Shimazaki and Laird [25] calculate that at about 70 km the mixing ratio is about 3 x 10^{-6}, and decreases at higher altitudes.

The result we obtain for ozone is, as for the other species, averaged over altitude, tropopause height, and location; it is therefore an average value which does not reflect any of the known seasonal trends. It would, for instance, have been interesting to make observations at latitudes more southerly than 40 S in order to attempt to detect any polar increase. However, the average

value we obtain is in good agreement with known values [26].

A point worthy of note at this stage is that, since the O_3 amount is known to vary considerably with time and location, and since some of the species of interest are thought to be associated with the O_3 (e.g., HNO_3, NO_2), it is at least possible that these species will exhibit similar fluctuations. In this sense, again, any real variations will tend to be lost in the variations of height, latitude, and tropopause height necessarily imposed during this experiment (Table 2).

Finally, though we have not quoted a result in Tables 2 and 3, we mention a first estimate which has been made for the mixing ratio of SO_2. This result, which is based on the tentative assignment of line 62 to SO_2, is approximate, and confirmation will have to await more accurate source data and better experimental resolution. However, at present we obtain an upper limit of 3.5×10^{-9} for V_{SO_2}.

The results given above, from the first experiment in a series to measure the concentrations of minor stratospheric species, indicate the power of the far-infrared for this purpose. Work is going ahead in several areas in order to improve the quality of data we can obtain. These areas include improvement of source spectroscopic data, increase of instrumental spectral resolution, and consideration of the derivation of the vertical profiles of mixing ratio with adequate height resolution.

ACKNOWLEDGMENTS

A large number of people have been involved in these experiments, and to thank them all would take too much space. We will, therefore, list significant group leaders.

At the NPL, the valuable assistance of Mr. N.R. Swann, who designed and built the control electronics, and assisted in the experiment itself, is fully acknowledged. At BAC the efforts of Mr. D. Vickery and Mr. J. Leach at Bristol, and the many people at Fairford working under the direction of Mr. B. Trubshaw, are gratefully acknowledged. The work is supported by the Committee on the Measurement of the Effects of Stratospheric Aircraft (COMESA) under Dr. R.J. Murgatroyd and Mr. P. Goldsmith, and forms part of the research program of the National Physical Laboratory.

REFERENCES

1. Harries, J.E., Swann, N.R.W., Beckman, J.E. and Ade, P.A.R., "High resolution observations of the submillimetre stratospheric emission spectrum," Nature *236*, 159, 1972: See also H.A. Gebbie, W.J. Burroughs, J.E. Harries and R.M. Cameron, "Submillimetre wave spectroscopy of the earth's atmosphere above 39,000 feet," Astrophys. J. *154*, 405, 1968.

2. Beckman, J.E., Ade, P.A.R., Huizinga, J.S., Robson, E.I., Vickers, D.G., and Harries, J.E., "Limits to the submillimetre isotropic background," Nature *237*, 154, 1972.

3. Harries, J.E., and Burroughs, W.J., "Measurements of submillimetre wavelength radiation emitted by the stratosphere," Quart. J. Roy. Met. *97*, 579, 1971.

4. Harries, J.E., and Burroughs, W.J., "Measurements of Submillimetre Wavelength Radiation Emitted by the Stratosphere, using Fourier Transform Techniques," NPL Divisional Report DES 7, 1971.

5. Burroughs, W.J., and Harries, J.E., "Observations of millimetre wave solar radiation at sea level," Infrared Phys. *11*, 99, 1971.

6. Harries, J.E., "Measurements of H-O-N Compounds in the Stratosphere from Concorde 002," NPL Divisional Report DES *16*, 1972.

7. Burroughs, W.J., and Harries, J.E., "Direct method of measuring stratosphere water vapour mixing ratios," Nature *227*, 824, 1970.

8. Stone, N.W.B., "Spectroscopy of some gases in the far infrared using a Michelson interferometer," PhD. Thesis, University of London, 1964.

9. Dowling, J.M., "Investigations in the Far Infrared with a Lamellar Grating Interferometer," Air Force Report SSD-TR-67-30, 1967.

10. Palik, E.D., and Rao, N.K., "Pure rotational spectra of CO, NO, and N_2O between 100 and 600 microns," J. Chem. Phys. *25*, 1174, 1956.

11. Harries, J.E., Burroughs, W.J., and Duxbury, G., "The pure rotation spectrum of HNO_3," Nature, Phys. Sci. *232*, 171, 1971.

12. Gora, E.K., "The pure rotation spectrum of ozone," J. Mol. Spec. *3*, 78, 1959, and private communication.

13. Bird, G.R., Hunt, G.R., Gebbie, H.A., and Stone, N.W.B., "The far infrared pure rotational spectrum of nitrogen dioxide (NO_2)," J. Mol. Spec. *33*, 244, 1970.

14. Goody, R.M., *Atmospheric Radiation*, Part 1, Oxford University Press, 1964.

15. Murcray, D.G., Kyle, T.G., Murcray, F.H., and Williams, W.J., "Presence of HNO_3 in the upper atmosphere," JOSA *59*, 1131, 1969.

16. Rhine, P.E., Tubbs, L.D., and Williams, D., "Nitric acid vapor above 19 km in the earth's atmosphere," Appl. Opt. *8*, 1150, 1969.

17. Houghton, J.T., Peskett, G.D., and Rodgers, C.D., "A Scientific Proposal to Employ the Pressure Modulator Radiometer to Sound the Temperature and Composition of the Stratosphere and Mesosphere," Clarendon Laboratory Report 40/71, Oxford University, 1971.

18. Schutz, K., Junge, C., Beck, R., and Albrecht, B., "Studies of atmospheric N_2O," J. Geophys. Res. *75*, 2230, 1970.

19. Goldman, A., Murcray, D.G., Murcray, F.H., Williams, W.J., Kyle, T.G., and Brooks, J.N., "Abundance of N_2O in the atmosphere between 4.5 and 13.5 km," JOSA *60*, 1466, 1970.

20. Bates, D.R., and Hays, P.B., "Atmospheric nitrous oxide," Planet. Space Sci. *15*, 189, 1967.

21. Abel, P.G., Ellis, P.J., Houghton, J.T., Peckham, G., Rogers, C.D., Smith, S.D., and Williamson, E.J., "Remote sounding of atmospheric temperature from satellites: II," Proc. Roy. Soc. *A320*, 35, 1970.

22. Ackerman, M., and Muller, C., "Stratospheric nitrogen dioxide from infrared absorption spectra," Nature *240*, 300, 1972.

23. Pick, D.R., and Houghton, J.T., "Measurements of atmospheric infrared emission with a balloon-borne multifilter radiometer," " Quart. J. Roy. Met. Soc. *95*, 535, 1970.

24. Mastenbrook, H.J., "The variability of water vapor in the stratosphere," J. Atmos. Sci. *28*, 1495, 1971.

25. Shimazaki, T., and Laird, A.R., "A model calculation of the diurnal variation in minor neutral constituents in the mesosphere and lower thermosphere including transport effects," J. Geophys. Res. *75*, 3221, 1970.

26. Godson, W.L., "Total ozone and the middle stratosphere over arctic and sub-arctic areas in winter and spring," Quart. J. Roy. Met. Soc. *86*, 301, 1960.

27. Meira, L.G., "Rocket measurements of upper atmospheric nitric oxide and their consequences to the lower ionosphere," J. Geophys. Res. *76*, 202, 1971.

28. Harries, J.E., Swann, N.R.W., Carruthers, G.A., and Robinson, G.P., "Measurements of the submillimetre stratospheric emission spectrum from a balloon platform," Infrared Phys., in press.

29. Lazrus, A.L., Gandrud, B., and Cadle, R.D., "Nitric acid vapor in the stratosphere," J. Appl. Met. *11*, 389, 1972.

30. Murcray, D.G., private communication.

DISCUSSION

BENSON: What type of measurements do you plan to make in the future, and how much data will be coming out? Do you plan to measure other gases?

GRAYSTONE: We plan to repeat the measurements from Concorde 002 in February 1973, but at higher spectral resolution, so as to improve the certainty of assignments and the accuracies of concentrations. This should give us more definite observations of NO_2 and SO_2, as well as the H_2O, O_3, HNO_3, and N_2O. We are going to make observations as a function of elevation angle from the Concorde some time late in 1973, to try to derive a vertical profile of concentrations. We also will make studies at much higher latitudes, and take measurements during consecutive day/night periods to monitor diurnal variations.

SCHAINKER: What is the noise intensity in your spectrum?

GRAYSTONE: The signal-to-noise ratio in the interferogram is about 10^3. In the spectrum, the integrated intensity of the weakest lines used is between two and five times the noise level; that of the strongest is of the order of 100 times the noise level.

KIRCHHOFF: Could you make any comment on stratospheric NO concentrations on the basis of your measurements to date?

GRAYSTONE: No indeed. We are only saying that 160 ppb is an *upper limit* for the concentration of NO, since our method would only be able to detect a higher level. It could be anywhere below that; we have no way of telling.

VERTICAL DISTRIBUTION OF MINOR ATMOSPHERIC CONSTITUENTS AS DERIVED FROM AIR-BORNE MEASUREMENTS OF ATMOSPHERIC EMISSION AND ABSORPTION INFRARED SPECTRA

D.G. MURCRAY, A. GOLDMAN, F.H. MURCRAY,
W.J. WILLIAMS, J.N. BROOKS AND D.B. BARKER
Department of Physics
University of Denver
Denver, Colorado

ABSTRACT: Mixing-ratio altitude profiles of minor atmospheric constituents have been derived from infrared balloon-borne spectroscopic observations. The observations were made from various altitudes using a solar spectrometer, spectral radiometers, and filter radiometers. The spectrometer is used to measure atmospheric absorption using the sun as a source; the radiometers are used to measure atmospheric emission. The current spectral resolution is ≈ 0.3 cm^{-1} for the absorption spectra and $\gtrsim 2$ cm^{-1} for the emission spectra. The available data cover the spectral region from 1 to 30μ. Results for vertical distributions of H_2O, CO and N_2O are presented, based on a line-by-line/layer-by-layer emission and absorption analysis, and for HNO_3, based on statistical band-model analysis.

INTRODUCTION

Our group at the University of Denver has been engaged in studies of the variation of the infrared atmospheric absorption and emission for a number of years. Data pertinent to this study have been obtained with balloon-borne spectrometers; they cover the spectral region from 1 to 30μ.

The data obtained with the instruments were recorded on board the balloon payload by means of a digital magnetic-tape recorder. Parallel outputs were also telemetered by means of an FM/FM telemetry system. The transmittance instrumentation is designed to measure the atmospheric transmittance at various altitudes. These data are obtained by studying the variation of the solar spectrum in various wavelength intervals with altitude. The system consists of a biaxial pointing control which is used to maintain the solar radiation on the entrance slit of the spectrometer and a 1/2 meter Czerny-Turner grating spectrometer which uses a small Littrow prism spectrometer as a predisperser and employs a Ge:Cu detector. This instrumentation is described in a previous article [1]. The current spectral resolution is ≈ 0.3 cm^{-1}. Two units are designed to measure the atmospheric emission in selected wavelength regions – a filter radiometer and a spectral radiometer. In the filter radiometer, all of the optical components in the field of view of the detector are cooled to 77°K. The radiation passes through a filter wheel with positions for 5 filters, after which it is focused onto a Ge:Cu detector. The field of view is 2°. The spectral radiometer employs a cassegrainian design with a Bausch and Lomb replica grating used as a dispersing element. Radiation passing through the exit slit is imaged onto a Ge:Cu detector. The whole unit is enclosed in a container which is cooled to 77°K by liquid nitrogen. The field of view is 12° and the spectral resolution is $\gtrsim 2$ cm^{-1}.

The vertical distribution of the minor constituents is derived by fitting the observed integrated radiance, or the integrated absorption, of selected isolated spectral regions, to the corresponding theoretical infinite-resolution integrals. Two methods are used, the line-by-line method and the band-model method. The necessary parameters – individual line parameters (frequencies, intensities, half-widths and energy levels) and band-model parameters (average intensities and average half-widths) – are available for most atmospheric molecules of interest. Elaborate computer programs have been developed for these computations and are currently being used on the CDC 6600/7600 computers at the National Center for Atmospheric Research, Boulder, Colorado.

METHODS OF ANALYSIS

Line-by-Line Method

The line-by-line analysis of the data is based on successive layer-by-layer calculations. Homogeneous atmospheric layers are defined by the actual altitudes of observations $h_1, h_2, \ldots, h_N$, where h_1 is the highest altitude. The basic equations are similar for emission and absorption spectra. The equations for emission spectra are [2]:

$$R(\nu,h_1) = E(\nu,1)\, B(\nu,1), \tag{1}$$

$$R(\nu,h_n) = T(\nu,n)\, R(\nu,h_{n-1}) + E(\nu,n)\, B(\nu,n), \tag{2}$$

$$n = 2, \ldots, N,$$

where $R(\nu,h_n)$ is the infinite-resolution radiance at ν (cm^{-1}) observed at h_n, $B(\nu,n)$ is the blackbody radiance of layer n, and $E(\nu,n)$ and $T(\nu,n)$ its infinite-resolution emissivity and transmittance respectively. The corresponding equations for absorption spectra are [3]:

$$A(\nu,h_1) = E(\nu,1), \tag{1a}$$

$$A(\nu,h_n) = T(\nu,n)\, A(\nu,h_{n-1}) + E(\nu,n), \tag{2a}$$

$$n = 2, \ldots, N,$$

where $A(\nu,h_n)$ is the infinite-resolution absorption observed at h_n. The infrared atmospheric emissivity is determined by the gas amounts and the vibration-rotation and pure rotation lines of the various molecular species. Eqs. (1) - (2) represent successive equations for $R(\nu,h_n)$, $A(\nu,h_n)$ where each step below h_1 involves two consecutive layers, and thus can yield concentrations of atmospheric constituents as a function of altitude.

Assuming no scattering, the relation $T(\nu) = 1 - E(\nu)$ can be substituted into Eqs. (1) - (2). $T(\nu,h_n)$ is a function of the amount of absorber $U(n)$ in the layer n between altitudes h_n and h_{n-1}. It seems now that once a theoretical model is developed for $T(\nu,h_n)$, Eqs. (1) - (2) can be solved successively for $U(n)$, $n = 1, \ldots, N$, thus yielding the desired absorber profile. However, the observed spectral radiance, $\bar{R}(\nu,h_n)$, or absorption, $\bar{A}(\nu,h_n)$, to be denoted by $\bar{S}$, are not at infinite resolution, but are rather a convolution of the infinite resolution $S(\nu,h_n)$, with the spectrometer slit function.

The integrated radiance, or absorption, is independent of the slit function. Thus, the integrated S is a suitable parameter for a fitting of theoretical integrated S, $\int S(\nu,h_n)d\nu$, to the experimental values, $\int \bar{S}(\nu,h_n)d\nu$, by successive solutions of the equations:

$$F[U(n)] = \int_{\nu_1}^{\nu_2} \bar{S}(\nu,h_n)d\nu - \int_{\nu_1}^{\nu_2} S(\nu,h_n)d\nu = 0, \tag{3}$$

for $U(n)$, $n = 1, \ldots, N$, where $S(\nu,h_n)$ is given by Eqs. (1) - (2).

It is not necessary here to use the entire band, but only to pick out an interval $[\nu_1,\nu_2]$ with a representative isolated group of lines. It is important that the spectral region chosen be isolated, so that the experimental integrated $\bar{S}$ can be accurately determined.

The above determination of $U(n)$ requires a suitable model for the calculation of $T(\nu,n)$. The most accurate transmittance is obtained by a line-by-line calculation. The monochromatic transmittance $T(\nu,n)$ is given by [4,5]:

$$T(\nu,n) = \exp[-k(\nu,n)\, U(n)], \tag{4}$$

where $k(\nu,n)$ is the absorption coefficient, which is a sum of the absorption coefficients of all spectral lines,

$$k(\nu,n) = \Sigma_i\, k_i(\nu,n), \tag{5}$$

which might contribute to the transmittance at ν.

The atmospheric infrared line shapes are given by the Voigt profile [4,5], which is a convolution of the Lorentz and Doppler shapes. For altitudes where the Doppler halfwidth is $\lesssim$ Lorentz halfwidth, the Doppler effects can be neglected. Thus

$$k(\nu,n) = \Sigma_i \frac{S^0{}_i(n)}{\pi} \frac{\alpha_i(n)}{(\nu-\nu_{0i})^2 + \alpha^2{}_i(n)}, \tag{6}$$

where ν_{0i}, α_i, and $S^0{}_i$ are the individual line centers, line halfwidths, and line intensities respectively. In the atmosphere, α_i and $S^0{}_i$ will vary from one layer to another as a result of temperature and pressure variations. The line intensities are assumed to depend on the temperature, θ, according to [5]:

$$S^0(\theta) = S^0(\theta_0)\,[\theta_0/\theta]^{Z+1} \times \exp\left[-1.439E''\left(1/\theta - \frac{1}{\theta_0}\right)\right] \times [1 - \exp(-1.439\nu_0/\theta)] \div [1 - \exp(-1.439\nu_0/\theta_0)]. \quad (7)$$

Here Z is the power of the temperature dependence of the rotational partition function. E'' (cm^{-1}) is the lower state energy, θ_0, θ are in degrees Kelvin, and ν_0 (cm^{-1}) is the line position. The induced-emission term, normally neglected in the near-infrared region, becomes significant at longer wavelengths such as 25μ.

The pressure dependence of α in a homogeneous layer is $\alpha \approx \alpha^0 P$, where P is the atmospheric pressure. The temperature dependence of α is assumed to be [2,3]:

$$\alpha^0(\theta) = \alpha^0(\theta_0)\,(\theta_0/\theta)^n, \quad (8)$$

where $n \approx 0.5$.

Atmospheric temperature and pressure profiles can be obtained from radiosonde data taken during the infrared measurements. The Curtis-Godson approximation [4] is then used to derive average temperature $\bar{\theta}_n$ and pressure $\bar{P}_n$ for each homogeneous layer. A constant absorber mixing ratio is assumed within each layer, so that [4]

$$\bar{P}_n = 0.5\,(P_n + P_{n-1}), \quad (9)$$

where P_n is the atmospheric pressure measured at altitude h_n. A similar relation is assumed for the temperature $\bar{\theta}_n$. These expressions for average pressures and temperatures are used for $n \geqslant 2$, while for $n = 1$, $\bar{P}_1$ is taken as $P_1/2$ and $\bar{\theta}_1$ as θ_1.

With the assumptions made above for the transmittance calculation, one can proceed to the solution of Eq. (3). The Newton-Raphson iterative method is very efficient for the solution for U (n) [2,3].

In the present study, vertical distributions of H_2O from emission data and of CO and N_2O from absorption data have been derived using the line-by-line/layer-by-layer method outlined above. A histogram, rather than a smooth curve, is shown for the mixing ratio profile to indicate the actual layers of the atmosphere considered in the profile derivation.

Band-Model Method

The derivation of the HNO_3 vapor distribution as a function of altitude is based on a band-model analysis of measurements of radiance $\bar{R}(\lambda,h_n)$ at wavelength λ. The atmosphere is divided as before into elementary layers corresponding to the actual altitudes of observation. The total amount of HNO_3 vapor in each layer, U (n), can then be derived, assuming homogeneous layers with constant mixing ratio within each layer.

The analysis starts at balloon float altitude, h_1, with the atmosphere above this altitude considered the first layer. Then the infinite-resolution radiance observed at wavelength λ and altitude h_1, $R(\lambda,h_1)$, is a one-layer emission with

$$R(\lambda,h_1) = E(\lambda,1)\,B_\lambda(\theta_1) = [1\text{-}T(\lambda,1)]\,B_\lambda(\theta_1), \quad (10)$$

where $E(\lambda,1)$ and $T(\lambda,1)$ are respectively the infinite-resolution emissivity and transmittance of layer 1, and $B_\lambda(\theta_1)$ is the blackbody radiance at wavelength λ and temperature θ_1 of layer 1.

According to the spectral statistical band model [4,5], the mean spectral transmittance $\bar{T}(\lambda)$ is given by

$$-\ln \bar{T}(\lambda) = \frac{(S^0/\delta)_\lambda\, U}{[1+(S^0/\gamma)_\lambda\,(U/\pi)]^{1/2}}, \quad (11)$$

where S^0($cm^{-2}atm^{-1}$) is the mean line intensity at unit pressure; $\gamma = \gamma^0 P$, where γ^0($cm^{-1}atm^{-1}$) is the mean line half-width and P is the atmospheric pressure; δ (cm^{-1}) is the mean line spacing; and U (atm-cm) is the amount of absorber present.

If we now consider the atmosphere above a certain altitude as a single homogeneous layer with an average temperature and pressure, we can combine equations (10) and (11) to get average radiance. Laboratory measurements [6] determined the band-model parameters at 40°C, so temperature corrections [5] were assumed to follow $S = S'\theta'/\theta$ and $\gamma = \gamma'(\theta'/\theta)^{1/2}$, where the primed quantities refer to 40°C. Equations (10,11) can then be solved for U (1). In all solutions to our data, U was found to be on the order of 10^{-4}(atm-cm) and the dimensionless Ladenburg-Reiche parameter ($S^0 U/2\pi\gamma$) was

always less than 10^{-3}. Thus, equation (11) can be simplified to

$$\bar{\epsilon}(\lambda) = (S^0/\delta)_\lambda U. \qquad (12)$$

The Ladenburg-Reiche parameter is $\ll 1$; hence, the analysis of the layered atmosphere is considerably simplified. The infinite-resolution radiance observed at h_2 can be derived as

$$R(\lambda,h_2) = E(\lambda,2)\, B_\lambda(\theta_2) + E(\lambda,1)\, B_\lambda(\theta_1) - E(\lambda,1)\, E(\lambda,2)\, B_\lambda(\theta_1). \qquad (13)$$

In the corresponding expression for average radiance $\bar{R}(\lambda,h_2)$ the overlap term can be neglected [7]. In addition, since $B_\lambda(\theta)$ is a slowly varying function of λ at a given θ, in comparison to the emissivity, we can choose θ as the average temperature of the layer (h_2 to h_1) and get an average $B_\lambda(\bar{\theta})$, where $\bar{\theta} = (\theta_1 + \theta_2)/2$, and then

$$\Delta\bar{R}(2,1) \equiv \bar{R}(\lambda,h_2) - \bar{R}(\lambda,h_1) = B_\lambda(\bar{\theta})\, E(\lambda,2). \qquad (14)$$

Combining relations (12) and (13) enables us to derive the amount of emitter in a layer between observations at two altitudes. This procedure can be generalized to any layer n so that

$$U(n) = \Delta\bar{R}(n,n-1)/B_\lambda(\bar{\theta})\,(S^0/\delta)_\lambda. \qquad (15)$$

This analysis was derived for spectral data, but it is also valid for a complete band if the "box" band-model parameters and the additional temperature correction $\delta_{band} = \delta'_{band}(T/T')^{1/2}$ are used [5].

It should be noted that Eq. (14) can lead to various errors when the overlap term in Eq. (13) is significant.

RESULTS

H_2O

Results for H_2O from Alamogordo, New Mexico, have been presented in detail [2]. Figures 1-4, selected from Reference 2, demonstrate the data, the method of analysis, and the resulting H_2O profiles.

Additional emission data in the 25μ region were obtained during a balloon flight made 21 April 1972 from Hyderabad, India. The resulting mixing ratio is presented in Figure 5. It shows a gradual decrease of the mixing ratio with altitude, from 10^{-5} gm/gm near 10 km to $\approx 10^{-7}$ gm/gm near 30 km. No obvious correlation could be observed with the tropopause location, which was near 18 km.

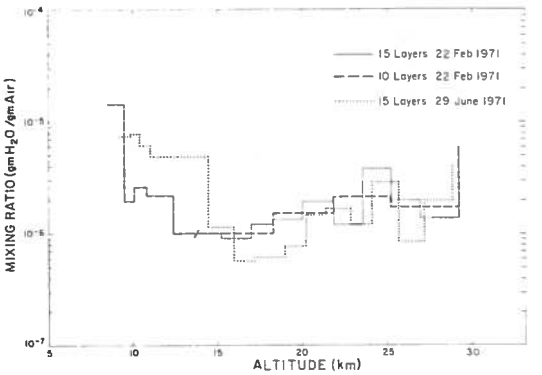

Figure 3. Mixing ratio of water vapor as derived from a 15-layer (solid line) and a 10-layer (broken line) calculation using the 25μ line group for the 22 February 1971 balloon flight. The slash near 14 km indicates the boundary between two layers with similar mixing ratio. The mixing ratio derived from a 15-layer calculation using the 25μ line group for the 29 June 1971 balloon flight is shown by the dotted line.

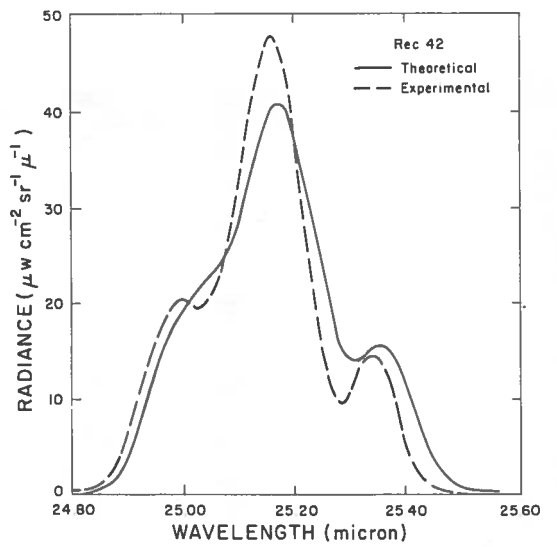

Figure 4. Comparison of theoretical and experimental radiance for the 25μ line group for Record 42 from the February 1971 flight. 15 layers were used in the calculated spectrum.

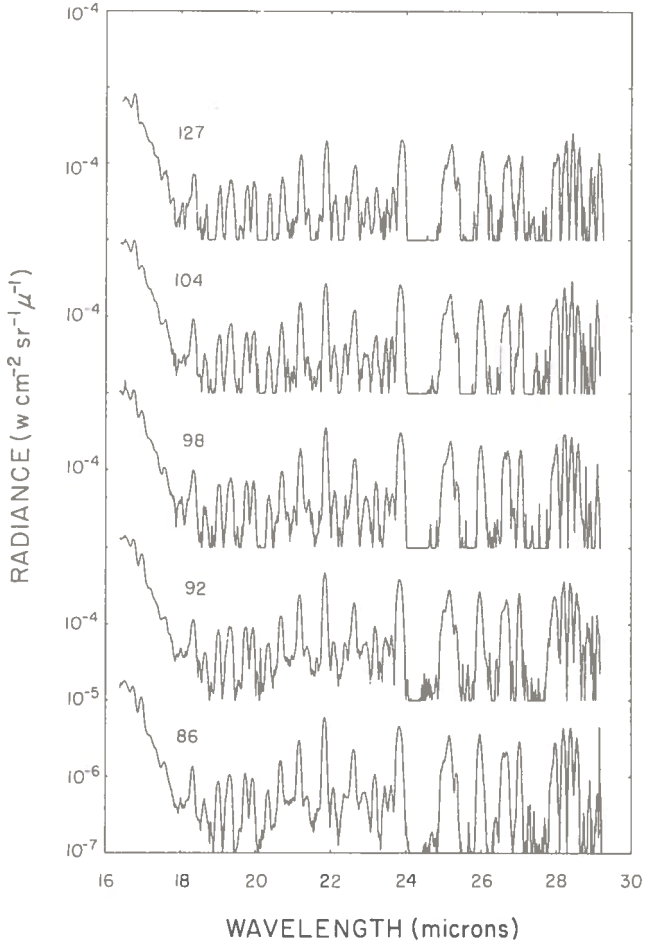

Figure 1. Samples of the reduced data obtained 22 February 1971 at Alamogordo, New Mexico, showing the downward night emission in the 16-30μ region as a function of altitude. The zenith angle was 45° for all records. Successive records are displaced by two decades of the log scale.

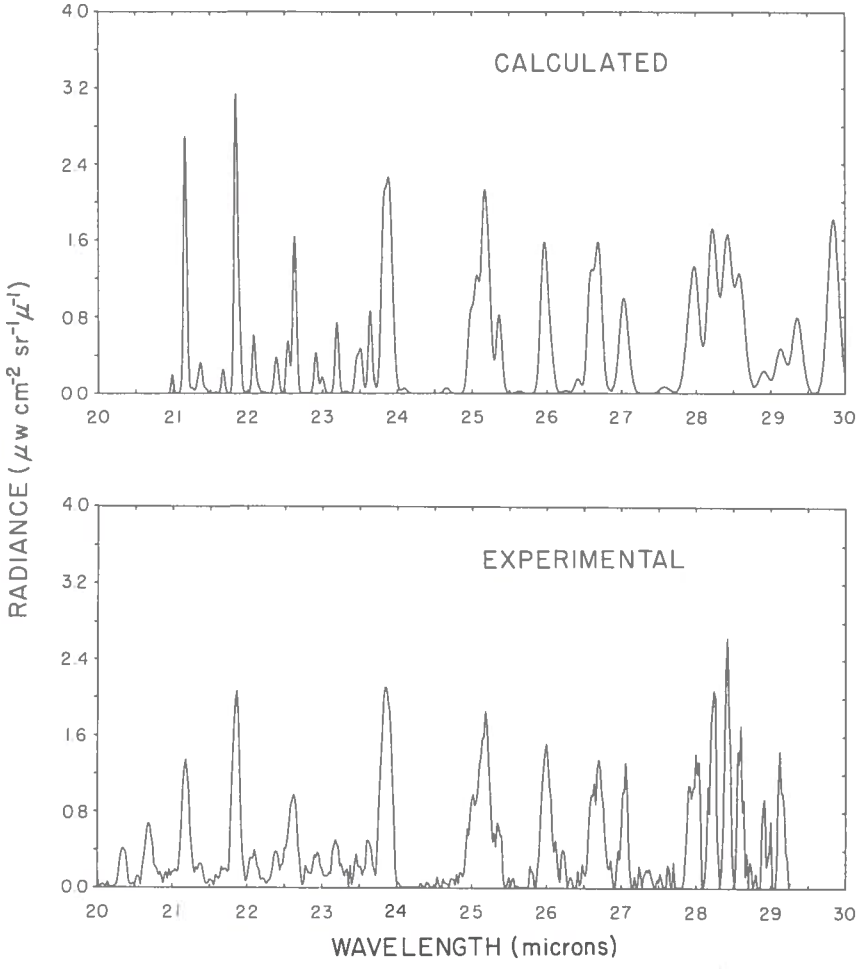

Figure 2. Comparison of calculated and measured emission spectra in the 20-30μ region for Record 127 of the February flight. U (1) is derived from the 25μ line group and corresponds to a mixing ratio of 5.8×10^{-6}gm/gm.

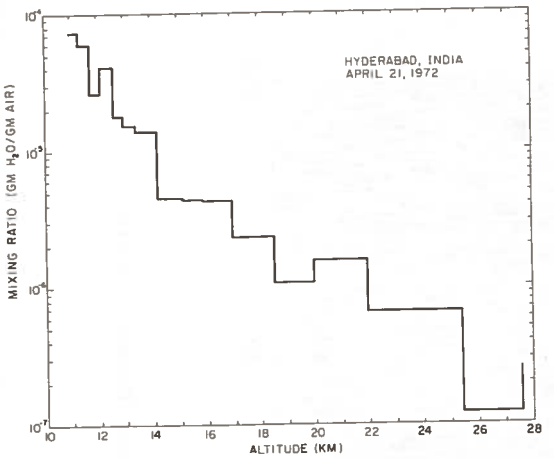

Figure 5. Mixing-ratio profile of H_2O as derived from a 16-layer calculation from the emission of the 25μ line group for the 21 April 1972 balloon flight made from Hyderabad, India.

CO

Data and results for CO from the 18 January 1972 balloon flight have been presented recently [3]. Figures 6-8 have been selected from Reference 3 to demonstrate some of the data and the results.

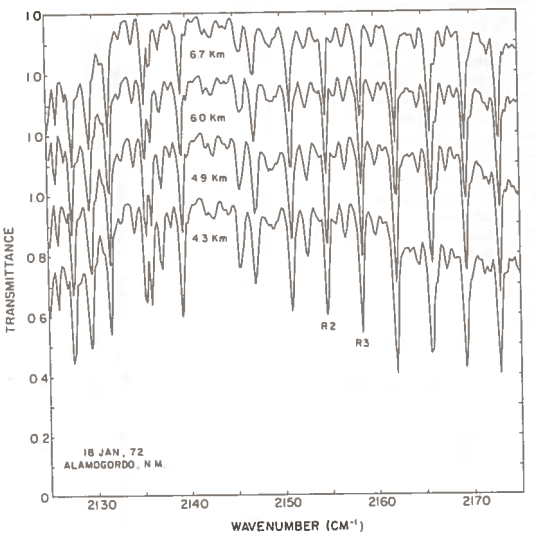

Figure 6. Atmospheric transmittance vs wavenumber from consecutive records at various altitudes for the 2125-2175 cm^{-1} region. The details of the records are given in Reference 3.

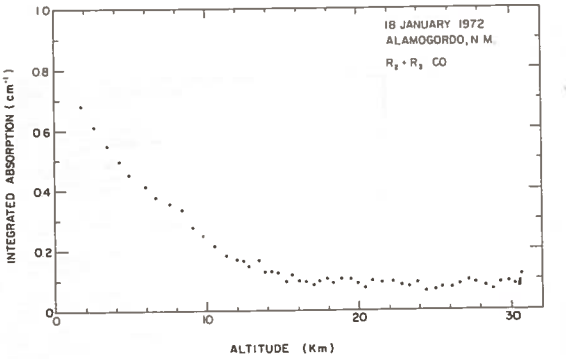

Figure 7. Integrated absorption vs altitude for the R (2) and R (3) lines of the fundamental (1-0) rotation-vibration band of CO.

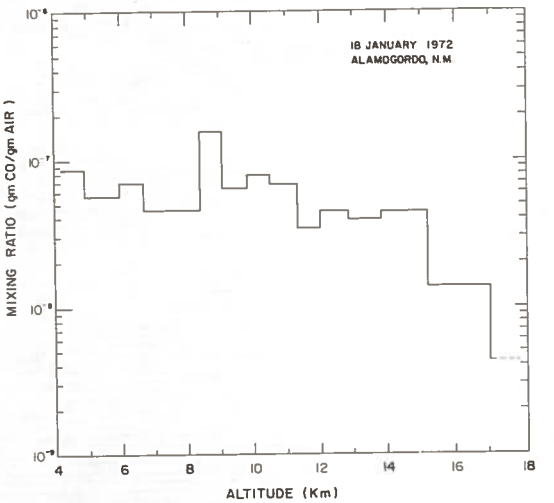

Figure 8. Mixing ratio of CO as derived from a 15-layer calculation using the R (2) and R (3) lines.

N_2O

An N_2O mixing ratio has been derived from line-by-line analysis of the 4.5μ region as observed during the 18 January 1972 flight. Figure 9 shows selected spectra obtained in the 2175-2250 cm^{-1} region. Each record is displaced by 20% in transmittance for clarity. The details of the records – altitudes, temperatures, pressures, and sun zenith angles – have been tabulated previously [3].

Both ends of this spectral region show significant interference from atmospheric constituents other than N_2O. On the short-wavelength side the N_2O lines are overlapped by

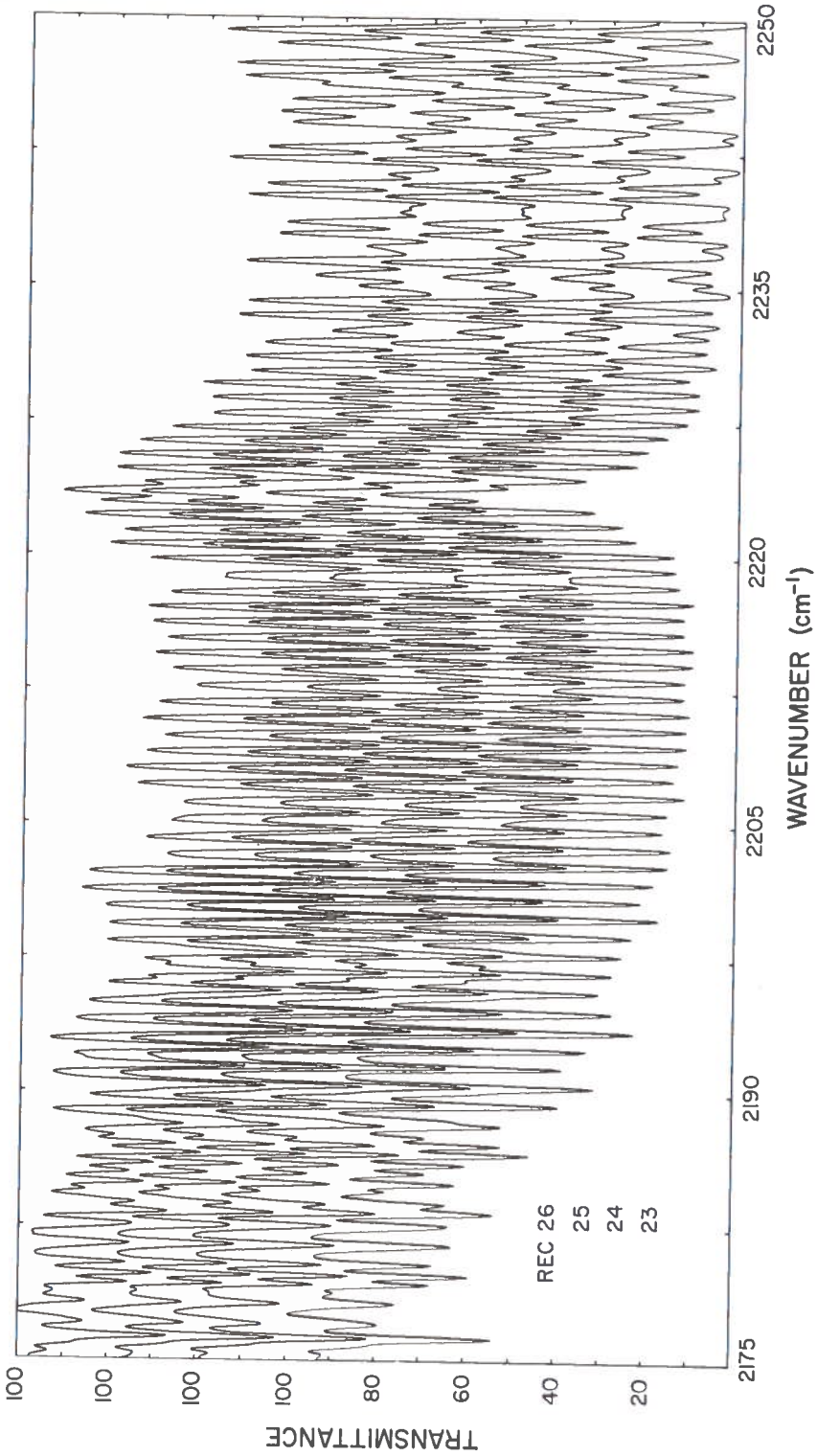

Figure 9a. Atmospheric transmittance vs wavenumber at various altitudes for the 2175-2250 cm^{-1} region, Records 23-26. (The record details are given in Reference 3.)

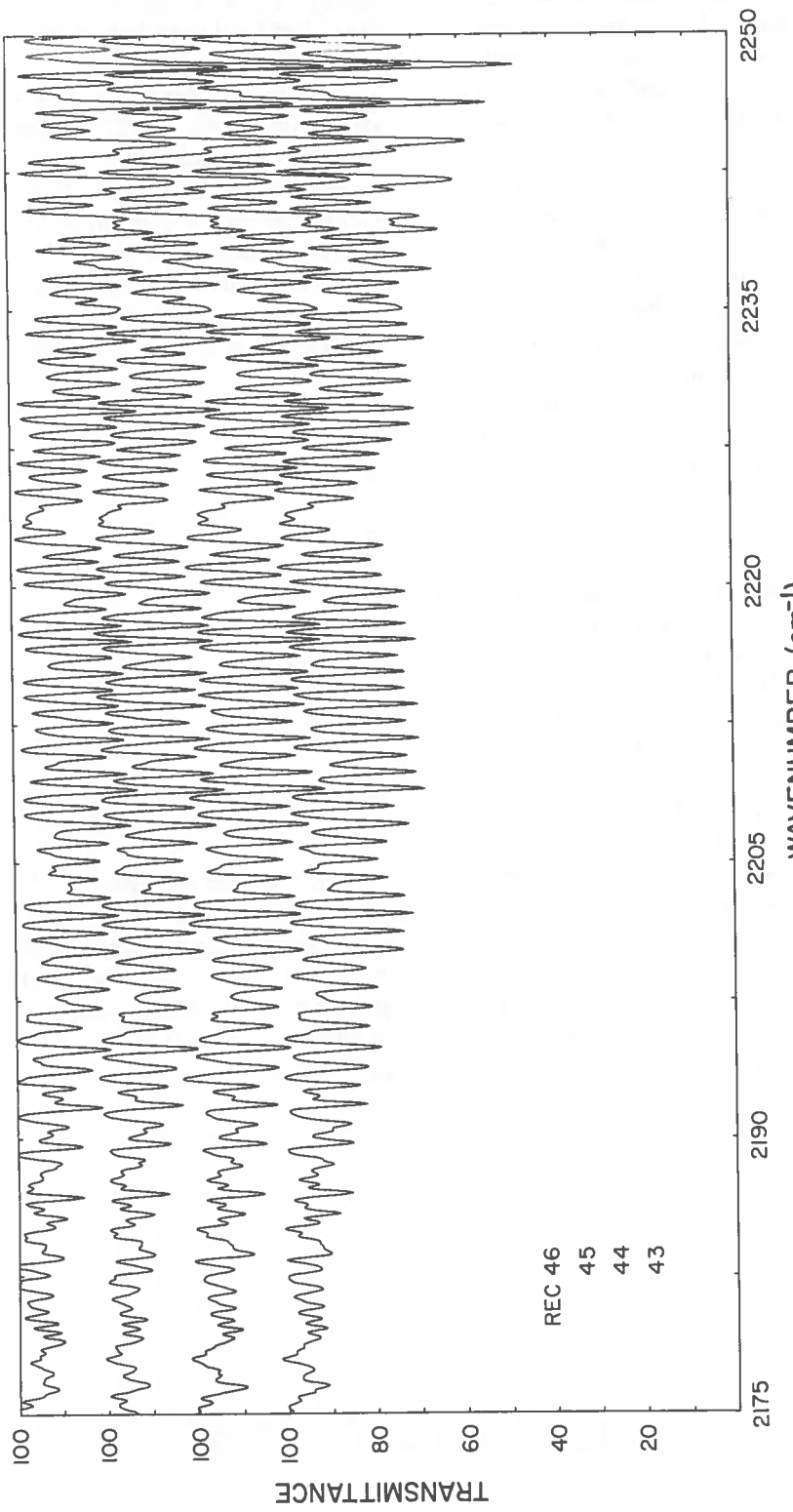

Figure 9b. Atmospheric transmittance vs wavenumber at various altitudes for the 2175-2250 cm^{-1} region, Records 43-46. (The record details are given in Reference 3.)

ν_3 ^{13}C $^{16}O_2$ P-branch lines, while on the long-wavelength side there is considerable interference with the (0-1) CO R-branch lines. However, near the ν_3 N_2O band center, the interference with CO_2 and CO is quite small, and for $2215 < \nu < 2225$ cm^{-1} the J values for CO R (J) lines and the CO_2 P (J) lines are $J > 20$ and $J > 60$ respectively. Thus the 2215-2225 cm^{-1} region is suitable for the derivation of the N_2O profile by assuming no interference from CO and CO_2 lines.

Boltzmann population ratios indicate that the strongest transitions in the band system near 4.5μ are the ν_3 fundamental band and the $\nu_3 + \nu_2 - \nu_2$ "hot" band, with an intensity ratio of ≈ 0.12. Isotopic N_2O ν_3 bands and the $\nu_3 + \nu_1 - \nu_1$ and $\nu_3 + \nu_3 - \nu_3$ "hot" bands are weaker by about an order of magnitude or more than the $\nu_3 + \nu_2 - \nu_2$ band and can be ignored for the present analysis.

Individual line parameters (positions, intensities, ground-state energies and half-widths) with J up to 80 were thus generated for the 4.5μ region by considering the ν_3 ($00^00 - 00^01$) and the $\nu_3 + \nu_2 - \nu_2$ ($01^10 - 01^11$) transitions. The line intensities were normalized to the band intensities by Lowder [10] and the line widths were taken from Tejwani and Varanasi [11] for an N_2O - air mixture. No vibration-rotation interaction was included in deriving the line intensities. Also, the ℓ-type doubling is not resolved here, and each line is actually a double.

The derived line intensities are plotted in Figure 10 as a function of ν; they show clearly the two bands used in the present analysis. It should be noted that the $\nu_3 + \nu_2 - \nu_2$ band is a $\pi - \pi$ transition with $\Delta\ell = 0$ and thus has a very weak Q branch, which hardly shows in the figure. The $\nu_3 + \nu_2 - \nu_2$ R-branch occurs at the center of the ν_3 band and contributes there significantly to the absorption contours.

Figure 11 shows the observed integrated absorption of the 2215-2225 cm^{-1} region as a function of altitude. Above 20 km it is difficult to separate the atmospheric N_2O lines from the background solar CO absorption, manifested as a nearly constant value from 25 to 30 km. The solar background can be subtracted from the atmospheric absorption, since practically none of the N_2O lines coincide with the solar CO lines [3].

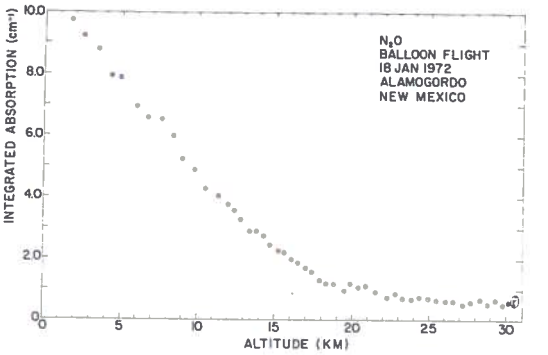

Figure 11. Observed integrated absorption vs altitude in the 2214.5-2225.5 cm^{-1} region.

On the basis of Figure 11, 21 records were selected for the line-by-line/layer-by-layer analysis. The resulting vertical distribution of N_2O is shown in Figure 12. The results indicate a gradual decrease of the mixing ratio as a function of altitude, from ≈ 0.35 ppm near 3 km to 0.15 ppm near 18 km.

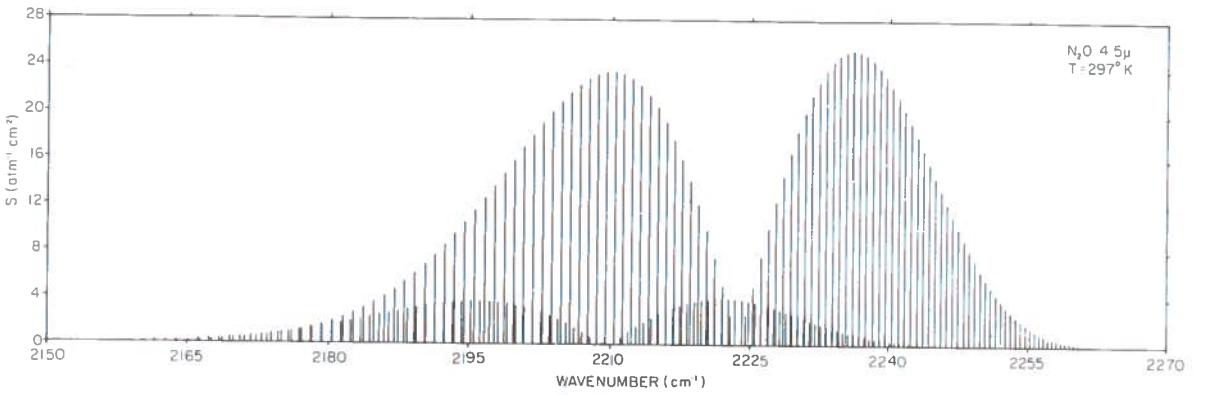

Figure 10. Line intensities of the ν_3 and $\nu_3 + \nu_2 - \nu_2$ bands of N_2O.

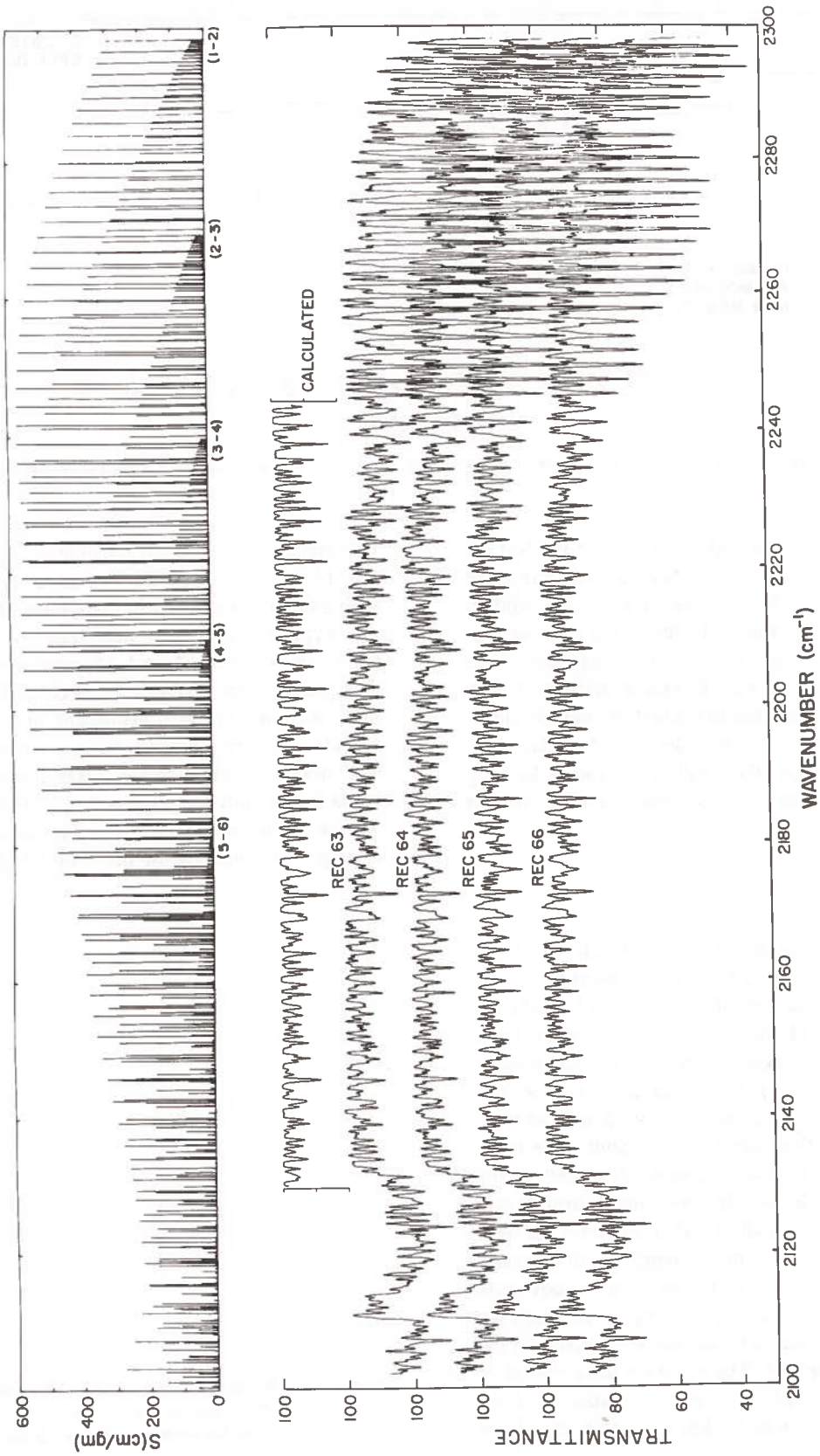

Figure 13. Solar absorption in the CO fundamental region, and its interpretation as solar CO at 4500 K. See Reference 8 for details.

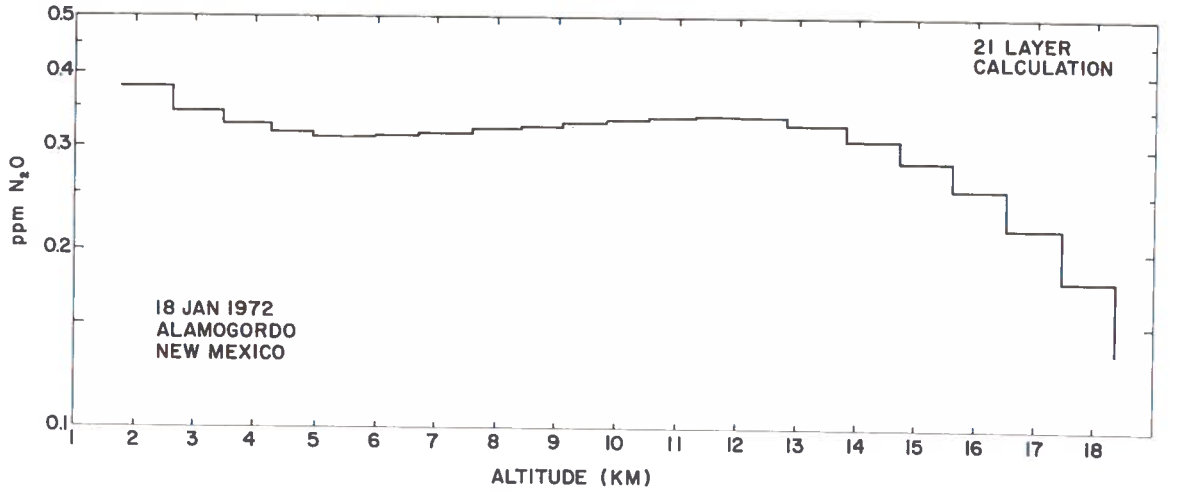

Figure 12. Mixing ratio of N_2O vs altitude as derived from a 21-layer calculation using the results in Figure 10.

It should be noted that both CO and N_2O in the spectral region used here are superimposed on solar CO lines. These have been studied separately [8]. Figure 13 shows the solar absorption in this region and the interpretation of the data in terms of solar CO bands with $\Delta v = 1$. It should be noted that the solar CO lines extend to $\nu > 2300$ cm^{-1} and thus have to be taken into account also in the analysis of the 4.3μ CO_2 atmospheric bands when observed with the sun as a source.

HNO_3

HNO_3 vibration-rotation bands at 5.9μ, 7.5μ, 11.3μ, and 21.9μ were observed in the absorption data with about a 0.3 cm^{-1} resolution [9]. Some of these bands have since been observed in emission spectra. For the present analysis, the 11.3μ band was chosen since it is centered in an atmospheric "window," with no overlap of other atmospheric bands. The emission data permit more accurate derivation of the HNO_3 altitude profile than the transmittance data, since for small absorber amounts emission measurements are more sensitive than transmission measurements. In the present study, data obtained from four balloon flights are analyzed to determine the altitude profile of HNO_3 in the lower stratosphere. The emission data consist of atmospheric radiance values obtained from several km to about 30 km in altitude by a filter radiometer with a 70 cm^{-1} bandpass centered at the 11.3μ region and by a spectral radiometer with a 6 cm^{-1} resolution in the same region.

Typical filter data and spectral data are shown in Figures 14 and 15 respectively. The data (see Figure 14) are not necessarily monotonic and smooth with decreasing pressure. The analysis, however, assumes plane stratified layers, and neglects any possible atmospheric differences in the emitting regions seen by the radiometers with increasing altitude. Our derivation of mixing ratio depends on the ratio of change of

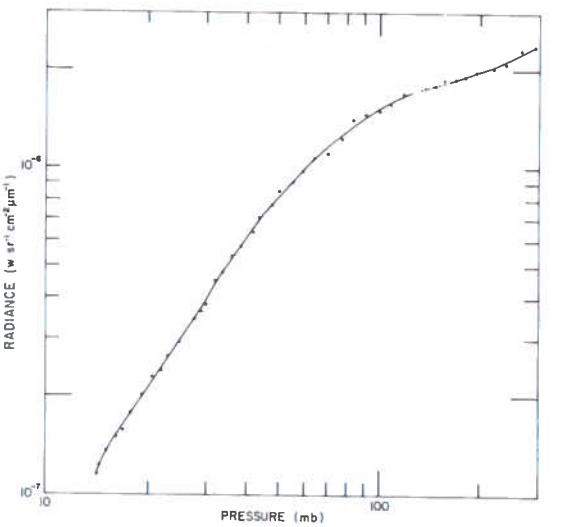

Figure 14. Radiance vs pressure for the 23 September 1970 measurements, with a smoothed curve between the observed points.

radiance, ΔR, to change of pressure, ΔP, and any non-monotonic behavior is smoothed. The only condition imposed on the smoothing technique was that the resultant data should be monotonic.

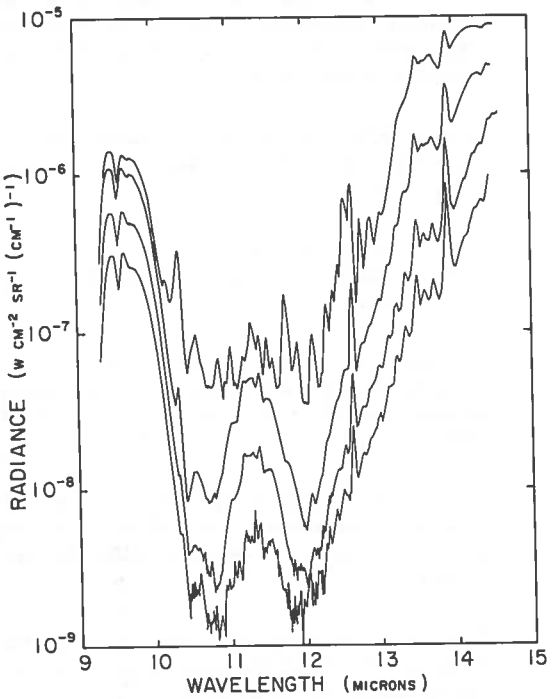

Figure 15. Typical spectral atmospheric radiance measured 10 December 1969 at altitudes of 3.4, 10.0, 20.1, and 24.7 km. The zenith angle was 45° for all records

The mixing ratio versus altitude is plotted in Figure 16 for four flights of the filter radiometer. Several prominent features are noticeable. First, the mixing-ratio profiles all have a maximum of about 2×10^{-8}gm HNO_3/gm air. Second, all the flights exhibit a gradual rise in mixing ratio with an increase in altitude until the maximum of about 2×10^{-8}gm/gm is reached between 20 and 24 km. The profiles then decrease to a relative minimum at about 27 km and, for the June flights, rise until the last record around 29 km. The total amount of HNO_3, U (atm-cm), is shown for each flight; it is the sum of the calculated amount of nitric acid in each layer considered in the analysis. The May, June, September, and November flights in 1970 had total amounts of 1.4, 2.1, 3.3, and 2.7 ($\times 10^{-4}$atm-cm); it should be noted that the May profile begins about 4 km higher in the atmosphere than the other flights. A variation of mixing ratio profiles with seasons and latitudes probably exists, but requires further study. The layering of nitric acid suggests a connection with ozone.

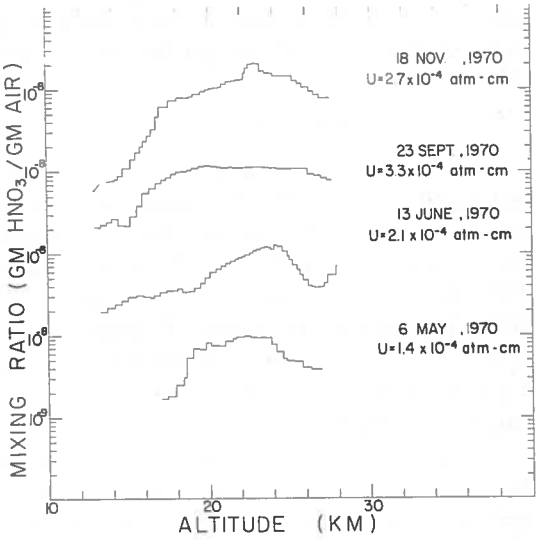

Figure 16. Mixing ratio profiles and total gas amounts for HNO_3.

SUMMARY

Results for vertical distributions of H_2O, CO, N_2O, and HNO_3 have been presented. H_2O profiles from three balloon flights have been derived by using a line-by-line/layer-by-layer analysis of emission spectra in the 24-29μ region. Two mixing-ratio profiles from Alamogordo, New Mexico, show a broad minimum near 15 km and a broad maximum near 25 km, with a range of values of $\approx 6 \times 10^{-7}$ gm/gm to $\approx 4 \times 10^{-6}$gm/gm. The H_2O mixing-ratio profile obtained from Hyderabad, India shows a gradual decrease with altitude, from $\approx 10^{-5}$gm/gm near 10 km to $\approx 10^{-7}$gm/gm near 30 km. A CO mixing-ratio profile has been derived from a line-by-line/layer-by-layer analysis of absorption spectra obtained in the 4.6μ region from Alamogordo, New Mexico. It shows a gradual decrease from $\approx 8 \times 10^{-8}$gm/gm near 4 km to $\approx 4 \times 10^{-8}$gm/gm near 15 km. A similar trend is also observed for N_2O, as derived from line-by-line/layer-by-layer analysis of absorption spectra in the 4.5μ region from the same flight. The N_2O mixing ratio decreases gradually from ≈ 0.35 ppm near 3 km to ≈ 0.15 ppm near 18 km. Four

HNO_3 profiles have been derived using a statistical band-model analysis of emission spectra in the 11.3μ region, also obtained from Alamogordo, New Mexico. The resulting profiles show that HNO_3 in the atmosphere has a multi-layer structure with a maximum mixing ratio of about 2×10^{-8}gm/gm between 20 and 25 km.

ACKNOWLEDGMENTS

The research was supported in part by the Advanced Research Projects Agency, monitored by the Air Force Cambridge Research Laboratories, and in part by the National Science Foundation – Department of Transportation (Climatic Impact Assessment Program) Grant GA-26228. The launch and recovery of the balloon instrumentation was capably handled by the AFCRL Balloon Group.

Acknowledgment is made to the National Center for Atmospheric Research, which is sponsored by the National Science Foundation, for computer time used in this research. The authors are indebted to T.G. Kyle of the National Center for Atmospheric Research, Boulder, Colorado, for a copy of his program for evaluating the line-by-line transmittance. C. Bauer, C.M. Bradford, W. Cochran, A. Csoeke-Poeckh, T. Dow, J.J. Kosters, J.R. Starkey, and J. Van Allen also took part in the program.

REFERENCES

1. Murcray, D.G., Murcray, F.H., and Williams, W.J., "A balloon borne grating spectrometer, " Appl. Opt. *6*, 191 (1967).

2. Goldman, A., Murcray, D.G., Murcray, F.H., Williams, W.J., and Brooks, J.N., "Distribution of water vapor in the stratosphere as determined from balloon measurements of atmospheric emission spectra in the 24-29μm region," to be published in Appl. Opt. 1973.

3. Goldman, A., Murcray, D.G., Murcray, F.H., Williams, W.J., Brooks, J.N., and Bradford, C.M., "Vertical distribution of CO in the atmosphere," in Proceedings of "Sources, Sinks, and Concentrations of Carbon Monoxide and Methane in the Earth's Environment," a joint meeting of the American Geophysical Union and the American Meteorological Society, Aug. 15-17, 1972, St. Petersburg Beach, Florida.

4. Goody, R.M., *Atmospheric Radiation*, Vol. I: Theoretical Basis, Oxford University Press, New York (1964).

5. Penner, S.S., *Quantitative Molecular Spectroscopy and Gas Emissivities*, Addison-Wesley Co., Inc., Reading, Mass. (1959).

6. Goldman, A., Kyle, T.G., and Bonomo, F.S., "Statistical band model parameters and integrated intensities for the 5.9μ, 7.5μ, and 11.3μ bands of HNO_3 vapor," Appl. Opt. *10*, 65 (1971).

7. Maclay, G.J., and Babrov, H.J., "Errors in spectral absorption measurements due to absorbing species in the atmosphere," J. Opt. Soc. Amer. *54*, 301 (1964).

8. Goldman, A., Murcray, D.G., Murcray, F.H., and Williams, W.J., "Solar absorption in the CO fundamental region," Submitted to Ap. J., 1972.

9. Murcray, D.G., Murcray, F.H., Williams, W.J., Kyle, T.G., and Goldman, A., "Variation of the infrared solar spectrum between 700 cm^{-1} and 2240 cm^{-1} with altitude," Appl. Opt. *8*, 2519 (1969).

10. Lowder, J.E., "Band intensity and line half-width measurements in N_2O near 4.5μ," J. Quant. Spectrosc. Radiat. Transfer *12*, 873 (1972).

11. Tejwani, G.D.T., and Varanasi, P., "Theoretical line width in N_2O-N_2O and N_2O-air collision," J. Quant. Spectrosc. Radiat. Transfer *11*, 1659 (1971).

DISCUSSION

SISSENWINE: Have you any physical explanation for the continued dropoff of water vapor over the tropics?

MURCRAY: Not yet. The signal-to-noise ratio on the emission spectra is quite good, and we can't find any obvious error.

LENA: Did you try to get a derived profile from a given altitude?

MURCRAY: No, since we doubt that it can be done. I think we would get a much better vertical distribution by using a layer-by-layer technique to determine the profile. Trying to do an inversion from a single altitude raises a lot of problems, such as pressure dependencies.

TOTH: In the 1800 to 1900 cm^{-1} region, did you see any NO or solar CO?

MURCRAY: A telluric CO_2 band goes through that region, but it is not very strong; we haven't seen much solar CO. We did not find any NO, nor would I care to guess at an upper limit for its concentration.

HIGH-RESOLUTION SPECTRA OF THE STRATOSPHERE BETWEEN 30 AND 200 CM^{-1}

J.P. BALUTEAU[1], E. BUSSOLETTI[2], P. LENA, AND A. MARTEN[3]
*Groupe Infrarouge Spatial**
Observatoire de Meudon
Meudon, France

ABSTRACT: We present here the preliminary results of the measurement of stratospheric emission spectra in the 30 - 200 cm^{-1} range. The spectra were obtained with a phase-modulated Michelson interferometer installed aboard a Caravelle. The flights were made at altitudes varying between 37,000 and 41,000 feet for a total of 16 hours of measurements. The preliminary results of one flight presented here show that the main features of the spectra are due, as expected, to H_2O lines. In addition, O_2 and O_3 lines are also easily identified. A comparison with the measurements of others, both in the laboratory and at altitude, show quite good agreement in the overlapping frequency regions.

It is worth noting that the spectrum of O_3 is known only to 89 cm^{-1}. We were able to identify the Q_R branches quite well up to this frequency in our spectra. In addition to the principal gases, other lines are tentatively identified as CO, NO, and N_2O. This is the first experiment ever to cover the frequency range beyond 125 cm^{-1} up to 200 cm^{-1}.

We also describe the future installation of this equipment aboard the Concorde, and present plans for improved instrumentation.

DESCRIPTION OF EXPERIMENT

Most of the previous far-infrared observations of the atmosphere have been performed from high mountain sites [1-3] and aircraft [4-8] by several authors in the frequency range 5-125 cm^{-1}. This paper reports preliminary results of recent aircraft measurements made by Baluteau and Bussoletti in the range 25-200 cm^{-1} using a step-scanning phase-modulated (10-Hz) Michelson interferometer. The instrument was carried aboard the experimental Caravelle 116 of the Centre d'Essais en Vol, Bretigny (France) on flights of May 8 and July 20, 1972, for a total of sixteen hours of observation time. The measurements were made at altitudes ranging from 37,000 feet to 41,000 feet. The spectra were taken in emission rather than in absorption, so the length of the observation time was limited only by the flight duration (about 4 hours). This procedure also allows night-time measurements, so that photochemical reactions may be studied.

The optical configuration of the instrument is shown in Figure 1. The sky is seen through a Mylar window of 40μ thickness at an angle of 30° above the aircraft horizontal. A metal shroud surrounds the interferometer-cryostat system, which is continuously purged by a flow of dry air. The maximum stroke of the moving mirror is 40 mm, so the instrument provides a maximum theoretical unapodized resolution of 0.063 cm^{-1}. Each step of the mirror is 20μ. The time between steps is 800 ms, while the signal integration time is 700 ms. The detector is a doped-germanium bolometer (Infrared Lab., Tucson, Arizona) with a measured noise-equivalent power (NEP) of 3×10^{-13} $W\text{-}Hz^{-1/2}$ at a typical working temperature of 2 K. The interferograms, which are the Fourier transform of the energy difference between the stratosphere ($\approx$ 220 K) and the experimental apparatus ($\approx$ 292 K), are recorded on magnetic tape during the flight. Data reduction is done on the ground, after digitization. The spectra are taken at resolutions varying from 0.2 cm^{-1} to 0.07 cm^{-1}, unapodized (Burroughs & Harries [9]).

No interference due to the aircraft's electrical system was observed. The entire apparatus

---

(1) J.P. Baluteau is also associated with the Laboratoire de Physique Stellaire et Planetaire, Verrières-le-Buisson.

(2) E. Bussoletti is on leave from the Laboratorio Plasma Spazio, C.N.R., Rome.

(3) A. Marten is also associated with the Centre National d'Etudes des Télécommunications.

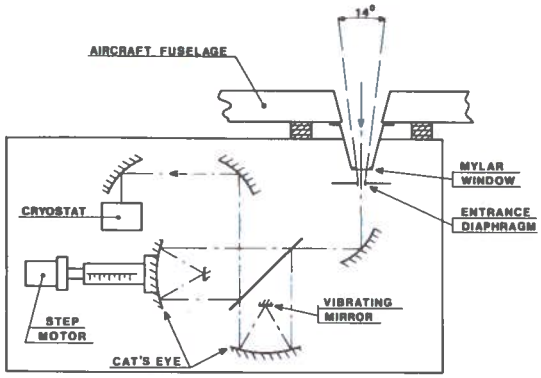

Figure 1. Schematic of the experimental system and its arrangment aboard the Caravelle. The instrument is a step-scanning Michelson interferometer with a cat's-eye configuration. The phase modulation is performed by the vibrating secondary mirror of the fixed cat's-eye. The Mylar beam-splitter has a thickness of 12.4μ. The moving mirror is mounted on a stepped micrometer. All the system interferometer-cryostat is enclosed in a metal shroud continuously purged by dry outside air. The flushing circuit contains a liquid N_2 trap and a heater.

was shock-mounted with a cut-off frequency of 7 Hz so that any effect of vibrations was eliminated. The details of the experiment are more extensively described elsewhere [10].

PRELIMINARY RESULTS

The following paragraphs describe preliminary results obtained during the flight of the night of May 8th at altitudes between 37,000 and 39,000 feet. These measurements were performed with a 12.3μ-thick Mylar beamsplitter which exhibits optimum efficiency over the wavelength range of interest. Figure 2 shows a typical interferogram. The noise level is evaluated from the fluctuations superimposed on the interference fringes observed at the end of the interferogram. The signal-to-noise ratio is typically 3000. Figure 3 shows two spectra obtained at a resolution of 0.18 cm^{-1}. The lower one was obtained by transforming the interferogram shown in Figure 2.

As can be seen, the reproducibility between the two spectra is very good; moreover, a general coincidence of many weak lines is also apparent. As expected, the noise increases toward the lowest frequencies, becoming essentially white noise beyond 20 cm^{-1}. Its peak-to-peak amplitude is evaluated at the end of the spectrum where no energy is expected, between 225 cm^{-1} and 250 cm^{-1}, and the subsequent rms value, σ, is computed.

An analysis of the spectra has been performed, considering as "really physical" only those lines whose peak amplitude is greater than 1 σ. The most prominent features are due to the H_2O rotational lines, the O_2 triplets, and the Q_R branches of O_3.

By operating the instrument in the laboratory with a blackbody source we obtained "ground-truth" spectra, at simulated aircraft altitude conditions, which confirm that none of the weak lines are instrumental artifacts.

The line assignments, as shown in Figure 3, have been carried out following Benedict [11] for H_2O (solid bars), and Gora [12] for O_3 (dotted bars). In addition, the O_2 lines (broken bars) are also identified. The bars for H_2O are plotted with a length proportional to the logarithm of the line strength, while for O_3 the length is proportional to the relative line strength, following Gora's Y values.

Comparison with the recent results of other authors [4,6] indicates good agreement in the overlapping frequency range. In some cases, our measurements show an improvement as a result of higher resolution and better signal-to-noise ratio.

Our attention has been devoted primarily to the identification of O_2 lines up to 200 cm^{-1}. Gora's calculations for O_3 up to 89 cm^{-1} allow positive identification of all the Q_R branches in this frequency range. Among the atmospheric trace gases, we have considered only CO, N_2O, and NO, because of their relatively high concentration (Dalgarno [13]).

Between 30 and 89 cm^{-1} many of the CO, NO, and N_2O lines fall close to the expected O_3 lines, so that positive identification becomes very difficult. A systematic analysis is in process to give definite assignments to the observed lines. In addition, calculations of the expected ozone transitions beyond 89 cm^{-1} are being carried out by A. Marten. These results will make possible an extension of the line assignments for trace gases.

Table 1 shows the calculated emission frequencies for O_2 between 30 and 200 cm^{-1}, with our observed emission frequencies listed in the

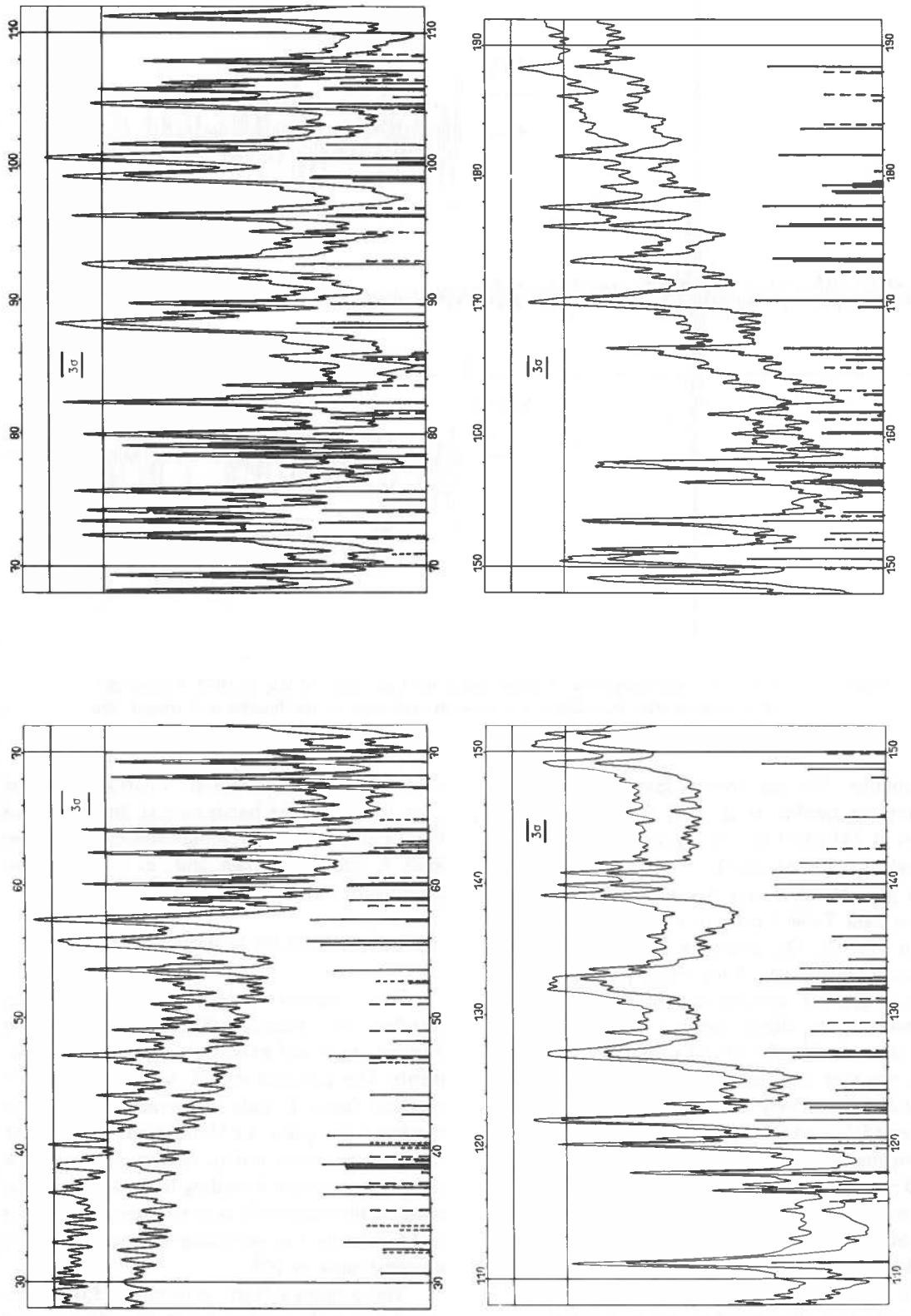

Figure 3. Example of two spectra obtained during the flight at a resolution of 0.18 cm^{-1}. The ordinates (in arbitrary units) are shifted to show the high quality reproducibility of the two runs. The H_2O lines (continuous bars), the O_2 lines (broken bars – – –), and the O_3 lines (dotted bars - - - - - - -) are identified. For H_2O and O_3 the bars' lengths are proportional to the logarithm of the line strength. For O_2 only the positions are given (bars of equal height). The figures show also the 3σ noise level (see text).

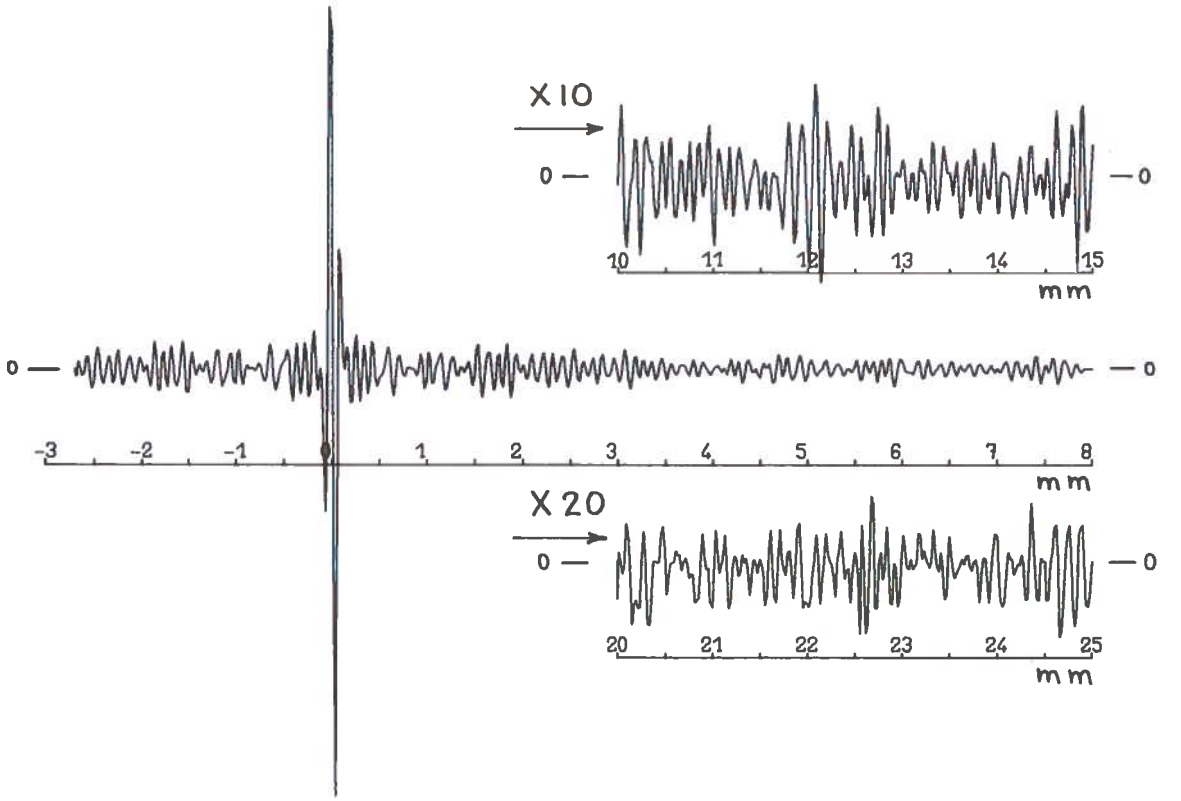

Figure 2. One of the interferograms obtained during the night flight of May 8, 1972. The last part of it is expanded in ordinate to show the presence of the interference fringes. The signal-to-noise ratio is typically 3000.

third column. The last column gives the values measured by Gebbie et al. [14] (30-65 cm^{-1}), Eddy et al. [4] (30-115.7 cm^{-1}), and Harries and Burroughs [6] (30-65 cm^{-1}).

In general, there is good agreement among all these data. Table 2 presents a similar comparison for the O_3 Q_R branches between Gora's theoretical frequencies, Eddy et al. [4], Harries and Burroughs [6], and our measurements.

Last, we tentatively assign a line found at 65.29 cm^{-1} to CO ($J = 13 \rightarrow J = 14$, $\tilde{\nu}_{th} = 65.24$ cm^{-1}), pointing out, nevertheless, that two O_3 lines fall respectively at the theoretical frequencies 65.13 and 65.39 cm^{-1}. More tentative is the assignment of the line at 80.53 cm^{-1} to CO ($J = 20 \rightarrow J = 21$, $\tilde{\nu}_{th} = 80.51$ cm^{-1}). In this last case, in fact, according to the rotational constants of N_2O given by Johnson et al. [15], the N_2O $J = 96$ transition falls at 80.59 cm^{-1}.

We should mention that one flight was performed at an altitude of 41,000 feet and data taken at a resolution of 0.07 cm^{-1} in an attempt to detect the OI line at 63μ. A narrow filter was used to reduce the bandpass and thus the noise level. Initial data analysis indicates that the noise level is still quite high and, as a result, the experiment was inconclusive.

PLANNED OBSERVATIONS ON CONCORDE

The instrument described above will be installed on Concorde 001 in early 1973 to improve upon and extend the previous measurements. The installation will differ from that of previous flights in only a few details. A quartz window will replace the Mylar window, and great care will be taken not to destroy laminar flow near the supersonic boundary layer. The dynamic range of the electronics is to be improved so as to make possible the recording of spectra with a dynamic range of 10^4.

The proposed flight altitude is 55,000 feet, about five scale heights for H_2O and one scale height for O_2 above the previous flight altitude.

Table 1. Identification of O_2 Lines

Transitions K'	K''	J'	J''	$\tilde{\nu}$ theor. cm^{-1}	$\tilde{\nu}$ obs. (present res.) cm^{-1}	$\tilde{\nu}$ obs. [4,6,14] cm^{-1}	Comments
		5	6	35.39	35.35	35.43 (G) 35.40 (E) 35.48 (H)	
5	7						
		6	6	37.38	37.52	37.39 (G)	
		6	7	39.36	39.38	39.35 (G) 39.35 (H)	
		7	8	46.90	–	–	B (H_2O)
		8	8	48.92	48.93	48.93 (G) 48.95 (E)	
7	9					49.03 (H)	
		8	9	50.88	50.88	50.88 (G) 51.00 (E) 50.82 (H)	
		9	10	58.40	58.36	58.36 (G) 58.50 (H)	
9	11	10	10	60.44	60.44	60.47 (G) 60.46 (H)	
		10	11	62.38	–	–	B (H_2O)
		11	12	69,89	69.93		
11	13	12	12	71.95	–		B (H_2O)
		12	13	73.87	–		B (H_2O)
		13	14	81.37	81.52-		S (H_2O)
13	15	14	14	83.45	83.43	83.45 (E)	
		14	15	85.35	85.44-		S (H_2O)
		15	16	92.83	–		B (H_2O)
15	17	16	16	94.93	94.96	95.00 (E)	
		16	17	96.82	96.78		
		17	18	104.28	–		B (H_2O)
17	19	18	18	106.40	–		B (H_2O)
		18	19	108.27	108.26		S (H_2O)
		19	20	115.70	115.68	115.70 (E)	
19	21	20	20	117.84	–		B (H_2O)
		20	21	119.64	–		B (H_2O)
		21	22	127.11	–		B (H_2O)
21	23	22	22	129.27	129.23		
		22	23	131.11	–		B (H_2O)
		23	24	138.50	–		B (H_2O)
23	25	24	24	140.67	–		B (H_2O)
		24	25	142.49	142.41		
		25	26	149.86	–		B (H_2O)
25	27	26	26	152.06	152.05		
		26	27	153.86	–		B (H_2O)
		27	28	161.20	161.22		
27	29	28	28	163.41	163.53		
		28	29	165.21	165.32		
		29	30	172.51	172.54		
29	31	30	30	174.74	174.83		
		30	31	176.52	–		B (H_2O)
		31	32	183.79	–		B (H_2O)
31	33	32	32	186.04	185.94		
		32	33	187.80	–		B (H_2O)
		33	34	195.05	194.98		
33	35	34	34	197.31	197.20		S (H_2O)
		34	35	199.06	198.95		

E = Eddy et al. [4], G = Gebbie et al. [14], H = Harries and Burroughs [6]
B = Blended, S = Shoulder

Table 2. Identification of O_3Q_R Branches

Transition $Q_R(J_K)$	Gora's Calculations J	Gora's Calculations $\tilde{\nu}$ theor. (cm^{-1})	$\tilde{\nu}$ obs. (cm^{-1}) present work	$\tilde{\nu}$ obs. (cm^{-1})
J_5	$12 \rightarrow 6$	$34.33 \rightarrow 34.34$	34.31	34.35 (E) 34.33 (H)
J_6	$14 \rightarrow 17$	$40.51 \rightarrow 40.52$	– (B)	–
J_7	> 25 $17 \rightarrow 8$	< 46.62 $46.66 \rightarrow 46.67$	46.57 (S)	46.51 (H)
J_8	≥ 22 $19 \rightarrow 9$	< 52.77 $52.78 \rightarrow 52.79$	52.69	52.75 (E) 52.75 (H)
J_9	> 10	< 58.87	– (B)	–
J_{10}	> 11	< 64.90	64.80	65.00 (E) 64.80 (H)
J_{11}	> 12	< 70.88	70.77	–
J_{12}	≥ 13	< 76.81	76.65	76.75 (E)
J_{13}	≥ 14	< 82.68	82.63 (S)	82.70
J_{14}	≥ 15	< 88.49	88.40	–

E = Eddy et al. [4], H = Harries and Burroughs [6]
B = Blended (H_2O), S = Shoulder

During flights at cruise altitude lasting one hour, from 44°N to 52°N, we expect to scan 1.5 to 60 air masses in zenithal distance. All measurements will again be emission spectra.

We expect, on the basis of the performance actually achieved on Caravelle, to obtain emission spectra, spanning 20 to 200 cm^{-1}, with a signal-to-noise ratio of 500 for one hour observing time, at a maximum resolution of 0.067 cm^{-1}. The equivalent amount of precipitable water overhead is estimated to be less than 1 micron.

A new instrument having a higher resolution (.02 cm^{-1}) is now under laboratory development and will be flown in early 1974. The better signal-to-noise ratio and resolution of this new instrument will make the identification of weak O_3 lines easier, which is the major task to be achieved before any firm conclusion can be reached on trace gases. Two factors will make this O_3 identification possible: first, at the altitudes where O_3 is formed, the pressure-broadened O_3 lines have a width of about .02 cm^{-1}. Trace gases, which are mostly concentrated around 15 km, have line widths of about 0.1 cm^{-1}. Second, ozone lines have a peak optical thickness equal to or larger than unity, and exhibit different characteristics in a sec z scan from the optically thin trace gases. Expected intensities for CO lines are on the order of a few percent, a factor of 8 above expected NO line intensities on the basis of theoretical estimates of stratospheric NO abundance.

Moreover, the large spectral range covered by these planned observations may allow the discovery and identification of new trace gases, since pure rotational signatures are relatively easy to identify. The high resolution offers the possibility of a detailed study of H_2O line profiles and the accurate determination of rotational temperatures at various altitudes.

Finally, the technique of measuring IR emissions could be a valuable tool in any real-time study of the exhaust of jet engines in the stratosphere.

ACKNOWLEDGMENTS

The authors are grateful to A. Langlet and J. Roucher for their invaluable work in the experimental operations, and to Mrs. J. Tualy for help in the data reduction. We also warmly thank the ground team and the crew of the Centre d'Essais en Vol (Bretigny, France).

E. Bussoletti's work at the Groupe Infrarouge Spatial is made possible by an E.S.R.O. postdoctoral fellowship.

REFERENCES

1. Gebbie, H.A., Chamberlain, J., and Burroughs, W.J., "Sub-millimeter wave solar observations", Nature *220*, 893 (1968).

2. Nolt, I.G., Martin, T.Z., Wood, C.W., and Sinton, W.M., "Far infrared absorption of the atmosphere above 4.2 km", J. Atmos. Sci. *28*, 238 (1971).

3. Biraud, Y., Gay, J., Verdet, J.P., and Zeau, Y., "Transmission atmosphérique et spectroscopie solaire en ondes submillimétriques", Astron. Astrophys. *2*, 413 (1969).

4. Eddy, J.A., Léna, P., and McQueen, R.M., "The far infrared transmission of the upper atmosphere", J. Atm. Sci. *26*, 1318 (1968).

5. Gebbie, M.A., Burroughs, W.J., Harries, J.E., and Cameron, R.M., "Sub-millimeter wave spectroscopy of the Earth's atmosphere above 39,000 feet", Astrophys. J. *154*, 405 (1968).

6. Harries, J.E., and Burroughs, W.J., "Measurements of submillimeter wavelength radiation emitted by the stratosphere", Quart. J.R. Met. Soc. *97*, 519 (1971).

7. Harries, J.E., Beckan, J.E., Ade, P.A.R., and Swann, N.R.W., "High resolution observations of the submillimeter stratospheric emission spectrum", Nature *236*, 159 (1972).

8. Nolt, I.G., Radostitz, J.V., and Donnelly, R.J., "Upper atmosphere emission at millimeter wavelengths", Nature *236*, 444 (1972).

9. Burroughs, W.J., and Harries, J.E., "On the use of apodization in submillimeter Fourier transform spectroscopy", Infrared Phys. *11*, 99 (1971).

10. Baluteau, J.P., Bussoletti, E., Langlet, A., and Roucher, J., "Determination des spectres d'émission du ciel dans l'infrarouge entre 45μ et 500μ a partir d'un interféromètre embarqué en avion", E.S.R.O./E.L.D.O. Scientific & Technical Review *4*, No. 4 (1972).

11. Benedict, W.S., private communication.

12. Gora, E.K., "The rotational spectrum of ozone", J. Mol. Spectroscopy *3*, 78 (1959).

13. Dalgarno, A., "Infrared day and night airglow of the Earth's upper atmosphere", Philosoph. Trans. Ray. Phy. Soc. *264* A, 153 (1968).

14. Gebbie, H.A., Burroughs, W.J., and Bird, G.R., "Magnetic dipole rotation spectrum of oxygen", Proc. Roy. Soc. A., *310*, 579 (1969).

15. Johnson, V.A., Trambarulo, R., and Gordy, J., "Microwave spectroscopy in the region from two to three millimeters", Phys. Rev. *84*, 1178 (1951)

Because of transportation difficulties, Dr. Dütsch was unable to present this paper at the conference.

THE PRESENT STATUS OF OZONE RESEARCH: PHOTOCHEMISTRY AND OBSERVATIONS

H.U. DÜTSCH
Laboratory for Atmospheric Physics, ETH
Zürich, Switzerland

ABSTRACT: Recent theoretical developments in the chemistry and transport of atmospheric ozone are discussed, with optimism for imminent answers to current questions. A plea is made for more observational data to keep pace with these developments.

INTRODUCTION

There is an interesting relation between the development of the observational knowledge on atmospheric ozone and that of the photochemical theory. In the first phase, the basic facts about the distribution of atmospheric total ozone content and its variation with season became known in the 1920's [1]. It was not, however, until Chapman's paper in 1930 [2] that the presence of that gas in the stratosphere was theoretically understood, and afterwards the theory made great progress on the basis laid by him. For almost 20 years after the war our theoretical knowledge (assuming the so-called "oxygen only" atmosphere, at least at stratospheric levels) seemed quite adequate, and it was felt that a considerable contribution to our knowledge of stratospheric circulation could be obtained from ozone research if reliable data on vertical distribution of the gas were available.

Starting about the time of the IGY, such data came along in increasing numbers and quality, obtained by direct and indirect methods [3-5]. Then it was found that it was difficult to fully reconcile these observations with theoretical results, even at those levels where near-equilibrium was to be expected [6].

Thus, the proposal by Hampson [7] and Hunt [8] that H-radicals produced by ozone-derived excited O-atoms, which in turn reduce the number of odd-oxygen particles, was readily accepted. Since then the theory has been in rapid motion. While it is now felt that the direct influence of H-radicals [9] on odd-oxygen particle concentration is small below 40 km, reactions with NO_x [10-12] have been considered, and quite recently it has become clear that the whole system could be fully understood only if some C-compounds [13] were also taken into account. Although at first this development looks very confusing, it seems now that a comprehensive system of atmospheric chemistry is developing, which fact provides some hope that a more stable solution is within reach. There is no doubt that the SST problem has been an effective catalyst towards this goal.

As mentioned, it was to some extent the big advances in ozone measurements during the early sixties which triggered the current theoretical effort. We may ask whether the observational side has kept pace with the theory; although further advances have certainly been made, we do not feel that the answer is a straight yes. If increased efforts are not made, the alternating imbalance between theoretical and observational knowledge which was typical of research in atmospheric ozone could easily develop again, this time with the observations lagging behind.

AN INTEGRATED PHOTOCHEMISTRY

During the last year or two it has become clear that the reactions between ozone and not only HO_2 but also OH are much slower than initially assumed [9]. The direct influence of water-vapor photochemistry on the odd-oxygen budget is therefore almost negligible below 35 to 40 km, although it remains dominant in the mesosphere, where reactions with atomic

oxygen are important. However, this does not mean that H-radicals can be neglected in any treatment of odd-oxygen particle photochemistry, because they interact strongly with other minor constituents which (we now think) influence the ozone budget in the middle and lower stratosphere.

It is now generally accepted that nitrogen oxides play a considerable role in ozone photochemistry below about 40 km, although it is not more than two years since this possibility was first stressed by Crutzen [10], Nicolet [11] and Johnston [12]. There are, however, still some doubts about the exact magnitude of the loss of odd oxygen produced by the catalytic destruction by NO_x.

It has also been realized that there is considerable interaction between the NO_x and the $\widetilde{H}$-system, producing mainly HNO_3 (which has already been observed) and probably HNO_2. A certain part of the NO_x becomes inactive by this transformation – and the reactions involved may under certain conditions (in the lowest part of the stratosphere) even produce some odd oxygen. Due to these interactions it now seems probable that an increase in water-vapor content in the lower stratosphere would not depress but rather raise the ozone concentration [14]. Under equilibrium conditions, however, the effect is small (of the order of 2% for a doubling of the water-vapor content) depending on the amount of NO_x present.

It is now possible to obtain a quite reasonable fit between observed and theoretically-calculated ozone concentrations from the stratopause down to the lower stratosphere, and also to reproduce the observed HNO_3 distribution within its limits of uncertainty (Figures 1 and 2), assuming a reasonable-looking NO_x distribution and using reaction rates which differ from the most recent laboratory determinations within tolerable margins [14].

The NO_x mixing ratios needed (Figures 1 and 2) to balance odd-oxygen production and destruction at the observed ozone concentration are, however, much higher (at many heights by an order of magnitude) than those recently reported by Ackerman [15] from the first direct spectrographic measurements of NO_x. Although it seems somewhat difficult to reconcile Ackerman's findings with the observed HNO_3 distribution [16], this discrepancy calls for

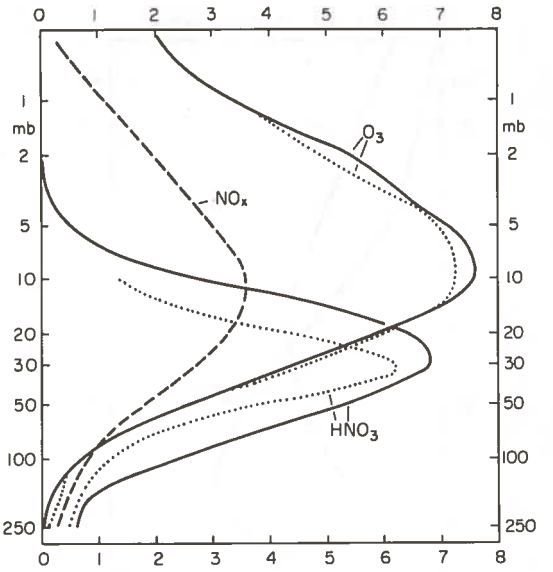

Figure 1. Comparison between observed (- - -) and calculated (——) vertical distribution of ozone and HNO_3 mixing ratios for mid-summer conditions at 45° lat, with an assumed NO_x distribution (– –). (Ozone in units 10^{-6}; HNO_3, 10^{-9}; NO_x, 10^{-8}.)

reconsideration of the intensity of the solar UV radiation in the window region around 2100 Å. If Brewer and Wilson's values [17] are used instead of Detwiler's [18] or Ackerman's [19], a much smaller NO_x content yields the necessary balance between production and destruction.

This question is of great importance to the SST problem. The influence of NO_x on ozone concentration is strongly non-linear, in that the same amount of artificially produced NO_x yields a much higher reduction of total ozone content in an atmosphere with a low natural nitrogen-oxides content than in an environment already rich in these gases.

In view of these uncertainties, the source problem for natural NO_x is of special interest. It is now largely agreed that NO_x is produced in the stratosphere by the reaction of N_2O (which originates in the troposphere) with $O(^1D)$, a photodissociation product of ozone [20-23]. The thermospheric source initially proposed now seems inefficient, because NO_x is photolyzed during its relatively slow downward transport through the mesosphere by mixing processes [22]. There may, however, be a certain contribution from production by cosmic rays [24].

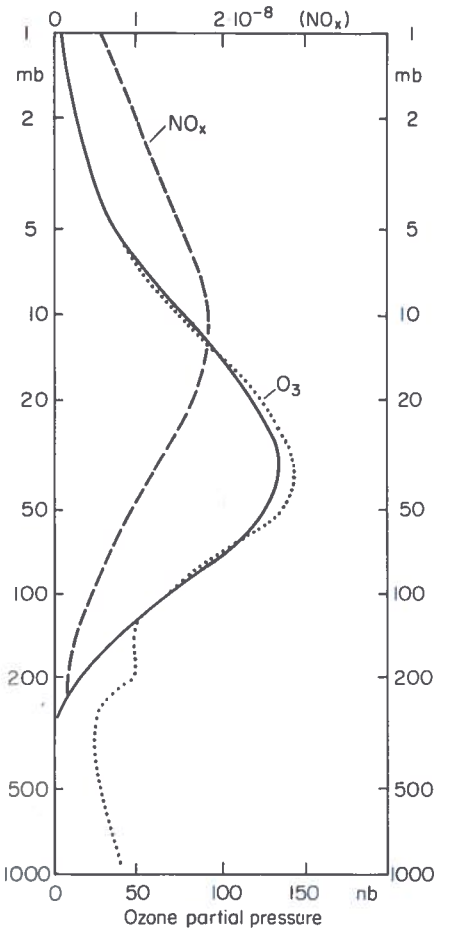

Figure 2. Vertical ozone distribution from theory (—) for 45° lat. and observations (- - -) (47° lat., 65 soundings) in midsummer and assumed mixing ratio of NO_x (– –).

Most recently, the importance of the interaction of the photochemical system described above (odd oxygen + active hydrogen + NO_x) with some carbon compounds (mainly methane [25,26] and its oxidation products, leading to H_2O, H_2, and CO) has been stressed. In particular, the discovery [26] that CH_4 is oxidized by reaction not only with excited oxygen atoms but also with OH, makes the interaction with the C-compounds rather important because it strongly influences the active hydrogen level in the lower stratosphere. Furthermore, odd-oxygen production seems to occur as a by-product of the CH_4 oxidation chain [13].

Although the complexity of the photochemical system in the stratosphere has increased rapidly with these recent developments, it has the great advantage that the chemistry of most of the trace substances at that level is merging into one comprehensive system which is depicted by Figure 3. It seems to me that this fact makes it more likely that a quantitatively satisfactory solution may be found within the near future. With an increasing number of interrelated and observable substances the number of degrees of freedom is actually reduced, and it may become possible to determine some not yet well-enough-known reaction or dissociation rates indirectly.

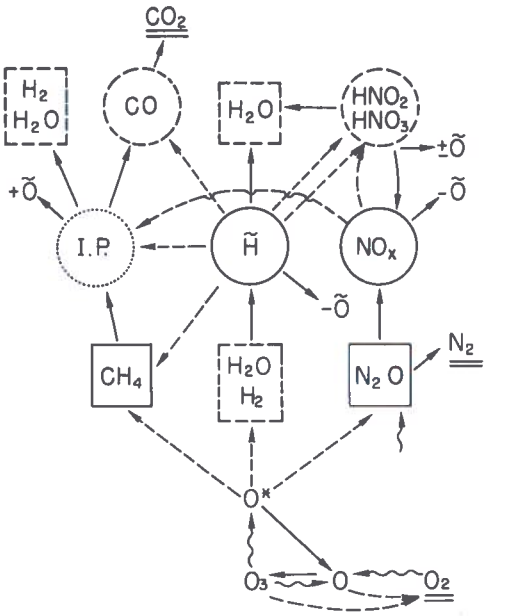

Figure 3. Schematic diagram of the photochemistry of minor constituents in the stratosphere.

- □ long-lived substances originating at the earth's surface, destroyed in the stratosphere.
- ⬚ same as above but also regenerated in the stratosphere.
- ○ reactive molecules and radicals produced in the stratosphere (I.P. = chain of intermediate products).
- ◌ partly produced by reactions between O substances.
- = semistable or stable substances with constant mixing ratio.
- ~~→ transformation by a primary photochemical process.
- A→B transformation of substance B by reaction with A.
- A→B indicates B is a product of a reaction of A, or gain or loss of odd-oxygen particles by reaction with A.

In speaking of a comprehensive system it is of some interest to note that the reactions of ozone and atomic oxygen with sulfur compounds, which were already being discussed ten years ago by Junge [27] in connection with an explanation of the stratospheric sulfate layer, are not presently included in this scheme. The main reason is that these reactions – even if they should be fast enough to explain the sulfate layer – do not catalytically destroy odd oxygen, and may therefore largely be disregarded in the integrated system described above.

A full solution of the photochemical problem is hampered not only by our still incomplete knowledge about reaction and dissociation rates – although considerable progress has recently been made in this direction – but in particular by the complication introduced by transport processes. While in the classical "oxygen only" photochemistry, only ozone was carried along by air motions as a more or less conservative substance, and all other involved trace gases were in at least near-equilibrium with it, the number of substances with long relaxation times has become large: in addition to ozone, N_2O, and NO_x (NO and NO_2 in rapid equilibrium among themselves), CH_4, H_2O, and H_2 certainly belong in this category and HNO_3 and CO at least partly do.

It is well known that the most simple transport model – namely, one assuming only vertical diffusion – does not suffice to treat ozone transport itself. Furthermore, the source for N_2O and CH_4, which is at the ground, is hardly uniform over the earth's surface. Therefore the full problem must be treated in at least a two-dimensional system (in the meridional plane). Some work in this direction has already been done [28], though without the complete photochemical system. One of the problems lies in the parameterization of large-scale exchange by mixing coefficients, which is not a very satisfactory procedure; correct specification of sources and sinks at the surface, and of the discontinuity at the tropopause, is another problem in such an undertaking.

An additional complication comes from the fact that there is a very pronounced seasonal variation in the pure photochemistry as well as in the transport processes. Steady-state models are therefore not useful, and their results cannot be compared with reality.

A fully satisfactory treatment will presumably be possible only using the three-dimensional numerical models of the general circulation with integrated photochemistry. However, in order to avoid unnecessary expense and allow some experimentation with the model, preliminary research with two-dimensional models is certainly very appropriate, when their limitations are kept in mind.

OBSERVATION OF OZONE AND OTHER TRACE GASES

As mentioned before, the impetus to the present development in photochemistry was given by the advance in our observational knowledge of atmospheric ozone distribution in the early sixties. Although the observational efforts have continued, they have not kept up with the present rapid expansion of the theory; if they are not stepped up, our ignorance of the actual situation in the atmosphere may finally slow down the solution of the problem.

Presently these observations must clearly be divided into two categories – measurements of ozone and measurements of the other trace substances. For most of the latter we have some relatively crude observational data on the vertical distribution (based on a rather small number of measurements) from which almost nothing is known about the dependence on latitude and season. With respect to ozone, however, we have a fair knowledge of the vertical distribution at different latitudes, of its dependence on season, and of its day-to-day variability [29].

The reasons for this discrepancy are twofold. First, ozone has some rather pronounced physical and chemical properties which can be used for constructing measuring devices. Second, its concentration in the stratosphere is one or several orders of magnitude higher than that of the other trace gases, except water vapor. Furthermore, there has been a long-lasting history of research on that gas, initially because of its biological interest and then because of its particular usefulness as a tracer.

It is certainly of prime importance to secure direct observational knowledge about all of the trace substances in the system described in the previous section. It is also important to find their dependence on season and latitude, and also their variability. Such measurements are most valuable

when as many as possible of these substances can be measured simultaneously.

Comparing our knowledge about ozone and the other trace substances, we may think that further O_3 observations are not needed, except for information on its quantity obtained together with measurements of the others. This is not so, however. Not only is ozone of prime interest because of the biological and climatic implications of a possible change introduced by human activities, it is also the central substance in the complex system under discussion, as can be seen from Figure 3.

It is therefore not only appropriate but absolutely necessary to know the vertical distribution of this gas and its variation in time and space much more accurately than that of the others, and considerably better than we do now. This may be seen from a short discussion of the six-year series of measurements of the vertical ozone distribution over Switzerland (47°N), which consisted of over 700 single ascents [30].

The mean of the total amount, measured concurrently with the vertical distribution, was compared with the 30-year average available for Arosa (Switzerland). Then, using the observed correlation of ozone concentrations at different levels with the total amount, approximate long-term climatological mean values of the seasonal variation at different levels were derived from the six years of data (Figures 4 and 5).

The big seasonal increase of ozone concentration at its peak around 40-50 mb is mostly concentrated within two months in early winter. This strongly indicates that poleward transport from the supposed source region in the tropical stratosphere is mostly directed into this layer, presumably carried by the downward leg of the stratospheric extension of the winter-hemispheric Hadley cell, which (in the troposphere) is almost ten times stronger than its summer-hemispheric counterpart and reaches its maximum intensity at this time of the year. This hypothesis is supported by the results of a similar observational series at Boulder, Colorado, 7° further south [5], which shows the same rise, starting about one week earlier and ending as much later, and is in good agreement with the findings of Newell [31] on ozone transport by the circulation observed during the International Quiet Sun Year.

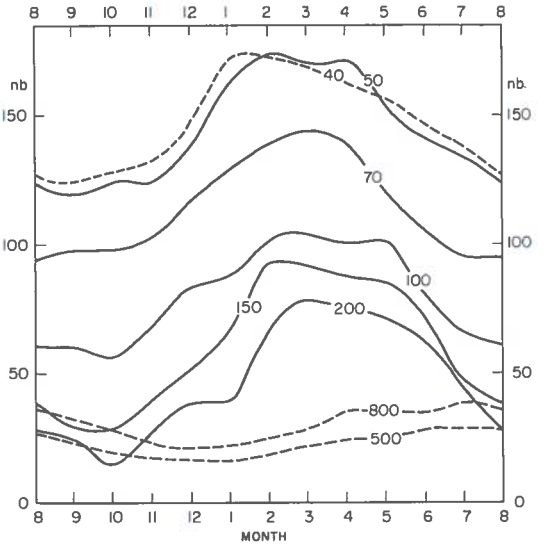

Figure 4. Seasonal variation of ozone partial pressure at different levels in the lower stratosphere and in the troposphere (contours labeled by total air pressure) from over 700 soundings over Switzerland, 47°N.

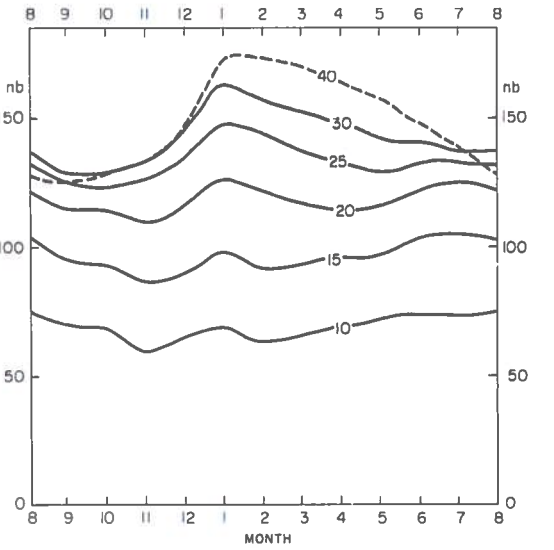

Figure 5. Seasonal variation of ozone partial pressure at different levels in the middle stratosphere.

From the 30-mb level upwards, a secondary maximum appears in summer and gradually becomes stronger than the winter peak. This shows at what level direct photochemical action (producing a summer maximum) becomes predominant over circulation influences (yielding

the winter increase). At the lower latitude (Boulder) the winter maximum is almost missing at the 10-mb level. The increase of much longer duration in the lower stratosphere, with its obvious interruption around 1 January, possibly indicating two different circulation mechanisms, is more difficult to explain. A comparison with similar data from other latitudes is needed even more here than for an explanation of the events at higher levels. Such a comparison would also be needed to assess the contribution of photochemical destruction in spring and summer to the decay of the excess ozone accumulated by circulation in the winter.

We are therefore convinced that similar observational series (about three soundings per week over several years) are needed for at least every 10° latitude to construct a meridional cross-section of ozone changes with time. This will really allow full comparison of photochemical models, including transport, with nature. Such cross-sections can be constructed from presently available data, but due to the too-short records and the inhomogeneity of the data, they are not reliable enough for the purpose. Also, they cannot give any further help in explaining the very interesting year-to-year variation which is indicated by the 6-year series over Switzerland.

The series also exhibited an interesting biennial variation at the height of the ozone maximum (Figures 6 and 7), with the high values in phase with the easterlies around 10 mb in the 26-month oscillation. This means (according to Reed [32]) an intensification of the downward leg of the stratospheric extension of the Hadley cell — which supports the explanation given above for the winter peak at this level.

The biennial variation is not shown by the total amount, however, because this mode is missing in the stronger year-to-year fluctuations in the lower stratosphere, which are regional in contrast to the presumably hemispheric oscillation higher up, and are produced by the deviations from normal of the large-scale weather patterns in the troposphere with their extensions in the lower stratosphere.

Several of the interpretations of this observational series need substantiation by a further extension of the measurements in time and (as already mentioned) to other latitudes. I am convinced that a full solution of the very

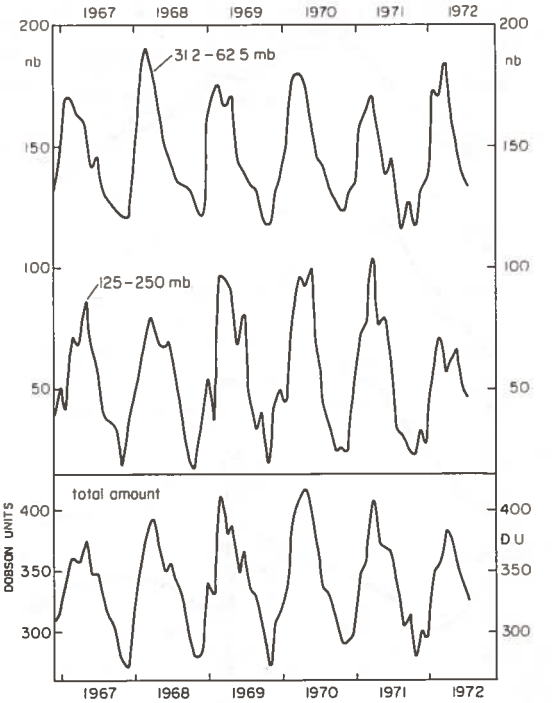

Figure 6. Year-to-year differences in the seasonal variation of ozone partial pressure at the bottom of the stratosphere (125-250 mb) and in the layer of maximum ozone concentration (31.2-62.5 mb) compared to the variation of the total amount.

complex problem which is before us can be obtained only if the big efforts on the theoretical side — photochemistry and modeling — are supported by a stepped-up observational program.

REFERENCES

1. Dobson, G.M.B., Harrison, O.N., and Lawrence, J. (1927), "Measurements of the amount of ozone in the earth's atmosphere and its relation to other geophysical conditions," Proc. Roy. Soc. A *114*, 521.

2. Chapman, S. (1930), "A theory of upper atmospheric ozone," Mem. Roy. Meteor Soc. *3*, 103.

3. Dütsch, H.U., and Mateer, C.L. (1964), "Uniform Evaluation of Umkehr Observations from the World Ozone Network," I, II, III, National Center for Atmospheric Research, Boulder.

4. Hering, W.S., and Borden, T.R. (1967), "Ozone sonde observations over North America," Vol. 4, AFCRL, Env. Res. Pap. No. 279, 365.

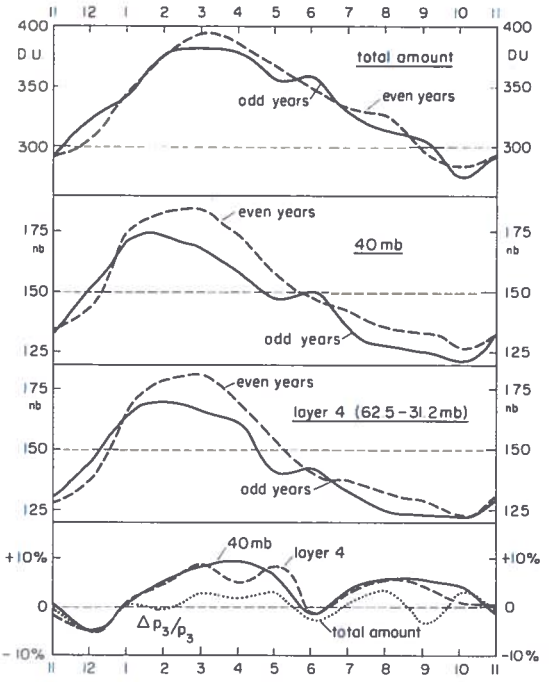

Figure 7. Seasonal variation in odd (avg. 1967+1969+1971) and even years (avg. 1968+1970+1972) of the ozone concentration at the level of the ozone peak (at 40 mb and in a layer between 31.2-62.5 mb), and of the total amount. At the bottom, percentage difference (even minus odd years divided by the mean value).

5. Dütsch, H.U., Züllig, W., and Ling, C.C. (1970). *Regular Ozone Observations at Thalwil, Switzerland and at Boulder, Colorado*, Lab. Atm. Phys., ETH, Zürich, 279 pp.

6. Hunt, B.G. (1966), "The need for a modified photochemical theory of the ozonosphere," J. Atm. Sci. *23*, 88.

7. Hampson, J. (1964), "Photochemical behaviour of the ozone layer," Can. Arm. Res. Develop. Estab., Tech. Note 1627, 164, Valcartier, Quebec, 280 pp.

8. Hunt, B.G. (1966), "Photochemistry of ozone in a moist atmosphere," J. Geophys. Res. *71*, 1385.

9. Langley, K.R., and McGrath, W.D. (1971), "The ultraviolet photolysis of ozone in the presence of water vapour," Planet. Space Sci. *19*, 413.

10. Crutzen, P.J. (1970), "The influence of nitrogen oxides on the atmospheric ozone content," Quart. J. Roy. Meteor. Soc. *96*, 320.

11. Nicolet, M. (1971), "Photochimie de l'ozone dans la stratosphère sous l'action des oxydes d'azote et de composés de l'hydrogène," Bull. Acad. Roy. Belgique *57*, 935.

12. Johnston, H. (1971), "Reduction of stratospheric ozone by nitrogen oxide catalysts from supersonic transport exhaust," Science *173*, 517.

13. Crutzen, P. (1972), "A discussion of the chemistry of some minor constituents in the stratosphere and troposphere," Proc. of the Symposium on Atmospheric Ozone, Arosa, to appear in PAGEOPH 1973 (Ozone Symposium).

14. Dütsch, H.U. (1972), "Recent developments in the photochemistry of atmospheric ozone," Proc. of the Symposium on Atmospheric Ozone, Arosa; to appear in PAGEOPH 1973 (Ozone Symposium).

15. Ackerman, M., and Muller, C. (1972), "Stratospheric methane and nitrogen dioxide from infrared spectra," Proc. of the Symposium on Atmospheric Ozone, Arosa; to appear in PAGEOPH 1973 (Ozone Symposium).

16. Williams, W.J., Brooks, J.N., Murcray, F.H., Fried, P.M., and Weinman, J.A. (1972), "Distribution of nitric acid vapour in the stratosphere as determined from infrared atmospheric emission data," J. Atm. Sci. *29*, 1375.

17. Brewer, A.W., and Wilson, A.W. (1965), "Measurements of solar ultraviolet radiation in the stratosphere," Quart. J. Roy. Meteor. Soc. *91*, 452.

18. Detwiler, C.R., Garret, D.L., Purcell, J.D., and Tousey, R. (1961), "The intensity distribution in the ultraviolet solar spectrum," Ann. Géophys. *17*, 263.

19. Ackerman, M., Frimout, D., and Pastiels, R. (1971), "New ultraviolet solar flux measurements at 2000 Å using a balloon borne instrument," in *New Techniques in Space Astronomy*, D. Reidel Pub., Dordrecht, 251.

20. McElroy, M.B., and McConnell, J.C. (1971), "Nitrous oxide, a natural source of stratospheric NO," J. Atm. Sci. *28*, 1095.

21. Nicolet, M., and Peetermans, W. (1972), "The production of nitric oxide in the stratosphere by oxidation of nitrous oxide," to appear in Ann. Géophys.

22. Brasseur, G., and Cieslik, S. (1972), "On the behavior of nitrogen oxides in the stratosphere," Proc. of the Symposium on Atmospheric Ozone, Arosa; to appear in PAGEOPH 1973 (Ozone Symposium).

23. Isaksen, I.A. (1972), "Production of nitrogen oxides in the lower stratosphere," Proc. of the Symposium on Atmospheric Ozone, Arosa; to appear in PAGEOPH 1973 (Ozone Symposium).

24. Warneck, P. (1972), "Cosmic radiation as a source of odd nitrogen in the stratosphere," J. Geophys. Res. *77*, 6589 (1972).

25. Nicolet, M. and Peetermans, W. (1972), "On the vertical distribution of carbon monoxide and methane in the stratosphere," Proc. of the Symposium on Atmospheric Ozone, Arosa; to appear in PAGEOPH 1973 (Ozone Symposium).

26. Nicolet, M. (1971), "Aeronomic reactions of hydrogen and ozone," in *Mesospheric Models and Related Experiments*, D. Reidel Pub., Dordrecht, 1111.

27. Junge, C.E. (1963), "Sulfur in the atmosphere," J. Geophys. Res. *68*, 3975.

28. Hesstvedt, E. (1972), "The effect of water vapour and nitrogen oxides upon the ozone layer, studied in a photochemical layer with meridional transport," Proc. of the Symposium on Atmospheric Ozone, Arosa; to appear in PAGEOPH 1973 (Ozone Symposium).

29. Dütsch, H.U. (1971), "Photochemistry of atmospheric ozone," Adv. in Geophys. *15*, 219-322.

30. Dütsch, H.U. and Ling, C.C. (1972), "Six years of regular ozone soundings over Switzerland," Proc. of the Symposium on Atmospheric Ozone, Arosa; to appear in PAGEOPH 1973 (Ozone Symposium).

31. Newell, R.E., Dopplick, T.G., and Boer, G.J. (1972), "Influence of the vertical motion field on ozone concentrations in the stratosphere," Proc. of the Symposium on Atmospheric Ozone, Arosa; to appear in PAGEOPH 1973 (Ozone Symposium).

32. Reed, R.J. (1965), "The present status of the 26-month oscillation," Bull. Am. Met. Soc. *46*, 375.

EVALUATED RATE AND PHOTOCHEMICAL DATA FOR MODELING OF THE STRATOSPHERE

DAVID GARVIN AND ROBERT F. HAMPSON
Physical Chemistry Division
National Bureau of Standards
Washington, D.C.

ABSTRACT: Three important types of input data for studies of the chemistry of the stratosphere are rate constants, absorption coefficients, and quantum yields for elementary processes. About 135 of these data items are needed for studies that will define the chemistry of the stratosphere. These data are being obtained both by experiment and by review and evaluation of existing measurements.

The data-evaluation program has two parts: evaluation by a group at NBS, and a cooperative survey by a large number of gas kineticists. The evaluated data now available are summarized in a table. The possible interactions among 42 species that may be present in the stratosphere are displayed on a reaction grid. Where possible the importance of a reaction and the status of its data are indicated.

Pollutants introduced into the stratosphere will interact with the existing complex $O_3/O_2/NO_x/HO_x$ photolytic system. Laboratory studies of the O_3/O_2 and O_3/H_2O_2 photolytic systems and rate measurements in an $O/O_3/NO_x$ system illustrate the types and magnitudes of effects to be expected.

INTRODUCTION

This paper is about stratospheric chemistry: the reactions that may occur, the data that are needed in order to determine which of them are important, and how these data are being obtained for use in the Climatic Impact Assessment Program (CIAP).

It will be taken as proved that chemical reactions are important in the stratosphere. This was demonstrated many years ago when the total ozone column was calculated from a simple photochemical mechanism by Chapman. Today a far more complex mechanism is being used to describe the natural stratosphere and the effects of the injection of the products of chemical combustion. Nicolet described this chemistry at the Survey Conference on the CIAP program [1] and has indicated the defects in the present data base.

The stratosphere is a highly dilute, cold, chemically reactive soup. The constituents known or suspected to take part in its chemistry are shown in Table 1. There are 42 in the list. Some are stable molecules that have been observed; others are free radicals and atoms that must result from the major photochemical reaction sequences.

Table 1. Species to be Considered in a Survey of the Chemistry of the Stratosphere

O	N	H	HNO
$O(^1D)$	NO	HO	HNO_2
$O(^1S)$	NO_2	HO_2	HNO_3
O_2	NO_3	H_2	NH
$O_2(^1\Delta)$	N_2	H_2O	NH_2
$O_2(^1\Sigma)$	N_2O	H_2O_2	NH_3
O_3	N_2O_5		
CHO	CO	SO	$h\nu$
CH_2O	CO_2	SO_2	
CH_3	CH_3OOH	SO_3	
CH_3O	CH_3ONO	S_2O	
CH_3O_2	CH_3ONO_2	H_2SO_4	
CH_4			

A system of 42 reacting species is too complex for direct laboratory study. Instead, data from simpler experiments must be combined in a model that can be used to predict the variation of the concentrations of the species as a function of time. Three important types of data that are required as input for the model (or computer simulation) are chemical rate constants

for elementary reactions, absorption coefficients, and quantum yields.

A major purpose of computer simulation of the chemistry of the stratosphere is to predict long-term changes in ozone concentration when various amounts of other trace reactants are present. The first problem is to determine what chemical reactions are, or are not, important. In order to do this the chemical modelers will consider many reactions besides the obvious ones, and test their influence on the system. Current models consider about fifty reactions. In all probability the necessary set will be much smaller, perhaps ten to twenty, but certainly not one or two.

The number required will depend upon how many species must be considered. An important part of the chemical modeling will be to determine which species are effectively at "steady state" concentrations. This term means that the time derivative of their concentration is very small, and is assumed to be zero. The mathematical importance of this condition is that it eliminates a species and its rate equation from the calculation. When the concentration of a "steady state" species is needed it can be calculated from those of other species.

CHEMICAL EXPERIMENTS RELATED TO THE STRATOSPHERE

Several conclusions can be drawn from an examination of the experiments that must provide the data needed in simulation studies. First, the chemistry in the natural and polluted stratosphere will be the same, qualitatively. The same species will be present in both. Differences in the predicted results for the natural and polluted cases will be caused not by new reactions but by changes in the concentration levels of the species. Second, various parts of the chemistry predicted for the stratosphere have been observed in laboratory experiments. Third, few experiments mimic either the concentration or the temperature regime in the stratosphere.

There is an important element of extrapolation in the simulations: qualitative extrapolation in selecting the applicable set of reactions, and quantitative extrapolation in taking numerical data measured in one temperature, pressure, and composition regime and applying it in another. Both of these extrapolations must be validated.

The remainder of this section is devoted to several examples of laboratory systems that are closely related to, and provide data for, stratospheric modeling. Where a choice can be made, the examples emphasize trace-gas reactions in air or oxygen. These examples supplement those given by Johnston at the CIAP Survey Conference [2]. In part they may help explain the chemistry to an interdisciplinary audience. They may also be systems against which the simulation mechanisms and techniques can be tested.

Ozone Photolysis

An abbreviated statement of the ultraviolet photolysis of ozone in dry air is shown in Table 2. When ozone is present at a few parts per million, with the total pressure 20 torr and the temperature 227 K, this process is very inefficient. The quantum yield, number of molecules of ozone destroyed per photon absorbed, is less than 10^{-4}. This estimate is an extrapolation from laboratory studies [3] using recently suggested mechanisms modified to include quenching of excited molecular oxygen. The extrapolation is from a few percent ozone in oxygen to parts per million and from 300 K to 227 K. It is unlikely that such a low quantum yield could be measured; the extrapolation is necessary.

Table 2. Reactions in the Ultraviolet Photolysis of Ozone

1	$O_3 + h\nu \rightarrow O(^1D) + O_2(^1\Delta)$	$\lambda < 310$ nm
2	$O(^1D) + M \rightarrow O(^3P) + M$	$M = N_2, O_2$
3	$O(^1D) + O_2 \rightarrow O(^3P) + O_2(^1\Sigma)$	
4	$O(^3P) + O_2 + M \rightarrow O_3 + M$	$M = N_2, O_2$
5 a	$O(^1D) + O_3 \rightarrow 2O_2$	
b	$O(^1D) + O_3 \rightarrow O + O + O_2$	
6	$O(^3P) + O_3 \rightarrow 2O_2$	
7	$O_2(^1\Sigma) + M \rightarrow O_2 + M$	
8	$O_2(^1\Delta) + O_3 \rightarrow O + 2O_2$	
9	$O_2(^1\Delta) + M \rightarrow O_2 + M$	
10	$O_2(^1\Sigma) + O_3 \rightarrow O + 2O_2$	

The major reactions that follow photon absorption (1) are quenching of $O(^1D)$, reactions (2,3), and reformation of O_3 from $O(^3P)$ and O_2 (4). All other chemistry competes with

these steps. Reactions that remove O (^{1}D) or O (^{3}P) also increase the net destruction of ozone. These species are, surely, in steady state: their concentrations depend strongly on the rates of reactions (2,3,4). It is vital to have accurate values for these primary steps.

The term "odd oxygen" is used in simulation studies. It means the sum of O_3 and O. Because reactions (2,3,4) are fast, O_3 and O are chemically equivalent. Any reaction scheme that decreases "odd oxygen" depletes the reservoir of ozone.

It is important to note that the only reaction *forming* O_3 is (4). This will be true for the other examples. This means that an oxygen atom is needed. Unless this atom comes from some source completely independent of ozone photolysis, the ozone concentration will never rise above the starting conditions. The obvious reaction is the photolysis of molecular oxygen. It now maintains the ozone level, competing with present destruction mechanisms.

Reactions of O (^{1}D)

The excited oxygen atom, O (^{1}D), is much more reactive than the ground state atom, O (^{3}P). For example, at room temperature $k_5/k_6 \approx 40{,}000$, showing more efficient attack on O_3. Some of the reactions of this excited atom with trace impurities in air are shown in Table 3. The first seven (5, 11-14) have high and comparable rates. These reactions are important for two reasons: they compete with the reaction sequence (2,4), increasing the net destruction of O_3, and they introduce new, reactive species. They are part of the chemistry of the natural stratosphere.

Reaction (11b) is particularly important because it introduces NO. This species is readily oxidized to NO_2 by O-atoms or O_3.

The rate date for reactions of O (^{1}D) are abundant. A large number of rate ratios have been measured. They are shown in Figure 1. (Only two absolute rates are available; they are for the reactions with O_3 and O_2.) The rate ratio data form an interconnected network, 31 different rate ratios connecting 11 species. This network is an over-determined set of linear algebraic equations that may be solved to give a self-consistent set of rate constants. Networks are unusual in kinetics, although common in thermochemistry.

Table 3. Reactions of Excited Oxygen Atoms, O(^{1}D)

5	a	$O(^1D) + O_3$	$\rightarrow 2O_2$
	b		$\rightarrow O + O + O_2$
11	a	$+ N_2O$	$\rightarrow N_2 + O_2$
	b		$\rightarrow NO + NO$
12		$+ CH_4$	$\rightarrow CH_3 + HO$
13		$+ H_2$	$\rightarrow H + HO$
14		$+ H_2O$	$\rightarrow HO + HO$
15		$+ N_2 + M$	$\rightarrow N_2O + M$
16		$+ CO + M$	$\rightarrow CO_2 + M$

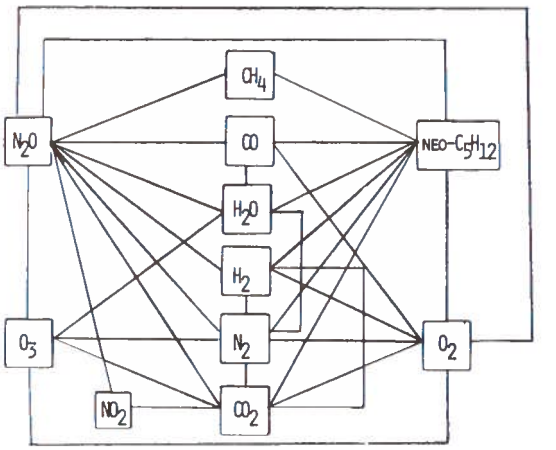

Figure 1. Rate ratio network for O (^{1}D) reactions. Each line indicates that the ratio of the rates of reaction of O^{1}D with the two species has been measured, e.g., k (O* + O_3)/k (O* + N_2O). Absolute rates have been measured only for the reactions with O_3 and O_2.

There are two crucial evaluation problems: (1) deciding which rate ratio studies are acceptable for use in the network analysis, and (2) putting the rates on an absolute basis. There are major inconsistencies in the ratio data. Even so, when almost all the data are used, the rates can be set to within a factor of two. Judicious selection should improve the reliability limits considerably. More absolute rate measurements are essential, since they set the scale for all the other

rates. They must be accurate; their errors propagate throughout the network.

Ozone-Nitrogen Oxide Interactions

The higher oxides of nitrogen, NO, NO_2, NO_3 and N_2O_5, can become part of the stratospheric soup. Reaction (11b) is one route. It converts N_2O, which is produced in the biosphere, to NO. Once this is present, various rapid reactions can form the others. Table 4 summarizes the NO_x chemistry that can occur in *pure dry air* in the presence of sunlight, either at ground level or in the stratosphere. It is by no means sufficient for a description of the chemistry in a moist atmosphere that also contains CO and organic molecules.

Table 4. Ultraviolet Photolysis of Nitrogen Dioxide

17	$NO_2 + h\nu \rightarrow NO + O\ (^3P)$	$\lambda < 390$ nm
4	$O + O_2 + M \rightarrow O_3 + M$	
18	$NO + O_3 \rightarrow NO_2 + O_2$	
19	$O + NO_2 \rightarrow NO + O_2$	
20	$NO_2 + O_3 \rightarrow NO_3 + O_2$	
21	$NO_3 + h\nu \rightarrow NO_2 + O\ (NO + O_2)$	
22	$O + NO + M \rightarrow NO_2^* + M \rightarrow NO_2 + h\nu$	
23	$NO_2 + NO_3 \rightarrow N_2O_5$	

Two reactions in this set, (18,19), form a cycle that destroys odd oxygen without removing NO_x. This cycle (and others) has been discussed in detail by Nicolet [1], Johnston [2,5], and Crutzen [6]. It has been applied to show that low concentrations of NO_x will reduce the ozone concentration in the stratosphere.

Recent laboratory studies demonstrate the effect. These are measurements of the rate of reaction of O with O_3 (6) under conditions where only reactions (6,18,19,22) are of any importance [4]. In effect, the time history of O-atoms was monitored in a previously prepared odd-oxygen mixture to which traces of NO were added. Figure 2 shows a distinct acceleration of the rate as the NO concentration is increased.

This cycle is not true catalysis. Reactions (18,19) are not the propagating steps in a chain reaction. Instead, they are "photo-catalytic".

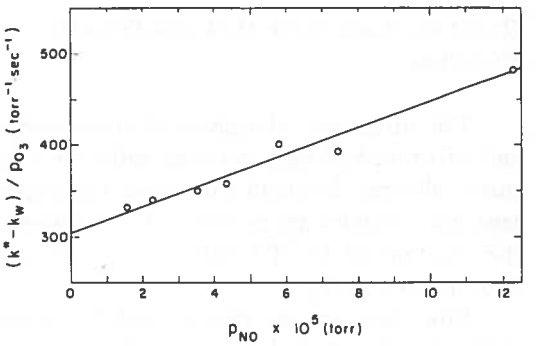

Figure 2. The effect of the addition of NO on the apparent rate constant for the reaction of O with O_3. Initial conditions: $[O_3] = 1.6 \times 10^{15}$, $[O_2] = 1.1 \times 10^{13}$, $[NO] = 1.1 - 3.9 \times 10^{12}$, [total] = 4.8×10^{16} molecules cm^{-3} (mostly argon), T = 298 K. The ordinate is the pseudo-first-order rate constant corrected for wall reactions. (Figure 3 of McCrumb and Kaufman, J. Chem. Phys. *57*, 1270 (1972). Used with the consent of the authors.)

The pair

$$NO + O_3 \rightarrow NO_2 + O_2 \qquad (18)$$

$$NO_2 + O \rightarrow NO + O_2 \qquad (19)$$

is equivalent to

$$O_3 + h\nu \rightarrow O + O_2 \qquad (1)$$

$$O + O_3 \rightarrow O_2 + O_2 \qquad (6)$$

since a photon is needed to produce the O-atom consumed in (19). Although this cycle can increase the destruction of ozone substantially above that in a pure O_2/O_3 system, it does not raise the maximum quantum yield. That would remain about 2, if we consider the set of reactions (1,2,3,7,9,10,18,19). This maximum level will not be reached because of the overwhelming importance of reaction (4).

Because of their catalytic effect, the rate constants for (18) and (19) must be known accurately. Good rate constants are also needed for other NO_x reactions, such as (20), (21), and (23). The pair (20,23) leading to N_2O_5 may provide additional destruction of O_3 at night. In turn, this means that the reactions and photochemistry of N_2O_5 must be considered.

Ozone-Water and Ozone-Hydrogen Peroxide Photolysis

The ultraviolet photolysis of moist ozone and of ozone-hydrogen peroxide mixtures both show enhanced destruction of ozone. The important intermediates are hydroxyl, HO, formed in the reaction of $O(^1D)$ with water (14), and hydroperoxyl, HO_2.

How these species interact with O_3 is not clear; the laboratory data are conflicting. When moist ozone, either in the presence or in the absence of O_2, is photolyzed under steady illumination the quantum yield can be very large, as much as 100 [7-8]. This indicates a chain reaction. One mechanism that has been suggested [7] is

$$HO + O_3 \rightarrow HO_2 + O_2 \qquad (30)$$

$$HO_2 + O_3 \rightarrow HO + 2O_2 \qquad (31)$$

This is true catalysis. Once initiated by HO formation, e.g., by reaction (14), it can continue indefinitely until the radicals are lost in termination steps. Another chain is

$$HO + O_3 \rightarrow HO_2 + O_2$$

$$HO_2 + O \rightarrow HO + O_2 \qquad (27)$$

This is catalysis of odd-oxygen disappearance in the same sense as the pair of NO_x reactions (18,19). It could not account for the long chains. These steady-state experiments may be giving minimum estimates for the chain lengths. The systems are optically thick, so all absorption occurs near the wall. Deactivation of excited species may be important.

Flash photolysis of moist ozone, in the absence of O_2, shows no effective chain. The total decomposition of ozone either decreases [9,10] or increases slightly [11]. The main effect at short times seems to be removal of $O(^1D)$ by reaction with water (14). These experiments suggest that (30) is slow. A direct measurement of the rate remains a high-priority item. We must be sure.

The photolysis of low concentrations of O_3 and H_2O_2 in the presence of a large excess of O_2 is more closely related to stratospheric conditions. It shows an increase in the destruction of ozone [12a]. (See Figure 3.) In all experiments the quantum yield is much less than one. Originally part of this enhanced decomposition was attributed to the reaction of HO with O_3. Recently the experiments have been reinterpreted in the light of $O(^1D)$ chemistry [12b]. The increased decomposition is due to the removal of $O(^1D)$ and $O(^3P)$ by reaction with H_2O_2 (29). No chain reaction involving HO or HO_2 reactions with O_3 occurs. These experiments should be considered as a "worst-case analysis" for the photolysis of dilute, moist ozone.

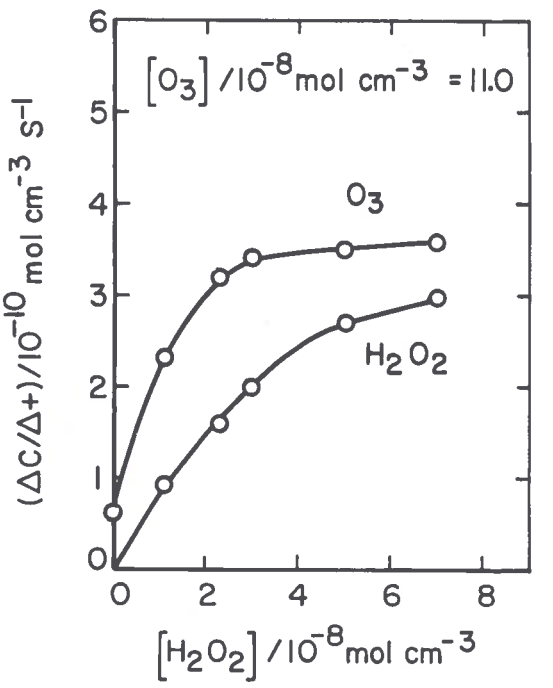

Figure 3. The effect of the addition of H_2O_2 on the photodecomposition of ozone. $\lambda = 254$ nm, $O_2 = 4.1 \times 10^{-5}$ molecules $cm^{-3} = 1$ atm, $T \approx 300$ K. The ordinate is the average rate of change of concentration per second during a 29-second period of illumination. $\Phi(-O_3) \approx 0.1$ for $[H_2O_2] = 0$. (Data from Table VI, Volman, J. Am. Chem. Soc. *73*, 1018 (1951)).

Table 5 shows some of the reactions that must be considered in the photolysis of dilute, moist ozone in excess O_2. If there is photocatalysis it could be via the sequence (24,25,27) or (24,25,28,29). Neither is attractive, because several steps are reactions between species present at very low concentrations. The mechanism for steady photolysis of concentrated moist ozone remains obscure.

Table 5. Reactions in the Ultraviolet Photolysis of Moist Ozone

1	$O_3 + h\nu \rightarrow O(^1D) + O_2(^1\Delta)$	
2	$O(^1D) + M \rightarrow O(^3P) + M$	
3	$O + O_2 + M \rightarrow O_3 + M$	
14	$O(^1D) + H_2O \rightarrow HO + HO$	
24	$HO + O \rightarrow H + O_2$	$O(^1D$ and $^3P)$
25	$H + O_2 + M \rightarrow HO_2 + M$	
26	$H + O_3 \rightarrow HO + O_2$	
27	$HO_2 + O \rightarrow HO + O_2$	$O(^1D$ and $^3P)$
28	$HO_2 + HO_2 \rightarrow H_2O_2 + O_2$	
29	$O + H_2O_2 \rightarrow HO + HO_2$	$O(^1D$ and $^3P)$
30	$HO + O_3 \rightarrow HO_2 + O_2$	
31	$HO_2 + O_3 \rightarrow HO + 2O_2$	
32	$HO_2 + h\nu \rightarrow ?$	
33	$H_2O_2 + h\nu \rightarrow HO + HO$	
34	$HO + H_2O_2 \rightarrow H_2O + HO_2$	

When these O_3-NO_x and O_3-water systems are combined, a new set of reactions links them (Table 6) with results that are not easily predictable, but are unlikely to retard the destruction of ozone.

Table 6. Some Reactions that Couple the O_3/NO_x and O_3/H_2O Photolysis Systems

35	$HO + NO + M \rightarrow HONO + M$	
36	$HO + NO_2 + M \rightarrow HNO_3 + M$	
37	$HNO_2 + h\nu \rightarrow HO + NO$	
38	$HNO_3 + h\nu \rightarrow HO + NO_2$	
39	$HNO_2 + O \rightarrow HO + NO_2$	
40	$HNO_3 + O \rightarrow HO + NO_3$	
41	$HNO_2 + HO \rightarrow H_2O + NO_2$	
42	$HNO_3 + HO \rightarrow H_2O + NO_3$	
43	$HO_2 + NO \rightarrow HO + NO_2$	
44	$HO_2 + NO + M \rightarrow HNO_3 + M$	?

This is a sufficient, although far from complete, description of the chemical reactions that must be considered in quantitative explanations of stratospheric chemistry. The emphasis has been on systems that are subsets of the complex air/O_3/NO_x/H_2O/RH/etc. system in the atmosphere. These subsets are also complex. Usually it is impractical to extrapolate the observed results to stratospheric conditions. Instead the subsets must be decomposed into their elementary reactions, and then these must be studied individually. *The rates and quantum yields for elementary reactions are independent of the systems in which they occur; they are transferable.* They may be combined in models to describe the stratosphere and also to describe the subsets discussed here. Indeed, quantitative reproduction of these simpler systems by simulation studies may be the only available test of the techniques used to describe stratospheric chemistry.

The Polluted Troposphere and Stratosphere

At ground level, in photochemical smog, ozone is a product, and it increases with time during the day. Photochemical smog is initiated by NO_2 photolysis, reaction (17). This fact is raised as an objection to the conclusion that NO_x will reduce the ozone concentration in the stratosphere. This objection will plague debate on stratosphere chemistry until there is a clear demonstration that these two views are compatible.

In our opinion, the CIAP program must make the demonstration. Two levels of explanation are necessary. One is a detailed explanation acceptable to photochemists familiar with tropospheric and stratospheric pollution. The other is a statement that will be convincing to an audience not familiar with chemistry. Both of these statements will be difficult to write. We are not satisfied with our own attempts, and urge chemical modelers to try their hands.

Because the starting conditions in the troposphere and stratosphere are widely different, there is little reason to expect the same overall effects from the operation of a common chemical mechanism. Photolysis of NO_2 is important at ground level, while that of O_3 is not: wavelengths below 290 nm do not penetrate. The ground-level photolysis occurs in an atmosphere with much higher water, CO, and reactive hydrocarbon levels. These species are important in the ozone buildup because they lead to paths for reoxidizing NO to NO_2 that do not involve ozone [13,14].

Most stratospheric chemistry models include the reactions that are also important in the troposphere. However, the two systems are so complex that simpler models should be used to demonstrate the similarities and differences. One possibility is the $NO_x/O_2/CO/H_2O$ system that has been used successfully by Demerjian et al. to explain certain smog-chamber results [14]. Another model could emphasize reactive hydrocarbons. A third approach would be to run a stratospheric chemical model under the ground-level starting conditions. These simulations could satisfy the chemists and provide the data upon which to base general statements for a wider audience.

COLLECTION OF DATA

Simulation studies of the chemistry of the stratosphere now use about 50 chemical reactions and photochemical processes. A larger number must be considered in making decisions about which ones will be important. Perhaps the total is 100 or 125.

What data are needed for these elementary chemical and photochemical steps? What special requirements must the data meet for them to be useful in the simulation studies?

The types of data are:

- Reaction rate constants for processes showing chemical change or energy transfer.
- Optical absorption coefficients for the photochemical steps.
- Efficiencies (quantum yields) for the photochemical steps. If more than one set of photo-products may follow absorption of light, efficiencies are needed for each such channel.

The special requirements imposed by the simulation studies are:

- Reaction rates must be applicable in the temperature range 220-280 K. Energy transfer efficiencies must be known for interaction of excited species with O_2 and N_2. In rare cases they may be needed for minor constituents of the atmosphere.
- Optical absorption coefficients are needed over the range of wavelengths that causes photodissociation. The wavelength ranges vary with the absorbing species; however, a rough guide is $180 < \lambda < 400$ nm.* If the molecule has important low-lying states, then the absorption coefficients should be applicable to the gas at temperatures of 220-280 K.
- Quantum yields are needed as a function of wavelength. It is particularly important to have good data near threshold (cut-off) wavelengths for the major absorbers.
- Reliability limits are needed for all these types of data. It must be possible, in the simulations, to estimate the range of results that can be expected.

There is one additional requirement that is characteristic of large-scale programs in which many people attack various portions of the problem: a common data base must be available to all.

The problem is a large one: much data is needed, and needed quickly. The requirements are severe. What resources are available? How are the needed data to be obtained?

The answer to the second question is:

- Use *acceptable* data that now exist, and
- Supplement these with new measurements as required.

Data evaluation addresses itself to both parts of this solution. The task is to determine:

- What data are available,
- Which are acceptable,
- What are the most reasonable numerical values,
- Which missing reaction rates can simply be estimated, and
- What new measurements are desirable.

What are the present resources? They are fairly large, the result of seventy years of chemical kinetics studies. Much of this work has been compiled and is reasonably easy to find, except, of course, for the most recent measurements. In addition, and more important, major programs have fostered the evaluation of rate data, particularly gas-phase rate data. CIAP is a direct beneficiary of this evaluation work.

*Ozone and NO_3 are important exceptions because of their weak absorption in the visible region of the spectrum.

This organized data evaluation work is international in scope. In the USA it is supported by the Office of Standard Reference Data, National Bureau of Standards. In the UK the work is fostered by the Office of Science and Technology. In the USSR the work is carried out by the Commission on the Compilation of Rate Coefficients of the Academy of Sciences. The international organization encouraging these programs is the Committee on Data for Science and Technology (CODATA) of the International Council of Scientific Unions.

Several of the more pertinent sources of evaluated and compiled rate data are listed in References 15-28. A larger list, covering all of chemical kinetics, has been published by CODATA [29]. (Interestingly enough, the first full-scale rate evaluation issued by the U.S. National Standard Reference Data Program was a treatment of the reactions of O, O_2, and O_3 by H.S. Johnston [22].) A rough estimate is that this pool of evaluations treats 650 to 800 reactions. It includes about 60 of direct interest to CIAP. This is an excellent legacy.

In order to obtain the remaining data and to determine whether or not they are applicable to stratospheric modeling, a special program for evaluating rate and photochemical data has been included in the CIAP program.

This has two parts. First, there is a group at the National Bureau of Standards that is issuing data sheets on reactions of particular interest. These data sheets summarize the available data, give a preferred value, and describe how it was selected or synthesized. These evaluations are being distributed to over 300 persons interested in stratospheric and tropospheric pollution problems. To date 27 data sheets have been issued [18,19]. Within the next few months another group of data sheets should appear, together with some revisions of earlier work. The current results of this work are summarized in Table 7. In addition, this group is distributing lists of rate constants that are the results of other evaluations [30]. Perhaps these lists are the forerunners of an agreed-upon, common data base.

However, this project is not enough. The CIAP time scale is short, modeling programs need data now, and decisions must be made about what measurements are needed. These facts were recognized by chemists who attended a workshop held in September. A group of them, the spokesman for which was R.J. Cvetanović, proposed a cooperative effort in which each chemist working on atmospheric chemistry would review the data on a few reactions closely related to his specialty. This is a very welcome suggestion. It could be a quantum jump for the chemical part of the CIAP program. It also is timely; it fits in with the plan for a comprehensive review of stratospheric chemistry in the forthcoming CIAP review volumes. A similar sounding-out of chemists had been planned by the chairman of the chemistry panel.

These two plans have been merged. A list of potential evaluators has been drawn up, and letters have been written to them inviting their participation. Descriptive material has been prepared and distributed which outlines what is needed and discusses some of the common problems that arise in evaluating data [31].

An important element in this cooperative project is a "reaction grid." This is a matrix showing the species present in the stratosphere as arguments and their potential interactions as intersections. It is both an aid in considering what chemistry might occur and a status report showing which reactions are believed to be important or unimportant and for which ones data are needed. Figure 4 is an abbreviated form of the current version of this grid.

This grid shows the interactions of 42 species with each other both in combination reactions, $A + B + M \rightarrow AB + M$, and in chemical exchanges, $A + B \rightarrow C + D + \ldots$, as well as the photoabsorption steps. A brief analysis is in order. There are 1674 intersections in the grid, 790 of which are marked "unimportant". At the other end of the scale, 134 intersections are labeled "important". Working values are available for 34 of these. (Overall, 59 of the reactions have been evaluated. Probably these evaluations will provide working values for 15 more reactions.) Thus, better than 100 items of data are needed. The largest groups of these for which working values are needed are: absorption coefficients and quantum yields (32), energy transfer reactions (15), and reactions of oxygen atoms (15), hydroxyl radicals (8), and oxygen molecules (7).

Any scientist should be able to evaluate the data closely related to his own research. The work requires careful attention to the techniques used, the method of data reduction, and the interpretation. The expert on a particular topic

Table 7. Rate and Photochemical Data for the Stratosphere

a. SUMMARY OF EVALUATED RATE DATA

Reaction			Rate Constant k ($cm^3 molecule^{-1} s^{-1}$)	Temperature Range (Deg. K)	Uncertainty in Log k
$H + HNO$	→	$H_2 + NO$	$>5 \times 10^{-14}$	211 – 703	
			7×10^{-12}	2000	±0.3
$H + HNO_2$	→	Products	No recommendation		
$H + HNO_3$	→	Products	$<1 \times 10^{-13}$	300	
$H + H_2O_2$	→	$H_2 + HO_2$	$2.8 \times 10^{-12} \exp(-1900/T)$	300 – 800	±0.3
		$H_2O + HO$	No recommendation		
$H + NO_2$	→	$HO + NO$	4.8×10^{-11}	300	±0.1
$H + O_3$	→	$HO + O_2$	2.6×10^{-11}	300	±0.1
$HNO + HO$	→	$H_2O + NO$	7×10^{-11}	1600 – 2100	±0.7
$HNO_2 + HO$	→	$H_2O + NO_2$	No recommendation		
$HNO_2 + O$	→	$HO + NO_2$	No recommendation		
$HNO_3 + HO$	→	$H_2O + NO_3$	$1.4 \times 10^{-12} \exp(-1000/T)$	300 – 650	±0.5
$HNO_3 + O$	→	$HO + NO_3$	$<1.5 \times 10^{-14}$	300	
$HO + H_2O_2$	→	$HO_2 + H_2O$	$1.7 \times 10^{-11} \exp(-910/T)$	300 – 800	±0.2
$HO + O_3$	→	Products	No recommendation		
$HO_2 + HO_2$	→	$H_2O_2 + O_2$	$3 \times 10^{-11} \exp(-500/T)$ (a)	300 – 1000	±0.3 (b)
$H_2O + NO + NO_2$	→	$2HNO_2$	$<1.1 \times 10^{-55}$ (c)	300	
$H_2O + N_2O_5$	→	$2HNO_3$	$<2 \times 10^{-18}$	300	
			$<1 \times 10^{-20}$	220	
$H_2O + O(^1D)$	→	$2HO$	3×10^{-10}	300	±0.3
$H_2O_2 + NO$	→	$HO + HNO_2$	$<1 \times 10^{-24}$	300	
			$\sim 2 \times 10^{-20}$	550	
$NO + O_3$	→	$NO_2 + O_2$	$9 \times 10^{-13} \exp(-1200/T)$	198 – 330	±0.11
$NO_2 + O_3$	→	$NO_3 + O_2$	6.1×10^{-17}	294	±0.11
$N_2O + O(^1D)$	→	$N_2 + O_2$	1×10^{-10}	300	±0.3
	→	$2NO$	1×10^{-10}	300	±0.3
$O + O_3$	→	$2O_2$	$2.0 \times 10^{-11} \exp(-2410/T)$	200 – 1000	±0.2
$O_2(^1\Delta) + M$	→	$O_2 + M$	$2.2 (T/300)^{0.8} \times 10^{-18}$ ($M=O_2$)	285 – 322	±0.1
			$<1 \times 10^{-19}$ ($M=N_2$)	300	
$O_2(^1\Sigma) + M$	→	$O_2 + M$	1.5×10^{-16} ($M=O_2$)	300	±0.12
			2.0×10^{-15} ($M=N_2$)	300	±0.1
			4×10^{-12} ($M=H_2O$)	300	±0.18

Notes:

a. $-d[HO_2]/dt = 2k[HO_2]^2$

b. Error in log k increases to ±1 at 1000 K

c. $-d[NO_2]/dt = k[NO]\ [NO_2]\ [H_2O]^2$. Value of k is for a surface reaction. This is adopted as the upper limit for the gas-phase rate constant.

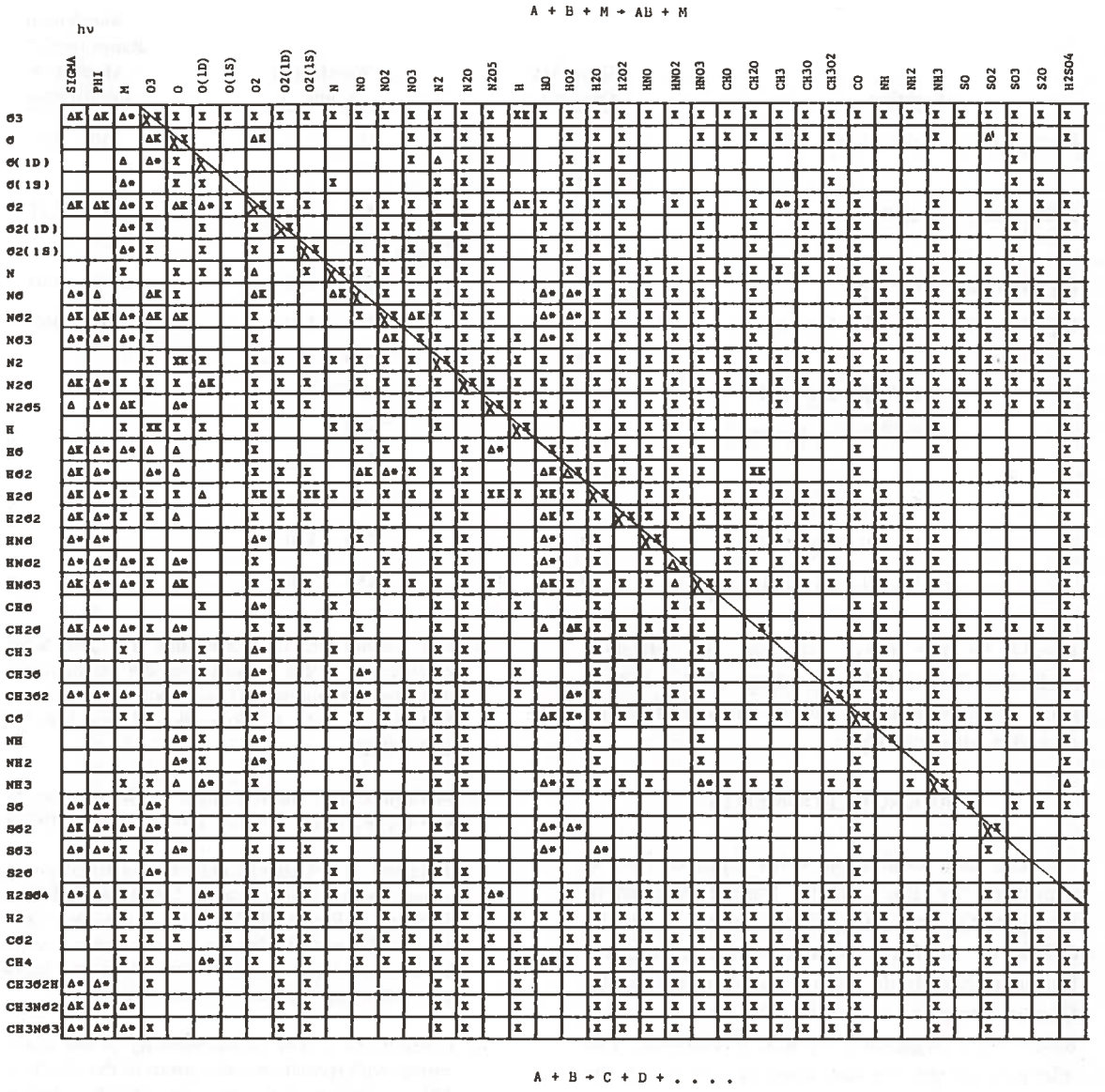

Figure 4. Reaction grid for stratospheric chemistry. The headings for rows and columns are species that are to be considered in stratospheric chemistry. A box in the grid represents their interactions. Combination reactions are above the diagonal, chemical exchanges below it. The first two columns are for absorption coefficients and quantum yields for photo-processes. The third, M, is for energy transfer. Interactions marked with a "Δ" are considered important. An "X" in a box means that the reaction is unimportant. A "K" means that a fairly good working value is available. An asterisk means that a value is needed.

Table 7. Rate and Photochemical Data for the Stratosphere (Cont.)

b. SUMMARY FOR EVALUATED PHOTOCHEMICAL DATA

Reaction	Quantum Yield $\phi(\lambda)$	at Wavelength λ, nm	Wavelength Range (nm) for Absorption Coefficients
$HNO_3 + h\nu \rightarrow HO + NO_2$	0.1	265	190 – 325
	0.3	254	
$H_2O_2 + h\nu \rightarrow 2HO$	1	200 – 300	185 – 225
			254
$O_3 + h\nu$ (vis) $\rightarrow O + O_2$	1	450 – 750	440 – 850
$O_3 + h\nu$ (uv) $\rightarrow O(^1D) + O_2(^1\Delta)$	1	250 – 310	200 – 360
	0	>310	
$\rightarrow O(^1D) + O_2(^3\Sigma\bar{g})$	0	<350	
$\rightarrow O(^3P) + O_2$ (singlet)	0	<310	
	≈1	310 – 350	
$\rightarrow O$ (total) $+ O_2$	1	250 – 350	
$\rightarrow O(^1D) + O_2(^1\Sigma\bar{g}^+)$	0	250 – 350	
$\rightarrow O(^3P) + O_2(^3\Sigma\bar{g})$	0	250 – 350	

should be the most effective and efficient evaluator. Before the proceedings of this conference are published we should know whether he *is*, and is willing to try.

ACKNOWLEDGMENTS

The data evaluation work reported here is supported by the Climatic Impact Assessment Program, Department of Transportation, by the Office of Standard Reference Data, National Bureau of Standards, and by the Measures for Air Quality Program, also NBS. The reaction grid is based on a suggestion of R.J. Cvetanović. The selection of species and markings on it are the work of H. Johnston.

REFERENCES

1. Nicolet, M. "Aeronomic chemistry of the stratosphere," Proc. Survey Conference, Climatic Impact Assessment Prog. (Cambridge, Mass., Feb. 15-16, 1972), DOT-TSC-OST-72-13, p. 44.

2. Johnston, H. "Laboratory chemical kinetics as an atmospheric science," Proc. Survey Conference, Climatic Impact Assessment Prog: (Cambridge, Mass., Feb. 15-16, 1972) DOT-TSC-OST-72-13, p. 90.

3. von Ellenrieder, G., Castellano, E., and Schumacher, H.J., "Die Kinetik und der Mechanismus des photochemischen Ozonzerfalls im Licht der Wellenlänge 2537 A," Zeit. Phys. Chem. N.F. *76*, 240 (1971).

4. McCrumb, J.L., and Kaufman, F. "Kinetics of the $O + O_3$ reaction," J. Chem. Phys. *57*, 1270 (1972).

5. Johnston, H., "Catalytic reduction of stratospheric ozone by nitrogen oxides," Lawrence Radiation Laboratory Report, UCRL-20568, Berkeley Calif. June 1971, and "Reduction of stratospheric ozone by nitrogen oxide catalysts from supersonic transport exhausts," Science *173*, 517 (1971).

6. Crutzen, P.J., "The photochemistry of the stratosphere with special attention given to the effects of NO_x emitted by supersonic aircraft," Proc. Survey Conference, Climatic Impact Assessment Prog. (Cambridge, Mass., Feb. 15-16, 1972), DOT-TSC-OST-72-13, p. 80; and "Ozone production rates in an oxygen-hydrogen-nitrogen oxide atmosphere," J. Geophys. Res. *76*, 7311 (1971).

7. Norrish, R.G.W., and Wayne, R.P., "The photolysis of ozone by ultraviolet radiation. II: The photolysis of ozone mixed with certain hydrogen-containing substances," Proc. Roy. Soc. (London) *A288*, 361 (1965).

8. Forbes, G.S. and Heidt, L.J., "The influence of water on the photolysis of ozone at λλ 280, 254 and 210 mμ," J. Am. Chem. Soc. *56*, 1671 (1934).

9. Langley, K.F., and McGrath, W.D., "The ultraviolet photolysis of ozone in the presence of water vapor," Planet. Space Sci. *19*, 413 (1971).

10. Biedenkapp, D., Hartshorn, L.G., and Bair, E.J., "The O (^{1}D) + H_2O reaction," Chem. Phys. Lett. *5*, 379 (1970).

11. Fortin, C.J., Snelling, D.R., and Tardif, A., "The ultraviolet flash photolysis of ozone and the reaction of O (^{1}D) with H_2O," Can. J. Chem. *50*, 2748 (1972).

12. *a.* Volman, D.H., "The photochemical reaction between ozone and hydrogen peroxide," J. Am. Chem. Soc. *73*, 1018 (1951).
b. Volman, D.H., correspondence with D. Garvin, Aug-Oct 1972.

13. Hecht, T.A., and Seinfeld, J.H., "Development and validation of a generalized mechanism for photochemical smog formation," Environmental Sci. Tech. *6*, 47 (1972).

14. Demerjian, K.L., Kerr, J.A., and Calvert, J.G., "The predicted effect of carbon monoxide on the ozone levels in photochemical smog systems," Environmental Lett. *3*, 73 (1972).

15. Baulch, D.L., Drysdale, D.D., and Lloyd, A.C., "Critical evaluation of rate data for homogeneous, gas phase reactions of interest in high temperature systems," *High Temperature Reaction Rate Data* (University of Leeds, England), No. 1 (May 1968). *Ibid*, No. 2 (Nov. 1968). *Ibid*, No. 3 (April 1969). Baulch, D.L., Drysdale, D.D., Horne, D.G., and Lloyd, A.C., *Ibid*, No. 4 (Dec. 1969). Baulch, D.L., Drysdale, D.D., and Horne, D.G., *Ibid*, No. 5 (July 1970).

16. Baulch, D.L., Drysdale, D.D., Horne, D.G., and Lloyd, A.C., *Evaluated Kinetic Data for High-Temperature Reactions*, Volume I: Homogeneous Gas Phase Reactions of the H_2-O_2 System, Butterworths, London, 1972.

17. Benson, S.W., and O'Neal, H.E., "Kinetics data on gas phase unimolecular reactions," NBS-NSRDS-21 (1970).

18. Hampson, R.F. (Ed.), Brown, R.L., Garvin, D., Herron, J.T., Huie., R.E., McKinley, J.D., and Tsang, W., "Chemical kinetics data survey: I. Rate data for twelve reactions of interest for stratospheric chemistry," NBS Report No. 10692 (Jan. 1972).

19. Hampson, R.F. (Ed.), Braun, W., Garvin, D., Herron, J.T., Huie, R.E., Kurylo, M.J., Laufer, A.H., Okabe, H., and Tsang, W., "Chemical kinetics data survey: II. Photochemical and rate data for fifteen gas phase reactions of interest for stratospheric chemistry," NBS Report No. 10828 (April 1972).

20. Herron, J.T., "An evaluation of rate data for the reactions of atomic oxygen (O^3P) with methane and ethane," Int. J. Chem. Kinetics *1*, 527 (1969).

21. Johnston, H.S., *Gas Phase Reaction Rate Theory*, The Ronald Press Co., New York (1966), Chapter 1.

22. Johnston, H.S., "Gas phase reaction kinetics of neutral oxygen species," NBS-NSRDS-20 (1968).

23. Kerr, J.A., and Parsonage, M.J., *Evaluated Kinetic Data on Gas Phase Addition Reactions: Reaction of Atoms and Radicals with Alkenes, Alkynes and Aromatic Compounds*, Butterworths, 1972.

24. Kondratiev, V.N., *Konstanty Skorosti Gazofaznykh Reaktsij Spravochnik* (Izdatelstvo "Nauka", Moskva, 1970); also issued as "Rate constants of gas phase reactions, reference book," R.M. Fristrom, Ed., translated by L.J. Holtschlag, COM-72-10014, Office of Standard Reference Data, NBS (1972).

25. Lloyd, A.C., "Evaluated and estimated kinetic data for the gas phase reactions of the hydroperoxyl radical," NBS Report 10447 (1971).

26. Schofield, K., "An evaluation of kinetics rate data for reactions of neutrals of atmospheric interest," Planet. Space Sci. *15* (643), 1336 (1967).

27. Schofield, K., "A scientific report on evaluated chemical rate constants for various gas phase reactions," Delco Electronics (General Motors Corp.), Santa Barbara, Calif. Report TR 71-57 (Dec. 1971).

28. Wilson, W.E., Jr., "A critical review of gas-phase reaction kinetics of the hydroxyl radical," J. Phys. Chem. Ref. Data *1*, No. 2 (1972).

29. CODATA Task Group on Data for Chemical Kinetics, "A catalog of compilation and data evaluation activities in chemical kinetics, photochemistry and radiation chemistry," CODATA Bulletin No. 3 (Dec. 1971).

30. Garvin, D., and Gevantman, L.H., "Selected rate constants for chemical reactions of interest in atmospheric chemistry," NBS Report No. 10867 (June 1972).

31. Johnston, H. and Garvin, D., "Working papers for a survey of rate data for chemical reactions in the stratosphere," NBS Report No. 10931 (Oct.1972).

RECENT KINETIC MEASUREMENTS ON THE REACTIONS OF $O(^3P)$, H AND HO_2

D. D. DAVIS
Department of Chemistry
University of Maryland
College Park, Maryland

and

W. W. WONG	*University of Maryland, College Park, Maryland*
S. D. FISCHER	*University of Maryland, College Park, Maryland*
R. L. SCHIFF	*University of Maryland, College Park, Maryland*
J. O. LEPHARDT	*University of Maryland, College Park, Maryland*
J. E. PRUSACZYK	*University of Maryland, College Park, Maryland*
W. A. PAYNE	*University of Maryland, College Park, Maryland;* *NASA Goddard Space Flight Center, Greenbelt, Maryland*
L. J. STIEF	*NASA Goddard Space Flight Center, Greenbelt, Maryland*
R. E. HUIE	*University of Maryland, College Park, Maryland;* *National Bureau of Standards, Washington, D. C.*
J. T. HERRON	*National Bureau of Standards, Washington, D. C.*

ABSTRACT: This paper examines the following systems, within the temperature ranges indicated.

(1) $O(^3P) + O_2 + M \rightarrow O_3 + M$ (200-346K)

$k_{Ar} = (6.57 \pm .59) \times 10^{-35} \exp[(1014 \pm 46 \text{ cal mol}^{-1})/RT] \text{ cm}^6 \text{ molec}^{-2} \text{ s}^{-1}$

$k_{Ar} : k_{He} : k_{N_2} = 1.0 : .92 : 1.6$

(2) $O(^3P) + NO_2 \rightarrow NO + O_2$ (230-339K)

$k = (9.12 \pm .44) \times 10^{-12} \text{ cm}^3\text{molec}^{-1}\text{s}^{-1}$ (temperature-independent)

(3) $O(^3P) + O_3 \rightarrow O_2 + O_2$ (220-355K)

$k = (2.0 \pm .8) \times 10^{-11} \exp[(-4522 \pm 150 \text{ cal mol}^{-1})/RT] \text{ cm}^3\text{molec}^{-1}\text{s}^{-1}$

(4) $H + O_2 + M \rightarrow HO_2 + M$ (220-360K)

$k_{Ar} = (6.75 \pm 1.1) \times 10^{-33} \exp[(685 \pm 128 \text{ cal mol}^{-1})/RT] \text{ cm}^6\text{molec}^{-2} \text{ s}^{-1}$

$k_{Ar} : k_{He} : k_{H_2} : k_{N_2} = 1.0 : .97 : 3.02 : 2.8$

(5) $HO_2 + CO \rightarrow CO_2 + OH$ (300K)

$k \leqslant 10^{-20} \text{ cm}^3\text{molec}^{-1}\text{s}^{-1}$

(6) $HO_2 + SO_2 \rightarrow SO_3 + OH$ (300K)

$k = 3 \times 10^{-16}$ (± factor 2) $\text{cm}^3\text{molec}^{-1}\text{s}^{-1}$

(7) $HO_2 + NO \rightarrow NO_2 + OH$ (300K)

$k = 3 \times 10^{-13}$ (± factor 3) $\text{cm}^3\text{molec}^{-1}\text{s}^{-1}$

INTRODUCTION

It has long been recognized that the neutral transient species $O(^3P)$, $O(^1D)$, OH, H, and HO_2 play a major role in defining the chemical dynamics of the stratosphere. In order to successfully model this atmospheric zone, it is therefore of major importance that reliable rate data be available for the reactions of these transients with other stratospheric species such as NO, NO_2, N_2O, HNO_3, O_3, O_2, H_2O_2, H_2O, CH_4, CO, and SO_2. In many cases, rate constants for possible key reactions are totally missing; in other cases, measurements are available only at 298K with the activation energy unknown; finally, there are many other reactions for which considerable rate data exist, but where the various measurements do not agree well.

This manuscript reports on several recent kinetic investigations carried out in our laboratories which attempt to fill in many of these existing knowledge gaps. Two different experimental techniques have been employed in making these measurements. The first of these is flash-photolysis/resonance-fluorescence, from which absolute rate constants were measured for the reactions of $O(^3P)$ and H. The second is the photochemical O_2 ^{18,18} isotope method, which was used for making relative rate-constant measurements of the reactions of HO_2.

EXPERIMENTAL

Flash-Photolysis/Resonance-Fluorescence

The application of the flash-photolysis/resonance-fluorescence technique to kinetic studies is now well established and has been discussed in numerous publications [1-7]. The basic design of this apparatus, shown schematically in Figure 1, consists of a thermostatted reaction cell centered in a vacuum housing, a spark-discharge flash lamp or tunable dye laser perpendicular to one face of the cell, an atomic-oxygen or hydrogen resonance lamp perpendicular to another face, and, finally, a photo-detector (a magnetic electron multiplier using either a copper-iodide or tungsten photocathode) perpendicular to the base of the cell. Windows in the apparatus were either LiF, CaF_2, or quartz, depending on the type of energy source used (dye laser vs. vacuum UV flash lamp) and the resonance lamp required.

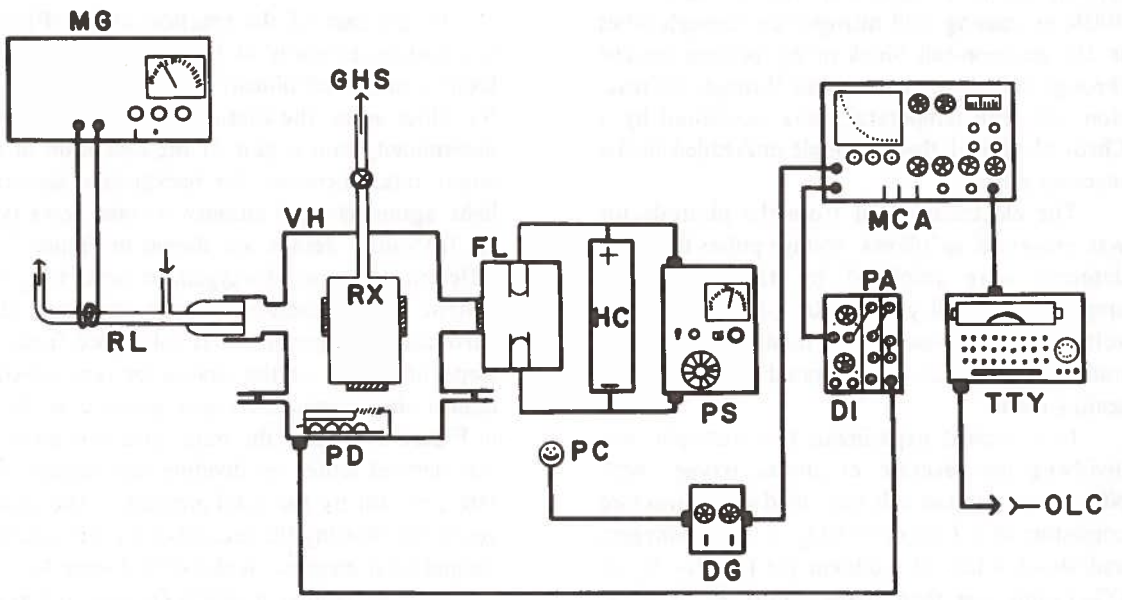

Figure 1. Schematic drawing of the flash-photolysis/resonance-fluorescence apparatus. DG – delay generator, DI – voltage discriminator, FL – flash lamp or tunable dye laser, GHS – gas-handling system, HC – high-voltage capacitor, MCA – multichannel analyzer, MG – microwave generators, OLC – on-line 1108 Univac computer for data processing, PA – pulse amplifiers, PC – photocell, PD – photon detector, PS – flash-lamp power supply, RL – resonance lamp, RXC – reaction cell, TTY – teletype, and VH – vacuum housing.

The atomic-oxygen and atomic-hydrogen resonance lamps were of the same construction as those described by Davis and Braun [8]. Ultrahigh-purity helium was pumped through a multicoiled liquid-nitrogen trap and then through the lamp at a pressure of about 1 torr. A microwave discharge through the ultrahigh-purity helium (which still contained traces of H_2O and O_2) produced both the oxygen triplet at 1303.5Å and the hydrogen Lyman-α line at 1216Å. Whenever the atomic-oxygen triplet needed to be isolated from the Lyman-α line, a CaF_2 filter window was placed in front of the lamp. For isolation of the Lyman-α line, on the other hand, an O_2 filter chamber was positioned between the output of the resonance lamp and the reaction cell.

When vacuum-UV radiation was used in the production of atomic species, a spark-discharge lamp was employed which used N_2 as a filling gas. In those experiments that used O_3 as a source of atomic oxygen, a tunable dye laser operating in the 5900-6200Å region of the spectrum was employed as the photo-flash; the laser dye was Rhodamine 6G.

The temperature of the reaction cell in this system could be controlled from about 190 to 400K by passing cold nitrogen gas through tubes in the reaction-cell block or by passing current through resistance wire wound through the reaction cell. The temperature was monitored by a Chromel-Alumel thermocouple embedded in the reaction cell.

The electrical signal from the photodector was processed as follows: voltage pulses from the detector were amplified by three wideband amplifiers (overall gain 1000), passed through a voltage discriminator, and finally stored in a multichannel analyzer operated in the multiscaling mode.

In a typical experiment (for example, one involving the reaction of atomic oxygen with NO_2), the reaction cell was filled with a mixture consisting of 1-7 mtorr of NO_2, 1 torr of oxygen, and about 4 torr of a diluent gas (Ar, N_2, O_2 or CO_2), and was then flash-photolyzed at wavelengths above 1050Å. Depending on the voltage at which the lamp was fired, from .05 to .005 mtorr of atomic oxygen was produced. A small fraction of this atomic oxygen was continuously excited by an atomic-resonance lamp, and the decay of the oxygen atoms in the mixture was monitored by following the fluorescence of the atomic-oxygen resonance radiation. The fluorescence signal was recorded on a multichannel analyzer, and more than 100 flashes were used to generate each kinetic decay curve. The reaction mixture was changed several times in the course of an experiment so that depletion of the NO_2 did not exceed 5%.

Since these experiments were conducted with the concentration of NO_2 in great excess over that of atomic oxygen, the observed loss of atomic oxygen was first-order. The first-order rate constant could, therefore, be determined from a plot of the logarithm of the count rate, corrected for background scattered light, against channel number or time. In every case, a good linear fit was found over at least a full-decade change in the count rate. This first-order rate constant was corrected for loss of atomic oxygen due to reaction with molecular oxygen, and for diffusion of atomic oxygen out of the reaction zone, and was then divided by the NO_2 concentration to derive the bimolecular reaction rate constant. The combined correction indicated above was typically less than 15% of the total first-order rate constant.

In the case of the reaction of O (^{3}P) with O_2, various amounts of O_2 were mixed with a fixed pressure of diluent gas, either Ar, He, or N_2. Once again, the first-order rate constant was determined from a plot of the logarithm of the count rate, corrected for background scattered light, against channel number or time. Some typical first-order decays are shown in Figure 2 for different pressures of oxygen. In the $O + O_2 + M$ system, the second-order rate constant at a particular total pressure was calculated from the slope of a plot of the first-order rate constant against the molecular-oxygen pressure as shown in Figure 3. Finally, the third-order rate constant was derived either by dividing the second-order rate constant by the total pressure of the diluent gas or by plotting the second-order rate constant against total pressure, as shown in Figure 4.

In those studies in which O_3 was used as the source of atomic oxygen, O (^{3}P), (e.g., $O + O_3 \rightarrow O_2 + O_2$), the treatment of the experimental data was similar to that already described for the $O + NO_2$ system. In the $O + O_3$ system, however, ground-state atomic oxygen was generated from the dye-laser flash-photolysis of O_3 in the

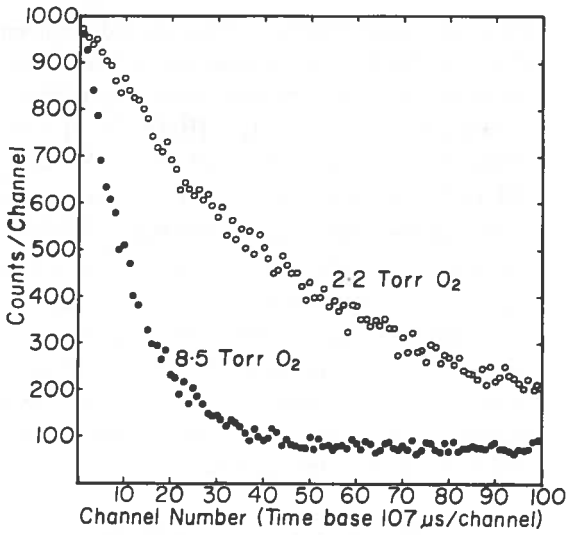

Figure 2. Typical exponential decay of $O(^3P)$ via reaction with O_2 where O_2 and M concentrations are in large excess.

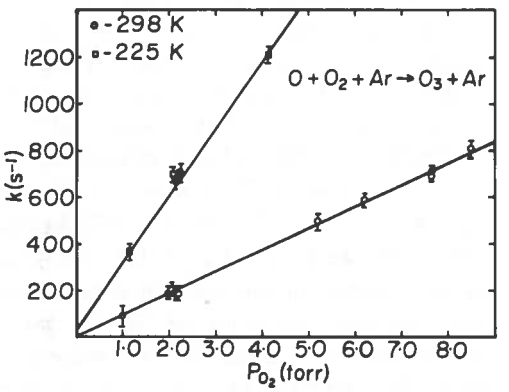

Figure 3. Plot of the pseudo-first-order rate constant for the reaction $O(^3P) + O_2 + M$, vs. the O_2 pressure.

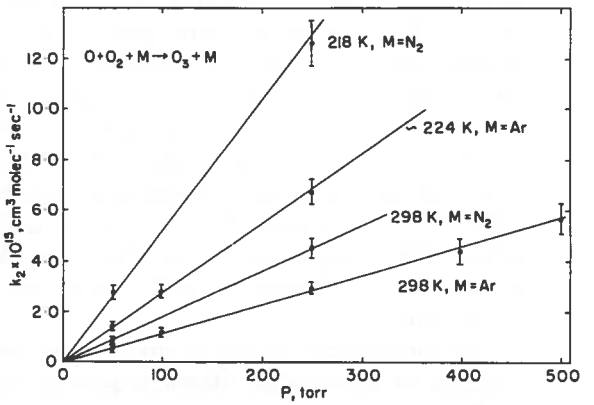

Figure 4. Plot of the pseudo-second-order rate constant for the reaction $O(^3P) + O_2 + M$, vs. the third-body concentration (M).

Chappuis band. The bandwidth of the photolysis radiation in this case was ≈ 200Å, with a maximum at 6000Å.

In the investigation of the reaction of atomic hydrogen with O_2, the source of atomic hydrogen was the vacuum UV flash photolysis of about 200μ CH_4. Treatment of the experimental data in deriving the third-order rate constant for reaction (4) was similar to that described above for reaction of $O(^3P)$ with molecular oxygen.

Photochemical $O_2{}^{18,18}$ Isotope Technique

In the photochemical $O_2{}^{18,18}$ isotope technique, measurements of the rate constants for reaction of HO_2 with CO, SO_2, and NO were made relative to the disproportionation reaction,

$$HO_2 + HO_2 \rightarrow H_2O_2 + O_2 \qquad (8)$$

The ratios of rate constants k_5/k_8, k_6/k_8, and k_7/k_8 were established from measurements of the photochemical rate of production of $CO_2{}^{16,18}$ and $CO_2{}^{16,16}$ which resulted from the low-intensity photolysis of mixtures of CO, H_2O, Ar, and $O_2{}^{18,18}$.

In most of the experiments reported here, HO_2 was produced via the third-order reaction (4). In a limited number of experiments, however, HO_2 was generated via the photolysis of H_2O_2. In the latter system, an excess of H_2O_2 over CO insured that most of the initially-formed OH would react with H_2O_2 to produce HO_2, e.g.,

$$H_2O_2 + h\nu \rightarrow 2OH \qquad (9)$$

$$OH + H_2O_2 \rightarrow HO_2 + H_2O \qquad (10)$$

The experimental apparatus used in the HO_2 kinetic studies is shown in Figure 5. This system consisted of a 300-cm^3 Pyrex photolysis cell equipped with a one-inch Suprasil window (transmits $\lambda > 1650$Å), a Hg resonance lamp, and a high-vacuum (10^{-6} torr) submanifold through which the gases H_2O, CO, $O_2{}^{18,18}$, and Ar could be metered into the photolysis cell. The output of the Hg resonance lamp was examined on a vacuum-UV monochromator and was found to consist of nearly equal amounts of the two lines 1849 and 2537Å. In these experiments, no attempt was made to block the 2537Å line, since neither the reactants (H_2O, CO, O_2) nor the products (CO_2) absorbed significantly at this

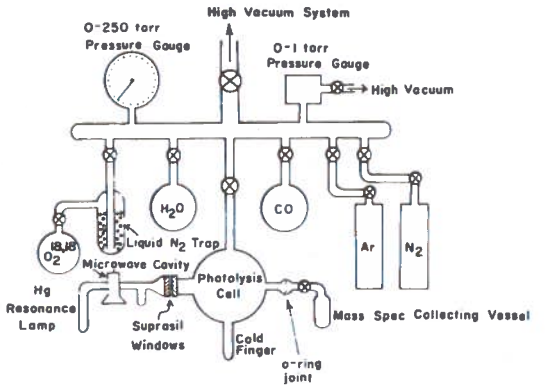

Figure 5. Apparatus used in the photochemical $O_2^{18,18}$ isotope technique.

wavelength. The products, $CO_2^{16,18}$ and $CO_2^{16,16}$, were analyzed with a CEC 21-620 mass spectrometer.

From the following reaction scheme

$$H_2O^{16} + h\nu \rightarrow H + {}^{16}OH \qquad (11)$$

$${}^{16}OH + CO^{16} \rightarrow CO_2^{16,16} + H \qquad (12)$$

$$H + O_2^{18,18} + Ar \rightarrow HO_2^{18,18} + Ar \qquad (4')$$

$$HO_2^{18,18} + CO^{16} \rightarrow CO_2^{16,18} + {}^{18}OH \qquad (5')$$

$${}^{18}OH + CO^{16} \rightarrow CO_2^{16,18} + H \qquad (12')$$

$$HO_2^{18,18} + HO_2^{18,18} \rightarrow H_2O_2^{18,18} + O_2^{18,18} \qquad (8)$$

$$H_2O_2^{18,18} + h\nu \rightarrow 2\,{}^{18}OH \qquad (9')$$

it can be seen that if the chain length for the reaction sequence (5'), (12') and (4') is unity or greater, the ratio $CO_2^{18,16}/CO_2^{16,16}$ will always be greater than unity.

A steady-state treatment of reactions (11), (12), (4'), (5'), (12'), (8) and (9') leads to the mathematical relationship.

$$\frac{R_{CO_2}^{18,18}}{(R_{CO_2}^{16,16})^{1/2}} = \frac{2k_{5'}[CO]}{(k_8)^{1/2}} + \frac{J_9,[H_2O_2^{18,18}]}{(J_{11}[H_2O^{16}]^{1/2})} \qquad (I)$$

where $R_{CO_2}^{16,18}$ and $R_{CO_2}^{16,16}$ are the rates of formation of labeled and unlabeled CO_2 in units of $molec^{-1}cm^{-3}s^{-1}$. (The second term on the right-hand side of equation (I) has been separated from the first term under experimental conditions such that $J_{9'}[H_2O_2^{18,18}] < k_8[HO_2^{18,18}]^2$ and $J_{9'}[H_2O_2^{18,18}] < J_{11}[H_2O^{16}]$.) From equation (I), it can be seen that a plot of the ratio $R_{CO_2}^{16,18}/(R_{CO_2}^{16,16})^{1/2}$ vs. $[CO^{16}]$ should yield a slope which is just equal to the rate-constant ratio $2k_{5'}/(k_8)^{1/2}$. The value of k_8 used in this study to evaluate $k_{5'}$ was 3.3×10^{-12} $cm^3molec^{-1}s^{-1}$ [9,10]. Expressions similar to equation (I) have also been derived for the case of reactions (6) and (7), and will be discussed later in the text.

RESULTS AND DISCUSSION

$$O(^3P) + O_2 + M \rightarrow O_3 + M$$

The third-order rate constant for reaction of ground-state atomic oxygen with molecular oxygen was measured for three different third bodies, Ar, He, and N_2. The rate constant observed for Ar at 298K was 3.63×10^{-34} $cm^3molec^{-1}s^{-1}$. The relative efficiencies of the above three gases at 298K were as follows: k_{Ar}: k_{He}: k_{N_2} = 1.0 : .92 : 1.6. At 218K the relative efficiencies were k_{Ar}: k_{N_2} = 1.0 : 1.7. Changes in the variables of this reaction system included total pressure variations of 50-500 torr, O_2 concentrations of about 1-8 torr, and variations in the flash intensity by a factor of ten. In every case, it was found that at a fixed temperature the third-order rate constant was invariant to the above changes in reaction conditions. Over the temperature range of 200-346K, an Arrhenius plot (see Figure 6) of the data from this work yielded the expression $k_{Ar} = (6.57 \pm .59) \times 10^{-35}$ exp $[(1014 \pm 46$ cal $mol^{-1})/RT$ cm^6 $molec^{-2}s^{-1}$. The stated uncertainties are the standard errors of the least-squares fit to the data. The maximum and minimum slopes which could be fitted through the error bars at each temperature corresponded to uncertainties in A and E of ± 2.15 $cm^6molec^{-2}s^{-1}$ and ± 180 cal/mol, respectively.

Of considerable concern in any study of the reactions of ground-state atomic oxygen is the possible kinetic influence of electronically-excited oxygen atoms and/or molecular oxygen. In these experiments, a minimum delay of 200 μs was employed between the flash photolysis of

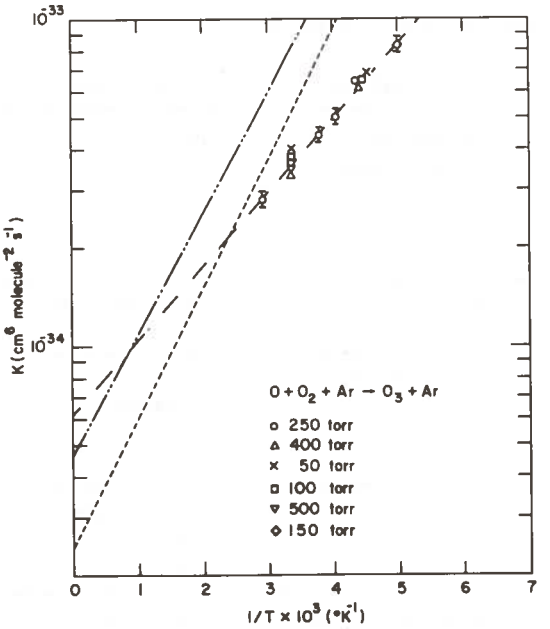

Figure 6. An Arrhenius plot of the rate data for the reaction $O(^3P) + O_2 + M \rightarrow O_3 + M$: – – – this work; - - - Clyne, McKenney & Thrush [11]; – - – - Mulcahy and Williams [12].

the reaction mixture and the atom-concentration measurements used in determining the rate constants. At the pressures used in this study, the 200-μs delay ensured that all atoms produced by the flash had reached the ground electronic state and were at thermal equilibrium. In the experiments employing He or Ar as the inert gas, most of the O (^{1}D) produced by the flash would be quenched by O_2, producing $O_2(^1\Sigma g^+)$. The excited molecular oxygen could then react with the ozone produced by the $O + O_2 + M$ reaction to regenerate atomic oxygen. However, since the concentrations of both O_3 and O_2 ($^1\Sigma g^+$) would be proportional to the flash intensity, any contribution from this reaction would depend upon the square of the flash intensity. To investigate the possibility that this reaction could have been important, the flash intensity was varied over about a factor of ten at both 298 and 225K. The observed invariance of the first-order rate constant with flash intensity demonstrates that the rate of atom loss was not being influenced by secondary reactions involving O_2 ($^1\Sigma g^+$) and O_3, or any other secondary processes such as $O + O_3 \rightarrow 2O_2$ or $O + O + M \rightarrow O_2 + M$.

In Table 1, the results of the present work are summarized along with rate measurements reported by other workers. Excluded are those discharge-flow measurements which were carried out under conditions for which the effects of active impurities and metastable molecular-oxygen species could have significantly influenced the final results.

As can be seen from Table 1, the only previous direct data on the temperature dependence of the rate of reaction of atomic oxygen with molecular oxygen are derived from flow system studies. Clyne, McKenney, and Thrush [11] studied the reaction in a plug-flow reactor, using a microwave discharge in oxygen as an atom source. The decay of the oxygen atoms down the reactor was determined by monitoring the chemiluminescence from the reaction $O + NO \rightarrow NO_2 + h\nu$. At room temperature, the results of these authors are in reasonable agreement with the present work (±15%). At lower temperatures, however, their data diverge from the present results and are about a factor of 3 higher at 220K. Mulcahy and Williams [12] also employed O + NO chemiluminescence to follow the atom concentration, but used the thermal decomposition of ozone as an atom source and carried out the study in a bulb reactor. These authors report a third-order rate constant for Ar which is a factor of 2 higher than our present results at 298K and a factor of 3 higher at 220K. In neither study were sufficient data given to allow detailed evaluation of the results.

In Johnston's review [22] of the kinetics of neutral oxygen species, the recommended value for the reaction of atomic oxygen with molecular oxygen was derived from the equilibrium constant and the recommended rate constant for the reverse reaction. The preexponential term obtained by this method is a factor of 5 lower than the present study's, and the exponential term is a factor of 2 higher. At 220K, this results in a rate constant a factor of 2 higher than that reported here. This discrepancy, however, is probably not as unreasonable as it first appears. For example, the ozone bond strength used by Johnston was 24.8 kcal mol^{-1}, and the activation energy used for the reverse reaction was 22.7 kcal mol^{-1}. An error of 5% in either of these values would be sufficient to account for

Table 1. A Summary of Rate Data on the Reaction $O + O_2 + M \rightarrow O_3 + M$

T (K)	M	k, $cm^6 molec^{-2} s^{-1}$	Method	Reference
298	He	3.33×10^{-34}	Flash-photolysis/ resonance-fluorescence	This work
298	Ar	3.63×10^{-34}		
200-346	Ar	$6.57 \times 10^{-35} \exp(1014/RT)$		
218	N_2	11.7×10^{-34}		
298	N_2	5.63×10^{-34}		
188-373	Ar	$2.44 \times 10^{-35} \exp(1800/RT)$	Discharge-flow	Clyne, McKenney & Thrush [11]
213-386	Ar	$4.7 \times 10^{-35} \exp(1680/RT)$	Thermal-decomposition/ flow	Mulcahy & Williams [12]
298	CO_2	23×10^{-34}		
298	O_2	9.0×10^{-34}		
298	He	6.33×10^{-34}		
298	CO_2	10.2×10^{-34}	Pulse radiolysis	Meaburn, Perner, LeCalve & Bourene [13]
298	N_2O	8.84×10^{-34}		
298	CO	4.42×10^{-34}		
298	He	4×10^{-34}	Thermal-decomposition/ flow	Kaufman & Kelso [14]
298	Ar	4×10^{-34}		
298	O_2	6.5×10^{-34}		
298	N_2	5.6×10^{-34}		
298	CO_2	15×10^{-34}		
298	N_2O	15×10^{-34}		
298	CF_4	16×10^{-34}		
298	SF_6	34×10^{-34}		
298	H_2O	60×10^{-34}		
298	O_2	6.4×10^{-34}	Flash-photolysis/ chemiluminescence	Stuhl & Niki [15]
298	N_2	5.4×10^{-34}		
298	CO	6.7×10^{-34}		
298	He	4.6×10^{-34}	Flash-photolysis/ absorption	Donovan, Husain, & Kirsch [16]
298	Ar	5.0×10^{-34}		
298	Kr	4.9×10^{-34}		
298	N_2	8×10^{-34}	Photolysis relative to $O + NO_2$	Hippler & Troe [17]
298	Ar	4.4×10^{-34}	Flash-photolysis/ resonance-fluorescence	Slanger & Black [18]
298	N_2	7.0×10^{-34}		
298	O_2	1.24×10^{-34}	Discharge flow	Francis [19]
298	Ar	2.28×10^{-34}	Pulse radiolysis	Sauer & Dorfman [20]
298	Ar	2.48×10^{-34}	Pulse radiolysis	Sauer [21]
298	CO_2	11.5×10^{-34}		
298	N_2O	9.6×10^{-34}		
298	He	1.92×10^{-34}		
	O_3	$4.63 \times 10^{-35} \exp(2100/RT)$	K_{eq} (review)	Johnston [22]
	Ar	$1.16 \times 10^{-35} \exp(2100/RT)$		
	O_2	$8.14 \times 10^{-35} \exp(890/RT)$	K_{eq} (review)	Benson & Axworthy [23]

the observed difference in the exponential factors.

In the present work, the rate constant for the reaction of atomic oxygen with molecular oxygen as a function of temperature has been determined in a static system free of the possible uncertainties associated with wall reactions. Rate constants have been measured at temperatures and pressures corresponding to stratospheric conditions. The reported rate measurements indicate that the rate of production of stratospheric ozone could be nearly a factor of 2 lower than that estimated from previously reported values of the third-order rate constant. This could be of considerable importance in estimating the magnitude of possible ozone-destruction mechanisms necessary to explain the observed ozone profiles.

$$O(^3P) + NO_2 \rightarrow NO + O_2$$

The rate constant for reaction (2), $O + NO_2 \rightarrow NO + O_2$, was measured over the temperature range of 230 to 339K. The results of these measurements have been plotted in Arrhenius form in Figure 7. A least-squares fit of all of the data to the Arrhenius equation gives the expression $k_2 = 8.70 \pm 0.65 \times 10^{-12} \exp[(26 \pm 41)/RT]$ $cm^3 molec^{-1} s^{-1}$. The error limits in this expression are the standard errors from the least-squares treatment of the data. The uncertainties calculated from a consideration of the lines with the maximum and minimum slopes which could be drawn through the attached error bars ($\approx \pm 4\%$) are $\pm 2.5 \times 10^{-12}$ $cm^3 molec^{-1} s^{-1}$ in the pre-exponential factor and ± 150 cal mol^{-1} in the activation energy.

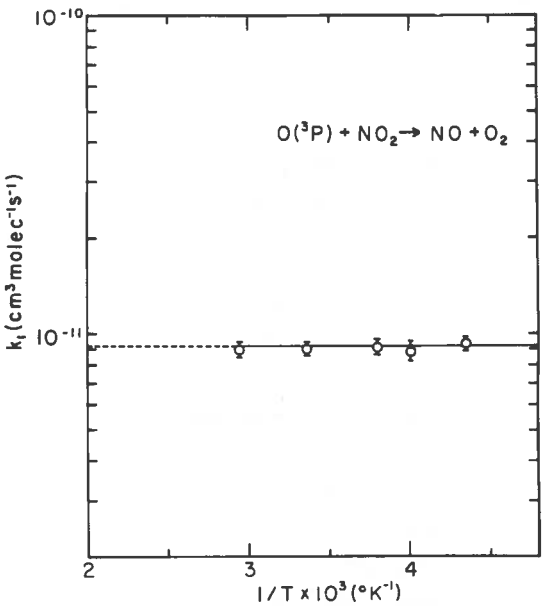

Figure 7. An Arrhenius plot of the rate data for the reaction $O(^3P) + NO_2 \rightarrow O_2 + NO$.

As is evident from the Arrhenius expression, the rate constant is, within the experimental uncertainty, independent of temperature. A simple average of all of the data from the tables gives, as a temperature-independent rate constant,

$$k_2 = 9.12 \pm 0.46 \times 10^{-2} \text{ cm}^3\text{molec}^{-1}\text{s}^{-1},$$

where the stated uncertainty is now the standard deviation of the data points from the mean. This value is within the standard error of the Arrhenius experssion over the entire temperature range.

At 298 and 339K, the kinetic data reported were measured using the glass reaction cell. The kinetic data taken using the brass cell at these temperatures were unreliable due to NO_2 decomposition. Since decomposition was not important at the lower temperatures (below 298K), data obtained with both the brass and the glass reaction cells were used. Identical answers, within experimental error, were obtained using the two cells at these temperatures. In these experiments the total pressure was limited to 5 torr to prevent a significant contribution to the measured rate from the fast third-order combination reaction between O and NO_2. Recent results from our laboratory indicate that the third-order reaction would not have influenced the measurement of the bimolecular rate constant by more than 2% at the operating pressure of 5 torr.

At several temperatures, both LiF and sapphire were used as flash lamp windows. Within the experimental error of the measurements, no effect on the rate constant was observed. As discussed before, this would indicate that the production of $O(^1S)$ was not complicating the reported rate measurements. In most of the rate measurements of reaction (2), Ar was used as the diluent gas. At 298K, however, N_2, O_2, and CO_2 were also used. At several other temperatures, both N_2 and Ar were employed. Within the experimental scatter of the data, no dependence of the measured rate constant on the

nature of the diluent gas was observed, which indicated that only the simple bimolecular reaction (2) was being studied. In addition, the lack of dependence on the diluent gas shows that the system was not complicated by secondary reactions involving $O_2(^1\Sigma_g)$, produced by the quenching of $O(^1D)$. This point was discussed in detail for the reaction system $O + O_2 + M \rightarrow O_3 + M$. Reactions of hot atoms formed in the primary photolytic process can also be discounted in this work, since the number of collisions with the diluent gas was over 1000 times greater than that with the reactant NO_2. Under these conditions, temperature equilibration of the O atoms would be insured.

As in the $O + O_2$ system, the flash intensity (and therefore the atom concentration) was varied by a factor of five at both 298K and 230K, to determine whether other possible secondary reactions were complicating the kinetic measurements. In addition, the NO_2 concentration was varied by a factor of four at 230K, and by a factor of six at 298K. The experimental results from each of those variations showed no change in the measured rate constant outside of the experimental error. These measurements indicate, therefore, that secondary reactions involving other reactive species produced by the flash, or products from the primary reaction, were of negligible importance in this study.

A comparison of the present results with those of previous studies is given in Table 2. It can be seen that only two previous temperature-dependence studies have been reported in the literature. As with the $O + O_2$ system, both of these previous studies were carried out in flow-discharge tubes. In the study by Klein and Herron [24], atomic oxygen was generated either by a discharge in a few percent O_2 in Ar or by means of the reaction $N + NO \rightarrow N_2 + O$. Atomic oxygen was detected by a mass spectrometer. At 298K the rate constant reported by Klein and Herron was about half the value measured in this work. The activation energy reported by these authors for reaction (2) was 1060 cal mol^{-1}, with the scatter in their data being about ±20%. Although it is not completely clear why the discharge-flow/mass-spectrometry results are lower than those reported in this work, the large decrease in the bimolecular rate constant observed by Klein and Herron at temperatures below 260K suggests that one or more side reactions were complicating the kinetic analysis. If similar processes were also significant at 298K, it might explain the lower values of the rate constant obtained by these authors.

Table 2. Summary of Reported Rate Measurements on the Reaction $O(^3P) + NO_2 \rightarrow NO + O_2$

T (K)	k ($cm^3 molec^{-1} s^{-1}$)	Reference
230-339	9.12×10^{-12} (temperature-independent)	This work
300	1.0×10^{-11}	Ford & Endow [25]
298	1.4×10^{-11}	Schuck, Stephens & Schrock [26]
298	3×10^{-11}	Nutt & Biddlestone [27]
298	2.5×10^{-12}	Phillips & Schiff [28]
278-375	3.24×10^{-11} exp (-1060/RT)	Klein & Herron [24]
298	5.41×10^{-12}	
297-543	1.7×10^{-11} exp (-580/RT)	Westenberg & deHaas [29]
298	6.26×10^{-12}	
298	8.3×10^{-12}	Clyne & Cruse [30]
298	5.6×10^{-12}	Smith [31]
410	8.1×10^{-12}	Smith [31]
298	4.4×10^{-12}	Stuhl & Niki [32]
280-550	1.7×10^{-11} exp (-600/RT)	Baulch, Drysdale & Horne (evaluation) [33]

Westenberg and de Haas [29] measured the temperature dependence of the rate constant for reaction (2), likewise using a discharge-flow system; however, atom detection in this case was made via esr measurements. They combined their data with those of Klein and Herron to obtain the following Arrhenius parameters: $A = 1.7 \times 10^{-11}$ $cm^3 molec^{-1} s^{-1}$ and $E = 580$ cal mol^{-1}. Their data showed little apparent temperature dependence, therefore, and gave an average value of $k_2 = 8.1 \times 10^{-12}$ $cm^3 molec^{-1} s^{-1}$. This is within 15% of the present temperature-independent rate constant.

In our study, the rate constant for reaction (2) was found to be a factor of two higher at stratospheric temperatures than the value extrapolated from the previously recommended [33] rate expression for k_2 ($1.7 \times 10^{-11} \exp[-600$ cal $mol^{-1}]/RT$ $cm^3 molec^{-1} s^{-1}$). This means that the ratio k_1/k_2 is a factor of four lower than the value used in earlier modeling calculations. This new ratio for k_1/k_2 seems to indicate that the amount of nitrogen oxide necessary to explain the experimentally-observed stratospheric ozone profile might be as much as a factor of four lower than previous estimates.

$$O(^3P) + O_3 \rightarrow O_2 + O_2$$

The reaction of $O(^3P)$ with O_3 has been examined over a total pressure range of 30-300 torr, an ozone concentration range of 100-1400 mtorr, and a temperature range of 220-355K. At 298K, the measured value of k_3 was found to be 1.06×10^{-14} $cm^3 molec^{-1} s^{-1}$. At this temperature a change in the total pressure (Ar) of a factor of six had no effect on the observed rate. In addition, a change in diluent gases from Ar to N_2 showed no effect on the rate constant within the experimental error of the measurements (±7%). Over the indicated temperature range, a fit of the bimolecular rate constant to the Arrhenius equation gave the expression

$$k_3 = (2.0 \pm .8) \times 10^{-11} \exp[-4.52 \pm .15 \text{ kcal mol}^{-1}/RT] \text{ cm}^3\text{molec}^{-1}\text{s}^{-1}$$

(see Figure 8). The stated uncertainties are the standard errors of the least-squares fit to the data. It should be noted that in this study of reaction (3), the problems of electronically excited oxygen atoms and molecular oxygen have been avoided by photodecomposing O_3 above 5900Å. At and above this wavelength the photolysis produces only ground-state atomic oxygen and ground-state molecular oxygen.

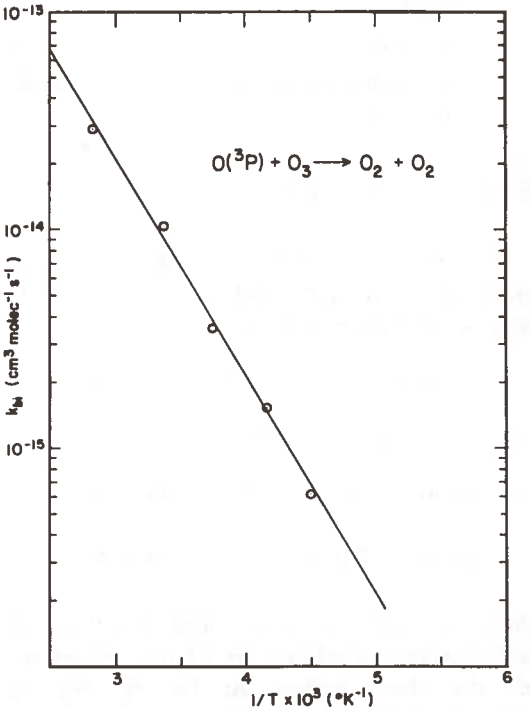

Figure 8. An Arrhenius plot of the rate data for the reaction $O(^3P) + O_3 \rightarrow 2O_2$.

A comparison of the data from this work with previous investigations of reaction (3) is given in Table 3. Only those studies which involved measurements of the temperature dependence of this reaction have been listed. It can be seen from this table that although the techniques employed in the study of reaction (3) have varied considerably, with the exception of the Arrhenius parameters given by Benson and Axworthy [23], the agreement between various studies on the value of k_3 at 298 and 220K is within about a factor of two. The agreement between the three most recent measurements of this reaction, Krezenski et al. [34], McCrumb and Kaufman [35], and this work, is within about 25% at both 298 and 220K. It appears, therefore, that the value of the rate constant for reaction (3) at stratospheric temperatures is now known to a reasonably high degree of accuracy.

Table 3. Reported Measurements of $O + O_3 \rightarrow O_2 + O_2$

Investigator	Temperature Range	Rate Expression ($cm^3 molec^{-1} s^{-1}$)
Benson and Axworthy [23]		5.6×10^{-11} exp (-5.7 kcal mol^{-1})/RT
Intezarova and Kondrat'ev [36]		$.48 \times 10^{-11}$ exp (-3.7 kcal mol^{-1})/RT
Johnston [22]		2×10^{-11} exp (-4.79 kcal mol^{-1})/RT
Schiff [37]		3.2×10^{-11} exp (-4.5 kcal mol^{-1})/RT
Krezenski et al. [34]	197-299K	1.2×10^{-11} exp (-4.3 kcal mol^{-1})/RT
McCrumb and Kaufman [35]	369-409K	1.1×10^{-11} exp (-4.3 kcal mol^{-1})/RT
This work	220-355K	2.0×10^{-11} exp (-4.5 kcal mol^{-1})/RT

$$H + O_2 + M \rightarrow HO_2 + M$$

At room temperature (298K), the third-order rate constants for the reaction $H + O_2 + M$ were found to be as follows:

$(1.95 \pm 0.28) \times 10^{-32}$ M = Ar

$(1.88 \pm 0.16) \times 10^{-32}$ M = He

$(5.90 \pm 1.18) \times 10^{-32}$ $M = H_2$

$(5.46 \pm 1.70) \times 10^{-32}$ $M = N_2$

Units are cm^6 $molec^{-2} s^{-1}$. The above set of rate constants establishes the relative efficiencies of the third bodies Ar : He : H_2 : N_2 as 1.0 : .97 : 3.02 : 2.8.

Due to the high quenching efficiency of the Lyman-α fluorescence signal by both N_2 and H_2, most of the temperature-dependence experiments were carried out using Ar as the third-body gas. Using the latter diluent gas, a temperature range of 220 to 360K was covered. At most temperatures at which measurements were taken, the total pressure was varied by nearly a factor of ten. An Arrhenius plot showing the temperature dependence of the third-order rate constant for k_{Ar} is shown in Figure 9. The data presented in this figure could be fitted to a simple straight line, and resulted in the expression:

$$k_{Ar} = (6.75 \pm 1.1) \times 10^{-33} \exp[(685 \pm 128)/RT] \ cm^6 molec^{-2} s^{-1}.$$

The error limits in the above expression were determined from consideration of the maximum and minimum slopes that could be drawn through the error bars on each third-order k value.

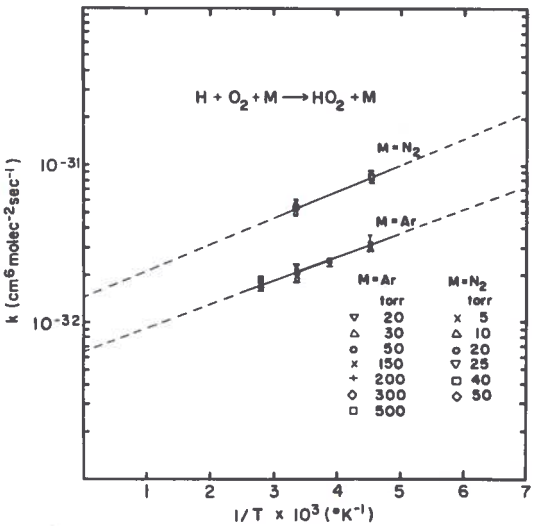

Figure 9. An Arrhenius plot of the rate data for the reaction $H + O_2 + M \rightarrow HO_2 + M$.

Due to the importance of the stratospheric reaction $H + O_2 + N_2 \rightarrow HO_2 + N_2$, the third-order reaction with $M = N_2$ was also investigated at 220K, and at total pressures of 10, 25, and 50 torr. The rate constant at this temperature was determined to be $(8.60 \pm .71) \times 10^{-32}$ cm^6 $molec^{-2} s^{-1}$, thus giving the relative efficiencies for M = Ar and $M = N_2$ as 1 : 2.7 at 220K.

As in previous studies involving the reactions of atomic oxygen, to test for the possible importance of secondary reactions in the study of $H + O_2 + M$, the flash lamp intensity was varied by a factor of 8 at 298, 360, and 220K. In each case, the rate constant was found to be invariant to changes in the light intensity within the experimental error of the measurements (±5%).

A comparison of the value of k_4 measured in this work with previous measurements is shown in Table 4. The only low-temperature study on this reaction previously reported was that of Clyne and Thrush [38]. They used a flow-discharge system with detection of H atoms by HNO emission. Over the temperature range of 250-800K, they derived an Arrhenius expression of the form $k_{Ar} = 1.3 \times 10^{-33}$ exp (1600/RT) cm^3 $molec^{-2}s^{-1}$. The value of k_4 recommended by Baulch et al. [39] was $k_{Ar} = 4.4 \times 10^{-33}$ exp [(1000 ± 1000)/RT] over the temperature range 300-2000K. Concurrent with the measurements made in this laboratory, Kurylo [40] of the National Bureau of Standards also investigated reaction (4) using the resonance-fluorescence technique and obtained the rate expression $k_{He} = (6.66 \pm 1.2) \times 10^{-33}$ exp [(473 ± 92)/RT] cm^6 $molec^{-2}s^{-1}$ over the temperature range 203-404K. He found the relative efficiencies for He, Ar, and N_2 to be 1.0 : 1.0 : 4.1. Thus, the two resonance-fluorescence studies on this reaction are in reasonably good agreement; they lead to a value of the rate constant for reaction (4) at stratospheric temperatures (around 230K) which is a factor of 2-3 times greater than the K values previously quoted in modeling calculations.

$HO_2 + CO \rightarrow CO_2 + OH$

The results of the experiments on reaction (5) are shown in Table 5. It is evident here that even for pressures of CO as high as 150 torr no significant amount of labeled $CO_2{}^{16,18}$ was formed. (The small but constant production of $CO_2{}^{16,18}$ in these experiments is believed to arise from the photolysis of $H_2O_2{}^{18,18}$, reaction (9).) It should also be mentioned that blank experiments, with H_2O absent from the photolysis mixture, indicated that production of CO_2 from mechanisms involving reactive species other than OH and HO_2 was always less than 2% of the total CO_2 product.

Figure 10 shows the results of a plot of $R_{CO_2{}^{16,18}}/(R_{CO_2{}^{16,16}})^{1/2}$ vs. [CO], the slope of which should be equal to $2k_5'/(k_8)^{1/2}$. The solid line here represents a least-squares fit of the four data points. It is apparent from this plot that the best fit to the data is a slope ≈ 0, thus indicating a vanishingly small rate constant for reaction (5). In an effort to obtain an upper limit for the value of the rate constant for reaction (5), error limits of ±30% were placed on each of the data points in Figure 10 and the maximum possible slope was then drawn through these error limits. Using the preferred value of k_8 [9,10] of 3.3×10^{-2} $cm^3molec^{-1}s^{-1}$, a maximum value of 1.5×10^{-20} $cm^3molec^{-1}s^{-1}$ was calculated for k_5. If it is assumed that chain termination occurs not via reaction (8) but rather via a process such as diffusion of HO_2 to the walls, the upper limit for the rate constant for reaction (5) is found to be $\approx 10^{-19}$ cm^3 $molec^{-1}s^{-1}$. On the other hand, if the principal loss mechanism for HO_2 is due to reaction with impurities, the upper limit for k_5 is $\approx 1 \times 10^{-18}$ $cm^3molec^{-1}s^{-1}$. In the latter case, the impurity level was placed at .1% [CO] and a rate constant of 10^{-13} $cm^3molec^{-1}s^{-1}$ was selected for reaction of HO_2 with this impurity. However, since hydrogen peroxide was observed to be a major product in related mass spectrometry studies, both of the above possibilities can probably be discounted.

The extremely low value of k_5 of $\approx 10^{-20}$ $cm^3molec^{-1}s^{-1}$ is to be compared with the value recently reported by Westenberg and de Haas [45] of $\approx 10^{-12}$ $cm^3molec^{-1}s^{-1}$. Because of the enormous disagreement in these values of k_5, careful consideration was given to possible sources of errors in each of the respective experimental systems. One such possibility would be the absence, or extremely low concentration, of HO_2 in this work as compared with Westenberg's system.

To test this hypothesis, a new experiment was performed in which the HO_2 was formed from the reaction sequence (9) and (10). In this experiment, 1.5 torr of H_2O_2 was photolyzed at 1849Å in the presence of 500 mtorr of CO and 1 torr of O_2. In this case the oxygen was not labeled, and the reactivity of HO_2 toward CO was indicated by a comparison of the total experimental yield of CO_2 with the theoretical or calculated yield. In this experiment, the 1849Å intensity was 5×10^{15} photons/cm^2/s and the photolysis time 10 minutes. Using the known extinction coefficient for H_2O_2 at 1849Å (35 cm^{-1} atm^{-1}), it was calculated that if each OH radical generated one HO_2 (reaction (10)), and this in turn reacted with CO to produce one CO_2 molecule, the yield of CO_2 would have been ≈ 300 mtorr. What was observed, in fact, was 6

Table 4. A Summary of Rate Data on the Reaction $H + O_2 + M \rightarrow HO_2 + M$

T (°K)	M	k_M $cm^6 molec^{-2} s^{-1}$	Technique	Reference
298	He	1.88×10^{-32}	Flash-photolysis/ resonance-fluorescence	This study
298	H_2	5.90×10^{-32}		
298	CH_4	42.0×10^{-32}		
298	Ar	1.95×10^{-32}		
220	Ar	3.25×10^{-32}		
220-360	Ar	6.75×10^{-33} exp (685 ± 128/RT)		
298	N_2	5.46×10^{-32}		
220	N_2	8.60×10^{-32}		
293	Ar	2.2×10^{-32}	Flow-discharge with HNO emission detection	Clyne and Thrush [38]
244	Ar	4.0×10^{-32}		
225	Ar	3.5×10^{-32}		
293	He	2.1×10^{-32}		
293	H_2O	$52 (\pm 40\%) \times 10^{-32}$		
250-800	Ar	1.3×10^{-33} exp (1600 ± 700/RT)		
293	Ar	3.7×10^{-32}	Calorimetric/ discharge-flow	Larkin and Thrush [41]
293	He	6.0×10^{-32}	Diffusion cloud with mass spec. probe	Dodonov, Lavrovskaya, and Talroze [42]
298	H_2	4.7×10^{-32}	Pulse-radiolysis/ fast Lyman-α absorption spectrophometry	Bishop and Dorfman [43]
298	Ar	2.35×10^{-32}		
298	H_2	4.7×10^{-32}	Pulse-radiolysis/ fast Lyman-α absorption spectrophometry	Hikida, Eyre and Dorfman [44]
298	Ar	1.64×10^{-32}		
298	CH_4	24.6×10^{-32}	Flash-photolysis/ resonance-fluorescence	M.J. Kurylo (1972) [40]
298	Ar	1.57×10^{-32}		
213	He	1.93×10^{-32}		
298	He	1.57×10^{-32}		
357	He	1.25×10^{-32}		
203-404	He	6.66×10^{-33} exp (473 cal mol^{-1}/RT)		
298	N_2	5.33×10^{-32}		
226	N_2	8.7×10^{-32}		
300-2000	Ar	4.42×10^{-33} exp (1000 ± 1000 cal mol^{-1}/RT)	Recommended value from the review by Baulch, Drysdale and Lloyd [39]	
298	Ar	2.33×10^{-32}**		
220	Ar	4.28×10^{-32}**		

* Only rate measurements made in the vicinity of room temperature and below are reviewed in Table 4. The high-temperature work by several investigators has been reviewed by Baulch et al. [39].

** Calculated from the corresponding Arrhenius expression.

Table 5. Reaction of HO_2 with CO

CO (torr)	Relative CO_2 Yield* 16,16	16,18
1	100	6.3
10	100	6.8
40	100	6.2
150	100	6.4

Concentrations of reactants: H_2O = 20 torr, $O_2^{18,18}$ = 1 torr

Total pressure: 200 torr (Ar + CO)

Photolysis time: ≈ 14 min.

Intensity: ≈ 3×10^{14} photons $cm^{-2}s^{-1}$

Total yield of CO_2: 8-14 mtorr

Blank experiment yield of CO_2: ≈ .4 mtorr

* The reproducibility of these experiments was ±15%. The results presented are the averages from 25 experiments.

mtorr of CO_2 product. From a consideration of the rate constants for reaction (10) and OH + CO, and the relative concentrations of H_2O_2 vs. CO, it can be calculated that 4-8% of the initially formed OH should have reacted with CO to form CO_2. The 2% yield observed experimentally indicates that within the uncertainty of the measurements and calculations (±10%), HO_2 generated via reactions (9) and (10) shows no greater reactivity toward CO than that produced in the original set of experiments from process (4).

$$HO_2 + SO_2 \rightarrow SO_3 + OH \text{ and } HO_2 + NO \rightarrow NO_2 + OH$$

In an effort to further demonstrate that HO_2 was being formed in the experiments described above (reaction 5), two additional reactants besides CO were examined. Those selected were SO_2 and NO. In these two new systems, reactions (7′) or (6′) would be competing with the extremely slow process (5),

$$HO_2^{18,18} + NO^{16} \rightarrow NO_2^{16,18} + {}^{18}OH \qquad (7')$$

$$HO_2^{18,18} + SO_2^{16,16} \rightarrow SO_3^{16,16,18} + {}^{18}OH. \qquad (6')$$

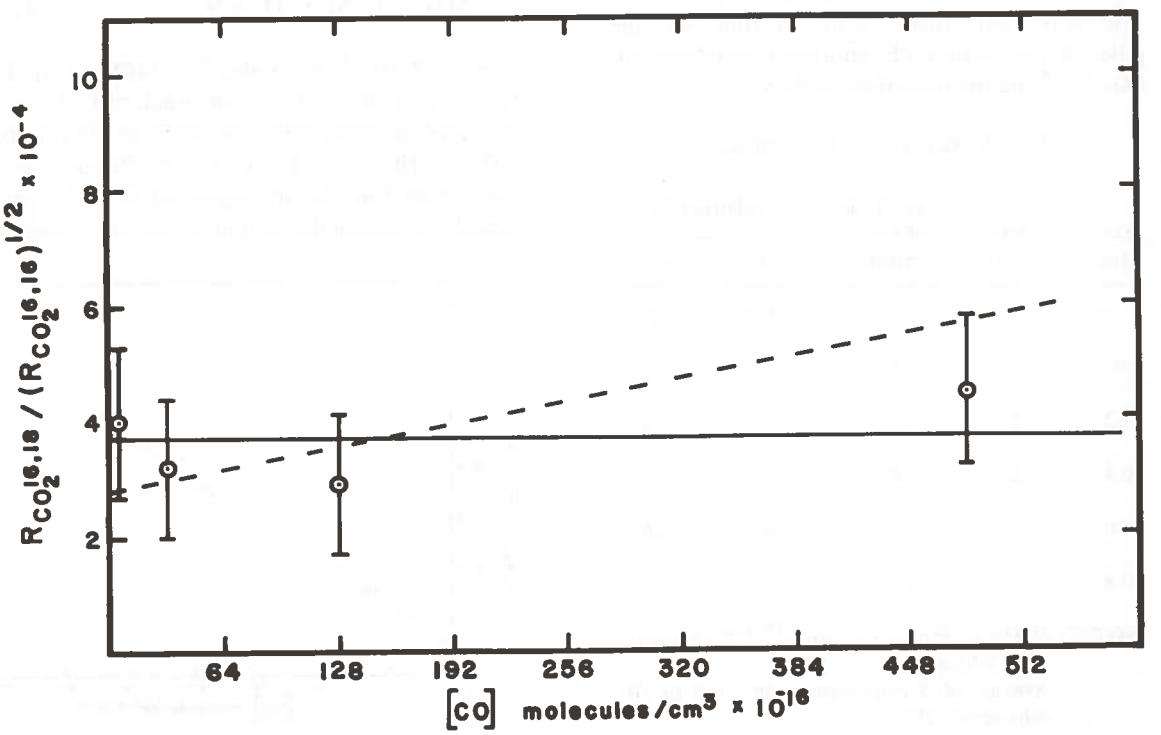

Figure 10. A plot of the ratio of $R_{CO_2}^{16,18}/(R_{CO_2}^{16,16})^{1/2}$ vs. concentration of CO. Slope = $2k_5'/(k_8)^{1/2}$.

Reaction (7′) or (6′) would then be followed by process (12′)

$$^{18}OH + CO \rightarrow CO_2{}^{16,18} + H, \qquad (12')$$

yielding an oxygen-18-labeled CO_2 molecule. Thus, a measure of the reactivity of SO_2 or NO toward HO_2 (versus that of process (8)) was once again made possible by measuring only the ratio $CO_2{}^{18,16}/CO_2{}^{16,16}$. In the experiments with added SO_2 the following conditions were maintained: $[H_2O] = 20$ torr, $[CO] = 1$ torr, $[O_2{}^{18,18}] = 1$ torr, $[N_2] = 20$ torr, $[SO_2] = .1 - .8$ torr and lamp intensity $\approx 5 \times 10^{15}$ photons $cm^{-2}s^{-1}$. The results of these experiments are given in Table 6. Unlike the system with only CO present as a reactant, the SO_2 experiments showed a definite trend of increased labeling with increasing $[SO_2]$. In the SO_2 system the ratio of $CO_2{}^{16,18}/CO_2{}^{16,16}$ reached a value of slightly greater than unity at pressures as low as 400 mtorr. In several control experiments on this system, it was shown that the dark reaction yielded < 1 mtorr CO_2. The photolysis of reaction mixtures in the absence of H_2O also resulted in < 2 mtorr of CO_2 product. The latter experiment tends to rule out the possible production of significant quantities of $CO_2{}^{16,18}$ via the photolysis of SO_2.

Table 6. Reaction of HO_2 with SO_2

SO_2 (torr)	Time (min)	Total Yield of CO_2 (mtorr)	Relative CO_2 Yield 16,16	16,18
0	a		100	17
0.1	1	41	100	32
0.2	2	68	100	42
0.4	2	42	100	122
0.6	3	141	100	166
0.8	3	102	100	170

NOTES: $H_2O = 20$ torr, $CO = 1$ torr, $^{18,18}O_2 = 1$ torr, $N_2 = 20$ torr
Average of 3 experiments, time = 2 to 10 min, error ±20%

Since reaction (6′) is clearly much faster than reaction (5) in the SO_2 system, the reaction sequence (11), (12), (4′), (6′) (12′) and (8) can be substituted for (11), (12), (4′), (5′), (12′) and (8) given earlier. From a steady-state treatment of this new sequence of reactions, the mathematical relationship

$$\frac{R_{CO_2}{}^{16,18}}{(R_{CO_2}{}^{16,16})^{1/2}} = \frac{k_{14}[SO_2]}{(k_8)^{1/2}} + K \qquad (II)$$

can be derived. Once again the units of $R_{CO_2}{}^{16,18}$ and $R_{CO_2}{}^{16,16}$ are molec $cm^{-3}s^{-1}$. As in the case of expression (I), a plot of the ratio $R_{CO_2}{}^{16,18}/(R_{CO_2}{}^{16,16})^{1/2}$ vs $[SO_2]$ gives a slope which is equal to the rate constant ratio $k_{6'}/(k_8)^{1/2}$. Figure 11 shows the results of this type of plot for the SO_2 system. Using the value of 3.3×10^{-12} $cm^3molec^{-1}s^{-1}$ for k_8, we calculate $k_{6'} = 3 \times 10^{16}$ $cm^3molec^{-1}s^{-1}$ (± factor of 2). The SO_2 results, therefore, tend to argue in favor of the presence of significant quantities of HO_2 in the previously-discussed CO system. From a comparison of the rate constant for reaction (6′) vs. the rate constant for the reaction

$$SO_2 + O + M \rightarrow SO_3 + M \qquad (15)$$

($k = 2.7 \times 10^{-33}$ $cm^6molec^{-2}s^{-1}$ [46]), it can be seen that at about 16-17 km reaction (6′) could be equal in importance to reaction (15) if the ratio of HO_2/O is 10 or greater. Reaction (6′) could therefore be an important reaction with regard to aerosol formation in the stratosphere.

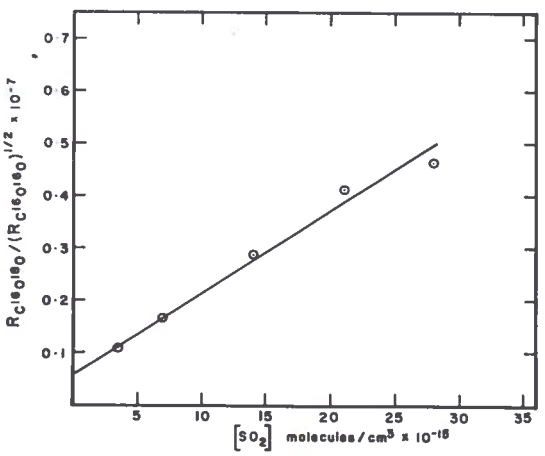

Figure 11. A plot of the ratio $R_{CO_2}{}^{16,18}/(R_{CO_2}{}^{16,16})1/2$ vs. concentration of SO_2. Slope = $k_{6'}/(k_8)^{1/2}$.

In the final set of experiments, varying amounts of NO were added to a gas mixture consisting of 20 torr of H_2O, 1 torr CO, 1 torr $O_2{}^{18,18}$, and 20 torr N_2. In the first experiment of this type, 50 mtorr of NO was added to the above gas mixture, with the result that the rate of production of CO_2 increased by about a factor of five. The ratio of labeled to unlabeled CO_2 was about 3 : 1. The absolute yield of $CO_2{}^{16,18}$ was nearly 400 mtorr, indicating not only that NO was reacting rapidly with HO_2 to form the product $NO_2{}^{16,18}$, but also that the NO_2 was being converted back to NO. (The most likely reaction to explain the latter observation is the reaction of NO_2 with atomic hydrogen.) In subsequent experiments the pressure of the NO was reduced to 1 mtorr, the photolysis time was reduced to about 30 sec, and the lamp intensity was reduced by nearly a factor of ten. Under these conditions the ratio of $CO_2{}^{16,18}/CO_2{}^{16,16}$ was still approximately 2 : 1. From a comparison of the ratio of $CO_2{}^{16,18}/CO_2{}^{16,16}$ for the NO system at 1 mtorr with the ratio of $CO_2{}^{16,18}/CO_2{}^{16,16}$ measured in the SO_2 system at higher pressures, it can be seen that the reaction of NO with HO_2 is probably 2×10^3 times faster than the HO_2-SO_2 reaction. This evaluation would place the rate constant for reaction (13) at 3×10^{-13} $cm^3 molec^{-1} s^{-1}$ (± factor of 3).

CONCLUSIONS

With the technique of flash-photolysis/resonance-fluorescence, a value of k_1 at stratospheric temperatures has been measured; it is a factor of two lower than previously suggested, whereas k_2 was found to be a factor of two higher. Since these key rate constants appear in modeling calculations as the ratio k_1/k_2, the value of this ratio will change by approximately a factor of four. Thus, the new ratio suggests that a smaller amount of nitrogen oxide is necessary to explain the experimentally observed stratospheric ozone profile, possibly less by a factor of four.

Studies completed on another of the Chapman reactions, reaction (3), have resulted in measured values of the rate constant which are in excellent agreement with those recently measured by other techniques [34,35]. It is believed, therefore, that this rate constant is now known with reasonably high accuracy.

The results from the investigation of reaction (4), both as reported here and as measured at NBS by Kurylo [40], indicate that this reaction is at least a factor of two to three times faster than previously assumed in modeling studies. The larger rate constant measured in both studies indicates that the dominant reaction of H atoms in the mid- and lower stratosphere is reaction (4).

The kinetic studies completed on the reactions of HO_2 at 300°K have shown that the reaction of thermalized HO_2 with CO is not significant in the conversion of CO to CO_2. In the lower stratosphere the reactions of HO_2 with SO_2 could be one of the major reactions responsible for conversion of SO_2 to SO_3. The SO_3 is expected to subsequently react with water vapor to form H_2SO_4, and then, still later, to form sulfate particulates [47]. The reaction of HO_2 with NO at low pressures to form NO_2 plus OH is quite fast. This appears to be the single most important reaction of HO_2 in the mid- and lower stratosphere.

ACKNOWLEDGMENT

The authors acknowledge the support of the Climatic Impact Assessment Program, Office of the Secretary, Department of Transportation, in this research.

REFERENCES

1. W. Braun and M. Lenzi, Discussions Faraday Soc. *44*, 252 (1967).

2. D.D. Davis, W. Braun, and A.M. Bass, "Reactions of Cl ($^2P_{3/2}$): absolute rate constants for the reaction with H_2, CH_4, C_2H_6, CH_2Cl_2, C_2Cl_4, and c-C_6H_{12}," Intern. J. Chem. Kinetics *2*, 101 (1970).

3. R.E. Huie, J.T. Herron, and D.D. Davis, "Absolute rate constants for the reaction of atomic oxygen with l-butene over the temperature range of 259-493°K," J. Phys. Chem. *75*, 3902 (1971).

4. R.E. Huie, J.T. Herron, and D.D. Davis, "Absolute rate constants for the addition and abstraction reactions of atomic oxygen with l-butene over the temperature range 190-491°K," J. Phys. Chem. *76*, 2653 (1972).

5. D.D. Davis, R.E. Huie, J.T. Herron, M.J. Kurylo, and W. Braun, "Absolute rate constants for the reaction of atomic oxygen with ethylene over the temperature range 232-500°K," J. Chem. Phys. *56*, 4868 (1972).

6. D.D. Davis, R.E. Huie, and J.T. Herron, "Absolute rate constants for the reaction $O(^3P) + NO_2 \rightarrow NO + O_2$ over the temperature range 230-339K," J. Chem. Phys. *58*, No. 2, 530 (1973).

7. D.D. Davis, M. Pilling, and R. Klemm, "A flash photolysis resonance fluorescence kinetics study of ground state sulfur atoms: I. absolute rate parameters for reaction of $S(^3P)$ with $O_2(^3\Sigma)$," Intern. J. Chem. Kinetics *IV*, 367 (1972).

8. D.D. Davis and W. Braun, "Intense vacuum ultraviolet atomic line sources," Appl. Opt. *7*, 2071 (1968).

9. A.C. Lloyd, "Evaluated and estimated kinetic data for the gas phase reactions of the hydroperoxyl radical," NBS Report 10447 (1971).

10. D.L. Baulch, D.D. Drysdale, and D.G. Horne, *Evaluated Kinetic Data for High Temperature Reactions:* Vol. 1, "Homogeneous Gas Phase Reactions of the H_2-O_2 System," Butterworth & Co. (1972).

11. M.A.A. Clyne, D.J. McKenney, and B.A. Thrush, "Rate of combination of oxygen atoms with oxygen molecules," Trans. Faraday Soc. *61*, 2701 (1965).

12. M.F.R. Mulcahy and D.J. Williams, "Kinetics of combination of oxygen atoms with oxygen molecules," Trans. Faraday Soc. *64*, 59 (1968).

13. G.M. Meaburn, D. Perner, J. LeCalve, and M. Bourene, "A pulsed radiolysis study of atomic oxygen reactions in the gas phase," J. Phys. Chem. *72*, 3920 (1968).

14. F. Kaufman and J.R. Kelso, "M effect in the gas-phase recombination of O with O_2," J. Chem. Phys. *46*, 4541 (1967).

15. F. Stuhl and H. Niki, "Measurements of rate constants for molecular reactions of $O(^3P)$ with NO, O_2, CO, N_2, and CO_2 using a pulsed vacuum-UV-photolysis-chemiluminescent method," J. Chem. Phys. *55*, 3943 (1971).

16. R.J. Donovan, D. Husain, and L.J. Kirsch, "Reactions of atomic oxygen," Trans. Faraday Soc. *66*, 2551 (1970).

17. H. Hippler and J. Troe, "High pressure recombination $O + O_2 \rightarrow O_3$," Ber. Bunsenges. Physik. Chem. *75*, 27 (1971).

18. T.G. Slanger and G. Black, "Reaction rate measurements of O^3P atoms by resonance fluorescence: I. $O(^3P) + O_2 + M \rightarrow O_3 + M$ and $O(^3P) + NO + M \rightarrow NO_2 + M$," J. Chem. Phys. *53*, 3717 (1970).

19. P.D. Francis, Brit. J. Appl. Phys., 1717 (1969).

20. M.C. Sauer and L.M. Dorfman, "Pulse radiolysis of gaseous argon-oxygen solutions. Rate constant for the ozone formation reaction," J. Amer. Chem. Soc. *87*, 3801 (1965).

21. M.C. Sauer, "A pulse-radiolysis study of the dependence of the reaction of atomic oxygen with oxygen on the nature of the third body," J. Phys. Chem. *71*, 3311 (1967).

22. H.S. Johnston, "Gas Phase Reaction Kinetics of Neutral Oxygen Species," USNBS Stand. Ref. Data Ser., NBS-NSRDS-20, (1968).

23. S.W. Benson and A.E. Axworthy, "Reconsideration of the rate constants from the thermal decomposition of ozone," J. Chem. Phys. *26*, 1718 (1957); *42*, 2614 (1965).

24. F.S. Klein and J.T. Herron, "Mass spectrometric study of the reactions of O atoms with NO and NO_2," J. Chem. Phys. *41*, 1285 (1964).

25. H.W. Ford and N. Endow, "Rate constants at low concentrations. III. Atomic oxygen reactions in the photolysis of nitrogen dioxide at 3660A," J. Chem. Phys. *27*, 1156 (1957).

26. E.A. Schuck, E.R. Stephens, and R.R. Schrock, J. Air Pollution Control Assoc. *16*, 695 (1966).

27. C.W. Nutt and A.J. Biddlestone, "Reaction of atomic oxygen with nitrogen dioxide," Trans. Faraday Soc. *58*, 1376 (1962).

28. L.F. Phillips and H.I. Schiff, "Mass spectrometric studies of atom reactions. I. Reactions in the atomic nitrogen-ozone system," J. Chem. Phys. *36*, 1509 (1962).

29. A.A. Westenberg and N. deHaas, "Atom-molecule kinetics using ESR detection. V. Results for O + OCS, O + CS_2, O + NO_2, and H + C_2H_4," J. Chem. Phys. *50*, 707 (1969).

30. M.A.A. Clyne and H.W. Cruse, "Studies of ground-state $^2P_{3/2}$ halogen atoms using atomic resonance absorption," Trans. Faraday Soc. *67*, 2869 (1971).

31. I.W.M. Smith, "Rate parameters for reactions of $O(^3P)$ with CS_2, NO_2 and olefins," Trans. Faraday Soc. *64*, 378 (1968).

32. F. Stuhl and H. Niki, "Detection of O^3P atoms in pulsed vacuum UV photolysis of NO and its application to O atom reactions," Chem. Phys. Letters *7*, 197 (1970).

33. D.L. Baulch, D.D. Drysdale, and D.G. Horne, *High Temperature Reaction Rate Data*, No. 5, University of Leeds (1970).

34. D.C. Krezenski, R. Simonaitis, and J. Heicklen, "The reactions of $O(^3P)$ with ozone and carbonyl sulfide," Intl. J. Chem. Kinetics *3*, 467 (1971).

35. J.L. McCrumb and F. Kaufman, "Kinetics of the O + O_3 reaction," J. Chem. Phys. *57*, 1270 (1972).

36. E.I. Intezarova and V.N. Kondrat'ev, "Thermal dissociation of ozone," Izv. Akad. Nauk SSR, Sev. Khim. *11*, 2440 (1967).

37. H.I. Schiff, "Neutral reactions involving oxygen and nitrogen," Can. J. Chem. *47*, 1903 (1969).

38. M.A.A. Clyne and B.A. Thrush, "Rates of elementary processes in the chain reaction between hydrogen and oxygen. II. Kinetics of the reaction of hydrogen atoms with molecular oxygen," Proc. Roy. Soc. *A275*, 559 (1963).

39. D.L. Baulch, D.D. Drysdale, and A.C. Lloyd, *High Temperature Reaction Rate Data*, No. 3, University of Leeds (1969).

40. M. Kurylo, National Bureau of Standards, private communication.

41. F.S. Larkin and B.A. Thrush, "Recombination of hydrogen atoms in the presence of atmospheric gases," Disc. Faraday Soc. *37*, 112 (1964).

42. A.F. Dodonov, G.K. Lavrovskaya, and V.L. Talroze, "Mass spectrometric measurements of elementary reaction rate constants. V. Reactions of hydrogen atoms with oxygen and helium," Kinetika i Kataliz *10*, 701 (1969).

43. W.P. Bishop and L.M. Dorfman, "Pulse-radiation studies. VI. Kinetics of the reaction of gaseous hydrogen atoms with molecular oxygen by fast Lyman α absorption spectrophotometry," J. Chem. Phys. *52*, 3210 (1970).

44. T. Hikida, J.A. Eyre, and L.M. Dorfman, "Pulse radiation studies. XX. Kinetics of some addition reactions of gaseous hydrogen atoms by fast Lyman α absorption spectrophotometry," J. Chem. Phys. *54*, 3422 (1971).

45. A.A. Westenberg and N. deHaas, "Steady-state intermediate concentrations and rate constants. Some HO_2 results," J. Phys. Chem. *76*, 1586 (1972).

46. M.F.R. Mulcahy, J.R. Stevens, and J.C. Ward, "The kinetics of reaction between oxygen atoms and sulfur dioxide: An investigation by electromagnetic resonance spectrometry," J. Phys. Chem. *71*, 2124 (1967).

47. J.P. Friend, New York University, private communication.

Because of the particular applicability of some very recent work done at the Stanford Research Institute, the following unscheduled paper was presented.

INVESTIGATION OF THE RATE COEFFICIENT FOR $O(^3P) + NO_2 \rightarrow NO + O_2$

TOM G. SLANGER, BERNARD J. WOOD, AND GRAHAM BLACK
Standford Research Institute
Menlo Park, California

The most recent measurements of the rate coefficient of the aeronomically important reaction $O(^3P) + NO_2 \rightarrow NO + O_2$ have been made by Davis, Herron, and Huie [1]. They obtained a value of 9.12×10^{-12} cm^3 $molec^{-1}$ sec^{-1}, which was temperature-independent in the range 230-339°K. At the low-temperature end, this value is about a factor of two higher than that given in current rate coefficient evaluations [2] and, if correct, has an important effect on atmospheric modeling at proposed SST altitudes.

The measurements of Davis et al. [1] were carried out in a system utilizing pulsed O_2 photodissociation and resonance fluorescence detection of $O(^3P)$ atoms. In our laboratory, we have a similar apparatus, and we have repeated their measurements, but in a somewhat different manner. We have photolyzed a mixture of O_2 and NO in a flow system by repetitive pulses of 1470 Å radiation, detecting $O(^3P)$ by its chemiluminescent reaction with NO. From the signal decay time, the $O(^3P)$ loss rate is established, and then, as NO_2 is added, the change in decay time directly gives the rate coefficient for the $O(^3P)$-NO_2 reaction. This system is almost identical to the one described by Stuhl and Niki [3], with which they determined a 300°K rate coefficient of 4.4×10^{-12} cm^3 $molec^{-1}$ sec^{-1}. The principal differences lie in the fact that we employed a premixed flowing NO_2 stream, that our source of $O(^3P)$ was O_2 – not NO – photodissociation, and that our system was Pyrex instead of stainless steel.

It is our belief that the variations in the room temperature rate coefficients determined in the 15 or so investigations of this reaction have two causes: the effect of the NO_2-N_2O_4 equilibrium, and wall reactions of NO_2. We felt that it was important to have the storage pressure of NO_2 low enough that the amount of N_2O_4 present was negligible, and also that a flow system be utilized to avoid significant wall losses of NO_2. Therefore, a tank of 0.2% NO_2 in nitrogen was used as the source; prior to delivery into the system, its precise concentration was determined by measuring its absorption of the 4358-Å Hg line, using cross-calibration against an accurately-known standard, and application of the equilibrium constant. An NO_2 absorption cross-section of 15.8 cm^{-1} atm^{-1} at 4358Å was measured. For the 1-atm storage pressure (1.5 torr NO_2) the equilibrium constant shows that NO_2 dimerization is 3.3% at 296°K. At the maximum reactor pressure of 2 mtorr, dimerization is less than 1% at 240°K.

Our measurements were carried out at two temperatures, 296°K and 240°K. Three runs were made at the higher temperature and two at the lower. Because of the relatively low intensity of the dissociating lamp, the $[NO_2] / [O(^3P)]$ ratio was always greater than 10^3, so pseudo-first-order kinetics are expected. Two typical plots of $O(^3P)$ decay time vs. $[NO_2]$ are shown in Figure 1, the slopes of which give the rate coefficient. The lines are practically parallel, with the 240°K line being slightly more steep. For the five runs, the 296°K average is 9.2×10^{-12} cm^3 $molec^{-1}$ sec^{-1}, whereas the 240°K average is 10.5×10^{-12} cm^3 $molec^{-1}$ sec^{-1}. We estimate that random and systematic errors set limits of ±15% on our data.

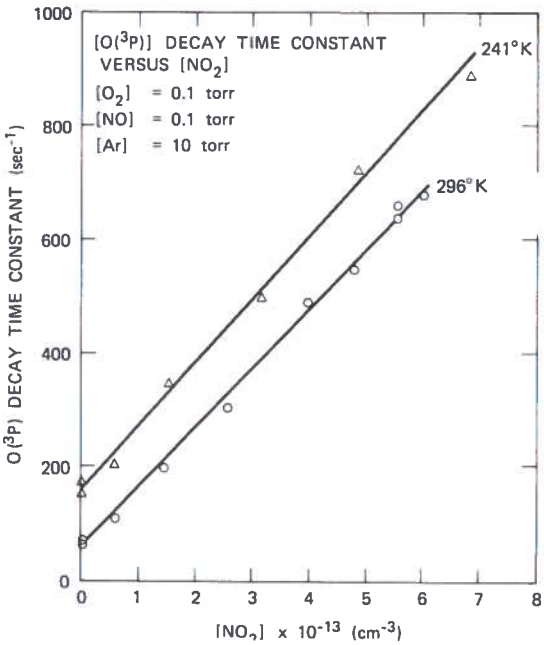

Figure 1. $[O(^3P)]$ decay time constant versus $[NO_2]$.

In Figure 2 are shown data of various investigators [1,2]. As may be seen, the line given by Davis et al.[1] actually extrapolates to fit all data above about 400°K, whereas our two points are in excellent agreement with theirs at room temperature and below. We believe it very likely that a number of earlier investigations have suffered from the problems mentioned above, both of which would tend to give low rate coefficients (assuming N_2O_4 to be less reactive to O (^{3}P) than NO_2).

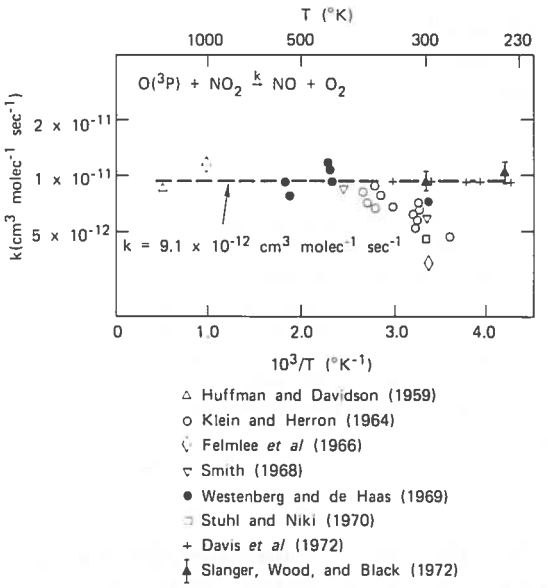

Figure 2. Arrhenius plot for the second-order reaction of O (^{3}P) with NO_2.

Our work is obviously less extensive than the measurements of Davis et al., and was undertaken principally to determine whether their results could be reproduced by another method, particularly one that had previously given lower rate coefficients. We are satisfied with the agreement between our data and theirs, and recommend that their values be used over the temperature range they investigated; however, their rate coefficient may also be valid out to 2000°K.

ACKNOWLEDGMENT

This work was supported by the Army Research Office, Durham, North Carolina, under Contract DAHC04-70-C-0034.

REFERENCES

1. D.D. Davis, J.T. Herron, and R.F. Huie. "Absolute rate constants for the reaction O (^{3}P) + NO_2 → NO + O_2 over the temperature range 230-339°K," J. Phys. Chem. (to be published).

2. D.L. Baulch, D.D. Drysdale, and D.G. Horne, "Critical evaluation of rate data for homogeneous, gas phase reactions of interest in high temperature systems," *High Temperature Reaction Rate Data*, No. 5, University of Leeds, England (July 1970).

3. F. Stuhl and H. Niki, "Detection of oxygen (^{3}P) atoms in pulsed vacuum UV photolysis of NO and its application to O atom reactions," Chem. Phys. Letters 7, 197 (1970).

DISCUSSION

NICOLET: Are you aware of the recent measurements by Clyne and Cruse at Cambridge?

SLANGER: The 300°K measurement reported by Clyne last year was 8.3 × 10^{-12} cm^3 $molec^{-1}$ sec^{-1}, which we consider quite acceptable. This year, he has reported a value of 6.1 × 10^{-12} cm^3 $molec^{-1}$ sec^{-1}, which he believes to be more accurate. My only comment is that we think that a system in which O(^{3}P) atoms are generated and are observed to disappear in situ gives kinetic data somewhat more directly than a discharge flow system, in which wall effects, which may vary as a function of NO_2, are important.

INSTRUMENTATION FOR NO MEASUREMENT IN THE STRATOSPHERE

B.A. RIDLEY, K.H. WELGE, AND H.I. SCHIFF
Centre for Research in Experimental Space Science
York University
Downsview, Ontario, Canada
and
L.R. MEGILL AND A.W. SHAW
Center for Research in Aeronomy
Utah State University
Logan, Utah

ABSTRACT: A chemiluminescence instrument has been developed for making in-situ measurements of NO in the stratosphere from either balloon or aircraft platforms. Optimization of its performance depends on addition of sufficient O_3 to the flow tube to ensure nearly complete consumption of NO, and on operation at as high a total gas-flow rate and temperature as practical. Provision is made for on-board calibration. Signal intensity was found to increase linearly with NO mixing ratio in the air sample and sensitivity was found to increase linearly with total sample flow rate. Laboratory simulation experiments showed a detection limit of at least 0.03 ppb at stratospheric pressures. Applications of the instrument include both balloon- and aircraft-borne experiments. Both configurations are designed for completely automatic operation.

PRINCIPLE OF THE METHOD

Our method of measuring NO is based on the chemiluminescence produced when ozone is mixed with nitric oxide. The important reactions which occur in the system are:

$$NO + O_3 \rightarrow NO_2^* + O_2$$
$$k_1 = 1.3 \times 10^{-12} \exp(-2.1 \times 1000/T)$$

$$NO + O_3 \rightarrow NO_2 + O_2$$
$$k_2 = 7 \times 10^{-13} \exp(-1.2 \times 1000/T)$$

$$NO_2^* \rightarrow NO_2 + h\nu \qquad k_3$$

$$NO_2^* + M \rightarrow NO_2 + M \qquad k_i$$

If the mixed gases flow down a tube long enough that virtually all the NO can react, the total number of photons per second which will be emitted within that tube is given by:

$$I = \frac{k_1 k_3}{(k_1 + k_2) \sum_i k_i [M_i]} \cdot F \cdot [NO]_0 \qquad (1)$$

where $[M_i]$ represents the concentration of each component in the system, $[NO]_0$ the initial concentration of NO in the sample, and F the flow rate of the gas in cm^3 sec^{-1}. The signal obtained from a photomultiplier viewing this tube will be proportional to I. Optimization of the signal for a given NO density will be obtained if (a) sufficient O_3 is added to ensure nearly complete consumption of NO within the flow tube; (b) the total flow rate F is as large as possible and (c) the temperature is kept as high as practical, since k_1 has a higher activation energy than k_2. These considerations formed the design principles of the instrument.

DESCRIPTION OF THE INSTRUMENT

The instrument is shown schematically in Figure 1. For balloon operation air is introduced from an 8-foot tube attached to the flange of the inlet baffle B, pulled by a fan through the instrument at flow rates of 200-300 cm^3 (STP) sec^{-1}, and exhausted through a flexible tube running up the balloon shroud. For aircraft operation the air inlet is equipped with a

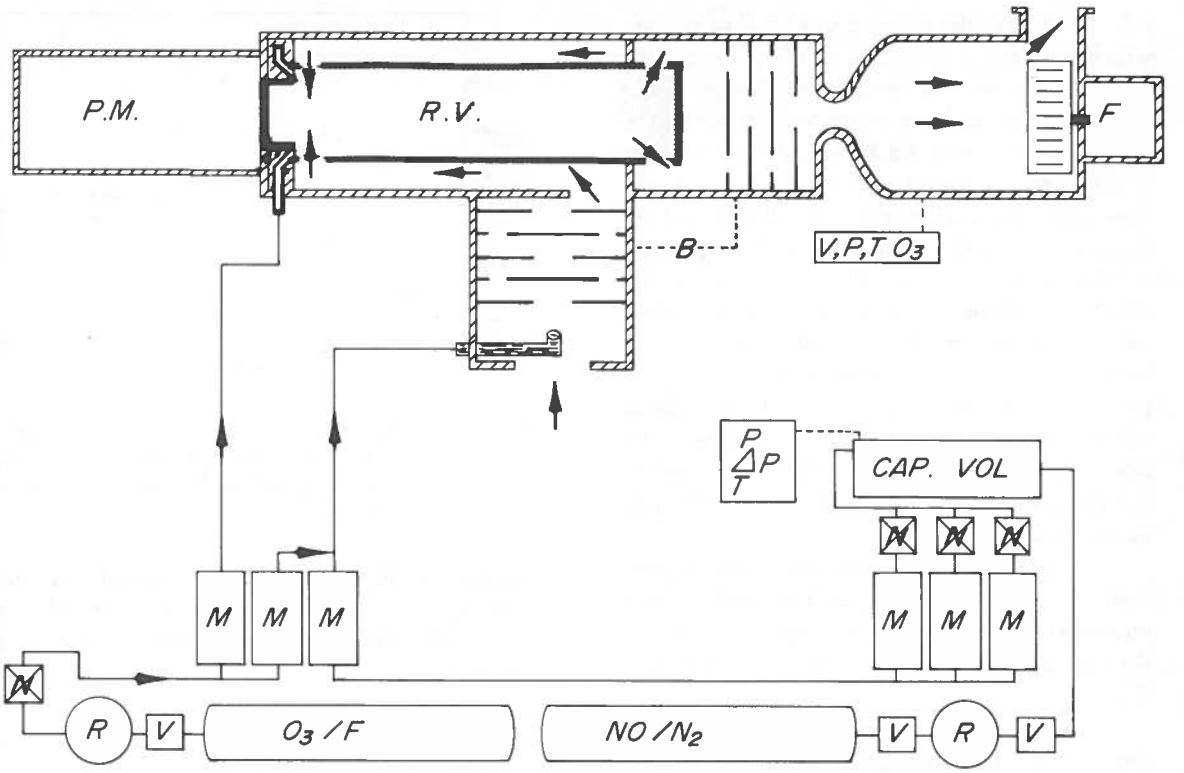

Figure 1. Schematic of the detection apparatus. O_3/F, cylinder containing approximately 10% O_3 in Freon-12; NO/N_2, cylinder containing 2 ppm NO in N_2; V, on-off valves; R, diaphragm gas regulators; N, needle valves; M, Magnalatch valves; CAP. VOL, ballast volume and capillary flow meters; P.M., photomultiplier; R.V., reaction vessel; F, fan blower.

servo-controlled inlet valve to provide the same flow rate. The forward movement of the aircraft obviates the need for the fan.

The incoming air passes through four baffle plates (B) containing 1-inch holes, which serve both to eliminate outside light and to heat the gas. It then flows through the outer annulus for further heating in order to provide a sufficiently long path for the zero reading described below. It then enters the reaction vessel which consists of an 8-inch length of Pyrex tubing 2 inches in diameter, gold-plated on the inside.

The ozone is taken from a storage bottle where it exists as an approximately 10% solution in Freon-12 (Matheson Gas Products Co.). The ozone-freon mixture flows through the cylinder valve V, regulator R, adjustable needle-valve N, and one of two normally closed Magnalatch valves (M). Typical O_3/Freon-13 flow rates are about 10 cm^3 (STP) sec^{-1}.

If introduced below the inlet baffles, the O_3 will react with most of the NO in the air sample before reaching the reaction vessel. This mode of operation is used to provide the zero reading, since we have found that a small but detectable signal is obtained even in the absence of NO in the system. For the actual sample measurement the O_3 is introduced through a series of inlet tubes into the reaction vessel just before the viewing window.

The mixed gases react before leaving the exit ports. They pass through additional light baffles before entering an analyzer region. Here the O_3 density is monitored by UV absorption, and the temperature, total pressure, and linear flow velocity by appropriate sensors.

Provision is made for on-board calibration. Calibrating gas, containing a known mixture of approximately 2 ppm NO in N_2, is carried in a stainless steel cylinder. This gas is drawn through

valves and a regulator into a small ballast volume which contains a calibrated capillary flowmeter. The temperature and pressure of the gas in the ballast volume and the pressure drop across the capillary are monitored by suitable transducers which permit evaluation of the calibrating gas's flow rate. These flow rates are determined by using one or more needle-valve and Magnalatch combinations. The needle-valve settings are selected in advance. For example, one set used in the laboratory simulation studies were: 0.07, 0.30, 0.55 cm^3, and (by using the last two in parallel) 0.85 cm^3 (STP) sec^{-1}. A Magnalatch valve is also inserted into the gas line before the inlet of the instrument to protect against one of the preceding Magnalatch valves being held open inadvertently.

For the calibration and simulation experiments at York University, an EMI 9558 photomultiplier was used to view the reaction cell through a Corning 2-60, 6100-Å long-wavepass filter.

Figure 2 shows a photograph of the instrument, which measures 14" X 18-1/2" X 8-1/2", excluding the ozone bottle, and weighs approximately 60 lbs. The outer shell is made of black-anodized aluminum wrapped with heating tape.

INSTRUMENT CALIBRATION AND FLIGHT SIMULATION

All transducers and sensors were calibrated over the range of environmental conditions anticipated for the actual flight experiment.

From equation (1) it will be seen that, for a given flow rate F, the signal should be linear in $[NO]_0$. Figure 3 shows a curve obtained by adding increasing amounts of calibrating gas to a flow of 230 cm^3 (STP) sec^{-1} of air (0 ppm NO). The slope of this line indicates the responsivity of the instrument. The detection limit can be defined as the rms noise of the background signal divided by the responsivity. For this experiment the detection limit is 0.05 ppb.

In terms of equation (1), the responsivity is proportional to $I/[NO]_0$, and should be linear in relation to the flow rate, F. Figure 4 shows such a plot. The experimental points were obtained using a variety of O_3 flow rates; the curve shows the relative insensitivity of the instrument to this parameter. It should be noted that the linearity

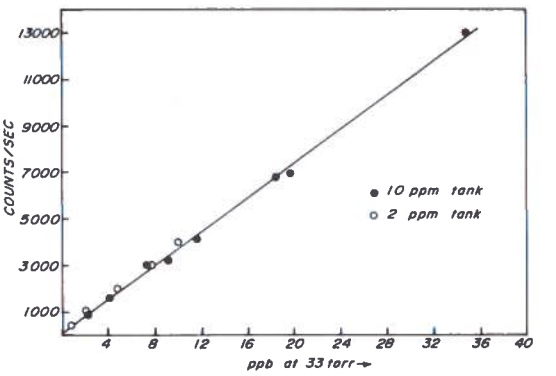

Figure 3. Sensitivity calibration curve using two NO/N_2 mixtures, 10 ppm and 2 ppm; total flow 230 cm^3 (NTP) sec^{-1}, $P_{O_3} \approx 1.5 \times 10^{-2}$ Torr.

shown in Figure 4 is not essential for the operation of the instrument because of the on-board calibration for the particular flow rate being used.

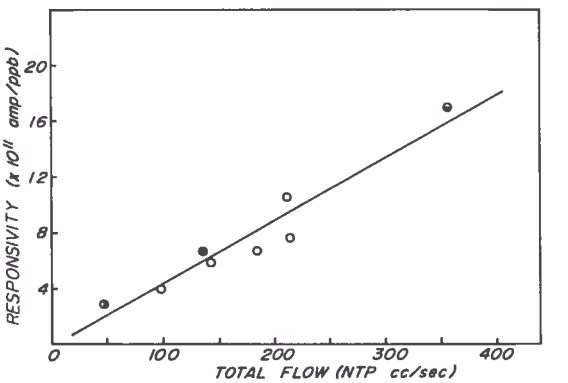

Figure 4. Sensitivity as a function of total gas flow, total pressure; 40 Torr. ○, 65 mTorr O_3; ●, 100 mTorr O_3; ◐, 320 mTorr O_3; ◒, 44 m Torr O_3.

Figure 5 shows an actual chart record of a laboratory simulation of a stratospheric measurement. Section A is the background signal obtained when the O_3 was introduced below the inlet baffle and the sample gas contained no NO. Section B was obtained under the same conditions when the sample gas contained a nominal 2.8 ppb of NO. The small increase in signal in B relative to A indicates that a small amount of NO still remained in the gas when it entered the reaction cell. Section C was obtained when the O_3 flow was directed into the reaction cell.

Sections D, E, F, and G were obtained with different amounts of calibrating gas added. In the actual flight experiment measurement of the ambient (Section C) will be repeated between each addition of calibrating gas.

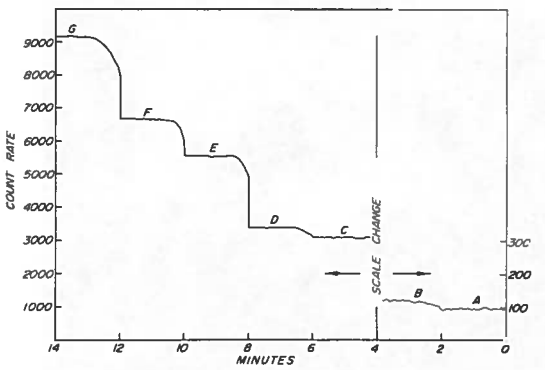

Figure 5. Chart record of simulated atmospheric experiment total flow, 290 cm^3 (NTP) sec^{-1}, pressure, 37 Torr. P_{O_3}, 50 mTorr.

The results are plotted in Figure 6. Extrapolation of the 'best' straight line to the abscissa gives the amount of NO in the sampled gas. The value of 2.6 ppb compares favourably with the 2.8 ppb in the sample, taking into account uncertainty in preparing the sampled gas mixture.

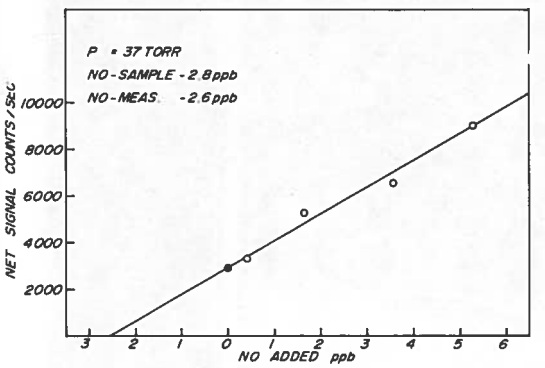

Figure 6. Signal vs. NO added in simulation experiment total flow, 290 cm^3 (NTP) sec^{-1}; press, 37 Torr; P_{O_3}, 50 mTorr.

The limit of detection for this experiment was 0.03 ppb. The noise characteristic of the RCA C31034A photomultiplier to be used in the flight experiment should provide some improvement in this limit.

APPLICATIONS

The NO measurement system described above will be useful, with slight modifications, on two types of vehicles. The first application will be a balloon-borne experiment in which the balloon will float at approximately 70,000 ft before initiation of the experiment sequence. At this altitude, the payload will be turned on by command from the ground, and the equipment will be purged for four minutes with O_3, after which three measurements and calibrations will be alternately performed at two-minute intervals, as shown in Figure 7. The cycle then repeats, beginning each time with a purge to supply a zero reading. This cycling continues until the "off" command is sent.

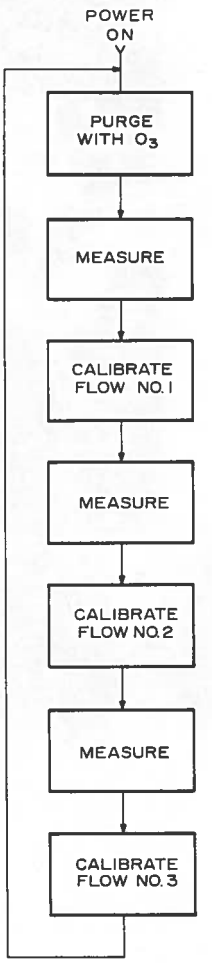

Figure 7. Measurement and calibration cycle for balloon-borne experiment.

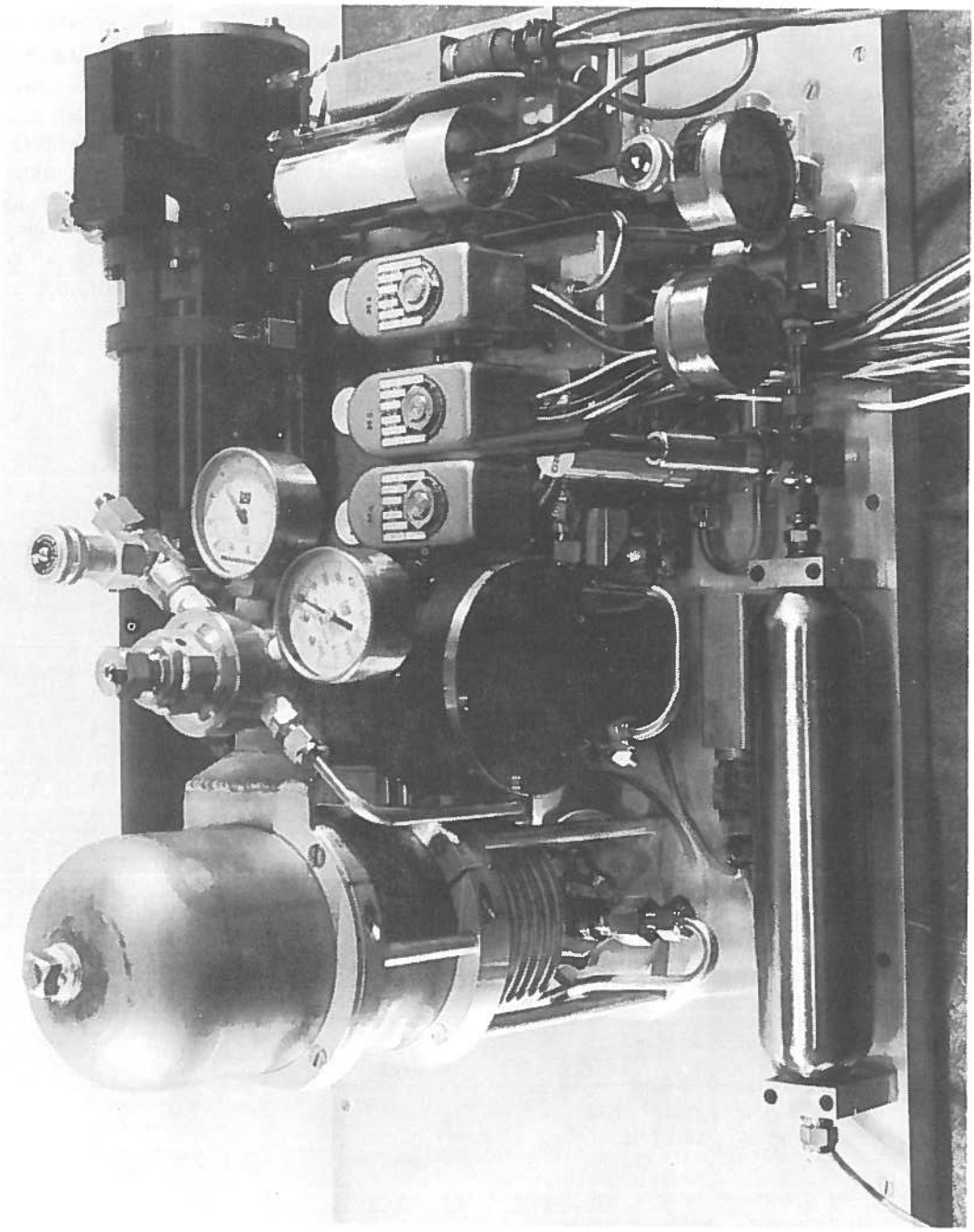

Figure 2. Photograph of detection apparatus.

Communications required for this experiment include an HF link from ground to balloon, which can command the experiment off or on. Data from the experiment are relayed to the ground over an S-band telemetry link. Three voltage-controlled oscillators are used to transmit 1) a linear dc signal, 2) a logarithmic signal, and 3) a commutated signal to record the housekeeping information. As a backup, all of the data transmitted will be recorded on an on-board digital tape recorder. Figure 8 shows a schematic layout of the signal-processing equipment and telemetry.

The signal-processing electronics consist of a cooled photomultiplier followed by a charge-sensitive preamplifier. This is followed in turn by a pulse height discriminator and a pulse-shaping circuit. After initial amplification, the pulses are passed into a rate meter that can give both a linear and a logarithmic response. The range of the linear response will be chosen on the basis of our best guess as to the expected signal level and will be adjusted for later flights on the basis of the results of the first. The logarithmic device (with a 5-decade dynamic range capability) is designed to cover the possibility of some substantial surprises in the density of NO.

The initial design for the balloon experiment anticipates a programmed balloon flight. As mentioned above, the experiment will be turned on at float ($\approx$ 70,000 ft); after purging, the routine of alternate measurements and calibrations will begin. During this time the balloon will be allowed to descend approximately 6000 ft, at which time the experiment will be commanded off. Ballast will then be dropped to allow the balloon to rise to the original altitude. Enough ozone, power, and ballast are available to allow operation for four descent cycles.

The gas will be pumped by means of a fan installed at the exit of the experiment. Gas will enter the entrance through a rigid tube extending approximately 8 feet below the experiment. The exhaust gases will be pumped into a flexible tube extending approximately 10 feet up the shroud

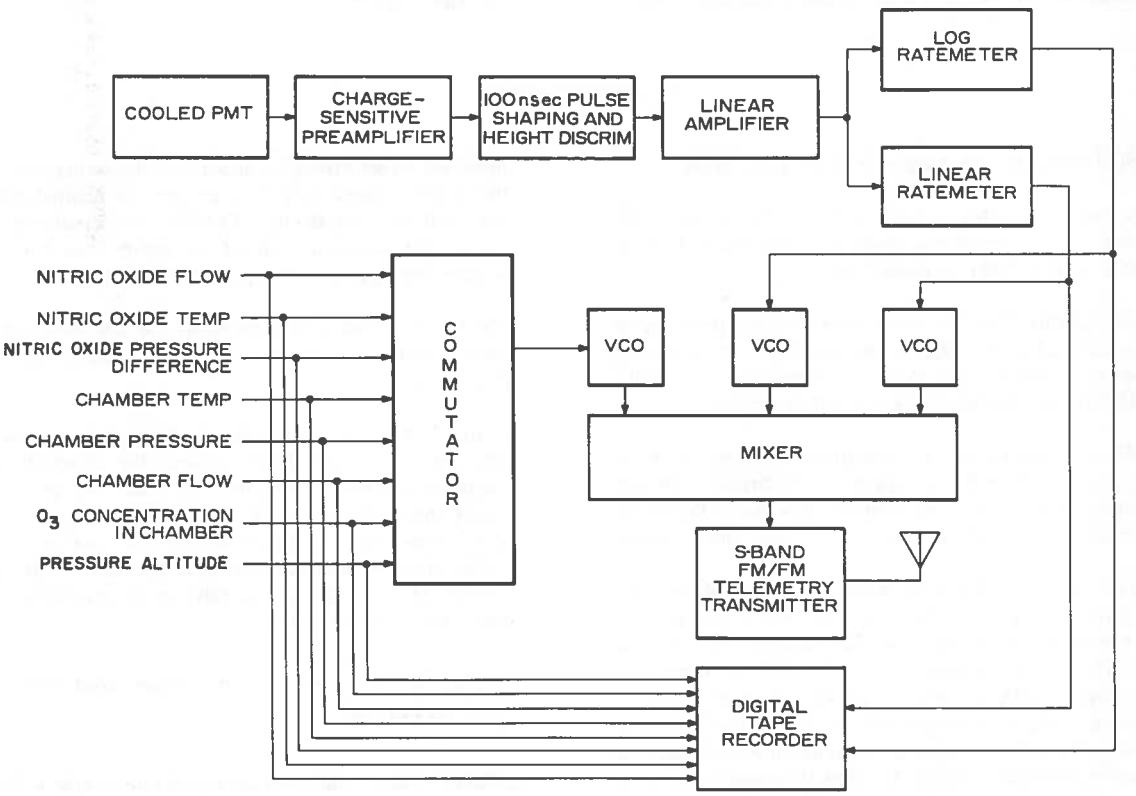

Figure 8. Schematic of signal-processing equipment and telemetry.

lines. This arrangement is designed to prevent the entry of exhaust gases into the system.

The entire experiment will be housed in an insulated container 28″ X 34″ X 19″ weighing 170 pounds exclusive of power. A total of 240 ampere hours at 28 V will be available. The weight of the batteries is approximately 70 pounds. Where necessary, heat will be applied to various elements of the payload. In particular, heat is to be applied at the reaction chamber; enough power must be available there to heat all the incoming gas to a temperature of 10°C to 15°C. A reasonable amount of temperature control is required in this experiment, since the chemiluminescence reaction is temperature-sensitive.

The aircraft-borne instrument differs from the balloon-borne unit in several details. The experiment hardware is to be mounted in the wing pod of an RB-57F aircraft. Power will be supplied from the aircraft, and all recording will be done on board. In order to extend the experiment time to the maximum flight time of the aircraft, the ozone supply will be doubled. Because of weight and balance considerations, the ozone is separated from the remainder of the payload and placed elsewhere in the pod. Instead of pumping the gas, as in the balloon experiment, the ram effect of the aircraft is utilized. Gas enters through a three-inch pipe protruding from the front of the pod and is exhausted out the side.

Because the measurements with their current calibrations depend upon maintaining a relatively constant flow rate, a throttle valve is installed in the entrance tube so that the flow rate can be servo-controlled with input from a flow sensor.

The aircraft experiment will be performed on a completely automatic basis. The experiment will be turned on by a pressure switch at about 60,000 ft and will operate continuously, utilizing the cycle described in Figure 7. Descent to an altitude below 60,000 ft will turn off the experiment. This altitude can, of course, be changed for special experiments.

The first balloon flight is currently scheduled for December 1, 1972. Integration of a payload into the aircraft is currently scheduled for January, 1973.

DISCUSSION

SCHAINKER: What are your future flight plans?

SCHIFF: We plan a balloon flight over White Sands, New Mexico. Our future program will be planned on the basis of that flight's information.

ASHENFELTER: We contemplate making three flights to determine the engineering feasibility. If everything works properly, this system may piggyback with the AEC routine particle and gas sampling method.

MEGILL: As for aircraft experiments, we plan to do an integration in an RB-57 sometime in February, and start flights in late spring or summer. How many flights are made will depend on how well the instrument works.

BRODERICK: There is some confusion about past measurements of stratospheric NO. We at TSC made a measurement last year on the Convair 990 with an instrument that is identical in principle but not quite so elaborate, with a sensitivity of 3.3 ppb at 45,000 feet. Going north from NASA Ames to Port Hardy, B.C., and back when the tropopause was at about 33,000 feet, we detected no nitric oxide. We think the experiment was a good one, but it is still only one piece of data. We left the instrument with NASA Ames, and they have since increased its sensitivity by about an order of magnitude, but I don't think they have gotten any unambiguous data to date. Thus, the only CIAP-funded experiment so far is that determination of an upper limit for the volume mixing ratio of 3.3 ppb at 45,000 feet.

SNELSON: Have you considered the possibility that some reaction could foul up the validity of the mechanism?

SCHIFF: Yes. You are probably thinking of reactions between ozone and hydrocarbons. We checked the chemiluminescence sensitivity of some olefins, and found that with our particular photomultiplier it was about three orders of magnitude less than that of nitric oxide. Methane does not give us any readings with O_3. Nevertheless, we do claim only to be measuring an upper limit of nitric oxide.

WHITTEN: Are you worried about contamination from the balloon?

SCHIFF: I don't think out-gassing of nitric oxide will be a serious problem, but we are going to make our measurements in the descent mode.

ASHENFELTER: We plan to take the balloon up to a specific altitude and float it for a while. Then we'll turn on the sampling system and have it descend at a rate of about 300 feet per minute; this should be faster than the free-fall rate for particles from the balloon surface. We'll repeat this procedure three or four times, and compare the data to see whether there was any contamination from the balloon or the payload.

SCHIFF: I expected to be asked about the fact that we were using NO as a calibrating gas, and exhausting it to the atmosphere by the fan. The balloon is free-floating, and we worried that adding nitric oxide to the stratosphere from the instrument itself might affect the data we obtained. Also, we are pumping ozone through the unit and into the atmosphere at a tremendous rate; we wondered whether this ozone might reduce the nitric-oxide concentration near the balloon. Because of these possible problems, we are sampling well below the gondola, in the descent mode, and exhausting high up the shroud. The balloon itself is a pretty good infrared radiator, so the convection currents will tend to alleviate these problems even more.

DAVIS: Have you tried putting SO_2 or formaldehyde into the system? Could either of them be another source of interference?

SCHIFF: We did put in hydrocarbons, so if any formaldehyde were going to be formed by ozone it would happen in our system. We did not put in SO_2.

SCHAINKER: What are the upper and lower limits of the altitude you will be sampling at? When you quote a concentration for a given altitude, what will be the implied uncertainty caused by motion of the balloon?

SCHIFF: Initially, we hope to start sampling when we get to 70,000 feet. Since we will be sampling for two minutes, at a descent rate of about 300 feet a minute, we'll have an uncertainty of 600 feet – 1000 at most. Eventually, we want to make concentration profiles up to as high as we can go in the balloon.

STRATOSPHERIC AERONOMY

PANEL DISCUSSION

MARCEL NICOLET
Institut d'Aéronomie Spatiale de Belgique
Chairman

FREDERICK KAUFMAN	*University of Pittsburgh*
PAUL J. CRUTZEN	*University of Stockholm*
MICHAEL B. McELROY	*Harvard University*
JULIUS LONDON	*University of Colorado*

NICOLET: I should like to begin with a short discussion of stratospheric aeronomy. My first slide shows the principal reactions in which stratospheric ozone is involved. First, in a pure-oxygen atmosphere the aeronomic processes involve the photodissociation of O_2 and O_3, the production of oxygen atoms and ozone molecules, and finally the re-formation of molecular oxygen through the reaction $O + O_3$. When hydrogen compounds are introduced, the two principal reactions are $O + OH \rightarrow O_2 + H$ and $O + HO_2 \rightarrow O_2 + OH$, both of which re-form oxygen molecules. Unfortunately, the rate coefficient of $O + HO_2$ has never been measured. Since the ratio $n(OH)/n(HO_2)$ in the upper stratosphere depends on the ratio a_7/a_5 (as given on this slide), it is clear that new laboratory measurements of these two reactions are badly needed. As far as the reactions of OH and HO_2 with ozone are concerned, a question mark indicates that more precision is needed and that they are not important, as was said earlier. Dr. Kaufman will speak on that subject later.

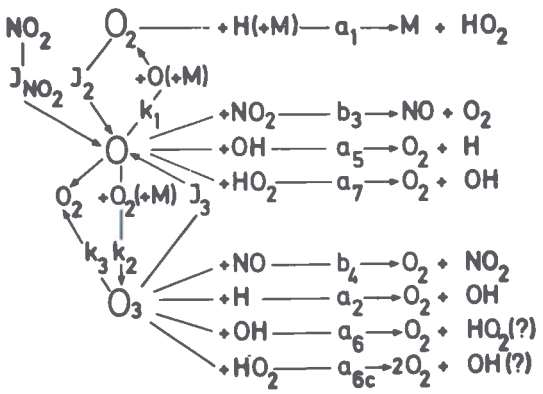

Slide 1. Reactions involving stratospheric oxygen and ozone.

The principal reactions with nitrogen oxides are: photodissociation of NO_2, reaction of O_3 with NO, and the reaction of NO_2 with O which leads to the re-formation of O_2. This last reaction has a rate coefficient which seems to be very well known: 9×10^{-12} cm^3 sec^{-1} according to Davis et al.

The second slide shows how the reactions begin in the stratosphere. These processes are all the result of dissociation of ozone by ultraviolet radiation. At $\lambda < 3100$ Å the photodissociation of an ozone molecule leads directly to an excited oxygen atom $O(^1D)$. For wavelengths greater than 3100 Å the efficiency of production of this excited atom is less than unity; the exact spectral distribution of this efficiency is not yet known. It is necessary to determine the real production of $O(^1D)$ in the photolysis of ozone for $\lambda > 3100$ Å, where the number of solar photons is increasing with wavelength and where the O_3 absorption cross-section is decreasing.

$$O(^1D) + H_2O \rightarrow OH + OH^*\ (v \leq 2) + 28.8 \text{ kcal}$$

$$O(^1D) + CH_4 \rightarrow CH_3 + OH^*\ (v \leq 4) + 43.5 \text{ kcal}$$

$$O(^1D) + H_2 \rightarrow H + OH^*\ (v \leq 4) + 43.5 \text{ kcal}$$

$$a^* = (3 \pm 1) \times 10^{-10} \text{ cm}^3 \text{ sec}^{-1}$$

Slide 2. Reactions of $O(^1D)$ that produce OH radicals.

In any case, the stratospheric chemistry of hydrogen compounds starts from the reactions of $O(^1D)$ with H_2O, CH_4, and H_2, which give OH radicals. These reactions are known with good accuracy; an average value of the rate coefficients is $(3 \pm 1) \times 10^{-11}$ cm^3 sec^{-1}. A difference of a factor of 2 is obtained if extreme minimum and maximum possible values are used.

The third slide shows another important reaction of excited oxygen atoms with nitrous oxide. Nitrous oxide cannot be formed in the stratosphere, since the three-body reaction with N_2 is negligible compared with the quenching reaction $O(^1D) + N_2 \rightarrow N_2 + O(^3P)$. The reaction of $O(^1D)$ with N_2O transported up from the troposphere leads to two nitric-oxide molecules with a rate coefficient which is well-determined, 1×10^{-10} cm^3 sec^{-1}.

$$O(^1D) + N_2(^1\Sigma) + M \rightarrow N_2O(^1\Sigma) + M$$

$$O(^1D) + N_2 \rightarrow O(^3P) + N_2 \quad ; \quad 5 \times 10^{-11} \text{ cm}^3\text{sec}^{-1}$$

$$N_2O + h\nu\,(\lambda < 3400\ \text{A}) \rightarrow N_2(X^1\Sigma) + O(^1D)$$

$$O(^1D) + N_2O \rightarrow N_2 + O_2 \quad ; \quad 1 \times 10^{-10} \text{ cm}^3 \text{ sec}^{-1}$$

$$O(^1D) + N_2O \rightarrow 2\,NO \quad ; \quad 1 \times 10^{-10} \text{ cm}^3 \text{ sec}^{-1}$$

Slide 3. Reactions of $O(^1D)$ with N_2 and N_2O.

Slide 4 shows an example of the possible production rates for nitric oxide. Two possibilities have been introduced for $O(^1D)$ concentrations: a minimum value corresponding to production only by $\lambda < 3100$ Å, and a maximum value where additional production is postulated for $\lambda > 3100$ Å. These two values lead to different production curves in the lower stratosphere. In addition to this production another aspect must be considered: the vertical distribution of the eddy diffusion and its absolute value. Here we adopted two working values: a minimum value (K_{min}) corresponding to an average value of about 10^3 cm^2 sec^{-1}, and a maximum value (K_{max}) corresponding to an average value of about 10^4 cm^2 sec^{-1}. You can see the important differences due to the different conditions which are adopted for transport conditions. With the small value of the eddy-diffusion coefficient the NO production peak is below 30 km, whereas the peak goes up to almost 40 km with the high value of the eddy diffusion. Such differences show how difficult it is to get a correct answer, and how important it is to know the principal rate coefficients with great accuracy.

Another origin of nitric oxide in the stratosphere is the dissociation of molecular nitrogen by cosmic rays. When the cosmic rays produce a certain number of ion pairs, there is also a direct dissociation of N_2 in addition to the effects of the dissociative ionization. The exact production of nitrogen atoms is not easy to determine but should be between 50 percent and 100 percent of the total ion production. This means that between 10 and 15 kilometers there is a maximum production of nitrogen atoms by galactic cosmic rays. Since the cosmic effect is also a nighttime ionization process, the total production of nitrogen atoms in the lower stratosphere becomes important at high latitudes where the production is about 10 times the equatorial production. And finally, we cannot forget in the analysis of all possible productions the effect of nuclear explosions. According to Foley and Ruderman, these have led to production of nitrogen atoms and, consequently, to significant formation of NO molecules.

Again, it must be said that more observational data are needed in order to study the action of nitrogen oxides; slide 5 shows how the total production of NO molecules depends on the eddy-diffusion coefficient and on the value of the $O(^1D)$ concentration. The total production of NO by oxidation of N_2O should be $(1.5 \pm 1.0) \times 10^8$ NO molecules cm^{-2} sec^{-1}, i.e., a factor of 5 between the minimum and maximum values.

Another important problem, which is introduced by slide 6, is the dissociation of nitric oxide in the beta, gamma, and delta bands. The principal dissociation comes from the δ (0-0) and δ (1-0) bands, which absorb solar radiation at $\lambda < 1908$ Å. The principal difficulty here is determining the penetration of the solar radiation through the discrete bands of the Schumann-Runge system of O_2 (slide 7). Computations of this, which must be made line by line, have been done in our laboratory. The vertical distribution of the photodissociation coefficient is about 10^{-5} sec^{-1} at zero optical depth,

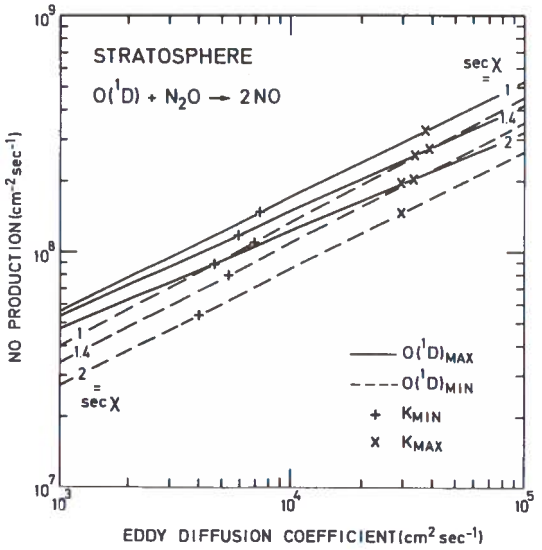

Slide 5. Column production rates of NO vs. eddy-diffusion coefficient, for various values of $O(^1D)$ concentration and solar zenith angle χ.

decreases to 4×10^{-6} sec^{-1} at 60 km, and reaches 1.5×10^{-6} at the stratopause for a solar zenith angle of 60°. Below 50 km there is a rapid decrease; the dissociation coefficient is only about 2×10^{-7} at 40 km. Such values show that the photodissociation of NO is still important in the lower mesosphere where there is practically no normal production of N and NO. Slide 8 shows how the conditions are different with and without dissociation of nitric oxide, and also the extreme importance of the values of the eddy diffusion coefficient.

As can be seen from slide 9, the production of nitric oxide in the lower stratosphere leads to a downward transport to the tropopause. In the upper stratosphere the loss term due to the photodissociation of NO is balanced by the transport from the lower stratosphere, not from the mesosphere. Thus, NO in the stratosphere is independent of the transport of mesospheric NO.

The final question in the problem of stratospheric nitrogen oxides is the formation of nitric acid. Among the production reactions shown in slide 10 (my 1965 diagram for nitric acid), the three-body reaction $OH + NO_2 + M \rightarrow HNO_3 + M$ is the most important in the stratosphere. Its rate coefficient is well known from the measurements of Simonaitis and Heicklen, McCrumb and Kaufman, and Morley and Smith; it is of the order of 2×10^{-30} $n(N_2)$ cm^3 sec^{-1}. The reaction $HO_2 + NO + M \rightarrow HNO_3 + M$ has not been measured. The reaction $H_2O_2 + NO_2 + M$

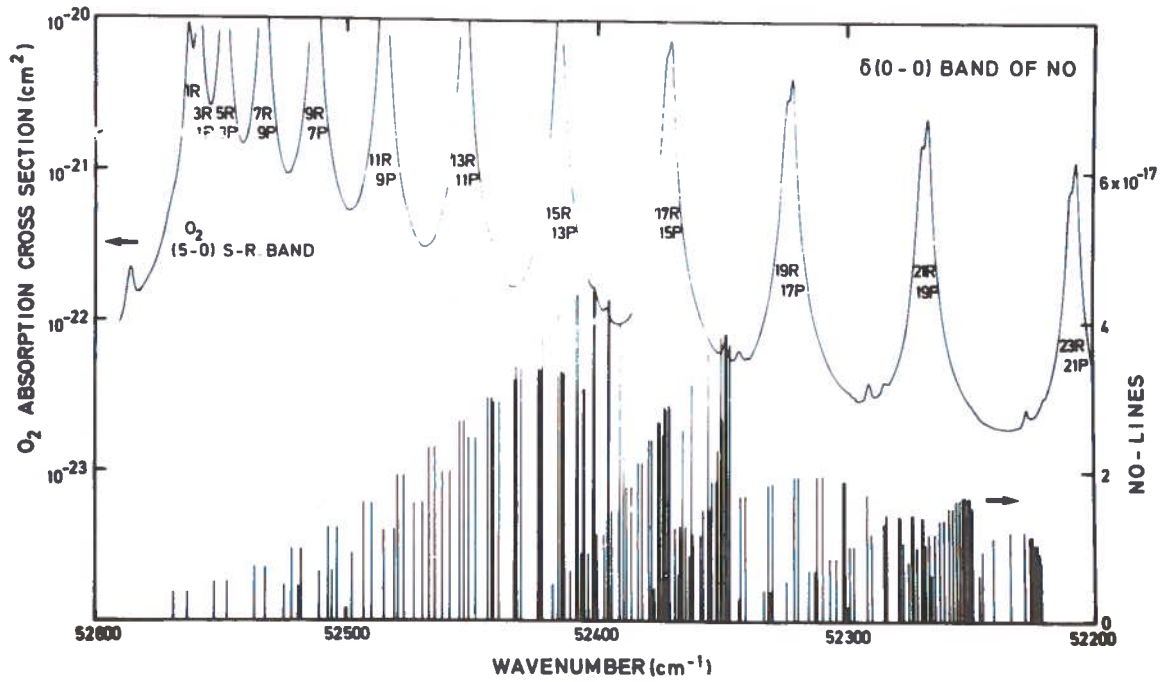

Slide 6. Overlap of the δ (0-0) band of NO with the Schumann-Runge bands of O_2.

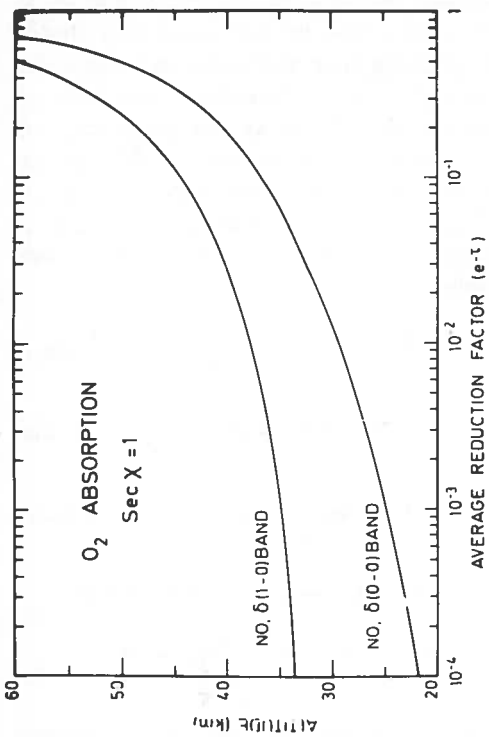

Slide 7. Absorption by O_2 at the wavelengths of the NO δ (1-0) and δ (0-0) bands, vs. altitude.

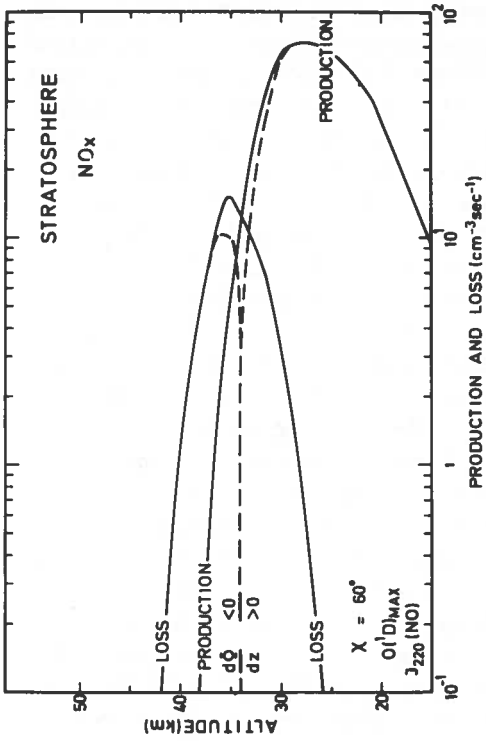

Slide 9. Production and loss of NO_x vs. altitude.

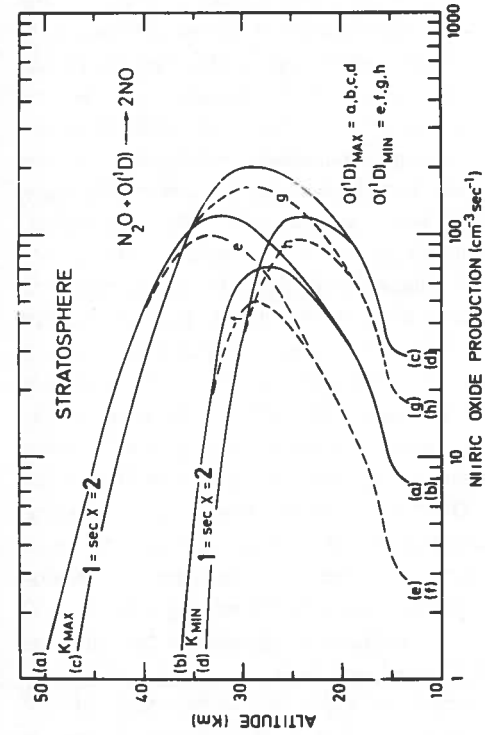

Slide 4. Production rates of NO vs. altitude for two values of the eddy-diffusion coefficient K, two values of the $O(^1D)$ concentration, and two values of solar zenith angle χ.

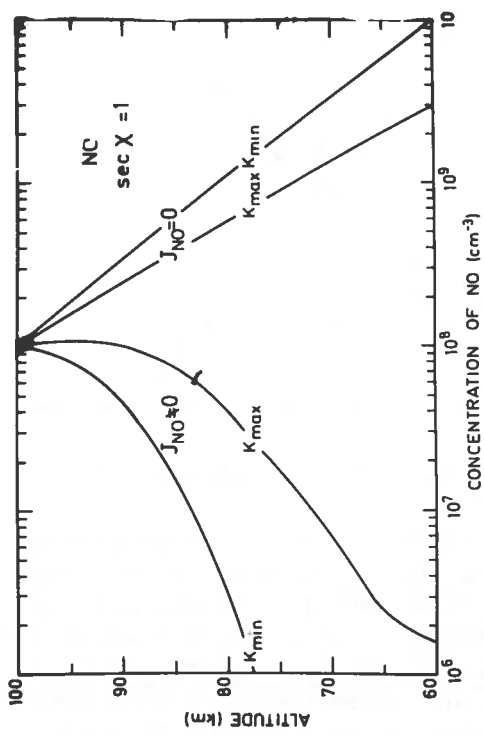

Slide 8. NO concentration vs. altitude, with and without predissociation of NO.

can be neglected, since Simonaitis and Heicklen have shown its rate coefficient to be very small. Among the loss processes for nitric acid, we have its reaction with OH and its photodissociation to $OH + NO_2$. Thus it is clear that stratospheric chemistry depends not only on nitrogen oxides but also on the hydrogen compounds. It is necessary to know with great accuracy the concentration of the hydroxyl and hydroperoxyl radicals in order to determine the ratio of the concentrations of nitrogen dioxide and nitric acid. The photodissociation coefficient of HNO_3 has been determined by laboratory measurements. From the measurements made in my laboratory, the following values have been obtained for solar zenith angles corresponding to 60°: about 2×10^{-5} sec^{-1} at 50 km, 5×10^{-6} sec^{-1} at 40 km, 1×10^{-6} at 30 km, 6.5×10^{-7} at 20 km, and 5×10^{-7} at 15 km. Thus the formation and dissociation of nitric acid must be introduced in the analysis of the action of nitrogen oxides in the stratosphere. Fortunately, there are very good observations of HNO_3 by Murcray et al. which make it possible to study the stratospheric behavior of nitric acid.

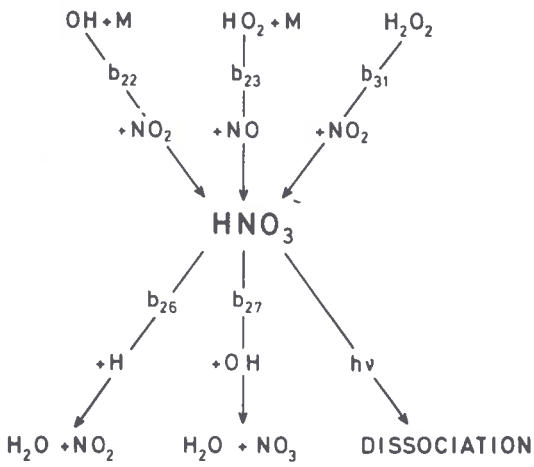

Slide 10. Source and sink reactions of HNO_3.

With slide 11 I come again to the reactions involving CH_4, i.e., reactions not only with $O(^1D)$ but also with $O(^3P)$ and particularly with OH. When the problem of CH_4 is introduced, it is necessary to add the CO problem, which was considered by McElroy, McConnell, and Wofsy in the stratosphere and troposphere. Dr. McElroy will speak on that subject later. In addition, the tropospheric problem, as it has been considered by Levy, must also be introduced as a stratospheric problem to enable us to understand the aeronomic behavior of the lower stratosphere. As an example, slide 12 shows that the production of CO comes from dissociation of CO_2 in the upper stratosphere, from the reaction of $O(^1D)$ with CH_4 in the middle stratosphere, and from the reaction of OH with CH_4 in the lower stratosphere.

(c_1) ; $O(^3P) + CH_4 \rightarrow CH_3 + OH - 2$ kcal

(c_1^*) ; $O(^1D) + CH_4 \rightarrow CH_3 + OH + 43$ kcal

(c_2) ; $OH + CH_4 \rightarrow CH_3 + H_2O + 15$ kcal

(a_{36}) ; $OH + CO \rightarrow CO_2 + H + 24$ kcal

Slide 11. Reactions of CH_4 and CO.

Slide 13 shows the two basic equations which must be used in the determination of the vertical distribution of CH_4 and CO in the stratosphere. CH_4 is not produced in the stratosphere, and a balance must be found between its loss processes and transport up from the troposphere. As far as CO is concerned, its stratospheric distribution as shown on slide 14 corresponds to a photochemical equilibrium at the stratopause but depends on the lower boundary conditions which are assumed at the tropopause. If the mixing ratio is of the order of 10^{-7} or 3×10^{-8}, as indicated on slide 14, there must be significant transport of CO from the troposphere through the tropopause. A condition of no transport from the troposphere requires a mixing ratio of the order of 10^{-8} at the tropopause. However, such a numerical value depends on the exact value of the rate coefficients of $OH + CH_4$ and of $OH + CO$. For this reason it is necessary to measure again with great accuracy the rate coefficients of these two reactions for stratospheric temperatures. A CO mixing ratio of 5×10^{-8} at the tropopause agrees with the observations of Warneck and Seiler.

In order to show the complexity of the chemistry of the lower stratosphere, I have a

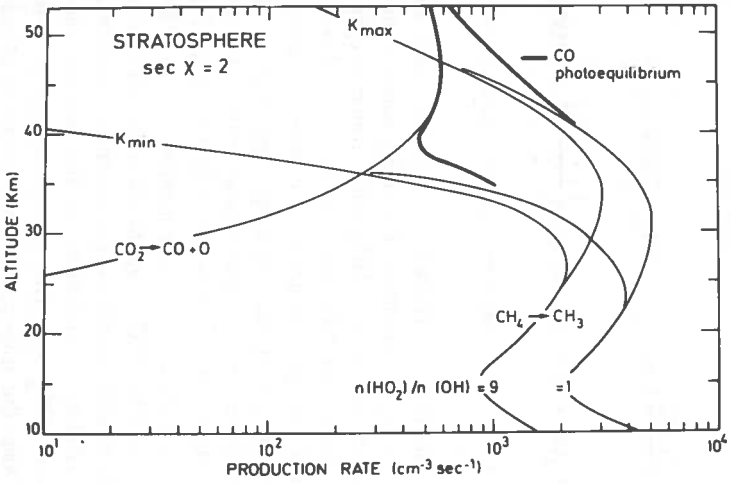

Slide 12. Production rates of CO vs. altitude.

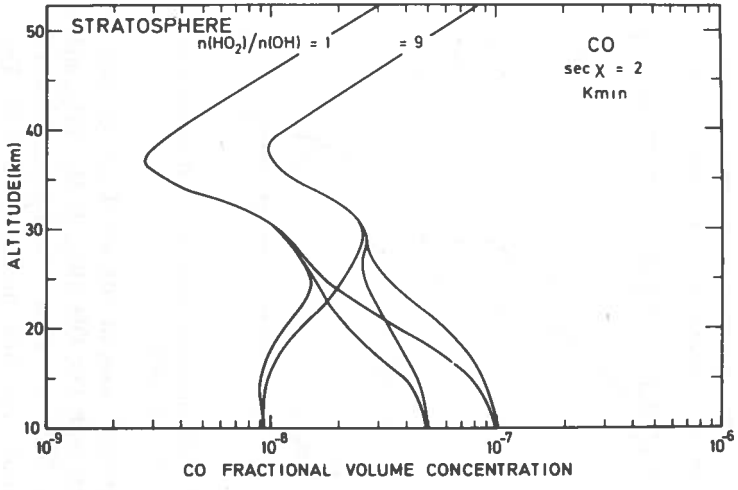

Slide 14. Calculated distributions of CO vs. altitude.

$$\frac{\partial n(CO)}{\partial t} + L(CO) + \frac{\partial \Phi(CO)}{\partial r} = P(CO).$$

$$\frac{\partial n(CH_4)}{\partial t} + L(CH_4) + \frac{\partial \Phi(CH_4)}{\partial r} = O$$

$$\Phi_i = n_i w_i = n_i K \left[\frac{1}{H_i} - \frac{1}{H} \right]$$

$$\frac{1}{H_i} = \frac{1}{n_i} \frac{\partial n_i}{\partial r} + \frac{1}{T} \frac{\partial T}{\partial r}$$

Slide 13. Equations determining the vertical distributions of CO and CH_4.

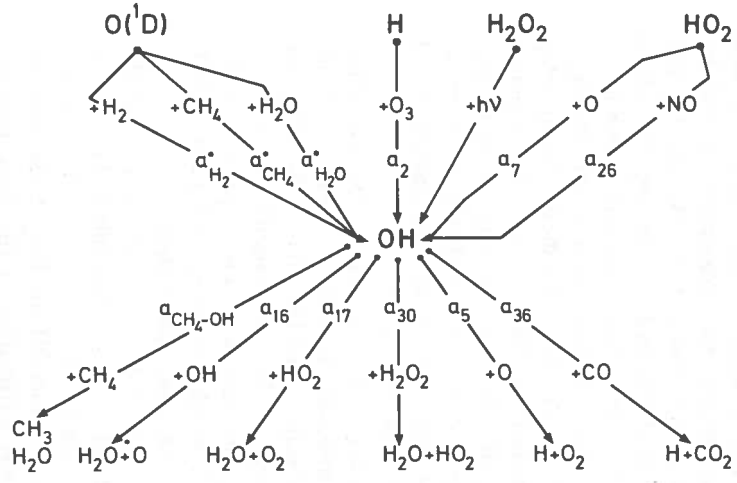

Slide 15. Reactions involving OH.

slide (15) indicating the various reactions in which OH is involved. As before, the first reactions involve the production of OH by reaction of $O(^1D)$ with H_2O, CH_4, and H_2. The reaction of atomic hydrogen with ozone leads to OH, and is particularly important in the mesosphere. The photodissociation of hydrogen peroxide leads to two OH radicals. Finally, HO_2 is transformed into OH by atomic oxygen and by nitric oxide. It must be kept in mind that nitrogen-oxide and hydroxyl-radical concentrations are connected through the reaction of NO with hydroperoxyl radicals.

The destruction processes of OH are numerous, as indicated on slide 15. Several of them, such as reactions with OH, HO_2 H_2O_2, CH_4, and HNO_3, lead to the re-formation of water vapor. Another important process is the reaction of OH with CO, which determines the ratio $n(OH)/n(HO_2)$ in the lower stratosphere.

In order to show the complexity of the aeronomy of the lower stratosphere, I have a few slides indicating the behavior of the principal reactions affecting OH and HO_2. Slide 16 shows the vertical distribution of the three principal productions of OH radicals, namely, reaction of $O(^1D)$ with H_2O, CH_4, and H_2. Slide 17 gives

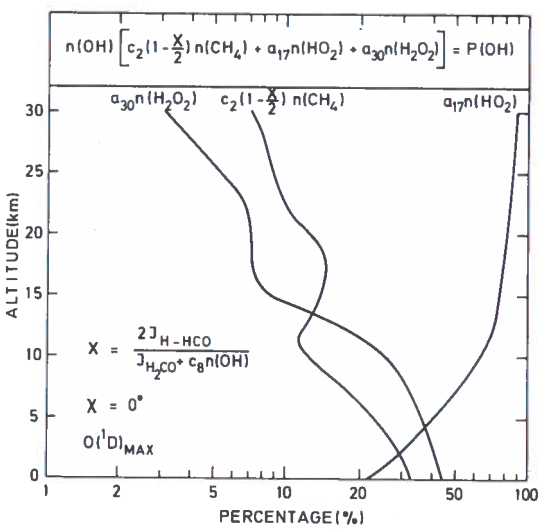

Slide 16. Percentage contributions of OH source reactions vs. altitude.

the principal losses of OH, which are its direct reactions with CO, OH, HO_2, H_2O_2, CH_4, and HNO_3. Slide 18 shows the balance between production and loss processes for OH. The principal loss process is the reaction of OH with

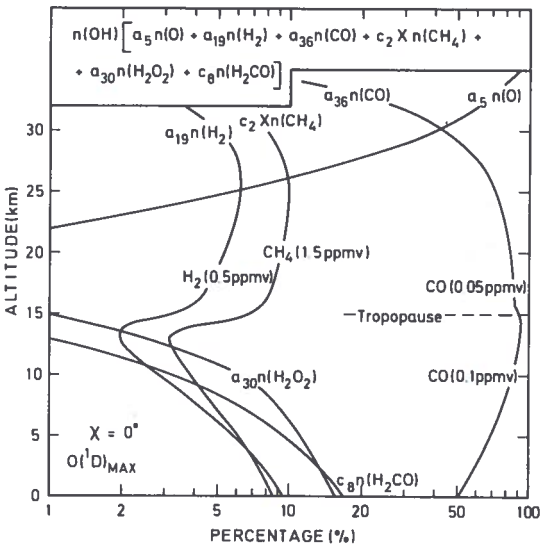

Slide 17. Percentage contributions of OH sink reactions vs. altitude.

HO_2, if the rate coefficient of the reaction OH + HO_2 reaches the 2×10^{-10} cm^3 sec^{-1} measured by Hochanadel et al. Again a very precise rate is required here in order to obtain the correct value of the product $n(OH) \cdot n(HO_2)$.

$$n(OH)\left[a_{17}\, n(HO_2) + a_{30}\, n(H_2O_2) + c_2\left\{\frac{1-X}{2}\right\} n(CH_4) + 2\, b_{27}\, n(HNO_3)\right] = \left[n(H_2O) + n(H_2) + n(CH_4)\left\{\frac{1+X}{2}\right\}\right] a^*\, n(O^*)$$

Slide 18. Equation balancing sinks and sources of OH.

The ratio $n(OH)/n(HO_2)$ as given in slide 19 is not easy to determine. Too many reactions are involved: reaction of HO_2 with atomic oxygen, OH, HO_2, and NO, and also that of OH with atomic oxygen, molecular hydrogen, carbon monoxide, methane, hydrogen peroxide, and even formaldehyde. The various curves of slide 14 indicate that the reaction of OH with CO plays a leading role in the determination of the ratio $n(OH)/n(HO_2)$ up to 30 km, where the reaction with atomic oxygen becomes important. The relative contributions of the reactions destroying HO_2 are given as percentages in slide 20. Near the tropopause level, the terms affecting HO_2 depend on nitric oxide, HO_2, and

OH. The term involving atomic oxygen plays the leading role above about 30 km.

$$n(HO_2)\left[a_7\, n(O) + a_{17}\, n(OH) + 2a_{27}\, n(HO_2) + a_{26}\, n(NO) + c_{16}\, n(CH_3O_2)\right] =$$

$$n(OH)\left[a_5\, n(O) + a_{19}\, n(H_2) + a_{30}\, n(H_2O_2) + a_{36}\, n(CO) + c_8\, n(H_2CO) + c_2 X n(CH_4)\right]$$

Slide 19. Equation from which $n(OH)/n(HO_2)$ can be derived.

In conclusion, more measurements are needed in order to determine the aeronomic structure of the stratosphere, particularly the lower stratosphere. The last slide (slide 21) shows a series of OH curves which have been computed with the conventional values of the rate coefficients. Errors of a factor of 2 and 3 are likely, since some of these rate coefficients have never been measured and are therefore estimated.

KAUFMAN: Since I cannot possibly discuss the chemistry of a large number of atmospheric reactions in any detail, let me first deal briefly

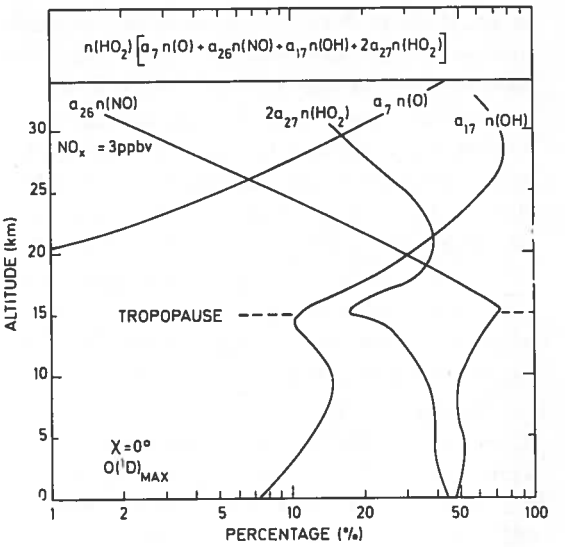

Slide 20. Percentage contributions of HO_2 sink reactions vs. altitude.

with some specific kinetic problems and then make several controversial remarks.

By way of introduction to the discussion of kinetics, it seems clear to me that the dozen or so groups around the world which work on atom and simple radical reactions are doing an excellent job and that, therefore, stratospheric chemistry and photochemistry is in surprisingly good

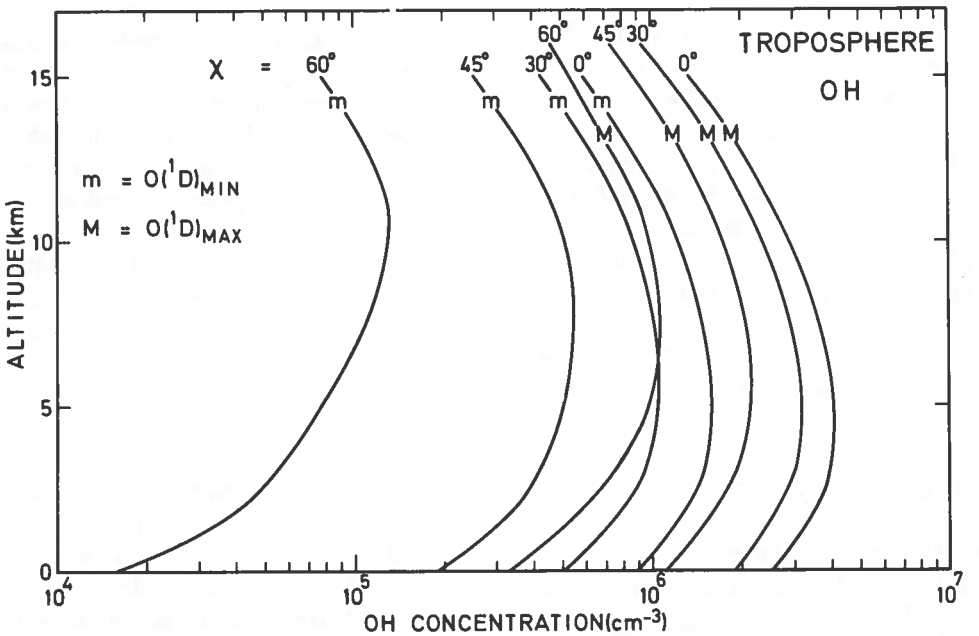

Slide 21. OH concentration vs. altitude, calculated for various solar zenith angles χ and $O(^1D)$ concentrations.

shape. If the problems of transport and residence times were in nearly equivalent shape, we might have some of the answers for CIAP right now. It is in this context that I must caution Prof. Nicolet when he asks for 20-30% accuracy for dozens of reaction rate constants (e.g., for $OH + HO_2 \rightarrow H_2O + O_2$, $O + HO_2 \rightarrow OH + O_2$, $OH + O_3 \rightarrow HO_2 + O_2$, $HO_2 + NO \rightarrow OH + NO_2$, $OH + NO_2 + M \rightarrow HNO_3 + M$, etc.) that he is making a vast amount of work for us kineticists at a time when the problems of transport are clearly in much worse shape than those of kinetics.

In the matter of OH reaction rates, Dr. Anderson and Mr. Margitan in my laboratory are well along to having reliable rate constants for the reactions $OH + NO_2 + M \rightarrow HNO_3 + M$ and $OH + NO + M \rightarrow HNO_2 + M$ for several M's (He, Ar, N_2) over a substantial temperature range. For the important HNO_3 production step, k seems to be about 2×10^{-30} cm^6 $molecule^{-2}$ sec^{-1} for M = N_2; the reaction has the expected negative temperature dependence, perhaps around T^{-3}, although these numbers must be considered preliminary. For HNO_2 formation, the rate is 2 to 3 times slower, and the temperature dependence is similar. For $OH + O_3$, we have gone through a comedy of misquotation, my early upper limit of 5×10^{-13} cm^3 $molecule^{-1}$ sec^{-1} having been variously made into an equality, and, in the Proceedings of the CIAP Survey Conference among others, by misprint into a lower limit. The very much smaller upper limit of 1×10^{-16} by Langley and McGrath, which is based on very indirect evidence, would remove the reaction from atmospheric importance. Dr. Anderson has quite recently begun direct rate measurements and finds a preliminary value of 6×10^{-14}, almost 3 orders of magnitude faster than Langley and McGrath's upper limit. Work on these reactions will be completed very soon. I reassert my earlier estimates of $OH + HO_2$ and $O + HO_2$ as being very fast atom-transfer processes with rate constants in excess of 10^{-11}, but am quite uncomfortable with Hochanadel et al.'s very large 2×10^{-10} for $OH + HO_2$, since I do not know of any molecule-molecule reaction which proceeds at anywhere near that rate.

At this point, let me put in a brief plug for reaction-rate theory. I was delighted to hear Dr. Garvin mention it. Correlation with, and estimates by, Benson's thermochemical transition-state theory or Johnston's BEBO theory of potential energy surfaces are always welcome, and experimentalists should make maximum use of rate theory at all levels of sophistication.

Now for the points of controversy. The first one has to do with Dr. Garvin's large matrix of potentially important atmospheric reactions. While I am in full agreement with the notion that we must not close out reaction channels prematurely, or forget about them altogether, I do want to caution against spreading ourselves too thin and perhaps expending an inordinate effort on a remote corner of that vast matrix. The obvious, common-sense remark is that some few processes must be very much more important than most of the other ones, and these merit study in greater depth and by several groups. It is here that the interaction of kineticists and modelers is particularly important, since it is the combination of atmospheric observations, simple models, and much insight which suggests the importance and need for study of certain reactions – such as, for example, the oxidation of NH_3 by OH which Prof. McElroy whispered to me just a little while ago is a potentially important source of NO_x.

My second point is perhaps just one of semantics, but I do object very strongly to the widely held notion that we are doing chemistry and photochemistry in order to provide input parameters for atmospheric models. It is my notion (clearly prejudiced) that one can do large-scale modeling in many different ways and get as many different answers. Surely, what we must try to understand are the basic physics and chemistry of atmospheric processes, and we are likely to accomplish this end through an optimum mix of atmospheric measurements, laboratory studies, theory, and imagination. I don't mean to belittle modelers; I just want to caution against the fascination (and large expense) of vast computer simulation programs which may become reminiscent of the story of the sorcerer's apprentice.

Last, I would like to mention the recent paper by Foley and Ruderman on the effects of past atmospheric nuclear tests, as a pressing issue and as a possibly very valuable past unplanned "experiment" on the modification of the ozone layer. I am doing so not because I find their conclusions compelling, but because a number of people here do not seem to be aware of the study.

Foley and Ruderman examined ozone records from various stations following the nuclear test series made by the U.S. and U.S.S.R., especially the latter's multi-megaton series in 1961/62, calculated NO production and stratospheric deposition to be equal to about a year's input due to a 1990 fleet of SST's, examined subsequent ozone records, and found no evidence of substantial ozone reduction.

CRUTZEN: Let me start by reminding you that above about 30 km, ozone is generally in a photochemical steady state (within 20%). Below that level, atmospheric motions are very important; meteorological processes have to be considered, and considered accurately. It is not just a matter of plugging simple eddy-diffusion coefficients into equations. Of course, atmospheric motions do influence ozone distribution, even above 30 km; ozone is probably dependent primarily on NO_x distribution, and NO_x distribution is influenced by both atmospheric motion and dissociation processes, which must also be considered.

The main region of ozone production – and this is another important point to remember – is between 25 and 35 km. Attention should be directed to this region as well as to the one in which SST's would fly. From this level ozone mixes downward by means of atmospheric motions which are difficult to describe, and supplies about half the total ozone content of the atmosphere.

By now we all know of the catalytic effect of NO and NO_2 in ozone destruction. When I pointed it out about three years ago, I estimated that about 20 ppb of NO_2 would be required at 30 km to help explain the "Chapman deficit." Theoretically, such an amount might be present, because experiments with photolysis of N_2O indicated that somewhere around 1850 Å about 10% of the photodissociation could give rise to N and NO. Using the data derived by Bates and Hayes, we got the required amount of NO_x.

Since then, it has been shown by Preston and Barr that the photodissociation process does not produce N and NO, but N_2O is still a source of NO via the reaction between $O(^1D)$ and N_2O. This process gives about 10 ppb of NO_x at 30 km, which is not sufficient to theoretically explain the observed ozone distributions. But then, thank heaven, Davis and his co-workers reevaluated the rate coefficients for the reactions $O + O_2 + M \rightarrow O_3 + M$ and $O + NO_2 \rightarrow O_2 + NO$, and the requirements for NO_2 mixing ratios at 30 km could be reduced to about 5 ppb, which can indeed result from the process $O(^1D) + N_2O$. In fact, Ackerman has reported a mixing ratio of 5 ppb for NO_2 somewhere around 30 km.

It may be that this is all a little too perfect. As we have heard, there are some very significant loss processes for NO_x, and dissociation of NO is also very important. It now seems to me that the theoretical amount of NO between 35 and 45 km may be so low that we might have difficulty in explaining the ozone profile in this region. Above 45 km, both the $O + O_3$ and the odd-hydrogen reactions become very important in determining the ozone concentrations. The fact that NO_x is so crucial, and its concentrations so sensitive to photodissociation processes, suggests the possibility of a solar-cycle influence on the ozone distribution. The dissociation of NO occurs at about 190 nm, rather low in the atmosphere, just above the ozone layer. Some of Heath's work indicates variations at 180 nm in solar flux over the solar cycle, so I would like to see UV radiation measurements made in this region over a complete solar cycle.

The importance of the conversion of NO_2 to nitric acid brings us to the problem of the balance of the odd-hydrogen species. The reaction $OH + HO_2 \rightarrow H_2O + O_2$ has been reported to be very fast, but two weeks ago I saw a report of a measurement indicating that it is slower at high temperatures by a factor of 10; I think that could do with some investigation. If that reaction is indeed ten times slower, then the reaction of OH with CH_4 becomes very significant.

The oxidation of methane is an exciting story which I will leave to Dr. McElroy. Let me say, though, that in the troposphere the methane and carbon-monoxide oxidation may lead to an important contribution to tropospheric ozone. The amount of ozone produced in the troposphere may equal or be larger than the estimated flux of ozone into the boundary layer of the troposphere. This possibility must be explored so that we can correctly set the lower boundary conditions for ozone on the dynamic models.

In closing, I would like to stress again that our research should certainly not merely concentrate on SST operating altitudes but should cover

the whole stratosphere so that we can understand all the processes.

McELROY: Professor Nicolet asked me to make some brief remarks on the importance of the methane/carbon-monoxide chemistry in the stratosphere. I think that the most important point is that the flux of methane into the stratosphere represents a very large source of free hydrogen for the stratosphere – some three orders of magnitude larger than the escaping amount of atomic hydrogen or oxygen. That indicates right away that the stratosphere should be sending free hydrogen down below the tropopause, rather than absorbing it.

In fact, the oxidation of methane probably represents a major source of stratospheric water, and the stratosphere is thus a source, rather than a sink, of tropospheric water. This seems to me nearly incontrovertible. It then raises a question as to the significance of the old Urey-Brewer 190° polar tropopause, and the idea that the stratospheric water mixing ratio is determined by the drying of air passing over the tropopause. These theories should be reexamined with methane as the source of water in mind.

Of course, having this large potential source of water in the stratosphere also introduces the possibility that some inhomogeneity in the mixing ratio of water exists in that region, or perhaps a variation with height.

As Nicolet said earlier, methane is a major source of stratospheric carbon monoxide; it is also probably the major source of total atmospheric carbon monoxide, more important than automobiles and the like. Carbon monoxide is important to the chemistry of the lower stratosphere. It is removed mainly by oxidation, absorbing the oxygen atom from OH, so, like methane, it can affect the equilibrium of H, OH, and HO_2, the dominant forms of odd hydrogen in the stratosphere. The reaction of OH with methane can influence the equilibrium concentration of OH in the stratosphere; I strongly endorse Professor Nicolet's remarks about the need for additional measurements of the rate coefficient for that reaction at stratospheric temperatures. I believe a factor-of-two change would introduce significant uncertainty into the problem of atmospheric photochemistry. Incidentally, it is possible that the carbon monoxide in the lower stratosphere is in photochemical equilibrium, rather than dynamically controlled, because of the faster rate of the CO + OH reaction.

The chemistry of methane is relatively simple, as Nicolet pointed out long ago. Methane is not re-formed in the atmosphere, so the chemistry is a one-way process of destruction. It is destroyed by OH, by photodissociation at high levels in the atmosphere, by $O(^1D)$, and by $O(^3P)$. The chemical time constant of methane varies from very long when the atmosphere is cold – perhaps 50 or 100 years at the tropopause – to very short at higher levels – months. That means that methane is potentially a very useful tracer of vertical motion. NCAR's recent measurements of methane at about 50 km indicate surprisingly large amounts of methane; this in turn implies that the stratosphere is a little less stable than some modelers, including myself, have thought in the past. The true state of the stratosphere may be closer to the curves that Nicolet labeled high or maximum eddy coefficients.

I think there is one incipient problem in the atmospheric chemistry that deserves mention: the total budget of atmospheric odd nitrogen. We know the rate at which the atmosphere is losing odd nitrogen; measurements have been made of the nitrate content of rain. However, the N_2O source is inadequate by some three orders of magnitude to balance this loss. The second most obvious possible source is industrial pollution, but Bates and Witherspoon counted that up and found that it too was too small. About the only thing left, as far as Jack McConnell and I can see, is oxidation of ammonia. The supply of ammonia is adequate to account for the odd nitrogen. The details of the oxidation path are still uncertain, but it is not unreasonable to suggest that oxidation is in part initiated by OH + NH_3 reactions. What we did was model, as best we could with the available chemistry, the aeronomy of atmospheric ammonia, bearing in mind that most of the ammonia condenses and is carried out of the troposphere by rain. A significant amount gets into the stratosphere, and if you compute the corresponding source of NO, you find that it is likely that ammonia is a larger source of NO_x in the stratosphere than N_2O is.

For the troposphere as a whole, ammonia is almost certainly a very significant source. It has some interesting properties, because it falls off

very rapidly with height in the stratosphere. Its time constant is rather short, so the associated NO_x production is confined to very low levels in the stratosphere. Above 20 km, N_2O is certainly the more important source. Ammonia is therefore probably a better natural indicator of the behavior of SST effluent, since it probably is providing a large source of NO_x in exactly the region of the atmosphere where the planes would fly.

LONDON: Let me say to begin with what a pleasure it is to finally see a *rapprochement* between those rivals of yore, the chemists and the meteorologists.

Until 10 or 15 years ago most atmospheric scientists regarded the Chapman reactions as playing the dominant, if not exclusive, photochemical role in the production and distribution of atomspheric ozone. Since then they have recognized that the photochemical system is much more complicated. Similarly, chemists and aeronomers used to treat the atmosphere as one-dimensional; now they realize that it must be viewed as multidimensional. Part of the reason for using the earlier approaches was to keep the analysis simple and gain some understanding of the major physical processes involved. It is now apparent, however, that a realistic solution to the ozone problem will require an understanding of the more complex photochemistry and dynamics. Paul Crutzen has already alluded to the fact that ozone in the troposphere and lower stratosphere generally has a long relaxation time, so the three-dimensional dynamics of the atmosphere plays a fundamental role in its distribution. The complexity of the photochemical-dynamic interactions makes modeling essential; it is absolutely necessary that the laboratory chemists and the modelers work together.

In my opinion, a reasonably complete understanding of the ozone budget and its variations will not be achieved for ten years or so — and even that may be an optimistic estimate. Most meteorologists agree that we still don't have a satisfactory theory of climate or long-term prediction of the state of the atmosphere. The non-linear interactive problem involves the transport of ozone and the effect of ozone as an active radiating gas that helps drive the circulation in the stratosphere, which in turn affects the photochemistry, which then varies the ozone distribution. As you can see, the process is a very involved, complicated one.

Even though it may take more than ten years to solve the entire problem, I think we can come up with some useful partial solutions in the next year and a half. We can tentatively identify the important factors in stratospheric ozone variations, and estimate their magnitudes within realistic uncertainties. Let me give you some illustrations. This first slide shows a distribution of the net atmospheric ozone production using an oxygen-hydrogen-nitrogen photochemical system involving 45 reactions. In this simple photochemistry, we have included the reaction of O_3 with OH, and assumed a coefficient for this reaction of 10^{-14}. At 10^{-13} the reaction would have been very important; at 10^{-16} it could be neglected. At 10^{-14} it has only a slight effect on the ozone system.

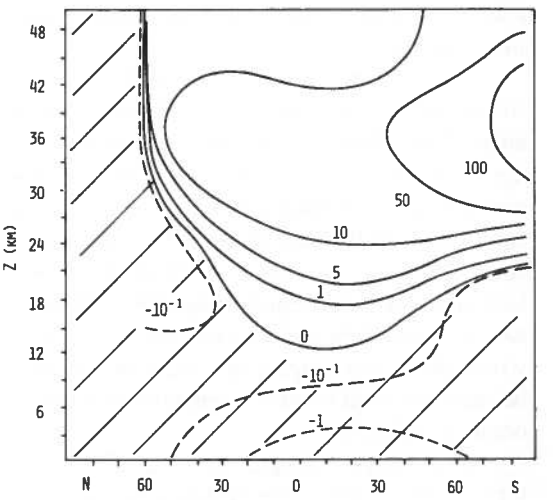

Slide 1. Ozone distribution (January 15, northern hemisphere) derived from an oxygen-hydrogen-nitrogen model. Photochemical source and sink = 10^5 cm^{-3} sec^{-1}. K_{O+NO_2} = 9.12 × 10^{-12} molec^{-1} cm^3 sec^{-1}. NO_x mixing ratio = 1 × 10^{-8} for Z > 30 km Global ozone net source, Z < 36 km: 2.88 × 10^{12} cm^{-2} sec^{-1}; 36 < Z < 50 km: 3.34 × 10^{12} cm^{-2} sec^{-1}. Total global ozone net source = 6.2 × 10^{12} cm^{-2} sec^{-1}

Also, we used a rate coefficient of 9 × 10^{-12} for the O + NO_2 reaction, which is about a factor of 3 higher than the values used previously. As a result, ozone destruction through the NO_x catalytic system is slightly more pronounced than before.

These calculations were made on the basis of an assumed vertical and mean-latitudinal global distribution of ozone. This assumed initial distribution is very important; if you assume too high a value, the production rate goes down considerably, and if you assume too low a value, the production rate goes up. In working with these model calculations you must be aware of their sensitivity to the original assumptions.

These calculations are by no means final. We do not have a source and a sink for the NO_x system. We assume a NO_x variation in the vertical, but no latitudinal variation. As has already been pointed out, an additional source of NO_x at high latitudes in the winter would mean a greater ozone sink there. On the other hand, in Nicolet's results showing the variation of NO production with zenith angle, about a factor of 10 less NO was produced at a very high zenith angle than for a vertical sun. Thus there would be less NO at high latitudes, and net ozone production would go up a little bit.

The net ozone production in this first slide is shown for winter with a mean January 15th sun angle. Production is very high in summer, with a maximum at an altitude of about 40 km. The net production is confined to the stratosphere, in the sunlit part of the atmosphere. NO_x destruction takes place in the region shielded from solar radiation. Various suggestions by Dr. Crutzen for ozone production and destruction in the lower stratosphere and troposphere were not included because we didn't want to get into that level of detail at this point.

Interestingly enough, with the NO_x mixing ratio above 30 km in the stratosphere assumed to be 10^{-8}, the total value of global production above 30 km is 6×10^{12} molec cm^{-2} s^{-1}. This is larger than the estimated sink at the ground, which is probably on the order of 5×10^{10} or 10^{11} molec cm^{-2} s^{-1}. The complicated photochemical system needs to be incorporated into a dynamic model involving atmospheric motions. Let me give you an example of the importance of ozone transport. We are presently working with the NCAR general-circulation model.* In this model, the atmosphere is divided into 12 layers, each 3 km deep, with a 5° by 5° horizontal grid mesh. The model goes from the ground up to 36 km, and from pole to pole. It is iterated every six minutes, and it takes 24 minutes to simulate one day. We put in an assumed ozone distribution, and then let the model transport the ozone, without any photochemistry. The second slide shows the results of some of the transport computations. The transport is separated into horizontal mean transport and large-scale horizontal eddy transport. The units here are relative to 3×10^{18} molec cm^{-1} s^{-1}. The solid line shows the effect of the ozone mean transport, and the dashed line the effect of the eddy transport.

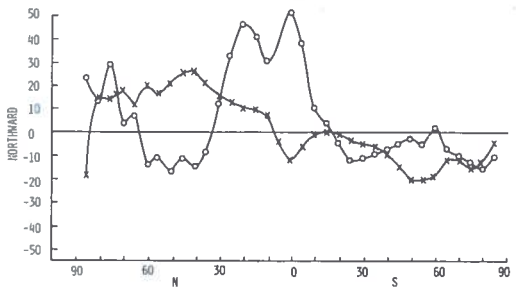

Slide 2. Vertically integrated transport of O_3 relative to 3×10^{18} molec cm^{-1} sec^{-1}. Positive = northward.

The slide clearly shows for the vertically integrated column the very marked effect of the Hadley circulation transporting ozone northward. Positive values here indicate ozone transport toward the North Pole. In the equatorial and sublatitude regions, the horizontal eddy transport is not very strong, and the mean transport decreases. In mid-latitudes, we have a return (negative) mean transport, so the eddy transport becomes very important; it is through this eddy transport that the ozone created in the equatorial region is transported poleward. A three-dimensional model shows that eddy processes also transport ozone downward into the lower stratosphere and upper troposphere, where it is conserved. In the southern hemisphere, horizontal ozone transport is much weaker. Even the eddies are much weaker in the southern-hemisphere summer than in the northern-hemisphere winter.

I think that these and other dynamic studies that couple atmospheric motions with the appropriate chemistry will eventually give us some reasonable indications of how perturbations in the atmosphere will actually affect the ozone distribution.

*The model is described in detail in Warren Washington's paper in this volume.

NARCISI: I have a question for Dr. McElroy about the balance of odd nitrogen and washout of nitrates. What about electrical discharges in the lower atmosphere as sources of dissociation of N_2, followed by a sequence of reactions going to nitric acid?

McELROY: That idea does appear in old textbooks, but when we put numbers into it, it fails by about two orders of magnitude to account for atmospheric NO_x.

STUHL: I have measured the rate constant of $OH + NH_3$ at room temperature; it is about 1.5×10^{-13}. If the published estimates of atmospheric OH are correct, and if the product NH_2 subsequently forms NO_x, the resultant NO_x would be much greater than the formation of NO_x by combustion processes, perhaps ten times greater.

McELROY: 1.5×10^{-13} is exactly what McConnell found necessary for the balance.

FRIEND: According to available estimates, the tropospheric mixing ratio of NH_3 is a few parts per billion, and the stratospheric mixing ratio of NO_x is several times greater. If we accept these estimates, how can tropospheric NH_3 be a major source of stratospheric NO_x?

McELROY: It's not as unreasonable as it sounds, and it depends on the rate coefficients for the production and loss processes in the nitrogen cycle. To the first order, the amount of NH_3 in the troposphere is determined by its rate of input from the ground and its mean residence time before rainout. Some fraction of this amount is oxidized to NO_x in the troposphere. The amount of NO_x in the troposphere depends on that oxidation rate and the mean residence time of NO_x before rainout. NO_x is less soluble than NH_3 in water, so in principle, the NO_x mixing ratio can exceed the NH_3 mixing ratio in the troposphere. The mixing ratios of both NH_3 and NO_x at the tropopause are determined by these considerations. The mixing ratio of NO_x will increase rapidly above the tropopause, reflecting downward flux of NO_x introduced in part by stratospheric oxidation of ammonia.

(UNIDENTIFIED): I have a question on the NO_x loss. Have you considered heterogeneous precipitation, and do you think it might be important?

NICOLET: We didn't consider such processes, but they would be slower than the homogeneous conversion of NO_2 to HNO_3 and the transport of HNO_3 vapor into the troposphere.

SISSENWINE: A few of us black-sheep meteorologists are unhappy about the inconsistency between the 190°K temperatures and the observed stratospheric humidity. Some of the humidity data are certainly questionable, but I think some of them are good. Yesterday Murcray showed good soundings indicating a humidity maximum around 20 to 25 km, which agrees with my soundings. Could this be explained by your suggestion that methane is a primary source of water vapor in the stratosphere? It struck me that it might be a better explanation than the convective-process one – evaluating the amount of cumulonimbus that gets up there, the surrounding temperature, and the mixing of the air, to show that a maximum is possible at this altitude.

McELROY: That depends on the details of the dynamics of the stratosphere. It seems to me that it is possible, at least in principle, for the methane source to lead to the kind of humidity inversion you are observing.

CRUTZEN: This finding really emphasizes the need for doing the analysis in more than one dimension.

BARRETT: Dr. McElroy, is there a reliable inventory of the production of methane from the ground, within a good order of magnitude?

McELROY: Yes. You have probably seen the paper which measured the methane produced by rice paddies, integrated that production, and found that the world's rice fields produced more non-CO_2 carbon than automobiles did. If you compute the necessary global source by calculating the sink of methane in the atmosphere, that source turns out to be ten times larger than

the rice-paddy source, which I think is not unreasonable if you consider the number of natural swamps contributing. The estimate is not really good enough, but I think it is within an order of magnitude.

(UNIDENTIFIED): Would someone on the panel give us a little more perspective on the day-to-night cycle? I am curious how far one can get without considering day-to-night effects on photochemistry.

LONDON: We have integrated over day and night in our own work. At these altitudes the nighttime effects are very small.

CRUTZEN: Day-night integrations are important for N_2O_5.

McELROY: Like Fred Kaufman, I'm concerned that the big models may get so far removed from the problem that we no longer understand what's going on. Big models have a very important place, but it is too easy to say that we'll solve the problem by building a big computer program – and then stop thinking. It would certainly be distressing, after running a program for 700 days, to suddenly find that it was missing the most important source of NO, or the most important sink. I think it is unrealistic to expect a global-circulation model to solve the very complex problem of stratospheric chemistry and dynamics, let alone give us definite answers to the ozone question within two years. Like Julius London, I think we'll be lucky if we get those in ten years. In any case, though, I think they will come from the combination of good measurements of the relevant constituents and imaginative thinking on the part of knowledgeable people.

ENGINE EXHAUST EMISSIONS SUBPROGRAM

A.K. FORNEY
Systems Research and Development Service
DOT Federal Aviation Administration
Washington, D.C.

ABSTRACT: The Engine Exhaust Emissions Subprogram will result in a projection of the amounts and types of effluents which will be deposited in the stratosphere by the high-altitude aircraft fleet projected for 1990. Progress on projects concerned with engine tests, fuels analysis, 1990 engine-emission predictions, and flight routes and frequencies is described.

SUBPROGRAM REVIEW

Exhaust Emissions from Today's Engines

Our first project covers the measurement of the exhaust emissions from existing aircraft engines: the YJ93-GE-3, the J85-GE-5, and the Rolls-Royce Olympus 593. The measurements are being made under conditions simulating flight in the stratosphere. The substances of interest to us are shown on Figure 1. We are not able to measure all these substances under the conditions of our tests; we have attempted measurements of the substances marked by the "X" on this figure. These substances are water, hydroxyl, hydrogen peroxide, nitric oxide, nitrogen dioxide, nitrous oxide, nitrogen pentoxide, carbon dioxide, carbon monoxide, total hydrocarbons, formaldehyde, sulfur dioxide, nitrous acid, nitric acid, and particulates. We used on-line instruments, spectroscopy, and laboratory analysis to make these measurements.

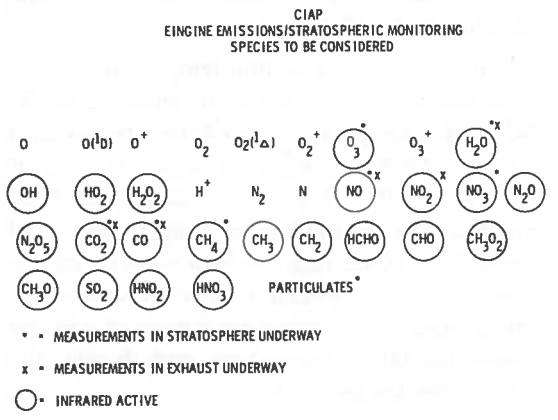

Figure 1. Species to be considered under Emissions Subprogram.

The YJ93 engine tests were designed to measure the emission levels at the engine exit plane over a wide range of flight speeds and altitudes. These tests were conducted at the USAF Arnold Engineering Development Center, Tullahoma, Tennessee. James Neely, Lloyd Grissom, and W.K. McGregor, all of that Center, report on various aspects of these tests in papers further on in this volume.

The J85 engine tests are scheduled for December 1972. They are being made in the propulsion wind tunnel at the Arnold Engineering Development Center. These tests are designed to determine what happens in the engine exhaust within the first 20 diameters of the engine exit plane, as the exhaust mixes with the high-speed airflow from around the engine. We hope that the results will be reported in Denver in June 1972.

Those of you who attended the Survey Conference here last February will remember that Rolls Royce generously offered to make emission measurements on an Olympus 593 engine, the engine being used in the Concorde supersonic transport, under conditions of interest to our program, and furnish the data to us. I am pleased to be able to report that these tests have been completed, and that M.R. Williams of Rolls-Royce reports the results in this book.

Fuels Analysis

The second project is a fuels analysis to determine the trace contaminants in aviation kerosene. The work under this project is being done by the Bartlesville Energy Research Center, Bureau of Mines, U.S. Department of the Interior. Richard Hurn from that Center describes this project in this volume.

1990 Engine Emission Levels

The National Aeronautics and Space Administration has agreed to conduct a study for the purpose of predicting the engine emission levels that can be expected in the year 1990. This study will include the engines of all vehicles that may be operating in the stratosphere. It is just now beginning, and its results will be reported at some time in the future.

1990 Flight Routes and Frequencies

The final project of this subprogram is the route projections study being conducted by the Engineering Systems Department, School of Engineering and Applied Science, University of California, Los Angeles. Its objective is to predict the flight routes, and flight frequencies along these routes, for the year 1990. Both technological and economic factors are being used to predict the upper and lower bounds of the routes and frequencies. These bounds, together with the engine emission levels for 1990, will determine the range of exhaust emission products injected into the stratosphere.

INTERPRETATION OF PUBLISHED EMISSIONS DATA

Now I should like to take a few minutes to clarify something that may have caused you some confusion, and has certainly caused me some concern.

There are several ways to specify the amount of the various trace substances in the exhaust of an aircraft engine. The way most used by the aircraft industry in the United States is called the emission index. Emission index is defined as the number of pounds of a substance in the exhaust per 1000 pounds of fuel consumed by the engine. (It has, of course, the same numerical value when specified as grams of the substance per kilogram of fuel consumed.)

The point I want to stress can be stated in this fashion: The emission index and the fuel consumed *both* vary with engine operating conditions, and these aircraft engine operating conditions are varying almost all the time. The existence of a varying emission index and fuel flow appear to have been overlooked entirely by both the SCEP [1] and SMIC [2] reports. Tables 1.5 and 1.6 in SCEP take the single set of GE4 engine data given in Table 1.4 and use it as if neither the emission indices nor the fuel flow change. SMIC makes the flat statement, "An engine consumes 33,000 lb of fuel per hour." (Section 9.2, second paragraph.)

The fact that emission indices for any given engine vary over the operating envelope of the engine may help explain why one sees so many different values reported by various engine manufacturers. In many cases they are reporting for different engine operating conditions, depending on the particular situation under consideration. Furthermore, the emission indices for one engine may be different from the indices of another engine because of design differences between the engines.

Let me explain. The emission index for nitric oxide, for example, is a function of three parameters: (1) the combustor inlet temperature, (2) the combustor inlet pressure, and (3) the combustor residence time. To simplify my explanation, I am going to discuss only the first of these three parameters. (I discard combustor inlet pressure on the basis that its influence is secondary, because the emission index for nitric oxide increases as the square root of the inlet pressure. I discard residence time by assuming, for the purpose of this explanation, that all combustors have essentially the same residence time under the same operating conditions.) Also, in the interests of simplification, let us ignore fuel nitrogen content, "non-standard" air temperature, and such variables.

The critical combustion temperature for the formation of nitric oxide is about 2000°K. Below that temperature, very little nitric oxide is formed; above that temperature, nitric oxide is formed rapidly. It can be readily seen from Figure 2 that the combustion temperature is well above 2000°K for high combustor-inlet temperatures. The next several figures show how the various engine operating conditions change the combustor inlet temperature, and thereby the combustion temperature.

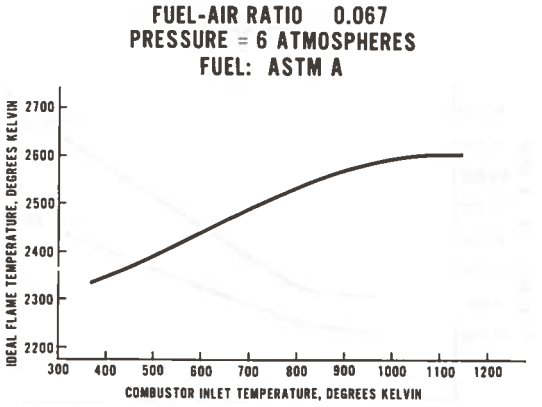

Figure 2. Ideal flame temperature dependence on combustor inlet temperature.

Figure 3 shows how the combustor inlet temperature increases with flight speed at a constant altitude and engine power setting. It also shows the difference between a typical subsonic engine, the Pratt & Whitney Aircraft JT9D engine used in the Boeing 747 airplane, and the GE4 engine that was planned for the U.S. SST airplane before its development was cancelled.

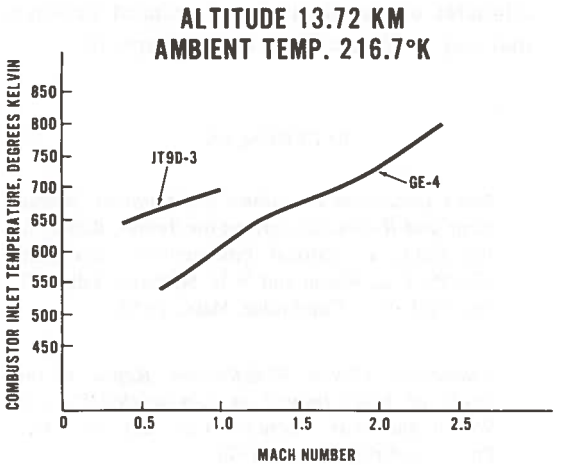

Figure 3. Combustor inlet temperature dependence on flight Mach number at 13.72 km.

Figure 4 shows the GE4 engine up to its cruise Mach number.

Figure 5 shows the effect of engine power setting at constant altitude and Mach number.

Figure 6 shows the effect of altitude at constant Mach number and engine power setting.

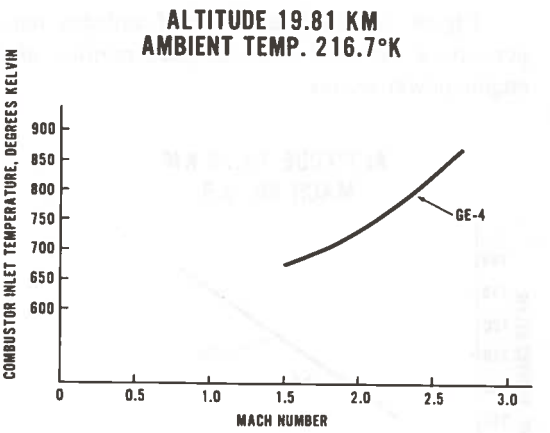

Figure 4. Combustor inlet temperature dependence on flight Mach number at 19.81 km.

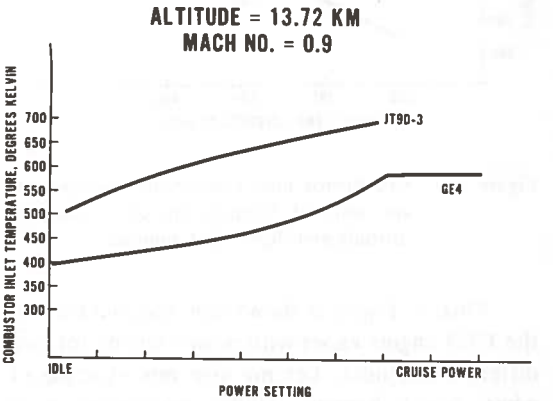

Figure 5. Combustor inlet temperature dependence on power setting.

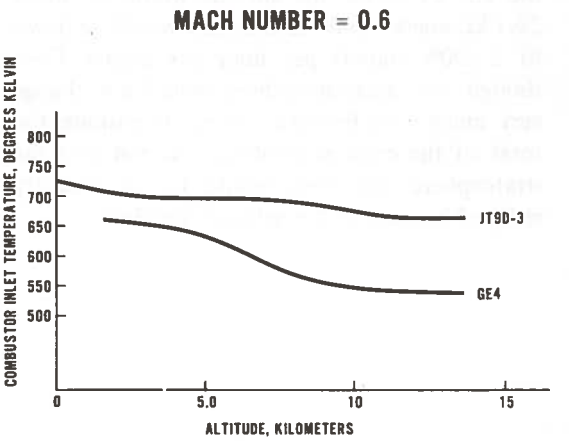

Figure 6. Combustor inlet temperature dependence on altitude at constant flight Mach number.

Figure 7 shows the effect of ambient temperature at constant altitude, Mach number, and engine power setting.

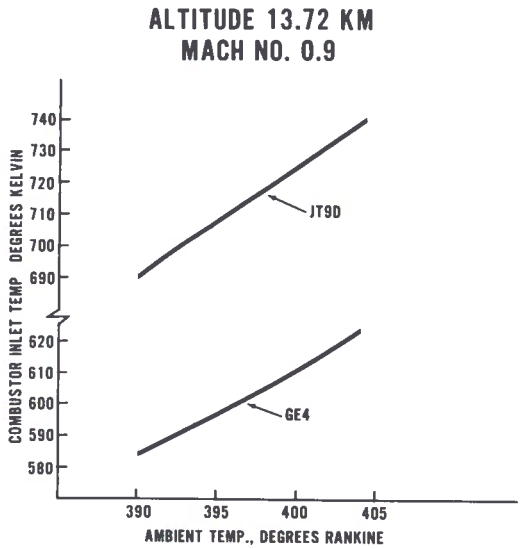

Figure 7. Combustor inlet temperature dependence on ambient temperature at a constant altitude and flight Mach number.

Finally, Figure 8 shows how the fuel flow of the GE4 engine varies with power setting for two different altitudes. Let me give one example of what could happen. Under maximum gross weight at takeoff, the U.S. SST would begin cruise at an altitude of 18 kilometers with a fuel flow of 34,000 pounds per hour per engine. At the end of cruise, the altitude would be about 20.1 kilometers and the fuel flow would be down to 23,000 pounds per hour per engine. Even though the emission indices would not change very much with this small change in altitude, the total of the exhaust products injected into the stratosphere per hour would be significantly reduced because of the reduced fuel flow.

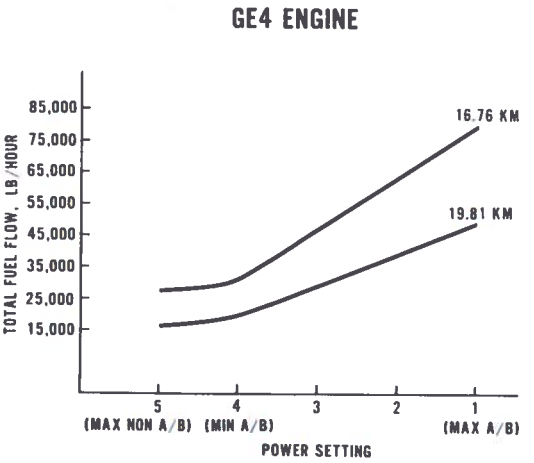

Figure 8. Total fuel flow dependence on afterburning power setting.

Later in this volume you will see the results of measurements of the emission indices of two different engines under simulated altitude conditions. Observe how these indices vary; observe how the fuel flow varies. Then the next time there is a SCEP or a SMIC conference I hope some representatives from engine and aircraft companies will be invited to help refine the estimates of the quantities of exhaust products that may be injected into the stratosphere.

REFERENCES

1. *Man's Impact on the Global Environment: Assessment and Recommendations for Action*, Report of the Study of Critical Environmental Problems (SCEP). C.L. Wilson and W.H. Mathews, Eds. MIT 162, MIT Press, Cambridge, Mass., 1970.

2. *Inadvertent Climate Modification: Report of the Study of Man's Impact on Climate* (SMIC). C.L. Wilson and W.H. Mathews, Eds. MIT 201, MIT Press, Cambridge, Mass., 1971.

EMISSION LEVELS OF THE OLYMPUS 593 ENGINE AT THE SUPERSONIC CRUISE CONDITIONS OF THE CONCORDE AIRCRAFT

M.R. WILLIAMS
Bristol Engine Division
Rolls-Royce (1971) Limited
Bristol, England

ABSTRACT: Emission levels of an Olympus 593 Mk 602 (production standard) engine have been measured under simulated cruise conditions for the Concorde aircraft. The methods used to predict emissions of carbon monoxide, unburnt hydrocarbons, and oxides of nitrogen are briefly discussed. A comparison of present measurements with earlier predictions indicates excellent agreement between the two sets of data.

The Olympus 593 Mk 602, illustrated in Figure 1, is a turbojet engine designed for efficient supersonic civil transportation at Mach 2. The flight profile is shown in Figure 2; it can be seen that the Mach 2 period of flight is of a cruise/climb nature in the stratospheric altitude range 15-18 km. The supersonic-cruise engine-pressure ratio is approximately 11:1, which, together with the substantial intake pressure ratio at this flight Mach number, results in combustion-chamber pressure and inlet temperature levels in the region of 565 to 915 kN/m^2 (5.6-9 atmospheres) and 770 to 830°K (925-1035°F). The combustion-chamber overall fuel/air ratio is comparatively weak, about 0.015.

The combustion chamber is of annular configuration, the fuel being injected into a primary zone by a 'vaporizer' fuel-injection technique. This system is conventional with Rolls-Royce (1971) Limited (Bristol Engine Division), and the Société Nationale d'Etude et de Construction des Moteurs Aéronautiques (SNECMA).

The tradeoff between engine specific fuel consumption and payload is very sensitive in the supersonic-transport application. A loss of 1% in combustion efficiency throughout the flight profile would incur a 5-6% payload deficit. For these reasons it is essential that the combustion efficiency be of a very high level; at the supersonic flight conditions it is approximately 99.9%, as can be seen in Figure 3. This figure is a correlation of combustion efficiency with combustion-chamber air loading; the air loading parameter is frequently used in aero engine combustion work.

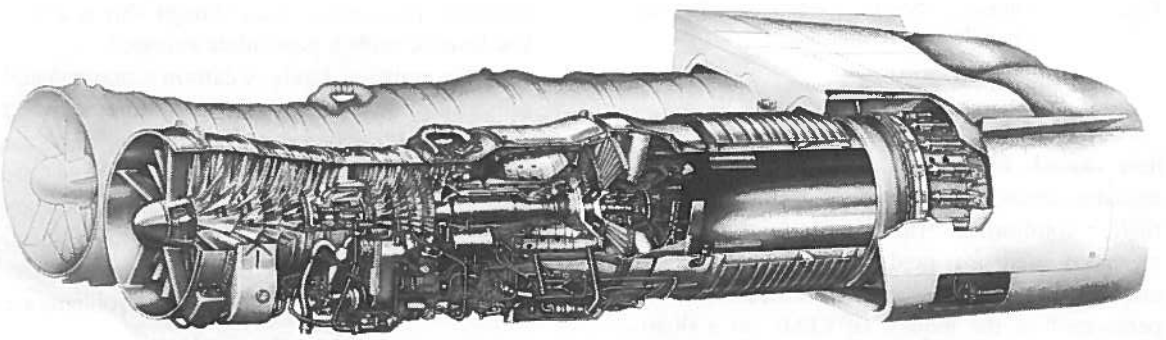

Figure 1. Installation of the Olympus 593 propulsion system.

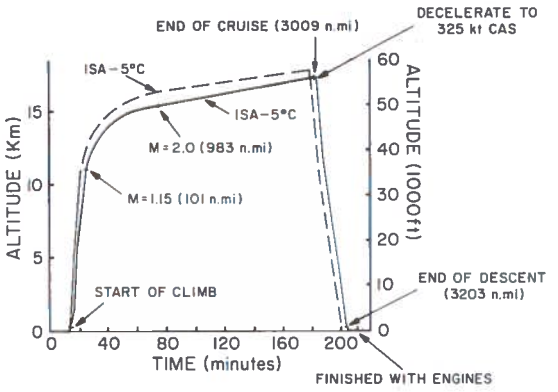

Figure 2. Time profile of a typical Paris – New York Concorde flight (Mk 602 engines).

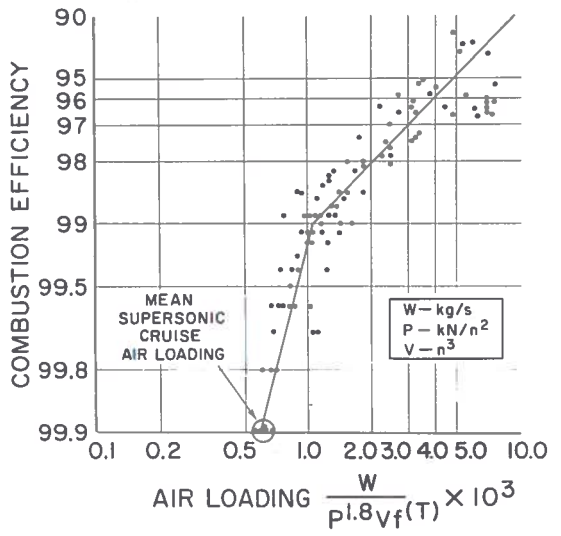

Figure 3. Olympus Mk 602: combustion efficiency versus loading relationship.

Over the last two years several organizations have asked for information on the exhaust emission levels of the Olympus engine at various flight conditions. This paper outlines the methods used for predicting supersonic-cruise emission levels and reports recent measurements, performed at the request of CIAP, on a flight-standard (production version) engine in the high-altitude test facility at the National Gas Turbine Establishment, Pyestock, England.

PREDICTION OF EXHAUST EMISSIONS AT MACH 2*

The major pollutant components of the exhaust are, of course, carbon dioxide and water vapor. Except for a very small correction for combustion inefficiency in the case of CO_2, the emission indices (g/kg of fuel) can be directly calculated from the composition of the fuel. (For CIAP purposes, this is being separately reported within the Engine Emissions Subprogram, though the values are expected to be approximately 3145 for carbon dioxide and 1270 for water vapor.)

The oxides-of-sulfur level is difficult to predict, simply because the sulfur content of aviation fuel currently in use throughout the world varies considerably. Calculations based only on the maximum fuel specification limits can be incorrect by an order of magnitude or more. Current average fuels give emission index values of 1.0 (U.S.) to 2.4 (U.K.) for sulfur levels of 0.05% and 0.12% respectively, expressed as SO_2. The fuels subprogram of CIAP will no doubt clarify this point.

The other main trace constituents are carbon monoxide, unburnt hydrocarbons, oxides of nitrogen, aldehydes, and carbon particulates. The emission level of the latter two pollutants is very difficult to predict, mainly because of a paucity of data on which to base an estimate. We have not attempted to estimate the low emission level of aldehydes that would be expected at this condition. If one assumes that the carbon particulate emission level of the combustor is solely a function of combustion pressure, then the emission index for carbon would be 0.1. This assumption seems too gross a generalization and probably pessimistic, even though this is a very low level of carbon particulate emission.

The emission levels of carbon monoxide and unburnt hydrocarbons can be estimated when the combustor efficiency level (Figure 3) and the composition of the inefficiency (Figure 4) are known. It can be seen that as the efficiency approaches 99.9%, the CO/C_3H_8 ratio varies considerably, principally because of inaccuracies in determining the C_3H_8 level. The problems are

*Throughout this paper I am discussing the emission levels at the exhaust primary-nozzle plane; I make no allowance for exhaust-plume or subsequent reactions.

probably due to several causes, e.g., sampling, line transfer, and sensitivity of flame-ionization detectors at levels approaching 2 ppm. We initially assumed the ratio to be approximately 40, but doubts arose as both the instrumentation and combustor were developed, and we decided to halve this ratio to ensure that we would not underestimate the unburnt-hydrocarbon level.

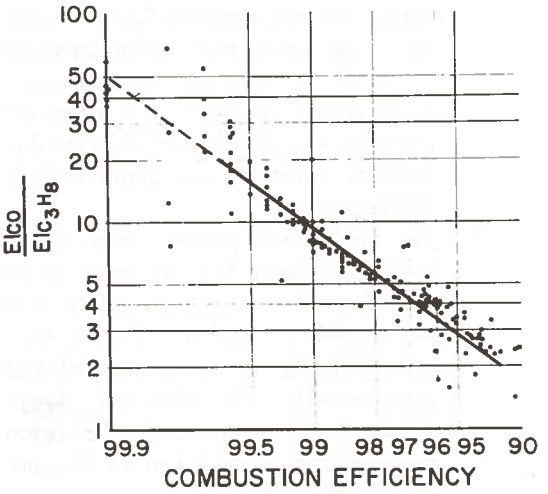

Figure 4. Combustion efficiency versus $EI_{CO}/EI_{C_3H_8}$.

The oxides-of-nitrogen emission estimates are basically corrected extrapolations of some rather limited, early ground-level measurements. The basic data was obtained by conventional sampling at the nozzle plane by means of a water-cooled averaging rake; the sample was transferred via a heated stainless-steel line operating at 150°C (302°F) and analyzed by the PDSA (phenol-disulfonic acid) wet-chemical technique. Figure 5 is an actual copy of the data available at the time of the prediction. The correlation method shown in the figure is basically the first step in the prediction technique. An outline of the method is as follows:

1. At the data test conditions available, the NO peak production rates are predicted. A fairly conventional "in-house" kinetic program is employed, which basically makes use of the Zeldovich mechanism. Humidity-level effects are ignored.
2. The NO emission level is assumed to be directly proportional to the relevant

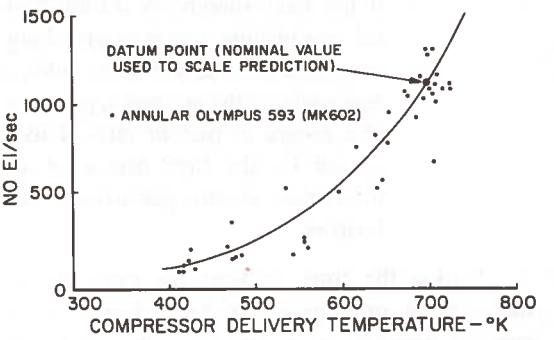

Figure 5. NO_X emission index as a function of compressor delivery temperature (T_3).

"residence time" (which is valid for the very short times being considered), which is assumed to be proportional to PV/WT (where P is the combustion pressure, V combustor volume, W combustion air mass flow, and T inlet air temperature), i.e., an overall combustor residence time.

3. A datum point is defined and a correlation constant obtained. (See Figure 5.)
4. An extrapolation to the Mach 2 conditions is now made from the datum conditions using steps 1 and 2.
5. Some further corrections, which have not been considered so far, may be required:
   a. *The effect of humidity:* The basic data contains typical fluctuations in sea-level humidity, which can be allowed for, but we have the uncertainties of extrapolating to the very dry conditions of the stratosphere. We have not found any experimental data on this effect, though many investigators, including ourselves, have increased the water-vapor levels and decreased NO production rates in good agreement with theory. Extrapolating this data to a dry atmosphere would imply increases in NO emission levels of between 10 and 25% over the correlated sea-level data, depending upon the data and method utilized.
   b. *The effect of combustor fuel/air ratio:* In correlating the sea-level data this effect was ignored because

it has been shown, by testing typical gas-turbine combustion chambers, that the NO emission index is essentially constant over representative ranges of fuel/air ratio. This is caused by the high degree of unmixedness in some gas-turbine combustors.

During the time between the early predictions, made principally for the National Academy of Sciences, and later estimates made for CIAP and other programs, we increased the estimated cruise-emission index for NO_x as NO_2 from 19 to 21 (at the average cruise/climb altitude). This increase was due principally to attempts to improve the correlation procedure by considering a local primary-zone residence time; it was also affected by changes in the predicted flight profile.

The predicted emission levels of carbon monoxide, unburnt hydrocarbons, and oxides of nitrogen at typical Mach 2 stratospheric flight conditions are summarized in Table 1.

Table 1. Estimated Olympus Mk 602 Emission Levels at Supersonic Cruise

Pollutant	Method of Measurement	Emission Index (g/kg of Fuel)*
NO_x as NO_2	Chemi-luminescence & PDSA	21
CO	NDIR	3.5
Total Hydrocarbons as CH_4	FID	0.2
Combustion Efficiency %	-	Approx 99.9%

*Altitude used for estimate - 16 km
Flight Mach Number - 2.0

ENGINE EMISSION MEASUREMENTS

An Olympus 593 bench-development-program engine No. 59337/2 was assembled to the Mk 602 production flight standard and installed in the No. 3 high-altitude test cell at NGTE, Pyestock. At this test facility it is possible to simulate the required Concorde flight profile. However, for the CIAP objective of determining the emission levels at Mach 2 and 15 to 18 kilometers altitude, there are two limitations:

1. The air-drying capacity is inadequate, in that it can only reduce the water mass mixing ratio to 300 to 500 ppm instead of the 1-3 ppm characteristic of the stratosphere. The design dryer performance was not achieved for the majority of the test points, and water-vapor levels up to 1200 ppm were encountered. A few test points were completed using sea-level ambient air when the day absolute humidity was approximately 2500 ppm.
2. The final nozzle pressure ratio is correctly simulated but, as there is no secondary flow around the engine, it is not possible to observe the wake reactions correctly. A rake was installed at approximately 20 diameters downstream, but it was not used; all emission measurements were taken at the primary nozzle exit plane.

A diagrammatic representation of the engine installed in the test cell is shown in Figure 6.

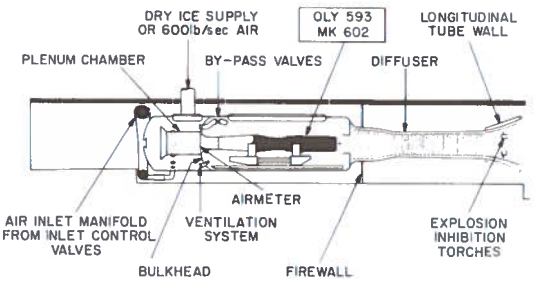

Figure 6. No. 3 cell at NGTE, Pyestock.

The water-cooled 7-point exhaust sampling rake was positioned horizontally 0.1 m downstream of the primary nozzle exit plane (see Figure 7). The sampling points were equally spaced and ganged to provide a single sample which was transmitted to the analysis area through an electrically heated stainless-steel line of 4 mm bore. There were two analysis stations, one just outside the engine test cell, with a line

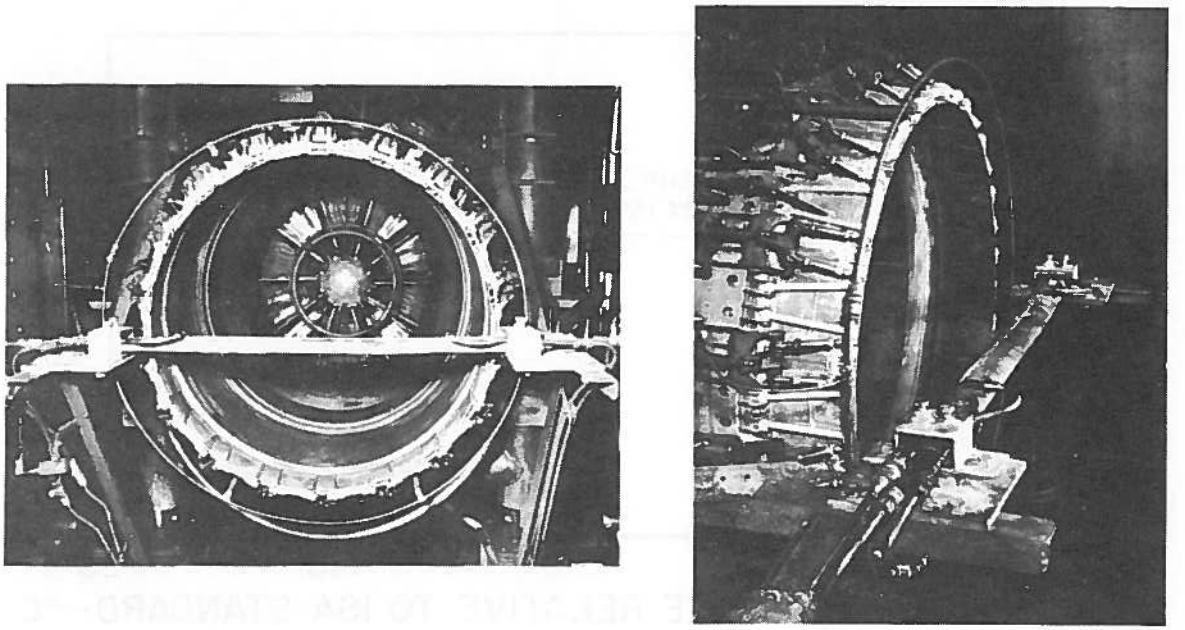

Figure 7. Exhaust sampling rake (primary nozzle exit).

length of 8 meters (Station 1), and the second in an analysis room, with a line length of 24 meters (Station 2). The residence time in the latter case was 1-3 sec, depending upon altitude.

The constituents determined and method of analysis used were as in Table 2.

Table 2. Location and Methods of Analysis

Constituent	Instrumentation	Station
Oxides of Nitrogen	PDSA	1 & 2
NO and NO_2	Chemiluminescence with converter	2
CO_2 and CO	Gas chromatograph	2
UB/HC	Flame ionization detector	2
C	Von Brand	2

RESULTS OBTAINED

The carbon dioxide levels were determined in order to assess the quality of the sample by comparing the sample fuel/air ratio with the calculated value obtained from a performance analysis of the engine. The error on this test series was approximately twice that normally seen for sea-level testing using the same technique, and was 10% on the "fuel rich" side of the calculated value. Why the error should increase over that of normal sea-level operation has yet to be determined.

The emission levels of oxides of nitrogen in terms of emission indices are shown in Figure 8, where it can be seen that the values obtained are somewhat below that for ISA-standard, zero-humidity conditions. However, the water-vapor level was considerably too high; also, the sample fuel/air ratio was incorrect and 10% fuel-rich, which may imply an error of similar magnitude between the measured value and the true mean.

The results quoted are those obtained by the chemiluminescence technique at Station 2. The agreement between PDSA and chemiluminescence was good and normally within 10%, the PDSA value usually being the lower. The chemiluminescence meter with converter indicated that only approximately 4% of the oxides of nitrogen was NO_2. This is in line with our non-reheated (non-afterburning) sea-level experience. There was no significant difference between the results at Stations 1 and 2.

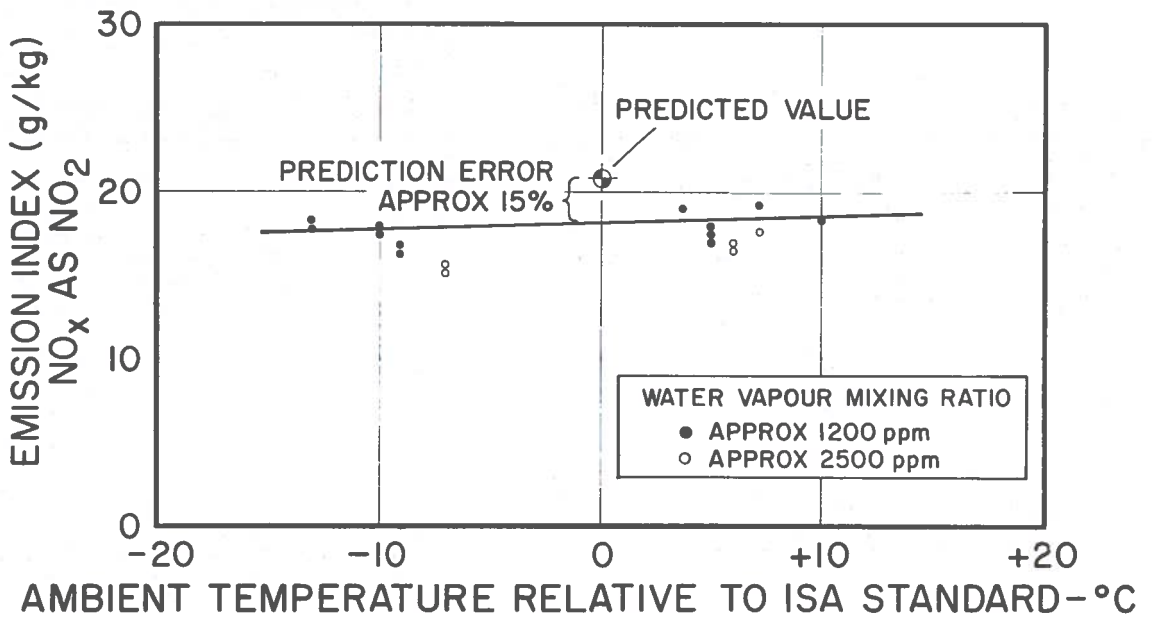

Figure 8. Olympus 593 Mk 602 NO_x emission index at altitudes of 15-18 km and flight Mach numbers 1.95-2.03.

The carbon-monoxide results in terms of emission indices varied between 1.4 and 4.6. Unfortunately, the FID installed was of the wrong calibration range; its minimum sensitivity level was equivalent to an unburnt-hydrocarbon emission index of 0.8, and all results were below this value, as would be expected. If we assume that the CO/C_3H_8 combustion-efficiency relationship is as shown in Figure 4, then the combustion efficiency is of the level anticipated, approximately 99.9%.

The carbon particulate level was approximately a Von Brand level 7, which, with our normal cross-calibration data, would confirm the estimated emission-index value of 0.1.

CONCLUSIONS AND RECOMMENDATION

Some aspects of this investigation into the emission levels of a production-standard Olumpus Mk 602 at typical Mach 2 stratospheric-cruise conditions were not entirely satisfactory, though the data obtained is in general agreement with the predicted emission levels. (The comparison between measured and predicted values is shown in Table 3.) The methods used for making these predictions from sea-level-static engine measurements appear to be reasonably accurate. We recommend that the predicted supersonic-cruise emission levels presented in Table 1 continue to be used as representative of the Olympus 593 Mk 602, the production version of the Concorde powerplant.

Table 3. Comparison of Estimated and Measured Olympus Mk 602 Emission Levels at Supersonic Cruise

Pollutant	Method of Measurement	Emission Index (g/kg of Fuel)	
		Estimated*	Measured**
NO_x as NO_2	Chemi-luminescence & PDSA	21	17.8 - 19.3
CO	NDIR	3.5	1.4 - 4.6
Total Hydrocarbons as CH_4	FID	0.2	< 0.8 (Instrument limit)
Combustion Efficiency %	–	Approx 99.9%	

*Altitude used for estimate - 16 km; Flight Mach Number - 2.0

**Simulated altitudes - 15.3 to 17.9 km; Flight Mach Numbers - 1.95 to 2.03

ACKNOWLEDGMENTS

Many people were involved in this investigation. I offer my thanks to all my colleagues involved at the National Gas Turbine Establishment, Pyestock, and in the Bristol Engine Division of Rolls-Royce (1971) Limited, who made this brief paper possible. I would particularly like to thank Colin Dawson and John Scott of Rolls-Royce who made an invaluable contribution in the areas of test-data analysis, correlation, and prediction. I also wish to thank the Directors of the Bristol Engine Division for permission to publish this paper as part of the Climatic Impact Assessment Program.

DISCUSSION

SCHIFF: Do you know what the efficiency of the NO_2-to-NO converter used in the chemiluminescence method is?

WILLIAMS: I was told that at the very low concentration level encountered, its conversion efficiency is pretty high, about 80 or 90%.

NARCISI: What was the NO emission level?

WILLIAMS: It was only 4% less than that of total oxides of nitrogen. 96% of the emission index is NO, even though NO_x levels are customarily reported as NO_2.

KIRCHHOFF: I am curious as to what chemicals you think are involved in the reduction of NO_x by injection of water vapor.

WILLIAMS: Our calculations indicate that water vapor merely suppresses the primary-zone peak temperature, which is the critical temperature in the production of NO.

(UNIDENTIFIED): How do you match stagnation temperatures in your experimental facilities?

WILLIAMS: We use a non-vitiating heater. The air from the compressors goes through a heat exchanger 60 or 80 feet tall, 10 feet in diameter, where it is warmed up to the 395 to 400°K necessary to simulate the ram effect.

SCHAINKER: Do you have any idea of the range of the emission-index values during ascent?

WILLIAMS: Predictions are available – FAA or CIAP people could give you them – but we have no estimates yet. The job is a difficult one, because of the reactions in the plume of the reheat system. A very expensive engine-test cell would be needed to actually take measurements.

(UNIDENTIFIED): What do you mean by "emission index per second"?

WILLIAMS: It is the combustor's emission index divided by residence time in the combustor, for that particular condition. The residence time is actually on the order of 1 to 1.5 milliseconds or so. It's a way of normalizing the emission index and is useful in combustor design engineering.

EMISSION LEVEL OF THE YJ93-GE-3 ENGINE, AN SST-LIKE ENGINE

JAMES NEELY AND DONALD L. DAVIDSON
ARO, Inc.
Arnold Engineering Development Center
Arnold Air Force Station, Tennessee

ABSTRACT: A test program was conducted in the J-2 altitude test cell of the Arnold Engineering Development Center to determine exhaust emissions of a YJ93-GE-3 afterburning turbojet engine.

The flight conditions at which data were taken varied from sea-level-static to 65,000 ft simulated altitude at Mach 2.7 and 75,000 ft at Mach 2.0, and included both afterburning and non-afterburning engine power settings. Emission measurements were made across the horizontal and the vertical centerline of a plane approximately two inches downstream of the secondary nozzle exit plane. A gas sampling system designed as nearly in accordance with SAE ARP 1256 as possible, consistent with the application, was used. An emissions-measurement package located approximately 60 feet from the probe, outside the cell, was used to make on-line measurements of CO, CO_2, C_xH_y, NO, NO_2, and NO_x. Off-line analyses were made by wet-chemistry methods from sample bottles and bag samples for gas, and electrostatic-grid capture and filter samples for particulates. In addition, NO and OH were measured in situ by narrow-line UV-absorption techniques.

Final data are just now becoming available from the test program, and data analysis is not yet complete. However, certain results are evident:

High-quality CO, CO_2, C_xH_y, NO, and NO_x emission data were obtained at each test condition, together with a limited amount of NO_2 data at three test conditions. Data trends with test-condition variables such as engine-inlet air temperature and pressure are generally consistent with those predicted by combustion technology. For example, CO concentrations decreased with increasing combustor-inlet pressure and temperature, while NO and NO_x concentrations increased under the same conditions. NO and NO_x levels increased with increasing equivalence ratio, while both CO and C_xH_y decreased. At all afterburning test conditions, there existed a central region of incomplete combustion at the exhaust plane. This region was characterized by high CO and C_xH_y levels (>2000 ppm), which can be explained by the annular-afterburner fuel-injection on the J93 engine. In the complete-combustion zone of the afterburning exhaust, NO_x concentrations (ppmv) increased no more than 50% relative to the levels at military power settings; CO levels increased up to 400% under the same conditions.

INTRODUCTION

The engine-emissions subprogram of the Climatic Impact Assessment Program is charged with the responsibility of obtaining emission data from engines as they are, and will be, operated in the atmosphere. Although jet engines have been in use for a number of years, engine testing has been viewed until recently from the standpoint of performance and safety. When the relationship of the engine and the environment was considered, it was to determine what effect the environment had on the engine. As concern for the quality of the environment has developed, the interaction of the environment/engine interface has come to be viewed from the other side – namely, what effect does the engine have on the environment? As it is impossible to approach the answer to this question directly, it has become necessary to separate it into a number of more simple questions which can be resolved. Some of these questions, in further simplified form, are presented in Figure 1.

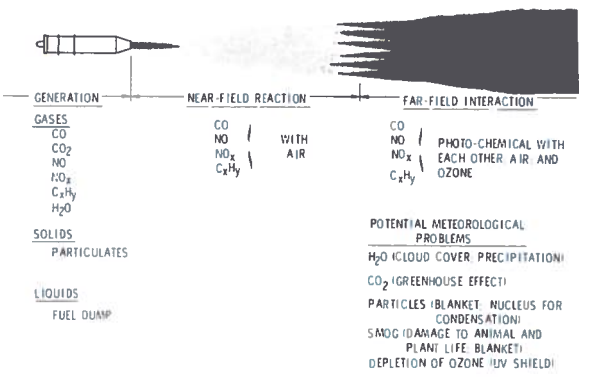

Figure 1. Environmental interactions of pollution emissions.

As the CIAP program began to get under way, there was a dearth of available reliable experimental data on the emissions from aircraft jet engines. This was graphically illustrated in February 1972 at the CIAP Survey Conference: the only presentation on the subject was a brief tutorial review of the emission characteristics of jet engines by Jack Grobman of NASA's Lewis Research Center [1]. Some emissions measurements have been made on several test stands in efforts to quantify the output of jet engines. A small amount of data has also been obtained at other than sea-level conditions; however, the test results are very limited. While the progress made to date in this field can hardly be classed as anything more than a beginning, it is at least that: a beginning.

SCOPE OF INVESTIGATION

As a part of the program to obtain data on the emissions output of aircraft engines at flight conditions, the DOT initiated a test program at the Arnold Engineering Development Center. The primary objective of this investigation was to determine the levels of emissions passing into the atmosphere from the jet engine as it operated at various simulated flight conditions. The scope of the program to be reported here was limited to a single engine, the YJ93-GE-3, operated at flight conditions as shown in Figure 2. Measurements were made at one plane approximately 2 inches downstream of the exit of the secondary nozzle. Other programs will investigate the reactions and interactions of the emissions with the environment; this program was limited to quantifying the emissions passing through the interface between the engine (generator) and the near field – in other words, making measurements at the nozzle exit plane.

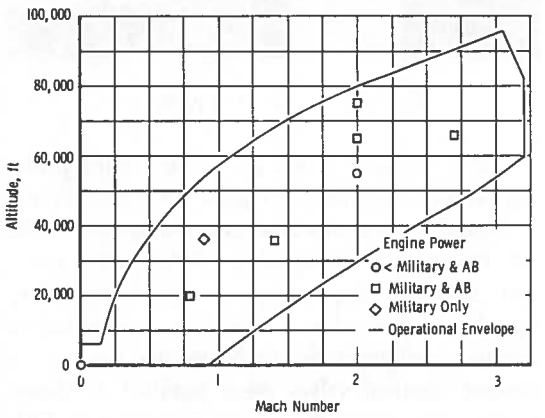

Figure 2. Simulated flight conditions investigated.

DESCRIPTION OF APPARATUS

Test Cell

The test was conducted in the J-2 test cell of the Engine Test Facility. The cell is 20 feet in diameter and 55 feet long. In it, aircraft jet engines may be tested at simulated flight conditions over a wide range of altitudes and Mach numbers. This simulation includes the production of the inlet total pressure and temperature associated with the flight altitude, Mach number, and inlet recovery, and the pressure surrounding the engine associated with the altitude. The internal chemical and fluid-mechanical performance of the engine during flight is thus reproduced in the test cell. Additional information about the cell and altitude testing capabilities may be found in Reference 2.

Engine

The General Electric YJ93-GE-3 engine was designed to power the XB-70, a Mach 3 bomber of the early 1960's. Although it does not represent current technology in some respects, it was the only available engine which would operate over the wide range of altitude and Mach numbers for which data were desired, and it is representative of much of today's engine technology.

The engine is a single-spool turbojet engine with afterburner, having a maximum sea-level-static thrust rating of 28,000 pounds, a maximum flight speed of Mach 3.2, and a maximum altitude capability of 95,000 feet. The engine is comprised of the following major components: an 11-stage compressor section, a combustion section, a 2-stage turbine section, a high-augmentation afterburner section, a variable-area ejector nozzle, and a control and accessory pod.

The engine compressor is an 11-stage stator unit having an 8.75 : 1 pressure ratio at sea-level-static, 100% corrected speed, and a corrected airflow of 261 lb/sec.

The main combustor is a fully annular type, with 32 fuel nozzles and a dual-energy ignition system, one for normal ground starts and the other for air starts.

The turbine is a two-stage air-cooled unit with a conical drive shaft, supported both front and rear by bearings.

The exhaust section consists of an afterburner and a guided expansion converging-diverging exhaust nozzle of fully variable area. The primary nozzle operates independently of the secondary nozzle. The afterburner incorporates two fuel-distribution systems, one for local burning and one for uniform burning. The flameholder contains three V-gutter rings and six catalytic ignitors.

Secondary airflow is directed aft between the engine shell and the aircraft engine shroud wall, providing a layer of air to cool the engine compartment and the jet nozzle components. Flow equivalent to 7 percent of the engine primary airflow is required at maximum afterburner operation. At certain non-standard operating conditions, the secondary airflow may exceed the 7 percent required for cooling. To provide aircraft inlet duct matching, the flow may reach as high as 20 percent of the primary airflow.

The engine control system is hydromechanical, with an electrical temperature override. Engine controls and accessories are enclosed in an insulated pod below the compressor for environmental, assembly, and maintenance purposes.

Major points of the engine configuration are shown in Figure 3. Additional details are available in Reference 3.

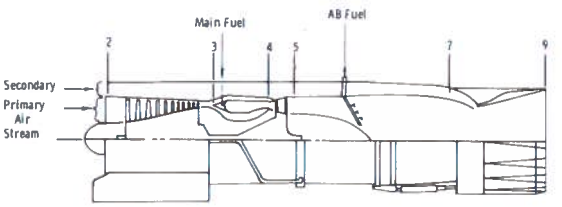

Figure 3. YJ93-GE-3 engine configuration.

Emissions Measurement

The major technical challenge of the program lay in the emissions measurement; it required the design, fabrication, and operation of a system to capture a sample of the exhaust at the nozzle exit, and transport it out of the cell to a sample-analysis package into which had been integrated analyzers and a calibration system to permit on-line measurements of the sample.

Sampling System

The SAE E-31 Committee has established guidelines for the design of a sampling system and testing approaches to the acquisition of emissions data on turbojet engines. These are contained in Aerospace Recommended Practice 1256 [4]. While this standard does not address some of the problems associated with the acquisition of data behind an afterburning engine, or from an engine in an altitude test cell, it was used for guidance in the design of the system.

Although data were taken only along the horizontal and vertical centerline of the exit plane, the design of the remotely controlled rake-actuation system, Figure 4, provided the capability of reaching any point in the exhaust plane. The rake itself contained a single sampling probe and an iridium/iridium-rhodium thermocouple, shown in Figure 5.

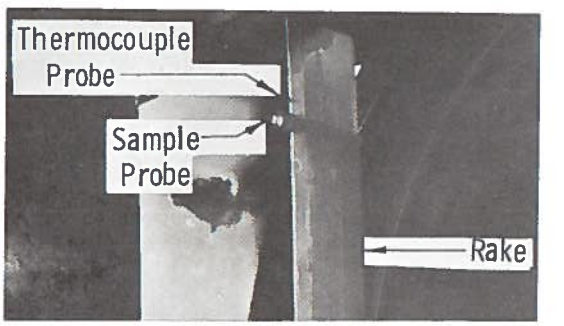

Figure 5. Sampling probe.

The pressure of the gas stream at the probe tip varied from 3.5 to 37 psia. Since the gas had to be delivered to the analyzer package at 15 psia for the proper functioning of the instruments, four bellows pumps were arranged so that they could be operated in a variety of series and/or parallel configurations to boost the pressure as needed; control valves were installed to dump excess gas when the pressure was too high (Figure 6).

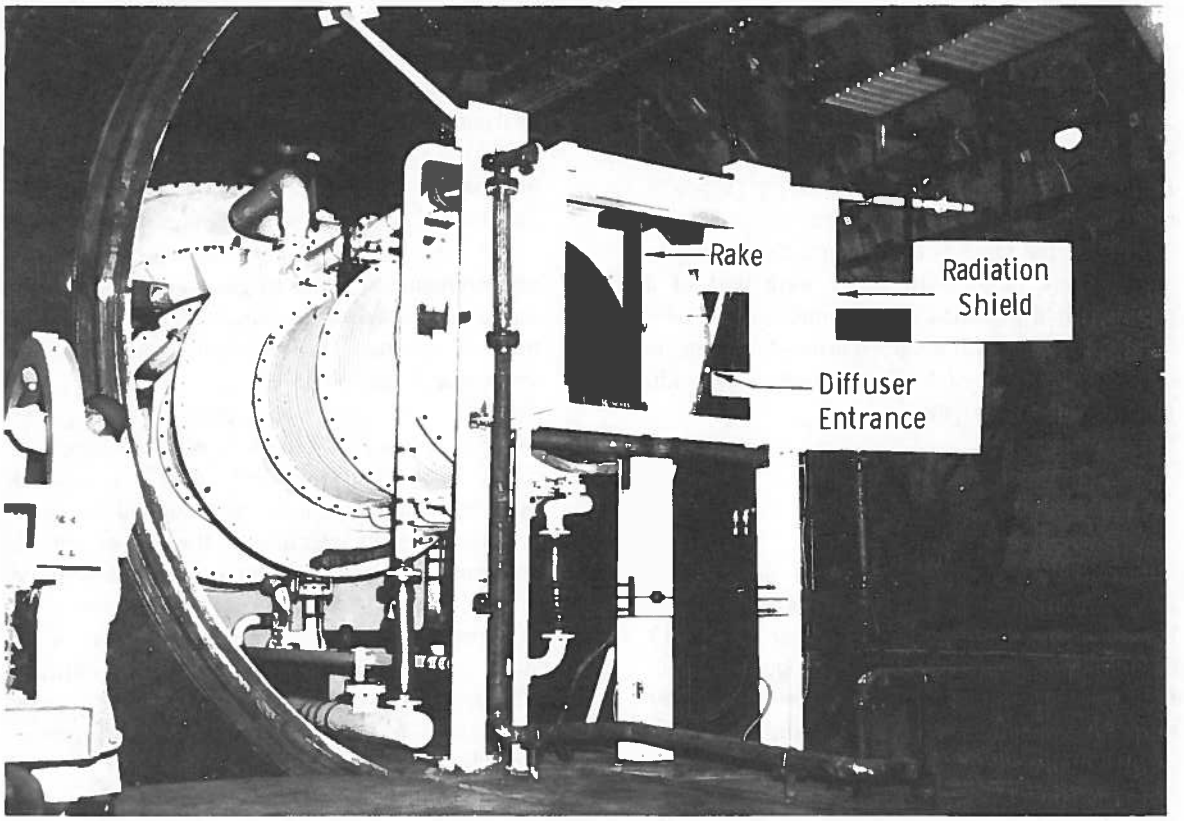

Figure 4. Emissions sampling rake and traversing system.

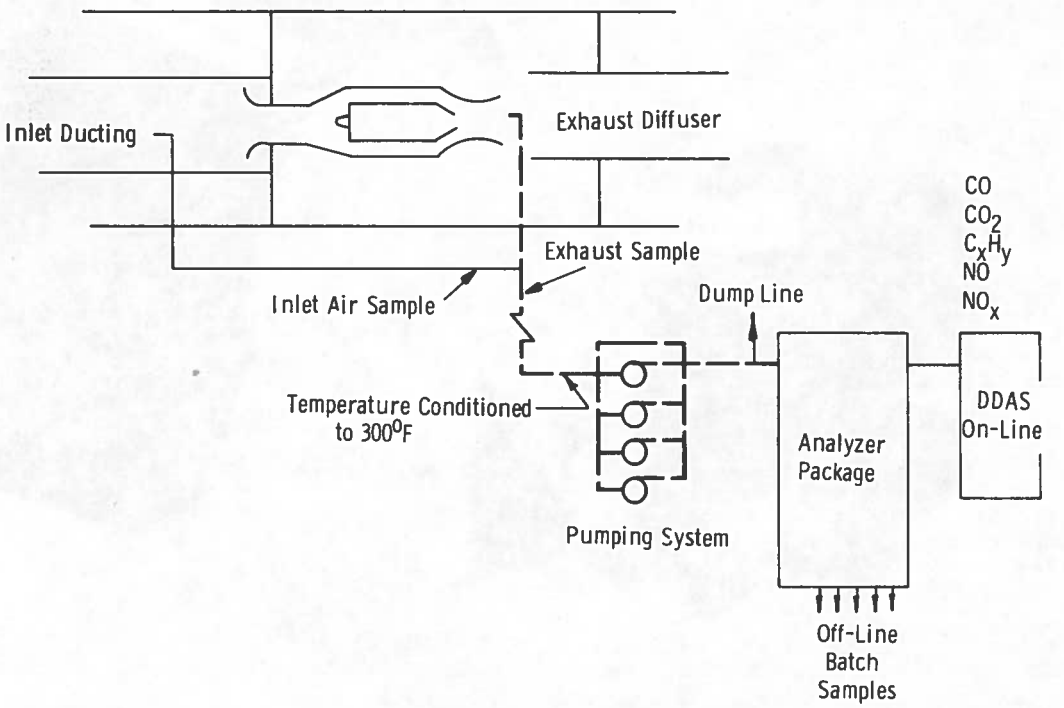

Figure 6. Emissions sampling system schematic.

The gas was cooled in the rake from total temperatures as high as 3000° F by the hot-water thermal-conditioning system. This water, at 300° F, flowed in a coaxial tube around the sampling line in the rake all the way to the tip. From the rake to the analyzer package (approximately 60 ft), the gas sample was maintained at 300° F by the same hot water counterflowing in an adjacent tube. Both tubes were part of a prefabricated insulated line. To make up for heat loss, heater tape was wrapped around the outside of the prefabricated line and covered by additional insulation (Figure 7).

Gas-Analysis System

The gas analysis system was designed to permit on-line analysis of eight gases plus particulates. This was accomplished by the use of 13 different analyzers, as shown in Figure 8. Real-time measurement of the samples was necessary to reduce the time required for testing.

In addition to the on-line analysis, off-line measurements were made. Both on-line and off-line measurements are shown in Table 1.

A more complete description of the gas-analysis system and its performance is presented by Lloyd Grissom in a paper entitled "Emissions Measurement System for Jet Engines in Altitude Test Cells," elsewhere in this volume [5].

A new and promising technique for in-situ measurement of exhaust-gas composition was successfully used to measure both NO and OH in the J-93 exhaust. This technique, which consists of passing a light beam through the exhaust and measuring the optical absorptivity of the gas at specific optical wavelengths, was developed at AEDC. It is very attractive because it avoids the flow disturbances of a sample rake and line, and permits, through selection of the proper optical wavelengths, the measurement of a wide variety of exhaust-gas constituents. Details of operation and performance are presented by Dr. W.K. McGregor in this volume in a paper entitled "Concentration of OH and NO in J-93 Engine Exhaust as Measured by Optical Instrumentation" [6].

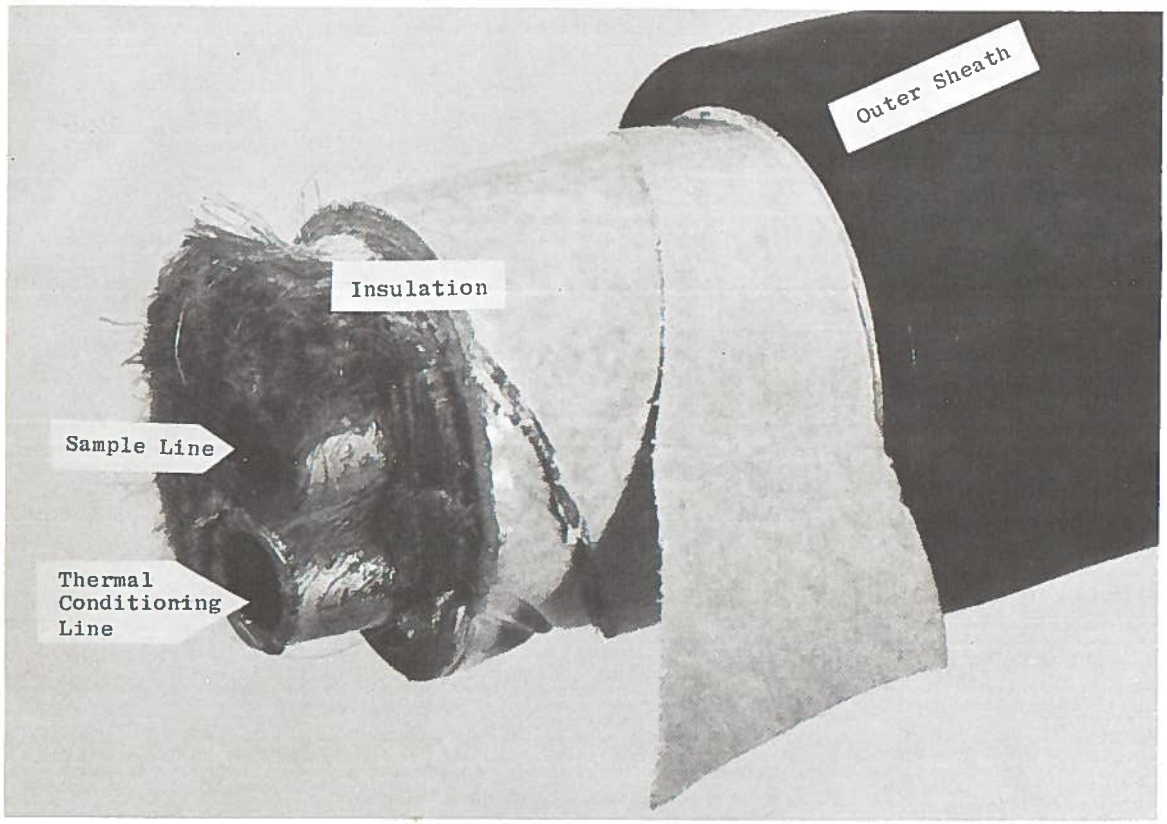

Figure 7. Sample transport line details.

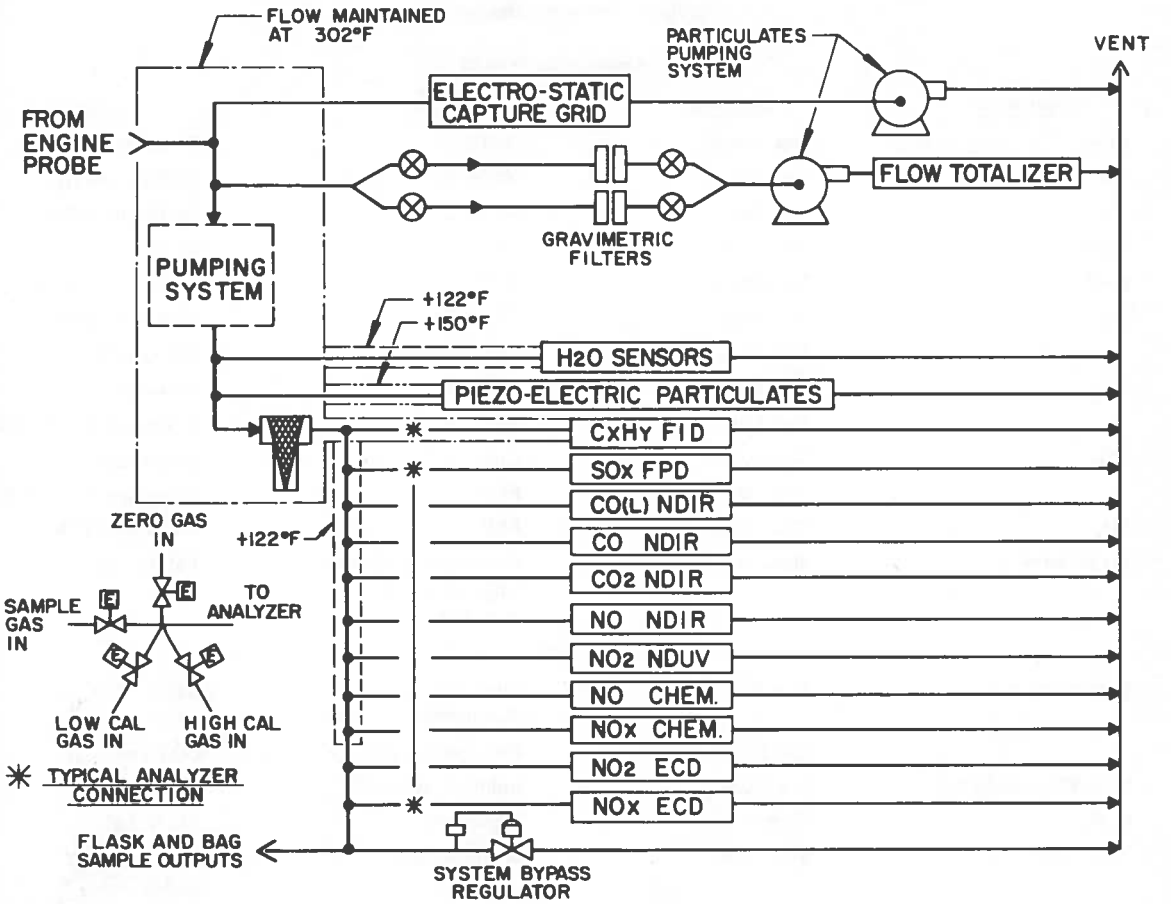

Figure 8. Emissions measuring system.

PROCEDURES

During the course of the testing, small deviations were made from some of the approaches described in this section. Nonetheless, the following discussion will provide the reader with a general knowledge of how the test data were obtained.

Gas Sampling

The instruments were calibrated in place by the use of standard zero and span gases. This was done before and after each test, and every 2-3 hours during tests which were of four hours' duration or more. After calibration, the engine was started and test conditions were set. The rake was moved into position, the gas pumps and pressure-control valves adjusted to establish the proper flow through the instruments, and the instrument output levels recorded by a digital data-acquisition system. An analog display from each instrument was monitored to ensure that the output levels were stable before the data point was recorded. After the data point had been acquired, the probe was moved to a new location in the stream and the acquisition procedure was repeated. At each point, engine and test-cell data were recorded as well. Data were also acquired through a probe at the front of the engine on each run, to provide a baseline for the air entering the engine.

ARP 1256 requires that at least 12 samples be taken in the plane being surveyed. In the initial plans for the program, it was decided that 13 measurements would be made, one on the centerline and three on the centroid of the three segments of equal area comprising each of the four quadrants. After several tests it was determined that, within the objectives of this program, more useful data would be obtained with fewer points in a shorter time by obtaining more than three points along a single

Table 1. Emissions Measurements

a. Continuous system

Component	Analysis	Sensor	Model
CO_2	Vol. Conc.	NDIR-S	Beckman 315B
CO	Vol. Conc.	NDIR-S	Beckman 315B
	Vol. Conc.	NDIR-L	Beckman 315BL
C_xH_y	Vol. Conc.	FID	Beckman 402
H_2O	Dew Point	VCD	Panametrics 1000
NO	Vol. Conc.	NDIR-L	Beckman 315BL
	Vol. Conc.	CID	TECO 10A
NO_2	Vol. Conc.	NDUV-L	Beckman 255BL
	Vol. Conc.	ECD	Dynasciences NR-210
NO_x	Vol. Conc.	CID	TECO 10A
	Vol. Conc.	ECD	Dynasciences NX-130
SO_x	Vol. Conc.	FPD	Meloy SA-160R
Particulates	Mass/Vol.	Electrostatic capture with piezoelectric microbalance	TSI 3210B

b. Batch system

Particulates	Mass/Vol.	Filter with gas total flowmeter	Gelman/PSC
	Size Distr.	Electrostatic capture	DOT Lab
SO_2, $SO_{\dot{x}}$, aldehydes	Vol. Conc.	Bubbler towers	AEDC Lab
C_xH_y	Carbon Distr.	Bag sample	AEDC Lab
Trace gases	Vol. Conc.	Bottle sample	BuMines Lab UCLA Lab
Fuel	H/C ratio, trace metals, aromatics, olefins, saturates	Wet chemistry and spectroscopy	AEDC Lab UT Lab
NO, OH	Remote absorption spectroscopy	Scanning UV	AEDC

radius to better define the profile. The 12 o'clock radius was used for the reference radius.

At some times, it was desired to obtain data for variables other than the flight conditions. To permit rapid acquisition of data from such a parametric investigation, a single measurement was made by leaving the probe at a fixed point on the 12 o'clock radius and varying the parameter under investigation.

Particulate Sampling

Particulates were sampled by two methods. One method was the electrostatic capture of particles on an electron-microscope grid. The method required the use of a custom-made device developed and constructed by personnel of the DOT Transportation Systems Center (TSC). After engine testing, the grids were packaged in test tubes and shipped to TSC.

The other method involved a filter pad for taking conventional filter samples. Prior to test, gravimetric filters were autoclaved, weighed, and placed in filter holders. The exhaust-gas flow through the filters was measured using a positive-displacement wet-test meter. After the test, the filters were sent to the chemical-analysis lab, where each was autoclaved and weighed. The weight difference was the particulate matter captured on the filter.

Flight conditions investigated during this program were those that provided information on specific points of interest and/or permitted parametric analysis of data. The engine-inlet pressure and temperature settings were determined from the geopotential (H) values from *The*

1962 Standard Atmosphere [7]. For the supersonic flight conditions, engine inlet pressure was reduced to take into account inlet recovery efficiency, according to MIL-E5008C.

RESULTS AND DISCUSSION

During the course of the test program, some 415 data points were obtained at the eight flight conditions investigated. Of these, 160 ultimately were reduced and are presented in a technical report on the program [8]. It is beyond the scope of this paper to present all the data acquired, but levels at certain representative points, and trends, will be given. While the data shown are valid for the test conducted, they are not comprehensive in the sense that no further experimentation is needed to establish the relationship of flight conditions to emissions.

No water-vapor or sulfur-oxide data will be presented, since neither analyzer worked properly during the test [5]. However, both quantities may be calculated from the fuel analysis by the following relationships:

$$\frac{\text{lb water}}{1000\ \text{lb fuel}} = \frac{9008\,\alpha}{12.01 + 1.008\,\alpha}$$

(where α is the hydrogen-carbon ratio)

= 1284 (for $\alpha = 2$; [4])

= 1234 (for $\alpha = 1.909$; fuel analysis)

$$\frac{\text{lb total oxides of sulfur (as } SO_2)}{1000\ \text{lb fuel}}$$

= 19.98 x % sulfur in fuel by weight

= 1.079 (sulfur content of 0.054%; fuel analysis)

No particulate data are presented from the on-line system [5], or from the sizing being done on the electron microscope. The latter will be reported at a later date. Data from the other off-line and batch samples will be reported either by the laboratory doing the analysis or by DOT.

Engine Inlet Samples

Although the inlet air was sampled at all flight conditions, the data at some of the points were not recoverable. The values shown in Table 2 will serve as baselines to indicate the typical content of the gas entering the engine.

Table 2. Engine Inlet Air Analysis

Pressure	16.21 psia
Temperature	487°F
CO_2	0.016%
NO	0.679 ppmv
NO_2	3.00 ppmv
C_xH_y	5.47 ppmv
H_2O (calculated)	345 ppmv

The unusually high hydrocarbon level results from the ethylene glycol which is sprayed in the air stream to prevent water from freezing on the air-cooling coils during the drying process in the compressor plant. Some of the material is carried along by the air stream directly to the test cell, or is deposited on the facility ducting, from which it is later re-entrained.

The air is dried in the compressor plant to approximately 345 ppmv of water for all of the high-altitude points. For the sea-level-static condition, the air contained approximately 1000 ppmv of water.

Nozzle Exit Profiles

Three flight conditions have been chosen for profile comparison because of their importance to the aviation industry: *Sea-level-static*, because that is where engines operate at the airport and because data may be obtained relatively inexpensively there; *36,000 ft, Mach 0.9*, because most commercial jet traffic today flies in that region; and *65,000 ft, Mach 2.7*, because of its importance to future possible SST flight regions. One might at first be inclined to assume that all parameters would change monotonically between sea-level-static and 65,000 ft, Mach 2.7; however, when these points are viewed on a plot showing combustion-zone pressure and temperature (Figure 9), it can be seen that this is not necessarily the case.

Total Pressure

Total pressure at the nozzle exit is presented in Figure 10a. This profile shows the presence of the low-energy secondary air flow which is bled around the engine and primary nozzle into the

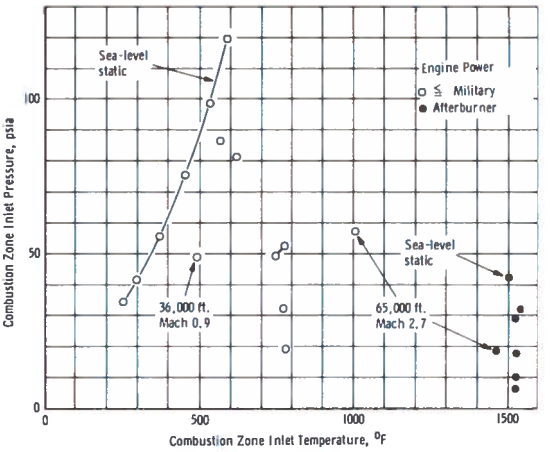

Figure 9. Combustion-zone pressures and temperatures.

secondary-nozzle entrance. The problem of designing a sample system for the widely varying probe inlet pressures is shown here, as related to both the radial variation and the changes due to flight conditions.

Total Temperature

The nozzle-exit temperature profiles at the three flight conditions are shown in Figure 10b. Here may be seen the effect of the dilution of the primary stream by the cool secondary stream in the boundary layer. Since overheating of the rake at sea-level-static flight conditions prevented the afterburner from being operated at levels higher than intermediate, no data are shown here at that flight condition.

Carbon Dioxide

The measured nozzle-exit radial profile of carbon dioxide (CO_2) is shown in Figure 10c. It should be noted that the emissions profiles in Figures 10c to 10g are shown on a radius-ratio basis. That is, they have been normalized to 100% nozzle radius for each set of flight conditions and engine power settings, instead of being shown in terms of distance (inches) as Figures 10a and 10b were. It can be seen that at the military power setting, the radial profiles are quite similar. The levels are changed, but remain essentially constant when the equivalence ratio (the ratio of the actual fuel/air ratio to the stoichiometric f/a value) is taken into consideration. Even at the idle and afterburning power settings, the CO_2 emissions are closely related to the equivalence ratio. (This will be shown in more detail in a later section.) The low level of CO_2 on the centerline is related to the facts that local values of the fuel-air ratio vary considerably in the afterburner, and that combustion is still in progress at the nozzle-exit plane, particularly along the centerline.

Carbon Monoxide

The radial profiles of carbon monoxide (CO) are presented in Figure 10d. They are shown in parts per million of volume (ppmv), as are the next three quantities. The relatively flat profile at military power is again readily observable. The engine design is optimized for this region of operation. Also, the products of combustion are quite well mixed by the time they have progressed through the turbine, the long afterburner, and the nozzle to the tailplane. The incomplete combustion along the centerline of this engine is seen at the 65,000-ft Mach 2.7 afterburning condition. The shape of the sea-level-static afterburner curve is directly influenced by the zoned fuel injection at the partial-afterburning power level at which data were taken.

Total Oxides of Nitrogen

The production of oxides of nitrogen (NO_x), which is closely related to temperature in the combustion zone, is shown in Figure 10e. As might be expected, the high-inlet-temperature, Mach 2.7 condition yields the highest level, but profiles are quite flat. At idle, the level is very low.

Nitric Oxide

The data indicate that nitric oxide (NO) (see Figure 10f) makes up most of the total oxides of nitrogen generated at the military power level. The profile at sea-level-static with afterburning is highly distorted, again due to the incomplete combustion and to interactivity with other gases in the stream.

Total Hydrocarbons

Hydrocarbon (C_xH_y) emissions were relatively low at the military power setting, although

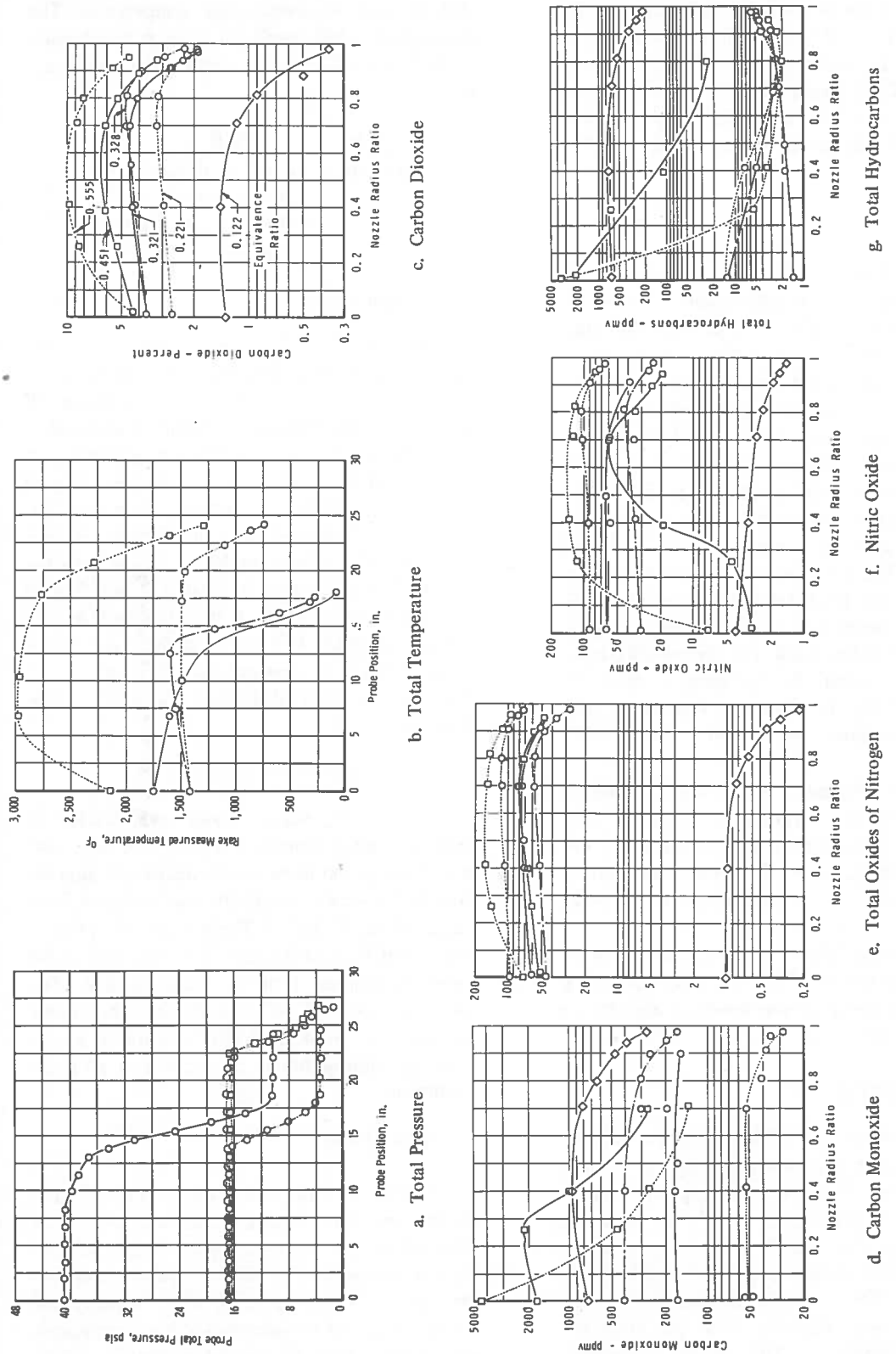

a. Total Pressure
b. Total Temperature
c. Carbon Dioxide
d. Carbon Monoxide
e. Total Oxides of Nitrogen
f. Nitric Oxide
g. Total Hydrocarbons

Figure 10. Nozzle exit profile. ◇, idle; □, afterburner; ○, military. —, 0 ft, Mach 0; – – –, 36,000 ft, Mach 0.9; ----, 65,000 ft, Mach 2.7.

the profile was quite different at sea-level-static from those at the two other conditions. The increased level near the nozzle wall is to some extent attributable to mixing with the secondary air which passed unaltered from the engine inlet to the nozzle. At idle and afterburning power settings, the much higher levels are readily evident.

Emission Index

One method of presenting the results of emission testing in a readily usable form is the use of an emission index: pounds of emission per 1000 pounds of fuel burned. These data, for the five gases measured, are presented in Figures 11a through 11e, as a function of equivalence ratio at flight conditions. Data are presented at six flight conditions from sea-level-static to 65,000 ft, Mach 2.7, and 75,000 ft, Mach 2.0. The flight conditions chosen will enable DOT to determine the influence of inlet conditions on emissions generation. The three Mach 2 flight conditions had a constant inlet total temperature, while inlet total pressure varied by more than a factor of 2. On the other hand, the engine-inlet total pressure was essentially the same at sea-level-static and 65,000 ft, Mach 2.7, but engine-inlet total temperatures were 60 and 500°F, respectively.

A review of Figures 10c through 10g shows that the probe at a radius ratio of 0.4 generally yielded data which represented an average of the output of the engine. Therefore, that probe setting was used as an indication of the total engine output in the following figures.

Power levels below military are shown at sea-level-static and at 55,000 ft, Mach 2.0; three different afterburner power levels are also shown at 55,000 ft, Mach 2.0.

Carbon Dioxide

The carbon-dioxide (CO_2) emission index is shown in Figure 11a. Over a range of engine conditions from idle to afterburning, the output varied only 8 percent. However, at constant power, the variation was less than 1 percent at military and only about 2 percent at afterburning power levels. This indicates an essentially constant combustion efficiency over this range of operating conditions. The index decreased slightly with increased altitude and increased slightly with increased inlet temperature. The theoretical index, based on uniform distribution of fuel, and 100 percent combustion efficiency, is:

$$\frac{\text{lb } CO_2}{1000 \text{ lb fuel}} = \frac{44{,}010}{12.01 + 1.008\alpha}$$

$$= 3138 \text{ (for } \alpha = 2; [4]\text{)}$$

$$= 3158 \text{ (for } \alpha = 1.909; \text{ fuel analysis)}$$

Carbon Monoxide

Whereas the CO_2 emission index is a measure of combustion efficiency, the carbon-monoxide (CO) emission index is a measure of combustion inefficiency. Figure 11b shows that this indicator decreases rapidly as engine power is increased to the military level. Also, as was seen in the CO_2 figure, as altitude increases, the combustors become more inefficient. In this case, the CO output of Mach 2 was approximately 5 times as great at 75,000 ft as at 55,000 ft. This was true for both the military level and afterburning. The CO output at the high temperature of Mach 2.7 was only about 15 percent of the value of sea-level-static at the same equivalence ratio.

Total Oxides of Nitrogen

Figure 11c, which shows total oxides of nitrogen (NO_x) expressed as NO_2, indicates that at military power there was a reduction of approximately 50 percent as altitude was increased from 55,000 ft to 75,000 ft. There was a 130 percent increase at 65,000 ft, Mach 2.7, over that at the same equivalence ratio at sea-level-static. The indicated level of NO_x at afterburning power settings was lower than that at military power levels by approximately 50 percent at all flight conditions.

Nitric Oxide

Indicated nitric oxide (NO) (Figure 11d) follows the same trends as the total oxides of nitrogen in the previous figure. It can be seen from a comparison of the two (when both are expressed as NO_2) that most of the military and afterburning NO emission-index levels presented are approximately 85 percent ±8 percent of the

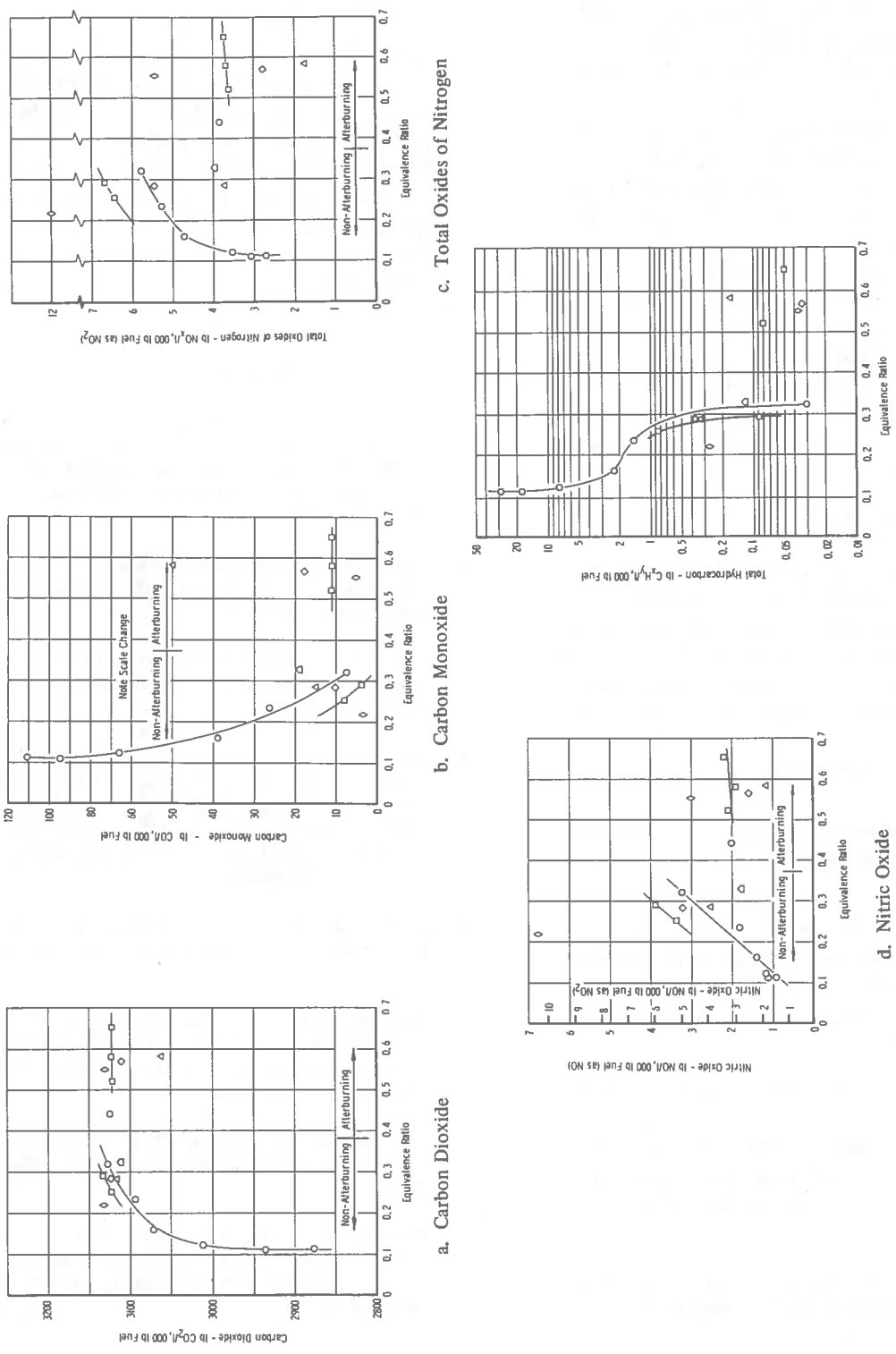

a. Carbon Dioxide

b. Carbon Monoxide

c. Total Oxides of Nitrogen

d. Nitric Oxide

e. Total Hydrocarbons

Figure 11. Flight conditions' influence on emissions index. ○, 0 ft, Mach 0; □, 36,000 ft, Mach 0.9; □, 55,000 ft, Mach 2.0; ◇, 65,000 ft, Mach 2.0; ◇, 65,000 ft, Mach 2.7; △, 75,000 ft, Mach 2.0.

NO_x value. At the cooler main-burner-inlet temperature points (sub-military power at sea-level-static; and 36,000 ft, Mach 0.9) the ratio of NO to NO_x tends to be lower (50-65 percent); the lowest main-burner inlet-pressure points (75,000 ft, Mach 2.0) had the highest ratio, approximately 95 percent.

The NO concentration measured by the spectroscopy method at 55,000 ft, Mach 2.0, was approximately twice the level measured by the basic probe method used for the data in this paper. Adequate end-to-end calibrations were conducted on the probe/instrument system to ensure the reliability of the data. If the spectroscopic data are correct, there is an inherent error in the basic method of sampling by probe; this would have a far-reaching effect on most of the data being acquired in the world today. Certainly this question is an important one, and needs early resolution.

Total Hydrocarbons

Figure 11e shows the hydrocarbon (C_xH_y) output of the engine. The values decrease quite rapidly as engine power is increased, until at the military and afterburning power level, the outputs are in the range of 0.1 lb/1000 lb fuel, a level so low that no significant trends can be ascertained.

CONCLUSIONS

The following conclusions can be reached from the foregoing data:

- A body of internally consistent data covering the broad range of flight conditions from sea-level-static to 65,000 ft, Mach 2.7, has been acquired by state-of-the-art practices.*
- Data trends were found to agree with those predicted from theory, and it has been possible to quantify the results in such a fashion as to permit reliable extrapolation to other flight conditions for this engine.
- Similar tests on other engines are needed to ensure that the same trends hold for other combustor types.
- Data obtained from in-situ optical measurements cannot as yet be reconciled with data obtained by sampling probes. Calibration techniques of the probe system have been verified; if errors are being introduced, the basic concept of probe-sensing is in question. Research efforts to certify measurement techniques appear to be of pressing importance.

* Requests for copies of the data should be addressed to the CIAP Office, Department of Transportation.

REFERENCES

1. Grobman, Jack, "Jet engine emissions," in *Proceedings of the Survey Conference*, February 15-16, 1972, Climatic Impact Assessment Program, Department of Transportation, DOT-TSC-OST-72-13, 25 (1972).
2. *Test Facilities Handbook* (Ninth Edition), "Engine Test Facility, Vol. 2." Arnold Engineering Development Center, July 1971.
3. "Operating and Service Instructions – YJ93-GE-3," Large Jet Engine Dept., General Electric Co., Cincinnati (1961).
4. *SAE Aerospace Recommended Practice – 1256*, "Procedure for the Continuous Sampling and Measurement of Gaseous Emissions from Aircraft Turbine Engines" (1971), available from the Society of Automotive Engineers, 2 Pennsylvania Plaza, New York, N.Y. 10001.
5. Grissom, J. Lloyd, "Emissions measurement system for jet engines in altitude test cells," in this volume.
6. McGregor, W.K., B.L. Seiber and J.D. Few, "Concentration of OH and NO in YJ93-GE-3 engine exhausts measured in situ by narrow-line UV absorption," in this volume.
7. *U.S. Standard Atmosphere, 1962*. U.S. Government Printing Office, Washington, D.C., December 1962.
8. Davidson, D.L., and Domal, A.F., "Emissions of a J93 turbojet engine for the DOT Climatic Impact Assessment Program (CIAP)," AEDC, to be published.

DISCUSSION

OLIVER: Why is your NO emission index for the J-93 a factor of three or so lower than the data Rolls-Royce showed for the Olympus 593?

NEELY: I don't know. A partial explanation may be that the Concorde data was presented as NO_2 rather than NO, which makes the difference a factor of two instead. The measurement techniques are similar, but since we don't know each other's equivalence ratios it would be premature to compare the indices.

OLIVER: Did you dry your air?

NEELY: The inlet air was dried to 200 ppm, but of course the gas coming from the engine contained water of combustion.

(UNIDENTIFIED): Does the cooling of the sample gas affect the amount of a substance measured, because of recombination at the lower temperature?

NEELY: The treatment of the sample gas was current state-of-the-art, but suspect. At the test conditions, not only was the air cooled, but the pressure was changed too; under some conditions the sample-line pressure was as low as 3.5 psia. This was a problem, since the air-quality measuring instruments we were using required the sample to be raised to atmospheric pressures.

TRACE COMPONENTS OF AVIATION TURBINE FUELS AND EXHAUSTS

A PROGRESS REPORT

R.W. HURN, J.W. VOGH, F.W. COX, AND D.E. SEIZINGER
Bureau of Mines
Bartlesville Energy Research Center
Bartlesville, Oklahoma

ABSTRACT: The objective of this work is to provide information on the amounts of non-hydrocarbon materials that may be present in aviation turbine fuels. A secondary objective is to determine the degree and manner in which trace components of the fuel can be associated with turbine emissions. This paper reports progress made to date in analyzing exhaust gas samples obtained from a YJ-93-GE-3 engine operating in the altitude cell at AEDC. Progress on the analysis of aviation turbine fuel samples gathered from four international airports is also presented.

INTRODUCTION

Turbine exhaust emissions are most readily conceived to be the products of the combustion of the hydrocarbon fuel. However, trace amounts of non-hydrocarbons are typically found in exhaust, and it follows that the amounts of any such trace contaminants that are ingested with the fuel consumed will also be discharged to the atmosphere in one form or another. Thus, if a complete inventory of aircraft emissions is to be drawn, information on the fuel's trace contaminants must be available. While much is known about the small amounts of non-hydrocarbon (principally metals) that may be found in turbine fuels, the information cannot be reliably associated with specific fueling operations or fuel origins. To obtain information which could be so associated, the Department of Transportation arranged for the Bureau of Mines to provide analyses of fuels from several major world air terminals.

As an adjunct to the fuels work, the Bureau has provided the sponsor with analytical data on samples of exhaust from an engine tested under altitude conditions at the Arnold Engineering Development Center (AEDC). These data were taken as a first gross attempt to inspect for what might be considered as "trace" exhaust components that could have special significance as atmospheric contaminants. Additional work with turbine exhausts is to be done to directly associate the trace components of the fuel with emissions from the engine.

EXPERIMENTAL WORK

Analyses of Samples from YJ93-GE-3 Altitude Cell Tests at AEDC

Exhausts produced during the course of tests of a J93 at simulated altitudes were collected (by AEDC personnel) into stainless steel tanks and shipped via air to the Bartlesville Center for analysis. Neither description of the engine tests nor information on measurements that were made on-site were available for reference in this progress report, but it is assumed that such information will be reported soon. Although information on the J93 work is not available from AEDC, earlier work with a J85-GE-5 engine may be of some interest in connection with the present study [1].

Analytical Methods

The analyses made on the samples covered a greater variety of components than have been examined in most experiments to date. Previous studies of turbine exhausts are represented by a field survey [2] which reported carbon monoxide (CO), carbon dioxide (CO_2), nitric oxide (NO), nitrogen dioxide (NO_2), total unburned hydrocarbons, and total aldehydes. The current work included all those plus hydrogen, methane, formaldehyde, hydrogen peroxide, nitrous oxide, and nitrite and nitrate ions.

Determinations were made by the following methods:

Oxygen was determined by gas chromatography on a Carbosieve-B column (4 ft X 1/8 in. outside diameter) at -30°C using a thermal conductivity detector.

Carbon monoxide and carbon dioxide were determined by nondispersive infrared (NDIR) analysis using the Beckman 315-A instrument.

Nitric oxide and NO_x were analyzed using the Thermo Electron chemiluminescence instrument.

Hydrogen was determined by gas chromatography on a Carbosieve-B column (8 ft by 1/8 in. O.D.) at -30°C using a helium ionization detector.

Methane and total hydrocarbons were determined by gas liquid chromatography (GLC) using established methods [3].

Nitrous oxide was trapped and concentrated on a Carbosieve-B sample collector and transferred to an analytical chromatographic system utilizing a temperature-programmed Carbosieve-B column (4 ft X 1/8 in. O.D.) and a 10% Carbowax 600 column (20 in. X 1/8 in. O.D.) held at room temperature. (The function of the Carbowax column was to delay the appearance of water in the chromatogram.) A thermal conductivity detector was used. This collection and analysis was somewhat similar to an established method [4].

Formaldehyde was determined by the chromatropic acid colorimetric method [5].

Total aldehydes were determined by the 3-methyl-2-benzothiazolone hydrozone (MBTH) colorimetric method [6].

Hydrogen peroxide analysis was carried out by oxidation of 1,2-di-(4-pyridyl) ethylene and conversion of the resulting aldehyde to the MBTH derivative [7].

Nitrite and nitrate were determined by a diazotization colorimetric reaction [8] with collection procedures as suggested by atmospheric photochemical studies [9]. The nitrite and nitrate were analyzed both as vapor samples, by collection in gas scrubbers, and as absorbed samples, by tank-washing procedures. The material collected in tank washings was analyzed and calculated as if it were vaporized; this value was corrected for the residual nitrite and nitrate in the gas phase and then combined with the gas-phase analysis level. Most of the nitrite and nitrate were found in the tank-washing solutions.

The procedures based on chromatographic, NDIR, and chemiluminescence methods were calibrated with gas blends of materials at suitable concentration levels. Methods based on colorimetric analysis were carried out using standardized instrument response curves and blank reference samples.

The sample tanks were held at 75-80°C during sampling for all analysis except the nitrite and nitrate tank-washing procedure. The 75-80°C temperature range was chosen to aid in the recovery of less volatile materials and to minimize adsorption on the tank walls. The temperature was not raised above 80°C in order to avoid excessive thermal degradation of the exhaust components.

Results

The results, summarized in Table 1, are reported on a volume basis, including the water vapor present. Hydrocarbon is reported as parts per million carbon; this is by common usage interpreted as the product of the molar concentration of hydrocarbon and the weighted average of the number of carbon atoms per molecule of hydrocarbon included in the measurement. In the flame ionization measurement the carbon atom value is obtained directly.

The components for which determinations were made differ greatly in chemical stability. Therefore, the holding or transport time had a varied effect on how reliably the measured values reflected those actually in fresh exhaust. Oxygen, carbon dioxide, carbon monoxide, hydrogen, methane, and nitrous oxide are all stable, so the values found should represent the fresh exhaust composition. Total hydrocarbon may be affected by reactions of olefins, by loss of organic oxygenates, and by retention of the high-molecular-weight components in the tank.

The other materials are unstable in varied degree. In our experience, formaldehyde and total aldehydes may either increase or decrease in aged samples, depending on the nature of the sample; in this instance, the values found

Table 1. Analyses of Exhaust Produced in Altitude Chamber Tests of a YJ93-GE-3 Engine

	Arnold Engineering Development Center sample number					
	1	3	6	8	10	9
Mode:						
Mach	2.0	2.0	2.0	2.0	2.7	2.7
Altitude (ft)	65,000	65,000	75,000	75,000	65,000	65,000
Power	Military	Mid-afterburner	Military	Mid-afterburner	Military	Mid-afterburner
Component, unit:						
O_2 (%)	15.9	8.6	15.2	10.8	17.8	9.8
CO_2 (%)	3.6	8.9	3.7	5.9	2.7	9.0
CO (ppm)	156	673	260	1,860	35	220
H_2 (ppm)	1.5	42.7	3.2	114.6	0.9	7.7
CH_4 (ppmC)	0.2	0.2	0.5	0.5	0.5	0.2
Total hydrocarbon (ppmC)	16.6	53.4	18.0	20.0	34.5	43.9
Formaldehyde (ppm)	0.53	1.49	0.25	0.42	0.02	0.17
Total aldehyde (ppm)	0.56	0.89	1.96	4.10	0.24	0.18
H_2O_2 (ppm)	—[a]	—	—	—	—	—
N_2O (ppm)	1.98	1.57	1.45	0.78	1.23	2.26
NO (ppm)	2.25	2.20	0.86	2.13	1.63	2.33
NO_x (ppm)	4.88	2.20	1.70	3.20	3.00	3.23
Nitrite[b] (ppm)	6.7	5.0	3.2	1.6	7.5	1.5
Nitrate[b] (ppm)	62.4	71.9	44.8	38.2	72.2	132.6

a. Dash (—) indicates not detectable (below 0.01 ppm).
b. Combined vapor and tank-washing samples. Interpreted as if all vaporized.

were low and less consistent than we would expect. We have little experience in hydrogen peroxide determinations, but the method as used was sensitive to 0.01 ppm in the gas phase. Hydrogen peroxide is known to react rapidly with nitrite under conditions that are used in chemical analysis [10]. It reacts fairly rapidly in gas phase with both NO and NO_2 [11]. Either course of reaction would be able to destroy all H_2O_2 before we could carry out analysis on the tank samples, and would account for our failure to observe it.

The NO and NO_x values are quite low in comparison to our usual experience with turbine and other engine exhausts; we expected this to occur because of reaction of the nitrogen oxides during the holding (i.e., transport) period. Estimates of NO_x levels in the raw exhaust based on the total NO_x, nitrite, and nitrate in tanks seem reasonable in comparison with data obtained elsewhere. These comparisons are best made on the basis of mass of NO_x emitted per unit mass of fuel burned.

These data corresponding to these samples are:

NO_x (as NO_2), (lb/1,000 lb fuel)	Mach No.	Altitude	Power
6.7	2.0	65,000	Military
10.1	2.7	65,000	Military
4.4	2.0	75,000	Military
2.9	2.0	65,000	Afterburning
5.0	2.7	65,000	Afterburning
2.3	2.0	75,000	Afterburning

Typical values from other tests of propulsion and auxiliary power units are on the order of 2 to 12 lb NO_x per 1000 lb fuel.

Note that these data are fairly self-consistent for given conditions (altitude and speed), and that NO_x emissions with the afterburner are approximately one-half those for the same conditions without the afterburner operating.

Analysis of Aviation Turbine Fuels

Samples of jet A turbine fuel were obtained from each of three different fuel suppliers both at New York Kennedy and at Los Angeles

International air terminals. Samples of jet A-1 were obtained from London Heathrow and Frankfurt International airports. In each case, a sample was drawn from the aircraft fueling hose during the course of a routine fueling operation. The samples were taken into acid-washed amber glass bottles and rigid precautions were taken against contamination of the sample at any stage of the sampling or handling operation.

The samples are being analyzed by a variety of standard techniques but with principal reliance upon atomic absorption for metals measurement. To date, trace metals and other analytical data have been obtained on the fuel samples from New York's Kennedy and the Los Angeles International airports. The currently available data, shown in Table 2, are based on replicated analyses of single fuel samples. Samples from the overseas airports have been received but analytical work has only just begun.

With regard to trace-metals content, one may note that the New York Kennedy samples consistently contain significantly greater quantities of copper and lead than were found in the Los Angeles samples. The differences in lead content are particularly striking, as is the high iron content of one New York sample. The significance of these differences is not addressed; they may in fact be totally insignificant. However, the metals content does appear to vary considerably. In additional work to be done, information will be gathered to reconstruct, as far as possible, the history of origin, processing, and transport for each sample. This information will then be used to determine whether some useful correspondence exists between the levels of specific trace components and the origin and/or process-transport history of the fuel.

The study will end with experiments in which turbine exhaust will be examined for those trace materials found in the fuel.

Table 2. Analytical and Trace Metals Data for Domestic Jet A Fuels

	Sample Number[a]					
	NY-1	NY-2	NY-3	LA-1	LA-2	LA-3
Specific gravity	0.8039	0.8050	0.8053	0.8156	0.8217	0.8138
API gravity	44.5	44.3	44.3	41.9	40.6	42.3
FIA[b], volume-percent:						
Paraffin	81.8	81.6	80.4	80.6	80.0	80.2
Olefin	2.5	2.1	2.1	2.6	2.4	2.5
Aromatics	15.7	16.3	17.5	16.8	17.6	17.3
Sulfur, weight percent	0.057	0.072	0.091	0.056	0.050	0.167
Nitrogen, ppm (μg/ml)	2	5	5	6	15	11
Phosphorous, ppm (w/w)	<1	<1	<1	<1	<1	<1
Element, ppb (w/w):						
Cadmium	3.8	1.2	0	0	0	0
Cobalt	0	0	0	0	0	0
Chromium	0	0	0	0	0	0
Copper	16.7	38.7	16.1	3.4	2.2	2.2
Iron	85.5	23.3	45.3	13.3	32.0	4.6
Magnesium	3.8	1.1	1.3	1.9	3.1	0.9
Manganese	1.5	1.5	3.3	1.5	1.5	1.5
Sodium	4.7	4.0	5.2	4.4	5.0	3.7
Lead	22.5	24.5	24.8	0	0	0
Strontium	0	0	0	0	0	0
Zinc	1.8	2.9	1.0	1.4	1.4	0

a. NY denotes New York Kennedy and LA denotes Los Angeles International.
b. Fluorescence indicating adsorption technique.

REFERENCES

1. Lazalier, G.R., and J.W. Gearhart, "Measurement of Pollutant Emissions from an Afterburning Turbojet Engine at Ground Level. II: Gaseous Emissions," AEDC-TR-72-70, 55, August 1972.

2. Cox, F.W., F.W. Penn, and J.O. Chase, "A Field Survey of Emissions from Aircraft Turbine Engines," BuMines Report of Investigation No. 7634, 28, 1972.

3. Dimitriades, B., C.F. Ellis, and D.E. Seizinger, "Gas Chromatographic Analysis of Vehicular Exhaust Emissions," *Advances in Chromatography*, *8*, (J.C. Giddings and R.A. Keller, ed.), Marcel Dekker, Inc., New York, 1969.

4. LaHue, M.D., H.D. Axelrod, and J.P. Lodge, "Measurement of atmospheric nitrous oxide using a molecular sieve 5A trap and gas chromatography," Anal. Chem. *43*, 1113, 1971.

5. Altshuller, A.P., L.J. Leng, and A.F. Wartburg, "Source and atmospheric analyses for formaldehyde by chromotropic acid procedures," Int. J. Air Water Poll. *6*, 381, 1962.

6. Coordinating Research Council, Inc. Report No. 415, "Oxygenates in automotive exhaust gas: Part I. Techniques for determining aldehydes by the MBTH method," 21, 1968.

7. Nauser, T.R., and M.A. Kolar, "Spectrophotometric determination of hydrogen peroxide in aqueous media with 1,2-di-(4-pyridyl) ethylene," Anal. Chem. *40*, 231, 1968.

8. Mullin, J.B., and J.P. Riley, "The spectrophotometric determination of nitrate in natural water, with particular reference to sea-water," Anal. Chem. Acta. *12*, 464, 1955.

9. Gay, B.W., and J.J. Bufalini, "Nitric acid and the nitrogen balance of irradiated hydrocarbons in the presence of oxides of nitrogen," Environ. Sci. Tech. *5*, 422, 1971.

10. Piccard, J., E.G. Peterson, and C.D. Bitting, "Determination of oxides of nitrogen (except nitrous oxide) in low concentration," Ind. Eng. Chem., Anal. Ed. *2*, 294, 1930.

11. Gray, D., E. Lissi, and J. Heicklen, "The reaction of hydrogen peroxide with nitrogen dioxide and nitric oxide," J. Phys. Chem. *76*, 1919, 1972.

EMISSIONS MEASUREMENT SYSTEM FOR JET ENGINES IN ALTITUDE TEST CELLS

J. LLOYD GRISSOM
Engine Test Facility
ARO, Inc.
Arnold Engineering Development Center
Arnold Air Force Station, Tennessee

ABSTRACT: An instrumentation system for the determination of selected exhaust emissions from jet engines operating under simulated flight conditions is described. The system functions over a total pressure range of 2.5 to 40 psia at the exhaust nozzle exit, and at exhaust temperatures up to 3600° R. Measured species include CO, CO_2, hydrocarbons, NO, NO_2, NO_x, SO_x, water vapor, and particulate matter. Redundant measurements of several species using different techniques are provided, and the results of these measurements are also discussed.

INTRODUCTION

Jet engine operations are the source of only a small part of those emissions defined as "air pollution" [1,2]. However, the species, concentrations, and the variations of these emissions with parameters such as altitude, flight Mach number and engine power setting, are of considerable interest. Also, because jet engines operate for long periods in a part of the atmosphere which is poorly understood in terms of chemistry [3], considerable concern has been expressed over the possible detrimental effects of high-altitude operations, particularly by supersonic aircraft.

Since facilities for testing jet engines under realistically simulated flight conditions over a wide range of altitudes and Mach numbers exist at the Arnold Engineering Development Center (AEDC), it was quite logical that the capability for evaluation of engine emissions be added when the need arose.

The system discussed in this paper was developed to characterize the emitted concentrations of the pollutant components deemed most important to a study of the impact of an operating stratospheric aircraft fleet upon the climate of the world (CIAP) [3]. This test series was conducted for the Department of Transportation (DOT). The DOT Transportation Systems Center also participated in developing the measurement systems, and furnished one of the particulate analysis systems. System design began in November, 1971. The system was first used in June 1972 in the Engine Test Facility's J-2 Test Cell at AEDC.

SPECIES MEASURED

Table 1 shows the constituents of the exhaust which the system was designed to measure. They comprised eight unique species: CO, CO_2, hydrocarbons, NO, NO_2, SO_x, H_2O, and particulates. In addition, NO_x ($NO + NO_2$) was also measured, permitting comparison with the sum of the individually measured NO and NO_2 values.

Both DOT and AEDC agreed that, as nearly as was practicable, the Society of Automotive Engineers Committee E-31 recommendations [4] would be followed, both as to analysis technique and gas-sample conditioning. As indicated in Table 1, the SAE recommendations covered only CO (measured by a non-dispersive infrared (NDIR) instrument), CO_2 (NDIR), unburned hydrocarbons (THC, measured by a flame ionization detector – FID), NO (NDIR or, provisionally, chemiluminescence), and NO_2 (non-dispersive ultraviolet – NDUV). The remaining compounds of interest were measured by the techniques which were judged to offer the most promise for our particular type of operation. These were NO_x (chemiluminescence), SO_x (flame photometric detector – FPD), H_2O (capacitance membrane), and particulates (by two methods – electrostatic grid for size distribution, and gravimetric filter for total weight per unit

Table 1. AEDC Engine Emissions Analyzer Types and Ranges

Constituent	Analyzer Mfr. and Model	Analysis Technique		Full-Scale Ranges
CO	Beckman 315B	Non-Dispersive Infrared	▲	0-1500, 0-3000, 0-7500 (ppm)
	Beckman 315BL	Non-Dispersive Infrared	▲	0-50, 0-100, 0-500 (ppm)
CO_2	Beckman 315B	Non-Dispersive Infrared	▲	0-5, 0-10, 0-20 (pph)
Hydrocarbons	Beckman 402	Flame Ionization	▲	0-5, 0-25, 0-50, 0-250, 0-500, 0-2500, 0-5K, 0-25K* (ppm)
NO	TECO 10A	Chemiluminescence	△	0-2.5, 10, 25, 100, 250, 1000, 2.5K, 10K (ppm)
	Beckman 315BL	Non-Dispersive Infrared	▲	0-50, 0-150, 0-500 (ppm)
NO_2	Beckman 255BL†	Non-Dispersive Ultraviolet	▲	0-50, 0-150, 0-500 (ppm)
	Dynasciences NR-210	Electrochemical Cell		0-25, 0-75, 0-250 (ppm)
NO_x	TECO 10A	Chemiluminescence with Converter		0-2.5, 10, 25, 100, 250, 1K, 2.5K, 10K (ppm)
	Dynasciences NX-130	Electrochemical Cell		0-100, 0-300, 0-1000 (ppm)
SO_x	Meloy SA-160R	Flame Photometric Detector		0-10 ppmv
H_2O	Panametrics 1000	Variable Capacitance Cell		-110°C to + 60°C (6 overlapping ranges) Dew/Frost-Point Temperature
Particulates	Thermosystems 3210B	Piezoelectric Mass Change Unit		0-.300, 0-.03, 0-.3, 0-3, 0-30, 0-300 (mg m^{-3})
	Gelman & Millipore	Gravimetric Filters		
	DOT/TSC	Electrostatic Precipitator		

▲ Techniques specified by SAE ARP-1256. (△ is an alternate.)
* Each range can be further desensitized by a factor of up to 10, yielding a minimum sensitivity of 0-250K.
† A "borrowed" 255A was used for the early part of the program.

volume). Also, to permit comparisons with other analysis techniques previously used in ground-level emissions testing at the AEDC, for which equipment was on hand, two additional analyzers, NO_2 (electrochemical cell – ECD) and NO_x (ECD), were added.

In addition, since the gravimetric-filter technique requires a long sample time, and involves much laborious hand work in evaluation of results, a particulates analyzer (piezoelectric mass change) which offered promise of continuous, instantaneous-rate, particulate-concentration measurement was included in the system design.

The appendix gives a brief description of the operating principles of the various analyzers, and indicates both their limitations and the precautions they require.

Table 1 lists the specific manufacturers and model numbers of the equipment chosen to implement the measurement concepts previously outlined. As may be seen from the table, considerable redundancy was employed. For CO, the wide variations in concentration expected over various flight conditions required the use of two instruments having widely different sensitivities. The units are basically very similar, differing only in optical path length of the sample and reference cells. The various full-scale ranges of each of the analyzers is shown in column 4. CO, CO_2 and THC data showed the widest range of values.

SYSTEM FLOW AND THERMAL CONFIGURATION

The essentials of the gas and particulate sample-handling system, and the general configuration of the entire emissions analyzer, are shown in Figure 1. The sample was divided into two parts upstream of the pumps, and one part was routed through the two particulates analyzers (gravimetric filter and electrostatic grid). A flow totalizer consisting of a positive-displacement gas flowmeter (wet-test meter) was used to measure

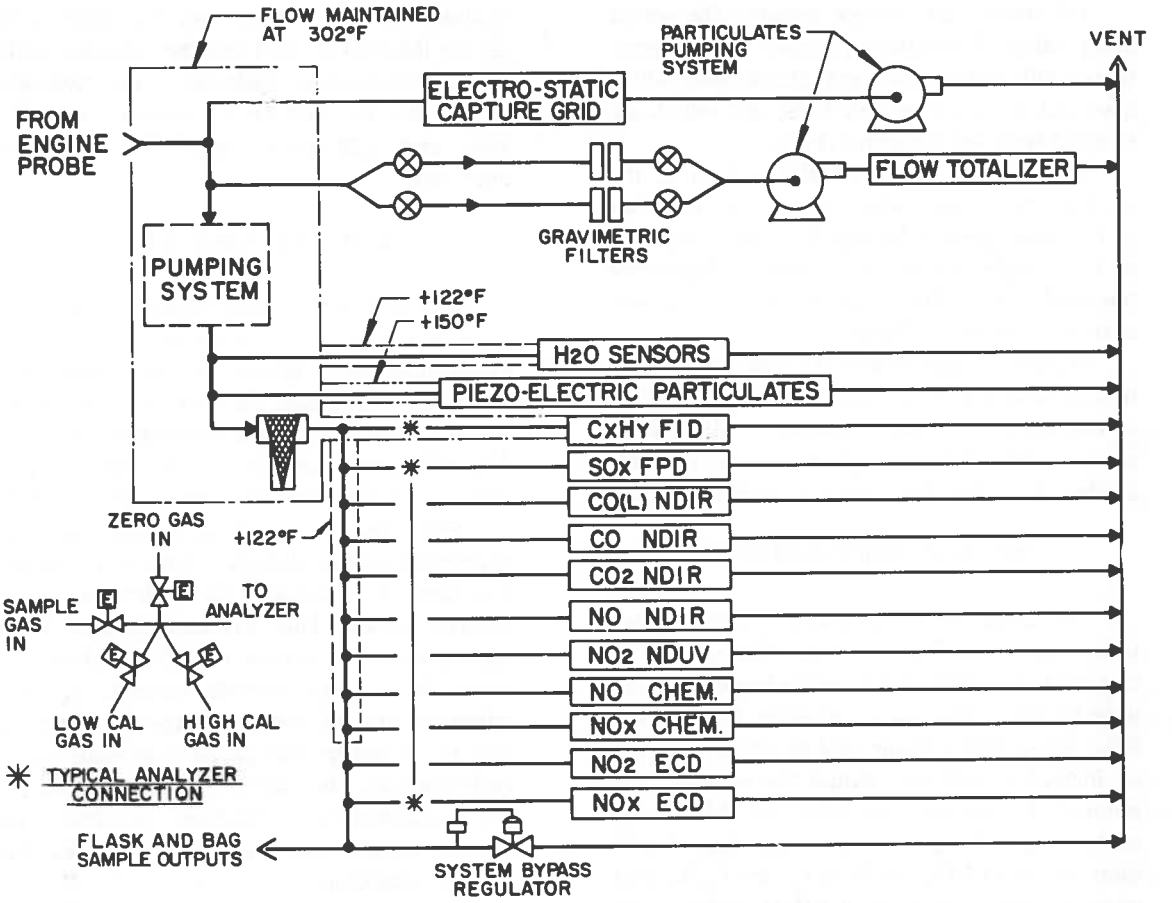

Figure 1. System flow and thermal conditioning.

the total integrated flow that corresponded to the loading of the gravimetric filter. Two identical filter legs were used alternately to expedite testing. The electrostatic grid was operated just long enough at each test condition to collect an adequate sample.

The second part of the sample stream was pressurized to 1 psig by means of the external pumping system described in [5], and a small portion (1 lpm) was passed through the piezoelectric microbalance particulates analyzer. Also, the water-vapor analyzer sensors were installed at this point in the flow system. The rest of the sample was then filtered to remove all particulates, and passed through the various analyzers for determination of the levels of the various gas species.

An automatic pressure controller was used to bypass and dump excess sample gas, holding the analyzer-inlet manifold pressure to within very close limits. Under all except the lowest engine total-pressure conditions, the bypass flow was several times larger than required for all of the analyzers, including particulates. The length and volume of the flow path from the analyzer-inlet manifold to the analyzer inlet was kept to the minimum possible in order to further minimize lag time in the system.

The sample temperature was regulated in three zones. The entire sample was conditioned to 302°F from the engine probe to the hydrocarbon analyzer to prevent condensation of heavier hydrocarbon compounds. In addition, the sample stream leading to the piezoelectric particulates analyzer was conditioned to 150°F. All other sample lines except for the electrochemical analyzers were conditioned to 122°F. The 302°F, the 150°F, and the 122°F systems consisted of hot-water-traced lines, with insulation applied over the tracing, and supplementary electrical heaters where needed.

Of course, the system required the use of many valves, flowmeters, pressure- and temperature-monitoring devices, and related items which have not been mentioned here, and which are omitted from the figure for clarity.

One unique aspect of this system is the valving arrangement, which allows zero or either of two span gases to be applied to each analyzer, or to a single analyzer, by means of electrically operated valves. The arrangement for a typical analyzer is shown in Figure 1.

Materials compatibility is a major consideration in such a system, since many of the species of interest are very easily destroyed. Materials in contact with the gases prior to analysis were limited to either 316 stainless steel or Teflon.

PHYSICAL ARRANGEMENT

The entire emissions-analysis system is contained within a 5-bay console. The console is mounted on casters and is approximately 120 in. wide by 80 in. high by 24 in. deep. Figure 2 is a front view of the console, and shows the location of individual analyzers within the console. Bay number 1 contains the long-path NDIR CO analyzer and the gravimetric filters. Bay 2 contains the ECD NO_2, ECD NO_x, and C_xH_y FID analyzer. Bay 3 contains the H_2O analyzer, the high-range NDIR CO, and the NDIR CO_2 analyzer. Bay 4 contains the FPD SO_x analyzer, the piezoelectric particulate analyzer, and the chemiluminescence NO and NO_x analyzers. Bay 5 contains the NDUV NO_2 and the NDIR NO analyzers.

The calibration and valve-control systems are also located in Bay 2, along with most of the individual analyzer flowmeters. The analyzer-inlet manifold-pressure-control system controls are located in Bay 3, as is the analyzer-output-signal and temperature-control-system monitor station. The electrostatic-grid particulates unit is located to the extreme right outside the enclosure.

A rear view of the console appears in Figure 3, which shows the amount of insulated tubing, control wiring, valves, and pumps required by the system. The bypass control valve is also visible in Figure 3 at the extreme right (exterior of Bay 5).

Equipment not shown, but very necessary, is approximately 20 bottles of service and calibration gases which must be located nearby. These include hydrogen/helium and hydrocarbon-free air for the FID (C_xH_y) analyzer, oxygen for the chemiluminescence analyzers, and hydrogen/helium for the FPD (SO_x) analyzer, as well as zero and calibration gases for the various analyzers.

CALIBRATION SYSTEM

Gas analyzers require frequent recalibration if accuracy is to be maintained. The AEDC emissions-analysis system has provisions for a three-step calibration for each analyzer, except for the water-vapor and particulates analyzers. The calibration gases chosen, and the analyzers with which they are used, are shown in Table 2.

Since test time is the most important (and expensive) part of altitude testing, it was deemed necessary to automate the calibration of the analysis system. This was accomplished by designing a control system which individually, by means of a single console control, or simultaneously for all analyzers, applied either the zero or the proper span gas (low- or high-span) to each analyzer. The individual mode was used for setup, adjustment, or checkout, to conserve gas, and the simultaneous mode was used to conduct system calibrations.

DATA RECORDING, DISPLAY, AND PROCESSING

The output of the analysis system consists of electrical signals, in addition to console indications. To permit assessment of the stability of the instruments (and the engine under test), graphic multichannel chart recorders, located in the analysis area, were used to monitor and record the console outputs. In addition, a digital data-acquisition system was used to record a short record (480 samples of each channel, over a 90-second interval) at each condition where data was desired. Calibrations were similarly recorded, using the calibration gases and system previously described. In general, the digitally recorded data were used for all processing and reduction, while the charts were used for stability determinations, system checks and tests, and "quick look" purposes.

The AEDC facility computer complex, consisting of an SEL 810A, a Raytheon R-520, and an IBM 370/155, was used for processing all

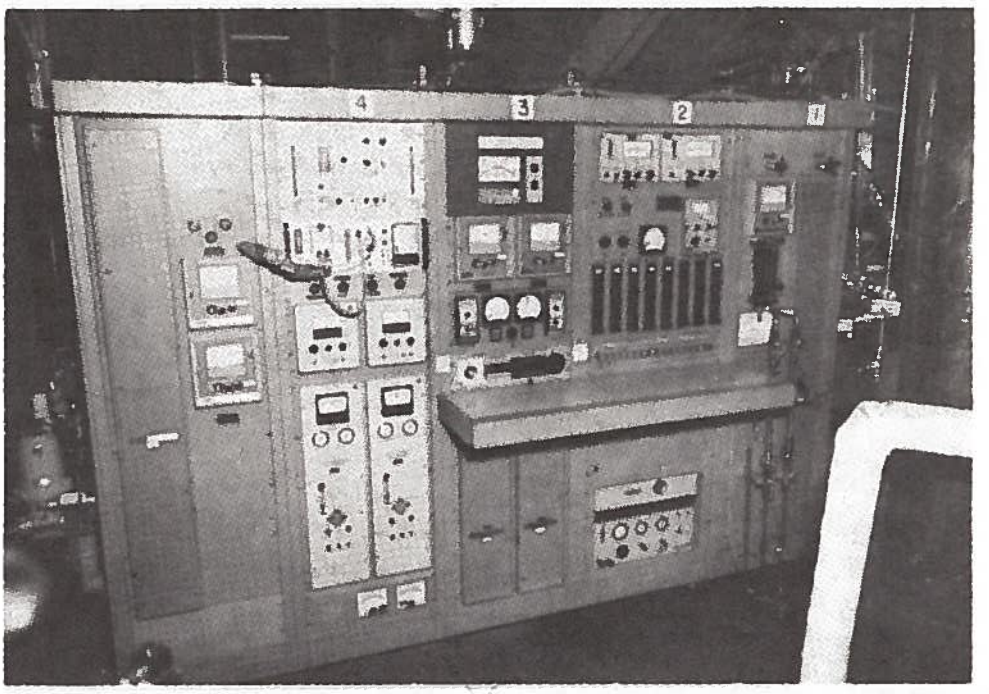

Figure 2. Front view, emissions analysis console.

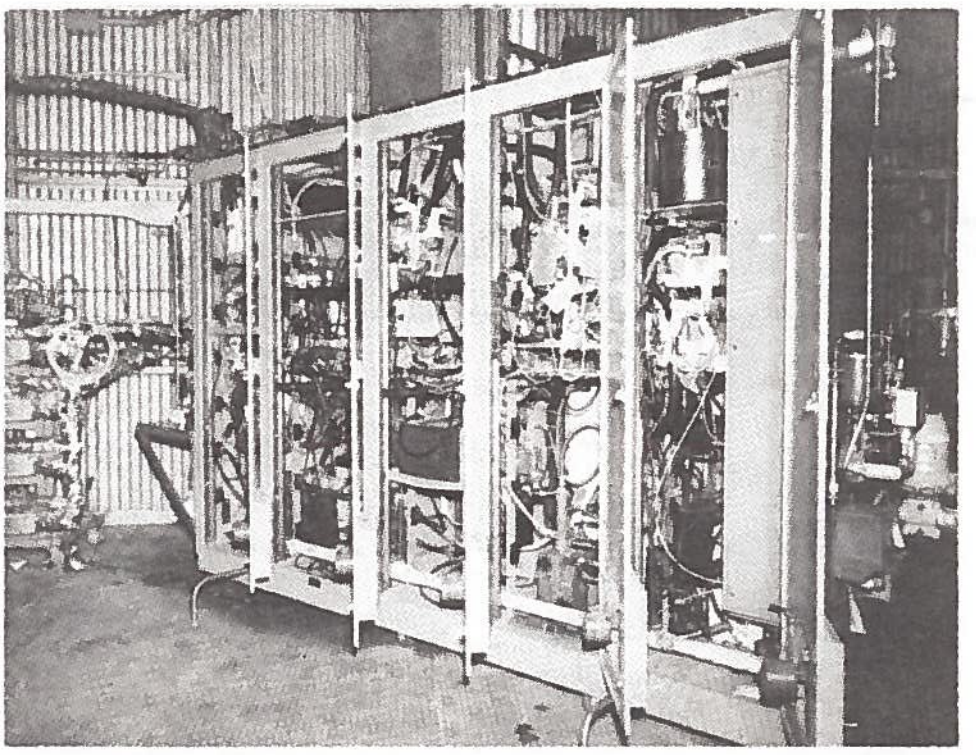

Figure 3. Rear view, emissions analysis console.

Table 2. Calibration Gases and Concentrations

Span Gas	Nominal Concentration	Analyzers Used With
NO	40 ppmv	NO Chemiluminescence, NO NDIR, NO_x ECD
NO	100 ppmv	
NO_2	40 ppmv	NO_x Chemiluminescence, NO_2 NDUV, NO_2 ECD
NO_2	200 ppmv	
CO	40 ppmv	CO NDIR (Low Range)
CO	400 ppmv	CO NDIR (High Range)
CO	3000 ppmv	
CO_2	2 pphv	CO_2 NDIR
CO_2	20 pphv	
C_xH_y (CH_4)	50 ppmv	C_xH_y FID
C_xH_y (CH_4)	500 ppmv	
SO_2	1 ppmv	SO_x FPD
SO_2	10 ppmv	
Zero Gas	–	All Analyzers

data. The system permits off-line correction for zero shifts, removal of interference-related errors, and graphic plotting of the data in many selectable formats, such as concentration versus probe position, fuel flow, altitude, or combinations of these. A block diagram of the system is shown in Figure 4.

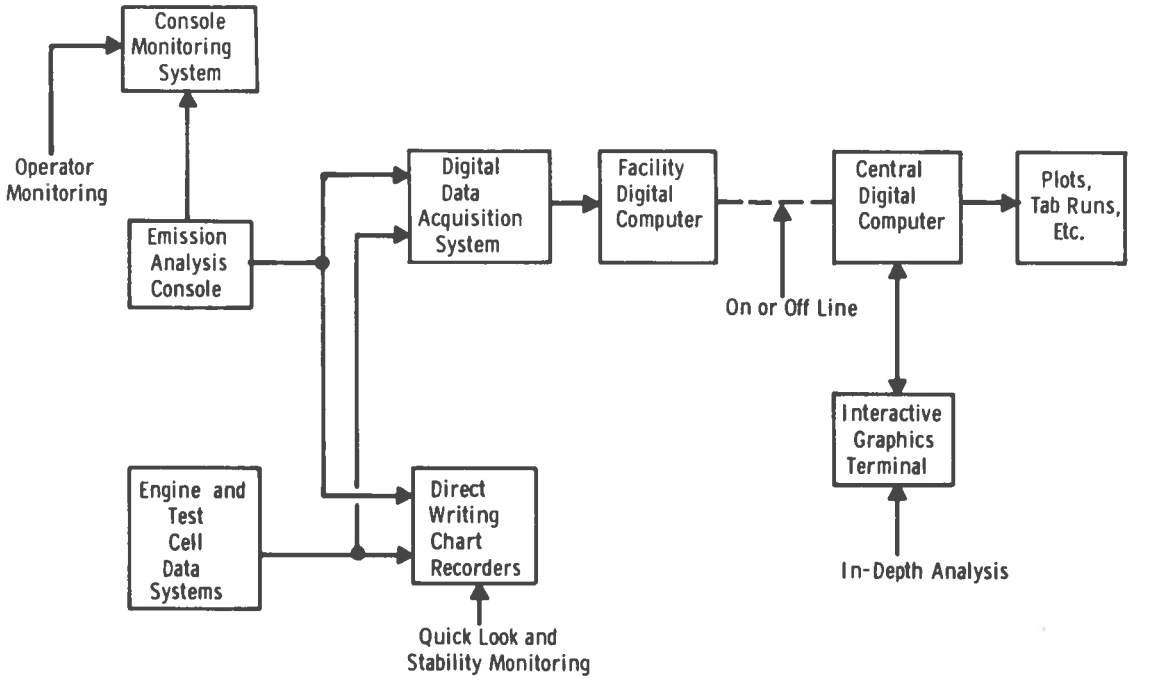

Figure 4. Data recording and processing system.

SYSTEM TEST AND RESULTS

Both before and after the engine-operating phase of the test program, validation tests were conducted for various known and possible problems with the analysis system. The tests which involved the behavior of the sample-handling system (i.e., sample probe lines, pumps, and materials compatibility) are described in the preceding paper [5]. In addition, several tests were made to determine pertinent characteristics of the instrumentation system. These included response time, thermal stability (effects of sample temperature, as well as console ambient temperature), effects of sample pressure and flow-rate variations, and the responses of different analyzers to various interfering gases.

a. *Time Response Characteristics.* As was expected, wide variation in analyzer lag time was noted, as Figure 5 shows. In general, these results were very close to manufacturer's quoted times, with allowances for the particular sample-handling system configuration employed. As is evident, some of the analyzer lag times are not wholly compatible with altitude test-cell time allowances, and slowed the testing rate considerably.

b. *Thermal Environmental Tests.* The thermal environmental tests had rather pleasant results; within reasonable limits of sample-conditioning system performance (±10°F) and for reasonable ambient temperatures (80 + 10°F), no temperature effects exceeding 1% of expected range were found.

c. *Sample Pressure and Flow-Rate Variation Tests.* Variations in the sample manifold pressure and flow rates likewise had little effect on system performance. It was necessary to maintain proper sample flow into those instruments which are flow-sensitive. However, the indicators supplied as part of the instruments were deemed adequate and sufficiently precise to permit the correct flows to be determined and set.

d. *Interference Tests.* One of the most prevalent sources of error in gas analysis, especially in the use of optical instruments, is interference from other gases which alters the readings produced by a constant concentration

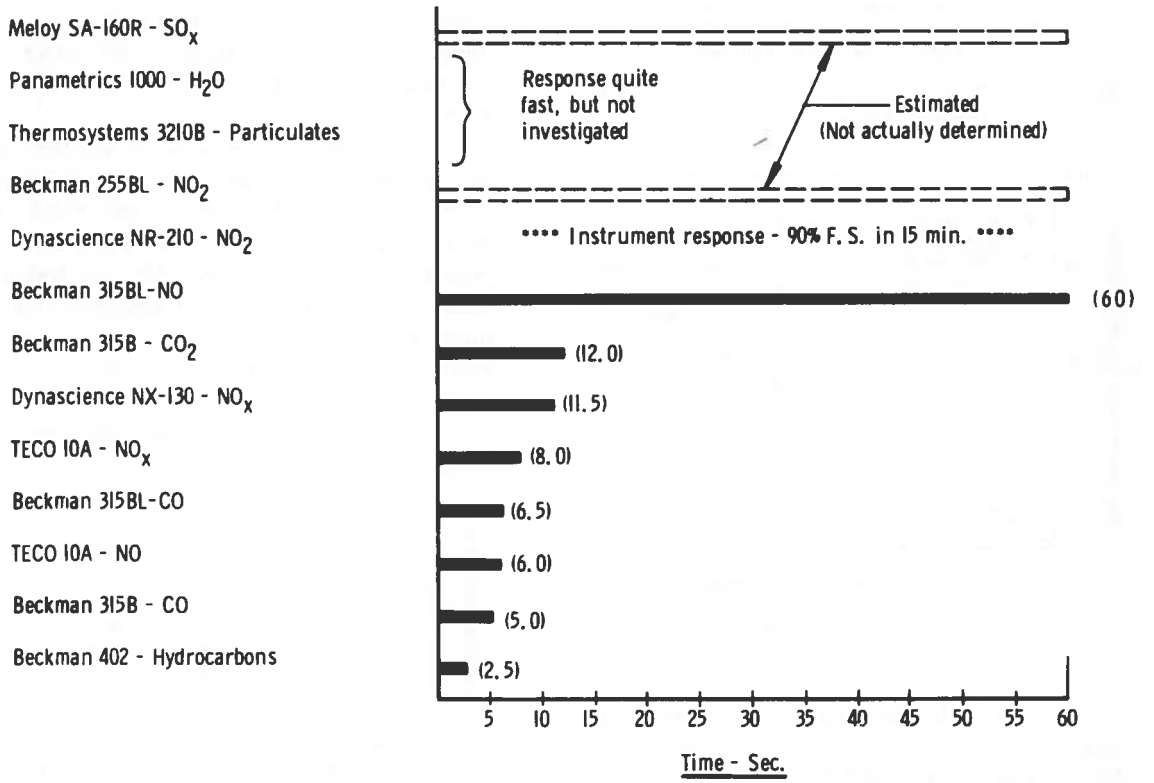

Figure 5. Initial response lag for step input.

of the species of interest. To characterize these interferences, a series of tests was made. The tests included the introduction of NO and NO_2 calibration gases into CO analyzers, and vice versa. All other combinations of gases and analyzers were also tested, and the responses noted. Also, some indications were noted during the engine test phase which dictated a need for still other interference tests involving species which were not being measured, such as O_2. Some of the results of these tests are shown in Figures 6 and 7.

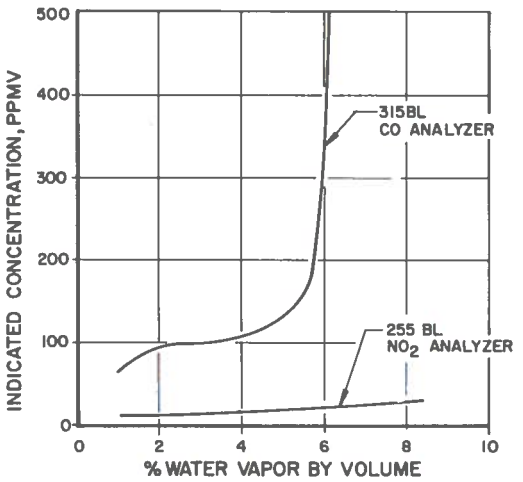

Figure 6. H_2O interference, NO_2 NDUV and CO NDIR (high-sensitivity) analyzers.

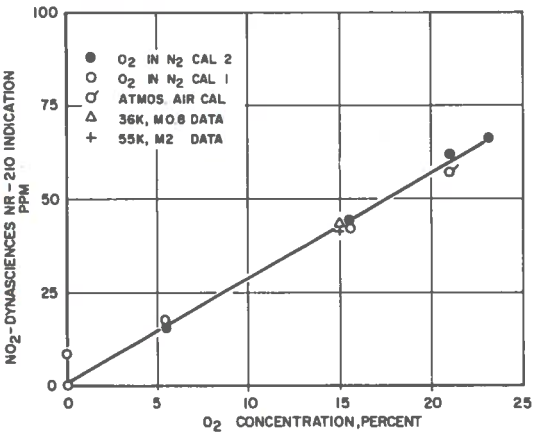

Figure 7. O_2 interference, NO_2 analyzer.

As can be seen, water-vapor interference was found to be present for both the NO_2 NDUV and the CO NDIR instruments. Water-vapor concentrations can be determined by calculation, however, and corrections can be applied to the data once the amount of interference has been determined. The interference characteristic of the NDIR analyzer was not, however, sufficiently systematic to permit its correction. The manufacturer has since changed the sample cells, and the unit no longer exhibits the effect shown in the figure.

Oxygen was found to be an interferent in the NO_2 electrochemical analyzer. Since oxygen concentration varies quite markedly in jet-engine exhaust, this interference was quite noticeable. Figure 7 shows the response of the electrochemical NO_2 analyzer to zero ppm of NO_2 in varying concentrations of oxygen. Also shown is the indication obtained from two data points where oxygen concentration has been calculated from fuel-air ratio and engine-operating data. These conditions were expected to produce very little NO_2, and this expectation has apparently been realized, since the data falls almost directly upon the zero-ppm line at the calculated oxygen concentration.

Another interference not illustrated was found in connection with the NO_x electrochemical analyzer. The introduction of acetylene from an unlighted torch was found to produce a severe overscale indication, from which the instrument did not recover for more than an hour.

The water-vapor analyzer was subject to contamination, although this was not an interference in the strict sense of the word. The instrument did not hold calibration after exposure to exhaust products for any length of time, as is shown in Figure 8. Dry-bulb temperatures were also very much a factor in this analyzer. The combination of contamination and dry-bulb temperature sensitivity was such as to render the water-vapor data unusable in our test.

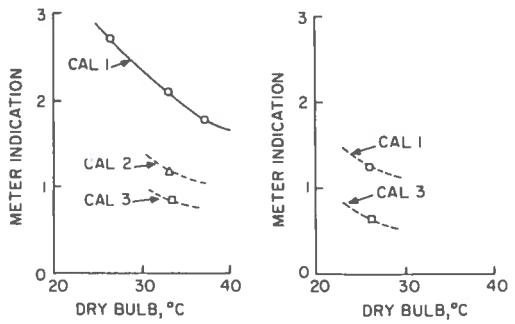

Figure 8. H_2O analyzer calibration.

Data Comparisons

Figures 9 through 13 illustrate the results produced by the differing techniques. As may be seen, agreement obtained varies markedly with engine conditions and other species of gases. Oxygen response is evident in the electrochemical cell (NO_2 analyzer) in Figure 9. The difference between the two curves in Figure 10 is probably the result of water-vapor interference. Hydrocarbon interferences are obvious in the data obtained from the electrochemical cell (NO_X unit) in Figure 11. Some response to water vapor may also be indicated in the NDIR NO analzyer (Figure 12.) Even though this analyzer incorporated a dryer, it was impossible to eliminate all water-vapor effects without increasing the system response time to an intolerable level. The NO + NO_2 sum as determined by the NDIR and NDUV analyzers correlated quite well with the NO_X data obtained from the chemiluminescence analyzer. Correction for water vapor was required, however, to achieve this agreement. Figure 13 shows these values for the 65 kft, Mach 2.6 non-afterburning condition. Agreement at afterburning was somewhat poorer due to larger amounts of water vapor, but either technique will apparently yield acceptable results.

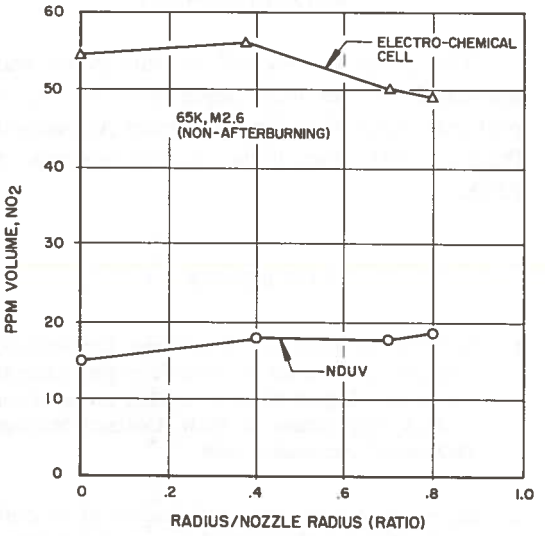

Figure 9. Nitrogen-dioxide concentration data.

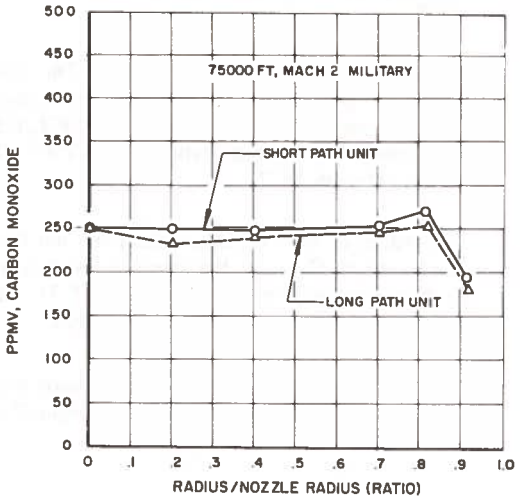

Figure 10. Carbon-monoxide concentration data.

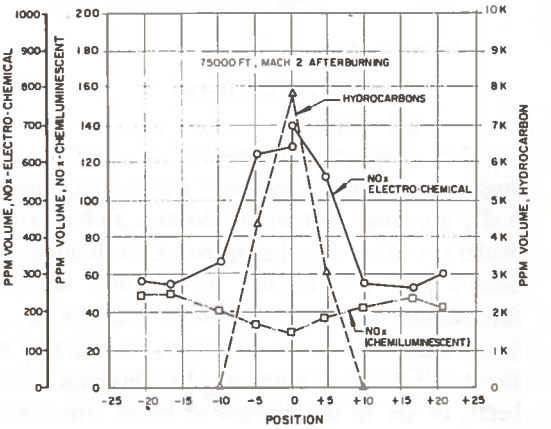

Figure 11. Total oxides-of-nitrogen concentration data.

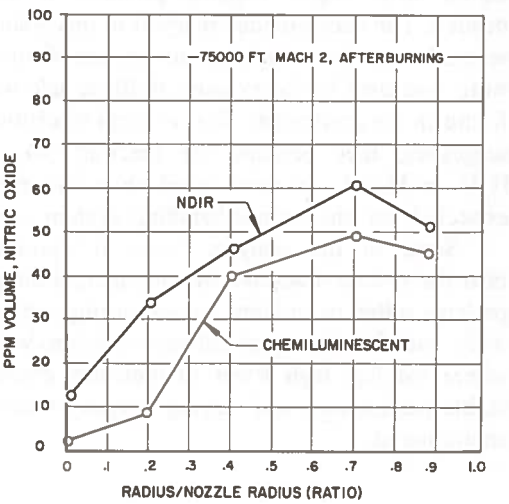

Figure 12. Nitric-oxide concentration data.

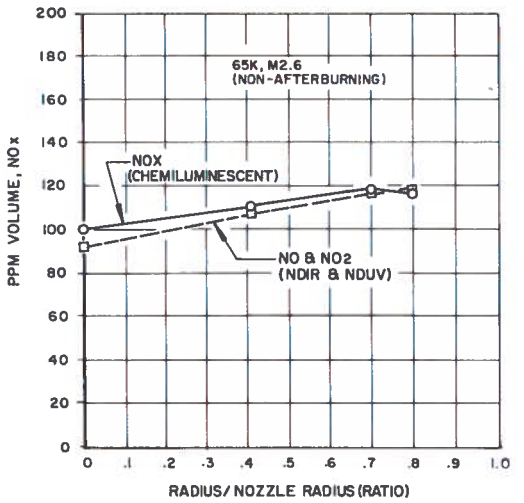

Figure 13. Total oxides-of-nitrogen data.

CONCLUSIONS

The acquisition of emissions data from jet engines operating at simulated flight conditions is really a science, not an art. Several problems are evident, however, and improvements in analyzer design and performance are needed. Recent discussions with manufacturers indicate their belief that some of the problems encountered in the use of the system described in this paper have been, or are in the process of being, overcome. Further testing and evaluation will be needed to verify this.

More study of the chemical processes associated with engine exhaust products is also needed. The sulfur-oxides analyzer in this system seemed to perform well, but no oxides of sulfur were measured in the exhaust. Sulfuric acid was found in the gravimetric filter in small quantities, suggesting that perhaps the reaction $SO_x + H_2O \rightarrow H_2SO_4$ is more rapid than had been expected for the sample-handling system used.

Some of the analyzer types incorporated into the system described in this paper, although perhaps suited to ambient air monitoring, are not really suited to jet-engine exhaust-emissions work where varying, high levels of moisture, considerable particulates, and varying oxygen levels are encountered.

The instrument list specified by the SAE E-31 Committee in ARP-1256 appears to have been a good selection at this particular time. However, it is hoped, and indeed expected, that significantly improved techniques and equipment will appear within the next few years.

Considerable work in the particulate-analysis area is needed. The gravimetric and microscope techniques for particulate analysis are not very efficient and require large investments in time, equipment, and skill. However, no suitable continuous analyzer for particulates is presently available.

ACKNOWLEDGMENT

The research reported in this paper was sponsored by the U.S. Department of Transportation under the Climatic Impact Assessment Program. ARO, Inc., is the contract operator of AEDC.

REFERENCES

1. Northern Research and Engineering Corporation, "Nature and control of aircraft engine exhaust emissions," Report Number 1134-1; prepared for NAPCA, Department of HEW, Contract Number PH22-68-27, November 1968.

2. Secretary of HEW, "National Control of Aircraft Engine Exhaust Emissions," report of the Secretary to the United States Congress pursuant to PL 90-148, The Air Quality Act of 1967, December 1968.

3. Grobecker, A.J., chairman's address: "The DOT Climatic Impact Assessment Program," *Proceedings of the Survey Conference*, Feb 15-16, 1972, U.S. Department of Transportation, DOT-TSC-OST-72-13, February 1972.

4. "Procedure of the Continuous Sampling and Measurement of Gaseous Emissions from Aircraft Turbine Engines," by SAE Committee E-31, Aircraft Exhaust Emission Measurements, 1971.

5. Neely, J.E., and D.L. Donaldson, "Emission level of the YJ93-GE-3 engine, an SST-like engine," in this volume.

APPENDIX
OPERATING PRINCIPLES OF ANALYZERS

Although a complete description of the operational principles, limitations, and other parameters of the analysis techniques mentioned above is beyond the scope of this paper, a brief description of each technique is presented.

Non-Dispersive Infrared (NDIR)

This type of analyzer (Figure 14) uses an infrared source, sample and reference cells, a detector, and an electronic signal processor. The detector is partitioned by a diaphragm, and is filled with the compound of interest, which must have a strong absorption band in the infrared. Infrared energy is coupled to the closed detector through a reference cell, which contains none of the compound of interest, and a sample cell, which contains the sample. Absorption by the compound of interest in the sample cell reduces the energy input to the sample-cell side of the detector, while no such absorption occurs in the reference cell. The gases within the two detector chambers are thus unevenly heated, and a pressure difference results. This pressure difference is proportional to the concentration of the compound of interest in the sample cell. The unit is calibrated by actually passing known concentrations of the compound of interest through the sample cell, and standardizing the readings obtained by adjustment of the signal processor. This technique is suitable for CO, CO_2, and NO, all of which absorb strongly in the infrared. Optical interferences from other absorbing gases are, of course, a problem. These are minimized by optical filtering of the source, and judicious choice of the particular infrared wavelength used. Cold-trapping or chemical dryers are sometimes required in addition to remove water-vapor interference.

Flame Ionization Detection (FID)

This type of analyzer, Figure 15, uses a hydrogen-rich flame into which a sample stream is introduced. Its operation depends upon the fact that when even traces of hydrocarbons are burned in such a flame, a large number of ions is produced. An ionization-current collector inserted in the area just above the flame thus produces an electrical current which is proportional to the hydrocarbon concentration. To provide a high speed of response, a significantly larger sample flow than is required by the flame is maintained up to very near the capillary, and is then dumped. The principal problems associated with this type of analyzer are 1) condensation of hydrocarbons on tube walls, and subsequent revaporization, and 2) maintenance of the proper fuel-air ratio. They can be ameliorated by enclosing the entire assembly in a 300°F oven, and metering and regulating of both fuel (hydrogen/helium mixture) and air inputs.

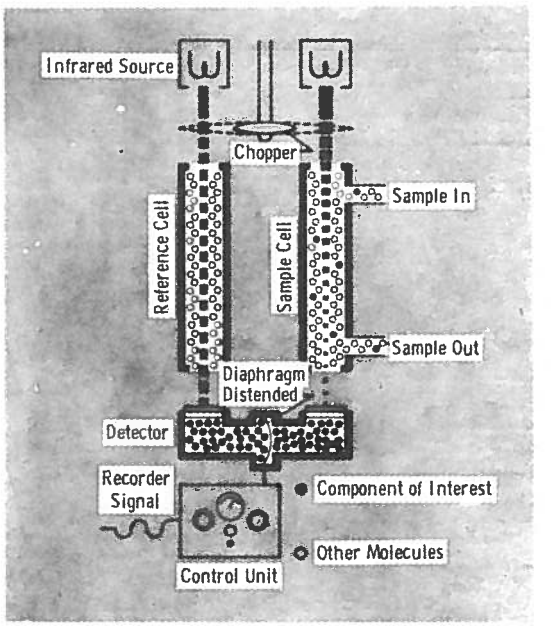

Figure 14. Principle of operation, NDIR analyzer (CO, CO_2, NO).

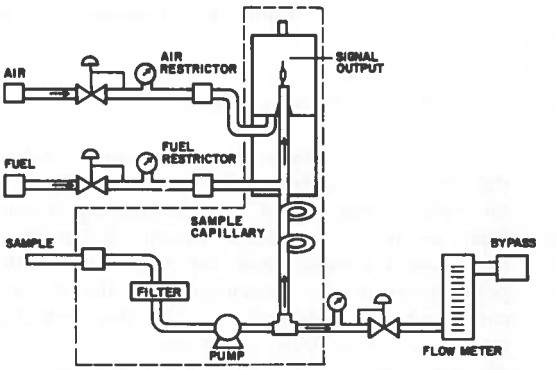

Figure 15. Principle of operation, flame ionization detector (THC).

Chemiluminescence

This type of analyzer (Figure 16) operates on the principle that when ozone combines with certain compounds, light is produced. The emitted light is proportional to the number of reacting molecules. If flow rates, pressures, and other factors such as temperature remain constant, and an excess of ozone is present, the emitted light is proportional to the concentration of the compound of interest. This type of analyzer is used for NO or, by adding a $NO_2 \rightarrow NO$ converter in the sample line, for NO_x ($NO + NO_2$). The principal difficulties with this instrument are variations in the reaction-chamber pressure, flow, and temperature. When it is used for NO_x, the thermal converter's efficiency, and poisoning or adsorption of the sample on its wall, must also be considered.

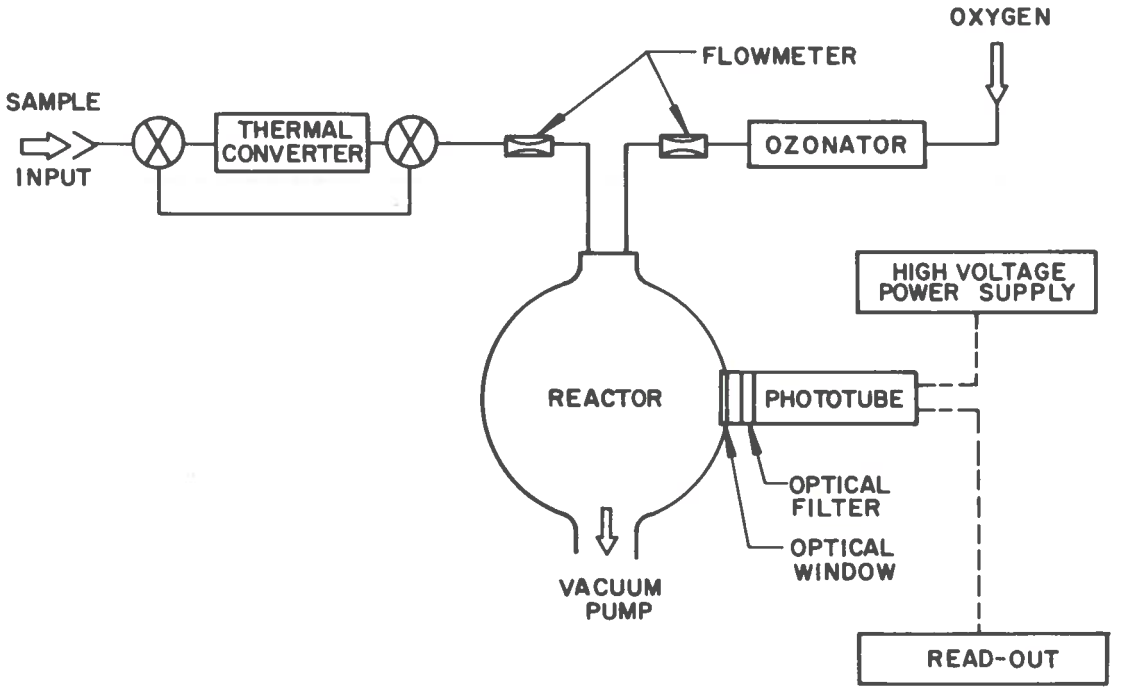

Figure 16. Principle of operation, chemiluminescence analyzer (NO, NO_x).

Non-Dispersive Ultraviolet (NDUV)

This type of analyzer (Figure 17) is quite similar to the previously described NDIR device, except that an ultraviolet source is used, and the partially absorbed beams are directly detected by a photocell. The ratio of the received energies from the two beams is then proportional to the concentration of the absorbing compound. The main problems with this method are interferences from other compounds which absorb in the ultraviolet, and, like all optical devices, vibration. They can be ameliorated by optical filtering and careful design of the installation. (ARP 1256 prohibits cold traps or dryers preceding the NDUV analyzer for NO_2 measurement, since water in a liquid state reacts with NO_2).

Electrochemical Cell

The electrochemical cell (Figure 18) depends on the principle that the permeation of a membrane by the compound of interest influences the rate of an electrolytic reaction involving a thin-film electrolyte. This electrolytic reaction produces a small electrical current which is proportional to the reaction rate. The cell, which is a proprietary item, and must be periodically renewed, can be sensitized to various compounds such as NO_2, NO_x, or SO_x. The principal difficulties include sensitivity to compounds other than the specific one for which the unit is sensitized (interferences), slow response, and a tendency of the electrolyte to become dry when exposed to a dry gas.

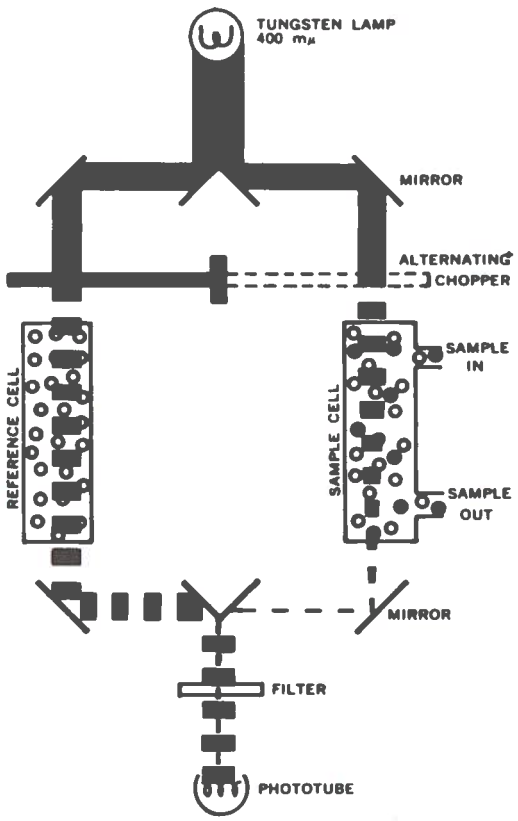

Figure 17. Principle of operation, NDUV analyzer (NO_2).

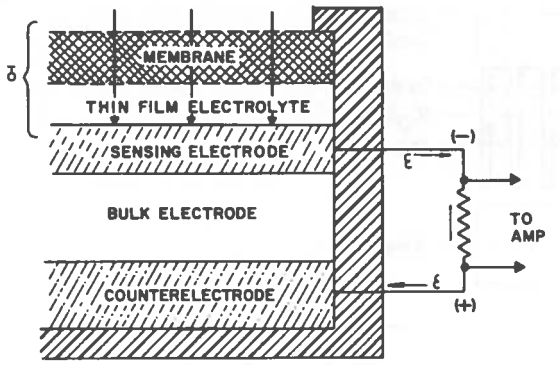

Figure 18. Principle of operation, electrochemical cell (NO_2, NO_x).

Flame Photometric Detector (FPD)

This type of analyzer (Figure 19) detects the characteristically colored light emitted by sulfur compounds burned in a hydrogen-rich flame. The light is detected by a photomultiplier and, after suitable processing, is used to indicate the sulfur concentration. By use of a "scrubber" in the inlet sample line, only oxides of sulfur are passed into the burner, thus permitting measurement of oxides of sulfur (SO_x) only. Since the detector flame in this instrument uses the oxygen from the sample, and since the oxygen content of jet-engine exhaust is variable (and quite low in some cases), a sample-dilution system is used to ensure that the oxygen content of the sample is adequate and relatively constant. The main difficulties with instruments of this type are the dilution ratio and the criticality of flow rates. Use of this type of analyzer is limited to sulfur compounds.

Capacitance Membrane

This sensor (Figure 20) consists of an aluminum substrate, which has a porous oxide layer created by anodizing the surface. A very thin porous layer of gold is evaporated over the oxide layer, forming a parallel-plate capacitor. Water vapor is transported through the porous top layer, and is absorbed onto the oxide structure, thereby changing the electrical impedance of the capacitor. This impedance is thus related to the water concentration of the gas in which the sensor is immersed. After suitable processing, a signal is obtained which is proportional to water-vapor concentration. Unfortunately, sensitivity to temperature, contamination, and extreme non-linearity are characteristic of this sensor.

Piezoelectric Microbalance

This particulate sensor (Figure 21) uses a pair of piezoelectric crystals, whose frequency of oscillation is proportional to the crystal mass (all other parameters held constant). An electrostatic precipitator is used in the inlet sample line to electrostatically charge the particles contained in the sample stream. These charged particles are drawn onto the crystal and captured, changing its mass and thus its frequency. The change of frequency is thus proportional to the particulate mass contained in a unit volume of the sample stream. The principal problems associated with this type of analyzer are the inability of the crystal to capture all of the particles (they are also captured by the needle, the housing, and the cavity), the shorting of the precipitator needle by moisture, hydrocarbons, and deposited particles, and excessive loading of the crystal by particulates. However, the crystal can be easily cleaned and the housing is thermally conditioned, which reduce these problems somewhat.

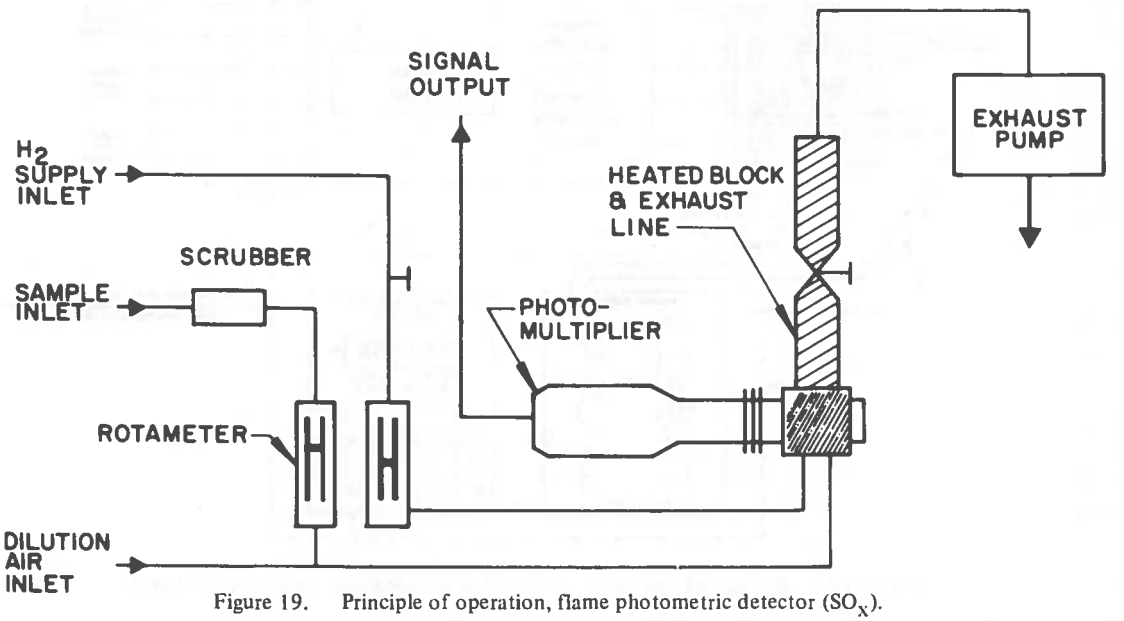

Figure 19. Principle of operation, flame photometric detector (SO_x).

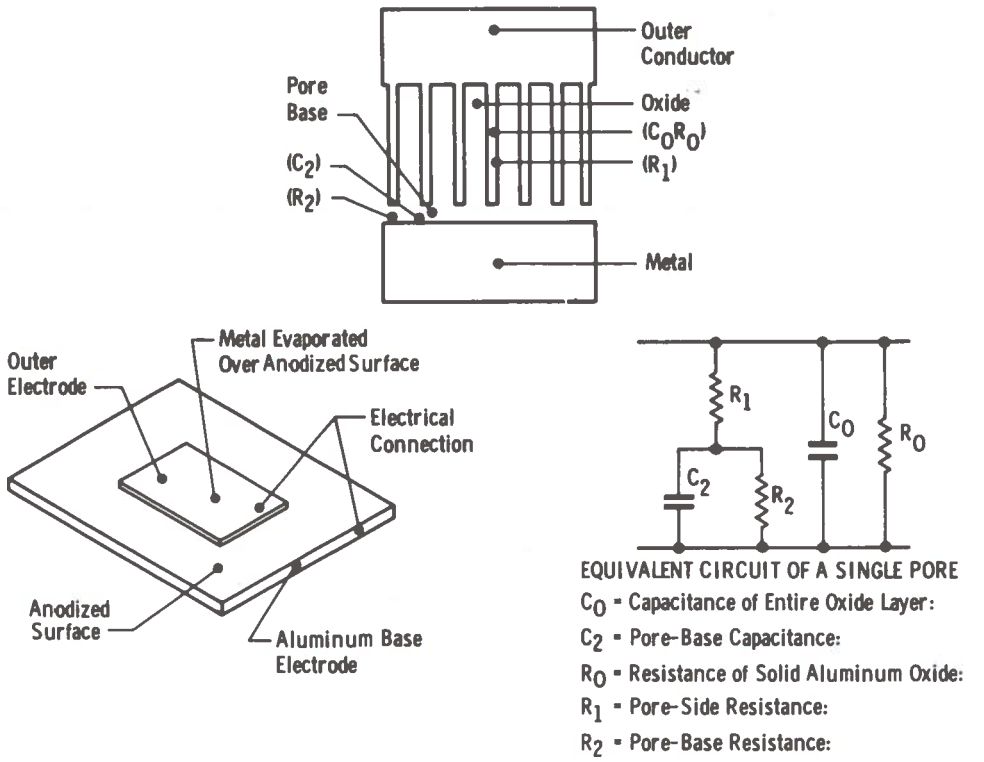

Figure 20. Principle of operation, capacitance membrane (H_2O).

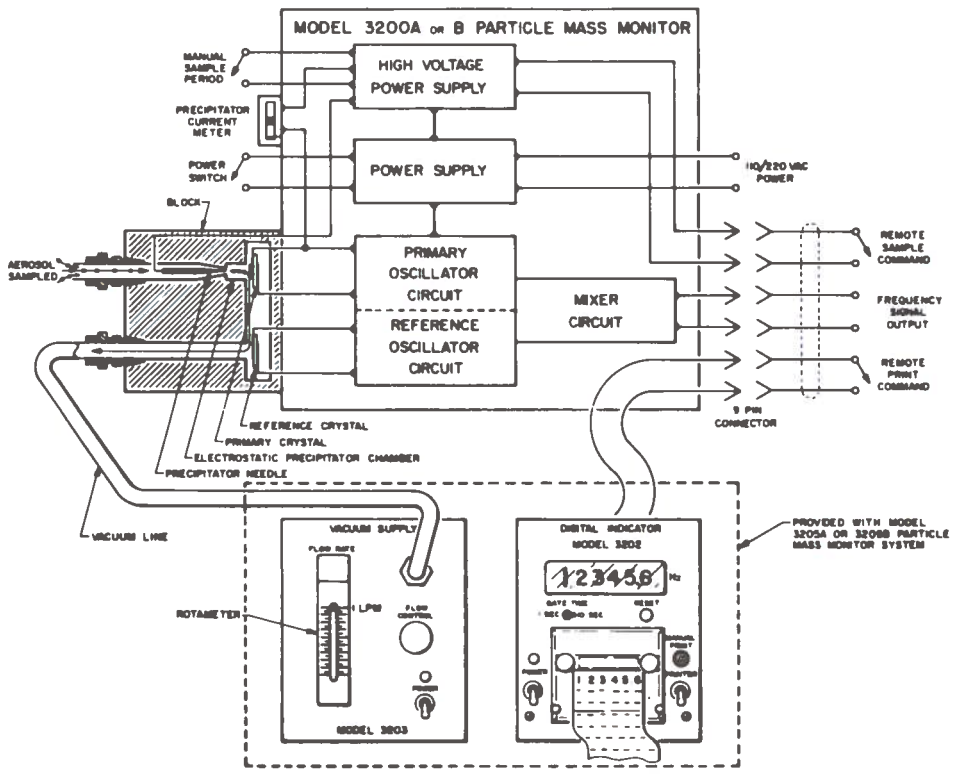

Figure 21. Principle of operation, piezoelectric microbalance sensor (particulates).

Gravimetric Filters

These are standard micron-sized absolute filters (Figure 22) made of materials which can be autoclaved. They are used in conjunction with a gas-flow totalizer. Each filter is autoclaved and weighed before and after exposure to a sample flow of known volume. The difference in weight is proportional to the particulate concentration in the exhaust during the time the filter was in use. The main difficulties associated with the use of this device are the need for 1) long periods of flow to produce discernible weight changes, 2) extreme care in handling, and 3) tedious and time-consuming data reduction.

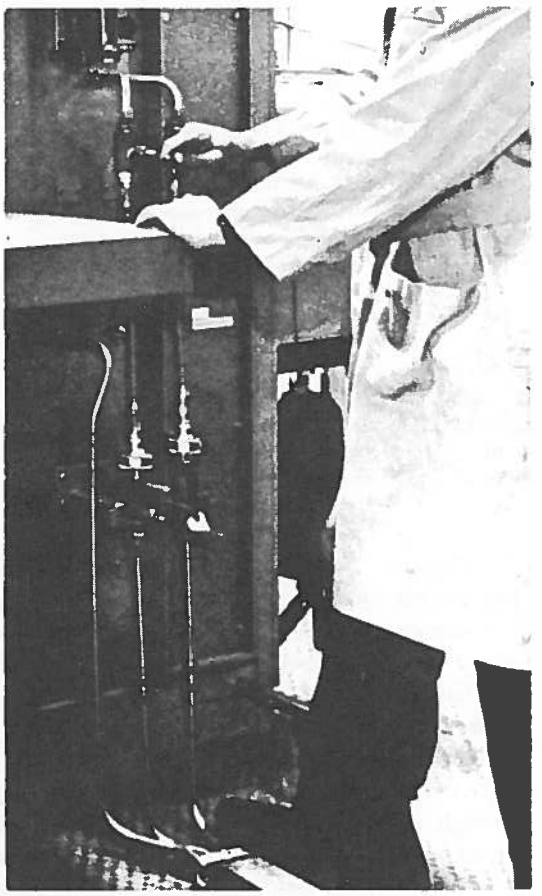

Figure 22. Gravimetric filters.

Electrostatic Capture Grid

This device (Figure 23) uses a principle similar to the electrostatic precipitator previously described, except that the particles are not captured for weighing. Instead, they are captured on a carbon-coated copper grid, and preserved for analysis by electron microscope. Data is obtained by manual analysis of photomicrographs, from which the size distribution of the particles is obtained. The principal problem encountered with this type of instrument is the tedious, time-consuming data-reduction process.

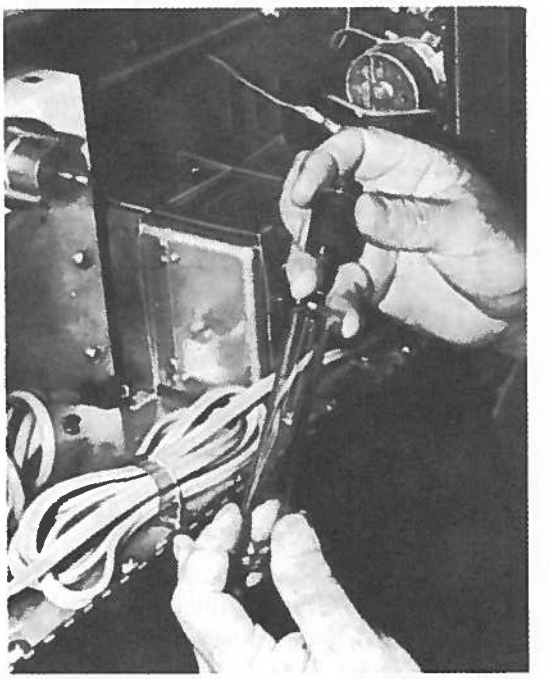

Figure 23. Electrostatic capture grid.

DISCUSSION

(UNIDENTIFIED): One point that has bothered me throughout your talk is the presence of that scrubber upstream of all your gas analyzers. Did you try bypassing it to see what the effect on the measurements would be? Is it removing volatiles, droplets, hydrocarbons, or what?

GRISSOM: That was merely a filter for taking out particulate matter. Since the entire filter unit was heated to above 300°F we did not expect it to affect hydrocarbons, but we did run tests on it with calibration gases. In addition, for some tests we introduced the calibration gases out at the probe and drew them through the filter to make sure that we were not losing concentration or getting conversion in the sample-handling system.

(UNIDENTIFIED): Did you try mixing all your calibration gases together and sending them through your input stream?

GRISSOM: Yes, we did analyze gas mixtures, though they did not include *all* the products in engine exhaust.

CONCENTRATION OF OH AND NO IN YJ93-GE-3 ENGINE EXHAUSTS MEASURED IN SITU BY NARROW-LINE UV ABSORPTION

W.K. McGREGOR, B.L. SEIBER, AND J.D. FEW
ARO, Inc.
Arnold Engineering Development Center
Arnold Air Force Station, Tennessee

ABSTRACT: The narrow-line absorption technique was applied to the resonance electronic vibrational-rotational bands of OH and NO to obtain the average absolute number density of OH and NO molecules at a position 12 inches downstream of the exhaust plume of a YJ93-GE-3 engine being operated under simulated flight conditions. The engine was operated over a range of power settings, including several afterburner fuel flow rates, at a number of simulated flight conditions from speeds of Mach 0 to Mach 2.6 and altitudes from sea level to 75,000 ft. The experimental apparatus and the method used to relate measurements of absorption coefficients to species densities are described in the paper. Levels of emission of OH ranged from a minimum of 1.5×10^{13} cm^{-3} at military power, Mach 1.4, 35,000 ft altitude, to a maximum of 10^{15} cm^{-3} at full afterburning, Mach 1.4, 35,000 ft altitude. NO densities ranged from a minimum of 1.4×10^{14} cm^{-3} at the Mach 2, 55,000-ft condition to a maximum of 2.3×10^{14} cm^{-3} at the Mach 2.6, 66,000-ft condition. OH emissions increase by an order of magnitude with the onset of afterburning, while NO emissions are not appreciably dependent on afterburning. The measured OH concentrations corresponded to those calculated at the thermodynamic conditions within the secondary combustion chamber. The NO concentrations measured by the absorption technique were a factor of 1.5 to 5 larger than those measured by sampling through a capture probe and analyzing the gas with chemiluminescence instruments.

INTRODUCTION

A number of molecular species produced during the combustion process within jet engines play roles in the chemical balance of the stratosphere [1]. Among these are nitric oxide, NO, and the hydroxyl radical, OH. In order to assess the impact of an additional source of these molecules, such as high-altitude aircraft, it is necessary to determine their rates of emission from typical jet engines. The concentration of highly reactive species such as OH must be measured by an in-situ technique, and it is also highly desirable to measure the more stable NO concentration in situ because of the uncertainty as to further chemical reactions within sampling probes and gas-analyzer instruments. This paper is devoted to a description of the application of a spectral-absorption technique to the measurement of OH and NO concentrations in the exhaust exit plane of a YJ93-GE-3 engine operated at several simulated flight conditions.

The measurements were made as part of a larger program of exhaust-emissions measurements on the YJ93-GE-3 engine at simulated flight conditions, conducted in the Propulsion Development Test Cell (J-2) at the Arnold Engineering Development Center (AEDC) [2]. The engine was operated over a range of simulated Mach numbers from zero to 2.6 and simulated altitudes from sea level to 75,000 ft, at power settings from idle to maximum afterburning. In the main program, emission levels of the constituents were measured by sampling through a probe which could be positioned anywhere in the exhaust plane, and analyzing the gas by means of a variety of commercial process instruments. The results of the sampling measurements are described in a companion paper [3]

The method used to make the in-situ measurements of OH and NO concentrations is usually referred to as the "narrow-line absorption" technique. In this method the transmission of a narrow-line source of radiation through a medium containing the species to be measured is determined and related, through either theoretical expressions or calibration, to the number of absorbing molecules along the path. (The source of radiation is a discharge lamp containing a fixed amount of the molecular species of interest.) The essentials of the method are contained in the standard text by Mitchel and Zemansky

[4], and the application to OH in combustion gases has been described by many investigators, including Kaskan [5] and Houghton and Jachimowski [6]. In the work described here, the resonance electronic bands of OH at 3064Å and NO at 2269Å were used. The details of the method used at AEDC are described by Davis, McGregor, and Mason [7], and two recent AEDC reports not yet published.

The main deterrent to such measurements is usually considered to be the harsh environment in which the laboratory-type instrumentation must be made to function. These hazards were overcome in this work and a large amount of data was obtained. This paper presents the details of the application and a first look at the measured OH and NO concentrations.

DESCRIPTION OF THE METHOD

Theory

The narrow-line absorption technique is based upon limiting the measured absorption to absorption at a line center in order to take advantage of the relation

$$\int_0^\infty k_\nu d\nu = \sqrt{\frac{\pi}{4 \ln 2}} \frac{k_{\nu_0} \Delta\nu_D}{\exp(a^2)\,\mathrm{erfc}(a)} \qquad (1)$$

where k_ν is the absorption coefficient at wavenumber ν defined by

$$k_\nu = 1/n \ln(I_0/I)_\nu \qquad (2)$$

with I_0 the incident intensity, I the measured intensity, and L the path length in cm. The other symbols have the following definitions:

k_{ν_0} = $(1/L)\ln(I_0/I)_{\nu_0}$, the absorption coefficient at the line-center wavenumber, ν_0.

$\Delta\nu_D = 2\nu_0\sqrt{\frac{2 \ln 2\, \kappa T}{Mc^2}}$, the Doppler width in cm^{-1}

where

κ = Boltzmann's constant, 1.38×10^{-16} ergs/°K

T = absolute temperature, °K

M = mass of absorbing molecule, gm

c = velocity of light, 3×10^{10} cm/sec

$a = \sqrt{\ln 2}\, \frac{\Delta\nu_N + \Delta\nu_c}{\Delta\nu_D}$, where $\Delta\nu_N$ is the natural width and $\Delta\nu_c$ is the collisional width of the line.

In almost all cases $\Delta\nu_N$ is much less than $\Delta\nu_c$ and may be neglected. For the OH molecule, several investigators have expressed "a" in terms of the pressure and temperature of the absorbing gas,

$$a = K(P/T) \qquad (3)$$

where K is an experimentally determined constant, P the pressure in atmospheres, and T the temperature in °K. Houghton and Jachimowski [6] list several determinations of K by different investigators, but the latest and most thorough work is by Nadler and Kaskan [8], who show that K depends upon which line of the (0,0) OH band is being used. Their value, K = 585 for the $R_2(3)$ line, will be used in this work.

For the NO molecule, Thorson and Badger [9] have shown that collisional broadening is much less than Doppler broadening, so that "a" is small and $\exp(a^2)\,\mathrm{erfc}(a) \approx 1$.

The absorption coefficient of a single line is expressed in terms of properties of the absorbing gas as follows:

$$\int_0^\infty k_\nu d\nu = \frac{\pi e^2}{mc^2} N_{v''J''} f_{v'v''J'J''} \qquad (4)$$

where:

e = electron charge, 4.8×10^{-10} esu

m = electron mass, 9.11×10^{-28} gm

$N_{v''J''}$ = number density of molecules in the rotational level J'' of the vibrational level v'' of the ground electronic state, cm^{-3}

$f_{v'v''J'J''}$ = Oscillator strength for the transition from the v'J' level of the upper electronic state to the v''J'' level of the ground electronic state.

Now, for Boltzmann equilibrium

$$N_{v''J''} = \frac{\exp[-G(v'')/\kappa T]}{\sum_{v''} \exp[-G(v'')/\kappa T]} \times \frac{(2J''+1)\exp[-F(J'')/\kappa T]\ N_0}{\sum_{J''}(2J''+1)\exp[-F(J'')/\kappa T]} \quad (5)$$

where $G(v'')$ is the vibrational energy of the v'' level, $F(J'')$ is the rotational energy of the J'' rotational level, and the summations are the vibrational and rotational partition functions. The oscillator strength for OH as given by Houghton and Jachimowski [6], 8.45×10^{-4}, and the rotational line strength as given by Dieke and Crosswhite [10], with Learner's [11] correction, will be used. Combining Eqs. (1), (4), and (5), and using the definitions given, the numerical equation for the number density of OH is:

$$N_{OH} = 7.16 \times 10^{15} \times \frac{Q_v\, Q_r}{W\, S_{J''} \exp[-F(J'')/\kappa T]}\ k_{\nu_0}\ \text{cm}^{-3} \quad (6)$$

The partition functions, Q_v and Q_r, as defined by the summations in (5), are easily calculable; W, defined as

$$W = \frac{\sqrt{4 \ln 2/\pi}}{\Delta \nu_D} \exp(a^2)\,\text{erfc}(a) \quad (7)$$

is also calculable for any given temperature and pressure. Values for $S_{J''}$ and $F(J'')$ are given for several R_2 lines in Table 1.

Table 1. Line Strength Factors and Term Energies for Several Lines of OH in the 3064Å (0,0) Band

	$S(J'')^a$	$S(J'')^b$	$F(J'')$, cm^{-1}
$R_2(1)$	2.7	2.7	126.4
$R_2(3)$	8.9	8.8	289.0
$R_2(4)$	12.8	12.6	429.5
$R_2(14)$	53.2	45.7	3841.5
$R_2(15)$	57.2	49.1	4371.2
$R_2(20)$	77.4	57.3	10,762.3

[a]Experimental value given by Dieke and Crosswhite [10]

[b]Value after applying Learner's correction [11]

In the case of NO, the oscillator strength as given by Perry-Thorne and Banfield [12], $f_{00} = 3.64 \times 10^{-4}$, should be used. The rotational line strengths are calculable from the formulae for $^2\Sigma \rightarrow {}^2\pi$ transitions given by Earls [13], with the $^2\pi$ state expressed as intermediate between Hund's cases "a" and "b". The resolvable lines are doublets arising from the same energy transition but different spin selection rules. Values for several useful lines arising from $Q_{22} + R_{12}$ transitions are given in Table 2. The numerical equation becomes

$$N_{NO} = 2.59 \times 10^{16} \times \frac{\Delta\nu_D\, Q_v\, Q_r\, k_{\nu_0}}{S_{J''} \exp[-F(J'')/\kappa T]}\ \text{cm}^{-3} \quad (8)$$

Table 2. Line Strength Factors and Term Energies for Several Lines of the Q_{22}, R_{12} Branch of the NO (0,0) γ-Band at 2269Å

(J'')	$S(J'')$	$F(J'')$, cm^{-1}
25/2	18.33	288.75
23/2	16.53	245.80
21/2	14.75	206.28
15/2	9.56	108.31
13/2	7.88	82.53
9/2	4.56	41.27

The lines of the NO gamma bands are much more closely spaced than those of OH, so they are not always resolvable with field instruments. This was true for the measurements reported on in this paper. In this case one can write [6]

$$\left(\frac{I}{I_0}\right)_{\nu_a}^{\nu_b} = \frac{I_1}{I_T} e^{-k_1 L} + \frac{I_2}{I_T} e^{-k_2 L} + \ldots \frac{I_i}{I_T} e^{-k_i L} \quad (9)$$

where $(I/I_0)_{\nu_a}^{\nu_b}$ is the transmission measured in the wavenumber interval $\nu_b - \nu_a$, $I_{1,2\ldots i}$ are the incident intensities of the individual lines within the interval, $k_{1,2\ldots i}$ are the absorption coefficients of the lines, and I_T is the sum of all the incident individual line intensities from the source. In principle, Eq. (9) can be solved for the density of a species if the temperature is known,

but it is generally easier to resort to a laboratory calibration. In the work reported here a laboratory calibration was performed for the NO molecule; the method of data reduction using the calibration is described in the next section.

When the source line width is not much narrower than the absorption line width, a correction is necessary to adjust the measured transmission to line-center transmission. Mitchel and Zemansky [4] show that for Doppler line shapes the measured transmission $(I/I_0)_m$ of a line is related to the transmission at line center $(I/I_0)_{\nu_0}$ by the integral relation

$$\left(\frac{I}{I_0}\right)_m = \frac{\int_0^\infty \exp[-\omega/\alpha)^2]\exp[-k_{\nu_0}L\exp(-\omega^2)\ ]\,d\omega}{\int_0^\infty \exp[-(\omega/\alpha)^2]\ d\omega} \qquad (10)$$

where

$$k_{\nu_0} = -\frac{1}{L}\ln (I/I_0)_{\nu_0}$$

$$\alpha = \frac{\Delta\nu_D\ (\text{source})}{\Delta\nu_D\ (\text{absorber})}$$

$$\omega = \frac{2(\nu-\nu_0)}{\Delta\nu_D}\sqrt{\ln 2}$$

This correction is applicable for OH when "a" is small, as it was in most cases under consideration in this work.

Experimental

The essential ingredients for application of the narrow-line absorption technique are a radiation source, optics for beaming the source radiation through the absorbing gas, a wavelength selective receiver (spectrometer), and a stable detector and signal-conditioning system. The arrangement of this hardware is illustrated in Figure 1. The most important requirement is that the source emit only radiation at the line center(s) of the absorbing gas. The most convenient way at present of assuring this condition is to create a gaseous discharge at low pressure and temperature in which the only radiation in the wavelength band of interest is the resonance radiation of the molecule to be studied. Several techniques are available for providing such a source; the one used here is described in the next section. Tunable dye lasers in the ultraviolet have potential, but they are not currently usable because of line-width and stability limitations.

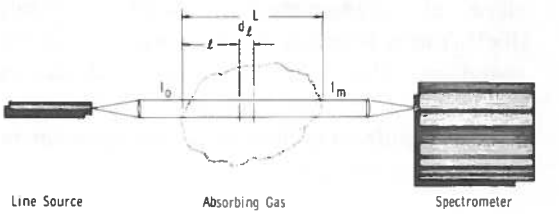

Figure 1. Illustration of physical arrangement for spectral line-absorption measurements.

It has been assumed, in the development of the analysis for the narrow-line absorption method, that the absorbing path was uniform in both temperature and concentration. When this is not the case, inversion techniques can be employed for certain simple geometries. For axisymmetric streams such as jet-engine exhausts, the Abel inversion can be applied. This is done by writing the fundamental absorption equation in the form

$$\ln(I(y)/I_0)_{\nu_0}(x) = -\int_{-y}^{+y} k_{\nu_0}\,dy \qquad (11)$$

where the appropriate geometry is as illustrated in Figure 2. This is in the form of an Abel integral transformation

$$k_{\nu_0}(r) = \frac{1}{\pi}\int_r^R \frac{\frac{d}{dx}\ln(I(y)/I_0)\nu_0}{\sqrt{r^2-x^2}}\,dx \qquad (12)$$

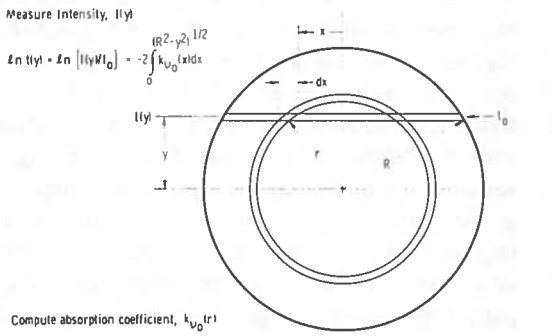

Figure 2. Illustration of Abel inversion of measured absorption coefficient.

Many routines are available for performing this inversion, and it is possible to obtain both local temperature and concentration from an axisymmetric source by its use. Unfortunately, a very rigid traversing platform is required for either the instruments or the engine (or else there must be many instrument stations located in the plane of measurement) in order to obtain $(I(y)I_0)$ as a function of the distance from the centerline. Thus, the inversion could not be employed in this work and it was necessary to assume a uniform path at some average temperature and concentration.

DESCRIPTION OF APPARATUS

Engine and Test Facility

The YJ93-GE-3 turbojet engine is fully described in [14], and the characteristics of the J2 test cell are given in [2]. It suffices to say here that the test was a direct-connect test in which ram air was supplied to the engine inlet at the temperature and pressure corresponding to a given air speed and altitude, and the static pressure at the engine exit was maintained at the pressure corresponding to the given altitude. The engine could be operated at any power setting, but data were taken only at "military power" and several afterburner power settings.

The conversion of the spectral absorption measurements to an absolute average number density of the species in question requires knowledge of the static gas pressure and temperature along the path. The concentration in parts per million requires also the gas density, which is found from the static pressure and temperature. In order to be consistent, since measurements of total pressure and temperature were not available for every condition at which absorption data were obtained, the unpublished YJ93-GE-3 PFRT Cycle Review, November 27, 1963, by D.P. Allen and R.J. Lewis, was used. The other engine variable required in the absorption measurements is the optical path length, or diameter of the engine exhaust stream. At the station 12 inches downstream of the nozzle exit, where the optical path intercepted the gas stream, it was found that the total pressure survey provided the best indication of the diameter of the stream, so this value was used as the path length.

Radiation Source

The source of narrow-line radiation was provided by a gas-discharge tube of special design shown schematically in Figure 3. A discharge is maintained through the capillary tube by two electrodes at either end, which are connected to a 2800-volt power supply. Gas flows continually through the tube; the pressure is adjusted to a value between 1 and 10 Torr, which seems to give the most stable operation. The tube is water-cooled to remove the heat transferred to the Pyrex walls and keep the gas cool as possible in order to minimize Doppler broadening of the spectral lines. Fused silica windows are mounted at either end of the tube to allow transmission of ultraviolet radiation. A monitoring photomultiplier tube with an interference filter is used at one window to record any drift in the radiative output that might occur.

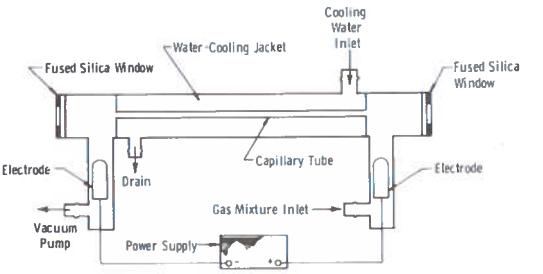

Figure 3. Discharge tube used to produce narrow-line radiation.

Experience has led to the use of special gas mixtures to provide spectra which are intense and unperturbed by bands from other molecules. To produce intense, narrow-line OH-resonance radiation, argon is bubbled through water at atmospheric pressure and then passed through a control valve, the discharge tube, and a vacuum pump. The argon evidently causes a selective excitation of the OH, producing the intense 3064Å band shown in Figure 4, which was obtained with a 1/2-meter Jarrell-Ash (JACO) spectrometer having a 2360 grooves/mm grating.

The NO γ-band radiation was found to be most intense when a 12:3:1 mixture of $Ar:N_2:O_2$ at a pressure of about 5 Torr was used. The (0,0) band of the γ system of NO is shown in Figure 5 as obtained in second order using a 1-meter JACO instrument having a 1180-grooves/nm grating. The lines of the γ band

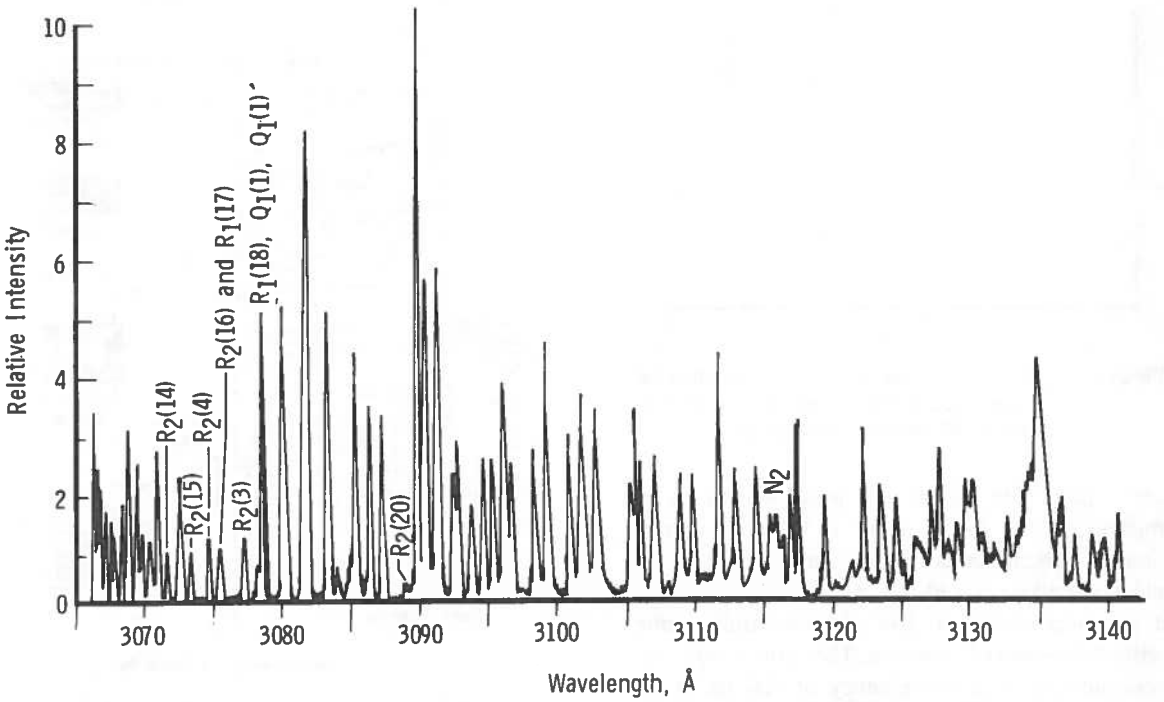

Figure 4. Line spectrum of the (0,0) OH band at 3064 Å produced by a discharge through flowing argon with entrained water vapor.

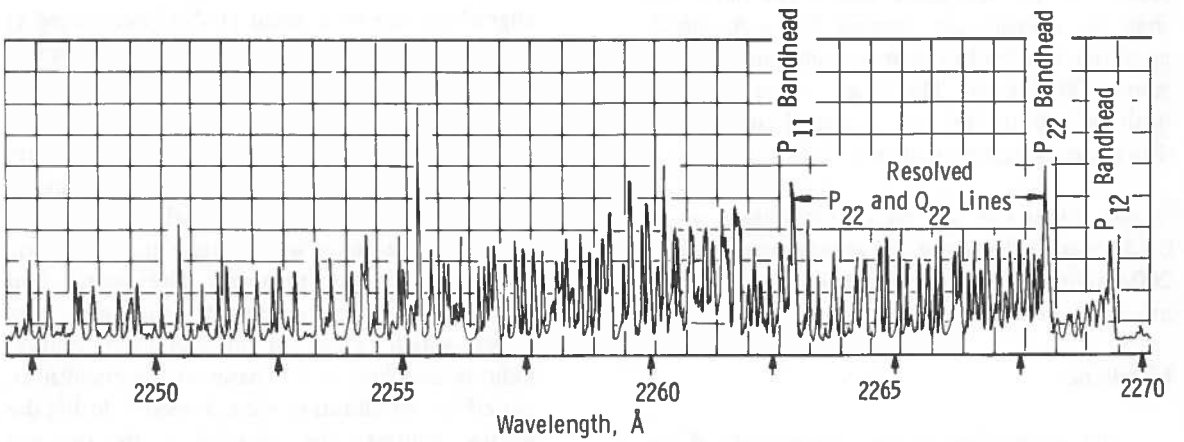

Figure 5. Line spectrum of the (0,0) γ-band of NO from a discharge through a 12:3:1 mixture of $Ar:N_2:O_2$.

are too closely spaced to be resolvable with the 1/2-meter instrument which had to be used in the test-cell installation, so an integrated-band spectrum as shown in Figure 6 had to be employed. The principles of the narrow-line absorption method are still applicable, however, since the source does emit narrow lines.

Receiver Unit

The receiver was a 1/2-meter Jarrell-Ash grating spectrometer with curved, adjustable slits, and a 2360 grooves/mm grating blazed for maximum reflection at 3000Å. The wavelength selector was operated remotely by a Selsyn motor/

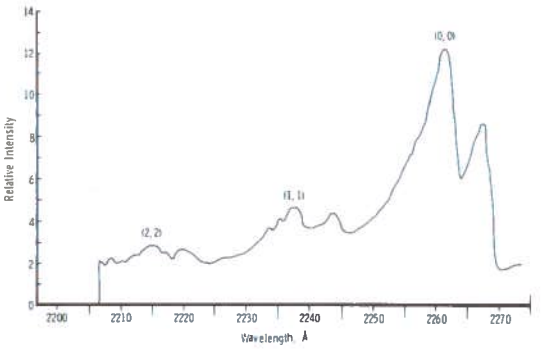

Figure 6. Integrated band spectra of NO obtained from discharge tube as mounted in propulsion development test cell (J-2).

servo pair. The wavelength position was transmitted by the signal from a 10-turn potentiometer, which served as the x-input for the x-y plotter used to record the data. The detector was a Hamamatsu-type R-106 photomultiplier tube with S-19 spectral response. The source radiation was modulated at a frequency of 400 Hz by an American Time Products Company tuning-fork chopper. The ac signal from the detector passed through a Philbrick Model 1003 preamplifier located within the spectrometer enclosure, and then to a Princeton Applied Research lock-in amplifier located in the instrument control room some 100 ft away. The data were recorded on both an x-y plotter and a strip-chart recorder. The instrumentation system is shown in Figure 7.

A 30-micron slit width (resolution about 0.2Å) was used for the OH measurements, and a 200-micron slit (1.6Å bandpass) for the NO measurements.

Installation

The orientation of the components of the measurement system with respect to the engine is diagrammed in Figure 8 and shown pictorially in Figure 9. In each case the view is toward the rear of the engine. A f/4.4 fused silica lens of 10 cm focal length was placed at one focal distance from the source, and another one focal distance from the spectrometer, so that a parallel beam of light was projected through a diameter of the engine exhaust at a point approximately 12 in. downstream of the nozzle exit plane. The distance from source unit to spectrometer was approximately 12 ft. The optical system was

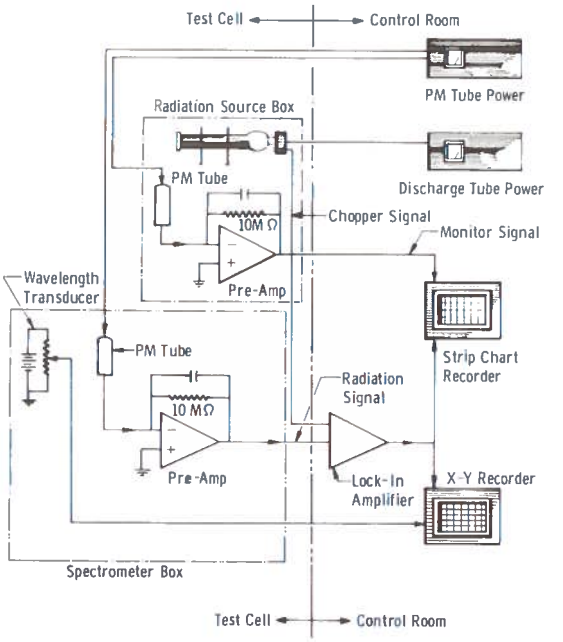

Figure 7. Circuitry for spectral-absorption data-recording system.

aligned by use of a small He-Ne laser placed at the centerline of the engine exhaust. No realignment was needed during the 4-week test period.

The source unit and spectrometer were housed in insulated, water-cooled aluminum enclosures mounted to the cell walls as shown in Figure 9. The boxes were purged at atmospheric pressure with dry nitrogen. The source and spectrometer were attached to 1-in.-thick steel plates which were set on vibration-isolation mounts attached to the bases of the enclosures. No effects of vibration were detected during the testing, although the vibration of the test cell itself was quite large. Thermocouples located inside the enclosures indicated that the temperature never rose above about 100°F, and no adverse temperature effects were observed. The fused silica windows through which the beam passed became coated with an oil-like substance during the tests, even though a stream of nitrogen was aimed at them at all times. The degradation of the signal due to window-coating did not seriously affect the measured results, but it made the data-reduction procedure more difficult, as will be discussed below.

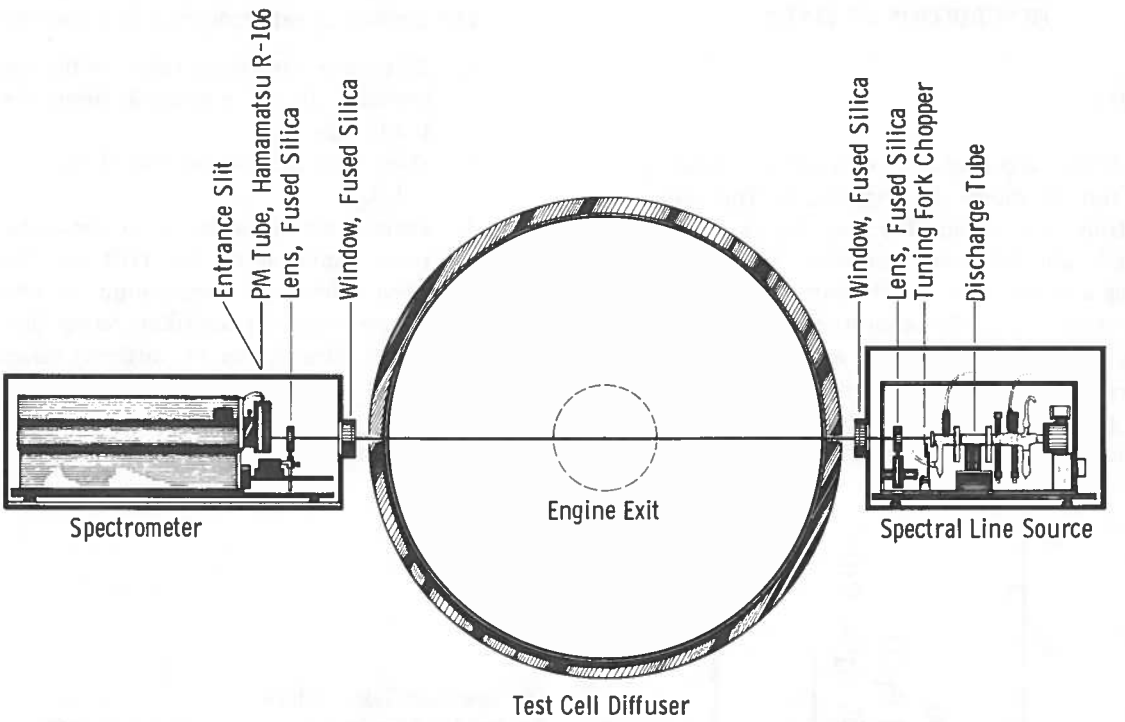

Figure 8. Diagram of installation of spectral-absorption apparatus in propulsion development test cell (J-2).

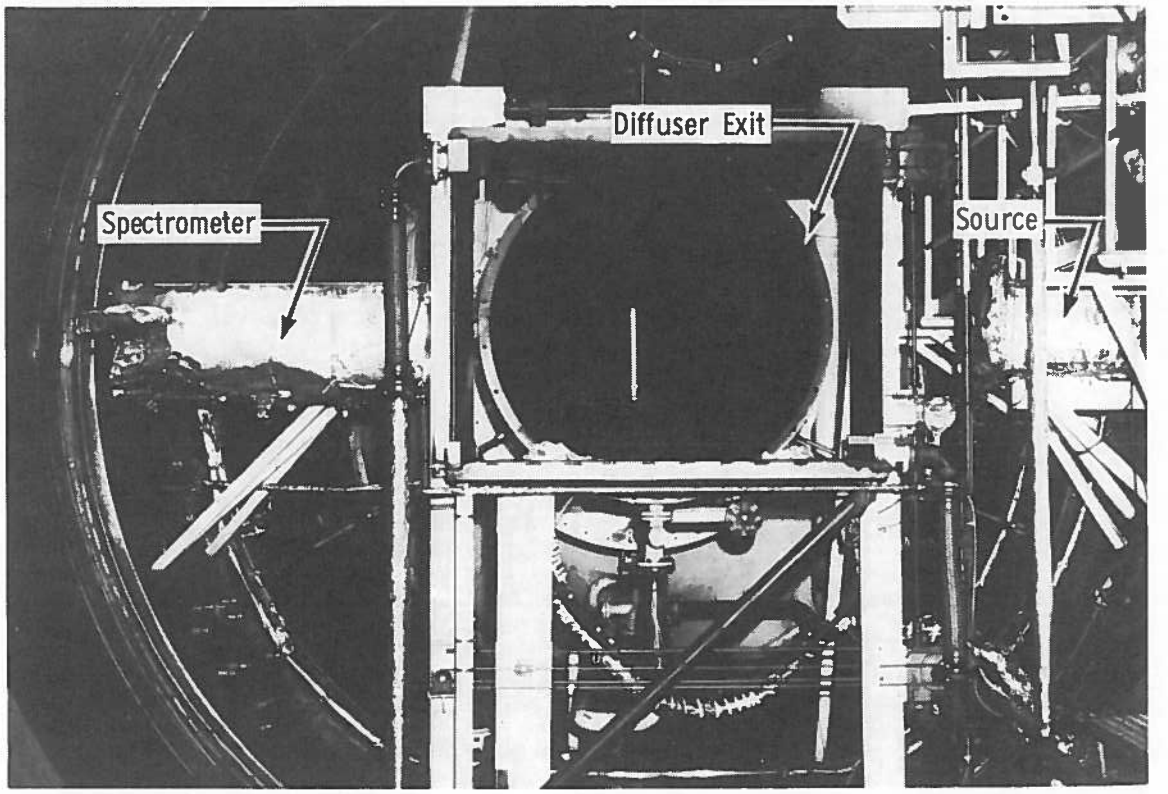

Figure 9. Photograph of installation of spectral-absorption apparatus in propulsion development test cell (J-2).

DESCRIPTION OF DATA

OH Data

A sample pair of OH spectra obtained during the test is shown in Figure 10. The upper spectrum was obtained before the engine was started, and the lower one some 3 hours later during acquisition of an afterburning data point. The magnitude of the absorption is noteworthy, as is the reduction in the reference intensity evidenced by the two spurious nitrogen bands and the lines from large rotational quantum-number states (note particularly $R_2(15)$).

The method of data reduction is as follows:

1. Determine a reference value for the line intensity to be measured using the $R_2(15)$ line, I_0.
2. Determine the transmission of the line, $(I/I_0)_m$.
3. Correct the transmission to line-center transmission, using Eq. (10) and the given exhaust-gas temperature. (A plot of measured transmission versus line-center transmission for different values of α was determined from Eq. (10) and used for correction to line-center transmission.)

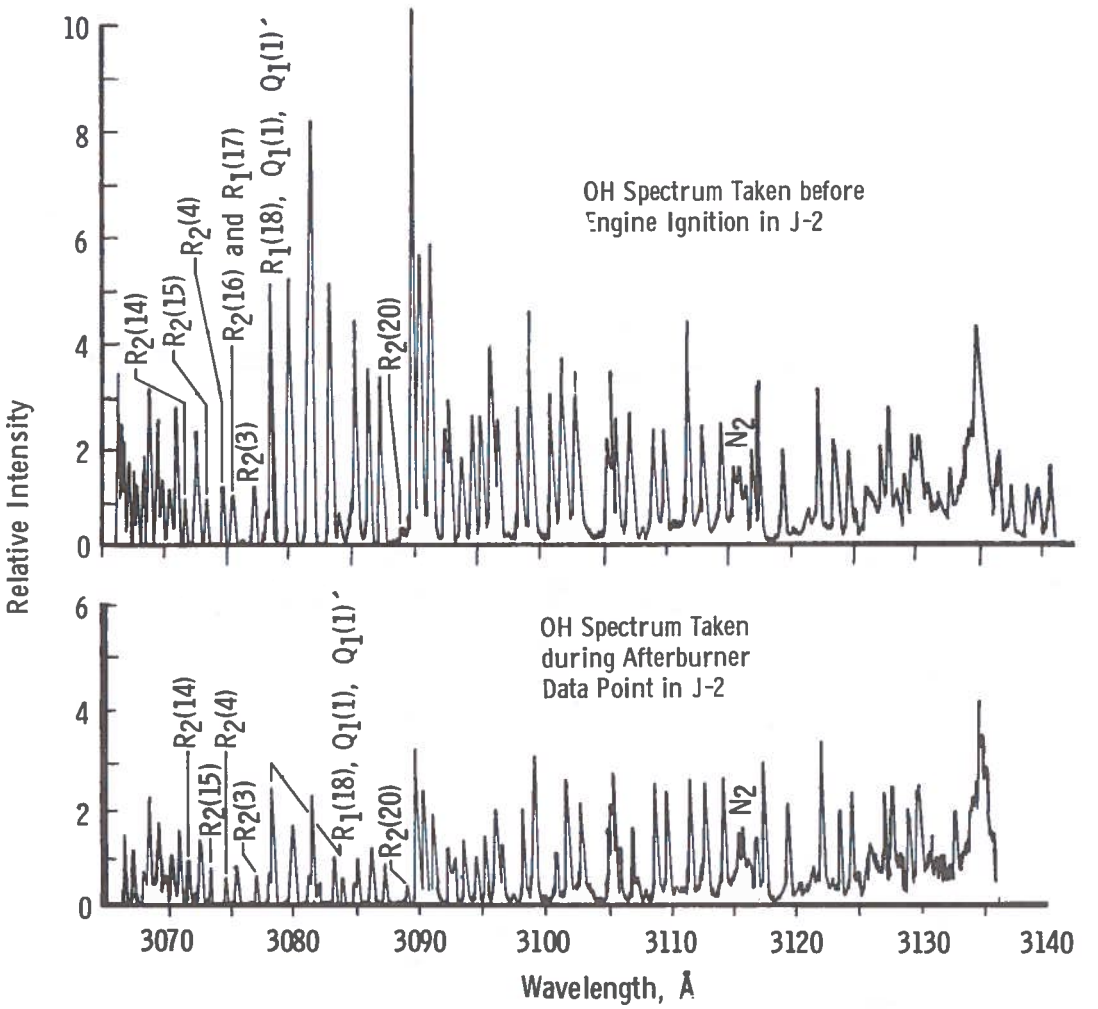

Figure 10. OH spectra taken before YJ93-GE-3 engine ignition and during afterburning.

4. Determine the number density from Eq. (6) using the appropriate gas pressure, temperature, and stream diameter, and the constants of Table 1.

The data reduction was carried out for only the $R_2(3)$ and $R_2(4)$ lines, for the purposes of this paper.

NO Data

A sample pair of NO spectra obtained during the test is shown in Figure 11. The upper trace is the reference spectrum, and the lower trace is for an afterburner data point. In this case the (1,1) and (2,2) bands from the source are also included in the spectral scans. The intensity of the (2,2) bandheads provides a convenient source of correction for source degradation, since they experience very little absorption at the temperatures encountered in the exhaust stream.

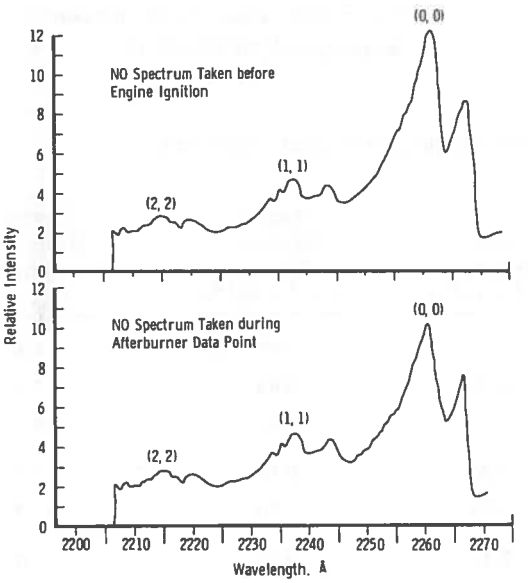

Figure 11. NO spectra taken before YJ93-GE-3 engine ignition and during afterburning.

A laboratory calibration was performed using an absorption tube of known length in which the pressure could be controlled. The spectra obtained in the laboratory at several different pressures are shown in Figure 12.

The method of calibration selected was as follows:

1. Measure the transmission at the peak of the second bandhead.

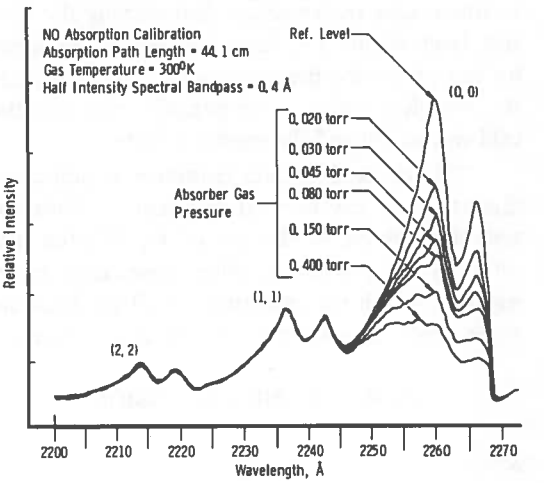

Figure 12. NO absorption calibration data for the (0,0) γ-band obtained with absorption cell in the laboratory.

2. Correct the measured transmission to line center, using Eq. (10).
3. Plot a calibration curve of N X L versus (I/I_0), as in Figure 13.

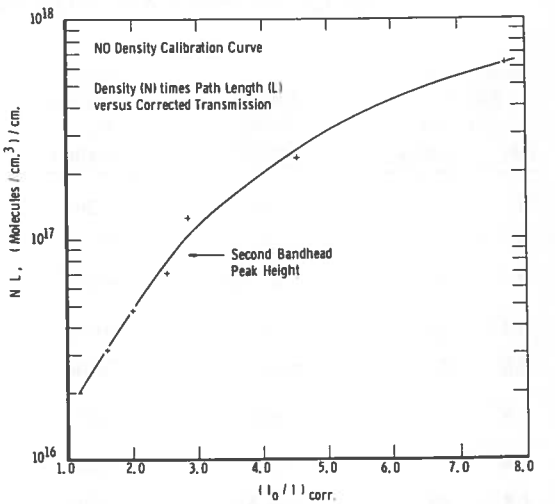

Figure 13. Calibration curve for NO density using second bandhead of the (0,0) γ-band (N = density of NO, cm^{-3}; L = path length, cm; $(I, I_0)_{\nu_0}$ = transmission at line center).

The data-reduction procedure was then straightforward. It consisted of correcting the reference intensity at the second bandhead using the (2,2) bandhead intensity, measuring the transmission at the second bandhead, correcting

to line-center transmission, determining the density from Figure 13, using the path length given by the pitot-tube pressure survey, and correcting for the difference in temperature between the calibration cell and the engine exhaust.

This method of data reduction is subject to alteration by any number of schemes. The most scientific would be the use of Eq. (9), but it is difficult to select a suitable wavelength increment in which the intensities of all the lines are measurable. Further work in this area is planned.

RESULTS AND DISCUSSION

Results

The "first-look" results of the emissions measurements on the YJ93-GE-3 engine using the data-reduction procedures just described are given in Tables 3 and 4 and Figures 14 and 15. A thorough analysis of these data is not an objective of this paper. Also, the numbers given may change somewhat as the data-reduction effort is iterated or altered. However, the relative values are not expected to change appreciably, nor are the absolute values expected to change by more than 20%.

Examination of the tables leads to the following observations:

1. OH densities are strongly affected by afterburning; values for maximum afterburning are larger than values for the military power setting by about an order of magnitude.
2. OH densities are directly related to total fuel flow rate.
3. NO densities are not noticeably dependent upon afterburning or total fuel flow rate, but remain about constant for all data points included.
4. NO concentrations measured by the in-situ method are factors of two to four larger than those measured by sampling and gas analyzers.

Table 3. Concentration of OH in Exhaust of YJ93-GE-3 Engine at Simulated Flight Conditions

Simulated Flight Conditions (M)	(h(kft))	Engine Power Setting	Total Fuel Flow Rate (lbm/hr)	Average Total Density ($cm^{-3} \times 10^{18}$)	Average Hydroxyl Density ($cm^{-3} \times 10^{14}$)	Average Hydroxyl Concentration (ppm)
0	0	mil	21200	11.3	0.50	4.4
0	0	min AB	29100	6.90	0.49	7.1
0	0	max AB	36300	4.45	6.41	144.
0.8	20	mil	15600	4.26	0.50	11.7
0.8	20	max AB	25800	2.96	2.70	91.2
0.9	37	mil	9040	2.43	0.17	7.0
1.4	35	mil	14300	2.65	0.15	5.7
1.4	35	min AB	19500	1.92	0.37	19.0
1.4	35	mid AB	23600	1.61	1.50	93.0
1.4	35	mid AB	24000	1.54	1.87	121.
1.4	35	mid AB	27600	1.47	4.29	292.
1.4	35	max AB	32000	1.34	10.4	776.
2.0	75	mil	3000	0.48	0.20	41.7
2.0	75	min AB	6200	0.39	1.77	454.
2.6	66	mil	7100	0.70	0.16	22.9
2.6	66	max AB	17900	0.35	2.08	594.

Table 4. Concentration of NO in Exhaust of YJ93-GE-3 Engine at Simulated Flight Conditions

Simulated Flight Conditions (M)	(h(kft))	Engine Power Setting	Total Fuel Flow Rate (lbm/hr)	Average Total Density ($cm^{-3} \times 10^{18}$)	Average Nitric Oxide Density ($cm^{-3} \times 10^{14}$)	Average Nitric Oxide Concentration (ppm)
1.4	35	mil	14500	2.65	1.98	74.8
2.0	55	mil	8470	0.96	1.58	165.
2.0	55	min AB	14900	0.81	1.42	175.
2.0	55	mid AB	17000	0.65	1.42	219.
2.0	55	max AB	18950	0.55	1.53	278.
2.6	66	mil	7100	0.70	2.26	323.
2.6	66	max AB	17900	0.35	2.16	617.

The uncertainty for these measurements is estimated to be about ±10%, on the basis of several repeated data points. The error in the absolute number densities cannot be estimated with any reliability, since it depends upon many factors. Among these are the true path length, the nonuniform distribution of concentration and temperature, static-temperature errors, and variations of source intensity during a spectral scan. However, for purposes of determining total emissions of OH and NO, the average molecular densities are believed to be accurate within ±20 percent.

Comparison of [OH] Results with Theoretical Predictions

In Figure 14 the density of OH is shown graphically for the flight conditions under which OH measurements were made, and for the power settings of military, minimum afterburning, and maximum afterburning. At the right of the figure is shown the average measured concentration in parts per million, and the equilibrium value calculated at the equivalence ratio and temperature corresponding to conditions in the afterburner combustion chamber. The theoretical value was obtained from the chemical-equilibrium calculation procedure given by Osgerby and Rhodes [15]. Note that there is reasonable agreement between the calculated and measured values for the afterburning cases. The values measured in the exhaust stream from the afterburning runs are consistently greater than those calculated in the combustion chamber except for one point, the sea-level-static minimum-afterburner run. The large discrepancy between the measured and calculated values for the nonafterburning firings is not yet understood. The important point is that the OH concentration is apparently governed by the finite rate chemistry in the flow, and is not altered very much in the millisecond or so between the two stations. The equilibrium value of [OH] at the static temperature and pressure existing at the measurement station is about two orders of magnitude less than the measured value. This observation is supported by the modeling results reported by the Lockheed research group [16].

Comparison of [NO] Results with Probe Measurements

Figure 15 shows the NO molecular density results of Table 4 in graphic form for the conditions run. Also, at the right of the figure are shown the concentrations determined by the absorption method and by the probe sampling method. The probe results were averaged [NO] data along the path taken from Reference 3. The total NO_x data from the sampling measurements are only slightly larger than the NO values. If both measurements are assumed to be correct, it is apparent that some of the NO must have been converted to some species other than an oxide of nitrogen along the path from the sample probe to the analyzer instrument. Further investigation is required to resolve this discrepancy.

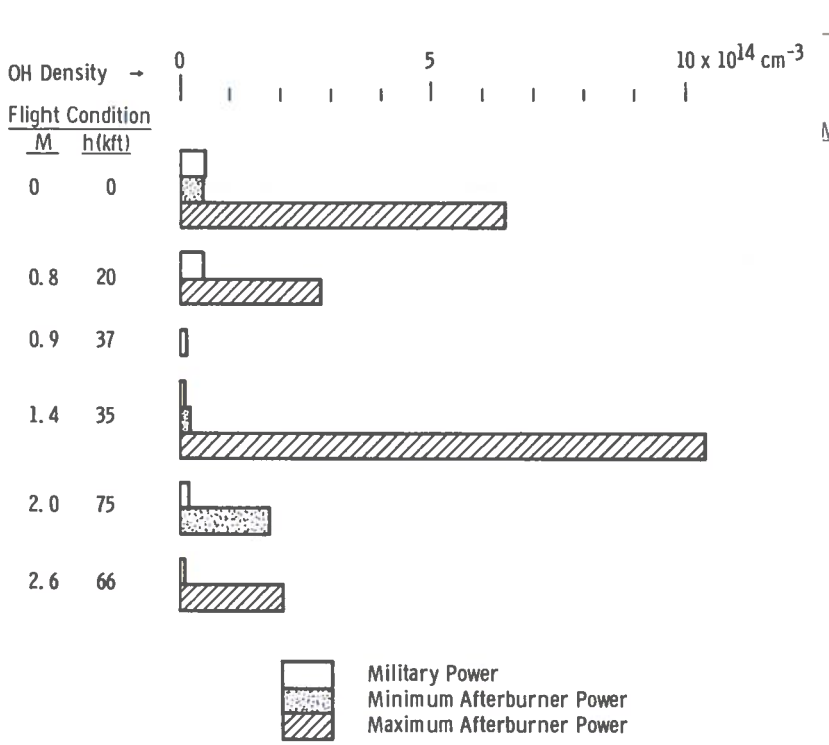

Figure 14. Average OH concentration in the exhaust of a YJ93-GE-3 engine compared with equilibrium values calculated at combustion conditions.

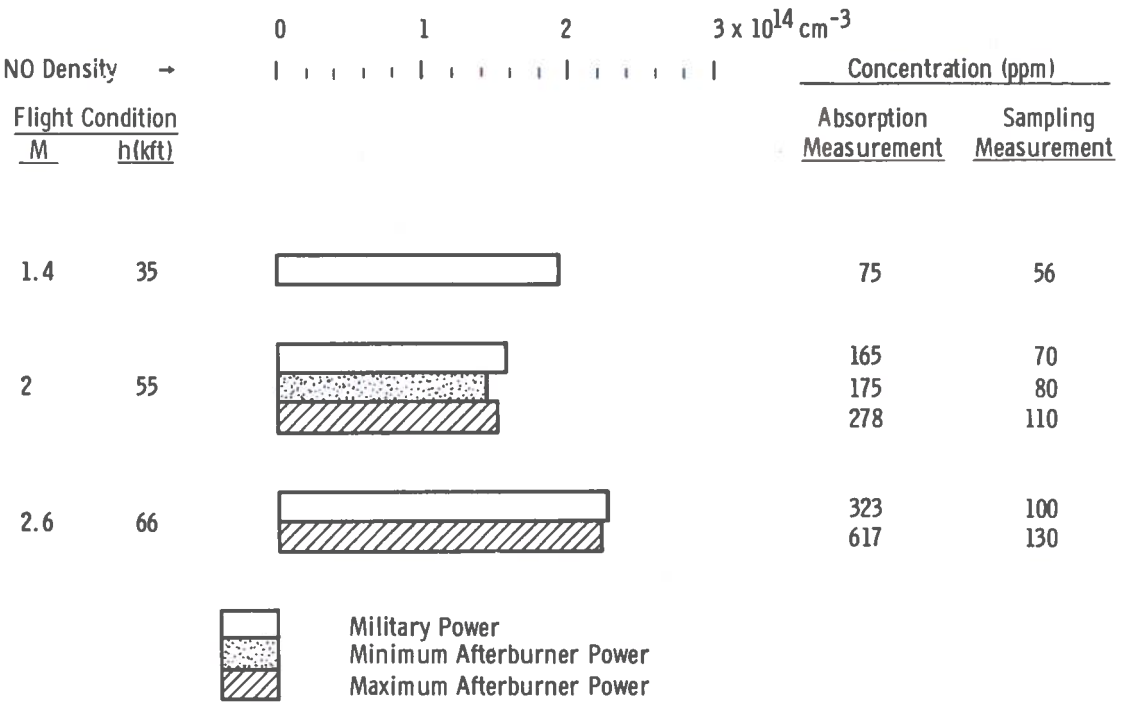

Figure 15. Average NO concentration in the exhaust of a YJ93-GE-3 engine; comparison of values measured in situ by UV absorption and those measured by sampling.

At this point it should also be noted that the rather constant NO molecular density means that the total rate of emission of NO is about constant, since the exhaust velocity and area do not vary much with engine flight speed and altitude. This fact is hidden when the measurement is expressed in terms of volume concentration (ppm) or emission index (weight of emissions/weight of fuel). Some absorption measurements were also attempted at the engine-idle power setting, but the attenuation was much less than for the military power setting. It is therefore suggested that the total rate of emission is a function only of the primary-combustor temperature, which is controlled by the equivalence ratio in the primary combustor.

Effect of Particulates on Absorption Measurements

One problem that was anticipated in making the UV transmission measurements never arose. It was predicted that the submicron soot particles in the engine exhausts would introduce scattering of the UV beam that would have to be distinguished from the absorption by the species of interest. However, no apparent reduction in transmitted intensity was detected at the engine-idle condition where the particulate loading is highest [17].

Further Possibilities for In-Situ Measurements

The use of in-situ techniques for measurement of the density of NO and OH has been demonstrated. It is possible to obtain concentrations of other minor species in the combustion gases, such as NO, CH, SO, and CN, using the same technique. Methods have also been developed at AEDC to determine concentration profiles of H_2O and CO_2 using measured infrared emission-absorption and band-model parameters [18]. This iterative technique may also provide the best method for obtaining static-temperature profiles. The emission-absorption method may also be applied to CO in the infrared, although this has not been done to date. Also, progress has recently been made in the detection of NO_2 by absorption of continuum emission in the 2400-2600Å range. It thus appears that the only species of interest which do not lend themselves to measurement by spectral techniques are the unburned hydrocarbons and the particulates.

SUMMARY

The results of the effort reported here on the in-situ measurement of hydroxyl and nitric-oxide concentrations in the exhaust of the YJ93-GE-3 jet engine by the resonance line-absorption technique may be summarized as follows:

- Spectral absorption techniques were successfully used to determine jet-engine emissions of OH and NO.
- OH emission densities of the YJ93-GE-3 engine were much larger for the afterburning engine than for the nonafterburning engine and, for the afterburner cases, corresponded to levels computed at the appropriate values of the afterburner-combustor fuel/air ratio, stagnation pressure, and stagnation temperature. The values ranged from 0.15×10^{14} cm^{-3} at Mach 1.4, 35,000 ft, and military power, to a maximum of 10.4×10^{14} cm^{-3} at Mach 1.4, 35,000 ft, and maximum afterburner power setting.
- NO emission densities for the YJ93-GE-3 engine were independent of whether the engine was afterburning or not afterburning, and changed only slightly with flight conditions for the military primary-combustor fuel flow. Values ranged from a minimum of about 1.4×10^{14} cm^{-3} at Mach 2, 55,000 ft, minimum AB, to about 2.3×10^{14} cm^{-3} at Mach 2.6, 66,000 ft, military.
- NO emission levels in ppm for the YJ93-GE-3 engine determined in situ by spectral absorption were larger by factors of about 1.5 to 5 than those measured by sampling through gas analyzers.

ACKNOWLEDGMENT

The research reported in this paper was sponsored by the U.S. Department of Transportation under the Climatic Impact Assessment Program. ARO, Inc., is the contract operator of AEDC.

REFERENCES

1. Barrington, A.E., editor, *Proceedings of the Survey Conference* Feb. 15-16, 1972, Climatic Impact Assessment Program, Department of Transportation, DOT-TSC-OST-72-13, (1972).

2. *Test Facilities Handbook* (9th Edition), Arnold Engineering Development Center, Arnold Air Force Station, Tennessee (July 1972).

3. Neely, J.E., "Emission level of the YJ93-GE-3 engine, an SST-like engine," in this volume.

4. Mitchel, A.C.G., and Zemansky, M.W., *Resonance Radiation and Excited Atoms*, the Macmillan Co., New York (1934).

5. Kaskan, W.E., "Hydroxyl concentrations in rich hydrogen-air flames held on porous burners," Combustion and Flame *2*, 229 (1958).

6. Houghton, W.M., and Jachimowski, C.J., "An absorption technique for measuring OH concentrations in shock tubes," Appl. Opt. *9*, 329 (1970).

7. Davis, M.G., McGregor, W.K., and Mason, A.A., "Determination of the Excitation Reaction of the OH Radical in H_2-O_2 Combustion," AEDC-TR-69-95 (Oct. 1969).

8. Nadler, M., and Kaskan, W.E., "Collisional broadening of OH $^2\Sigma - {}^2\pi$ lines in flames," J. Quant. Spec. Rad. Trans. *10*, 25 (1970).

9. Thorson, W.R., and Badger, R.M., "On the pressure broadening in the gamma bands of nitric oxide," J. Chem. Phys. *27*, 609 (1957).

10. Dieke, S.H., and Crosswhite, H.M., "The ultraviolet bands of OH," J. Quant. Spec. Rad. Trans. *2*, 97 (1962).

11. Learner, R.C.M., "The influence of vibration-rotation interaction on intensities in the electronic spectra of diatomic molecules," Proc. Roy. Soc. London *A269*, 311 (1962).

12. Perry-Thorne, A., and Banfield, F.P., "Absolute oscillator strength of the (0,0) band of the gamma system of nitric oxide by the Hook method," J. Phys. *B 3*, 1011 (1970).

13. Earls, L.T., "Rotational strength factors for transition," Phys. Rev. *48*, 423 (1935).

14. Ward, T.R., Kistler, S.M., and Edwards, Z.B., "Performance Evaluation of the YJ93-GE-3 Turbojet Engine in an Altitude Test Cell," AEDC-TDR-62-173 (June 1963).

15. Osgerby, I.T., and Rhodes, R.P., "An Efficient Numerical Method for the Calculation of Chemical Equilibrium in the H/C/O/N/A System," AEDC-TR-71-256 (April 1972).

16. Hoshizaki, H., Anderson, L.B., and Conti, R.J., "High-altitude aircraft wake dynamics," in this volume.

17. Gearhart, J.W., and Benek, J.A., "Measurement of Pollutant Emissions from an Afterburning Turbojet Engine at Ground Level: I. Particulate Emissions," AEDC-TR-72-64 (June 1972).

18. Brewer, L.E., and Limbaugh, C.C., "Infrared band model technique for combustion diagnostics," Appl. Opt., *11*, 1200 (1972).

DISCUSSION

SCHAINKER: Do you have any estimates of the accuracies of your concentrations? Also, are you getting interference from other species in the exhaust?

McGREGOR: Let me answer the last question first. We are generating the narrow-line spectrum on one side of the engine; I didn't mention that we are chopping at that point, so we are discriminating against any radiation that might be coming from within the engine exhaust. There is some radiation at these wavelengths which could interfere. However, we are discriminating against this by chopping the source, and since the source is pure radiation from the molecule in question, there is no interference.

As for accuracy, we are essentially calculating the molecular density from first principles, using the best data we have for the oscillator strength, and I have confidence in our results for OH number density. I am somewhat less confident about the parts per million, because this value is sensitive to temperature. In the case of NO, we have to rely on laboratory calibrations, but the conversion of absorption coefficients to density is fairly insensitive to temperature, since in the theoretical relationship there is the ratio of Doppler width over Boltzmann distribution. In the temperature range in which we are working, a factor-of-two change in temperature alters that ratio by very little. We could do almost anything to it and probably not change it by more than about 20%.

SCOTTO: Have you made any estimates of the error introduced by the diameter of the exhaust stream?

McGREGOR: We use the total-pressure profiles across the exit plane to get our path width, so there would have to be a big tailoff of the concentrations in the mixing zone for our values to change by more than about 5%.

SCOTTO: How would temperature gradients affect your measurements?

McGREGOR: They turned out to be less important than I had feared; you can arbitrarily change the temperature in the calculation by a fairly large amount without changing the final result much. If I had more time to make such measurements, though, I would do it differently. Rather than taking one shot through the center, I would take a profile across the stream. I would then do an Abel inversion of the transmission, inferring temperature and concentration at the same time.

KAUFMAN: Could you tell me how long the exhaust gas takes to pass from the high-temperature region in the burner through the secondary nozzle and out to where you see it?

McGREGOR: It's supersonic at these conditions, 10^{-4} or 10^{-5} seconds.

ANDERSON: You said that the trends were consistent, although the numbers were generally higher. If, with maximum afterburning, 80% of the NO_x were present as NO_2 and you were looking at NO, would you be able to see a violation of the trends?

McGREGOR: I am fairly certain that in all cases total NO_x measured by the sampling probe was actually *less* than the NO numbers we got with remote optical techniques – which of course doesn't make sense unless other nitrates are formed or something is adsorbed on the walls of the sampling system. I would very much like to make simultaneous NO and NO_2 measurements under similar circumstances, using remote optical techniques.

THE PERTURBED ATMOSPHERE: A REVIEW OF CIAP ACTIVITIES

ROBERT L. UNDERWOOD
Office of the Secretary
U.S. Department of Transportation

ABSTRACT: Major Climatic Impact Assessment Program (CIAP) activity is structured to estimate perturbations to the 1990 stratosphere and the 1990-2020 troposphere that could result from projected 1990 world high-altitude fleet operations. While models must be relied upon for these estimations, experimental and observational data are utilized where they can give insight into model validity or provide necessary model parameterizations. The spectrum of models necessary for estimation of the perturbed atmosphere may be categorized by the time and motion scale resolved, by model dimensionality, and by degree of coupling between fluid motions and chemistry in the model. Model intercomparisons, comparisons with observed climatology, and model sensitivity studies are essential for placing confidence levels upon model predictions.

Ongoing CIAP activities related to estimation of the perturbed atmosphere are described. Although the emphasis is on activities funded under the CIAP, related activities are described which are not funded by CIAP but are considered important to its success. Expected program outputs are summarized, and current problem areas are addressed.

The objective of the Climatic Impact Assessment Program (CIAP) is to assess, in the form of a report in 1974, the impact of climatic changes resulting from perturbation of the upper atmosphere by the propulsion effluents of a world high-altitude aircraft fleet as projected to 1990. In order to meet the CIAP objectives by the required 1974 date, the program is proceeding in six steps: 1) determine the nature of the existing stratosphere, 2) determine the nature and amounts of propulsion effluents to be introduced into the stratosphere at about the year 1990, 3) estimate perturbations to the stratosphere resulting from the introduction of the projected engine effluents, 4) estimate perturbations to the troposphere which may result from changes in the stratosphere, 5) determine the biological effects of the estimated tropospheric changes upon man, animals, and plants, and 6) assess the economic impacts of the environmental effects. Figure 1 schematically depicts the interaction of these steps.

This paper reviews CIAP activities related to estimation of the perturbed atmosphere – that is, the third and fourth steps in the study. Papers by A.J. Grobecker, S.C. Coroniti and A.J. Broderick, A.K. Forney, and D. Sheldon provide similar surveys of CIAP activities pertinent to the remaining steps in the program.

Description of the perturbed 1990 timeframe stratosphere requires combined consideration of the propulsion effluents introduced (step 2 of the study) and the natural unperturbed stratosphere (step 1 of the study). Outputs must include description of mass transport, chemical reactions, sources and sinks, and energy transport in the perturbed stratosphere, and the resulting distribution of species densities in the stratosphere and insolation at the tropopause. With knowledge of the perturbed stratosphere, the perturbed 1990-2020 troposphere is to be estimated. Outputs must include mean values and standard deviations of temperature, winds, and precipitation as well as surface radiative flux. The thirty-year time interval was chosen to allow consideration of longer-term tropospheric perturbations that could result from changes in heating of the oceans.

It is evident that models – whether based upon solutions of analytical equations governing pertinent physical processes or upon correlation of empirical data – must be relied upon to provide estimates of projected atmospheric perturbations. The scope of CIAP modeling activities will depend on the answers to the following three questions:

- What considerations must be made in the simulation of the stratosphere by computer?
- What abridgements of a complete model of the stratosphere/troposphere/ocean,

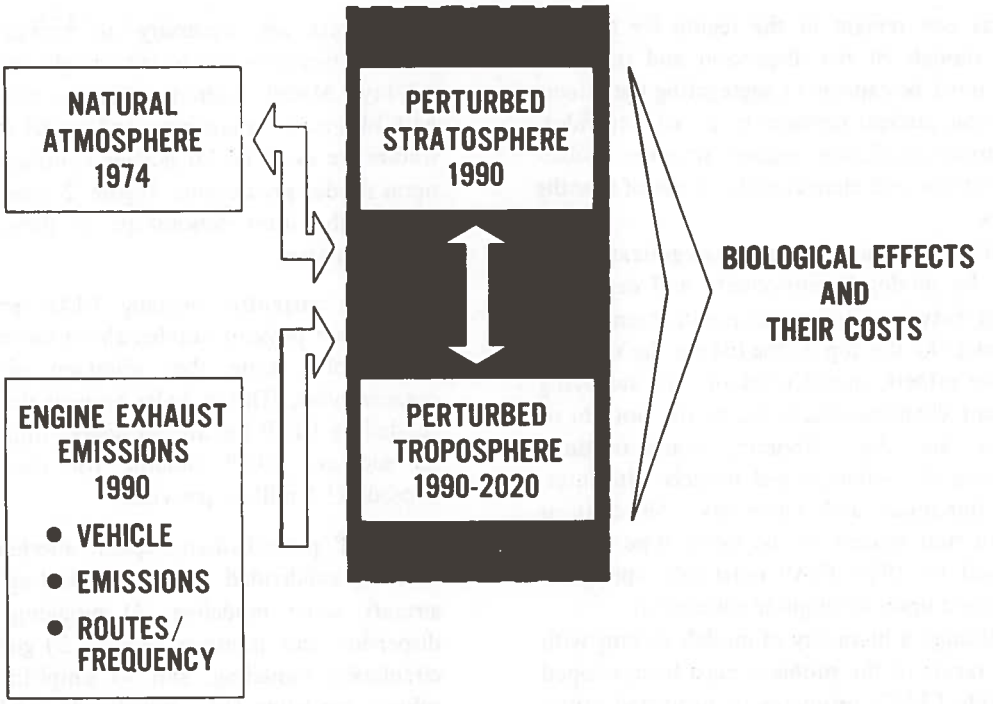

Figure 1. Structure of Climatic Impact Assessment Program.

such as that planned for future development by NOAA's Geophysical Fluid Dynamics Laboratory, may seem appropriate to derive answers desired by CIAP?

- What are the expected limitations of the stratospheric simulation to be done in the next two years?

Computer and schedule constraints may force compromises in the comprehensiveness of the models which can be utilized to derive answers desired by CIAP.

The spectrum of models necessary for estimation of the perturbed atmosphere may be categorized in various ways. Among these are categorization by the time and motion scale resolved, by model dimensionality, and by degree of coupling between fluid motions and chemistry in the model. Table 1 shows a categorization of regimes for analysis of atmospheric perturbations by the time and scale of motion resolved. The wake regime extends from the point at which engine exhaust products are deposited in the flow field behind a high-flying aircraft to distances at which the influence of atmospheric dynamics becomes significant or dominant in comparison with aerodynamically induced flow

Table 1. Modeling Regimes

REGIME	CHARACTERISTIC TIME	HORIZONTAL SCALE (M)	VERTICAL SCALE (M)	REGION CHARACTERISTICS
WAKE • JET PLUME • VORTEX/POST VORTEX	MINUTES	10^2 - 10^3	10^2 - 10^3	• AERODYNAMICALLY INDUCED MOTIONS PREDOMINATE • TEMPERATURE DECREASES TO AMBIENT • $V_{wake} \neq V_{ambient}$
DISPERSION AND TRANSPORT	DAYS, WEEKS	10^2 - 10^4 TO 10^5 - 10^6	10^2 - 10^4 TO $5 \cdot 10^4$	• LOCAL ATMOSPHERIC DYNAMICS DOMINATES • EFFECTS OF MULTIPLE AIRCRAFT IN TRAFFIC CORRIDOR
GLOBAL CIRCULATION	MONTHS, YEARS			• GLOBAL-SCALE MOTIONS • LONG-TERM EFFECTS OF AIRCRAFT FLEET

perturbations. In this regime the propulsion effluents cool rapidly to ambient temperature and spread horizontally and vertically over distances on the order of hundreds of meters. The propulsion effluents remain in the region for times on the order of minutes. The dispersion and transport regime is influenced dominantly by the small-scale structure of the atmosphere, which produces convection and atmospheric diffusion of engine effluents from the line in which the aircraft wake is deposited. The regime terminates when the propulsion exhaust products spread to dimensions compatible with the grid size of global circulation models. Since exhaust

products can remain in the region for days or weeks, models of the dispersion and transport regime must be capable of aggregating the effects of multiple aircraft passages in a traffic corridor. The global-circulation regime involves global-scale motions and characteristic times of months or years.

Table 2 is an alternate categorization of models by model dimensionality and degree of coupling between fluid motions and chemistry in the model. At the top of the list are the simplest modeling efforts, useful primarily for surveying important chemical reactions. At the bottom of the list are the elaborate, computer-time-consuming three-dimensional models with interactive dynamics and chemistry. Since it is doubtful that models of the latter type can be developed by 1974, CIAP must rely upon estimates based upon incomplete simulation.

Although a hierarchy of models dealing with various facets of the problem must be developed to provide CIAP's estimates of projected atmospheric perturbations, experimental and observational data are necessary to provide model parameterizations and to give insight into model validity. Model intercomparisons, comparisons with observed climatology, and model sensitivity studies are essential for placing confidence levels upon model predictions. Figure 2 schematically depicts the interrelationships of these various CIAP activities.

The currently ongoing CIAP perturbed-atmosphere projects number about twenty-seven, and involve more than eighteen performing organizations. (This includes projects that are not funded by CIAP but are considered important to its success.) CIAP funding for the projects exceeds $1.5 million per year.

CIAP perturbed-atmosphere modeling projects are subdivided into those dealing with 1) aircraft wake modeling, 2) modeling of the dispersion and transport regime, 3) global-scale circulation modeling, and 4) simplified atmospheric modeling (i.e., global-scale models with parameterized transport). The major CIAP

Table 2. Classes of Computational Models

MODEL DIMENSIONALITY	TYPICAL EXAMPLES	USEFULNESS
CHEMICAL REACTIONS ONLY, NO DYNAMICS	UNIV. WASHINGTON (Harrison) V.P.I. (Levine)	INITIAL SURVEY OF SENSITIVITY OF CHEMICAL REACTIONS
ONE-DIMENSIONAL WITH PARAMETERIZED TRANSPORT	NOAA (Shimazaki) NASA Ames (Whitten)	SURVEYS OF SENSITIVITY OF CHEMICAL REACTIONS USING PARAMETERIZED DIFFUSIVE TRANSPORT
	LMSC (Hoshizaki)	STUDIES OF WAKE DYNAMICS
TWO-DIMENSIONAL WITH PARAMETERIZED DYNAMICS	LLL (MacCracken) NOAA (Shimazaki)	EFFECTS OF DIFFUSIVE TRANSPORT ON CHEMISTRY
	LMSC (Hoshizaki)	STUDIES OF WAKE DYNAMICS
THREE-DIMENSIONAL WITH DYNAMICS	GFDL (Mahlman) MIT (Cunnold) NCAR-Colorado (Washington, London) UCLA (Mintz)	STUDIES OF DYNAMICS AFFECTING CHEMISTRY, BUT NOT DYNAMICS AFFECTED BY CHEMISTRY
TWO-DIMENSIONAL WITH INTERACTIVE DYNAMICS AND CHEMISTRY	LLL (MacCracken)	STUDY OF DYNAMICS AND CHEMICAL INTERACTION OF LIMITED SCOPE
THREE-DIMENSIONAL WITH INTERACTIVE DYNAMICS AND CHEMISTRY	(Post-1974 only)	COMPLETE ATMOSPHERIC SIMULATION

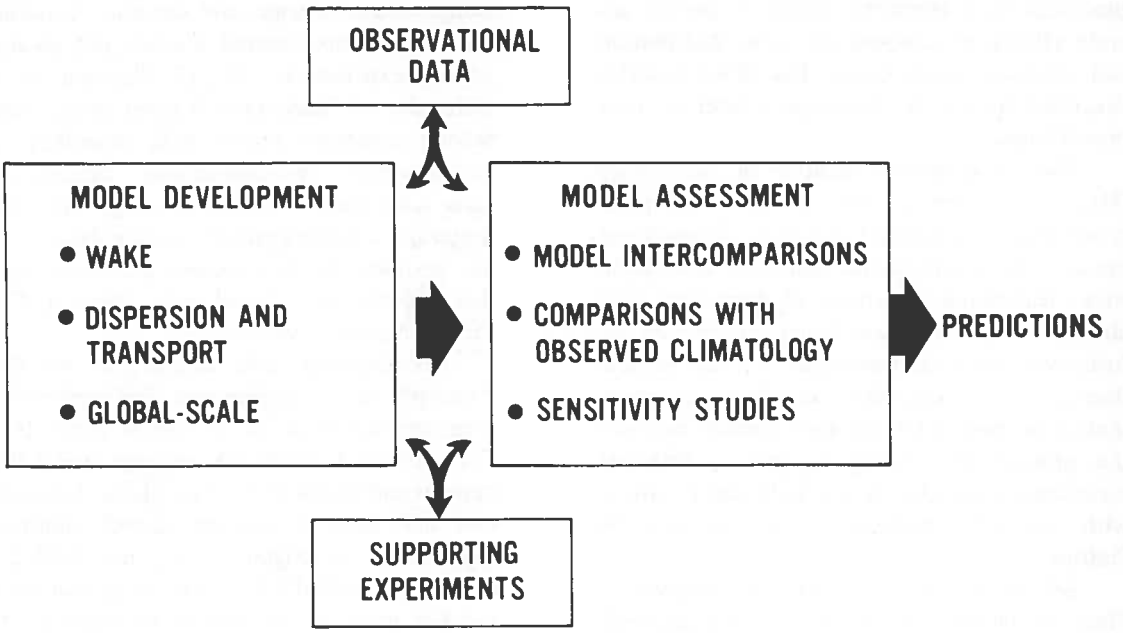

Figure 2. Perturbed atmosphere activities.

aircraft-wake modeling project is being conducted by Lockheed Missiles and Space Company (LMSC), Palo Alto Research Laboratory. LMSC is developing and utilizing a model for the chemically reacting wake of an aircraft flying at subsonic or supersonic speeds in the stratosphere or upper troposphere. Model outputs are wake size and composition for input to dispersion and transport models. The principal investigator, H. Hoshizaki, describes the model in greater detail in this volume. In a related effort, Aeronautical Research Associates of Princeton, Inc. (ARAP) is examining fundamental chemical and fluid-mechanical processes in aircraft wakes, under NASA sponsorship.

Modelers of the dispersion and transport regime include the Aerospace Corporation, Lawrence Livermore Laboratory (LLL), and ARAP. Aerospace is developing a model for dispersion and transport of engine exhaust products to provide pollutant distributions for input to global-scale models. Principal investigator is Dr. T. Taylor. LLL is adapting and extending existing nuclear-cloud diffusion/transport models to transport and chemically transform exhaust constituents over lateral scales from hundreds of meters to hundreds of kilometers. Principal investigator is Dr. J. Walton. ARAP's efforts support those of Aerospace and LLL through simulation of small-scale atmospheric diffusion to calculate effective eddy diffusivities, and through estimation of the effects of non-uniform mixing on chemical reactions. Dr. G. Hilst is principal investigator.

As part of CIAP's global-scale circulation modeling activities, LLL is extending and improving the LLL zonal atmospheric model (ZAM) to make it suitable for CIAP application in estimating perturbations to the stratosphere and troposphere due to aircraft operations. ZAM is a two-dimensional model (latitude, altitude). Dr. M. MacCracken, principal investigator, further discusses the model in this volume.

The University of California at Los Angeles (UCLA) is extending its existing three-dimensional global circulation model into the stratosphere, incorporating stratospheric radiation dynamics and photochemistry, and coupling the model to an ocean model. The extended model is to be used, in time, to investigate the natural and perturbed atmosphere. Principal investigators include Professors Y. Mintz, A. Arakawa, and S. V. Venkateswaran.

In a cooperative effort, the National Center for Atmospheric Research (NCAR) and the University of Colorado are combining results from NCAR's three-dimensional atmospheric circulation model with a University of Colorado

time-dependent chemistry model to predict aircraft effects on atmospheric ozone distribution and ultraviolet transmission. The NCAR model is described by Dr. W. Washington later in these proceedings.

The Massachusetts Institute of Technology (MIT) is developing a three-dimensional, quasi-geostrophic, spherical-harmonics atmospheric model with stratospheric dynamics and chemistry. Horizontal variations of dependent variables in the model are being represented by forty-two spherical harmonics. In the vertical direction, the dependent variables are represented on twenty-six pressure surfaces between the ground and seventy kilometers. Principal investigators are Drs. D. Cunnold and F. Alyea, with scientific guidance from Professor N. Phillips.

Several activities of NOAA's Geophysical Fluid Dynamics Laboratory (GFDL), although not funded by CIAP, are considered important to the program's success. Included, for example, are development of a fifty-vertical-level, three-dimensional, global-circulation model that is to incorporate stratospheric chemical and transport processes, and three-dimensional stratospheric tracer experiments. The latter are the subject of a paper in this book by Dr. J. Mahlman.

Global-scale models under development within the CIAP include simplified models with parameterized transport as well as general-circulation models. Among the simplified models is a global box model under development at LLL for use in screening important chemical processes and in indicating worldwide equilibrium distributions. Dr. J. Chang is principal investigator. Similarly, Dr. T. Shimazaki and D. Wuebbles at NOAA's Environmental Research Laboratories are developing a two-dimensional steady-state atmospheric-chemistry model with parameterized motion that emphasizes the 10-40 km altitude region. The model is to be extended to include time dependence and possibly three-dimensional transport. Mr. Wuebbles further describes the model in a paper below. An analogous model is under development by Dr. R. Whitten at the NASA Ames Research Center with NASA funding. Dr. F. Hudson of the Sandia Corporation is performing theoretical and modeling studies of normal and disturbed stratospheric chemical kinetics in order to determine significant stratospheric species and reactions, time dependence of compositional change, and optimum conditions for in-situ experimental studies and chemical release experiments. Dr. H. Harrison of the University of Washington is developing a stratospheric computer model with chemistry and parameterized two-dimensional dynamics to guide laboratory and field investigations. Other simplified modeling projects not funded by CIAP but pertinent to its objectives are under way in this country and abroad (e.g., Belgium, Great Britain, Norway, Sweden).

Observational data obtained in the CIAP Atmospheric Monitoring and Experiments Subprogram, described in an earlier paper by S. Coroniti and A. Broderick, support model development and assessment. Atmospheric data collection and analysis projects provide additional support. In an ongoing effort not funded by CIAP, MIT and GFDL are collecting and analyzing ten years of radiosonde atmospheric data (1963-72). Data to be made available include wind speed and direction, temperature, and relative humidity at more than twenty levels up to seven millibars. NCAR has similar ongoing activities. In an effort that is related to and complements that of MIT/GFDL, Environmental Research and Technology, Inc. (ERT) is establishing a data bank for trace constituents in the stratosphere, and is collecting and analyzing nonradiosonde atmospheric data. Dr. N. Gaut is principal investigator. Under CIAP funding, Professor R. Newell and other MIT staff members are analyzing five years (1963-67) of stratospheric data for parameters of modeling significance (e.g., horizontal fluxes of momentum, heat, and energy). Dr. D. Deirmendjian of the Rand Corporation is estimating the effects of particulates upon solar radiation; he will use the results to perturb a general circulation model.

CIAP experiments also support model development and assessment. The CIAP Atmospheric Monitoring and Experiments Subprogram experiments are pertinent. Also pertinent are laboratory chemistry studies conducted as part of the CIAP Chemical Dynamics Subprogram. Professor H. Johnston of the University of California at Berkeley is investigating in the laboratory chemical reactions affecting stratospheric ozone. He is obtaining spectroscopic properties of O_2, O_3, NO_2, HNO_3, N_2O, and NO_3 and performing thermal kinetic studies involving NO_2+O_3, $HO+O_3$, $HOO+O_3$, HOO+NO, and $O(^1D)+N_2O$.

Professor D. Davis of the University of Maryland is developing improved techniques for the measurement of OH, $O(^1D)$, and HO_2, and measuring reaction kinetics involving $O(^3P)$, $O(^1D)$, H, OH, and HO_2. The National Bureau of Standards is advising CIAP on significant chemistry in the stratosphere, obtaining and evaluating rate and photochemical data, and performing pertinent laboratory measurements. Dr. M. Scheer is principal investigator. In addition, numerous laboratory chemistry studies relevant to, but not funded by, CIAP are being conducted in this country and abroad.

Several CIAP experimental studies are of special interest in consideration of the perturbed atmosphere. LMSC is conducting ground-based and flight experiments to examine horizontal and vertical growth of wakes behind high-flying aircraft. NASA, without CIAP funding, is examining the feasibility and desirability of a stratospheric jet wake experiment to verify wake models. If such an experiment proves attractive, NASA plans to conduct it. N. Farlow of the NASA Ames Research Center is principal investigator for the project. Dr. F. Hudson of Sandia, as noted previously, is examining optimum conditions for an NO chemical release experiment. His studies are described later in this volume. LMSC is examining a stratospheric photochemistry experiment to yield data on the potential alteration of atmospheric composition by chemical reactions with species present in jet engine exhaust gases.

One model assessment project is presently funded by the CIAP. The Rand Corporation is comparing results from global models (e.g., UCLA, LLL) with climatic data and performing parametric studies of model sensitivities to changes in input data. Dr. R. Rapp is principal investigator. Dr. M. Warshaw of Rand discusses this project in more detail further on.

Tables 3 and 4 summarize these perturbed-atmosphere projects. Figure 3 summarizes the flow and interfaces of the ongoing CIAP modeling activities pertinent to estimation of the perturbed atmosphere.

Certain problem areas require special attention if CIAP perturbed-atmosphere objectives are to be met:

- Extension/refinement of models to incorporate stratosphere
- Selection of simplified models for CIAP use
- Coupling wake/dispersion and transport/global models
- Model data requirements and their satisfaction
- Accuracy requirements vs. model capabilities
- Model verification
- Model sensitivity studies

Modeling of the dispersion and transport regime and model sensitivity studies appear especially critical at this time.

Further background material on the subject of this paper is available in References [1] through [3].

Table 3. CIAP Perturbed-Atmosphere Projects (Modeling)

WAKE REGION	DISPERSION AND TRANSPORT	GLOBAL CIRCULATION	SIMPLIFIED MODELS
LMSC	AEROSPACE	2-D: LLL	LLL
ARAP*	ARAP	3-D: GFDL* MIT NCAR*/U. COLO. UCLA	NASA AMES* NOAA ERL SANDIA U. WASH. OTHERS*
	LLL		

*NOT CIAP-FUNDED

Table 4. CIAP Perturbed Atmosphere Projects

ATMOSPHERIC DATA COLLECTION AND ANALYSIS	SUPPORTING EXPERIMENTS	MODEL SENSITIVITIES/ INTERCOMPARISONS
ERT	AM&E SUBPROGRAM	RAND
GFDL*	LMSC	
MIT	NASA*	
NCAR*	SANDIA	
RAND	C D SUBPROGRAM	

*NOT CIAP FUNDED

REFERENCES

1. Barrington, A.E., editor, *Proceedings of the CIAP Survey Conference, 15-16 February 1972,* DOT Report DOT-TSC-OST-72-13, 1972.
2. Underwood, R.L. editor, *Proceedings of the CIAP Workshop on Computational Modeling of the Atmosphere, 11-14 April 1972,* DOT Report DOT-TST-90-1, 1972.
3. Greenstone, R., and Underwood, R.L., *Summary Proceedings of the CIAP Joint Atmospheric Modeling and Chemical Dynamics Workshop, 12-13 September 1972,* DOT Report DOT-TST-90-2, 1972.

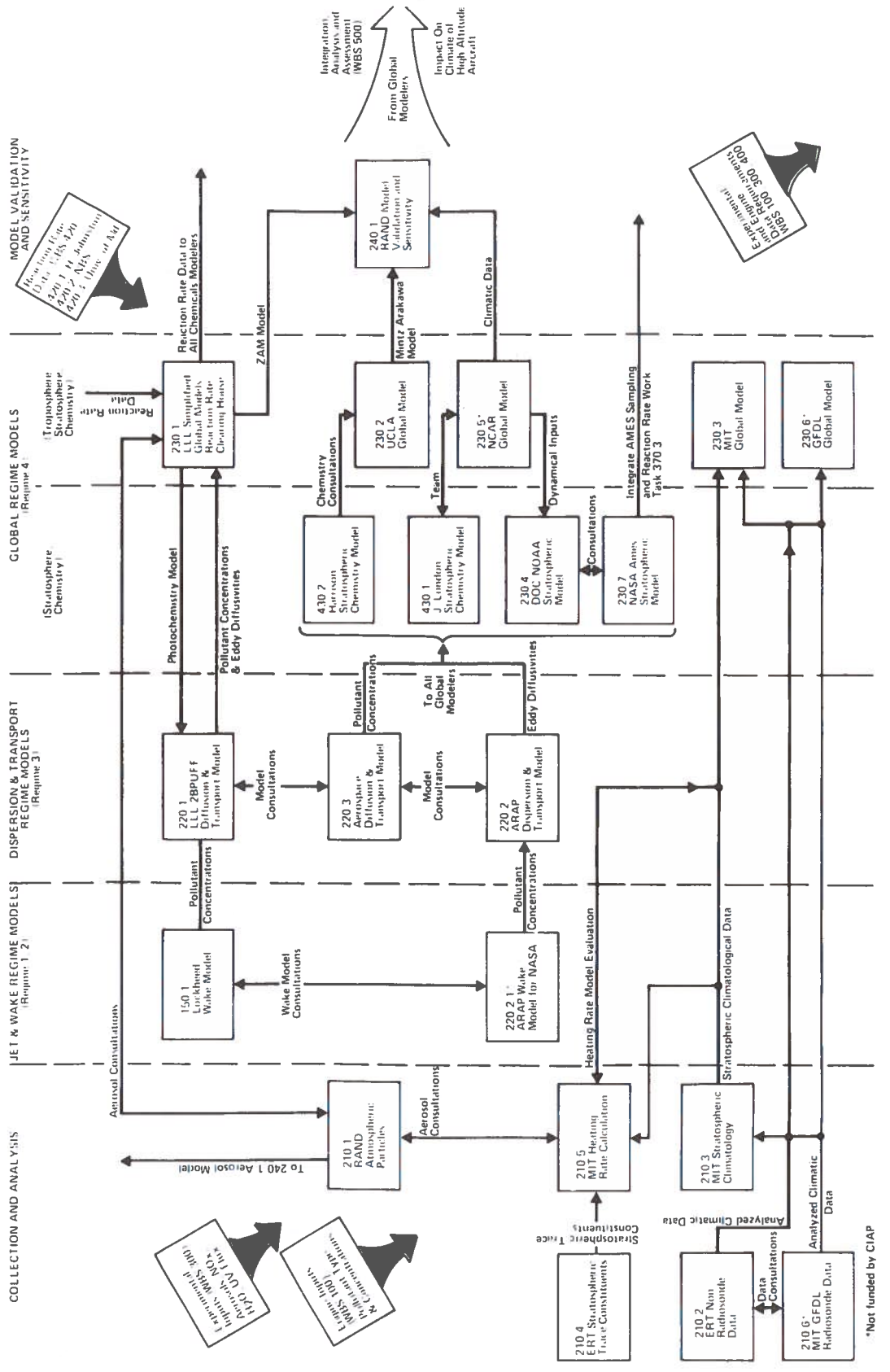

Figure 3. Atmospheric modeling task flow.

THE DESIGN OF CHEMICAL-RELEASE EXPERIMENTS IN THE STRATOSPHERE

FRANK HUDSON
Sandia Laboratories
Albuquerque, New Mexico

ABSTRACT: The interaction of mathematical simulation with the design and interpretation of experiments is explored, first for a laboratory study and then for a chemical release in the stratosphere. Several chemical-release experiments are simulated, in order to learn which ones would give measurable and meaningful results. It is concluded that a real experiment would be difficult and complex, but that none of the unsolved problems seems insurmountable.

INTRODUCTION

The Climatic Impact Assessment Program and the problem it addresses are unusual in many ways: for example, its motivation and initiation, the broad scope of both its investigation and the applications of the answers it yields, the variety of disciplines involved, the strongly predictive nature of the undertaking, and the large number of diverse groups whose studies must be combined to form a coherent picture. In a more directly technical sense, the range of time and space scales involved is disconcerting; studies whose characteristic times and distances are microseconds and nanometers must be correlated with those measured in years and thousands of kilometers.

Such a program might understandably require some unusual technical approaches in certain critical areas. One such project that has been frequently suggested is chemical-release studies of the chemical kinetics induced by the trace-gas effluents while they are being dispersed in the stratosphere. This direct simulative approach is appealing, but gives rise to a number of very difficult problems with time scales, instrumentation, and field operation. I have been asked to make an exploratory study of the kinetic aspects of such a program to better delineate the parameters involved, and to develop an approach that would optimize the design of experiments. The preliminary results of this study are presented here; they emphasize the need for iterative correlation of calculations based on laboratory experiments with in-situ measurements. This is *not* a proposal for, or a specific design of, chemical-release experiments; an actual program would require much more detailed calculations and investigation.

In an earlier talk, Dr. Garvin expressed an idea that should have more prominence in CIAP: that of "simulation." I do not mean just mathematical simulation, but experimental simulation as well. Of necessity, a great deal of CIAP's work involves mathematical simulation, but none as yet utilizes experimental simulation of the disturbed stratosphere. A central theme of the approach discussed here is close iterative coupling of mathematical and experimental simulation.

The characteristics of mathematical simulation of atmospheric chemica' kinetics are two: (1) It is based almost entirely on experimental data, supplemented by calculations which use established physical and chemical principles. Models assemble, order, and express in mathematical equations these data and the relationships among them. (2) The results obtained by model calculations have limited meaning and validity unless they match well with measurements made in the atmosphere for similar conditions. The model must satisfy these criteria as far as possible; once it has done so, it becomes an excellent tool for correlating data, investigating hypotheses, studying species and processes not measured, extrapolating in time and space scales, and making predictions.

For the normal stratosphere, several workers have compiled models that satisfy the first criterion very well and the second one to some degree. For the chemically disturbed stratosphere, the first criterion can be reasonably met,

but there are no field data to allow validation by comparison under the second criterion. It can of course be argued that the same general chemistry applies to the disturbed stratosphere as to the normal, and matching with the normal should be sufficient for the disturbed situation. However, matching the highly variable and complex ambient conditions is marginal at best, and not satisfactory. Extrapolation to disturbed conditions is neither warranted nor advisable.

If chemical-release experiments are to be made in the CIAP program, they must be done with only minor modifications of existing instrumentation and modes of operation, because of the limited time available. Such experiments would therefore be extremely difficult, and would require extremely efficient, coordinated use of several methods of studying the atmosphere. I would like to present past examples of successful work to show the feasibility of parts of such a project, and discuss results of the preliminary calculations exploring the characteristics of chemical-release experiments. Let me again emphasize that this is *not* a proposal for an experiment, but a study of means of optimizing the chances for success of future experiments.

EXPERIMENTS AND MATHEMATICAL SIMULATION*

Let me give you an example which shows the great benefits that can be derived from close iterative coupling of an experimental program and a mathematical simulation of the experiments. Frank K. Truby of Sandia Laboratories designed the experiments as a laboratory study of the temperature dependence of the attachment/detachment of electrons in oxygen. The system used involved flash photo-ionization of a small amount of nitric oxide in oxygen, and time-dependent mass analysis of the negative ions produced. The reaction vessel had dimensions of about an inch, and an experimental run lasted a few milliseconds. The characteristics are therefore completely different from those of in-situ stratospheric studies, but the mode of coupling calculations and experiments, and the potential benefits, are the same.

A set of equations describing as exactly as possible the geometrical, physical, and chemical characteristics of the experimental set-up were composed into a computer code while the laboratory system was being constructed. The mathematical simulation included all the postulated chemical species and reactions, and the exact geometry of the reaction vessel. Also included were molecular diffusion, ambipolar diffusion, and wall effects. We first "ran" a number of experiments in the computer to choose real experimental runs that would be pertinent, to determine the optimum parameters, and to study the time-dependent "results." The real experiments were then run, and the results compared with the calculated results to correct the computer program and improve its validity. The cycle was then repeated until we had reasonable confidence in the validity of the model. Then a very detailed computational analysis of the processes was made, interpolating in time in the real experiments, and extrapolating to earlier and later times, and to other combinations of parameters not measured. Whereas the experimental measurement gave particle densities of only a few species (mass units 32, 46, 62, and 64), the calculations provided information on other species as well. More important, though, they could identify and characterize processes.

The range of experimental conditions included oxygen pressures from one to three torr, about one to two millitorr of nitric oxide, and photo-ionization production of 1 to 3 $\times$ 10^8 electrons and NO^+ ions per cubic centimeter. Even in this very simple system initially composed of O_2, NO, e, and NO^+, it was necessary to consider 19 species:

O	NO	NO^+
O_2	NO_2	$NO^+ \cdot NO$
O_3	NO^-	$NO^+ \cdot H_2O$
O^-	NO_2^-	H_2O
O_2^-	ONO^-	e
O_3^-	NO_3^-	
O_4^-	$OONO^-$	

In addition to the physical processes mentioned earlier, 81 chemical reactions were included in the first calculations; 45 were found to be significant

*An expanded version of the material in this section was presented at the December 1971 meeting of the Division of Electron and Atomic Physics of the American Physical Society in Atlanta.

The negative-ion reaction scheme shown in Figure 1 is based principally on the work of Eldon Ferguson and the Boulder group. The initial step is the very rapid attachment of electrons to oxygen molecules, followed by the charge-exchange and reactions forming complex molecules as shown. Figure 2 shows one example of the matching of computed time histories of species with an experiment; the dots, circles and crosses are experimental values for masses 62, 32, and 46 respectively. The particle density scale is logarithmic and the time scale linear. The lines are the calculated particle densities for the species designated as $OONO^-$, O_2^-, and ONO^- in Figure 1. These are the computed results after adjusting parameters in the model to match the experimental results. The matching was done for relative peak heights, for the time at which maximum densities occur, and for the slope of decay of the densities. It would have been easy to match just one set of curves; here the parameters were adjusted until a large number of sets of curves, over a wide range of total pressures, partial pressures, and temperatures, were well matched.

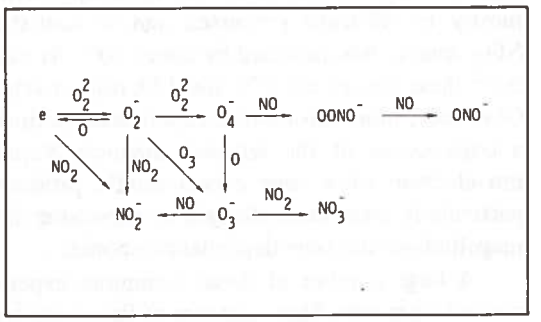

Figure 1. Diagram of the negative-ion reaction sequence.

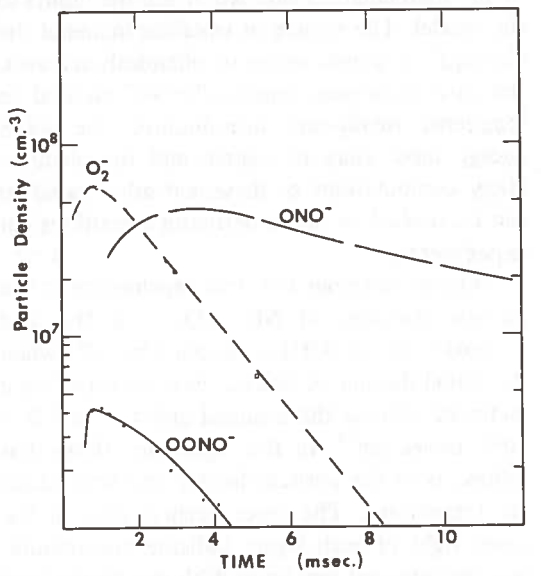

Figure 2. Comparison of experimental results with those calculated from the corrected model.

Assuming that this degree of matching indicates that the model is a reasonably good simulation of the "reality" of the experiments, what can the calculations now show that was not available in the experimental results? Figure 3 is a plot of calculated particle densities of six negative species. In this graph the time-scale is logarithmic in order to show the earlier and later time development. Thus the histories of more species, the early time behavior, and extrapolation in time are readily obtainable. The rate at which each of the 45 reactions is occurring can be obtained to identify the important processes in the production or loss of any species, again as a function of time. Modifications to the system can be checked out quickly, and a wide range of hypothesized experiments investigated by calculation.

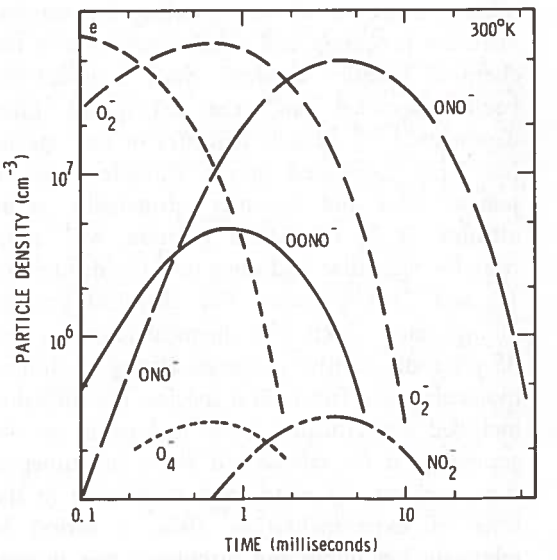

Figure 3. Results from the corrected model shown in greater detail.

EXPLORATORY CHEMICAL-RELEASE CALCULATIONS

Now let us consider the results of calculations of a range of stratospheric chemical-release experiments. These are not proposed experiments; they are intended to explore the characteristics of such experiments by mathematical simulation in order to study feasibility, establish time-scales, and optimize selection of parameters.

First, chemical-release experiments are local, with dimensions measured in meters or tens of meters, and short-term, with periods of minutes or at most a few hours under ideal conditions. Obviously, some measurements (e.g., rates or cross-sections) can be made better in the laboratory; the stratosphere is a very complex system, and it is this *system* that is best studied with in-situ measurements. Chemical-release experiments therefore do not attempt to approach simulation of either single processes or the global, long-term cumulative problem.

A chemical-release experiment is the controlled introduction of a specified amount of one or more chemical species into the stratosphere, and measurement of the subsequent changes in certain atmospheric parameters which can be attributed to transport and chemical reactions brought about or modified by the released species. A mathematical simulation of the experiment should include the characteristics of the release, a means of incorporating the variable diffusion processes, and a full description of the chemical kinetics involved. Such a model has been assembled, and the anticipated time-dependence of particle densities of key species has been calculated over a suitable range of release rates and amounts – principally at an altitude of 20 kilometers at noon, with some runs for nighttime and some runs for altitudes of 15 and 25 kilometers. The chemical kinetics incorporated about 130 chemical reactions and 35 photodissociative processes among 32 atomic, molecular, and free-radical species. The diffusion included was arbitrary, since it depends on the geometry of the release and of the instrumentation, and on the winds and turbulence at the time of experimentation. Here, a period of relatively low winds and turbulence was chosen, but diffusion was still a dominating factor.

The figures below graphically represent some of the simulated experiments. Figure 4 is for 20-kilometer altitude, daytime releases; the ambient particle densities of ozone (O_3), nitric oxide (NO), nitrogen dioxide (NO_2), and nitric acid (HNO_3) are taken to be approximately 2.0×10^{12}, 7.0×10^{9}, 7.5×10^{9}, and 1.0×10^{10} molec cm^{-3} respectively. Note that a small increase in total density of one species does not affect the particle densities of other species sufficiently for instrumental detection. For example, doubling the nitric-oxide particle density (to 1.4×10^{10} cm^{-3}) induces negligible change in the ozone density (less than half a percent in the one- to three-hour range). In ten minutes, 75% of the excess NO has disappeared, mostly by diffusive processes, and in turn the NO_2 density has increased by about 10%. At one hour these figures are 97% and 12% respectively. Obviously, more informative experiments require a large excess of the released chemical. Rapid introduction of a large excess should produce particularly instructive changes by increasing the magnitude of the time-dependent response.

A large number of these "computer experiments" were run. This sequence of figures shows a variety of modes of chemical-release studies. Each has its own characteristic results, and is therefore a different way of checking the validity of the mathematical simulation and the inputs to the model. The choice of variables included the chemical or combination of chemicals released; the rate of release, from a "pulse" method to long-term steady-rate introduction; the solar-energy input (day or night); and the altitude. Many combinations of these and other variables can be studied to select optimum conditions for experiments.

Figure 4a shows the time dependence of the particle densities of NO, NO_2, and O_3, and hydroxyl radicals (OH) (multiplied by 10^4) when the initial density of NO has been increased by a factor of 10 over the assumed ambient to 7.0×10^{10} molec cm^{-3}. In this figure and those that follow, both the particle-density and time scales are logarithmic. The three vertical lines at the lower right of each figure indicate one minute, ten minutes, and one hour. With this simple (and unreal) sudden increase of NO density at $t = 0$, the diffusion processes included tend to swamp

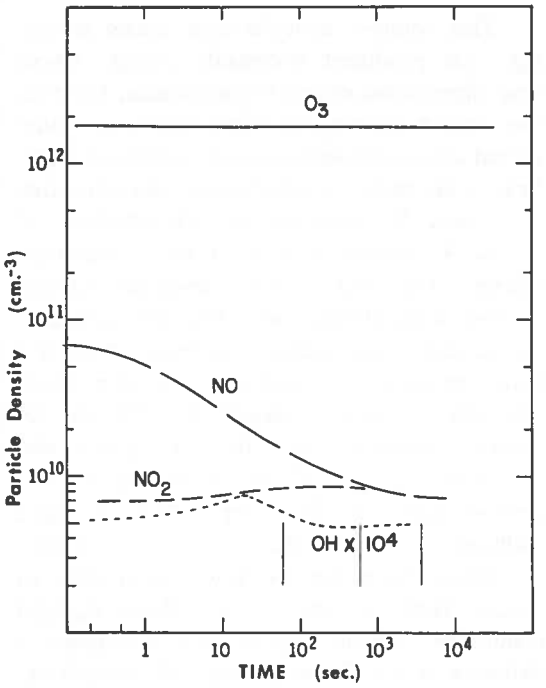

a. Initial assumed NO density, ambient X 10. Diffusion included.

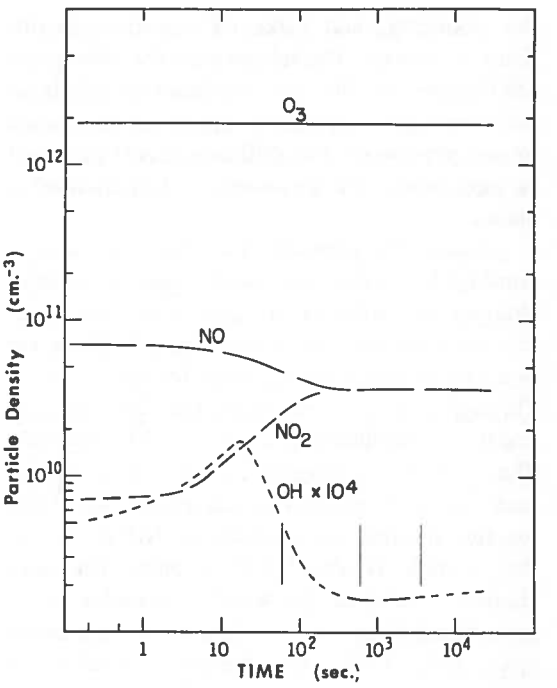

b. Initial assumed NO density, ambient X 10. Additional NO release to compensate for diffusion.

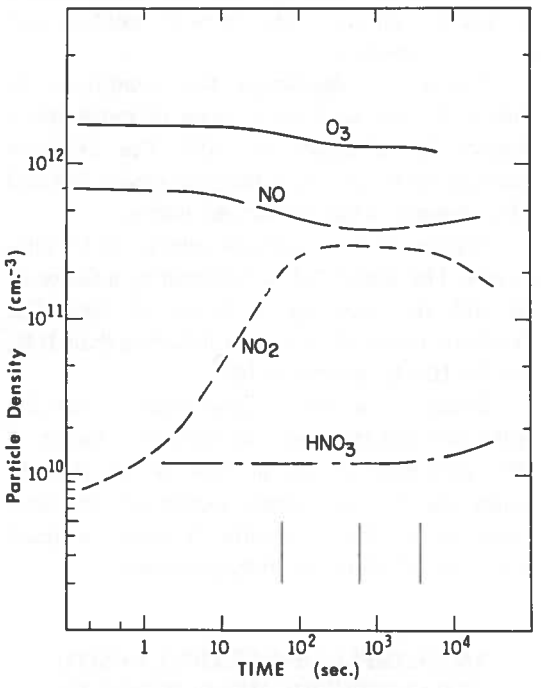

c. Initial assumed NO density, ambient X 100.

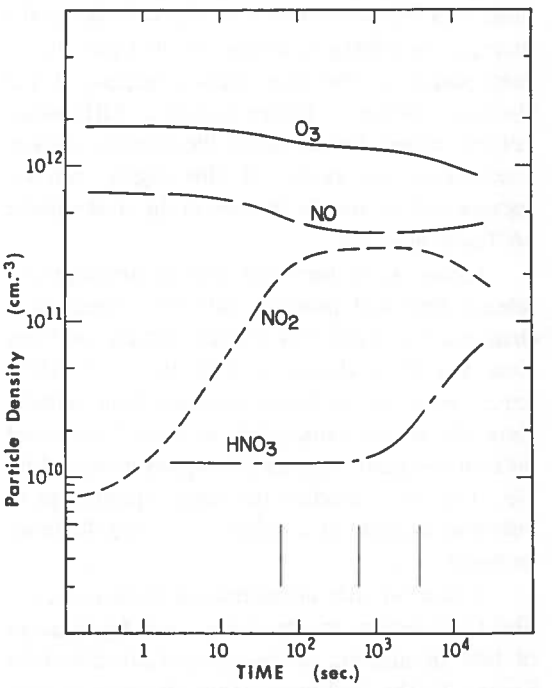

d. Initial assumed NO density, ambient X 100; initial H_2O, ambient X 100.

Figure 4. Time dependence of the particle densities of several important species. Daytime; altitude, 20 km.

the chemistry, and make its consequences difficult to extract. The release used for subsequent calculations was therefore modified to include an additional time-dependent release of the species to compensate for the diffusion loss at the point or path where the measurement (calculation) is made.

Figure 4b presents the results of such a combined release. The ozone particle density changes very little in the time span covered; at one hour the decrease is less than 3%. There are two sets of characteristic times for the reactions. Through the early reactions, the NO and NO_2 reach an equilibrium in about 500 seconds. The NO + O_3 reaction is the most important factor in producing this equilibrium. The reactive lifetime for removal of NO by O_3 at this altitude is about 150 seconds. The later chemistry involves the series of complex nitrogen-oxygen compounds leading to an increase in nitric acid, HNO_3. This species is therefore of vital concern in the overall problem. The reactive lifetime for three-body conversion of NO_2 to HNO_3 by the hydroxyl radical probably approaches 10^6 seconds for non-perturbed conditions at 20 kilometers. With this calculation the increase of HNO_3 is about 1% in three hours. Also shown is the very rapid response of the hydroxyl radical to the perturbation. OH cannot yet be measured at 20 km at the densities shown. Techniques for study of this highly reactive species and of atomic oxygen in the stratosphere are badly needed.

Figure 4c is the next step in developing a release that will produce sufficient measurable changes. The initial NO particle density has been increased by a factor of 100, to 7.0×10^{11} cm^{-3}, plus the diffusion-compensation release. Here the ozone density has decreased by about 30% in one hour, and the HNO_3 has increased by 1%. The NO_2 reaches the early equilibrium in 300-400 seconds at a value more than 40 times ambient.

Figure 4d adds an additional realistic factor. The H_2O density has been increased by a factor of 100, in addition to the changes calculated for Figure 7. The first-hour ozone decrease is now about 33%, and the HNO_3 increase is almost 70%. The NO_2 early equilibrium is reached in the same time span, but at a value 2.5% lower than the previous case.

This complex dual-chemical release in daylight has produced reasonable changes whose time dependence should be measurable. The final five figures present equivalent results for other potentially useful experimental situations: nighttime, other release methods, and other altitudes.

Figure 5a duplicates the characteristics of Figure 4d except that it is for a nighttime release. The NO density decreases rapidly because of the elimination of NO_2 photodissociation, and the NO_2 increases correspondingly by a factor of almost 100 over the assumed ambient. The HNO_3 increase is slightly less. The O_3 decreases considerably more than in Figure 8, also principally because of the elimination of NO_2 photodissociation. The OH radical is again included to tantalize the instrument developers.

Figure 5b is for a different mechanism of release. Here, we start with ambient daylight conditions, introduce an artificial step-function darkness at t = 0, and, from 100 seconds on, increase the NO particle density at a rate of 10^8 molec cm^{-3} sec^{-1}. This release stops at 3600 seconds, as shown by the arrow. Part of this situation is unrealizable, but for calculational purposes it allows study of both build-up and decay characteristics.

Figure 5c duplicates the conditions of Figure 5b, but with an increase of initial water density by a factor of 100. The principal resulting difference is a damping of the NO and NO_2 changes in the 100-second region.

Figure 5d is a daylight release at 15 kilometers. The initial NO is increased by a factor of 10 and the H_2O by a factor of 100. The first-hour ozone decrease is a little less than 10%, and the HNO_3 increase is 14%.

Figure 6 is for a 25-kilometer altitude; initial NO and H_2O are increased by a factor of 100. This level of NO increase at this altitude causes the NO to become dominant, and produces rather drastic results. A lesser increase would be sufficient for study purposes.

AN EXAMPLE OF MULTIPLE IN-SITU STRATOSPHERIC MEASUREMENTS

Let us leave the relatively easy world of calculations and say a few words about an actual operation. Even the simplest experiments in the

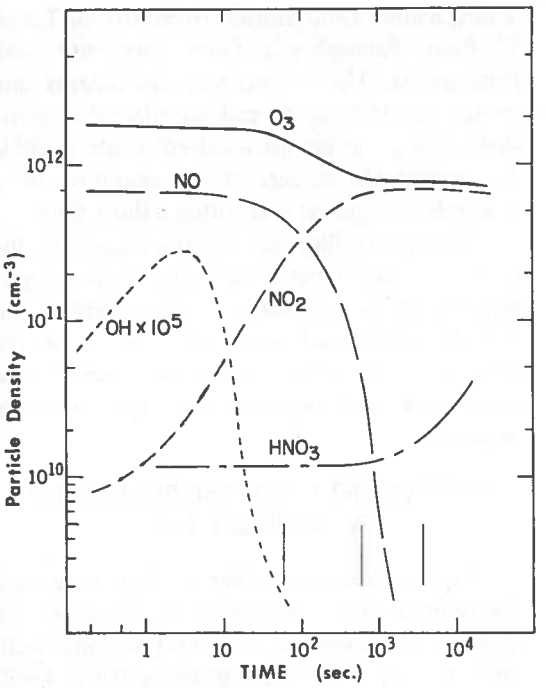

a. Initial assumed NO density, ambient X 100; initial H_2O, ambient X 100. Nighttime. Altitude, 20 km.

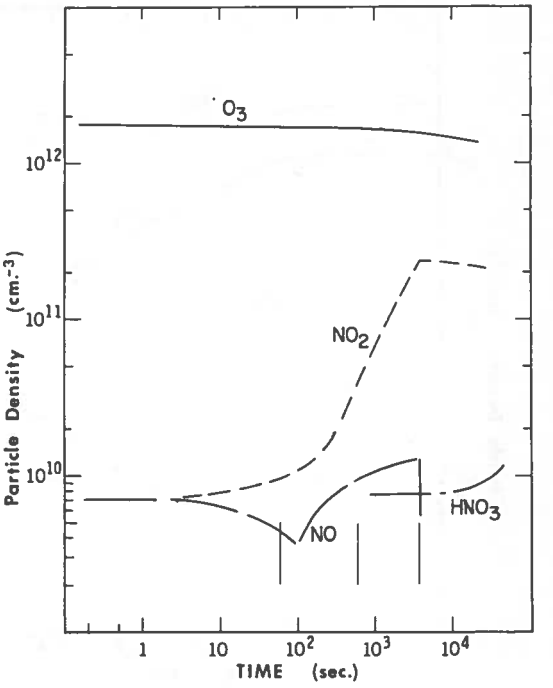

b. Initial assumed densities, ambient for daylight. Increase of NO density, 10^8 molec cm^{-3} sec^{-1} from 100 to 3600 seconds. Nighttime. Altitude, 20 km.

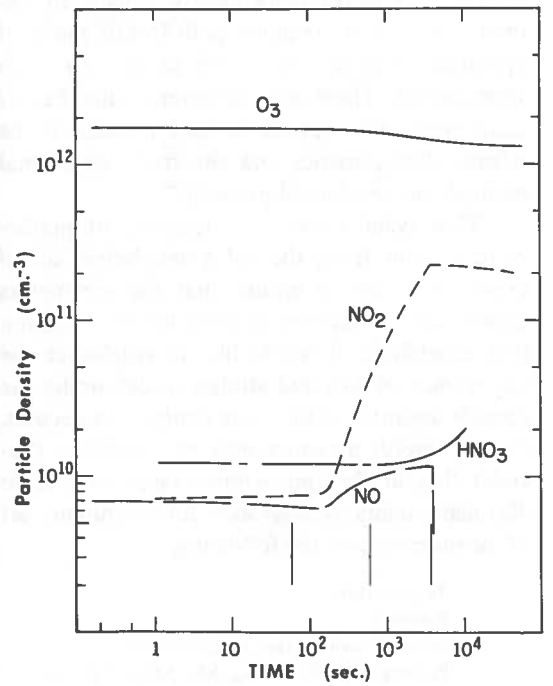

c. Initial assumed H_2O density, ambient X 100; other densities, ambient for daylight. Increase of NO density, 10^8 molec cm^{-3} sec^{-1} from 100 to 3600 seconds. Nighttime. Altitude, 20 km.

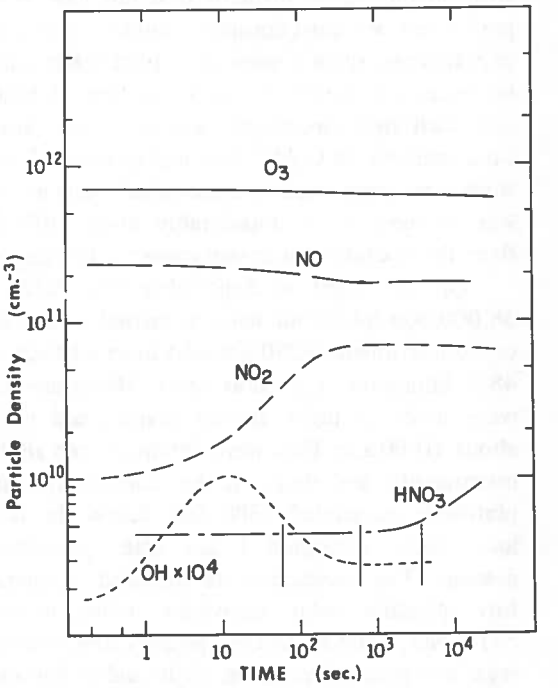

d. Initial assumed NO density, ambient X 10; initial H_2O, ambient X 100. Daytime. Altitude, 15 km.

Figure 5. Time dependence of selected particle densities for various conditions.

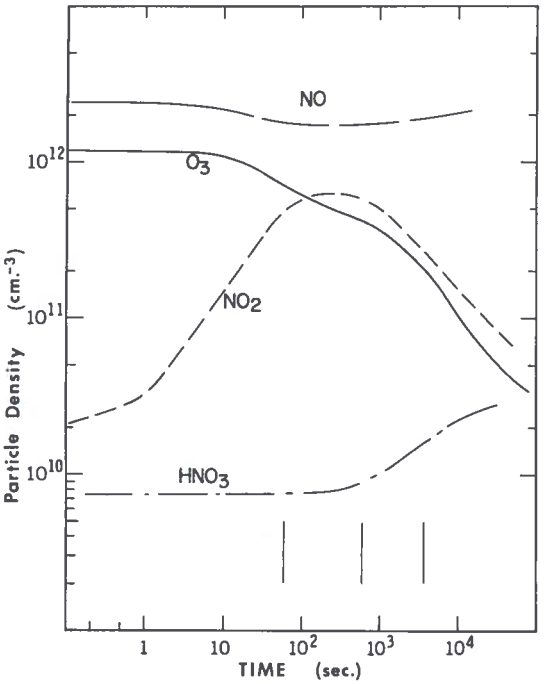

Figure 6. Time dependence of selected particle densities at 25 km, daytime. Initial assumed NO and H_2O densities, ambient X 100.

stratosphere are so difficult that few have been performed. We must consider complex correlated experiments, since a number of parameters must be measured, preferably as a function of time. Are such field operations feasible in the short time available to CIAP? The answer is yes. I can show you a very successful example – one which was in some ways considerably more difficult than the operation discussed earlier in this paper.

On the night of September 17, 1972, a 38,000,000-cubic-foot balloon carried a payload of 20 instruments (250 pounds) to an altitude of 48.7 kilometers (159,000 feet). Measurements were made at night, during sunrise, and until about 10:00 a.m. Data were obtained from all 20 instruments, and those on the main instrument platform, suspended 1300 feet below the balloon, were recovered intact after parachute descent. The measurements included temperature, pressure, solar ultraviolet, water, ozone, NO + NO_2, carbon dioxide, positive ions, cosmic rays, and parameters of the flight and of balloon behavior.

The balloon operation was handled by the Air Force Cambridge Research Laboratories. The measurements program included personnel from the Atmospheric Sciences Laboratory at White Sands; Sandia Laboratories; University of Texas, El Paso; Pennsylvania State University; and Panametrics. Use of existing instruments and operational techniques, and exceptional cooperation among the groups involved, made possible the remarkable success of the operation on a relatively low budget and within a short time.

Two points illustrated by this success are the desirable characteristics of balloons as support vehicles for stratospheric experimentation, and the advantages in selecting flight times during the periods of minimum stratospheric winds and disturbance that occur in late April and late September.

INSTRUMENTATION AND SUGGESTED MEASUREMENTS

Papers presented earlier at this conference discussed results of stratospheric measurements made with current instrumentation, and indicated the types and capabilities available. I will not develop the topic further. In my opinion, instrumentation is one of the two greatest difficulties in chemical-release experiments. At present, no instruments clearly satisfy all criteria – sensitivity, required path length, mode of operation, response time, and so on – for such experiments. There are, however, a number of instruments that appear to have promise if the release characteristics and the field operational method can be adapted properly.

This again shows the necessity of mathematically simulating the full system before actual experimentation to ensure that the parameters chosen will be compatible with the instrumentation capabilities. I would like to emphasize the importance of infrared studies to determine the particle densities of the more complex molecules, and of careful measurements of the solar ultraviolet flux in the approximate range of 270 to 400 nanometers. A suggestion for a minimum set of measurements is the following:

- Temperature
- Pressure
- Solar ultraviolet flux (270-400 nm)
- Particle densities of O_3, NO, NO_2, H_2O, and HNO_3
- Altitude
- Winds
- Instrument platform altitude
- Precise specification of release characteristics
- Optical characterization of the dispersion of the release "cloud."

DISCUSSION

The foregoing is only one example of a proposed approach to the study of the stratosphere, one that can be called the method of "induced perturbations." To date, stratospheric studies have been almost entirely passive; the experimenter measures one or more parameters in an environment that is relatively static with reference to the time span of the experiment. A more aggressive approach would be to produce controlled, well-defined atmospheric disturbances of sufficient magnitude that the time dependence of key parameters can be measured during perturbation and recovery. In this way, the basic processes responsible for atmospheric behavior can be characterized, and its physical and chemical aspects explored. The characteristics of the means by which the perturbation is induced, such as identity, intensity, duration, and geometry, must be precisely specified. In the studies of natural perturbations made to date, the source has not been well-defined. This topic is too extensive to discuss further here.

In closing, I want to emphasize a few points relative to the specific problem of chemical-release perturbation of the stratosphere to simulate certain aspects of aircraft-effluent perturbations. First, the experiments are for relatively small volumes and short times. Balloon-supported instrument platforms and days with minimum winds and turbulence are required. A large number of coordinated in-situ measurements are needed, and reasonably precise time-dependent characterization of the release cloud is an absolute necessity. Definition and control of the means of perturbation are also necessary. Operational methods and potentially suitable instrumentation are available. Central to the method, however, is detailed iterative coordination of the mathematical simulation of the very complex interactive system and the experiments.

The greatest understanding will be gained from time-dependent studies of critical parameters during perturbation and recovery. Expected levels of effluent chemicals are not sufficient to produce identifiable time-dependent results. Higher levels, particularly "chemical-pulsing" to very high densities of the release species, along with optimum geometry, will help overcome the diffusion and time-scale problems inherent in present chemical-release experiments. The relative importance of specific processes in the high-level release cannot be linearly scaled down and applied to releases at the expected levels. Model calculations and comparisons must be used. Information on species other than those discussed should also be sought; an outlook based on present knowledge may prove too limiting. Our knowledge of the atmosphere has taken occasional surprising turns in the past. With a problem as broad and complex as the present one, we should anticipate additional "surprises." Chemical-release experiments would be one good way of investigating this possibility.

This exploratory study indicates that meaningful chemical-release studies would be very difficult and complex, but very valuable. Although a number of problems remain to be solved, none seems insurmountable. Such studies would initiate a new method of studying basic stratospheric processes, and represent a worthy challenge to the atmospheric-research community.

DISCUSSION

KIRCHHOFF: I think one might ask whether a *chemical*-release experiment is useful. Why not measure naturally-occurring concentrations in the stratosphere, measure chemical reaction rates in the laboratory, and check your predictions in small reaction chambers? You mentioned two reasons: the possibility that species or reactions we have not considered will turn out to be important, and the interaction between atmospheric dynamics and chemistry, which cannot be simulated in the laboratory or simply by sending up a balloon. Both are significant, and sophisticated ways of releasing chemicals and of resolving the spatial and time distributions are needed if we are to accurately define the role of small-scale dynamic motions – and I think that these dynamics are the most important thing to learn.

HUDSON: You have to know the characteristics of the release and the structure as a function of time so you can tell what you're measuring.

KAUFMAN: The program as you have described it seems a little vague; it is not clear to me what you will get out of it that hasn't been adequately done in the laboratory, or how you expect to compare it with computer models.

HUDSON: Remember, I wasn't talking about a specific experiment or specific items to be learned; the studies explored the characteristics of *potential* experiments, to optimize the design approach. We are dealing with a systems problem, and I am discussing an approach to the study of one of its subsystems.

In general, I think the scientific community is pretty good at making laboratory measurements, integrating them into a complex system such as the atmosphere, and obtaining meaningful results. But in a program like CIAP we are responsible to Congress, to concerned American taxpayers, and to our international audience for the integrity and quality of the experiments on which we base our conclusions. In such a situation I think we should simulate the conditions of the perturbed atmosphere as closely as possible. Even if we don't find any "surprises", we would at least validate our present concepts and extrapolations.

GOLOMB: I have a more specific question. How are you going to increase the number density of the released material a thousandfold? It seems to me that the number density will be determined by the ambient density. To modulate the number density of NO, for example, you would have to dilute it with a lot of another carrier, such as N_2, which I should think would make the experiment tenuous and the vehicle payload enormous.

HUDSON: I was discussing the local increase of particle density – i.e., partial pressure – for one or two species. The problem you mention is indeed one of the great difficulties of such experiments, and is why I indicated the need for compensation by time-dependent release of additional amounts of the chemical in question.

TRANSPORT MEASUREMENTS IN THE STRATOSPHERE

N.W. ROSENBERG, R.E. GOOD, AND S.P. ZIMMERMAN
Air Force Cambridge Research Laboratories
Bedford, Massachusetts

ABSTRACT: The objective of this AFCRL study is to determine the atmospheric transport processes in the 15-30 km altitude region where SST emission products are deposited. Studies will extend to the higher altitudes to which these products may be carried by transport processes.

Field trips are scheduled for January and July 1973 to examine seasonal differences; techniques developed by AFCRL will be used for dispensing, observing, and analyzing visible trails of smoke tracers for flow fields to scales as small as a few meters. The experiments are designed to provide simultaneous measurements of temperature, wind velocity, and ozone concentration. The eddy diffusion coefficient will be estimated independently from fluctuations in wind shear, photographic trail image density, and temperature.

EXPERIMENTAL TEST PLAN

Figure 1 shows the experimental test plan. Smoke trails will be released from rockets over the White Sands Missile Range (WSMR). Three rockets will be launched, using two sites 12 km apart. Each rocket will release a vertical smoke trail, which will be photographed with high-resolution cameras. Other probes will be flown simultaneously to telemeter high-resolution ozone and temperature profiles, which also provide information on turbulence structure as a function of altitude. An RB-57 aircraft will dispense smoke trails from similar canisters in two horizontal passes through the same region at heights of 22 and 19 km, for near-simultaneous observation of horizontal profiles and input measurements to vortex trail formation and decay. The instrumented RB-57F will also be flown during the program to allow on-board experimenters to simultaneously measure solar flux, O_3, NO, H_2O, and additional minor species.

This experiment will be repeated for two successive morning periods. In addition, each rocket experiment will be accompanied by an AWS meteorological rocket (wind and temperature measurement up to 60 km altitude), to obtain a more complete picture of stratospheric-mesospheric circulation processes.

The two launch sites will provide spatial separation of 12 km. Two releases will be made from one site to provide time separation of 2000 seconds. The three trails will then permit assignment of $\partial V/\partial t$, $\partial V/\partial r$, and $\partial V/\partial Z$ versus altitude to N and E components of the horizontal wind. Two horizontal passes by the aircraft will also permit photography of aircraft-wake dispersal characteristics.

The tracer is a TiO_2 micron-sized particulate formed by simultaneous release of $TiCl_4$ and H_2O deposited at the rate of 1 kg/km. This deposition rate leaves a 0.1% contaminant in air at 25 km altitude on initial entrainment to a 5 m radius. Over the maximum expected observation period of 10 minutes, the radius expands to about 50 m and the contaminant level falls to 10 ppm.

Two cameras will be used at each observation site, with 300 mm and 1600 mm focal length. At a 40-km slant range these will give trail resolutions of 7 meters and 1 meter with a film scan of 50 microns.

Since the first experiment is scheduled for January, the following discussion treats miscellaneous relevant data obtained elsewhere.

SPATIAL FREQUENCIES OF THE WIND PROFILE

Figure 2 shows two AFCRL smoke releases covering 30 to 70 km altitude, and separated by 30 km horizontally [1]. Two features should be noted: first, the high spatial frequencies in the vertical profiles, and second, the extreme similarity of the two profiles separated by 30 km. These lead to an estimate that horizontal scale size is at least 1000 times vertical scale size, and emphasize the sheet-like nature of the flow field.

Figure 3 presents velocity profiles derived from two NASA releases [2] which show little

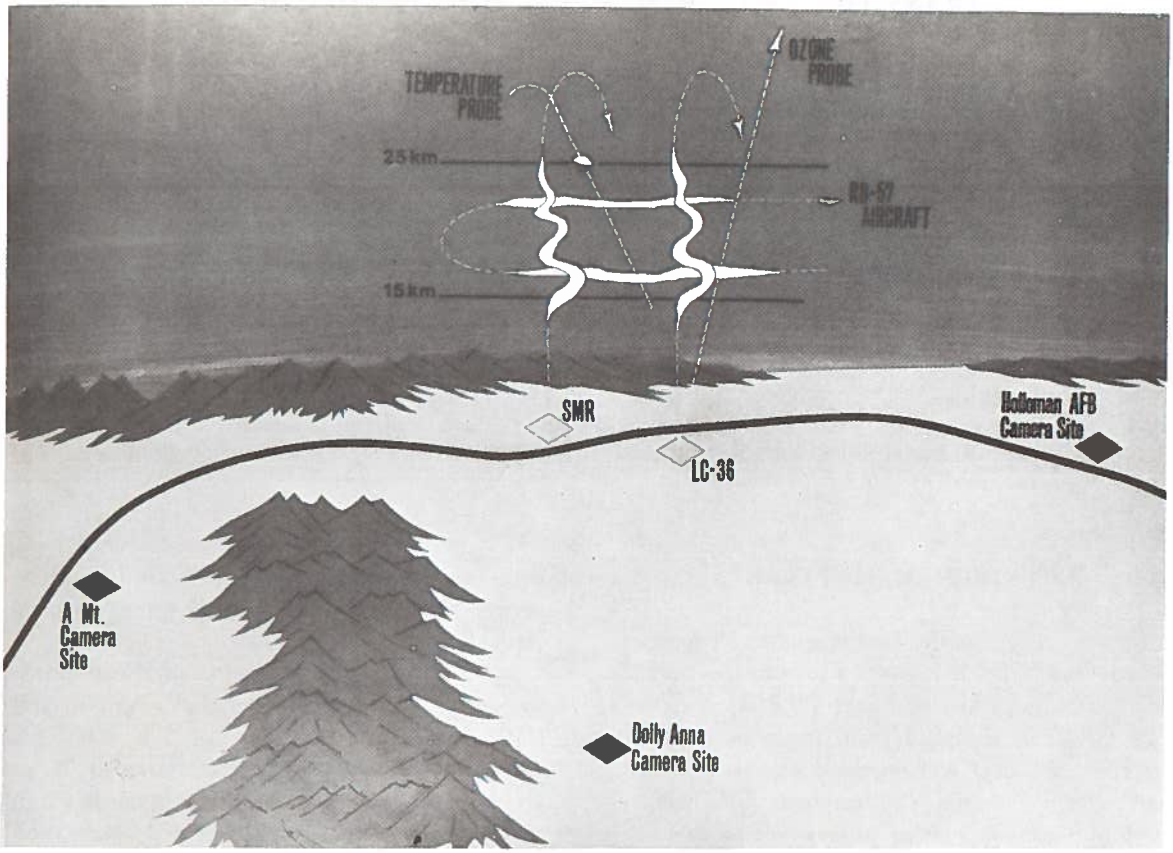

Figure 1. Stratosphere transport experiment.

Figure 2. AFCRL smoke trails, 30 to 70 km, two minutes after release.

variation over 2000 seconds in time. This is just what might be expected, since the same sheet-like structure exists, i.e. the winds from 40 km away are overhead after 2000 seconds at an average velocity of 20 m/s.

TURBULENT STRUCTURE

Figure 4 shows a telescopic view of a trail deposited from 38 to 40 km [3]. The width of the frame is 500 m, and the resolution is about 2 m. The turbulent structure was calculated to extend to a radius of 20 meters 100 seconds after release, while the wake from the burned-out vehicle (a 6-cm radius ARCAS) could have reached only a 3-m radius at that time. It is therefore believed that the trail released from the rocket, unlike the aircraft-released trail, will be a tracer for turbulent structure in the ambient atmosphere. The effective diffusion coefficient in

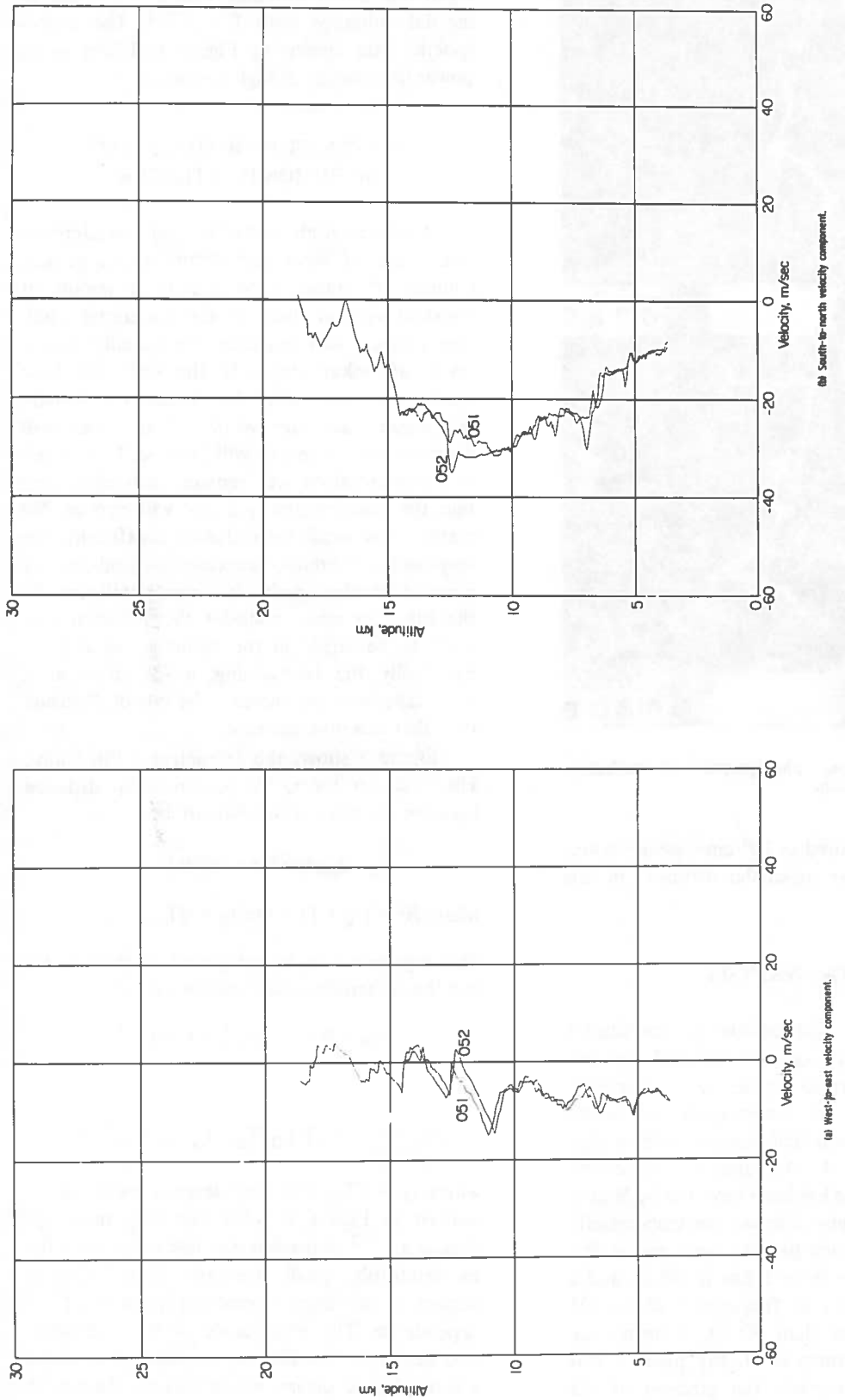

Figure 3. NASA wind profiles of smoke trails 051 and 052 obtained May 6, 1964 at 1318 and 1343 EST.

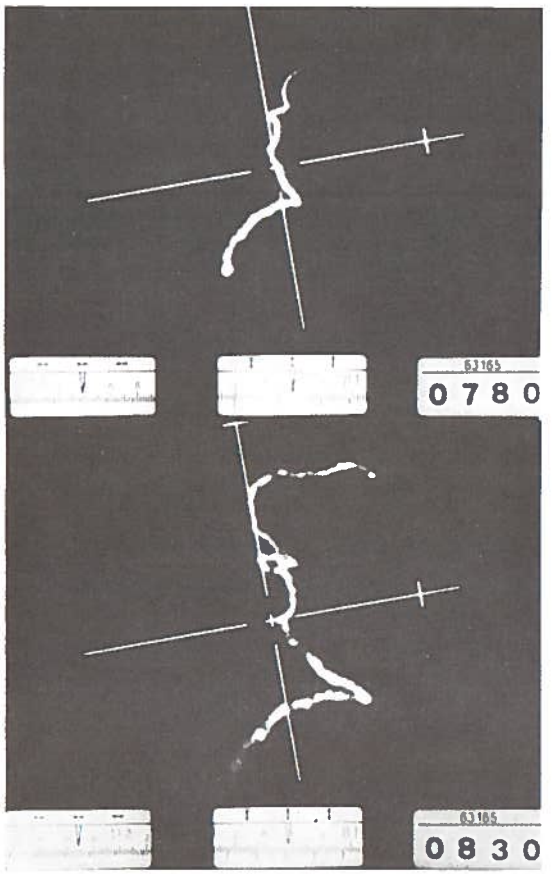

Figure 4. Telescopic photographs of turbulent smoke trails.

this trail was measured as 10^4 cm^2/sec at 40 km, which is 200 times molecular diffusion in this altitude.

DATA ANALYSIS

Amplitude (or autocorrelation amplitude) vs. spatial frequency can be obtained for anv profile – i.e., a vertical profile of a horizontal wind component, or temperature, or ozone density, or a turbulent trail structure such as that shown in Figure 4. An analysis of several temperature profiles has been reported by Mantis and Pepin [4]. Figure 5 shows the tropospheric temperature spectrum to have one spatial frequency dependence from 1 km to 30 m, and a different dependence at frequencies above .03 (wavelengths shorter than 30 m). A turbulence analysis by Zimmerman et al. [5] predicts this behavior in two regimes: the gradient of the mean dominated subrange with $E \sim f^{-3}$, and an inertial subrange with $E \sim f^{-5/3}$. The stratospheric data shown in Figure 6 differs in its power dependence at high frequency.

INTERACTION OF SHEAR AND DIFFUSION IN A TRACER

A current study at AFCRL [6] considers the interaction of shear and diffusion in a vertical column of tracer deposited in a region of constant vertical shear of the horizontal wind. The column will lengthen horizontally like a stack of poker chips. If the diffusion time constant is very long, the volume will remain unchanged, but the width of the trail will decrease, and its length will increase. The centerline concentration will remain unchanged, and thus the concentration gradient will increase. No matter how small the diffusion coefficient, the lengthening *eventually* increases the gradient to a point at which diffusion becomes significant. At the other extreme, consider the diffusion constant to be large, so the radius grows at $t^{1/2}$. Eventually the lengthening, which grows at t, must take over and increase the rate of diffusion over that of a no-shear case.

Figure 7 shows the geometry of this study. The equation for r, the perpendicular distance between the sides of the column, is

$$d(r/B)^2/dt = 4D/B^2$$

where $B^2 = (t_S^2 + 1)^{-1}$ and $t_S = t/T_S$

This equation can be integrated to define r (t) and the centerline concentration c (t) as

$$r/r_0 = B\,[1 + t_D\,(t_S^2/3 + 1)]^{1/2}$$

and

$$c/c_0 = \left\{1 + t_D\,[(T_D/T_S)^2\, t_D^2/3 + 1]\right\}^{-1/2}$$

where $t_D = t/T_D$. The time dependence of c/c_0 is plotted in Figure 7. Note that c/c_0 must approach a $t^{-3/2}$ dependence at late times, even for an arbitrarily small non-zero shear, whereas neglect of the shear interaction leads to a $t^{-1/2}$ dependence. The importance of this consideration lies in the fact that any atmosphere contains a hierarchy of shears, which become the source

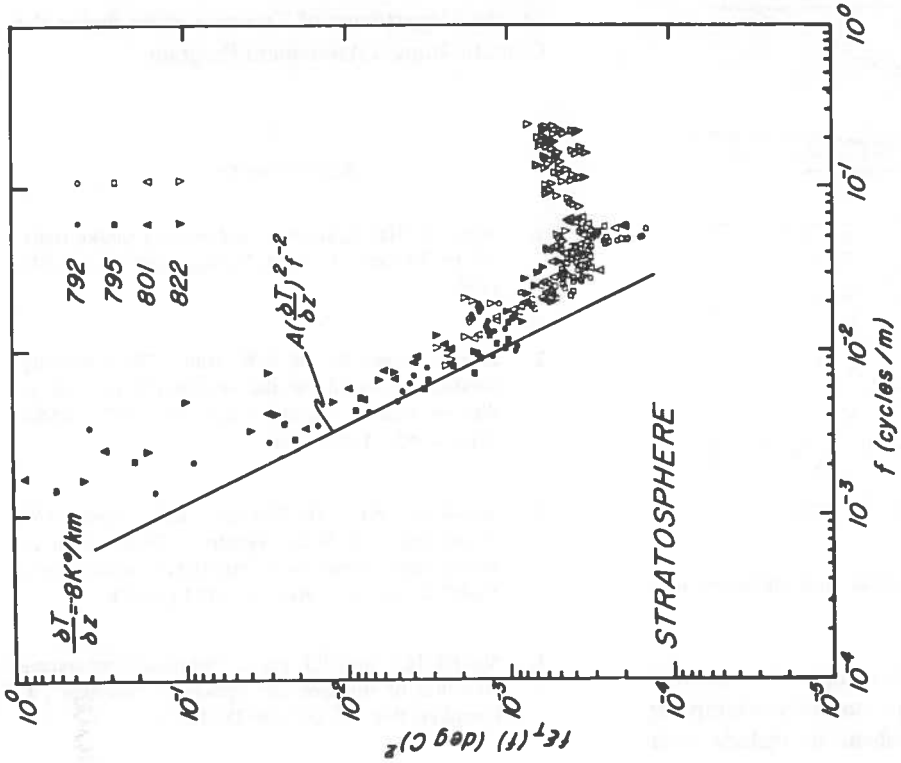

Figure 6. Energy spectrum of stratospheric temperatures. Each flight's open data points indicate spectral estimates, for which the error may exceed 1/2 of the reported value. (From Reference 4.)

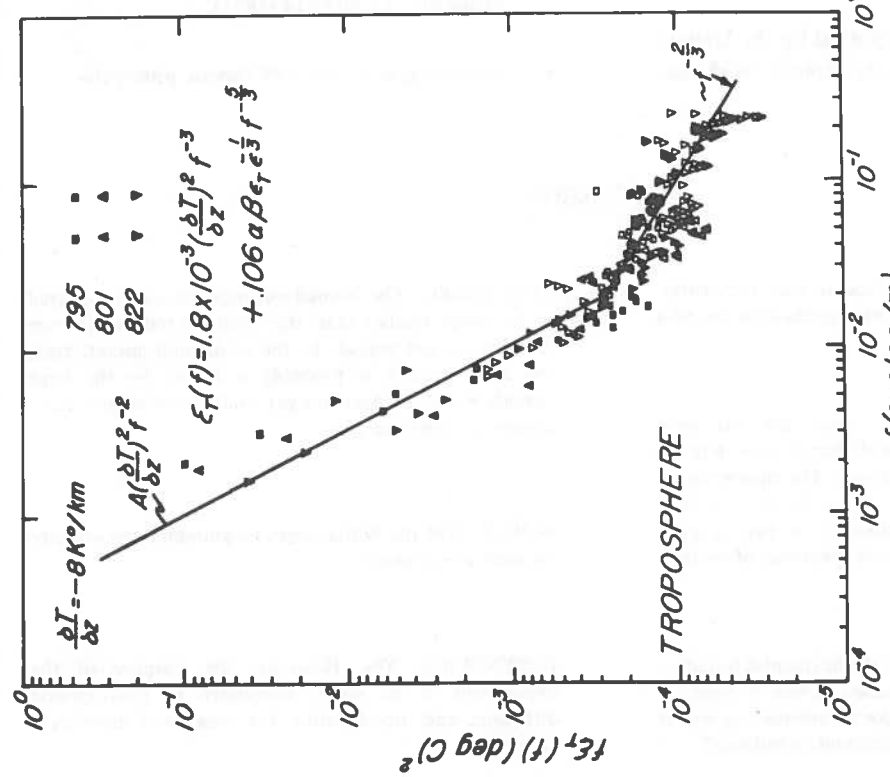

Figure 5. Energy spectrum of tropospheric temperatures. Each flight's open data points indicate spectral estimates, for which the error may exceed 1/3 of the reported value. (From Reference 4.)

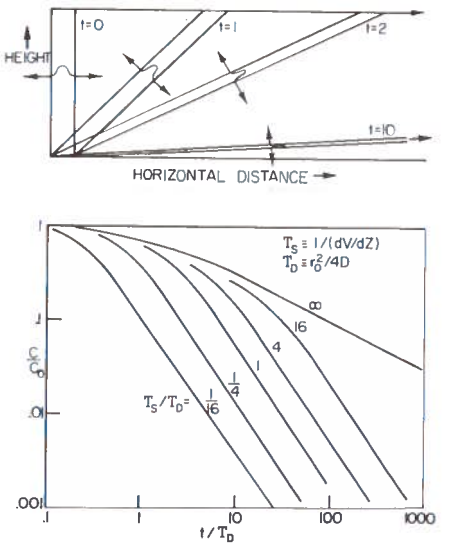

Figure 7. Interaction of shear and diffusion in a tracer.

of an eddy-diffusivity high compared to molecular diffusion alone. We are currently attempting to extend the above analysis to include such hierarchies of shears.

ACKNOWLEDGMENTS

This work is being supported by the Department of the Air Force under Project 7635, and by the Department of Transportation under the Climatic Impact Assessment Program.

REFERENCES

1. Marshall, Maj. James C., "Behavior of smoke trails, 30 to 70 km", J. Appl. Meteorology *8*, 641-648 (1969).

2. Henry, Robert M. and R.W. Miller, "Wind velocity profiles measured by the smoke-trail method at Wallops Island, Virginia, 1963 and 1964", NASA TN D-4365, March 1968.

3. Beaudoin, P.E., D. Golomb, T.M. Noel, N.W. Rosenberg and W.K. Vickery, "Observation of mesosphere winds and turbulence with smoke trails". J. Geophys. Res. *72*, 3732 (1967).

4. Mantis, H.T. and T.J. Pepin, "Vertical temperature structure of the free atmosphere at mesoside", J. Geophys. Res. *76*, 8621-8628 (1971).

5. Zimmerman, S.P., C.A. Trowbridge and I.L. Kofsky, "Turbulence spectra observed in passive contaminant gasses in the upper atmosphere", Space Res. *XI*, 907-914 (1971).

6. Rosenberg, N.W. and E.M. Dewan, principals.

DISCUSSION

(UNIDENTIFIED): The photograph of the trail centerline appeared to be uniform. What conclusions can you draw about shears?

ROSENBERG: The large-scale photo did not have sufficient resolution to show local fluctuations, but the telescopic photo showed them clearly. The shears can be measured only to spacing of about 20 m (the trail width). Diffusion will be estimated in two ways – growth of trail width, and spatial spectrum of vertical shears.

ALBER: Is the radial growth in the horizontal found to be proportional to the three-halves power of time, as expected from an isotropic wake turbulence, or will it be a measurement of the environmental turbulence?

ROSENBERG: The burned-out rocket wake is expected to be much smaller than the observed trail width over the observation period. In the horizontal aircraft trail, the early growth is probably a tracer for the large aircraft wake. We have not yet studied sufficient data to answer the question fully.

WOFSY: Will the White Sands measurement be affected by local topography?

ROSENBERG: Yes. However, the purpose of the experiment is to study variability in stratospheric diffusion, and any location (or time) will have local effects.

MILLER: Our group has also found that small-scale features in temperature and wind components are very similar to paired observations. A study of stratospheric chemical releases at Eglin in 1969 reported vertical motions of these features on the order of meters per second. Would you comment on the reliability of these vertical motions?

ROSENBERG: We have not studied Eglin data. We have found *apparent* vertical velocities of meters per second at higher altitudes; we assign these to convection of the released material, which is significantly heated by the large, rapid momentum transfer to the ambient atmosphere on release from the rocket which was moving at 1.5 km/sec.

DISPERSION OF TRACERS IN THE STRATOSPHERE

ERNEST BAUER
Institute for Defense Analyses
Arlington, Virginia

ABSTRACT: Data on the dispersion of tracers as a function of time after injection are presented for a variety of altitude regimes over times from seconds to a year, supplementing the compilations of Hage [1,2]. It is shown that within the admittedly wide range of variability of the data there is no evidence of different behavior for the horizontal dispersion between the atmospheric boundary layer ("Ekman layer"), troposphere, and stratosphere. Some comments are made on possible theoretical interpretations of the data and on its utility in predicting exhaust dispersion and reactant concentrations at distances from 100-1000 km behind a vehicle flying in the stratosphere.

INTRODUCTION

One of the most important factors in determining the environmental impact of the injection of materials into the atmosphere is the rate of dispersion of the injected species, i.e., the rate at which they mix with the ambient atmosphere. This mixing takes place by a combination of turbulent and molecular diffusion and convection, arising from the injection mechanism and the ambient atmosphere. In the Climatic Impact Assessment Program, the injection mechanism is being analyzed, mainly by Lockheed [3], in terms of jet mixing of the engine exhaust, and somewhat larger-scale mixing by the vortices generated at the aircraft wing tips. This paper discusses the subsequent problem, of how one proceeds from effective initial conditions at a point some 100-1000 km behind a stratospheric aircraft, where the wing-tip vortices have spread the engine exhaust gases into a coarsely, uniformly mixed region some 100-1000 m in cross-section, to a region some 500-1000 km further downstream, where one may begin to talk about synoptic-scale disturbances which provide input conditions for a global climatological model. The approach adopted here is to emphasize existing data, and in particular its range of variability and the uncertainties and limitations of our present understanding; it thus complements Walton's analysis [4].

First, the physical mechanisms of the dispersion range (on decreasing scales of distance) from mesoscale convection through turbulent diffusion to molecular diffusion. The emphasis in such studies is on the analysis of experimental data, and when the expansion of a cloud of tracer is examined it is impossible to separate the various scales of motion. Furthermore, even when a cloud of given size is formed it is not *a priori* clear that the tracer species (or any other constituent of the cloud) is uniformly mixed on a molecular scale characterized by the minimum turbulent eddy size λ_0 [5], rather than on some larger scale of inhomogeneity or "marble caking" ℓ_M.

(The dimension of the minimum turbulent eddy – the "internal scale" of turbulence, λ_0 – is related to the Reynolds number, R, and the dimension of the maximum turbulent eddy – the "external scale" of turbulence, ℓ – by

$$\lambda_0 \approx \ell/R^{3/4}.$$

The Reynolds number may be expressed in terms of the external scale, the kinematic viscosity, ν, and the approximate velocity variation, Δu, in a turbulent eddy of characteristic dimension ℓ as:

$$R = \ell \Delta u/\nu.$$

Since the turbulent dissipation rate, ϵ, is equal to $\Delta u3/\ell$, we may write

$$\lambda_0 \approx \left(\frac{\nu^3}{\epsilon}\right)^{1/4}$$

Thus, at an altitude of 20 km, where $\epsilon \approx 1\text{-}10^3$ erg gm^{-1} sec^{-1}, λ_0 is on the order of 0.3-2 cm. This is much larger than the gas-kinetic mean free path, which is on the order of 10^{-4} cm. It is more

difficult to provide a similar estimate for ℓ_M, but values of 1-100 m may be representative.)

Our data will be expressed in terms of cloud standard deviations in the horizontal and vertical, σ_h and σ_v. For a smoke, dust, or other such particulate or molecular cloud one assumes a Gaussian profile; the distribution of mass concentration $\chi = \chi(x,y,z,t)$ relative to the center of mass of the cloud at time t is then given by an expression of the form

$$\chi(x,y,z,t) = \frac{Q}{(2\pi)^{3/2}\,\sigma_h^2(t)\,\sigma_v(t)} \exp - 1/2 \left\{ \frac{x^2 + y^2}{\sigma_h^2} + \frac{z^2}{\sigma_v^2} \right\}$$

where x,y are local quasi-horizontal coordinates, z is the vertical coordinate with origin at the center of mass of the cloud, and Q is the total mass contained within the cloud. For balloon or tetroon pairs an equivalent σ_h value can be defined by the relation

$$\sigma_h = \left\{ \frac{1}{2} \overline{x^2(t)} \right\}^{1/2},$$

where $\overline{x^2}(t)$ = mean square balloon or tetroon separation distance at time t. It should be noted that in general the horizontal and vertical cloud widths or standard deviations are not the same, i.e., the cloud dispersion is anisotropic because of the atmospheric stratification due to gravity.

It is customary to parametrize the dependence of σ_i on travel time t by introducing a *horizontal* or *vertical diffusivity* K_i:

$$\sigma_i^2 = 2\,K_i\,t;$$

i = horizontal (σ_h, K_h) or vertical (σ_v, K_v)

The diffusivity K applies to dispersion of the cloud by eddies whose length scale is less than that of the cloud being dispersed, i.e., it combines both turbulent small-scale diffusion and mesoscale convection in an appropriate manner.

EXISTING EXPERIMENTAL DATA ON DISPERSION

While CIAP is interested in dispersion in the *stratosphere*, many of the experimental results to date were obtained in other atmospheric regions: in the atmospheric surface layer or Ekman layer, up to roughly one kilometer above the ground, and in the troposphere, below 8 or, at most, 15 km. As Table 1 shows, these regions are quite different in character. In addition, the dispersion results were obtained by a variety of different techniques, as is shown in Table 2.

Table 2. Experimental Techniques

Technique	Altitude Range	Time Scale	References
Growth of Smoke Puffs (includes Plumes, Spores, Rocket Trails)	Ekman Layer to Mesosphere	to 10 minutes	Hage [1,2]
Chemical Release Cloud	Mesosphere	1-30 minutes	Blamont & DeJager [6] Justus [7] Zimmerman [8]
Balloons, Tetroons, etc.	Ekman Layer to Stratosphere	hours-months	Angell et al. [9] Hage [1,2] Heffter [10]
Dust Cloud from (Nuclear) Cratering	Troposphere	hours-days	Randerson [11]
Radioactive Debris from Nuclear Explosions	Troposphere/Stratosphere	months	Hage [1,2] Heffter [10]
Fluorescent Particles	Lower Atmosphere	1-30 minutes	Hage [1,2]
Meteor Trails	Mesosphere	1-30 minutes	Blamont & DeJager [6] Greenhow [12] Zimmerman [8]

Table 1. Characteristics of Different Atmospheric Regions

Region	Altitude Range	Temperature Gradient	Wind Speed	Wind Shear	Turbulence	Clouds	Residence Time of Tracers	Notes
Ekman Layer (Atmospheric Surface Layer)	0-1 km above local surface	$\partial T/\partial z$ sometimes positive, sometimes negative: strong day-night variation	relatively low ($\leq$ 10m/sec)	may be large[1]	often present: due to buoyant instability or wind shear	often present	1 day	2
Free Troposphere	1 km to tropopause (which is at 8 km in polar regions, 11 km in mid-latitudes, 16 km in tropics)	usually negative; sometimes unstable	moderate; variable	may be large[1]	often present: generally due to buoyant instability	often present	1 week	3
Stratosphere	Tropopause to temperature maximum at 50 km arising from photodissociation of atmospheric ozone	generally positive	may be very large ($\geq$ 100 m/sec)	may be large[1]	sometimes present; due to wind shear	rare	1 year (at 20 km-increasing with increasing height)	4

[1] Measured values of wind shear are generally less than $\partial u/\partial z \sim$ 1-10 m/sec/km $\sim 10^{-3} - 10^{-2}$ sec^{-1}; however, these are limited by resolution in height measurement Δz, so that actual values may be larger.

[2] This region shows strong day-night variability. It is a boundary layer produced by Coriolis force-turbulence interactions, and water condensation-evaporation interchange with the ground is predominant here: clouds and fog are often found. Tracers have a relatively short residence time. This region contains about the lowest 10% of the atmospheric mass.

[3] In this region the temperature decreases with height, sometimes sufficiently strongly for turbulent convective (buoyant) overturning. The bulk of the atmosphere (70% of mass) is in this region, the atmospheric circulation is largely driven by it, and thus both weather and climate are largely determined by the region, in particular by the (variable) amounts of water.

[4] In this region the temperature increases with height, so that there is in general no buoyant overturning. There is occasional strong jet-stream-related turbulence near the lower boundary, and generally wind-shear-induced turbulence is occasionally present in the region. This region, which contains about 15% of the atmospheric mass, is strongly coupled to the troposphere. Ozone (present to 10^{-6} mole fraction) is the most significant minor species.

Representative results for both horizontal and vertical dispersion as a function of travel time are given in Figures 1 and 2. While the results show a rather large spread, presumably as a result of inherent atmospheric variability, there is no evidence from the experimental data of any altitude variation in horizontal dispersion between the Ekman layer and the stratosphere. In general, however, the results obtained in the Ekman layer and in the troposphere apply only to rather short times, since the mean residence time of material in these atmospheric regions is relatively short because of rainout or washout. Furthermore, most of these results refer to the dispersion of "test particles" such as smoke or balloons, rather than to molecules. However, there seems no reason to doubt that these test particles do trace the flow reasonably accurately, though the dispersion of energy, linear and angular momentum may follow quite different laws – see, for example, reference 13. Note also that the results presented here correspond to a

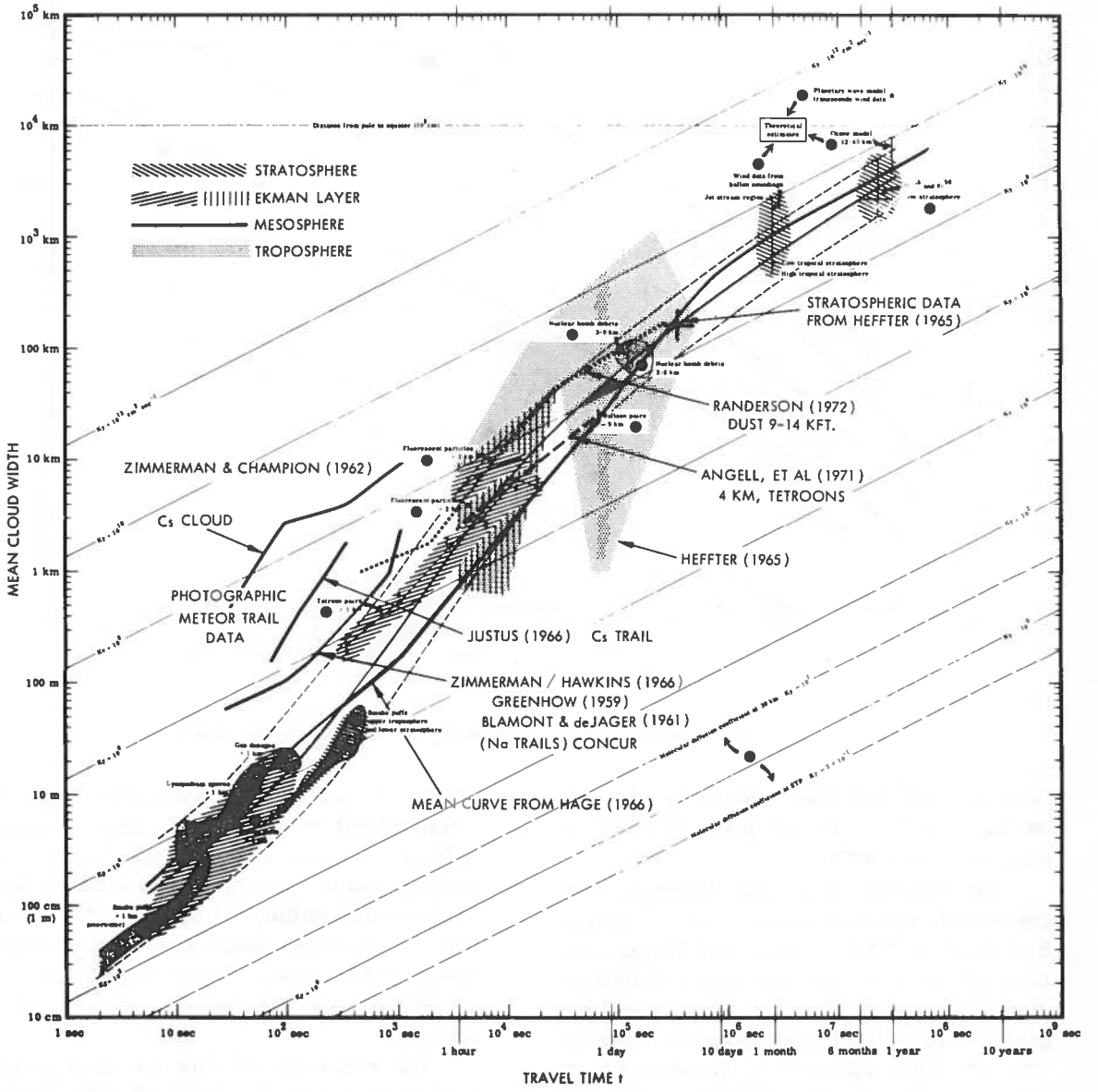

Figure 1. Horizontal dispersion as a function of travel time.

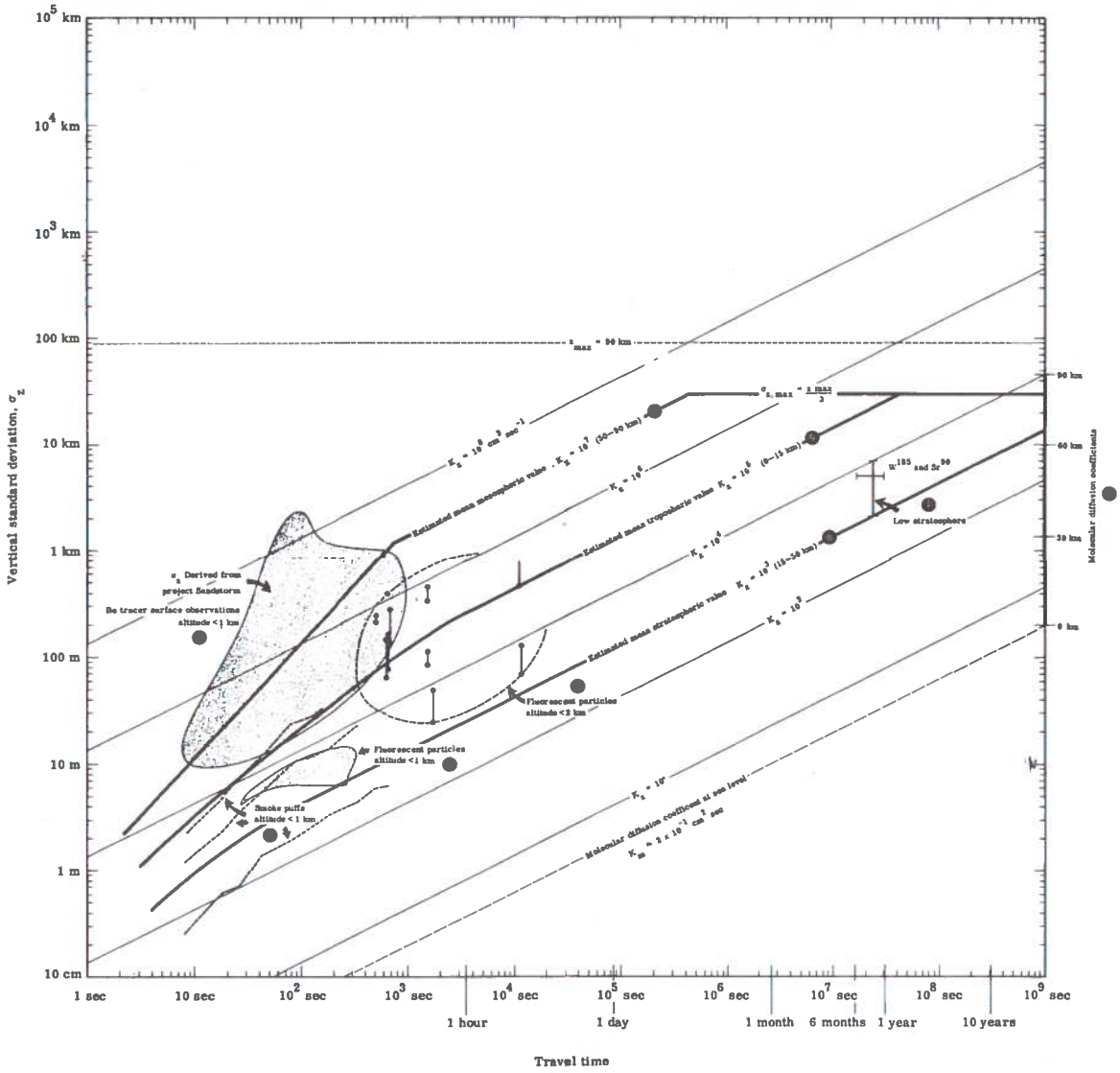

Figure 2. Vertical cloud width as a function of travel time. From Hage et al. [2].

time- or length-dependent value of K_h; the data on K_v (Figure 2) is too poor to permit a comparable statement.

The variation of vertical diffusivity with atmospheric region shown in Figure 2 is derived by Hage et al. [2] from the general discussion of Lettau [14]; while this represents a distillation of much experience it is not based on identifiable experimental data. (The characteristic residence time for vertical diffusion, τ_c, is obtained from the one-dimensional diffusion equation $\partial\chi/\partial t = K_v\, \partial^2\chi/\partial z^2$ by assuming a characteristic distance of the order of the atmospheric scale height, $H \approx kT/Mg \approx 7$ km. This gives $\tau_c \approx H^2/K_v$. If one takes representative values, K_v (stratosphere) $\approx 10^4$ cm^2/sec gives τ (stratosphere) ≈ 2 years, and K_v (troposphere) $\approx 10^6$ cm^2/sec gives τ (troposphere) ≈ 1 week. Obviously vertical diffusion is not the only mechanism for removing traces from a given atmospheric region; thus, effective vertical diffusion coefficients may be smaller than the values quoted.)

The anisotropy of data for times greater than an hour or so, i.e., for cloud widths greater than a kilometer, arises from gravitational stratification of the atmosphere with a scale height $\approx$ 5-7 km, and will be discussed further below.

It must be stressed that this data is incomplete: without information on wind speed and wind shear, diffusion cannot be separated from convection.

SOME INTERPRETIVE COMMENTS

As was pointed out above, for a sufficiently large scale the motion is anisotropic because of gravitational stratification. A critical-length scale ℓ_B may be defined on dimensional considerations in terms of the turbulent dissipation rate, ϵ, and the relevant frequency for anisotropic motion, which may be the Brunt-Väisälä frequency $N (\approx 10^{-3} - 10^{-2}$ sec$^{-1})$ for lapse rate instabilities, or the wind shear $\omega_s \mp \partial u_h/\partial z$ $(\approx 10^{-3} - 10^{-2}$ sec$^{-1})$ for strong vertical variations in the horizontal wind. Thus, following Tchen [15], we may write

$$\ell_B = 2\pi A_\ell (\epsilon/N^3)^{1/2} \text{ or } 2\pi A_s (\epsilon/\omega^3)^{1/2}$$

for lapse rate or shear instabilities, respectively. Here A_ℓ and A_s are numerical constants of order unity. Reasonable numerical values give $\ell_B \approx$ 200 m - 2 km, which is somewhat smaller than the atmospheric scale height, about 7 km.

For distances $\sigma \ll \ell_B$ the effect of gravitational stratification is negligible. The turbulence will then be isotropic, and will tend to follow a Kolmogoroff $k^{-5/3}$ spectral law. For distances $\ell_B < \sigma < \ell_C \approx$ 100-500 km the turbulence will be anisotropic because of either lapse rate or wind-shear instabilities, and in this "buoyancy subrange" the spectral law will be of form k^{-3} – cf. Tchen [15]. The choice of ℓ_C is somewhat arbitrary, but is characterized by the synoptic scale of meteorological motions; in any case ℓ_C is sufficiently large compared to the scale height H that for $\sigma \gg \ell_C$ the dispersion is essentially two-dimensional.

One example of this can be seen in the motion of radioactive W^{185} from nuclear tests. Extensive modeling by Gudiksen, Fairhall and Reed [16] – see also [17] – who work with data 3 to 12 months after the release, yields eddy diffusivity values in the range

$$K_h \approx 10^9\text{-}10^{10} \text{ cm}^2/\text{sec};$$

$$K_v \approx 10^3\text{-}10^4 \text{ cm}^2/\text{sec}$$

It can be seen from Figure 1 that this value of K_h is appropriate for time scales of this order, while the value of K_v is the maximum range of values of three-dimensional isotropic turbulence.

Another way to present the data is by expressing K_h as a function of time or distance, as is done in Figures 3 and 4. It is more convenient to use the mean values and the bounds as given by Hage in [1] rather than in [2]; the latter's mean value is shown, and it falls within the bounds of the earlier estimate. The three regimes of dispersion outlined at the beginning of the present section are displayed separately in Figure 3, although in Figure 4 the first two regimes coincide for $\sigma < \ell_C$, giving

$$K_h \approx \sigma_h^{1.13}$$

Randerson [11] finds an exponent 1.17, which is also obtained in sea water near the ocean surface (cf. Okubo [18]); however, the magnitude of the eddy diffusivity in sea water is smaller by a factor of 100 than that in the atmosphere. This is understandable, since near the ocean surface $\epsilon \approx 10^{-4}\text{-}10^{-3}$ erg/gm sec. These values may be compared with the early analysis of Richardson [19], which gives

$$K_h \approx \epsilon^{1/3} \sigma_h^{4/3}.$$

It may be noted that results of the type

$$K_h \approx \sigma_h u_d \approx u_d^2 t$$

where u_d is a mean diffusion velocity are readily understandable in terms of a mixing-length theory: a cloud of size σ_h is most efficiently spread into the ambient atmosphere by an eddy of the same size, and it is plausible to suppose that eddies grow linearly with time, with a representative diffusion velocity $u_d \approx$ 30-50 cm/sec.

DISCUSSION

The available dispersion results can be used for CIAP or similar applications in the absence of anything better. However, the limitations of the data must be noted.

First, the data is incomplete; it provides a crude measure of dispersion as a function of time, but does not supply information on the

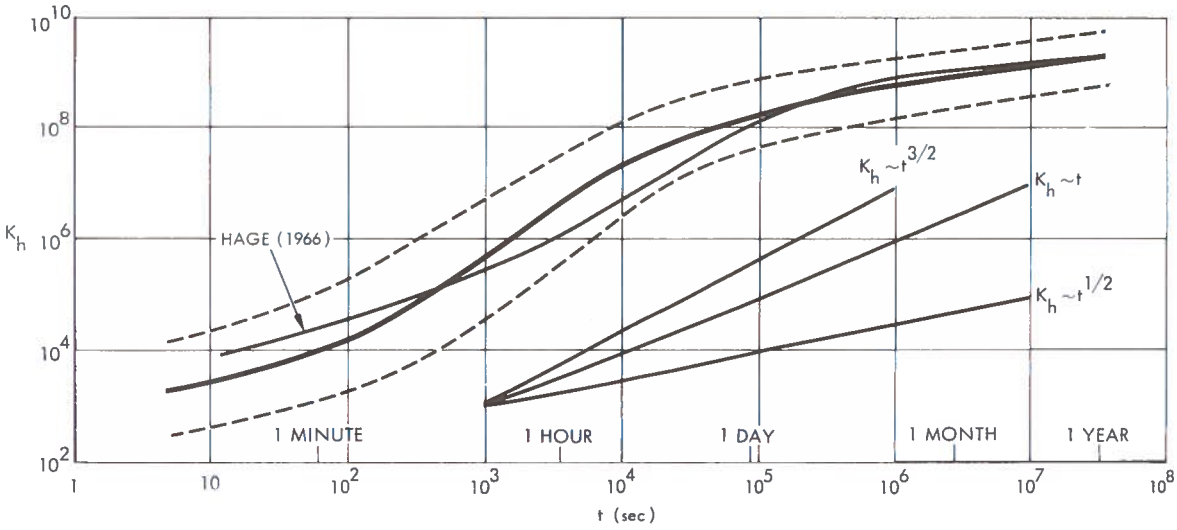

Figure 3. Horizontal "eddy diffusivity" K_h (cm^2/sec) as a function of travel time.

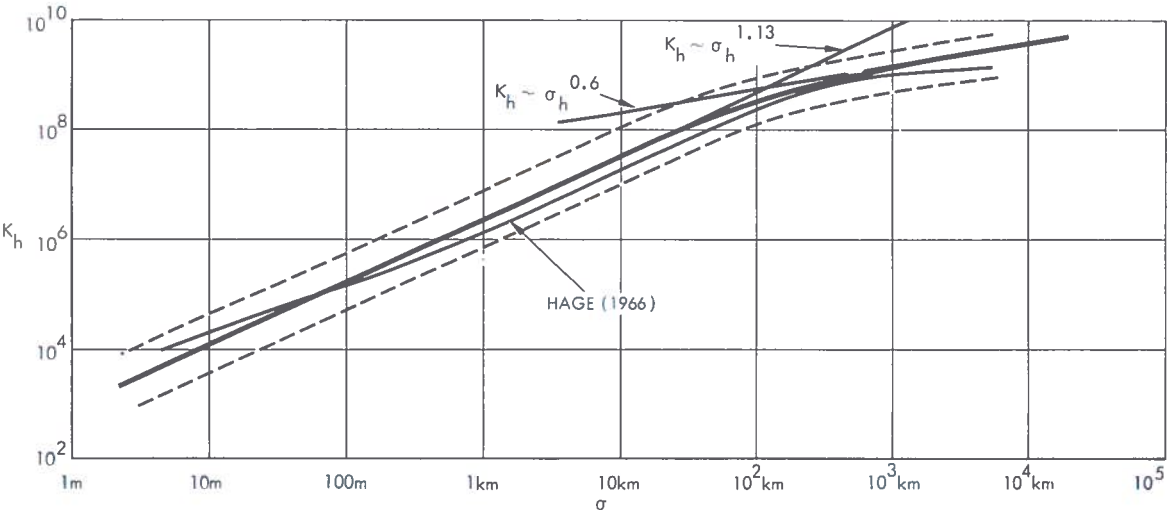

Figure 4. Horizontal "eddy diffusivity" K_h (cm^2/sec) as a function of mean cloud width σ_h.

underlying wind, wind shear, lapse rate, turbulent dissipation rate, etc.* In other words, no detailed inference on the operative mechanism of turbulence, or on the local mesoscale convection, can be drawn from the existing data. This can clearly be seen by comparing the dispersion results of Figure 1 with the characterization of different atmospheric regions in Table 2: within the spread of the data there is no noticeable altitude variation in horizontal dispersion between Ekman layer, troposphere, and stratosphere, despite the very different physical conditions in these regimes.

Furthermore, while the data gives the gross dispersion or overall cloud size as a function of travel time, it does not provide information on the small-scale irregularities or "marble caking" within the cloud, which give a measure of the actual rate of air entrainment. This is particularly important when these dispersion results are used

*In fact, measurements will be undertaken under the CIAP program to correct this deficiency, at least to time scales of the order of 30 minutes or less – see Rosenberg, Good, and Zimmerman's paper in this volume.

to treat the chemistry, because the effective rate of chemical reactions in a nonuniformly mixed atmosphere may be different from that in a uniformly mixed atmosphere, and thus a model such as of Donaldson and Hilst's [20] should be used if necessary.

If we assume accurate experimentation, the spread in the dispersion data is due to the inherent atmospheric variability: in a given region ϵ does vary by a factor of 10 to 100 (or more) over times of the order of hours, and there are comparable variations in the other parameters characterizing atmospheric dispersion. It is not obvious that a more precise measure of dispersion would be very useful, since it would still be necessary to average over atmospheric conditions later. It may be more accurate (or conceptually more satisfying) to do the averaging over atmospheric conditions after rather than before estimating the mean dispersion, but this point ought to be established before a more elaborate experimental or analytical program is undertaken.

ACKNOWLEDGMENTS

I should like to thank Drs. I.W. Alber (TRW); J.K. Angell and S.R. Hanna (NOAA); H. Hidalgo, R.C. Oliver, and P.A. Selwyn (IDA); T. Taylor (Aerospace); and C.M. Tchen (CUNY) for helpful comments.

REFERENCES

1. K.D. Hage (1964), "Particle Fallout and Dispersion Below 30 km in the Atmosphere," Travelers Research Center Report, prepared for Sandia Corp., available as SC-DC-64-1463 from NTIS.

2. K.D. Hage, G. Arnason, N.E. Bowne, P.S. Brown, H.D. Entrekin, M. Levitz, J.S. Sekorski (1966), "Particle Fallout and Dispersion in the Atmosphere," Travelers Research Center Report Prepared for Sandia Corp., available as SC-CR-66-2031 from NTIS, Springfield, Virginia.

3. H. Hoshizaki, L.B. Anderson, R.J. Conti (1972), "High-altitude wake dynamics," in this volume.

4. J. Walton (1972), "Scale-Dependent Diffusion," LLL Report UCRL-74-134, to appear in J. Appl. Meteor.

5. L.D. Landau and L.M. Lifshitz (1959), *Fluid Mechanics*, Addison-Wesley, Reading, Mass.

6. J.E. Blamont and C. de Jager (1961), "Upper atmospheric turbulence near the 100 km level," Ann. de Géophys. *17*, 134.

7. C.G. Justus (1966), "Energy balance of turbulence in the upper atmosphere," J. Geophys. Res. *71*, 3767.

8. S.P. Zimmerman (1966), "An anomalous molecular type of diffusion measured in the study of chemical releases and long-lasting, visible meteor trails," Space Research *6*, 425.

9. J.K. Angell, P.W. Allen, E.A. Jessup (1971), "Mesoscale relative diffusion estimates from tetroon flights," J. Appl. Meteor, *10*, 43.

10. J.L. Heffter (1965), "The variation of horizontal diffusion parameters with time for travel periods of one hour or longer," J. Appl. Meteor. *4*, 153.

11. D. Randerson (1972), "Temporal changes in horizontal diffusion parameters of a single nuclear debris cloud," J. Appl. Meteor. *11*, 670.

12. J.S. Greenhow (1959), "Eddy diffusion and its effect on meteor trails," J. Geophys. Res. *64*, 2208.

13. V.P. Starr (1968), *Physics of Negative Viscosity Phenomena*, McGraw-Hill, New York.

14. H. Lettau (1951), "Diffusion in the upper atmosphere," in *Compendium of Meteorology*, T.F. Malone, Ed., Amer. Meteor. Soc., p. 320.

15. C.M. Tchen (1972), "Fluid motions and some of their effects on chemistry in the upper atmosphere," private communication. See also Tchen, paper to appear in Phys. Fluids, January 1973, or Bauer, Selwyn, Tchen (1971), Institute for Defense Analyses Paper P-756.

16. P.H. Gudiksen, A.W. Fairhall, and R.J. Reed (1968), "Roles of mean meridional circulation and eddy diffusion in the transport of trace substances in the lower stratosphere," J. Geophys. Res. *73*, 4461.

17. L. Machta and K. Telegadas (1972), "Examples of stratospheric transport," in this volume.

18. A. Okubo (1971), "Oceanic diffusion diagrams," Deep Sea Rsch. *18*, 789.

19. L.T. Richardson (1926), "Atmospheric diffusion shown in a distance-neighbour graph," Proc. Roy. Soc. (London) *A110*, 709.

20. C.D. Donaldson and G.R. Hilst (1972), "Effect of inhomogeneous mixing on atmospheric photochemical reactions," Environ. Sci. and Tech. *6*, 812.

DISCUSSION

ZIMMERMAN: I don't agree with the diffusivity results your slides showed. Kellogg, and Frenkiel and Katz, have made measurements by releasing smoke puffs from balloons in the altitude range from ground level to about 17 km. Gifford and I have both analyzed this work; the growth rate measured in some of the tracer-release studies argues strongly against your results up to scale sizes of about 300 meters.

ALBER: In interpreting data from release experiments, we must remember that the experiments involved scales of only a few hundred meters, and correlations of this type are being made with scales going from a few hundred meters to 1000 kilometers. With the latter, the rates of dissipation vary with altitude, longitude, and latitude, and thus can give rise to wide variations in an overall comparison.

ZIMMERMAN: In the stratosphere and mesosphere, the inertial type of diffusion is controlled by scales of up to a couple of kilometers. It is these smaller scales that are at work when airplanes deposit chemicals.

BAUER: At those times the airplane turbulence is dominant.

(UNIDENTIFIED): The basic point, surely, is that the choice of an appropriate diffusion coefficient is a function of the scale size of the turbulence. However, when the transport processes at work in the ozone question are on the order of a year or so, why do we need to bother with these smaller-scale effects?

BAUER: I think we have to start with what happens in the exhaust regimes, since those details can be important to the chemistry on which the quantitative exhaust-emissions data used as an "input" to the larger-scale models depends.

HIGH-ALTITUDE AIRCRAFT WAKE DYNAMICS

H. HOSHIZAKI, L.B. ANDERSON, AND R.J. CONTI
Lockheed Palo Alto Research Laboratory
Palo Alto, California

ABSTRACT: An analysis of the chemically reacting wake behind an aircraft has been performed. It was found that wakes behind aircraft first grow principally in the vertical direction, due to detrainment from the sinking vortex pair, and then primarily in the horizontal direction, due to wind shear, wake turbulence, and gravitational collapse. At the point at which aircraft-induced effects become negligible and the atmospheric environment begins to control the wake growth, the wake dimensions are approximately 1000 m in width and 500 m in height. Chemical reactions were found to be significant only in the near field of the jet engine exhaust. Hydrocarbon oxidation was found to reduce the H, OH, and O levels by many orders of magnitude. No significant conversion of NO_2 to HNO_3 was found to take place.

INTRODUCTION

This paper is based on analyses and results of the High-Altitude Aircraft Wake Dynamics Study program currently being conducted by the Lockheed Palo Alto Research Laboratory for the Department of Transportation as part of the Climatic Impact Assessment Program. Only major results and conclusions are presented herein, since details of the study are presented in Reference 1.

The relationship of the wake dynamics study to other modeling studies within the CIAP is illustrated in Figure 1. The wake regime extends from the time engine exhaust emissions are deposited in the atmosphere up to about 10^3 sec later. A wake model presently under development will describe fluid-mechanical and chemical behavior of engine exhaust emission in the wake regime. It will also provide input data to the diffusion and transport regime, which begins at the end of the wake regime and lasts for days. The diffusion and transport regime is currently under study at the Lawrence Livermore Laboratory. Finally, global circulation models will extend analysis of the interaction of engine exhaust emissions with the atmosphere up to a period of years.

The basic objective of the wake dynamics study is to examine the interaction of high-altitude aircraft engine emissions with the aircraft wake flow field and determine the extent to

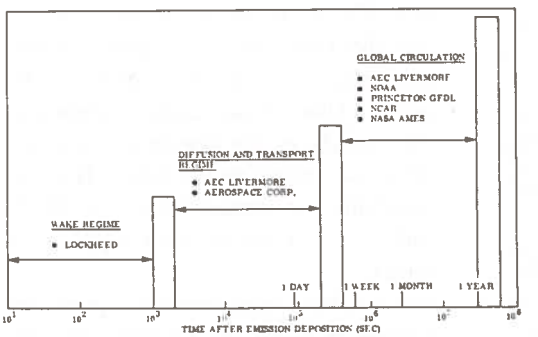

Figure 1. Relationship of wake dynamics model to other CIAP models.

which this flow regime must be considered in specifying the types and amounts of effluents entering the global circulation as a result of high-altitude aircraft operations. The general approach was to look simultaneously at the fluid-mechanical and chemical behavior of the engine exhaust emission to identify and evaluate, where possible, the important mechanisms by which the engine emissions can interact with the atmosphere. The dependence of the parameters that control those mechanisms on aircraft characteristics, flight conditions, and the atmospheric environment was established. Different flight conditions and the differences in the atmospheric environment between the troposphere and stratosphere were thus taken into account.

The important features of the wake fluid-mechanical model were found to be the dominance of the early wake growth (up to a few

minutes) by the engine exhaust jet flow field, and the rolled-up vortex pair flow. Late-time wake growth is affected equally by aircraft-dependent parameters and by atmospheric environment. At early times, the wake growth is primarily in the vertical direction because of mass detrainment from the sinking vortex pair. At later times, the wake grows principally in the horizontal direction because of wind shear, wake turbulence, gravitational collapse, and buoyant rise. The wake width at the end of the wake regime is of the order of 1,000 m (for commercial airliner-type aircraft), with a corresponding height of the order of 500 m.

The important conclusions from the wake chemical kinetics analyses are:

- In an engine operating mode with relatively low HC emissions, finite reaction-rate effects are an important aspect of the chemistry in the engine exhaust-expansion nozzle and exhaust jet regime. There is substantial oxidation of CO to CO_2 in the nozzle and jet, and the concomitant production of H atoms maintains the concentrations of H, O, and OH well above their equilibrium values.
- Hydrocarbon oxidation has a profound scavenging effect on the inorganic radicals. Introduction of large HC quantities reduces the H, OH, and O levels by many orders of magnitude.
- Significant oxidation of NO to NO_2 cannot be accomplished in the exhaust regime. In the absence of HC, the NO_2/NO ratio is kept very small through reduction of NO_2 by H atoms. When HC is abundant, the effect is to freeze NO_2 in the nozzle near its initial throat value. Similarly, oxidation of SO_2 to SO_3 appears not to be significant.
- OH concentrations can be high in the jet, but under such conditions the NO_2 would be very low – thereby precluding formation of HNO_3 from the reaction

$$NO_2 + OH \rightarrow HNO_3$$

Even if OH and NO_2 were both initially plentiful in the hot exhaust, significant conversion to nitric acid is forestalled through the rapid consumption of OH by the competing reaction

$$OH + OH + M \rightarrow H_2O_2 + M.$$

The wake chemical model, which will provide inputs to the diffusion and transport regime chemistry, can be either simple or complex depending on the requirements of the diffusion and transport regime model. This is an area that requires further study and coordination with other CIAP program elements.

The results of the present studies have indicated that radiative cooling of the exhaust jet and wake buoyancy due to radiative transport are not important. The transport of particulates in the wake regime was also found to be unimportant because the small size of the emitted particulates causes the particulate motion to coincide with the gas motion.

AIRCRAFT EXHAUST TRAILS

Observed Features

A study of the data gathered in this program and other reported data [2] yields a consistent picture of the major features of aircraft exhaust trails, as shown in Figures 2 and 3.

The near trail, labeled "jet" in these figures, lasts for times on the order of 10 sec. In this region the exhaust trail occupies a fraction of the overall aircraft wake, since it is confined to turbulent jets issuing from the engines. The jet regime is characterized by rapid growth of the exhaust trail, which starts on a meter scale at the engines and grows more than an order of magnitude to become comparable to the aircraft size at the end of the jet (point A, Figure 3), at which point the exhaust occupies most of the aircraft wake. The end of the jet is marked by a sharp decrease in horizontal rate of growth, as shown in Figure 3.

The intermediate trail is labeled "vortex" because in this region the trailing vortex pair, associated with wind lift, dominates the wake. The striking feature of this regime is a horizontal growth that is practically nil, while the vertical growth proceeds at a substantial rate, as shown in Figures 2 and 3. The vortex regime lasts for times on the order of 100 sec, corresponding to distances of about 20 km behind the aircraft.

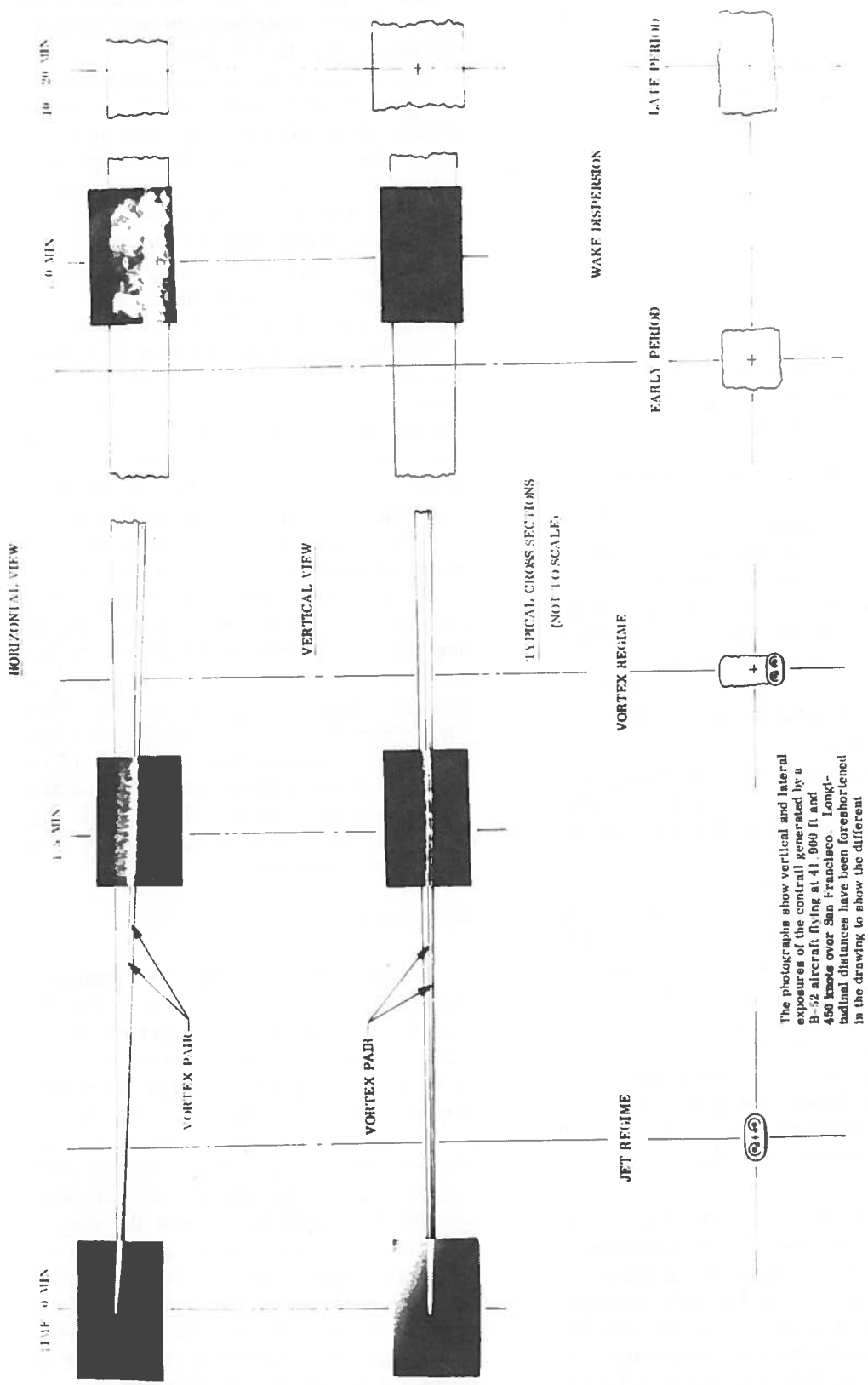

Figure 2. Wake physical features.

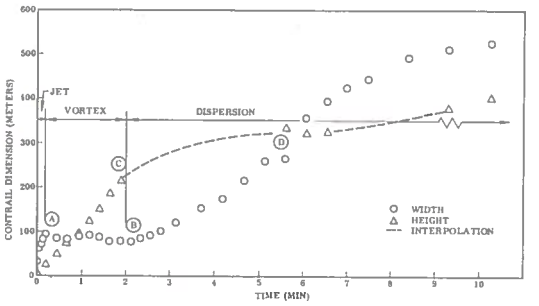

Figure 3. Time history of B-52 exhaust trail shown in Figure 2.

The end of the vortex regime (points B and C of Figure 3) is marked by a reversal of the growth pattern; that is, the trail stops growing vertically and starts to grow horizontally.

After the vortex pair has broken down, the exhaust trail starts dispersing by a variety of mechanisms to be discussed later. The horizontal growth overtakes the vertical dimension (point D of Figure 3), and the wake flattens and continues growing horizontally for hours. The main characteristic of the dispersion regime is a horizontal growth rate that decreases with time (at least for times of 0.5 hr or so), a feature that has important implications with regard to the mechanism of dispersion.

Microdensitometer traces of the wake photographs at 1.5 and 7.0 minutes (Figure 2) were made to obtain a qualitative description of the mass distribution across the wake. The traces are shown in Figures 4a through 4c. In Figure 4a the vortex pair is clearly visible in the lower portion of the wake; the microdensitometer traces show a greater concentration of light-scattering particles in the vicinity of the vortex pair. The scattering particles are probably ice crystals; if their dimensions are in the submicron range, their distribution should be a good indicator of the exhaust gas distribution. Figure 4b is the corresponding horizontal trace, which clearly shows the mass concentration due to the vortex pair.

Figures 4c and 4d are vertical and horizontal scans at 7.0 minutes, well into the wake dispersion regime where organized aerodynamic motion has ceased to exist. The microdensitometer traces indicate a slightly rounded distribution with a ragged top. The concentration of mass at the bottom of the wake evident in Figure 4a is no longer discernible. The breakup of the vortex evidently redistributes the mass uniformly throughout the wake cross-section.

The procedure for obtaining the data shown in Figures 2 and 3 consists of still and motion pictures taken simultaneously from two locations – one directly underneath the flight path, and one from the side at an elevation angle of about 10°. The pictures are taken in sequence, tracking a particular feature of the contrail. The apparent dimension of the contrail is measured with an optical comparator, and the corresponding height and width are obtained by solving a set of simultaneous equations involving the azimuth and elevation from both cameras. In a few selected cases, a microdensitometer has been used to obtain accurate definition of the contrail edge. The drift velocity of the contrail is obtained by geometric addition of the longitudinal drift and lateral displacement, measured from the motion-picture film. Atmospheric conditions are obtained from the local sounding.

As mentioned above, the exhaust trail is assumed to coincide with the observed condensation trail. This assumption is based on the fact that only persistent contrails are used to generate data. This type of contrail is produced at low temperatures (below -61°C) and persists many hours, which indicates that it consists of ice crystals in a supersaturated environment. Under these circumstances reevaporation would be negligible, and the condensation trail is a good indicator of the exhaust trail.

Wake Flow Regimes

A theoretical model of the major features of aircraft exhaust trails has been developed on the basis of data discussed in the previous section and from theoretical consideration of the physical factors affecting aircraft wakes. For present purposes, the end of the wake is defined as a point at which the sum of aircraft-induced effects has become negligible, and the exhaust is entirely subject to the natural atmospheric environment. For modeling purposes the wake is subdivided into jet, vortex, and dispersion regimes (as illustrated in Table 1), corresponding to the observed behavior discussed previously. A summary of the main features of the model follows, and a more detailed description of each regime is included in the following sections.

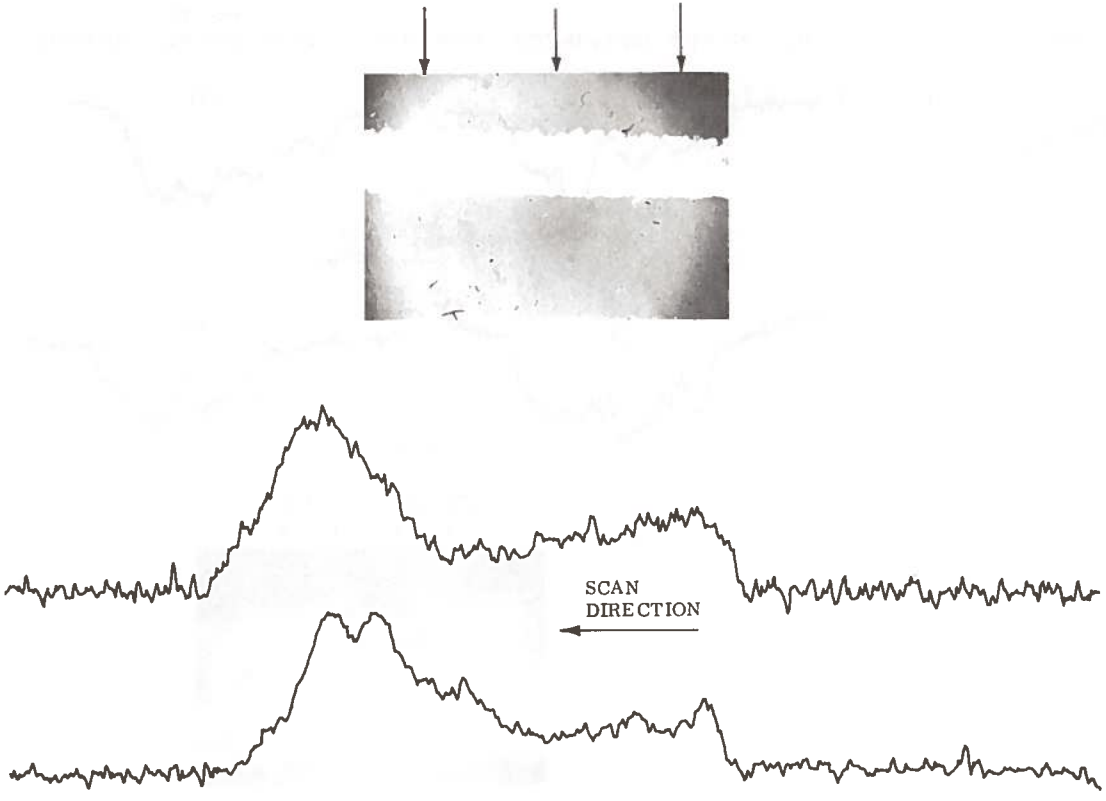

Figure 4a. Vertical microdensitometer scans – B-52 at 42 kft, wake age = 1.5 minutes.

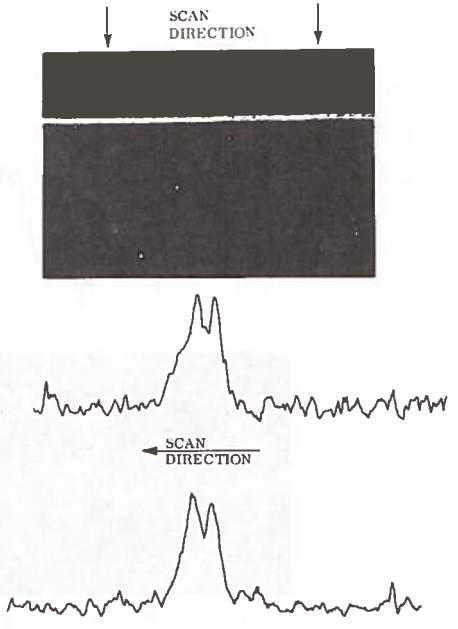

Figure 4b. Horizontal microdensitometer scans – B-52 at 42 kft, wake age = 1.5 minutes.

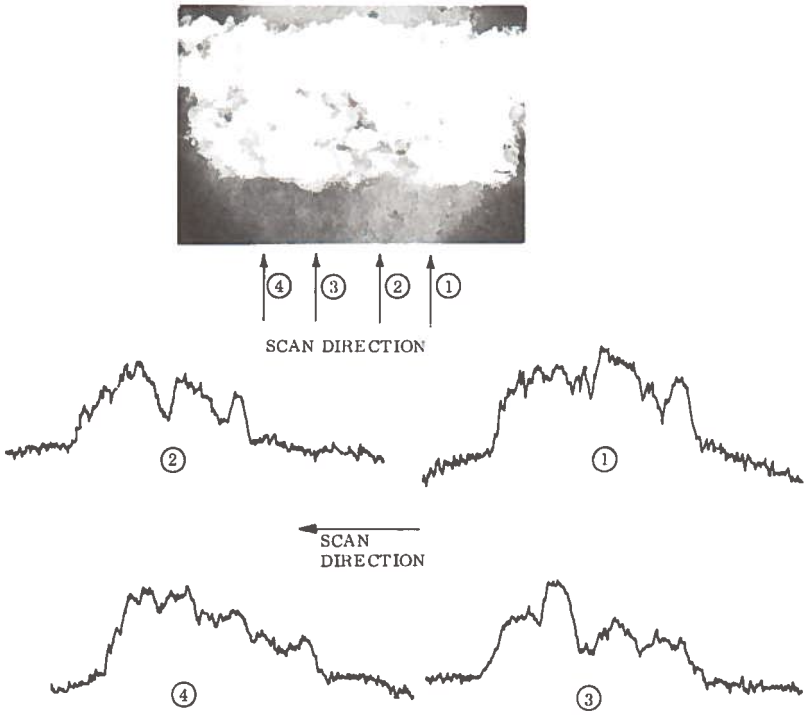

Figure 4c. Vertical microdensitometer scans – B-52 at 42 kft, wake age = 7.0 minutes.

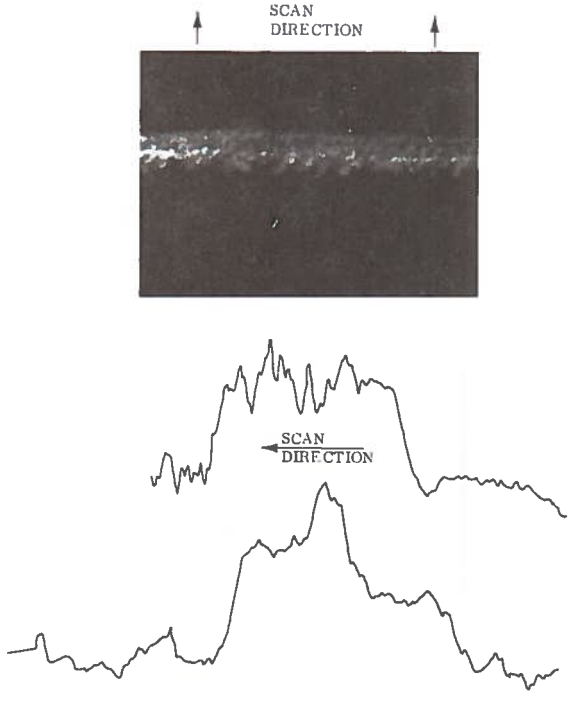

Figure 4d. Horizontal microdensitometer scans – B-52 at 42 kft, wake age = 7.0 minutes.

Table 1. Wake Model Regimes*

Jet Regime	Vortex Regime	Wake Dispersion Regime
Time ≈ (10 sec)	Time ≈ [illegible] (10^2 sec)	Time ≈ 0 (10^3 sec)
Jet exhaust energy dominates jet flow Jet grows symmetrically in vertical and horizontal Atmospheric environment secondary	Horizontal wake growth restricted by vortex pair circulation Vortex pair sinking causes vertical growth Atmospheric environment secondary	Aircraft-induced perturbations comparable to atmospheric perturbations Wake dispersion Mechanisms • Wind shear • Wake turbulence • Gravitational collapse • Buoyant rise

* See Fig. 2 for physical features

The jet regime extends from the engines to where the jets occupy all the recirculating region associated with the trailing vortex pair (indicated as point A in Figure 3). This corresponds to a time of about 10 sec and a distance of about 2 km. In this region, the exhaust gases mix with the aircraft wake according to the classical laws of turbulent jets. The jets are immersed in the developing vortex field and are attracted to the cores because of jet buoyancy, but the interference seems to be minor, since the rate of growth is that of classical jets immersed in a uniform coflowing stream. The details of jet-vortex interaction and appearance of the exhaust trail are dependent on the detailed aircraft configuration, such as number and placement of the engines, but by the time point A is reached at the end of the jet regime, the exhaust occupies the whole vortex and the details of entrainment into the aircraft wake become unimportant. In view of the foregoing arguments, the jet regime is modeled using the classical laws of a turbulent jet in a coflowing stream.

The vortex regime extends from the end of the jet regime to the point at which the vortex pair breaks up because of hydrodynamic instability, as described by Crow [3] and others [4]. This regime lasts for times on the order of 100 sec and extends over distances on the order of 20 km. The unusual feature of this regime – namely, vertical growth with little or no horizontal growth – can be explained by the fact that the wake in this regime is dominated by the trailing vortex pair. The exhaust gases, which originally fill the recirculating flow associated with the sinking vortex pair, become detrained from the pair and are deposited in a region of roughly rectangular cross-section, with the top at the original flight level and the bottom at the vortex pair. Thus, the vortex pair restrains the exhaust from horizontal growth and promotes vertical growth instead. It is believed that the exhaust detrainment is due to buoyancy forces, which detract from the downward linear momentum of the vortex pair, causing a decrease of circulation, detrainment of mass, and increase in sinking speed. This phenomenon is the opposite of that observed in thermals and nuclear fireballs, where buoyancy acts to increase the upward momentum of a vortex pair or ring, causing mass entrainment and slowing down its ascent. The upper central photograph in Figure 2 shows the cores of the sinking vortex pair and the detrained exhaust above them. This effect, which is induced entirely by the aircraft, has a lasting impact on the wake because the vertical growth exposes it to wind shear, which is one of the major mechanisms for further dispersal in the wake dispersion regime. The vortex regime is modeled using the theory of ideal vortex pairs [5].

The characteristics of the vortex pair, such as circulation strength, pair separation distance, time to vortex-sheet roll-up, and sinking rate, are related to aircraft and flight characteristics. Some of the more important parameters are aircraft weight, flight velocity, lift distribution, and wing span. Given the aircraft and flight characteristics, the major features of the vortex pair can be predicted.

In the vortex regime, atmospheric environment again plays a secondary role. The structure of the vortex pair is determined primarily by the characteristics of the aircraft and flight parameters. The rotational motion and the sinking of the vortex pair are part of the aerodynamics of the aircraft.

The wake dispersion regime lasts for about 1000 sec from vortex breakup, during which time the exhaust wake changes from an aircraft-dominated condition to a mode of natural atmospheric dispersal. This regime generally has been associated with pure atmospheric dispersion, and an unexpected finding of this program is that the aircraft-induced effects last for times about an order of magnitude larger than the vortex breakup time. At the beginning of the dispersion regime (points B and C in Figure 3) the vortex pair breaks up, allowing the horizontal growth to resume while the vertical growth decreases markedly. Eventually, the horizontal spread overtakes the height (point D) and, at very long times, the exhaust trail assumes the

flattened shape characteristic of atmospheric dispersion under stable conditions.

Several dispersion mechanisms have been assessed and approximate computations made to estimate their relative importance. However, the scarcity of data (only one contrail has yielded long-time data) makes clear-cut discrimination difficult to establish at this time. Nevertheless, three modes of dispersal seem to play a major role – wind shear, residual wake turbulence, and gravitational collapse. Lateral growth due to buoyant rise has been proposed as a dispersal mechanism [6], but present evidence indicates that this effect is less important than the foregoing three.

The general approach in the wake dispersion regime is to relate the dispersing mechanisms to the appropriate aircraft parameters and the atmospheric environment. In this manner, given the aircraft and flight characteristics and the atmospheric environment, the wake growth in the wake dispersion regime can be estimated.

Jet Regime

The jet regime extends from the engines to the point at which the exhaust occupies the entire trailing vortex pair. In this region, the exhaust is confined to turbulent jets issuing from the engines and submerged in the aircraft wake. This regime is important because it determines the environment in which the exhaust may still be chemically active because of the relatively high temperatures. As indicated in the discussion of the chemical-kinetics model further on, it has been found that the important chemical reactions occur either in the engine or in its immediate vicinity, which limits the need for detailed knowledge of the jet to a region out to about 10 exit diameters. A special study of this region has been made and is described below. Although the rest of the jet regime (about 2 km in length) is not of crucial importance for pollution purposes, it also has been addressed to provide a complete description of the exhaust trail.

Near Field

The near field of the jet regime is of special interest because it is the hottest section and closest to the engine, and therefore is a region with potential for sustaining exhaust reactions. A detailed study of the near field must take into account the differences in engine configuration, particularly whether or not the engine has a secondary nozzle. Most modern jet engines are equipped with a variable-area primary nozzle that sustains sonic flow at the exit. Thus, under most operating conditions, the exhaust is underexpanded at the exit plane and undergoes further expansion in the jet. On the other hand, some high-performance engines, such as the GE-4 built for the Boeing SST, are equipped with primary and secondary nozzles able to expand the exhaust and deliver it to the atmosphere at ambient pressure. This feature makes an important difference because it gives rise to two different cooling mechanisms: the underexpanded jet behind a primary nozzle cools rapidly by adiabatic expansion with very little mixing, whereas the ideally expanded jet behind a secondary nozzle cools by turbulent mixing with atmospheric air. Botn types of jet have been calculated, and the results used as inputs for the chemical-kinetics calculations.

For the case of ideally expanded (constant-pressure) jets behind a secondary nozzle, calculations have been carried out using various turbulent jet theories. Downstream of the exhaust nozzle, the mixing layer at the edge of the jet grows until it reaches the centerline, after which the jet becomes fully developed. In the region between this point and the exit plane, there is a conical region of constant properties where mixing has not yet taken place. Abramovich [7] gives the following length for the conical core:

$$\frac{x_c}{r_0} = \frac{1 + \dfrac{u_{ext}}{u_{jet}}}{0.27\left(1 - \dfrac{u_{ext}}{u_{jet}}\right)\left(0.214 + 0.144\,\dfrac{u_{ext}}{u_{jet}}\right)^{0.5}}$$

The results for the jet flow field are presented later, in the chemical kinetics section.

Far Field

The turbulent jets containing the exhaust grow in the developing vortex field generated by the wing. The detailed interaction between jets

and aircraft wake is a fairly complicated process, involving the buoyancy of the jets and the roll-up process of the vortex sheet behind the particular type of wing. For present purposes, these details are secondary; the main objective is to estimate the overall rate of jet growth and location of the point at which the exhaust fills the vortex pair. To this end the calculations of Reference 8 have been used to estimate the trajectory of various points, originally on the wing trailing edge, as they proceed to roll up around the vortex core. The conclusion of this study is that, for wing-mounted engines, the jets turn about one revolution around the vortex core; at this point they can be considered as fully entrained in the vortex. This situation is confirmed by field observations and the study of photographs of smoking or contrail-producing engines. The time required to turn one revolution around the core is as follows:

$$t_A = \pi^3 \left(\frac{\ell}{b}\right)^2 \frac{\rho V b^3}{W} \qquad (1)$$

where

- ℓ = distance from the engine to the centerline of the vortex
- b = aircraft span
- V = speed
- W = weight
- ρ = ambient density.

This time period is sensitive to aircraft configuration because of the squared dependency on ℓ, but a rough average is $\ell/b \approx 0.2$, which yields

$$t_A \approx 1.5 \frac{\rho V b^3}{W} \qquad (2)$$

The growth of the jet up to time t_A has been calculated using several turbulent jet theories, in particular that of [7], which gives the jet radius in the implicit form

$$\frac{x}{r_0} = 4.55 \left\{ \frac{r}{r_0} + \frac{0.69}{p^2} \left[\left(\frac{r}{r_0}\right)^2 - p^2 \right]^{1.5} + \left[\left(\frac{r}{r_0}\right)^3 - p^2 \right] \right\}$$

where x is the distance downstream, r_0 the exit radius, and p a parameter dependent upon the ratio of external velocity to jet velocity

$$p = 8.04 \frac{1 - \frac{u_{ext}}{u_{jet}}}{\left(\frac{u_{ext}}{u_{jet}}\right)^2}$$

Calculations using these formulas and photographic data show that at the time t_A the jets have grown to approximately the size of the trailing vortex pair. For modeling purposes, the time t_A is taken to be the end of the jet regime, at which time the exhaust occupies the entire vortex system and further horizontal growth is curtailed, as shown in Figure 3. The time

$$\tau \equiv \frac{\rho V b^3}{W} \qquad (3)$$

is a characteristic time for the jet regime. It will be shown in the section entitled "Scaling Model" that this is also a characteristic time for the vortex regime, and therefore a convenient time-scaling parameter to reduce the data and extrapolate results.

Vortex Regime

The vortex regime covers the section of exhaust trail extending from the end of the jet regime to about where the trailing vortex pair breaks up. This corresponds to a time of about 100 sec. The vortex pair in this regime dominates the dynamics of the wake. This vortex pair results from the roll-up of the vortex sheet that is shed from lifting surfaces, notably the aircraft wing. It can be shown that the edge of such a vortex sheet is unstable and rolls up because of mutual induction between the vortex filaments that make up the vortex sheet. This mutual induction is analogous to the electromagnetic phenomenon, and, in fact, obeys the same law (Biot-Savart). The roll-up of a trailing vortex sheet has been studied extensively [8], and it is a well documented fact that after a time of approximately $\tau/10$ the edges have rolled up tightly about the two cores that contain most of the velocity associated with the wing circulation. Thus, at times on the order of τ, that is, at the beginning of the vortex regime, the vortical wake of a finite wing is well represented by a classical vortex pair. This pair consists of two linear counter-rotating vortices with cores that are small compared with the aircraft size and set

apart a distance d of about one wing span [d = (π/4) b for elliptically loaded wings].

The dynamics of a vortex pair as described above is well understood [5]. The pair cannot be stationary; due to mutual induction between the vortices, it travels at a steady speed. Thus

$$U = \frac{\Gamma}{2\pi d} \tag{4}$$

where Γ is the strength of either vortex. It can be shown that there is a mass of recirculating fluid, bounded by a closed streamline, that travels with the pair. In practice, the bounding streamline may sustain a weak shear layer due to velocity mismatch between the recirculating flow and the ambient fluid; otherwise, the boundary between vortex and ambient fluid is sharp. This explains the containment effect that the vortex has on the horizontal spread of the exhaust. For the case of a trailing vortex pair generated by a wing, the pair moves downward with a linear momentum per unit length

$$P = \rho \Gamma d \tag{5}$$

that balances the wing lift (which is related to Γ).

The vortex pair sinks at the speed U given by Eq. (4), which is relatively insensitive to buoyancy effects because the decreases in circulation and size tend to compensate for each other. In a perfectly still environment, this process would continue for a long time because the dissipative effects are small. It is well known that frictional losses cannot account for the disappearance of the vortex pair in a matter of minutes, which is usually the case. The most likely mechanism for destruction of the vortex pair seems to be the hydrodynamic instability studied in Ref. 3. According to this source, the time for instabilities to grow one e-fold is

$$t_B = 3.7\,\tau$$

where τ is defined by Eq. (3). A correlation of data from free flights and laboratory experiments [4] shows that the time for the vortex cores to loop and start breaking up is best fitted by

$$t_B \approx 10\,\tau \tag{6}$$

For modeling purposes, it will be assumed that the vortex pair sinks at a steady speed given by Eq. (4) or, equivalently, the wake in the vortex regime grows vertically at the rate

$$\frac{dh}{dt} = \frac{8}{\pi^3}\,\frac{W}{\rho V b^2}$$

From the previous discussion, it is clear that τ is a scaling time for the vortex regime. Thus, if lengths are referred to the aircraft span b and times to τ, the last equation becomes

$$\frac{d\,(h/b)}{d\,(t/\tau)} = \frac{8}{\pi^3}$$

and a universal description of the vortex regime can be constructed as follows:

Initial time $\quad \frac{t_A}{\tau} = 1.5$

Final time $\quad \frac{t_B}{\tau} = 10$

Vertical rate of growth $\quad \frac{8}{\pi^3}$

It was previously noted that the jet regime can also be described in relation to the time τ. Therefore, a simple model for jet and vortex regimes can be assembled, as will be shown in the following section.

Scaling Model

Scaling of both the jet and vortex regimes can be accomplished with the same characteristic time τ and can be represented in a unified way as shown in Figure 5.

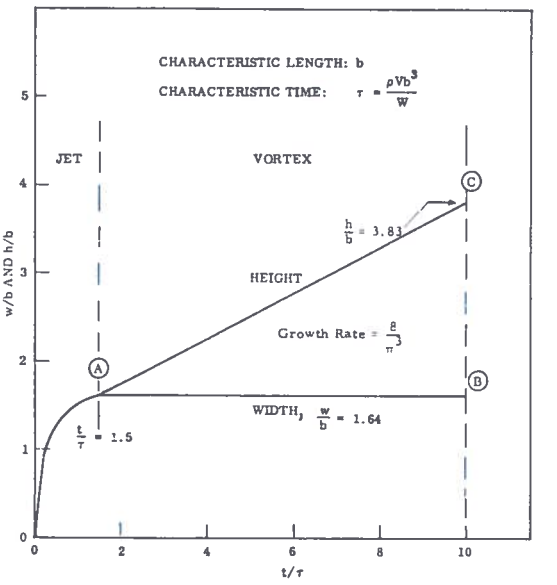

Figure 5. Scaling model for jet and vortex regimes.

The jet regime starts at time zero and ends at $t_A/\tau = 1.5$, according to Eq. (2), which defines the abscissa of point A in the previous figure. The ordinate of point A is the width (dimensionless) of the vortex pair which, according to Ref. 5, is given by

$$w = 2.09\ d = 2.09\ (\pi/4)\ b = 1.64\ b$$

or

$$\frac{w}{b} = 1.64$$

for elliptically loaded wings. In the vortex regime, the width remains constant at this value (line AB), whereas the height grows at a rate $8/\pi^3$. The end of the vortex regime is at $t_B/\tau = 10$. This sets the final height of the wake (at vortex breakup) at w/b = 3.83. It is interesting to note that the height and width of the wake at vortex breakup depend on the aircraft span alone. Figures 6 and 7 show data plotted in dimensionless form according to this scaling model for width and height, respectively.

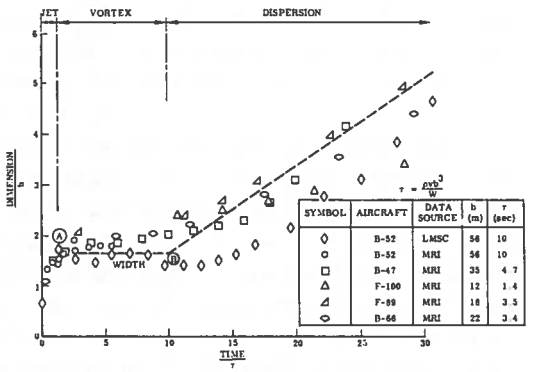

Figure 6. Comparison of contrail width data with scaling model.

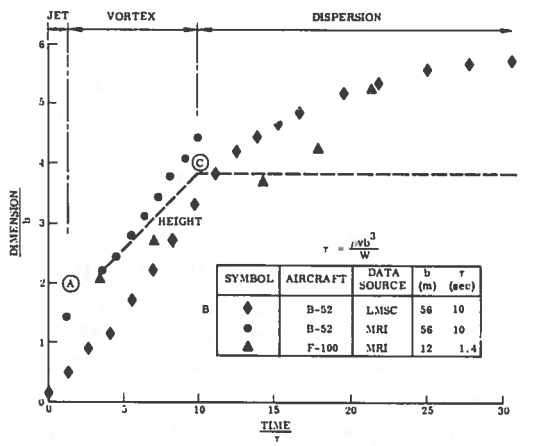

Figure 7. Comparison of contrail height data with scaling model.

It seems that in spite of its simplicity, the model is reasonably good. The experimental data generally follow the scaling-model predictions for both the width and height over an order of magnitude range of τ. This scaling model should be adequate for estimating the dimensions of the wake in the jet and vortex regime.

Wake Dispersion Regime

General Features

The wake dispersion regime extends from vortex breakup to the time at which the atmospheric dispersion is independent of the aircraft that deposited the exhaust trail. Thus, this regime spans the gap between the aircraft-dominated early regimes and the purely atmospheric processes. The wake dispersion regime is the most complex of the three presently defined regimes because it involves several modes of dispersal, and because both aircraft-induced and atmospheric-induced processes coexist and are of comparable importance.

It was an unexpected finding of the present study that aircraft-induced effects last for relatively long times. At the beginning of the wake dynamics program it was known, through the data of Ref. 2, that after vortex breakup the horizontal rate of growth is different for different aircraft. However, only short-time data were available, up to times on the order of a few minutes. It had been generally assumed that aircraft effects die out rapidly after vortex breakup. Our acquisition of long-time data and a closer look at the major processes contributing to wake dispersal indicate that aircraft-induced effects may be present in significant amounts up to times one order of magnitude larger than vortex breakup, that is, on the order of thousands of seconds. This conclusion is partly based on the data shown in Figure 3. The observed rate of horizontal growth in Figure 3 at times longer than 2 min tends to decrease with time. This is the opposite of the expected trend for natural dispersion, which proceeds at an *increasing* rate for diffusion coefficients proportional to the wake width.

Other evidence to support the long-lasting effects of the aircraft comes from examination of the major mechanisms of dispersal, namely, wind shear, diffusion due to wake turbulence, gravitational wake collapse, and buoyant rise. The

effect of wind shear is aircraft-dependent because the rate of growth is proportional to the initial wake height, which in turn is proportional to the aircraft span. The growth due to wake turbulence depends on the turbulent energy in the wake after vortex breakup, which in turn is a function of the energy the aircraft must deposit in the wake to maintain steady flight. Gravitational collapse is proportional to wake height, which, as stated above, is a function of aircraft span. Buoyant rise has the shortest persistence, and is the weakest of the growth mechanisms.

Wind Shear

Wind shear contributes to dispersal of the exhaust trail by advection of the top and bottom of the exhaust trail at different speeds. For simplicity, the wind velocity may be assumed to be linear through the trail height. This assumption seems justified in view of the coarseness and uncertainty associated with wind data. Under this assumption, the rate of growth of the trail width is given by

$$\frac{dw}{dt} = h \sin\theta \frac{dv}{dz} \qquad (7)$$

where

- h = trail height
- θ = angle between the wind and the trail axis
- v = wind speed
- z = vertical coordinate.

An indication of the relative importance of wind shear is given in Figure 8, where the contribution of wind shear to horizontal dispersal was calculated on the basis of the local atmospheric sounding at the time the contrail was produced. The horizontal growth due to wind shear is referenced to the wake width at the end of the vortex regime.

Stratospheric exhaust trails can be expected to be subjected, on the average, to less wind shear than was that shown in the figure, which was deposited in the high-shear region near the tropopause. It can also be expected that wind-shear will affect dispersal of the exhaust trail for a long time into the dispersion regime, since these effects should be the slowest to decay.

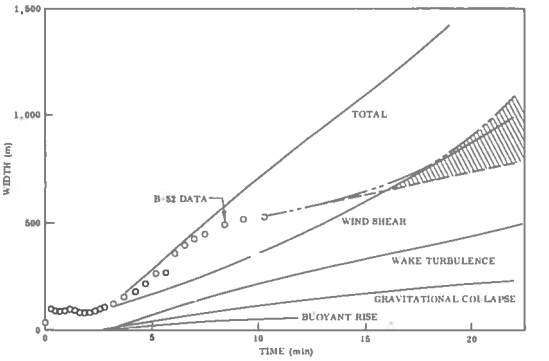

Figure 8. Comparison of estimated growth with observed wake width.

Wake Turbulence Diffusion

In the present model, it is assumed that wake growth by turbulent diffusion in the dispersion regime is due entirely to turbulence deposited in the wake by vortex breakdown. The scale of turbulence created by vortex breakdown is assumed to be about one wake width at the time of breakdown. The turbulent energy in the wake at wave lengths comparable to the wake width is initially much greater than that present in the free atmosphere. As the wake grows in width and height, mixing with the atmosphere and internal dissipation will continuously decrease the wake turbulence level until it attains the turbulence level of the free atmosphere. Additional turbulence will be deposited into the wake by the turbulent boundary layer and by viscous shear and mixing at the edge of the engine exhaust jets. The scale of this turbulence is probably of the order of 1 meter or less and therefore should not play an important role in diffusing the overall wake.

The kinetic energy in the wake due to the vortex pair was estimated by equating it to the induced drag and by assuming that the kinetic energy was uniformly distributed over the entire wake cross-section. This estimate for the aforementioned B-52 flight yielded an average turbulence velocity of 2.4 m/sec. If it is further assumed that all of this energy is at the wave length equal to the wake width, the resulting spectral density is somewhat higher than that present in what is qualitatively termed severe clear-air turbulence. This estimate can be considered an upper bound, since the turbulence

would be expected to distribute itself over some wave length interval. According to the findings of many investigators, severe turbulence corresponds to a dissipation rate of about $\epsilon = 700$ cm^2/sec^3. A more realistic value for the wake dissipation rate is probably about 100 cm^2/sec^3.

Given the dissipation rate, an estimate can be made of the wake growth by wake turbulence diffusion. Walton [9], for example, has obtained a solution to the diffusion equation of the form

$$\sigma^2 = \sigma_0^2 + 2\epsilon^{1/3}\sigma_0^{4/3}\, t + \frac{4}{3}(\epsilon\sigma_0)^{2/3}\, t^2 + \frac{8}{27}\epsilon t^3 \qquad (8)$$

where

σ = cloud size = standard deviation of the concentration distribution
σ_0 = initial cloud size
ϵ = dissipation rate
t = time

In this solution, the diffusion coefficient is taken to be

$$K = \epsilon^{1/3}\, \sigma^{4/3}\, (t)$$

In the present method of solution, the dissipation rate is assumed to be proportional to the turbulent kinetic energy, and is therefore decreased by atmospheric dilution as the wake cross-sectional area increases with time. The decrease in the dissipation rate due to internal dissipation has not been taken into account.

The results of this quasi-steady approximation are shown in Figure 8 for a value of the initial wake-dissipation rate ϵ_0, equal to 100 cm^2/sec^3. The horizontal growth due to wake turbulence is referenced to zero wake width at the end of the vortex regime to more clearly illustrate its contribution. The standard deviation has been equated to the wake width in these estimates.

Wake Collapse

When a well-mixed region is created locally in a stable stratified environment, the fluid in the well-mixed region tends to acquire neutral stability while the surrounding fluid remains stable. As a consequence, local buoyancy forces are created, with the top of the mixed region becoming negatively buoyant and the bottom positively buoyant with respect to the environment. This creates a vertical collapse of the well-mixed region, which flattens and spreads horizontally as every parcel of mixed fluid seeks its own density level in the stratified environment. The initial phases of collapse are dominated by gravitational and inertia forces. In theory, this process should continue until the originally mixed region flattens out into a lamina. In practice, after the initial phases of collapse, viscous forces come into competition with the driving gravitational forces, and the nature of the motion is changed.

A number of laboratory experiments to study these effects have been carried out in water tanks containing stratified solutions [10, 11, and 12]. It has been observed that mixed regions created with various agitators or by self-propelled bodies collapse as described above. These experiments are necessarily limited to short times because of wall effects that slow down and eventually stop the horizontal growth. Reference 11 suggests that the early collapse can be subdivided into two regimes where lateral growth is given by

$$\frac{y - y_0}{y_0} = 0.29\left(\frac{t}{\lambda}\right)^{1.08} \qquad 0 < \frac{t}{\lambda} < 2.5$$

and

$$\frac{y}{y_0} = 1.03\left(\frac{t}{\lambda}\right)^{0.55} \qquad 2.5 < \frac{t}{\lambda} < 6.75$$

Here y is the half-width of the collapsing region; y_0 is its initial radius; and λ is the reciprocal of the Brunt-Vaisala frequency:

$$\lambda = \left[-g\,\frac{1}{\rho}\,\frac{d\rho}{dz}\right]^{-1/2}$$

where

ρ is the environmental density and z the vertical coordinate.

The experiments were conducted over a range of stratifications, corresponding to λ from 0.6 to 4.0 sec, and the well-mixed region was originally of circular cross-section. Application of these results to the present problem should be made cautiously, since the atmospheric stratification is much weaker (λ about 75 sec for the B-52 data), and the characteristic radius of the well-mixed region of the wake is uncertain. Nevertheless, the above equations are the best available

estimate of the wake collapse effect at the present time, and have therefore been used to obtain order-of-magnitude estimates. Figure 8 also shows the estimated magnitude of the collapse effect for the B-52 data, assuming that only the vortex is well mixed. For this application, the time λ has been computed using the potential density deduced from the actual sounding at the time of flight.

Buoyant Rise

Buoyant rise of the exhaust trail has been proposed as a growth mechanism at late times [13]. The growth results from entrainment of ambient air, much like what occurs in chimney plumes. The source of buoyancy in the wake is the thermal energy in the engine exhaust. A quick calculation shows that the temperature rise in the wake is not large; however, small temperature differences can produce significant buoyant rise. In Reference 13, the buoyant rise and associated rate of growth are calculated using chimney-plume theories. To check the conclusions, the problem was approached from a different point of view, namely, by considering the exhaust trail as a line thermal deposited instantaneously. Initially the thermal is assumed to have a finite, circular cross-section and a finite amount of buoyancy per unit length, represented by the temperature difference above ambient. At time zero the thermal is allowed to rise freely in an environment of arbitrary stratification. The theoretical approach of Reference 14 for instantaneous point sources was followed, with the proper reformulation for the case of a line source. The basic assumptions are that the rate of turbulent entrainment is proportional to the speed of rise through an entrainment coefficient α, and that an incompressible formulation can be used for the atmosphere provided potential rather than physical density is used throughout.

The differential equations expressing conservation of volume, mass, and momentum are

$$\frac{dr^2}{dt} = 2r\alpha\mu$$

$$\frac{d}{dt}(\rho r^2) = 2r\rho_a\alpha\mu$$

$$\frac{d}{dt}(r^2\rho\mu) = gr^2(\rho_a - \rho)$$

where r is the radius, ρ the potential wake density, and ρ_a the potential ambient density, an arbitrary function of altitude. This system can be solved in closed form in terms of quadratures containing the arbitrary ambient density. For present purposes it was simpler to calculate numerical solutions to the differential equations with a high-speed computer. The entrainment coefficient suggested by Reference 14 ($\alpha \approx 0.3$) was used, and the buoyant rise was calculated from time zero to the equilibrium height of first velocity reversal. The initial temperature difference was given as an input parameter.

The estimated growth for the B-52 is shown in Figure 8 along with the observed wake growth. We conclude that although buoyant rise is potentially a mechanism for wake growth (the magnitude depending on aircraft, flight, and atmospheric parameters), this effect seems to be overshadowed by the effects of wind shear, turbulent diffusion, and gravitational collapse.

CHEMICAL KINETICS MODEL

The technical approach for the chemical kinetics model has been to screen the many possible chemical reactions to determine their probable importance in the engine exhaust jet, the near wake, and the far wake – i.e., to as late as 20 min after passage of the aircraft. To examine the reactions in the exhaust jet, however, it has been necessary for the calculations to cover areas even farther upstream, within the engine nozzle. The rate histories for many of the species must be examined before they reach the nozzle exit so that their concentrations at the exit plane can be established. Many atoms and radicals have been found to be present, and it cannot be reasonably anticipated that experimental test data on representative turbojet engines will be capable of quantitatively identifying all of the important species. Thus, the engine nozzle kinetics work is a necessary part of the chemical-reaction screening process. In this approach, simplifying relationships have been sought, such as steady-state and partial-equilibrium relationships among minor species, and efforts have been made to discover when such relationships can be used for making reliable predictions. The reliability of the simplifying methods is ascertained by comparison of the results with fully coupled computer solutions of the reacting flow problem.

The scope of the chemical screening process is broad; thermochemical reactions, photochemistry, and chemical particulate-formation reactions are all considered. Because oxides of nitrogen are thought to play a particularly important role in the stratosphere, their reactions are given special attention.

For studies of thermal reactions in the engine exhaust jet regime, the analytical approach involves setting up a chemical kinetics model using those elementary reactions that play a role in changing the concentrations of engine emissions in the exhaust nozzle and the near jet, downstream from the engine exit plane. Numerical methods are used to integrate the resultant governing chemical rate equations up to the point at which the exhaust flow mixes with the ambient atmosphere. Initial conditions for the computations are compatible with available data on engine exhaust composition.

The reactions and their respective rates are summarized in Table 2. Reverse reaction-rate constants are calculated from equilibrium constants. References for the rate data are given in the table. These data constitute a preliminary set used during model development, and are not necessarily recommended "best" values.

The analysis of the chemical reactions in the engine exhaust nozzle and exhaust plume was carried out using the NASA Lewis general kinetics program and other Lockheed programs [15]. The NASA program is capable of treating reacting flows with the fluid-mechanical equations coupled to the chemical rate equations.

The GE-4 engine operating at maximum power at a 65,000-ft altitude and flight Mach number 2.7 was taken as a conservative case for evaluating exhaust reactions. This operating condition gives the highest engine temperatures and a correspondingly great possibility of significant chemical reaction in the wake.

The engine exhaust nozzle conditions as determined from engine manufacturer's data are as follows:

Nozzle throat radius: 57.9 cm
Throat static temperature: 1730°K
Throat static pressure: 0.839 atm
Equivalent fuel: C_8H_{18}, $\phi = 0.715$

The nozzle shape is approximately conical, with the radius given by

$$r - r^* = 0.26x$$

where r is the nozzle radius, x is the length, and * indicates the throat. The nozzle is designed to expand the flow to ambient pressure, 0.0562 atm at 65,000 ft.

With the pressure-matched condition at the nozzle exit plane, the exhaust flow continues at constant temperature and pressure until the shear layer generated at the exhaust-jet/ambient-atmosphere interface closes in and mixes with the exhaust jet. Under these conditions, the constant temperature and pressure region

Table 2. Chemical Reactions in the $CO_x/NO_x/SO_x/CH_4$/Air System

Reaction Number	Reaction	Reaction Rate Variables*			Ref.
		A	n	E	
1	$H + N_2O = N_2 + OH$	3.01×10^{13}	0	10,800	16
2	$N + OH = NO + H$	4.21×10^{13}	0	0	16
3	$O + N_2O = N_2 + O_2$	3.61×10^{13}	0	24,000	17
4	$N_2 + NO_2 = NO + N_2O$	1.41×10^{14}	0	83,000	17
5	$H + NO_2 = NO + OH$	7.25×10^{14}	0	1,930	18
6	$HO_2 + NO = OH + NO_2$	6.00×10^{11}	0	0	19
7	$O + N_2 = NO + N$	1.44×10^{14}	0	75,580	17
8	$NO + O = N + O_2$	4.10×10^{9}	0	38,340	17
9	$M + NO_2 = O + NO + M$	1.10×10^{16}	0	65,000	17
10	$NO + O_2 = O + NO_2$	3.05×10^{12}	0	47,400	17
11	$NO + NO = N_2O + O$	7.05×10^{11}	0	65,000	17
12	$M + N_2O = N_2 + O + M$	6.30×10^{14}	0	56,800	17
13	$CO + OH = CO_2 + H$	4.20×10^{11}	0	1,080	20
14	$H + O_2 = OH + O$	2.20×10^{14}	0	16,800	21
15	$OH + OH = H_2O + O$	6.30×10^{12}	0	1,100	
16	$O + H_2 = H + OH$	1.80×10^{10}	1	8,900	
17	$H_2 + OH = H_2O + H$	2.20×10^{13}	0	5,150	
18	$M + H_2 = H + H + M$	2.20×10^{14}	0	96,000	
19	$M + H + OH = H_2O + M$	1.40×10^{23}	-2	0	21
20	$M + O_2 = O + O + M$	2.50×10^{18}	-1	118,500	18
21	$M + H + O_2 = HO_2 + M$	1.50×10^{15}	0	-1,000	21
22	$H + HO_2 = OH + OH$	2.50×10^{14}	0	1,900	
23	$OH + HO_2 = H_2O + O_2$	1.00×10^{13}	0	1,000	
24	$O + HO_2 = OH + O_2$	5.00×10^{13}	0	1,000	
25	$H + HO_2 = H_2 + O_2$	2.50×10^{13}	0	700	
26	$H + HO_2 = H_2O + O$	1.00×10^{13}	0	1,000	21
27	$NO_2 + OH = HNO_3$	2.90×10^{12}	0	0	22
28	$H_2O_2 + OH = H_2O + HO_2$	1.00×10^{13}	0	1,800	21
29	$OH + OH + M = H_2O_2 + M$	7.1×10^{14}	0	-5,100	21
30	$HO_2 + HO_2 = H_2O_2 + O_2$	6.5×10^{13}	0	0	21
31	$SO_2 + O + M = SO_3 + M$	4.5×10^{14}	0	0	23
32	$SO_3 + H = SO_2 + OH$	6.5×10^{14}	0	10,800	23
33	$SO_3 + O = SO_2 + O_2$	6.5×10^{14}	0	10,800	23
34	$CH_4 + H = CH_3 + H_2$	6.9×10^{13}	0	11,900	15
35	$CH_4 + OH = CH_3 + H_2O$	7.2×10^{13}	0	5,900	
36	$CH_4 + O = CH_3 + OH$	2.0×10^{13}	0	9,200	
37	$CH_4 + O_2 = CH_3 + HO_2$	1.0×10^{13}	0	63,000	
38	$CH_3 + O = CH_2O + H$	1.9×10^{13}	0	0	
39	$CH_3 + O_2 = CH_2O + OH$	7.5×10^{10}	0	0	
40	$CH_2O + H = HCO + H_2$	1.0×10^{13}	0	2,000	
41	$CH_2O + OH = HCO + H_2O$	7.0×10^{10}	0.7	1,000	
42	$CH_2O + O = HCO + OH$	4.0×10^{11}	0.6	4,000	
43	$HCO + O = CO + OH$	1.8×10^{11}	0.5	0	
44	$HCO + OH = CO + H_2O$	1.1×10^{11}	0.5	0	
45	$HCO + H = CO + H_2$	1.5×10^{12}	0.5	0	15

*Reaction rate constant $k = A T^n \exp(E/RT)$. Units are moles, cm, sec, °K, cal.

extends out to 22 meters beyond the nozzle exit plane.

The complete chemical-kinetic model analysis then involves two steps. First, the model is run subject to the constraint of the conical nozzle flow, and second, the calculations are continued at exit-plane temperature and pressure, out to the end of the unmixed region. The pressure, temperature, and time profiles as functions of position, shown in Figure 9, were used for all calculations presented here. Possible reactions in the mixing zone and beyond are considered in later sections.

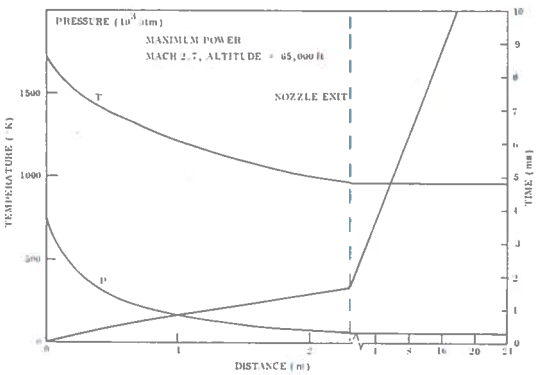

Figure 9. GE-4 jet exhaust flow properties.

The initial species compositions for nozzle expansion calculations were determined by chemical equilibrium computations at the nozzle throat, with the exception of CO, NO, NO_2, and CH_4. The equilibrium calculations were performed using the Lockheed "P Chem" thermochemical equilibrium program. The species CO, NO, NO_2, and CH_4 are well known to be out of equilibrium in jet exhausts because of chemical-kinetic freezing and mixing effects in the combustor and afterburner regions. The CO and NO initial concentrations were estimated by reviews of available data, i.e., to give exit-plane concentrations consistent with typical test results. The NO_2 concentrations at the throat were arbitrarily increased above typical combustor exhaust levels to account for about 10% of the total NO_x. The concentration of CH_4, taken to represent all unburned hydrocarbon, was treated as a parameter. Initial throat concentrations of all species are given in Table 3.

Table 3. Initial Throat Concentrations

Species	Mole Fraction
H	7.57-07
N_2O	8.11-08
N_2	7.47-01
OH	3.33-04
N	9.41-12
NO	2.99-04
O	1.56-05
O_2	5.59-02
NO_2	2.99-05
HO_2	1.36-07
CO	2.99-03
CO_2	9.10-02
H_2O	1.02-01
H_2	1.28-05
HNO_3	6.43-12
SO_2	1.00-04
CH_4	zero to 3.00-03

Results for the Case CH_4 = Zero

For the above starting conditions, the model calculations yield the concentration profiles shown in Figure 10. Excluded from Figure 10 are the trace species SO_3, N, and HNO_3, whose concentration levels remain at all times less than 1 ppb, and the major species CO_2, O_2, N_2, and H_2O, for convenience in plotting.

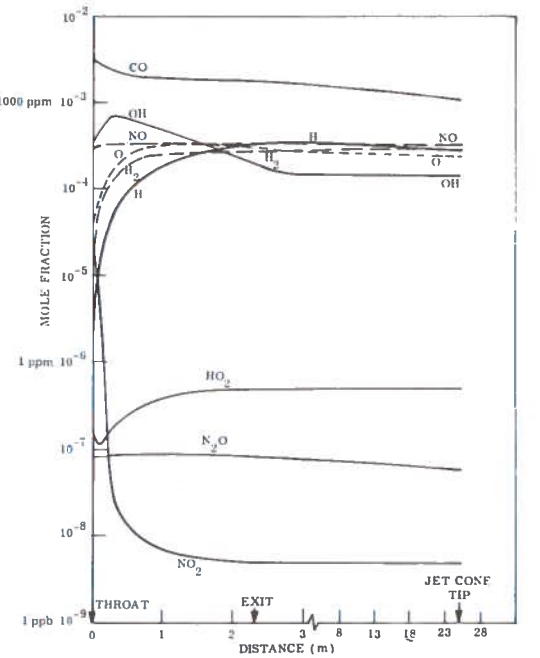

Figure 10. Species concentration profiles in GE-4 secondary nozzle and jet exhaust, zero hydrocarbons.

These results show that a non-equilibrium but only slowly changing chemical balance exists in the exhaust plume. Evidently the low density at 65,000 ft greatly slows recombination. It is found that nearly all of the active inorganic radical and atomic species exist in superequilibrium concentrations.

The origin and maintenance of these radicals is largely a consequence of carbon monoxide oxidation. Near throat temperatures, the reaction $CO + OH \rightarrow CO_2 + H$ is essentially a branching step because the H atoms produced react via $H + H_2O \rightarrow H_2 + OH$ and $H + O_2 \rightarrow O + OH$ followed by $O + H_2O \rightarrow 2OH$. In the cooler exhaust jet, the CO oxidation still represents a chain mechanism, where $CO + OH \rightarrow CO_2 + H$ is followed primarily by $H + O_2 + M \rightarrow HO_2 + M$, with $H + HO_2 \rightarrow OH + OH$ regenerating the OH.

The notion that the high radical concentrations are an eventual result of carbon monoxide oxidation is confirmed by computations in which the CO oxidation rate is arbitrarily reduced to negligible values. The model output then shows concentrations of O, OH, and H radicals in the nozzle which are lower by about one order of magnitude.

Results with Hydrocarbons Included

Test data are scarce for SST engines, but those which exist show that quantities of unburned hydrocarbons (measured as total C) may be quite large with afterburning [24]. To take some account of the effect of hydrocarbons on the exhaust chemistry, methane oxidation reactions 34-45 are included in the model.

The major effect of the methane reactions was found to be a sacrifice of radicals defined as $P \equiv H + OH + O$ in favor of CH_2, CH_2O, HCO, and CO. The magnitude of the P-radical reduction is dependent on the unburned hydrocarbon quantities assumed.

Two sets of concentration profiles are shown in the accompanying figures (Figures 11 and 12). Both are for conditions corresponding to the GE-4 engine at maximum power and 20-km altitude. Starting throat concentrations of all species are taken as before, except that the portion of CH_4 is assumed initially to be 500 ppm in Figure 11 and 3000 ppm in Figure 12. In the first case, most of the CH_4 is oxidized in the

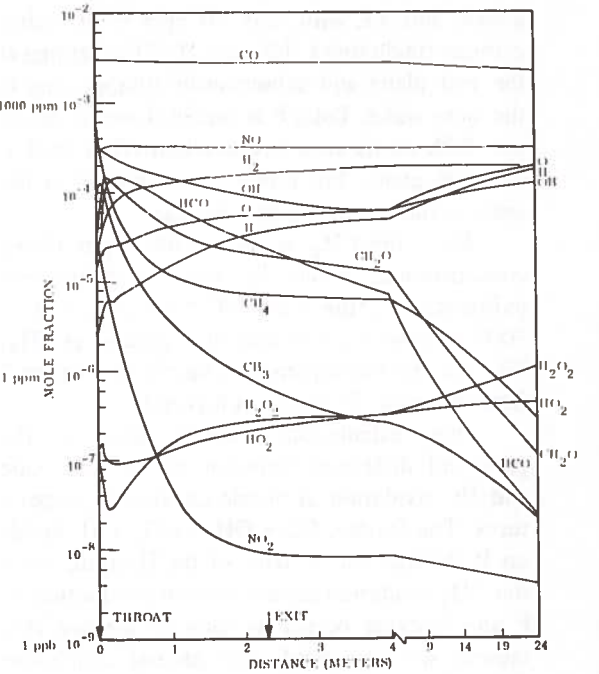

Figure 11. Species concentration profiles in GE-4 secondary nozzle and jet exhaust, 500 ppm hydrocarbons at throat.

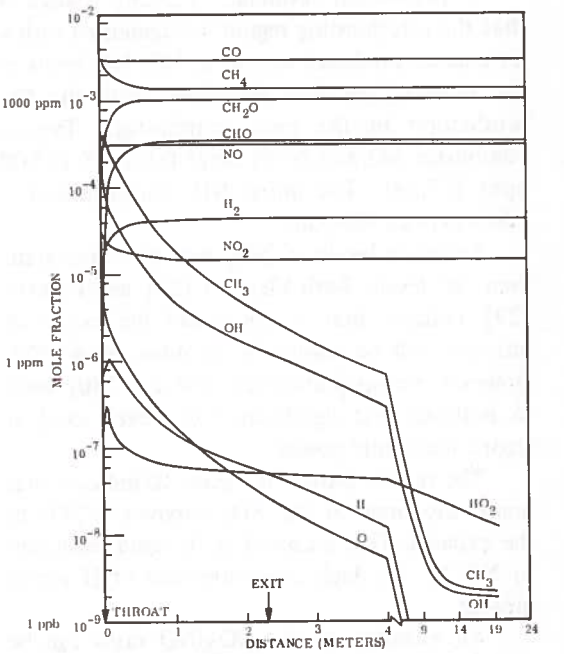

Figure 12. Species concentration profiles in GE-4 secondary nozzle and jet exhaust, 3000 ppm hydrocarbons at throat.

nozzle and jet, with only 50 ppm total hydrocarbons (including CHO and CH_2O) remaining at the exit plane and subsequently disappearing in the near wake. Total P is forced down to about one fifth of its zero hydrocarbon (HC) level at the exit plane, but builds up somewhat in the wake as the last of the HC vanishes.

When the CH_4 is set at 3000-ppm throat concentration, practically none is completely oxidized; i.e., the wake HC level is frozen at 3000 ppm with about half of it present as CH_4. This has the consequence of nearly eliminating P from the wake, as shown in Figure 12.

These calculations serve to point out the profound difference between carbon monoxide and HC oxidation at nozzle expansion temperatures. The former, $CO + OH \rightarrow CO_2 + H$, builds up P through the activity of the H atom, while the CH_4 oxidation cannot sustain production of P and freezing occurs as soon as the available radicals are scavenged. The general conclusion drawn here is that if the unburned HC levels are high, then the radicals H, OH, or O cannot be present at significantly high concentrations.

Discussion of NO_x *Results*

Experimental evidence [25,26] indicates that the afterburning region in augmented turbojet engines produces very little NO. NO levels in the exhaust are thus associated with the NO production in the main combustors. Typical combustor NO exit levels range from 100 to 500 ppm [27,28]. The initial NO concentration is taken here as 300 ppm.

Emission levels of NO_2 are more uncertain than NO levels. Both Fletcher [28] and Caretto [29] indicate that at full power the oxides of nitrogen will be essentially all nitric oxide, NO. However, recent preliminary test data [30] seem to indicate that significant NO_2 levels exist at engine maximum power.

The results shown in Figure 10 indicate that practically none of the NO_x survives as NO_2 in the exhaust. This is caused by its rapid reduction to NO by the high concentrations of H atoms present.

An estimate of the NO_2/NO ratio can be made by applying the steady-state approximation to the two dominant reactions:

$$NO + O + M \xrightarrow{k_a} NO_2 + M$$

$$H + NO_2 \xrightarrow{k_b} NO + OH$$

The NO_2 formation rate is

$$\frac{d\,[NO_2]}{dt} = k_a\,(NO)\,(O)\,(M) - k_b\,(H)\,(NO_2)$$

The assumption that NO_2 is in a steady state produces the relationship

$$\frac{(NO_2)}{(NO)} = \frac{k_a\,(M)\,(O)}{k_b\,(H)}$$

Therefore with $k_a = 1.05 \times 10^{15} \exp(1870/RT)$, and $k_b = 7.25 \times 10^{14} \exp(-1930/RT)$

$$\frac{(NO_2)}{(NO)} = [1.45 \exp(3800/RT)]\,\frac{(M)\,(O)}{(H)}$$

This expression is only weakly temperature-dependent, so, since (M) is constant, the (O)/(H) ratio is the controlling factor.

Substituting the zero-CH_4 exit-plane concentrations of M, O, and H in the latter expression yields

$$\frac{(NO_2)}{(NO)_{\text{exit, steady state}}} = 0.62 \times 10^{-5}$$

This compares favorably with the results of the full computer solution, i.e.,

$$\frac{(NO_2)}{(NO)_{\text{exit, finite rate}}} = 1.1 \times 10^{-5}$$

Figures 11 and 12 demonstrate that when sufficient CH_4 is present, the steady-state value of NO_2/NO is not reached. The above expression is still a good approximation in the case of 500 ppm CH_4, but with 3000 ppm it fails badly, since with the very low H-atom levels the destruction of NO_2 virtually stops. Of course, the formation is also slowed. Significantly, at no point in the nozzle or jet does there appear to be a net formation of NO_2; the fraction NO_2/NO_x freezes at 1/2 its originally assumed throat value.

A comparison between the H and NO_2 profiles at the three values 0, 500, and 3000 ppm initial CH_4 is shown in Figure 13. The inverse relation between the H and NO_2 concentrations is apparent.

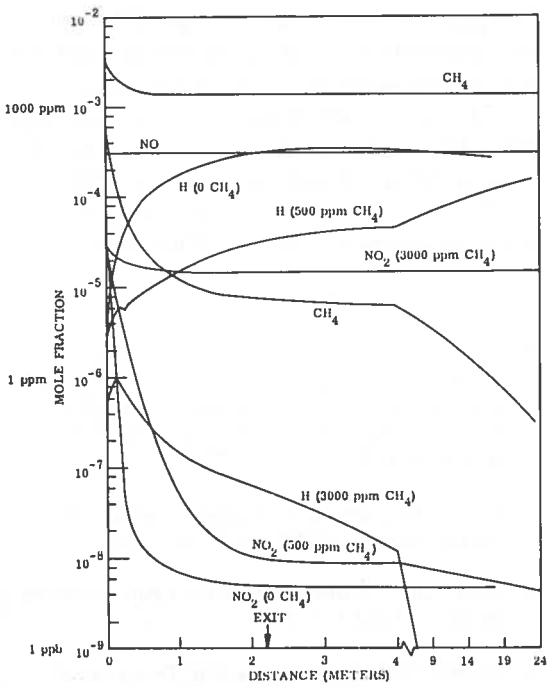

Figure 13. Effect of hydrocarbon on NO_2 in GE-4 secondary nozzle and jet exhaust.

CO *Oxidation*

The phenomenological aspects of CO oxidation have been discussed. Numerical results show that a considerable decrease in CO can occur in the nozzle and jet under cruise conditions with low unburned HC concentrations. Calculations for the zero HC run, presented in Figure 10, show that the proportion of CO in the exhaust is decreased from 3000 ppm in the nozzle throat to 1780 ppm CO at the exit, and then is further reduced to 1150 ppm at the tip of the conical jet core.

The corresponding CO levels for the run with 500 ppm CH_4 initially present are 2810 ppm CO at the exit, and 2180 ppm finally. When the portion of CH_4 was set at 3000 ppm, the CO level remained nearly frozen throughout.

Oxides of Sulfur

At the combustor exit, both thermodynamic and kinetic considerations predict the well-known result that virtually all sulfur is present as SO_2. In the nozzle and jet, the kinetics of the sulfur oxides will be dominated by three reactions [23]. These are the homogeneous formation of SO_3

$$SO_2 + O + M \xrightarrow{k_a} SO_3 + M$$

and its reduction by H or O atoms

$$SO_3 + H \text{ (or O)} \xrightarrow{k_b} SO_2 + OH \text{ (or } O_2)$$

This mechanism is analogous to the NO-NO_2 cycle in the nozzle and jet discussed previously.

A steady-state analysis can be applied as before, with SO_3 replacing NO_2 as the steady-state species. The analysis gives the expression:

$$\frac{(SO_3)}{(SO_2)_{SS}} = \frac{k_a\,(O)\,(M)}{k_b\,[(O) + (H)]}$$

Recent published values [23] for k_a are in the range $k_a = 1.5 \times 10^{15}$ to 10^{16} cm^6 $mole^{-2}$ sec^{-1}. For k_b, the expression $k_b = 6.5 \times 10^{14}$ exp (-10800/RT) cm^3 $mole^{-1}$ sec^{-1} has been used [23]. Using k_b, $k_a = 4 \times 10^{15}$, and nozzle exit properties (T = 954°K), the steady-state relationship yields

$$\frac{(SO_3)}{(SO_2)_{SS}} = 6 \times 10^{-4} \quad \text{(nozzle exit)}$$

Therefore, it can be concluded that at the nozzle exit there is only a negligible quantity of SO_3.

Nitric Acid Formation by NO_2 *Oxidation*

Although there appears to be little chance for appreciable NO_x to exist as NO_2 in the hot exhaust, it is true that with rapid cooling due to air entrainment the recombination

$$NO + O + M \rightarrow NO_2 + M$$

and the reaction with ambient O_3

$$NO + O_3 \rightarrow NO_2 + O_2$$

are fast. Furthermore, the NO_2 thus formed will no longer be destroyed by H-atom attack because of the activation-energy barrier involved.

Then at low temperature, stable nitric acid can be formed by

$$NO_2 + OH \xrightarrow{k_{27}} HNO_3$$

Of course, a necessary requirement for this to be significant is that OH not be removed faster by

some other process. Such a process does exist, however, namely,

$$OH + OH + M \xrightarrow{k_{29}} H_2O_2 + M$$

One may compare the rate of OH loss by the above reaction to that in the NO_2 + OH reaction. Defining Z as the ratio

$$Z \equiv \frac{\left(\frac{d\,OH}{dt}\right)_{29}}{\left(\frac{d\,(OH)}{dt}\right)_{27}} = \frac{2k_{29}\,[OH]^2\,[M]}{k_{27}\,[OH]\,[NO_2]}$$

one has

$$Z = \frac{2k_{29}\,[OH]\,[M]}{k_{27}\,[NO_2]}$$

Z is independent of air entrainment because OH and NO_2 are diluted together. If $Z \gg 1$ then HNO_3 will not be formed.

Using rate data from Table 2, and assuming $T = 220^\circ K$ and $[OH] = [NO_2]$, one finds.

Z = 100 at 25 km
= 230 at 20 km
= 490 at 15 km

Thus, it appears that HNO_3 formation can be ruled out. The rate constants, especially k_{29}, may be very uncertain. We have used the expression given by Baulch for k_{29}. This has an activation energy of -5.1 kcal and an asserted temperature range of validity of 700 to 1500°K.

A recent critical review of OH radical kinetics by Wilson [31] recommends a k_{27} value at 300°K of about half of what is computed using Baulch's expression. Thus the condition $Z \gg 1$ remains, and the conclusion that NO_x is not converted to HNO_3 appears to be valid.

ACKNOWLEDGMENTS

The authors would like to acknowledge the very considerable contributions made by several other members of the wake dynamics study project. Drs. W. McLean and J. Meyer have contributed significantly to the development of the chemical kinetics model, while Mr. K.O. Redler has been instrumental in the planning, collection, and analysis of aircraft contrail data. This paper would not have been possible without the contributions of these individuals, and the authors express appreciation for their efforts.

The authors would also like to acknowledge that this work has been supported by the Climatic Impact Assessment Program, Office of the Secretary, Department of Transportation, under the direction of Dr. R.L. Underwood.

REFERENCES

1. Hoshizaki, H., R.J. Conti, L.B. Anderson, K.D. Redler, J.W. Meyer, W.J. McLean, and D.E. Cassady, *Study of High-Altitude Aircraft Wake Dynamics, Final Report:* Task I, Problem Definition, DOT-TST-90-3, Dec. 1972.

2. Smith, T.B., and K.M. Beesmer, *Contrail Studies for Jet Aircraft*, AFCRL TR-59-251, 1969.

3. Crow, S.C., "Stability theory for a pair of trailing vortices," AIAA J. *8*, 2172.

4. *Aircraft Wake Turbulence and Its Detection*, ed. J. Olsen and A. Goldburg, Plenum Press, 1971.

5. Lamb, H., *Hydrodynamics*, Dover, 1945.

6. Overcamp, T.J., and J.A. Fay, "Dispersion of SST trails in the stratosphere," AIAA Paper 72-650, 1972.

7. Abramovich, G.N., *The Theory of Turbulent Jets*, MIT Press, 1963.

8. Spreiter, J.R., and A.H. Sacks, "The rolling up of the trailing vortex sheet and its effect on the downwash behind wings," J. Aero. Sci. *18*, 21, 1951.

9. Walton, J.J., Scale Dependent Diffusion, UCRL-74134, Lawrence Livermore Laboratory, August 1972.

10. Schooley, A.H., and R.W. Stewart, "Experiments with a self-propelled body submerged in a fluid with a vertical density gradient," J. Fluid Mech. *15*, 83.

11. Schooley, A.H., "Wake collapse in a stratified fluid," Science *157*, 421.

12. Wu, J., "Mixed region collapse with internal wave generation in a density-stratified medium," J. Fluid Mech. *35*, 531.

13. Overcamp, T.J., and J.A. Fay, "Dispersion of SST Trails in the Stratosphere," AIAA Paper 72-650, 1972.

14. Morton, B.R., G.I. Taylor, and J.S. Turner, "Turbulent gravitational convection from maintained and instantaneous sources," Proceed. Roy. Soc., Series A *234*, 1, 1956.

15. Bittker, D.A., and Scullin, V.J., *General Chemical Kinetics Computer Program for Static and Flow Reactions, With Application to Combustion and Shock Tube Kinetics,* NASA TN D-6586, 1972.

16. Fletcher, R.S., R.D. Siegal, and E.K. Bastress, *The Control of Oxides of Nitrogen Emission From Aircraft Gas Turbine Engines*, Vol. 1, "Program Description and Results," Report No. FAA-RD-71-111, 1, 1971.

17. Laurendeau, N., *The Thermal Decomposition of Nitric Oxide and Nitrogen Dioxide*, University of California at Berkeley, Report No. TS-72-4, April 1972.

18. Garvin, D., and L.H. Gevantman, *Chemical Kinetics Data Survey*. III: Selected Rate Constants for Chemical Reactions of Interest in Atmospheric Chemistry, NBS Report 10-867, June 1972.

19. Davis, D.D., University of Maryland, private communication.

20. Baulch, D.L., D.D. Drysdale, and A.C. Lloyd, *High Temperature Reaction Rate Data, No. 1*, School of Chemistry, University of Leeds, May 1968.

21. Baulch, D.L., D.D. Drysdale, D.G. Horne, and A.C. Lloyd, *Evaluated Kinetic Data for High Temperature Reactions*, Butterworths, London, 1972.

22. Simonaitis, R., and J. Heicklen, "The kinetics of the reaction of OH with NO_2," Transactions, American Geophysical Union (EOS) *52*, Nov. 1971, Abstracts.

23. Levy, A., E.L. Merryman, and W.T. Reid, "Mechanisms of formation of sulfur oxides in combustion," Envir. Sci. Tech. *8*, 563, 1970.

24. Diehl, L.A., *Preliminary Investigation of Gaseous Emissions from Jet Engine Afterburners*, NASA-TM-X-2323, July 1971.

25. *SST Powerplant Exhaust Emission Characterizations*, Scott Research Labs 1220 01 0371, 1971.

26. Palcza, J.L., *Study of Mach Number Effects on Exhaust Gas Emissions of an Afterburning Turbofan Engine*, Naval Air Propulsion Test Center ATD-212, Dec. 1971.

27. Starkman, E.S., and R.F. Sawyer, "The role of chemistry in gas turbine emissions," Trans. ASME, J. Eng. Power, 333, July 1971.

28. Fletcher, R.S., and R.D. Siegal, *The Control of Nitrogen Emissions from Aircraft Gas Turbine Engines*, Vol. 2: The NO_x Formation Process, Report No. FAA-RD-71-111, 2, 1971.

29. Caretto, L., "The formation of NO in combustion processes," presented at Central States Section/Combustion Institute, March 1968.

30. Lazalier, G.R., and J.W. Gearheart, *Measurement of Pollutant Emissions from an Afterburning Turbojet Engine at Ground Level*, Arnold Engineering Development Center TR-72-70, Aug. 1972.

31. Wilson, W.E., "A critical review of the gas-phase reaction kinetics of the hydroxyl radical," J. Phys. Chem. Ref. Data *1*, No. 2, 535, 1972.

DISCUSSION

(UNIDENTIFIED): Would you expect any major differences in the near-wake dynamics at 65,000 feet, compared to the lower-altitude ones you studied?

HOSHIZAKI: No, I think the basic wake features would be the same.

ANDERSON: The reason that we were so interested in whether NO is converted to NO_2 early in the wake was that if all the OH were co-existing with the NO_2, nitric acid could form and provide an early sink for NO_x.

(UNIDENTIFIED): Isn't there a study by Steve Crow which gives a theoretical prediction of the vortex pair as it breaks up? Also, can we be certain that the extent of the condensation or ice nuclei distribution is truly representative of the wake size?

HOSHIZAKI: As to your first question, I believe Crow predicts vortex breakup at a normalized characteristic time (t/τ) of 3.6 or so, and we adjusted that to 10 on the basis of experimental data.

CONTI: As regards ice nuclei, we feel that the wake is supersaturated with respect to the environment. There might be some detailed exchanges in it, like agglomeration or coagulation, but by and large it is a tracer for the engine exhaust. The non-persistent contrails are not supersaturated, and disappear in seconds or minutes.

CORRIN: I suspect that in the supersaturated situation the water vapor itself in the wake can be seriously perturbed, much as siver-iodide nuclei will perturb cumulonimbus clouds. The freezing of the supercooled liquid droplets liberates a great deal of energy and

significantly changes the dynamics of the cloud. Incidentally, the most persistent contrail I ever observed lasted one hour and five minutes.

(UNIDENTIFIED): Do you intend to make any calculations to see the effect of the non-uniformity of the exhaust plume?

HOSHIZAKI: Yes; on the basis of this work, we are developing a model for CIAP which will compute the chemistry off the centerline. However, we will model only the constant-pressure region in the exhaust plume. We will not consider the mixing region, between the wake and the ambient air, but we doubt that it would be useful for the purposes of CIAP anyway.

TRAUGOTT: Are the gravitational effects you mentioned large enough to influence wake turbulence? What sort of Richardson number do you have in regime 3?

HOSHIZAKI: I don't know what the turbulence levels and shear gradients in that regime are. I think they are probably comparable to those of the atmosphere after about 10 to 30 minutes.

COMMENTS ON PHOTOCHEMICAL MODELING

EIGIL HESSTVEDT
Institute of Geophysics
University of Oslo
Oslo, Norway

ABSTRACT: Rates of formation and destruction of $O(^3P)$, odd oxygen, OH, HO_2, H_2O_2, odd hydrogen, H_2, and H_2O, derived without transport, are presented as a function of altitude from 10 to 70 km. When an earlier two-dimensional model of the ozone layer with transport is modified by the NO_x profile recently observed by Ackerman and Muller*, the agreement between calculated and observed ozone distribution is improved.

RATES OF FORMATION AND DESTRUCTION OF OXYGEN-HYDROGEN COMPONENTS IN THE STRATOSPHERE AND LOWER MESOSPHERE

The number of reactions considered in atmospheric photochemical models has increased steadily, and will continue to do so. Earlier, when the models were less complex than the present (and future) ones, it was easier to remember the reaction rates for the relatively few reactions considered in the models. But today the list of reactions is becoming so long that only experts can distinguish the important reactions from the unimportant ones off-hand. It may therefore be of interest to present, in the form of tables or diagrams, a survey on the production and destruction rates of some of the components usually considered in the more conventional oxygen-hydrogen atmosphere models. My report therefore does not pretend to present any scientific news; it is merely meant to serve as a guide and a reference. The reaction rates are diagrammed as a function of altitude in Figures 1-10; from these diagrams one may sort out the important reactions for each chemical constituent.

The reactions and rate coefficients used are listed in Table 1. Data for the number densities of the oxygen and hydrogen components, as well as NO, NO_2, CO, and M, are given in Table 2. Composition data are taken from time-dependent photochemical models computed by myself. In

*Ackerman, M., and Muller, C., "Stratospheric nitrogen dioxide from infrared absorption spectra," Nature *240*, 300, 1972.

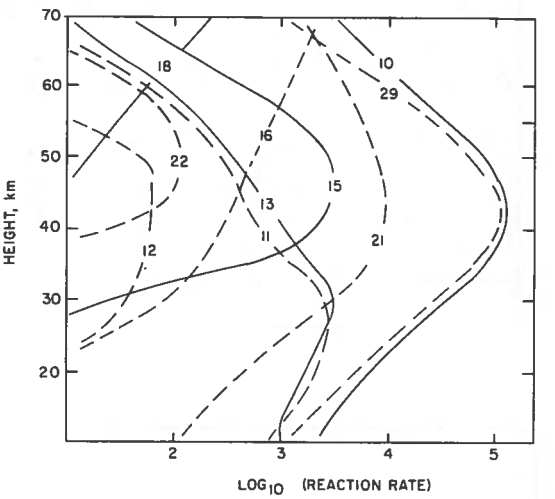

Figure 9. Rates of production (- - -) and destruction (—) of odd hydrogen, H + OH + HO_2.

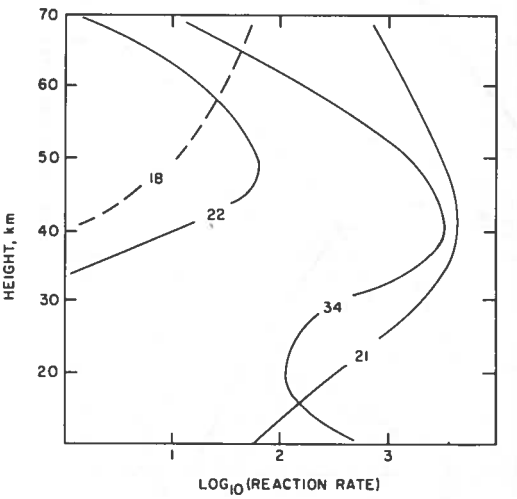

Figure 10. Rates of production (- - -) and destruction (—) of H_2.

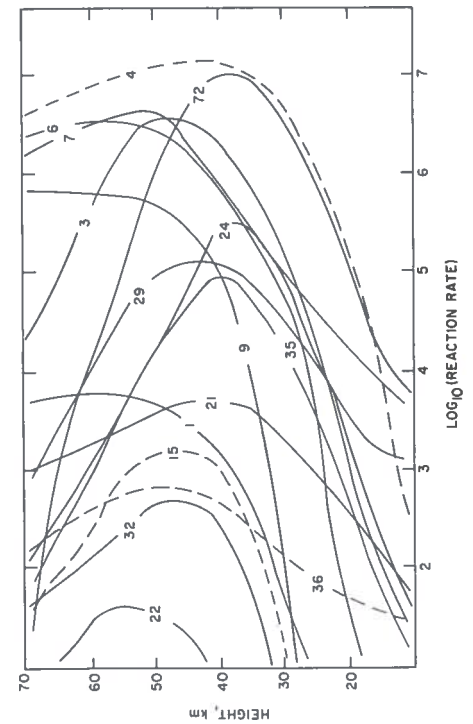

Figure 2. Rates of production (- - -) and destruction (—) of odd oxygen, $O(^3P) + O(^1D) + O_3$.

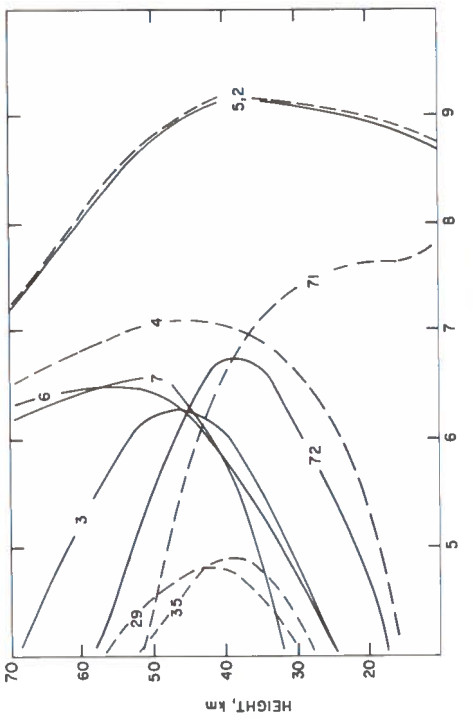

Figure 1. Rates of production (- - -) and destruction (—) of $O(^3P)$. The numbers on the curves refer to the reactions listed in Table 1.

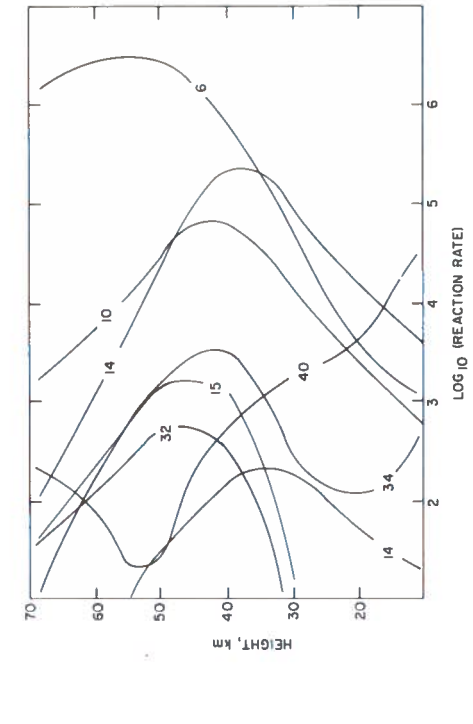

Figure 4. Rates of destruction of OH.

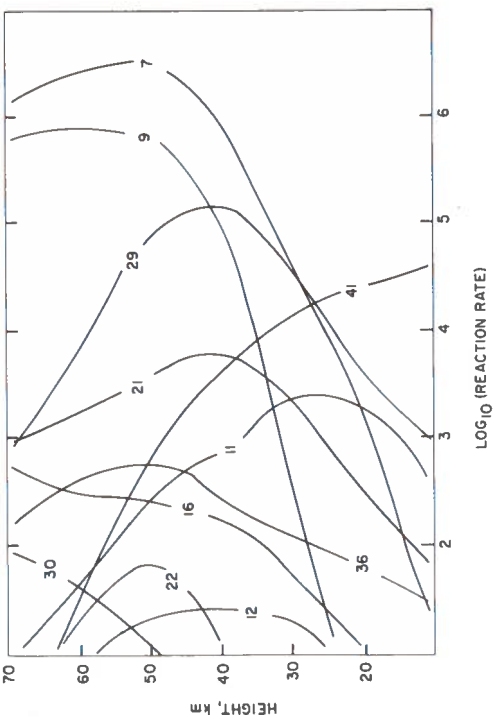

Figure 3. Rates of production of OH.

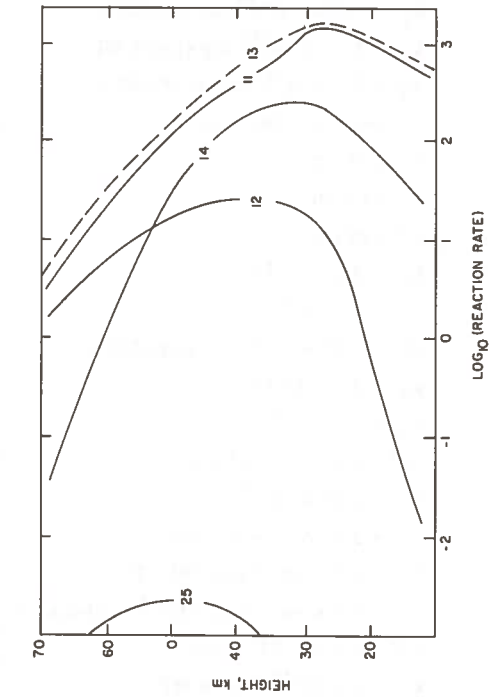

Figure 6. Rates of production (- - -) and destruction (—) of H_2O_2.

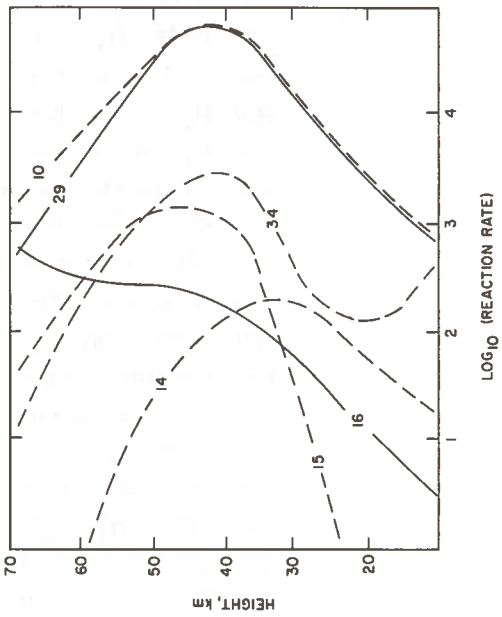

Figure 8. Rates of production (- - -) and destruction (—) of H_2O.

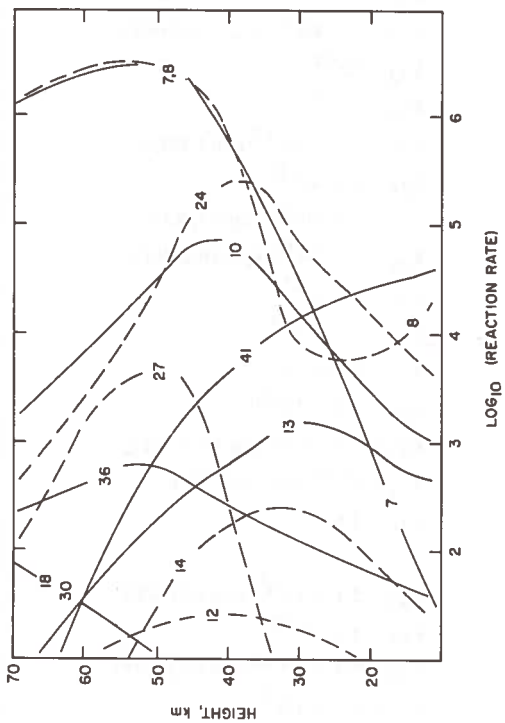

Figure 5. Rates of production (- - -) and destruction (—) of HO_2.

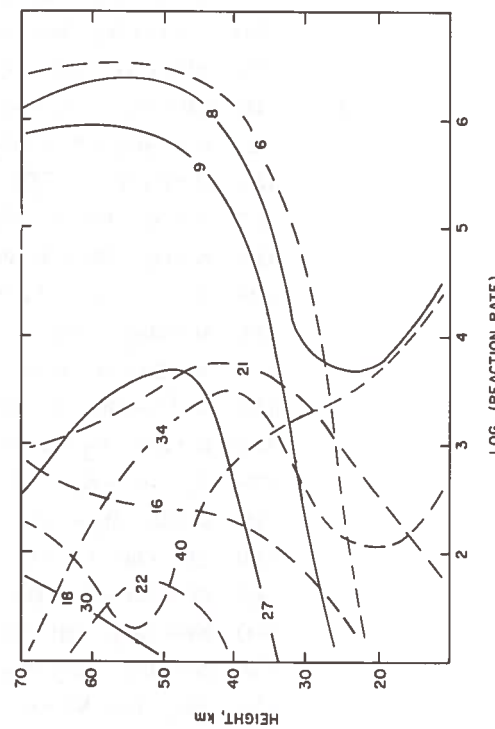

Figure 7. Rates of production (- - -) and destruction (—) of H.

Table 1. Reactions and Reaction Rates

(1)	$O(^3P) + O(^3P) + M \rightarrow O_2 + M$	$k_1 = 1.50 \times 10^{-34} \exp(1.4/RT)$
(2)	$O(^3P) + O_2 + M \rightarrow O_3 + M$	$k_2 = 1.05 \times 10^{-34} \exp(1.014/RT)$
(3)	$O(^3P) + O_3 \rightarrow 2\,O_2$	$k_3 = 2.1 \times 10^{-11} \exp(-4.91/RT)$
(4a)	$O_2 + h\nu \rightarrow O(^3P) + O(^3P)$	$175\ nm < \lambda < 242.4\ nm$
(4b)	$O_2 + h\nu \rightarrow O(^3P) + O(^1D)$	$\lambda < 175\ nm$
(5a)	$O_3 + h\nu \rightarrow O(^3P) + O_2$	$\lambda > 310\ nm$
(5b)	$O_3 + h\nu \rightarrow O(^1D) + O_2$	$\lambda < 310\ nm$
(6)	$OH + O(^3P) \rightarrow H + O_2$	$k_6 = 2.5 \times 10^{-11}$
(7)	$HO_2 + O(^3P) \rightarrow OH + O_2$	$k_7 = 7 \times 10^{-11}$
(8)	$H + O_2 + M \rightarrow HO_2 + M$	$k_8 = 1.89 \times 10^{-32} \exp(0.685/RT)$
(9)	$H + O_3 \rightarrow OH + O_2$	$k_9 = 2.6 \times 10^{-11}$
(10)	$OH + HO_2 \rightarrow H_2O + O_2$	$k_{10} = 2 \times 10^{-10}$
(11)	$H_2O_2 + h\nu \rightarrow 2\,OH$	$187.5\ nm < \lambda < 382.5\ nm$
(12)	$O(^3P) + H_2O_2 \rightarrow OH + HO_2$	$k_{12} = 1.87 \times 10^{-15}$
(13)	$HO_2 + HO_2 \rightarrow H_2O_2 + O_2$	$k_{13} = 3 \times 10^{-11} \exp(-500/T)$
(14)	$OH + H_2O_2 \rightarrow H_2O + HO_2$	$k_{14} = 1.7 \times 10^{-11} \exp(-910/T)$
(15)	$OH + OH \rightarrow H_2O + O(^3P)$	$k_{15} = 8.3 \times 10^{-11} (T/273)^{1/2} \exp(-2/RT)$
(16)	$H_2O + h\nu \rightarrow OH + H$	$135\ nm < \lambda < 237.5\ nm$
(17)	$H + HO_2 \rightarrow H_2O + O(^3P)$	$k_{17} = 2 \times 10^{-10} \exp(-4/RT)$
(18)	$H + HO_2 \rightarrow H_2 + O_2$	$k_{18} = 3 \times 10^{-12}$
(19)	$H + H + M \rightarrow H_2 + M$	$k_{19} = 1.2 \times 10^{-32} (273/T)^{0.7}$
(20)	$O(^1D) + M \rightarrow O(^3P) + M$	$k_{20} = 3.8 \times 10^{-11}$
(21)	$O(^1D) + H_2 \rightarrow OH + H$	$k_{21} = 3 \times 10^{-10}$
(22)	$O(^3P) + H_2 \rightarrow OH + H$	$k_{22} = 7 \times 10^{-11} \exp(-10.2/RT)$
(23)	$HO_2 + O_3 \rightarrow OH + 2\,O_2$	$k_{23} = 10^{-20}$
(24)	$OH + O_3 \rightarrow HO_2 + O_2$	$k_{24} = 10^{-14}$
(25)	$H + H_2O_2 \rightarrow H_2 + HO_2$	$k_{25} = 2.8 \times 10^{-12} \exp(-1900/T)$
(26)	$H + O(^3P) + M \rightarrow OH + M$	$k_{26} = 8 \times 10^{-33}$
(27)	$H + O_3 \rightarrow HO_2 + O(^3P)$	$k_{27} = 2 \times 10^{-10} \exp(-4/RT)$
(28)	$H + O_2 \rightarrow OH + O(^3P)$	$k_{28} = 1 \times 10^{-9} \exp(-16.8/RT)$
(29)	$O(^1D) + H_2O \rightarrow 2\,OH$	$k_{29} = 3 \times 10^{-10}$
(30)	$H + HO_2 \rightarrow 2\,OH$	$k_{30} = 3 \times 10^{-12}$
(31)	$H + OH + M \rightarrow H_2O + M$	$k_{31} = 2.5 \times 10^{-31}$
(32)	$O(^3P) + OH + M \rightarrow HO_2 + M$	$k_{32} = 1.4 \times 10^{-31}$
(33)	$H + HO \rightarrow H_2 + O(^3P)$	$k_{33} = 3 \times 10^{-11} \exp(-8.3/RT)$
(34)	$H_2 + OH \rightarrow H_2O + H$	$k_{34} = 10^{-10} \exp(-5.9/RT)$
(35)	$O(^1D) + O_3 \rightarrow 2\,O_2$	$k_{35} = 3 \times 10^{-10}$
(36)	$HO_2 + h\nu \rightarrow OH + O(^3P)$	
(40)	$CO + OH \rightarrow H + CO_2$	$k_{40} = 2.1 \times 10^{-13} \exp(-115/T)$
(41)	$NO + HO_2 \rightarrow OH + NO_2$	$k_{41} = 3 \times 10^{-13}$
(70)	$NO + O_3 \rightarrow NO_2 + O_2$	$k_{70} = 9.3 \times 10^{-13} \exp(-1235/T)$
(71)	$NO_2 + h\nu \rightarrow NO + O$	$J_{NO_2} = 7 \times 10^{-3}$
(72)	$NO_2 + O \rightarrow NO + O_2$	$k_{72} = 3 \times 10^{-11} \exp(-300/T)$

Table 2. Number Densities (Noon Values) of Oxygen-Hydrogen Components

Height km	$O(^3P)$	$O(^1D)$	O_2	O_3	OH	HO_2	H_2O_2	H	H_2O	H_2	CO	NO	NO_2	M
70	1.5+10	1.9+2	4.7+14	1.7+ 9	4.9+6	1.2+6	2.4+4	1.3+7	6.3+ 9	1.1+10	3.4+ 8	3.4+ 6	1.5+ 2	2.3+15
65	1.3+10	2.6+2	9.0+14	4.5+ 9	7.5+6	1.9+6	8.4+4	5.7+6	1.8+10	1.5+10	1.8+ 8	1.2+ 7	2.4+ 3	4.3+15
60	1.2+10	3.6+2	1.6+15	1.1+10	1.1+7	3.0+6	2.6+5	2.7+6	4.1+10	1.8+10	4.8+ 7	3.4+ 7	2.6+ 4	7.7+15
55	9.0+ 9	4.5+2	2.9+15	3.1+10	1.6+7	4.4+6	7.0+5	1.0+6	8.8+10	2.1+10	7.1+ 6	1.1+ 8	4.1+ 5	1.4+16
50	6.6+ 9	5.6+2	5.2+15	9.7+10	2.4+7	6.6+6	1.9+6	3.5+5	1.8+11	1.7+10	6.5+ 6	3.0+ 8	4.9+ 6	2.5+16
45	4.1+ 9	6.5+2	9.9+15	3.3+11	3.5+7	1.0+7	5.4+6	9.0+4	3.4+11	2.6+10	2.6+ 7	7.9+ 8	6.2+ 7	4.7+16
40	1.1+ 9	3.1+2	2.0+16	9.0+11	2.9+7	1.1+7	1.3+7	5.2+3	6.8+11	4.9+10	1.2+ 8	1.3+ 9	5.8+ 8	9.4+16
35	2.6+ 8	1.1+2	4.0+16	1.9+12	1.5+7	1.7+7	1.5+7	1.6+2	1.5+12	9.6+10	5.6+ 8	1.5+ 9	2.0+ 9	1.9+17
30	4.5+ 7	1.9+1	8.6+16	2.6+12	3.4+6	2.1+7	2.2+8	2.1	2.3+12	2.0+11	2.7+ 9	2.2+ 9	4.0+ 9	4.1+17
25	8.0+ 6	3.8	1.9+17	2.8+12	1.4+6	2.2+7	3.7+8	2.2−1	4.9+12	4.4+11	1.3+10	3.3+ 9	5.6+ 9	8.9+17
20	1.2+ 6	7.8−1	4.1+17	2.4+12	7.8+5	1.8+7	3.0+8	7.5−2	1.1+13	9.8+11	5.5+10	4.3+ 9	5.5+ 9	2.0+18
15	1.4+ 5	1.4−1	9.1+17	1.4+12	4.8+5	1.2+7	1.6+8	3.2−2	2.4+13	2.2+12	2.0+11	9.0+ 9	6.2+ 9	4.4+18
10	3.2+ 4	4.2−2	1 8+18	1.0+12	3.5+5	1.0+7	1.5+8	1.5−2	4.8+13	4.4+12	4.4+11	1.4+10	1.1+10	8.8+18

these models atmospheric transport is neglected, but is indirectly taken care of by using profiles for CO and NO_x (and O_3 below 30 km) taken from one-dimensional transport models. Some of the components have a diurnal variation, but in all cases the noon values for 45° latitude, summer, are given.

Other authors may prefer different values for the rate constants, and may also arrive at a composition which is different from the one presented here. Furthermore, it is true that other reactions are important and should be included. I feel that it will be useful to revise and extend the data presented here as progress is made in atmospheric chemistry.

FURTHER STUDIES IN A TWO-DIMENSIONAL OZONE MODEL WITH TRANSPORT

At the CIAP meeting in Gaithersburg in September I gave a report on a theoretical study of the ozone layer, using a two-dimensional model with transport. Since it is very likely that many in this audience already know about the basis for and the results of my work, I shall not bore you with too many details.

This two-dimensional model extends from 35 km down to the tropopause, which is taken as 10 km in high latitudes, increasing to 18 km in the equatorial region. The photochemical reactions considered are the same as in the foregoing section. A parameterized atmospheric transport is used. Two models are computed, one for summer and one for winter conditions. Photochemical equilibrium is assumed for ozone at the upper boundary (35 km), while a fixed value of 10^{12} molecules/cm^3 is assumed at the lower boundary.

In the previous model a constant value was used for the mixing ratio of NO_x. Recently I have recomputed the model using a fixed vertical profile for this mixing ratio which is in agreement with the measurement of NO_2 by Ackerman and Muller. Furthermore, computed profiles are used for the dissociation rate of NO_2, rather than a constant value as in the older model.

While the latter point is of less significance, the change of profile for the NO_x mixing ratio has a marked effect upon the computed O_3 distribution, especially for the summer case. The result is shown in Figure 11.

The use of a curved NO_x profile brings the model into much closer agreement with observations. This is particularly true for high-latitude summer, where the old model failed to reproduce the observed strong ozone layer.

As was done for the old model, computations were repeated for other profiles of NO_x. For example, if the NO_x content is increased by 50%, the total ozone is reduced by 10%. The relationship between NO_x and total ozone, derived for the old model, is found to be valid also for the improved model with its curved NO_x profile.

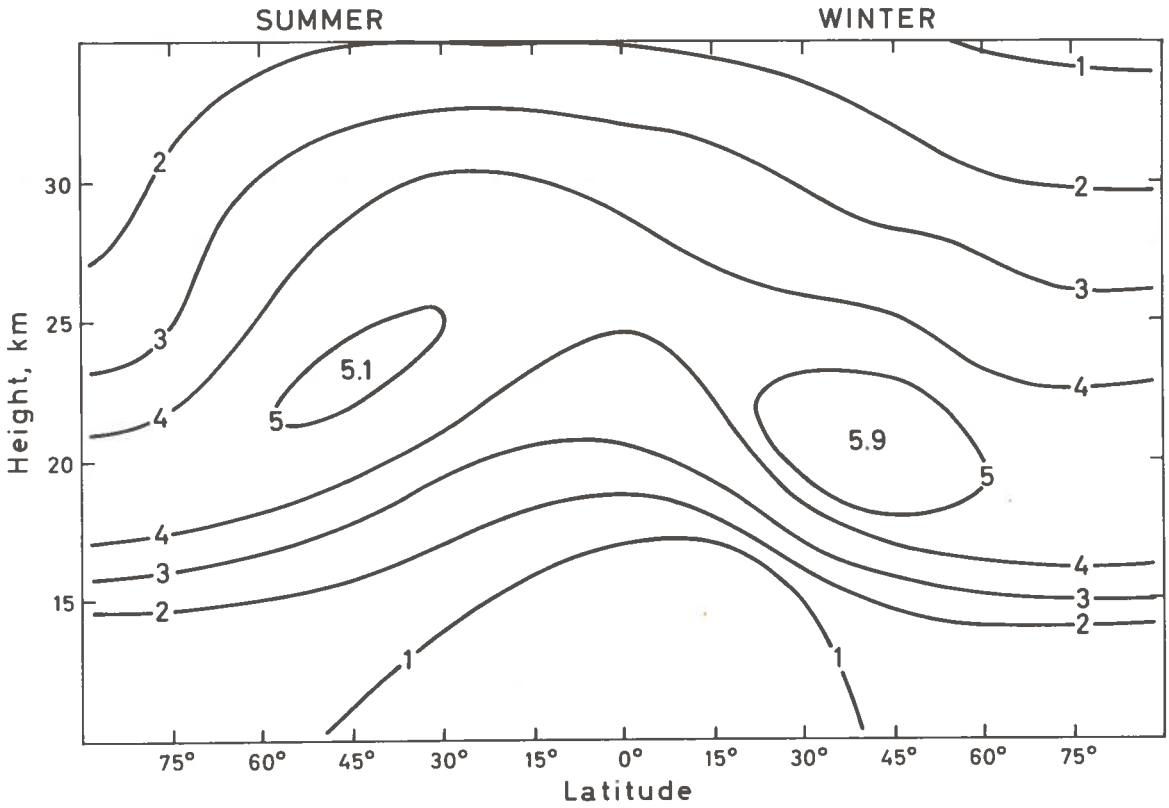

Figure 11. Ozone distribution obtained with Ackerman and Muller's NO_X profile.

DISCUSSION

GARVIN: I am delighted to see charts of reaction rates as a function of altitude. This is an unusually simple presentation of modeling results, and I think it will be very helpful to laboratory chemists in deciding what to study and refine for use in models. I hope others doing large-scale modeling will present their results in a similar format.

ELLSAESSER: I think it is important to look at the effect of NO injection on ozone as a function of latitude. Adding NO to the stratosphere might reduce mid- and high-latitude ozone without disturbing the vertical column over the Equator. Such an addition can be judged only by examining the resultant increase in UV exposure at various latitudes, and comparing it to a permissible maximum; global figures are not really meaningful.

TIME-DEPENDENT TWO-DIMENSIONAL PARAMETERIZED MODEL

T. SHIMAZAKI AND D.J. WUEBBLES
Aeronomy Laboratory
ERL, National Oceanic and Atmospheric Administration
Boulder, Colorado

ABSTRACT: Because of the importance of horizontal as well as vertical transport for the minor constituents' distributions in the stratosphere, especially in the lower stratosphere, any model in this region must be at least two-dimensional. This paper describes our time-dependent two-dimensional model, which is currently being developed under DOT contract. Introducing temperature, mean meridional circulation, and eddy diffusion as parameterized values, we solve the two-dimensional continuity equation for a 360-degree meridional plane by an alternating-direction implicit line-iterative method. The boundary conditions are given by photochemical equilibrium at the upper boundary (50 km), the same vertical flux at the lowest two grid points at the lower boundary (10 km), and a cyclic boundary condition at the side boundaries. A preliminary result of the photochemical pure-oxygen model obtained by our method is compared with the recent Nimbus 4 BUV measurements. The future development of this modeling is briefly discussed.

INTRODUCTION

The distributions of minor neutral stratospheric constituents, especially ozone, play an important role in the global energy budget and radiation balance of the atmosphere. For instance, stratospheric ozone, while comprising only 3×10^{-7} of the atmosphere, strongly absorbs solar ultraviolet radiation and provides the principal heat-energy deposition in the atmosphere.

Various exhaust constituents released from SST flights may affect the ozone distribution leading to a change in the amount of sola. ultraviolet radiation reaching the earth, which may be hazardous to man. Johnston [1] and Crutzen [2] have shown that a reduction of ozone density might result from the injection of NO into the stratosphere by aircraft engines. However, before we completely understand the possible effects of stratospheric flight, we need more sophisticated modeling of the distributions of ozone and the other minor constituents in the stratosphere, including the transport effects.

Both vertical and horizontal transport are important and must be included in the model of minor stratospheric constituents. The problem must also be treated as time-dependent, since the effects of engine exhausts are essentially time-dependent. The day-night difference in particular may cause very different chemical reaction schemes and dynamics.

In this paper we describe briefly the modeling technique of our time-dependent two-dimensional model, discuss how this modeling can fit the CIAP requirements, and present its current status and plans for future development.

BASIC CONSIDERATIONS

A realistic model of stratospheric ozone cannot be obtained on the assumption of photochemical equilibrium. If an atmospheric constituent requires more than a day to reach photochemical equilibrium, then transport due to eddy diffusion and atmospheric winds becomes important in the determination of the distribution of that constituent. For ozone in the stratosphere, the time to reach equilibrium increases from less than a day at the stratopause to more than a year at 25 km [3,4]. Therefore, below approximately 45 km atmospheric dynamics becomes increasingly important.

Prabhakara [5] has shown that with the addition of dynamics a meridional model of the ozone layer predicts ozone density distributions much closer to those observed than does the model of photochemical equilibrium. Hesstvedt [6] has improved the Prabhakara model by including water vapor and nitrogen compounds.

However, because of their boundary conditions, which assume either constant or observed ozone density at the lower boundary (tropopause) and an awkward side boundary condition at the equator, neither model may be able to adequately calculate the effects of engine exhausts, since these effects should change the ozone density distributions at the boundaries.

For a general circulation model of the mean atmosphere, horizontal motions are of primary importance, and vertical motions are only secondary. For determining the height distributions of the chemically active minor constituents, however, vertical transports are essential, because chemical sources and losses are strongly height-dependent. In the stratosphere both vertical and horizontal transport should be important, and must be included in any model of that region; therefore, any model for the stratosphere should be at least two-dimensional.

It would be ideal to solve the thermodynamic equation and the equations of motion simultaneously with the continuity equation in the three-dimensional domain, as is being done in the global-circulation models. However, presently available global-circulation models will require major refinements and extensions to be applicable to the CIAP problem [7]. At present, most of the global-circulation models use observed distributions of ozone, rather than calculating the ozone distribution. Even if the ozone density distribution is calculated theoretically, it is not certain to give a reasonable temperature distribution and circulation.

While stratospheric ozone chemistry will be included in some of the global-circulation models, it is unlikely that a three-dimensional, global-circulation model with fully interactive chemistry, fluid dynamics, and thermodynamics can be developed by the 1974 CIAP deadline. For the ozone problem, less comprehensive, simplified models may be able to obtain similar results without the large amount of computer time and memory needed by the global-circulation models.

Parameterized, simplified models should be able to obtain some useful results by the CIAP deadline for the exhaust effects on the distribution of minor constituents in the stratosphere. In parameterized modeling, a value for temperature, eddy diffusion, and mean wind is assigned at each grid point of the model, whereas in the global-circulation models each of these parameters is recalculated at each time step. The term "simplified" indicates that the model does not simultaneously solve the three kinds of equations, i.e., the equations of motion, energy, and continuity; the modeling technique itself is not simple. Although we do not recalculate the temperature structure at each time step, we will examine the consistency of the results *for the normal stratosphere* by calculating the temperature structure for the calculated ozone-density distributions; chemistry and dynamics must be those which reproduce the originally assumed temperature structure. This examination of consistency is needed before we put the SST exhaust gases into the model. (We implicitly assume that the dynamics is not seriously affected by chemistry or the redistribution of ozone density.)

Details in the atmospheric motion, especially in the various scales of motion and in the time variability of these motions, are difficult to represent by parameterization. However, it appears that the transport of minor constituents in the stratosphere is dominated by large-scale motions that can be represented in terms of mean motion (or wind) and eddy (or turbulent) diffusion. The accuracy with which these parameters describe the motions of the atmosphere rests heavily on observational data, which is quite limited at present.

Because of the long time-constants of many of the constituents in the stratosphere, it would be useful to find the steady-state solution of the continuity equation and then use it as the initial condition for the time-dependent (diurnal) solution. Because of the large differences between day and night density distributions for some of the constituents, such as atomic oxygen, it may be necessary to use a time-dependent model to adequately determine the effects of any changes in chemistry between day and night.

OUR TWO-DIMENSIONAL TIME-DEPENDENT MODELING METHOD

We are developing a two-dimensional time-dependent model for the stratosphere by extending our previous one-dimensional models for the mesosphere and lower thermosphere [8-12]. In this model, temperature, mean meridional

circulation, vertical mean winds, and horizontal as well as vertical eddy diffusion are included by way of parameterized values. In our two-dimensional model, the meridional plane of 360 degrees is considered for the height range of 10 to 50 km, comprising most of the stratosphere for each 10 degrees of latitude. By using the 360-degree meridional plane we can set a side boundary condition which is more reasonable than those of the other two-dimensional models (180-degree in the Prabhakara model and 90-degree plane in the Hesstvedt model). As can be seen in Figure 1, which shows the meridional plane used in the study, with the sun at an angle δ from the equator, our model has also the advantage that the day-night and the seasonal differences can be calculated simultaneously.

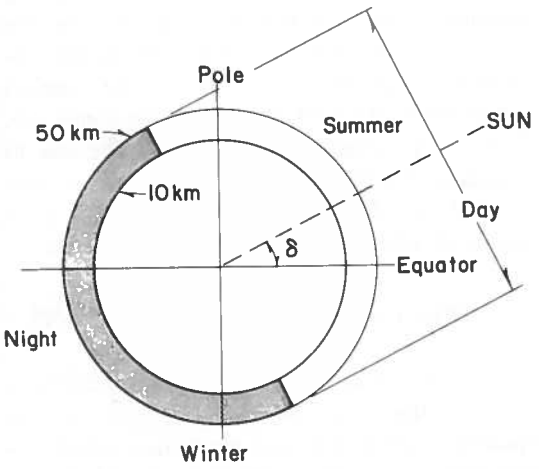

Figure 1. 360-degree meridional plane showing day-night and seasonal differences, as used in our two-dimensional model of the stratosphere.

We solve the continuity equation using a thermal and dynamic structure based on observations. The three-dimensional continuity equation (in spherical coordinates) can be written as

$$\frac{\partial n}{\partial t} = Q - Ln + \frac{\partial}{\partial z}(nw) + \frac{\partial}{\partial y}(nv) - \frac{\tan\theta}{r}(nv) + \frac{1}{r\cos\theta}\frac{\partial}{\partial x}(nu) + \frac{\partial}{\partial z}\left\{K_{zz}\left(\frac{\partial n}{\partial z} + n\left(\frac{1}{T}\frac{\partial T}{\partial z} + \frac{1}{H}\right)\right) + K_{zy}\frac{\partial n}{\partial y}\right\} + \frac{\partial}{\partial y}\left\{K_{yy}\frac{\partial n}{\partial y} + K_{yz}\frac{dn}{dz} + K_{yx}\frac{\partial n}{\partial x}\right\} - \frac{\tan\theta}{r}\left\{K_{yy}\frac{\partial n}{\partial y} + K_{yz}\frac{\partial n}{\partial z} + K_{yx}\frac{\partial n}{\partial x}\right\} + \frac{1}{r\cos\theta}\frac{\partial}{\partial x}\left\{K_{xx}\frac{\partial n}{\partial x} + K_{xy}\frac{\partial n}{\partial y} + K_{xz}\frac{\partial n}{\partial z}\right\} + K_{zx}\frac{\partial n}{\partial x}\right\} \quad (1)$$

where n is the number density, x represents the zonal or longitudinal direction, y the meridional or latitudinal direction, and z the vertical direction; u, v, and w are the components of mean motion in the x, y, and z directions, respectively; K_{zz}, K_{yz}, etc. represent the effective eddy diffusion coefficients, T is temperature, H is mean scale height, r is the earth's radius, and θ is latitude. The term including tan θ arises from the convergence of the meridians toward the poles in the spherical coordinate system. Taking the zonal average of equation (1), we obtain the two-dimensional continuity equation (terms of $\partial/\partial x$ vanish)

$$\frac{\partial n}{\partial t} = Q - Ln + \frac{\partial}{\partial z}(nw) + \frac{\partial}{\partial y}(nv) - \frac{\tan(\theta)}{r}(nv) + \frac{\partial}{\partial z}\left\{K_{zz}\left(\frac{\partial n}{\partial z} + n\left(\frac{1}{T}\frac{\partial T}{\partial z} + \frac{1}{H}\right)\right) + K_{zy}\frac{\partial n}{\partial y}\right\} + \frac{\partial}{\partial y}\left\{K_{yy}\frac{\partial n}{\partial y} + K_{yz}\frac{\partial n}{\partial z}\right\} - \frac{\tan(\theta)}{r}\left\{K_{yy}\frac{\partial n}{\partial y} + K_{yz}\frac{\partial n}{\partial z}\right\} \quad (2)$$

Since we are considering the 360-degree meridional plane, each quantity in equation (2) represents the zonal average for the day and night sides separately. The day side represents the noon condition and the night side the midnight condition. Initially, we consider the time-independent or steady-state solution of (2). The result will be used as an initial condition for the time-dependent solution. Later, when we solve the time-dependent problem, the effects of zonal motion could be included by way of parameterization. Under the assumption that the time variation corresponds to the longitudinal or zonal variation, the model could be considered three-dimensional

The grid used in representing the stratosphere is shown in Figure 2. Grid points are taken in intervals of 10 degrees latitude in the horizontal direction and 1 km in the vertical direction. At each grid point, the continuity equation must be solved for each minor constituent to be studied, giving us a set of continuity equations to be solved simultaneously. In solving a set of time-dependent continuity equations by the numerical finite-difference method, the so-called implicit method gives faster and better convergence than the explicit method.

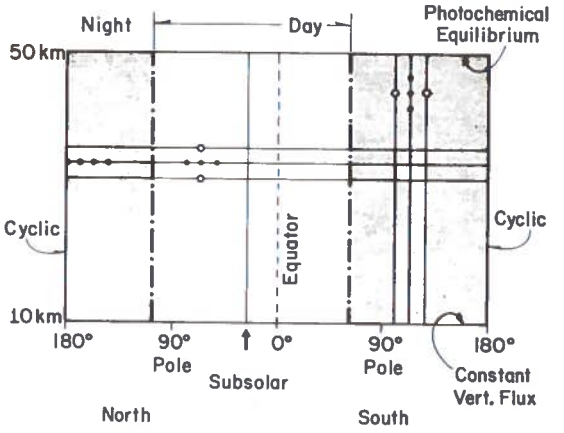

Figure 2. Grid used in representing the stratosphere, extending from 10 to 50 km and over the 360-degree meridional plane.

In our two-dimensional time-dependent model, we use the implicit line-iterative method [13,14]. With this method the continuity equation is first reduced to a linear equation of n's in a row at a constant height K by the use of finite difference equations

$$n(J+1,K) = A(J,K)\,n(J,K) + B(J,K)\,n(J-1,K) + C(J,K) \quad (3)$$

where J and K indicate the horizontal and vertical co-ordinates, respectively, and A, B, and C are complex functions independent of the unknowns, n (J−1,K), n (J,K), and n (J+1,K). C is a function, however, of values of n at heights K+1, K, and K−1 from the previous iteration (for K+1 and K) or previous time step (for K−1). The line iteration starts from the top. In Figure 2 the three values to be determined in the row of constant height, K, are shown by dark circles; the values taken from the previous iteration or time step are shown by light circles. All unknown values in the row of K will be determined simultaneously so that the values at both ends, separated by 360 degrees, may be the same (cyclic boundary condition). If necessary, we will apply a similar method to columns as well as rows; the method is then called the alternating-direction implicit line-iterative method.

Photochemical equilibrium is normally assumed at the upper boundary (50 km); however, for constituents whose chemical time constants are too long for this, fixed values are assumed on the basis of observations or theoretical considerations at the upper boundary. At the lower boundary (10 km), the vertical flux is assumed to be the same at the lowest two grid points (constant flux with height).

The model will be tested for consistency by calculating the temperature structure for the resultant ozone density distribution. If the calculated temperature is close to the original temperature structure, the solution is consistent. From such consistency tests we may be able to determine which dynamics is best, and we may be able to adopt such dynamics in our later model calculations for examining SST effects.

CURRENT STATUS AND FUTURE PLANS

For the model calculations we need information on the solar radiation intensity and its spectrum; absorption and photodissociation coefficients of the main absorbers in the stratosphere at various wavelengths; chemical reaction coefficients and their temperature dependence for the important chemical reactions; global temperature structure; meridional and zonal mean wind in the stratosphere; and horizontal and vertical eddy-diffusion coefficients.

The temperature structure is tentatively taken from Murgatroyd [15]. (See Figure 3.) The solar flux data and the photodissociation cross-sections for O_2 and O_3 are taken from Ackerman [16]. The reaction rate for $O + O_2 + M \rightarrow O_3 + M$ is based on Johnston [17], and the reaction rate for $O + O_3 \rightarrow 2O_2$ is from NBS Report 10828 [18].

We have initiated our study by determining the distribution of O and O_3 from Chapman reactions assuming photochemical equilibrium. Programming of this simplest case could be useful

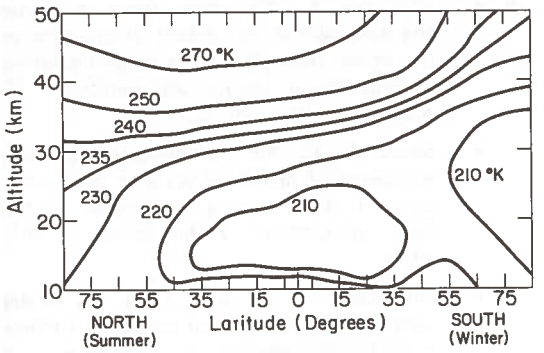

Figure 3. Contours for constant temperature in the stratosphere, based on data presented by Murgatroyd [15].

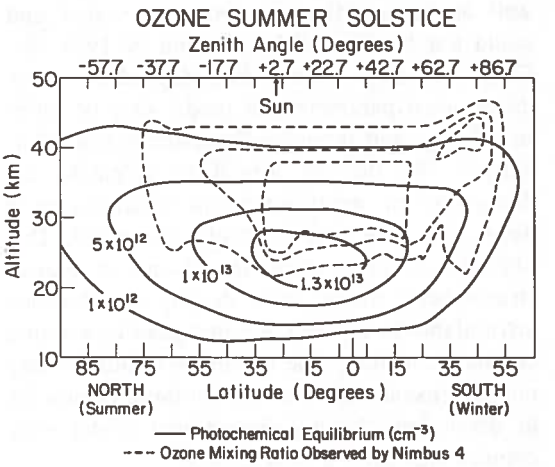

Figure 4. Comparison of the contour map of constant ozone number density calculated on the assumption of photochemical equilibrium by our method, with the contour map of the observed ozone mixing ratio from the Nimbus 4 BUV satellite.

for solving the basic problems which we will meet in the more complicated programs at the later stages of our study. The result will also be valuable for comparison with the later models that will include nitrogen and hydrogen chemistry and dynamics, and for determining their effects.

The results for the calculation of O_3 are shown in Figure 4, along with observations of O_3 taken from the Nimbus 4 BUV satellite [19] The contours of Nimbus data show the constant mixing ratio, whereas the contours of the model represent constant number densities. Both the model and the observed ozone distributions are for the summer solstice. As expected, the calculated photochemical-equilibrium ozone-density distribution varies in both altitude and magnitude from the observed ozone distribution; this indicates the necessity of including the dynamic effects in the model. In particular, the photochemical model cannot explain the higher O_3 concentration at winter high latitudes.

Calculations are now being done for the steady-state pure-oxygen model, including dynamics. The relative importance of eddy diffusion, horizontal mean motion due to meridional circulation, and vertical winds will be determined by comparing the model result of the $[O_3]$ distribution with observations and by testing the consistency of the result with the original temperature structure, as outlined in the method section.

Once dynamics has been added to the steady-state model, minor constituents other than pure-oxygen components will be added, along with their chemistry. An oxygen-nitrogen-hydrogen model will first be calculated by the addition of compounds such as NO, NO_2, NO_3, N_2O_5, HNO_3, OH, H_2O, HO_2, and H_2, and their related photolysis and chemical reactions. Eventually, carbon-containing constituents, such as CH_4, CO, CO_2, and CH_2O, will be added to the steady-state model. The time-dependent model will then be calculated, proceeding in a series of steps similar to the steady-state calculations.

Once the time-dependent two-dimensional model of the natural stratosphere has been completed, the perturbations by SST aircraft exhaust will be calculated. The exhaust gases will be added to the time-dependent model at a specific rate, varying with time and latitude, and the effects will be analyzed by extending the model calculation for an appropriate period of time.

CONCLUDING REMARKS

The inclusion of horizontal transport is essential to the modeling of stratospheric ozone. For evaluating the effects of NO_x emitted by stratospheric flights, the time-dependent model is preferable. The development of the global-circulation model for stratospheric minor constituents, calculating temperature and motions as

well as composition, is too complicated and could not be finished by the end of 1974, the CIAP deadline. The time-dependent two-dimensional parameterized model may be easier to develop, and should still provide useful information. We do not intend to calculate the day-to-day or month-to-month variations as is done with the global circulation model. Our objective is to estimate the change in typical stratospheric mean ozone density distributions attributable to the SST exhaust gases to within a certain error limit. The technique of our existing one-dimensional chemical model should be useful in developing the two-dimensional model with coupled chemistry and dynamics.

REFERENCES

1. Johnston, H., "Reduction of stratospheric ozone by nitrogen oxide catalysts from supersonic transport exhaust", Science *173*, 517, 1971.

2. *a.* Crutzen, P.J., "Ozone production rates in an oxygen-hydrogen-nitrogen oxide atmosphere", J. Geophys. Res. *76*, 7311, 1971.

   b. Crutzen, P.J., "The photochemistry of the stratosphere with special attention given to the effects of NO_x emitted by supersonic aircraft", *Proceedings of the DOT CIAP Survey Conference*, Cambridge, Mass., February 1972, DOT-TSC-OST-72-13, p. 80.

3. Nicolet, M., "Aeronomic chemistry of the stratosphere", *Proceedings of the DOT CIAP Survey Conference*, Cambridge, Mass., February 1972, DOT-TSC-OST-72-13, p. 44.

4. Dütsch, H.U., "Current problems of the photochemical theory of atmospheric ozone", in *Chemical Reactions in the Lower and Upper Atmosphere*, Interscience Publishers, New York, 1961, p. 167.

5. Prabhakara, C., "Effects of non-photochemical processes on the meridional distribution and total amount of ozone in the atmosphere", Mon. Wea. Rev. *91*, 411, 1963.

6. Hesstvedt, E., "The effect of water vapor and nitrogen oxides upon the ozone layer, studied in a photochemical model with meridional transport", presented at the Symposium on Atmospheric Ozone, Arosa, Switzerland, August 1972; to appear in PAGEOPH, 1973.

7. *Proceedings of Asilomar DOT-CIAP Workshop*, ed. R. Underwood, DOT Report TST-90-1, 1972.

8. *a.* Shimazaki, T., "Dynamical effects on atomic and molecular oxygen density distributions in the upper atmosphere: a numerical solution to equations of motion and continuity", J. Atmos. Terr. Phys. *29*, 723, 1967.

   b. Shimazaki, T., "On the boundary conditions in theoretical model calculations of distributions of minor neutral constituents in the upper atmosphere", Radio Science *7*, 695, 1972.

   c. Shimazaki, T., and A.R. Laird, "A model calculation of the diurnal variation of minor neutral constituents in the mesosphere and lower thermosphere", J. Geophys. Res. *75*, 3221, 1970. (See also *77*, 276, 1972).

   d. Shimazaki, T., and A.R. Laird, "Seasonal effects on distributions of minor neutral constituents in the mesosphere and lower thermosphere", Radio Science *7*, 23, 1972.

   e. Shimazaki, T., and D.J. Wuebbles, "On the theoretical model for vertical ozone density distributions in the mesosphere and upper stratosphere", presented at the Symposium on Atmospheric Ozone, Arosa, Switzerland, August, 1972; to appear in PAGEOPH, 1973.

9. Peaceman, D.W. and H.H. Rachford, "The numerical solution of parabolic and elliptic differential equations", J. Soc. Indust. Appl. Math. *3*, 28, 1955.

10. Douglas, J. and H.H. Rachford, "On the numerical solution of heat conduction problems in two and three space variables", Trans. Amer. Math. Soc. *82*, 421, 1956.

11. Murgatroyd, R.J., "Winds and temperatures between 20 and 100 km – a review", Quart. J. Roy. Met. Soc. *83*, 417, 1957.

12. Ackerman, M., "Ultraviolet solar radiation related to mesospheric processes", in *Mesospheric Models and Related Experiments*, ed. G. Fiocco, D. Reidel Publishing, Dordrecht, Holland, 1971, p. 149.

13. Johnston, H., "Gas phase reaction kinetics of neutral oxygen species", National Standard Reference Data Series, NBS-NSRDS-20, 1968.

14. NBS Report 10828, ed. R.F. Hampson, "Chemical kinetics data survey, II. Photochemical and rate data for fifteen gas phase reactions of interest for stratospheric chemistry", 1972.

15. Krueger, A.J., D.F. Heath, and C.L. Mateer, "Variations in the stratospheric ozone field inferred from Nimbus satellite observations", presented at the Symposium on Atmospheric Ozone, Arosa, Switzerland, August, 1972; to appear in PAGEOPH, 1973.

DISCUSSION

(UNIDENTIFIED): What estimate are you using for your eddy-diffusion coefficients?

WUEBBLES: Right now we are using the eddy-diffusion coefficients obtained by Reed and German (1965).

(UNIDENTIFIED): What uncertainties exist in your boundary conditions, and how do they propagate into the results?

WUEBBLES: At the top boundary we assume photochemical equilibrium, which is particularly good for ozone because of the short chemical time constants. At the lower boundary we assume constant flux between the lower boundary and the first row above it. I don't think that will propagate into the results for the steady-state solution except for the first few kilometers above the lower boundary.

ZIMMERMAN: It seems to me that the upper boundary condition might be a problem. In our calculations ozone becomes dominated by transport at night at altitudes over 70 km.

SHIMAZAKI: So far, we have worked out the steady-state calculation only for the daytime. I agree that O_3 is not in photochemical equilibrium at night; in our time-dependent model, we will use the flux condition as the boundary condition at night.

(UNIDENTIFIED): Could you tell me what you mean by cyclic boundary conditions? And what is your numerical method for solving the differencing equations?

WUEBBLES: Cyclic boundary conditions mean that every 360° around the globe we must give the same distribution for the constituents studied. The numerical method we are using is called the line-iterative implicit method.

(UNIDENTIFIED): How do you handle the non-linear terms? Do you describe the velocities?

WUEBBLES: We don't calculate the velocities. At the moment we are calculating just [O] and $[O_3]$ in the model; there is a non-linear term in the continuity equation describing $[O_3]$. At present we linearize the $[O_3]^2$ term by splitting it into an implicit term and an explicit one.

ZONAL ATMOSPHERIC MODEL ZAM2

MICHAEL C. MACCRACKEN
Lawrence Livermore Laboratory
University of California
Livermore, California

ABSTRACT: The zonal atmospheric model (ZAM2) is a two-dimensional general-circulation model with a 5°-latitude grid; it is presently being extended vertically into the stratosphere. Although longitudinal derivatives are set to zero and a mechanism simulates the meridional transport by horizontal waves and eddies, proportional surface coverage at each latitude allows for continental and oceanic contrast. The thermodynamics and hydrology of a moist atmosphere, including the effects of solar and long-wave radiation, cloudiness, condensation, evaporation, surface frictional drag and subgrid-scale convection, are simulated. Surface temperature and water vapor are determined by a surface energy-balance calculation. The computational cycle involves a time step of 15 minutes; it can be iterated for several years of atmospheric time. Application to the Climatic Impact Assessment Program will involve sensitivity and perturbation studies, introduction of interactive kinetics, and analysis of the potential effect of several pollutant species distributions.

INTRODUCTION

As part of the Climatic Impact Assessment Program (CIAP), we have been updating the zonal atmospheric model (ZAM) developed by MacCracken [1,2] to study the climatic impact of the pollutant-species distributions forecast for upper-atmospheric flight systems. This two-dimensional approach is intended to provide indications of potential climatic effects within the CIAP timetable, a schedule that will be difficult to meet with the present three-dimensional models at GFDL, NCAR, and UCLA [3]. This paper represents a progress report on our efforts.

The original ZAM model was derived from the three-dimensional general-circulation model developed by Leith [4]. Many of the atmospheric processes included in the present model are taken directly from Leith. The objective in going from three to two dimensions (latitude and the vertical) was to increase model running speed by focusing on the perturbations of the global energy balance (climate) rather than on the day-to-day weather. MacCracken [5] incorporated many surface interactions into the ZAM model and then applied it to the evaluation of several hypotheses concerning the causes of ice ages. Omission of longitudinal derivatives requires that a mechanism be established to simulate nonzonal wave and eddy motion. This is still the subject of considerable discussion and investigation.

In applying the model to the CIAP, significant improvements and refinements have been undertaken, both to increase the sensitivity of the model to the more subtle perturbations caused by aircraft and to extend the model to handle the new mechanisms through which effluent could interact with the climate. This paper describes the structure and basis for the updated zonal model (ZAM2) and the plans for its application.

MODEL STRUCTURE

The model uses the fluid dynamic and thermodynamic conservation equations to treat the evolution of a moist atmosphere for an average meridional section of the earth (Figure 1), taking into account such external influences as long- and short-wave radiation, evaporation, condensation, and surface friction. Plans are under way to treat both conservative and reactive pollutants and their interaction with the atmospheric radiation balance.

The earth is assumed to be spherical, with a radius of 6366 km. The meridional grid extends from pole to pole and uses a 5°-latitude staggered grid. Vertically, a mass-coordinate system is used and the atmosphere is divided into pressure levels. Originally, ZAM had six layers with even

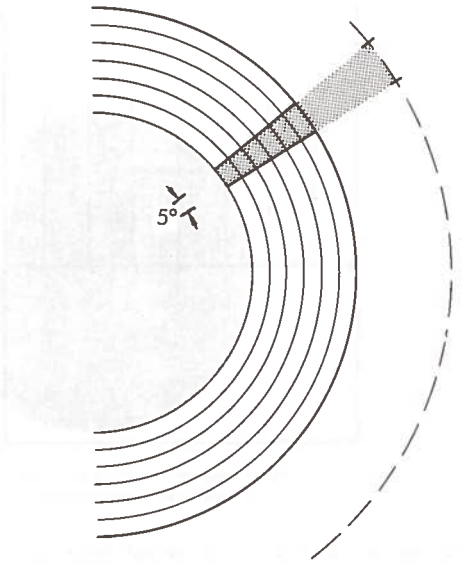

Figure 1. Latitudinal (5°) and vertical (pressure coordinates) grid used in the zonal atmospheric model.

mesh points at 100, 200, 400, 600, 850, and 1000 mbar and odd mesh points midway between the even levels. A seventh layer extending from 1000 mbar to the surface is assumed to be a constant-flux layer for energy, water, and angular momentum. ZAM2 is now being extended to include stratospheric levels at 10, 20, and 50 mbar. The prognostic variables that determine the dynamic state of the atmosphere are the temperature T and water-vapor mixing ratio μ. These are centered at even vertical and horizontal mesh points. The zonal and meridional winds, u and v, are centered at odd vertical and horizontal mesh points. In addition, with a pressure coordinate system, the surface pressure p_s is computed in order to completely define the system.

Because the surface energy balance is very important in determining the climate, the surface at each latitude is divided proportionally into land (several different types are permitted) or ocean, either of which can be or become covered or uncovered by ice or snow or both. This division by surface type is done in a "pointillist" fashion – that is, neither a longitudinal grid nor a continental structure is established. Vertical fluxes (e.g., radiation, precipitation) are calculated on the basis of individual surface type. The prognostic variables in the lowest atmospheric layer above each surface are identified by surface type. In calculating meridional fluxes, and above the lowest layer, the effects of surface type are averaged at each latitude.

In the case of land, a fraction at each latitude can be treated as elevated to simulate the effect of mountain ranges protruding to any designated even pressure level. These "mountains" not only maintain their own energy and water balance, but block meridional winds in proportion to their fractional coverage. At each latitude belt, the ocean is assumed to be a well-mixed layer of water (i.e., surface fluxes interact with the total depth of the layer), with a thickness approximately equal to the depth of the thermocline (i.e., the level below which seasonal temperature variations are negligible). At present, this depth is taken to be from 25 to 50 m, as suggested by Shaw and Donn [6].

In treating the surface energy balance for land, ice- and snow-covered land, or ice-covered ocean, a vertical layering totaling not more than ten layers, which increase in thickness with depth, is imposed. Atmospheric fluxes interact only with the top layer; the thermodynamics between the layers is determined by the heat equation, which is set up to conserve energy even in cases where there are combinations of layers each having different heat capacities, conductivities, and thicknesses. For land, the bottom layer is assumed to be insulated from any geothermal heat flux from below; for ice-covered ocean, the ocean below the ice is coupled to the bottom layer of ice.

Figure 2 portrays this treatment of the surface types at one latitude, showing open ocean, sea ice, land, and mountain. The prescriptions for the melting and spreading of sea ice and the buildup and melting of snow and ice on land are discussed later.

GOVERNING PHYSICAL EQUATIONS

The ZAM2 model is a general-circulation model that uses the laws of conservation of mass, angular momentum, total potential energy (internal plus potential), and water vapor to advance an initial field of prognostic variables.

Conservation of Mass

In a pressure coordinate system, conservation of mass is assured if the divergence of the wind field is zero, that is,

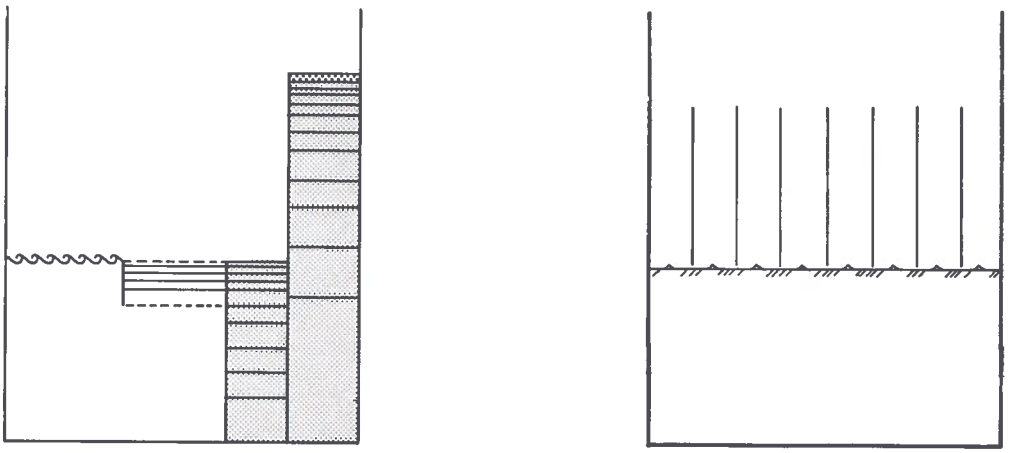

(a) Surface type division at latitude ℓ viewed from latitude ℓ

(b) Surface type division at latitude ℓ viewed from other latitudes

Figure 2. Conceptual view of fractional surface coverage in calculating: (a) vertical fluxes at latitude ℓ; (b) meridional fluxes that affect latitude ℓ.

$$\left[\frac{1}{a\cos\theta}\frac{\partial u}{\partial \lambda}\right] + \frac{1}{a\cos\theta}\frac{\partial (v\cos\theta)}{\partial \theta} + \frac{\partial \omega}{\partial p} = 0, \quad (1)$$

where the vertical velocity ω is defined as the total time derivative of pressure (positive downward). (Symbols are defined in Appendix A.) In ZAM2, the term in brackets allowing longitudinal divergence is set to zero. Given the boundary condition $\omega = 0$ at the top of the atmosphere ($p = 0$), the vertical velocity at any pressure level can be found by integrating down through the atmosphere. At the surface this yields a tendency equation for surface pressure such that

$$\frac{dp_s}{dt} = \omega_s, \quad (2)$$

where d/dt is the total derivative.

Hydrostatic Equilibrium

The model assumes hydrostatic equilibrium based on a scale analysis of the conservation equation for vertical momentum. This means that the pressure at a given point is determined by the weight per unit area of the air above that point. The differential expression representing this assumption is the hydrostatic relation

$$dp = -\rho g dz, \quad (3)$$

where ρ is the air density and g (assumed constant) is the gravitational acceleration. This expression is used in replacing the altitude z by the pressure as the vertical coordinate. In making this replacement, p must also be replaced by z, or more usually by the geopotential $\phi = gz$. The geopotential at any pressure level can be determined by integrating Eq. (3) upward from the surface, using virtual temperature to correct for the effects of moisture.

Conservation of Angular Momentum

On the surface of a sphere, the tendency equations for the horizontal velocities are based on conservation of angular momentum, yielding a transformed version of the Navier-Stokes equation. Formulated in flux divergence form [7] with an eddy-diffusion term to simulate subgrid-scale diffusion (and dissipation of kinetic energy), the conservation equations can be written

$$\frac{\partial u}{\partial t} - \left\{\frac{1}{a\cos\theta}\left(\left[\frac{\partial F_Z(u)}{\partial \lambda}\right] + \frac{\partial F_M(u)}{\partial \theta}\right) + \frac{\partial F_V(u)}{\partial p}\right\} - \left(2\Omega\sin\theta + \frac{u\tan\theta}{a}\right) v = \left[-\frac{1}{a\cos\theta}\frac{\partial \phi}{\partial \lambda}\right] + \frac{F_\lambda}{a\cos\theta} - \left\{\frac{1}{a\cos^2\theta}\left(\frac{\partial F_M^d(u)}{\partial \theta} + \left[\frac{\partial F_Z^d(u,-v)}{\partial \lambda}\right]\right) + \frac{\partial F_V^d(u)}{\partial p}\right\} \quad (4)$$

and

$$\frac{\partial v}{\partial t} - \left\{\frac{1}{a\cos\theta}\left(\left[\frac{\partial F_Z(v)}{\partial \lambda}\right] + \frac{\partial F_M(v)}{\partial \theta}\right) + \frac{\partial F_V(v)}{\partial p}\right\}$$
$$+ \left(2\Omega\sin\theta + \frac{u\tan\theta}{a}\right) u = -\frac{1}{a}\frac{\partial \phi}{\partial \theta} + \frac{F_\theta}{a}$$
$$- \left\{\frac{1}{a\cos^2\theta}\left(\frac{\partial F_M^d(v)}{\partial \theta} + \left[\frac{\partial F_Z^d(v,u)}{\partial \lambda}\right]\right)\right. \quad (5)$$
$$\left. + \frac{\partial F_V^d(v)}{\partial p}\right\},$$

where the advective and diffusive fluxes in the zonal, meridional, and vertical directions, respectively, are

$$F_Z(x) = -ux$$
$$F_Z^d(x,y) = -\frac{K_H}{a}\left(\left[\frac{\partial x}{\partial \lambda}\right] + 2y\sin\theta\right)$$
$$F_M(x) = -vx\cos\theta$$
$$F_M^d(x) = -\frac{K_H}{a}\cos^3\theta\,\frac{\partial}{\partial \theta}\left(\frac{x}{\cos\theta}\right) \quad (6)$$
$$F_V(x) = -\omega x$$
$$F_V^d(x) = -K_V\frac{\partial x}{\partial p}.$$

In these expressions, F_λ and F_θ are surface friction terms, Ω is the angular velocity of the earth's rotation, and K_H and K_V are the horizontal and vertical eddy-diffusion coefficients, respectively.

In making the two-dimensional approximation, the terms in brackets become zero. However, the effect of these terms on u and v cannot be neglected because they are essential in describing the energy and momentum transport of such atmospheric phenomena as Rossby waves. The most important assumption made in constructing a zonal model is in approximating these terms by an additional term or terms on the right-hand side of Eqs. (4) and (5).

Ideally, the formulation of the turbulent-eddy transport should be based on variables internal to the model. In the original version of ZAM, this was only partially achieved by increasing the horizontal eddy-diffusion coefficient for momentum, temperature, and water vapor by a factor of 2. This use of an Austausch diffusion coefficient is discussed by Clapp [8], including cases in which it is a function of latitude and season. Often it is meant to include the effects of mean transport as well. It was our feeling that externally varying the diffusion coefficient in time would prejudice any results in studying ice-age hypotheses since, with drastically different surface conditions, one could not predetermine the appropriate diffusion coefficient. In ZAM, this approach worked reasonably well in mid-latitudes. In tropical latitudes, however, it was evident that the diffusion away from the equator was too large, leading to too weak a Hadley cell and too-low temperatures.

For ZAM2, this problem is again being studied. At least three approaches might be improvements on the use of a constant diffusion coefficient. The first is to vary the diffusion coefficient with latitude and season, determining the values so that the model matches the atmosphere [9,10,11]. This can be done for the CIAP if one assumes that the maximum climatic effect will be a small perturbation on the circulation patterns of the atmosphere. The perturbation would then evidence itself as a difference in the mean circulation between the perturbed and control runs (e.g., in the u, v fields calculated using Eqs. (4) and (5)). This ability of a perturbation to feed back into the basic transport calculations of the model is an important advantage of a general-circulation model, even a two-dimensional one, over completely parameterized transport models often used in the study of the kinetics.

The second approach is to externally impose on the model the observed eddy transport, or perhaps even some results computed from three-dimensional general-circulation models. This approach requires the same assumption as above and would evidence itself the same way. It is related to it in that observations are generally those used in determining the diffusion coefficient.

The third, and more basic, approach is to introduce transport based on internal model parameters, such as the meridional temperature gradient. The theoretical formulation of such a term poses significant difficulties, although work by Saltzman [12] and others certainly offers a start on the problem. The added advantages to

this approach, however, are well worth the effort, since the perturbation assumption no longer need be made and an additional feedback mechanism is introduced to permit model response. We expect to report further on this effort in the near future.

Because the eddy-diffusion terms for angular momentum are not formulated to conserve kinetic energy, no tendency equation can be written for this quantity. A balance does develop, however, during the running of the model, thus permitting extended computational runs.

Conservation of Total Potential Energy

Atmospheric temperature in the model is determined by the thermal tendency equation

$$\frac{\partial T}{\partial t}-\left\{\frac{1}{a\cos\theta}\left(\left[\frac{\partial F_Z(T)}{\partial\lambda}\right]+\frac{\partial F_M(T)}{\partial\theta}\right)+\frac{\partial F_V(T)}{\partial p}\right\}=\frac{\kappa\omega T}{p}+\frac{\dot{q}}{c_p}, \tag{7}$$

where $\dot{q}$ is the nonadiabatic heating rate due to long-wave and solar radiation, eddy transport, latent heat release during condensation, and boundary interactions. Again, the bracketed term is assumed to be zero by ZAM2. The first term on the right-hand side of Eq. (7) is the buoyancy term (we assume that the atmosphere is an ideal gas). The term results in heating when air is adiabatically compressed as it descends. Thus, the term serves to convert total potential energy to kinetic energy and vice versa. The considerations mentioned in the eddy-diffusion discussion apply here. The parameterization of each of the other nonadiabatic terms is discussed in the next section.

Conservation of Water Vapor

Water vapor is treated only in its vapor form in the model atmosphere, with precipitation of any amount in excess of saturation. If we denote by $\dot{r}$ the rate of precipitation, evaporation, and eddy transport of water vapor, we can write the conservation equation for the water-vapor mixing ratio μ as

$$\frac{\partial\mu}{\partial t}-\left\{\frac{1}{a\cos\theta}\left(\left[\frac{\partial F_Z(\mu)}{\partial\lambda}\right]+\frac{\partial F_M(\mu)}{\partial\theta}\right)+\frac{\partial F_V(\mu)}{\partial p}\right\}=\dot{r}. \tag{8}$$

When pollutants are introduced into ZAM2, each species will be treated by an equation similar to Eq. (8) (except for those for which an instantaneous steady-state assumption is made). In the case of pollutants, $\dot{r}$ will contain a chemical species transformation term.

In the model, the conservation Eqs. (1), (4), (5), (7), and (8) are finite-differenced explicitly. Beginning with initial values at each grid point, the current values of the winds are used to calculate new values of T, p_s, and μ, which are then used to update the wind field. As this happens, of course, the sun rises and sets, snow forms, and so on. The finite-difference methods used have been discussed previously by Leith [4] and MacCracken [2]. Stability considerations require a 15-min time step. Rather than discuss the details again, the updated versions of the parameterizations of physical processes will be considered here.

MODELING OF PHYSICAL PROCESSES

All general-circulation models are based on the same basic conservation equations, although coordinate systems, grids, and methods of solution vary. They often differ significantly in how they represent various physical processes; for example, whether they fix various quantities or allow them to interact dynamically with the model dynamics. The philosophy followed in developing ZAM2 has been to provide for as much dynamic interaction as possible. Even in cases where the data and physical understanding to formulate a prescription are not completely clear, permitting feedback through the physical process offers another way of seeing in what direction and magnitude the atmosphere will respond to a perturbation of the control situation. However, care must be taken in interpreting the results. This usually involves ensuring that the chain of responding mechanisms is intuitively understood and believable. Because of ZAM2's shorter computer running time, the chain is often

most easily traced through the use of additional model runs, an option not as readily available with three-dimensional models.

This section discusses many of the mechanisms used in the model to simulate atmospheric processes. Numbers and coefficients are included, but considerable effort is now being spent in refining and documenting them, so the values presented here are subject to change.

Cloud Cover

Although the model forecasts water-vapor mixing ratio, for radiation and precipitation prescriptions the cloud cover must be determined diagnostically from the prognostic variables. Because of the complex nature of clouds in the atmosphere, empirical formulae rather than theoretical formulations are generally used. From one-dimensional model studies at tropical latitudes, Leith [13] developed a cloud-fraction (α) prescription such that at each layer

$$\alpha = 0.7r^2, \tag{9a}$$

where r is the local relative humidity. Clouds are assumed to be vertically correlated; however, this assumption is being reviewed. Recent comparisons with observations at LLL indicate that this prescription may be adequate in the tropics, but it underestimates total cloud cover at higher latitudes. Although we are still developing the prescription, it is expected to be of the form

$$\alpha = \text{Minimum } [\alpha_{max}, \alpha_1(r-\alpha_2)^2 + \alpha_3], \tag{9b}$$

with the coefficients α_{max}, α_1, α_2, α_3 being a function of latitude.

We have not yet introduced a dependence on vertical velocity, as has been done in the NCAR model [14]. Because a zonal model cannot develop the intense convective systems occurring in three-dimensional models, we expect that if such a dependence were introduced into ZAM2 it would be quite different in format from the NCAR approach.

Vertical Convection

As discussed by Leith [13], vertical transport of heat, momentum, and water vapor takes place mainly by means of convective processes on a scale too small to be explicitly calculated in general-circulation models. If we do not take these processes into account, we compute, for example, precipitation occurring only when the atmosphere becomes supersaturated at a given latitude and pressure level.* Since precipitation is the only sink of water vapor, the model will tend to run at near-saturation conditions, even if the actual intensity of the atmospheric water cycle is correct. In the real atmosphere, small-scale convection often leads to precipitation when the average relative humidity in a zone is only 50%.

The ZAM model incorporates Leith's convection prescription, which is coupled to the extent of cloud cover. A differential velocity between the slightly warmer, saturated cloud fraction α and the cooler, drier clear air is specified as a function of a convective-intensity function C. This quantity is taken to be a function of the stability (i.e., the lapse rate) between the two layers. The choice of C promotes strong ascending of the clouds for unstable air; the inclusion of a relatively small vertical-diffusion term promotes slight descending for stable air. As the saturated air of the clouds rises adiabatically, it expands and cools, releasing convective precipitation. The heat release associated with this is treated as a source in the energy equation. The convective-intensity function is also used to calculate an upward heat flux resulting from small-scale convective motion, a process that is used in addition to very limited vertical energy diffusion.

Figure 3 illustrates this process and specifies the significance of the constants. In this figure,

$$C = \begin{cases} 1 - \dfrac{C_k(\partial\Theta_S/\partial p)}{X_0^2} & \text{for } \dfrac{\partial\Theta_S}{\partial p} \geqslant C_k \\ \dfrac{C_k}{\partial\Theta_S/\partial p} - \dfrac{C_k(\partial\Theta_S/\partial p)}{X_0^2} & \text{for } \dfrac{\partial\Theta_S}{\partial p} < C_k \end{cases} \tag{10}$$

where the saturated equivalent potential temperature is given by

$$\Theta_S = \left(T + \frac{L}{c_p}\mu_S\right)p^{-\kappa}.$$

* This is also true in three-dimensional models.

Our model sets C_k equal to -15 and assumes that X_0 is a function of pressure.

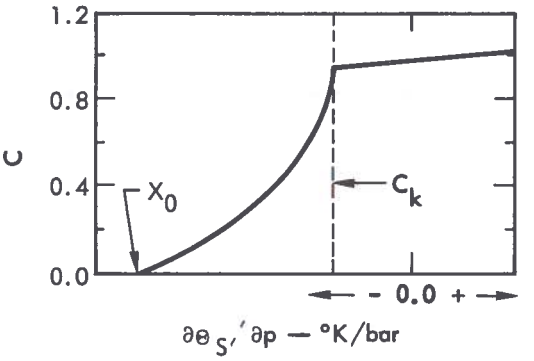

Figure 3. Plot of the convective-intensity function (after Leith [13], with adjustments).

Vertical diffusion of angular momentum is made proportional to the convective intensity by setting K_V in Eq. (6) equal to $2.4 \times 10^5 C$ cm^2/sec. With more vertical levels being introduced to represent the stratosphere, these values will certainly change.

Evaporation of the precipitation from higher layers is also allowed and is assumed to be proportional to 0.25 (1 − r). This process is really a vertical energy-transport mechanism, and hence has a stabilizing effect on atmospheric convection.

Solar Radiation

Solar radiation, which is assumed to result from a solar constant of 2.0 cal cm^{-2} min^{-1}, is absorbed in the present model by water vapor and clouds. In extending the number of layers vertically into the stratosphere, we include absorption by ozone, using as our first approximation the mechanism developed by Hering et al. [15] and modified by Luther [16]. The clouds are assumed to scatter both forward and backward as well as to absorb; the parameters are primarily a function of pressure. A conceptual diagram of the solar radiation prescription is shown in Figure 4. The scattered radiation is assumed to be diffuse and is not correlated with cloud position. Its actual path length through the water vapor is assumed to be 1.66 times the vertical-path length. A pressure-broadening term is also included. Table 1 details some of the cloud parameters; Appendix B gives the actual solar-radiation equations.

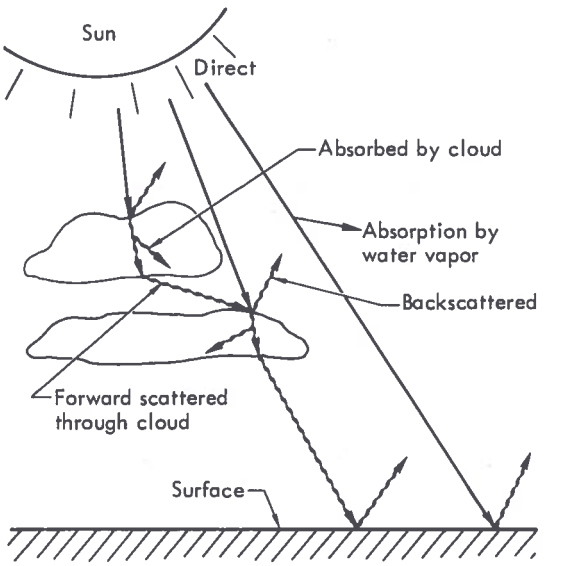

Figure 4. Schematic view of treatment of solar radiation interacting with cloud cover. Straight lines indicate path of unscattered beam; wavy lines indicate paths of scattered radiation.

Table 1. Cloud Albedo and Absorptivity

Pressure level (bars)	Cloud albedo*	Cloud absorptivity*
0.100	0.21	0.01
0.200	0.21	0.01
0.400	0.48	0.04
0.600	0.48	0.04
0.850	0.69	0.06
1.000	0.69	0.06

* Based on values taken from Houghton [17].

The direct solar-radiation calculation is made first; then an iterative process is performed to determine the upward and downward diffusive fluxes as a function of pressure. This must be done because the equations are coupled; the known boundary conditions are that the downward diffuse radiation is zero at the top of the atmosphere, and that the albedo relates the downward diffuse radiation plus the solar radiation to the upward diffuse radiation at the surface. This calculation is performed for each surface type and its appropriate albedo. For the atmospheric layers more than one layer above the surface, the absorption is averaged proportionally to the fractional surface coverage.

With the introduction of photochemically reactive pollutants, we expect to represent, at least crudely, their spectral dependence.

Long-Wave Radiation

Long-wave radiation is calculated with a spectrally-averaged transmission coefficient using a scheme developed by Leith and fully described by Coffin [18], included here as Appendix C. The calculation employs the same cloud prescription as that for solar radiation, assuming every cloud is both a blackbody absorber and radiator. The model divides the atmosphere into up to twenty slabs of equal transmissivity, the flux being calculated for each slab. The divergence of the radiative fluxes yields the net temperature change. Typical values are 1 to 3°C per day in the free atmosphere and up to 10°C in the near surface layers.

The only atmospheric absorber presently included, besides water, is carbon dioxide, which, in the lower layers, is assumed to absorb 18% of the radiative flux in the slab where the emission occurs. In the stratosphere, carbon-dioxide emission is based on an empirical scheme developed by Leovy [19], recalibrated on data from Newell [20]. With the extension of the model into the stratosphere, we plan to improve the treatment of long-wave radiation in the upper atmosphere.

Again, as for the solar radiation, the calculation is made for each surface type on the basis of its temperature; then, for all but the bottom layer of the atmosphere, the temperature change is averaged. The importance of doing this is most evident in polar regions, where the open water and sea ice often differ in temperature by 20°C.

Surface-Atmosphere Interactions

Fluxes of angular momentum, energy, and water vapor occur across the air-surface interface. In ZAM2 each surface type is treated independently. To calculate the surface drag, a surface velocity (V_s) is defined as the square root of the sum of the squares of its components (u_s and v_s). The angular-momentum flux from the surface into the atmosphere is then

$$F_{\lambda s} = \rho c_D |V_s| (-u_s)\, a \cos\theta \qquad (11a)$$

due to the zonal wind, and

$$F_{\theta s} = \rho c_D |V_s| (-v_s) a \qquad (11b)$$

due to the meridional wind, where c_D is a dimensionless drag coefficient. However, the vertical angular-momentum fluxes due to vertical eddy transport calculated in Eqs. (4) and (5) give

$$F_{\lambda d} = K_V \frac{\partial (ua \cos\theta)}{\partial p} = K_V \frac{u_s - u_{s-1/2}}{p_s - p_{s-1/2}}\, a \cos\theta \qquad (12a)$$

and

$$F_{\theta d} = K_V \frac{\partial (va)}{\partial p} = K_V \frac{v_s - v_{s-1/2}}{p_s - p_{s-1/2}}\, a, \qquad (12b)$$

where the subscript s-1/2 indicates the odd-mesh pressure level just above the surface, thus bounding the pressure layer across which the flux flows. It should be noted that the vertical fluxes of angular and linear momentum differ only by a constant at a given latitude. The required non-divergence of the flux in the thin bottom layer allows $F_{\lambda s}$ and $F_{\lambda d}$, as well as $F_{\theta s}$ and $F_{\theta d}$, tc be equated, which permits the surface velocitie: and fluxes to be determined.

Surface fluxes of sensible heat (F_T) and water vapor (E) (i.e., convection and evaporation) are derived from relations similar to Eqs. (11a) and (11b). Thus,

$$F_T = \rho c_T |V_s| (T_s - T_{s-1/2}) \qquad (13)$$

and

$$E = \rho c_\mu |V_s| (\mu_s - \mu_{s-1/2}), \qquad (14)$$

where here the s-1/2 pressure level is the even level just above the surface.

The values for c_T, c_μ, and c_D, which are determined empirically from model-behavior studies, are given in Table 2. At present these coefficients are not a function of surface type; however, this is being reviewed, in view of the results of Delsol et al. [21]. Changes in the surface temperature and the water-vapor content affect the fluxes into the atmosphere, thus permitting the surface to interact with the atmosphere.

Although mountains are treated as protruding into the atmosphere and as blocking meridional and zonal winds, the fluxes of angular momentum, energy, and water vapor associated with the sides of mountains are currently assumed to be zero.

Table 2. Surface Characteristics

Surface	Albedo	Density (g/cm^3)	Heat capacity (cal/g°k)	Thermal conductivity (cal/cm hr°K)	Atmosphere — interaction coefficient: Surface drag, c_D	Thermal, c_T	Evaporation, c_μ	Runoff coeff. (fract. loss per day)
Ocean	Minimum $\left[0.40, 0.07 + \frac{0.01}{(\cos\Phi + 0.03)}\right]$	1.025	1.000	—	4.7×10^{-3}	4.0×10^{-4}	8.0×10^{-4}	—
Snow	0.70 for fresh snow 0.55 for melting snow	0.400	0.210	3.672	4.7×10^{-3}	4.0×10^{-4}	8.0×10^{-4}	0.50
Ice	0.70 for fresh ice 0.55 for melting ice	0.917	0.480	19.25	4.7×10^{-3}	4.0×10^{-4}	8.0×10^{-4}	0.25
Tundra	0.15 if r < 0.35 0.30 if r > 0.70	1.600	0.200	21.0	4.7×10^{-3}	4.0×10^{-4}	8.0×10^{-4}	0.25
Savanna	0.10 if r < 0.35 0.25 if r > 0.70	1.600	0.200	21.0	4.7×10^{-3}	4.0×10^{-4}	8.0×10^{-4}	0.25

Surface Characterization

As indicated earlier, at each latitude the surface can be divided proportionally among surface types having different thermal, radiative, and hydrologic properties and can be treated as being at sea level or one of several possible higher altitudes. Although the particular choices described here are being reviewed and updated, they indicate the variability that is possible.

The first surface type represents open ocean, which is a well-mixed layer of water, the depth of which can vary with latitude. We are now using a constant depth of 50 m. Rainfall and evaporation from the ocean are assumed not to change the depth. All atmospheric fluxes interact with the ocean as a whole; thermal and radiative properties are shown in Table 2. Because ocean currents provide an important mechanism for meridional energy transport, externally chosen fluxes are imposed (Table 3) independent of any temperature gradient or sea-ice coverage.

The second surface type is ice-covered ocean. (There may be snow on the ice.) The fractional coverage at each latitude varies in time as a function of the energy balance of both the ocean and the sea ice itself. Starting with open ocean, sea ice 20 cm thick is formed if the ocean temperature decreases below the freezing point (271.4°K); the extent of ice formed is sufficient to provide energy by heat-of-fusion to return the ocean temperature to 271.4. Once sea ice is present it spreads or contracts horizontally (i.e., the fractional coverage changes), depending on whether the open ocean is continuing to cool or warm. However, the open ocean is not allowed to contract beyond a specified minimum fraction of open leads, which can be a function of latitude.

Table 3. Ocean-Current Heat Fluxes

Latitude	Northward flux (10^{19} cal/day): Model*	Sverdrup [22]: Atlantic	Sverdrup [22]: Pacific	Emig [23]
90°S	0.0	–	–	–
80°S	0.0	–	–	–
70°S	-0.01	–	–	0.0
60°S	-0.55	–	–	-0.8
50°S	-1.25	–	–	-1.7
40°S	-2.20	–	–	-3.5
30°S	-2.10	–	–	-5.2
20°S	-1.40	–	–	-5.7
10°S	-0.25	–	–	-5.1
0	0.85	0.58	0.0	-2.8
10°N	2.30	1.2	1.0	0.1
20°N	2.80	1.6	0.86	1.9
30°N	2.70	1.9	0.58	2.1
40°N	1.90	1.2	0.0	1.6
50°N	0.95	0.86	0.0	1.1
60°N	0.51	0.43	0.0	0.6
70°N	0.35	–	–	0.3
80°N	0.09	–	–	0.0
90°N	0.0	–	–	–

* These values are actually given at odd latitudes. To simulate the climate in the Atlantic, the ocean-flux values in the northern hemisphere have been increased slightly to represent the strong currents. The effect is small in comparison to the atmospheric fluxes. Emig's values for the southern hemisphere have been reduced to smooth the transition between the two hemispheres.

Physically, the open-lead fraction is a function of surface wind stress, ocean currents, and so on, but this dependence is not internally functionalized in the model. Any energy deficit of the leads at the minimum allowable fractional coverage is made up by increased thickness of the adjacent sea ice.

The sea ice also changes thickness on the basis of its own energy balance. The depth of ice and the snow on top of it is divided into a total of ten layers, the upper layers being thinner than the lower layers to more closely match their thermal inertia with the diurnal variations of the atmosphere. The bottom layer of ice is thermally coupled to the ocean below, which is held at 271.4°K by adjusting the ice thickness. The heat equation is solved for the layered structure; each layer may have its own thermal and conductive properties. (See Table 2 for snow and ice.) The atmospheric fluxes, however, act only on the top layer. Precipitation onto the sea ice is assumed to be snow if the ice temperature is below freezing and rain if the ice is melting. Rain is assumed to melt its equivalent mass of snow. A surface-layer water balance is maintained; the depth is determined by the rain, melting snow and ice, evaporation, run-off, and refreezing to ice. If this water balance is positive – that is, melted water is present on top of the snow or ice – the albedo of the surface is reduced.

As the ice and snow melt, a minimum thickness of 20 cm is maintained by reducing the fractional sea-ice coverage appropriately. Thus, the sea ice can grow and retreat as a dynamic function of the model's energy balance.

The third surface type is land; there are at present two types of land (tundra and savanna) that can be treated separately at each latitude. Further choices and refinements are being considered. As for the sea ice, the land (and any overlying snow and ice) are divided into layers and the heat equation is solved. Precipitation can take the form of rain or snow, depending on surface temperature. Evaporation is limited by the balance of surface water, the relative humidity for the surface being reduced if evaporation and runoff exceed precipitation and melting. This variation in r changes the albedo, as shown in Table 2; a linear interpolation is used between the wet and dry conditions. Finally, a fraction of the land area at each latitude can be taken as elevated to represent mountain ranges. This is clearly important in the Antarctic regions, but the effect at other latitudes should also be considered. By doing this, we can expect to get snow buildup, which otherwise would not be possible, on mountains at mid-latitudes. The mountain elevations that may be selected are given in Table 4.

Table 4. Mountain Heights

Mountain height (km)	Approx. surface pressure (bar)
1.417	0.870
3.655	0.620
7.011	0.420

The particular choices of surface characteristics are given when model results are discussed.

PRESENT MODEL RESULTS

Because the updated ZAM2 is undergoing final checkouts, the results described here are based on earlier model runs, which did not allow proportional surface coverage or extend into the stratosphere. The presentation is intended only to indicate the general features of the results, not to serve as a detailed validation study; thus, only qualitative comparisons with the observed climate are included. In updating the model, we also plan to use altitude as the vertical axis for displaying output. This will permit easier comparison with observed results.

Table 5 shows the particular choice of surface types used in the run; the choices of snow and ice coverage are typical of the summer solstice, when the calculation was begun. Only six vertical pressure levels are included, and this is insufficient to represent the stratosphere. Thus, the upper atmosphere results should not be expected to be particularly good.

The results discussed are after the atmosphere-surface system has come to near steady state, as evidenced by the temperature variation for corresponding seasonal averages differing by only about 1°K. In the Arctic there are larger changes because the all-or-nothing ice-cover prescription leads to larger variations due to slight changes in the date of refreezing of the sea ice.

Table 5. Initial Surface Conditions for Simulation of the Present Time

Latitude	Surface type	Mountain height	Ocean thermocline depth (cm)	Ice thickness (cm)	Snow cover (cm)
90°S	Land	Medium		300,000	1,000
85°S	Land	Medium		300,000	986
80°S	Land	Medium		300,000	974
75°S	Land	Medium		300,000	949
70°S	Land	Low		300,000	244
65°S	Ocean		20,000	0	0
60°S	Ocean		20,000	0	0
55°S	Ocean		15,000	0	0
50°S	Ocean		12,000	0	0
45°S	Ocean		10,000	0	0
40°S	Ocean		10,000	0	0
35°S	Ocean		10,000	0	0
30°S	Land	Sea level		0	0
25°S	Ocean		10,000	0	0
20°S	Ocean		10,000	0	0
15°S	Ocean		10,000	0	0
10°S	Ocean		10,000	0	0
05°S	Land	Sea level		0	0
00°Q	Ocean		10,000	0	0
05°N	Ocean		10,000	0	0
10°N	Ocean		10,000	0	0
15°N	Ocean		10,000	0	0
20°N	Land	Sea level		0	0
25°N	Ocean		12,000	0	0
30°N	Ocean		12,000	0	0
35°N	Ocean		15,000	0	0
40°N	Land	Sea level		0	0
45°N	Land	Sea level		0	0
50°N	Ocean		15,000	0	0
55°N	Land	Sea level		0	0
60°N	Land	Sea level		0	0
65°N	Land	Sea level		0	0
70°N	Ocean		20,000	0	0
75°N	Ocean[a]		20,000	124[a]	0
80°N	Ocean[a]		20,000	268[a]	0
85°N	Ocean[a]		20,000	467[a]	14
90°N	Ocean[a]		20,000	473[a]	101

[a]When sea ice is present, open leads are assumed to be 4%.

Temperature

A meridional cross-section of the annual mean temperature computed by the model is shown in Figure 5. The surface temperature distribution is compared with observed data in Figure 6. The overall pattern in the lower atmosphere is in good agreement with observations [26], but the annual mean temperatures in the equatorial region are several degrees too low at all levels. Although it is not yet confirmed, we suspect that this is the result of using a diffusion coefficient that is representative of the mid-latitude transport (i.e., Rossby-wave transport) rather than of the much lower tropical-eddy transport. A similar effect also appears in the zonal and meridional wind fields. The upper-level temperatures at all latitudes lack the structure shown by observations. This is the result of using a simplified vertical mesh for the tropopause and stratosphere and an incomplete treatment of radiation transport in the stratosphere. By adding additional levels and ozone absorption, we expect to reduce these discrepancies.

Relative Humidity

The computed annual mean relative-humidity profile shown in Figure 7a is contrasted in Figure 7b with values observed by London [27]. The familiar subtropical minima occur in the upper troposphere, and the general pattern compares well with the relative humidity distribution used by Manabe and Wetherald [28] in their radiation studies. This correlation with observation is doubly important, since the cloud-cover distribution in the model is a function of relative humidity. The surface relative humidities appear high because they are set to 100% over oceans and sea ice, but this should improve when we use proportional surface types.

Zonal Wind

The annual mean of the computed zonal wind field (Figure 8a) in each hemisphere shows symmetric jets of greater than 70 km hr^{-1} at 30° N and 30° S. We hope that, with more levels in the model, the upper edge of the jets may be better defined. Although zonal wind was at a minimum at the equator, easterlies did not, in general, occur except in the subtropics very near the surface. The reasons for this disparity are not clear, but they may again relate to the value of the diffusion coefficient used to accomplish horizontal transport of sensible heat (i.e., to the inclusion of simulated cyclonic activity in equatorial latitudes where little or none exists) and to the lack of a longitudinal dimension. Observed values, as summarized by Manabe [29], indicate a jet centered at 35° latitude with a strength of about 90 km hr^{-1}, and easterlies extending to the top of the atmosphere, equatorward of about 15° latitude in each hemisphere.

The computed mean zonal winds for particular seasons contain much greater structure than the annual mean field (Figure 8b). The southern-hemisphere winter jet is very strong and centered more toward the equator than the annual mean jet. A meridional section of the zonal wind field shows that the jet lies at the southern edge of a strong Hadley cell. The upper-level easterlies north of the equator lie at the northern extent of this cell. Displacement of the cell so far from the equator is a result of the choice of the land band located at 20° N, a problem that should be alleviated by going to fractional coverage.

Meridional Circulation

The annual means of the meridional and vertical winds are given vectorially in Figure 9a. Symmetric Hadley cells with ascent centered near the equator are evident. In addition, there is a strong katabatic wind off the Antarctic ice sheet, a phenomenon noted by Byrd and Scott during their explorations. Neither a middle-latitude indirect (Ferrel) cell nor a polar direct cell appears, partly because of the effect of annual averaging. As is evident in Figure 9b, seasonal motions are considerably stronger and more varied. The land-sea contrast in the northern (summer) hemisphere causes strong convection. The southern-hemisphere Hadley cell and monsoon are clearly evident. Failure of the model to produce a Ferrel cell is not surprising, given the particular diffusion prescription being used to simulate the cyclonic disturbances. Improved representation of the horizontal-wave and eddy-transport mechanisms should yield better results.

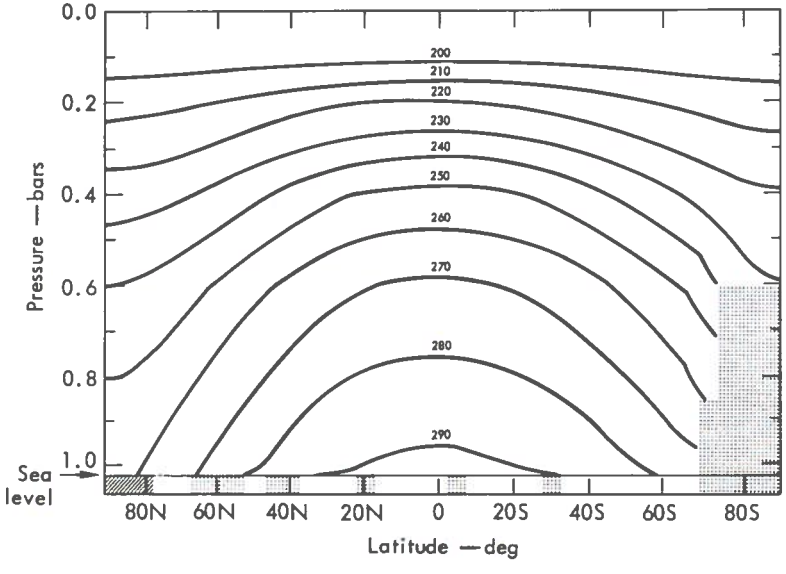

Figure 5. The latitude-height distribution of annual mean temperature (°K) computed by ZAM. Surface types indicated are sea ice (hatching), land and mountains (dots), and open ocean (blank).

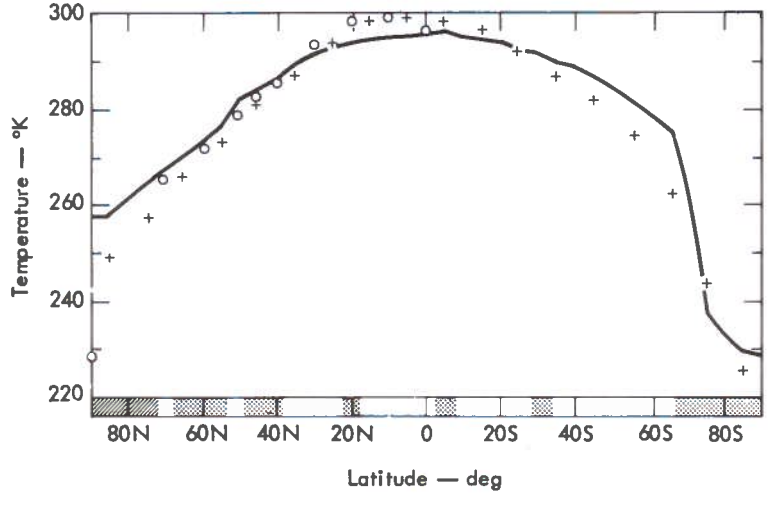

Figure 6. The latitudinal distribution of annual mean surface temperature. Solid line, computed by ZAM; cross-marks (+), observed by Sellers [24]; circles (○), observed at 1000 mb by Peixoto [25].

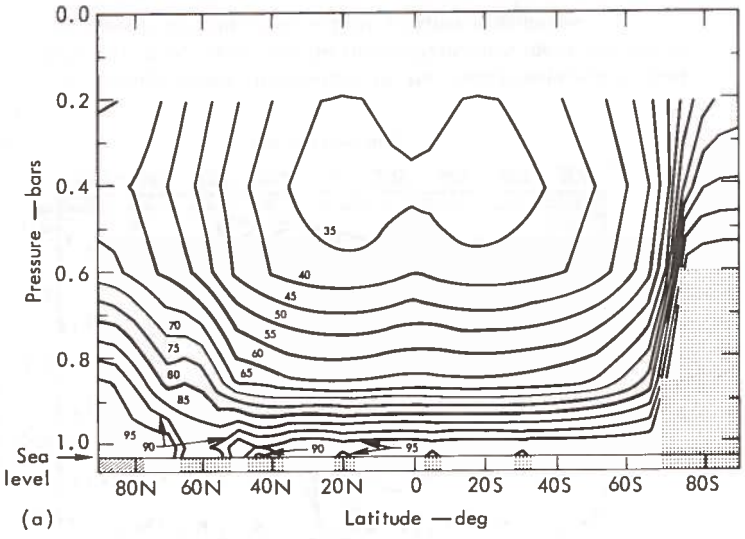

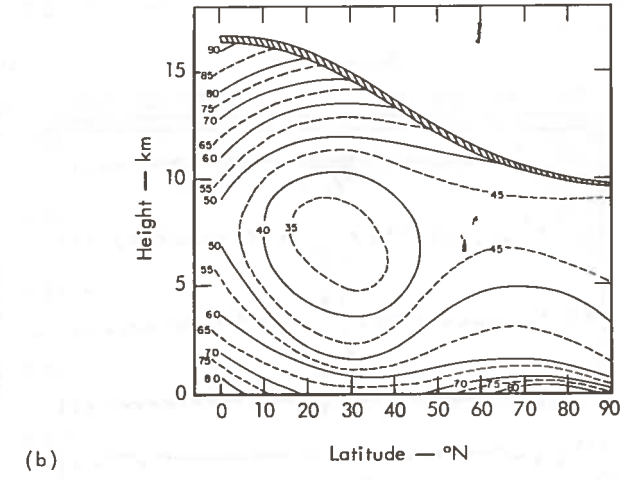

Figure 7. The latitude-height distribution of zonal relative humidity (percent): (a) annual mean computed by ZAM, and (b) spring average observed by London [27] for the northern hemisphere.

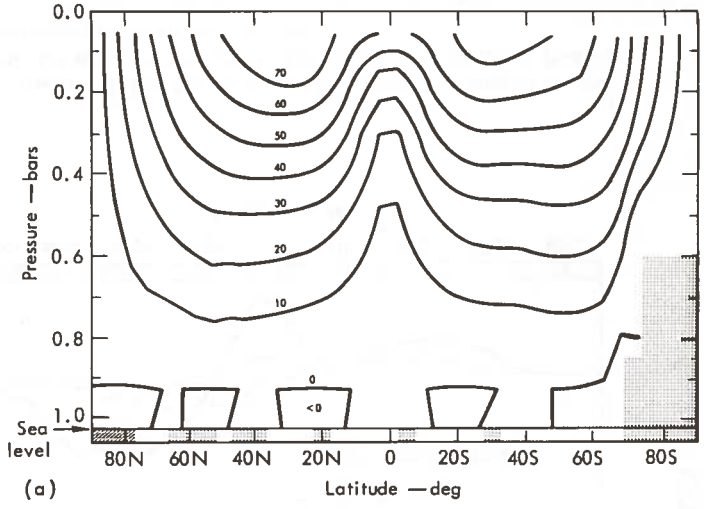

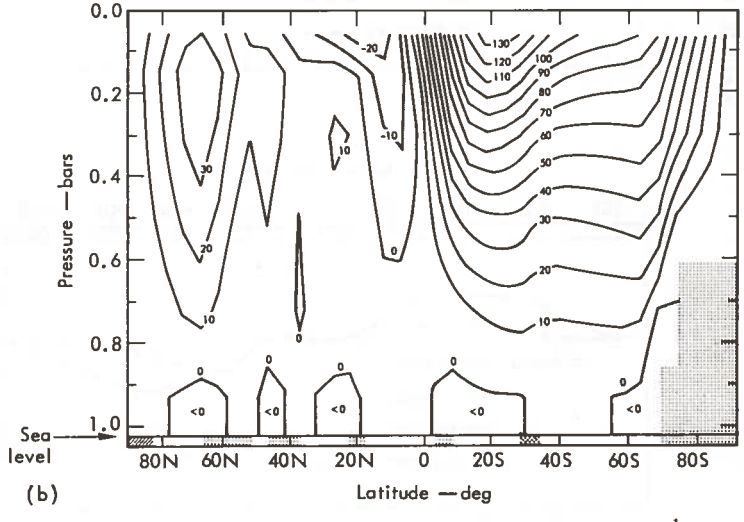

Figure 8. The latitude-height distribution of the zonal wind (km hr^{-1}): (a) annual mean, and (b) June-to-September mean. Positive numbers indicate westerly winds; negative numbers (shaded regions) indicate easterly winds.

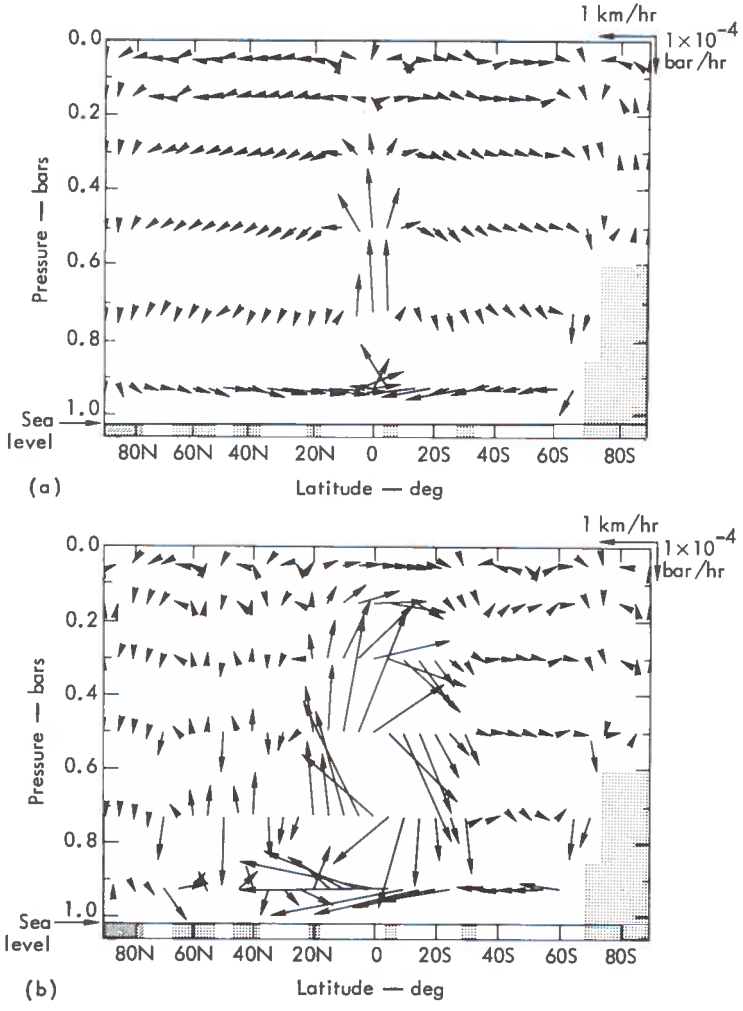

Figure 9. The latitude-height distribution of the meridional-vertical wind field: (a) annual mean, and (b) June-to-September mean. The key in the upper right-hand corner indicates relative magnitudes.

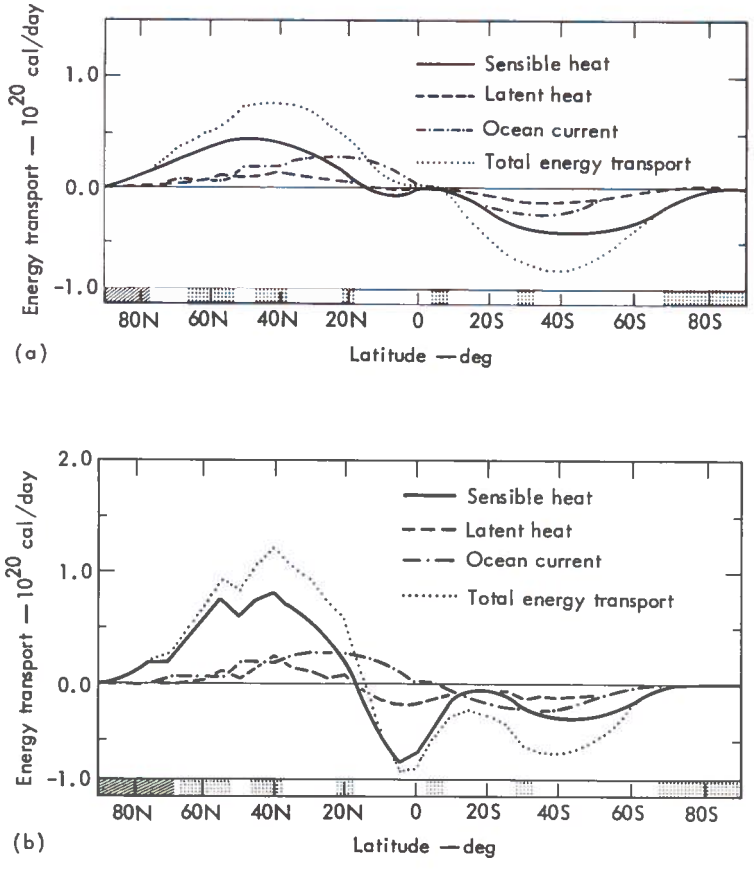

Figure 10. The latitudinal distribution of meridional energy transport components: (a) annual mean, and (b) December-to-March mean. Positive values indicate northward transport.

Meridional Energy Transport

Annual mean computed energy transports are given in Figure 10a. As one might expect, the transport is toward the pole in each hemisphere. No distinction is made between transport by advection and transport by diffusion. However, examination of other computer results indicates that transport by eddy diffusion is dominant at middle latitudes, where advective transport often has the opposite sign, and that advection is dominant in tropical latitudes. The total energy transport peaks at 7.5×10^{19} cal day^{-1} at a latitude of about 40° N. Sellers [24] compiled observations ranging from 5.5 to 13.7×10^{19} cal day^{-1}. He observed a peak energy transport of 7.1×10^{19} with a best-estimate value of 10.7×10^{19} cal day^{-1}. Most observations indicate that the maximum occurs at 40° N.

The energy transport in Figure 10a vanishes near the equator as well as at the poles, indicating that there is no net annual energy transport between hemispheres. The negative dip of the sensible-energy-transport curve just north of the equator reflects the strength of the Hadley cell, with warm surface winds advecting total potential energy (internal plus potential) toward the equator, while colder high-altitude winds carry less potential energy toward the pole. The total energy transport (kinetic plus potential) is still poleward, however, carrying away the radiation excess of the equatorial regions. The dip is much more noticeable in certain seasonal-average calculations (Figure 10b) where the Hadley cell is more apparent.

Precipitation

The computed annual precipitation is shown in Figure 11, together with the water-equivalent depth of snowfall. The most obvious feature is the lack of a strong precipitation peak at the equator. The discrepancy in rainfall at the equator results, in part, from the lack of longitudinal (particularly land/sea) variations and, in part, from too little evaporation at all latitudes. The marked depressions over the subtropical land bands are the result of winter circulation patterns in which air descends over the cool land. Also to be noted is that precipitation in the form of snow is heavy on land just poleward of the ocean regions.

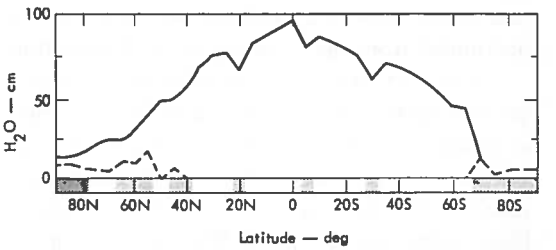

Figure 11. The latitudinal distribution of annual precipitation (solid lines) and snowfall (dashed lines) in equivalent centimeters of water.

PLANS FOR ZAM2 IMPROVEMENT AND VALIDATION

Before ZAM2 can be utilized for the CIAP, it is clear that detailed validation studies will have to be made, comparing ZAM2 results with observations and with the calculations of three-dimensional models. An early, very preliminary comparison was made with the Mintz-Arakawa model by Graham and Warshaw [30] at Rand before they were funded by the CIAP for such comparisons. Such tests are not completely straightforward because of the different mechanisms, grids, and so forth. The best test usually starts with conditions as similar as possible and then compares the results of both models with the real climate. I think it is fair to say that in a comparison of our model with the UCLA model, each had shortcomings, and it would be difficult to determine which model gave better zonal-average results. Although we expect the updated ZAM2 to give improved results, the main purpose of the improvements is to make the model more sensitive to potential CIAP inputs.

Incorporation of kinetics and stratospheric radiative physics into ZAM2 is being considered in association with other efforts at LLL sponsored by CIAP. Although detailed radiative-absorption prescriptions are being developed, our first step will be to introduce empirically-derived formulae based on the observed species concentrations.

After this, tracer studies will be undertaken, probably of the spread of radioactive debris, and possibly for volcanic debris. Ozone as a passive

tracer can also be treated, although specification of its sinks and sources will require some effort. Without further refinement of the radiation calculation, however, the dynamics would still be uncoupled from the evolving ozone distribution.

The next step is to base radiative absorption on the instantaneous species distribution. Then, in conjunction with the kinetics effort at LLL, we plan to introduce a simplified species list and reaction set. Because of the model's relatively high computational speed, this should permit a range of experiments to be undertaken in which the pertinent parameters can be varied.

ZAM2 USE FOR CIAP

The general goal for our program is to assess, within the DOT timetable, the effects of potential pollutant distributions on the global climate. The results from this model must be carefully scrutinized, as must the results from all models, but the extent and diversity of atmospheric feedback mechanisms included in ZAM2 should make it a useful tool for determining what the important processes may be.

In working to meet this objective, several important problems must be faced. The first is determining the pollutant input parameters initially and as a function of time. Since both the grid scale and the computer-time requirements will not allow the treatment of a single SST, ZAM2 must interface with models that treat these scales. In addition, since kinetic equilibrium for many species in the stratosphere may take many years, it seems appropriate to initialize ZAM2 with input for a near-equilibrium species distribution. Thus, we propose to interface with a two-dimensional model that has already distributed the reacting pollutants throughout the stratosphere, using a parameterized transport mechanism* and assuming that the kinetics do not interact with the transport. Such a model is being developed at LLL by Chang and others.

A second problem is whether we can expect the model to be sufficiently sensitive to react to a modified species distribution. Since, in a deterministic model, any change will manifest itself in the results in some fashion, comparison of model runs (control versus perturbed) is viewed as providing the most useful information. How much the model will react, however, is not completely clear. We are planning some early tests to determine the magnitude of the species modification required to perturb surface temperatures, for example, by perhaps half a degree.

When a perturbation does occur, the question is whether it is of the proper sign and magnitude. Since there is a very limited set (almost the null set) of well-defined climatic situations against which to validate a climatic model, and these perturbations are often large and their mechanisms not well understood, this question is probably best answered by tracing the operative mechanisms through the model to gain an intuitive understanding. One can also hope that the first-order discrepancies will be removed in comparing the results of model runs, since the same discrepancies will occur in each run.

We will seek confirmation of any unusual or significant results in other models. Not only will this provide an independent assessment of the impact, but also the filtering of many possibilities by ZAM2 might increase the effectiveness of the three-dimensional models and reduce the number of expensive runs that lead to inconclusive results.

SUMMARY

The updated LLL Zonal Atmospheric Model (ZAM2) is a two-dimensional (latitude and vertical) general-circulation model, for simulating the atmospheric mass and energy fluxes that determine climate. The atmospheric physics is governed by the primitive equations, but omission of longitudinal derivatives requires that a mechanism be established to simulate meridional transport by horizontal waves and eddies. At each latitude, the lower boundary dynamically interacts with the atmosphere and can be divided proportionally among ocean, sea ice, land, and mountains. Radiatively- and kinetically-interactive chemistry is planned, so that the model may be used for extended runs in studies with a wide variety of probable distributions of trace constituents. These studies, involving comparisons between the perturbed and control runs, should improve our understanding of the coupling of dynamics and kinetics, and should also

* Perhaps based on averages from a ZAM2 control run.

indicate the mechanisms by which SST effluent might affect the climate, thus providing guidance that will be helpful in selecting situations to be studied in three-dimensional models.

ACKNOWLEDGMENTS

This work has been in part performed under the auspices of the U.S. Atomic Energy Commission and in part supported by the Climatic Impact Assessment Program, Department of Transportation. I am also indebted to Hugh Ellsaesser for his continual advice and review.

REFERENCES

1. MacCracken, M.C., "Ice age theory analysis by computer model simulation," Ph.D. thesis, University of California, Davis/Livermore, 1968.

2. MacCracken, M.C., *A Zonal General Circulation Model,* Lawrence Livermore Laboratory Rept. UCRL-50594, 1969.

3. Underwood, R.L. (ed.), "Proceedings of the Climatic Impact Assessment Program Workshop on Computational Modeling of the Atmosphere," Asilomar, Pacific Grove, California, 11-14 April 1971, Report No. DOT-TST-90-1, Department of Transportation, 1972.

4. Leith, C.E., "Numerical simulation of the earth's atmosphere," in *Methods of Computational Physics*, Vol. 4, 1-28, Academic Press, Inc., New York, 1965.

5. MacCracken, M.C., *Tests of Ice Age Theories Using a Zonal Atmospheric Model*, Lawrence Livermore Laboratory Rept. UCRL-72803, 1970.

6. Shaw, D.M., and W.L. Donn, "A thermodynamic study of arctic paleoclimatology," Quaternary Res. *1*, 175-187, 1971.

7. MacCracken, M.C., *The Atmospheric Conservation Equations in Flux Divergence Form*, Lawrence Livermore Laboratory Rept. UCRL-50593, 1969.

8. Clapp, P.F., "Parameterization of macroscale transient heat transport for use in a mean-motion model of the general circulation," J. Appl Meteorol. *9*, 554-563, 1970.

9. Adem, J., "On the theory of the general circulation of the atmosphere," Tellus *XIV*, 102-115, 1962.

10. Sellers, W.D., "A global climatic model based on the energy balance of the earth-atmosphere system" J. Appl. Meteorol. *8*, 392-400, 1969.

11. Reed, R.J., and K.E. German, "A contribution to the problem of stratospheric diffusion by large-scale mixing," Mon. Wea. Rev. *93*, 313-321, 1965.

12. Saltzman, B., "Steady state solutions for axially-symmetric climatic variables," Pure Appl. Geophys. *69*, 237-259, 1968.

13. Leith, C.E., *Convection in a Six-Level Model Atmosphere*, Lawrence Livermore Laboratory Rept. UCRL-12415-T, presented at the International Symposium on Dynamics of Large-Scale Processes in the Atmosphere, Moscow, June, 1965.

14. Oliger, J.E., R.E. Wellck, A. Kasahara, and W.M. Washington, *Description of NCAR Global Circulation Model*, NCAR Technical Note NCAR-TN/STR-56, Boulder, Colorado, 1970.

15. Hering, W.S., C.N. Touart, and T.R. Borden, Jr., "Ozone heating and radiative equilibrium in the lower stratosphere," J. Atmos. Sci. *24*, 402-413, 1967.

16. Luther, F.M., personal communication, October 1972.

17. Houghton, H.G., "On the annual heat balance of the northern hemisphere," J. Meteorol. *11*, 1-9, 1954.

18. Coffin, M.D., "A numerical investigation of the energy balance of the planet Mars," Ph.D. thesis, University of California, Davis/Livermore, 1967 (published as Lawrence Livermore Laboratory Rept. UCRL-50309).

19. Leovy, C., "Simple models of thermally driven mesopheric circulation," J. Atmos. Sci. *21*, 327-341, 1964.

20. Newell, R.E., "The global circulation of atmospheric pollutants," Sci. Amer. *224* (1), 32-42, 1971.

21. Delsol, F., K. Miyakoda, and R.H. Clarke, "Parameterized processes in the surface boundary layer of an atmospheric circulation model," Quart. J. Roy. Meteorol. Soc. *97*, 181-208, 1971.

22. Sverdrup, H.U., "Oceanography," in *Handbuch der Physik*, Vol. XLVIII, Springer-Verlag, Berlin, 1957.

23. Emig, M., "Heat transport by ocean currents," J. Geophys. Res. *72*, 2519-2530, 1967.

24. Sellers, W.D., *Physical Climatology*, University of Chicago Press, Chicago, 1965.

25. Peixoto, J.P., *Hemispheric Temperature Conditions During the Year 1950*, Scientific Report No. 4, Dept. of Meteorology, Massachusetts Institute of Technology, Cambridge, 1960.

26. Manabe, S., and R.F. Strickler, "Thermal equilibrium of the atmosphere with a convective adjustment," J. Atmos. Sci. *21*, 361-385, 1964.

27. London, J., *A Study of the Atmospheric Heat Balance*, Final Report, AFCRL Contract AF 19(122)-165, Research Division, College of Engineering, New York University, 1957.

28. Manabe, S., and R.T. Wetherald, "Thermal equilibrium of the atmosphere with a given distribution of relative humidity," J. Atmos. Sci. *24*, 241-259, 1967.

29. Manabe, S., "Climate and the ocean circulation. I: The atmospheric circulation and the hydrology of the earth's surface," Mon. Wea. Rev. *97*, 739, 1969.

30. Graham, W., and M. Warshaw, personal communication, 1971.

31. Goody, R.M., *Atmospheric Radiation, I: Theoretical Basis*, Oxford, Clarendon Press, 1964.

32. Manabe, S. and F. Möller, "On the radiative equilibrium and heat balance of the atmosphere," Mon. Wea. Rev. *89*, 503-532, 1961.

APPENDIX A

SYMBOLS

A = clear-air absorption coefficient

a = radius of the earth

a_c = cloud albedo

B = blackbody flux

C = convective intensity

c_p = specific heat of air at constant pressure

F = advective or frictional flux (specified by a subscript)

F^d = diffusive flux of angular momentum (direction specified by a subscript)

g = acceleration due to gravity

H = subscript indicating horizontal direction

I = radiation intensity

K = diffusion coefficient (specified by a subscript)

k_λ = radiation absorption coefficient

L = latent heat of vaporization

M = subscript indicating meridional direction

m = index associated with pressure level

p = pressure

$\dot{q}$ = sensible-heat rate in the atmosphere

R = gas constant for dry air

$\dot{r}$ = relative humidity; as a subscript indicates a reference quantity

r = water-vapor source rate in the atmosphere

S = subscript indicating saturated equivalent condition

s = quantity evaluated at the surface of the earth; path length

T = temperature

t = time

u = eastward (zonal) component of wind velocity

V = subscript indicating vertical direction

v = northward (meridional) component of wind velocity

w = optical depth coordinate

z = vertical coordinate

Z = subscript indicating zonal direction

α = fractional cloud cover

γ = cloud absorptivity

δ = declination angle of the sun

Θ = potential temperature

θ = degrees of latitude

κ = R/c_p

λ = degrees of longitude, wavelength

μ = water-vapor mixing ratio

ν = frequency

ρ = density of the atmosphere

τ = radiation transmissivity

$\bar{\tau}_F$ = flux transmissivity defined by Eq. (C-20)

$\tilde{\tau}_F$ = flux transmissivity defined by Eq. (C-21)

Φ = zenith angle of the sun

ϕ = geopotential, vertical angle

Ω = angular-rotation rate of the earth

ω = vertical velocity

APPENDIX B
SOLAR-RADIATION CALCULATIONS

The direct-beam solar-radiation flux (F_s) is calculated, from the top of the atmosphere to the surface, from the equation

$$F_s(p_{m+1/2}) = F_s(p_{m-1/2}) \left[1 - \frac{\alpha_m - \bar{\alpha}_{m-1}}{1 - \bar{\alpha}_{m-1}} - (1 - \bar{\alpha}_m) A^s_m \right], \quad \text{(B-1)}$$

where $\bar{\alpha}_m$ is the maximum cloud fraction above m and A is the clear-air absorption of the beam by water vapor. Specifically,

$$A^s_m = 0.172 \left(\Delta z^{0.3}_{m+1/2} - \Delta z^{0.3}_{m-1/2} \right), \quad \text{(B-2)}$$

where

$$\Delta z_{m+1/2} = \frac{\sum_{m'=1}^{m} \mu^D_{m'} \Delta p_{m'}}{\cos \Phi} \left(\frac{p_{m'}}{p_s} \right)^{0.6} \quad \text{(B-3)}$$

is the water-vapor path length (D indicates dry air);

$$\mu_m = \alpha \mu_{saturation} + (1 - \alpha) \mu^D_m \quad \text{(B-4)}$$

allows the water-vapor content in dry air to be determined; and

$$\cos \Phi = -\cos\delta \cos\theta \cos\left(\frac{2n\pi\Delta t}{24} \right) + \sin\delta \sin\theta \quad \text{(B-5)}$$

yields the zenith angle of the sun (δ is a function of the time of year and n is the a time-step counter).

Physically, the second term in the square brackets in Eq. (B-1) accounts for cloud obstruction, and the third term accounts for clear-air absorption by water vapor. The numerical values appearing in Eq. (B-2) are the result of comparing our model's calculations to the scheme used by C.E. Leith. Ozone absorption in the top layer is an additional term included in A^s_1.

The upward-diffusive flux ($F^\uparrow$) and the downward-diffusive flux ($F^\downarrow$) are governed by the equations

$$F^\uparrow(p_{m-1/2}) = F^\uparrow(p_{m+1/2}) \left[\alpha_m \left(1 - a_{c_m} \right)(1 - \gamma_m) + (1 - \alpha_m) A^\uparrow_m \right] + a_{c_m} \frac{\alpha_m - \bar{\alpha}_{m-1}}{1 - \bar{\alpha}_{m-1}} F_s(p_{m-1/2}) + a_{c_m} \alpha_m F^\downarrow (p_{m-1/2}) \quad \text{(B-6)}$$

and

$$F^\downarrow(p_{m+1/2}) = F^\downarrow(p_{m-1/2}) \left[\alpha_m \left(1 - a_{c_m} \right)(1 - \gamma_m) + (1 - \alpha_m) A^\downarrow_m \right] + \left(1 - a_{c_m} \right) (1 - \gamma_m) \frac{\alpha_m - \bar{\alpha}_{m-1}}{1 - \bar{\alpha}_{m-1}} F_s(p_{m-1/2}) + a_{c_m} \alpha_m F^\uparrow (p_{m+1/2}). \quad \text{(B-7)}$$

Here, $A^\uparrow_m$ and $A^\downarrow_m$ are based on an appropriate average water-vapor path length multiplied by 1.66, since the radiation is diffuse. The cos Φ term shown in Eq. (B-3) is not included, however. The terms in the square brackets account for cloud and clear-air losses in the flux from the previous level. The other two terms include direct-beam and opposite-direction diffuse-beam contributions.

In calculating the diffuse-radiation fluxes, the direct-beam fluxes are known, as are the two boundary conditions

$$F^\downarrow (p = 0) = 0 \quad \text{(B-8)}$$

and

$$F^\uparrow (p = p_s) = a_s \cdot [F^\downarrow (p = p_s) + F_s (p = p_s)], \quad \text{(B-9)}$$

where a_s is the surface albedo. Solution is achieved by guessing $F^\uparrow (p = 0)$ and then solving the system of equations down through the atmosphere, checking the agreement with Eq. (B-9), adjusting if necessary, and calculating to the top of the atmosphere. This yields a value of $F^\uparrow (p = 0)$ upon which to base a new guess. The cycle is continued until Eq. (B-9) agrees within a specified limit.

The effect of solar radiation on the atmosphere and the surface is then determined by taking the divergence of the fluxes last calculated.

APPENDIX C*

FLUX OF LONG-WAVE RADIATION

Starting with Schwartzschild's equation,

$$dI_\lambda = k_\lambda \rho \, ds[f(\lambda,T) - I_\lambda], \tag{C-1}$$

define w as the optical depth measured from the top of the atmosphere parallel to the z-coordinate direction:

$$dw = -\rho \, dz = \rho \cos\phi \, ds, \tag{C-2}$$

$$\frac{dI_\lambda}{dw} = -k_\lambda \sec\phi \left[I_\lambda - I_{b_\lambda}(T) \right] \tag{C-3}$$

$I_{b_\lambda}(T)$ is the blackbody intensity at wavelength λ and temperature T.

Differentiating Beer's Law,

$$I_\lambda = I_{0_\lambda} e^{-k_\lambda w \sec\phi}, \tag{C-4}$$

and assuming k_λ independent of w leads to

$$\frac{dI_\lambda}{dw} = \frac{dI_{0_\lambda}}{dw} e^{-k_\lambda w \sec\phi} - k_\lambda \sec\phi \, I_{0_\lambda} e^{-k_\lambda w \sec\phi} \tag{C-5}$$

Combining Eqs. (C-3) and (C-5),

$$\frac{dI_{0_\lambda}}{dw} = k_\lambda \sec\phi \, I_{b_\lambda}(T) e^{k_\lambda w \sec\phi}; \tag{C-6}$$

$$I_{0_\lambda}(w) = k_\lambda \sec\phi \int_0^w I_{b_\lambda}[T(w')] e^{k_\lambda w' \sec\phi} dw'; \tag{C-7}$$

$$I_\lambda(w) = I_{0_\lambda} e^{-k_\lambda w \sec\phi} = k_\lambda \sec\phi \int_0^w I_{b_\lambda}(w') e^{-k_\lambda \sec\phi (w-w')} dw'; \tag{C-8}$$

$$I_\lambda(w) = k_\lambda \sec\phi \int_0^w I_{b_\lambda}(w') e^{-k_\lambda \sec\phi (w-w')} \int_0^w I_{b_\lambda}(w') e^{-k_\lambda \sec\phi (w-w')} d(w-w'). \tag{C-9}$$

Define:

$$\tau_\lambda(w-w') = e^{-k_\lambda \sec\phi (w-w')}; \tag{C-10}$$

$$\frac{d\tau_\lambda(w-w')}{d(w-w')} = -k_\lambda \sec\phi \, \tau(w-w'); \tag{C-11}$$

$$I_\lambda(w) = k_\lambda \sec\phi \int_0^w I_{b_\lambda}(w') \, \tau(w-w') \, d(w-w') = -\int_0^w I_{b_\lambda}(w') \frac{d\tau(w-w')}{d(w-w')} d(w-w'); \tag{C-12}$$

$$I_\lambda(w) = -\int_1^{\tau_\lambda(w)} I_{b_\lambda}(w') \, d\tau(w-w') = \int_{\tau_\lambda(w)}^1 I_{b_\lambda}(w') \, d\tau(w-w'). \tag{C-13}$$

In order to go from this expression for intensity to an expression for flux, a generalized transmission function, τ_i', must be obtained by averaging over elemental spectral intervals. A generalized absorption coefficient, L_i, takes the place of the absorption coefficient, k_λ; thus, an averaged transmission function $\tau'(L_i \sec\phi \, w)$ takes the place of $e^{-k_\lambda \sec\phi w}$. Goody [31] discusses the rather complex nature of this averaging.

In order to obtain slab transmissivity, required for flux calculations, from beam transmissivity, an averaging over angular directions is necessary. This is accomplished by assuming an average value of the angular direction of $\sec\phi = 1.66$. The generalized flux transmission function for the *i*th spectral interval evolves as follows:

$$\tau_{F_i}(w) = \tau'_F(L_i w) = \tau'(1.66 \, L_i w). \tag{C-14}$$

An expression for flux in the *i*th spectral interval corresponding to Eq. (C-13) is

$$F_i(w) = \int_{\tau_{F_i}(w)}^1 B_i(w') \, d\tau_{F_i}(w-w'). \tag{C-15}$$

For the *i*th spectral interval, $F_i(w)$ is the downward flux at level w', $B_i(w)$ is the blackbody flux at the temperature of position w', and τ_{F_i} is the generalized flux transmission function.

Considering the limit where spectral intervals become infinitesimally small so that associated functions become continuous, Eq. (C-15) may be written

$$F_\nu(w) = \int_{\tau_{F_\nu}(w)}^1 B_\nu(w') \, d\tau_{F_\nu}(w-w'). \tag{C-16}$$

*Appears as Appendix B in [18].

Integrating this by parts leads to

$$F_\nu(w) = B_\nu(w) - B_\nu(0)\,\tau_{F_\nu}(w) - \int_0^w \tau_{F_\nu}(w-w')\,\frac{dB_\nu(w')}{dT(w')}\,dT(w'). \quad \text{(C-17)}$$

The following averages are defined:

$$F(w) = \int_0^\infty F_\nu(w)\,d\nu; \quad \text{(C-18)}$$

$$B(w) = \int_0^\infty B_\nu(w)\,d\nu; \quad \text{(C-19)}$$

$$\bar{\tau}_F(w,T) = \frac{\int_0^\infty B_\nu\,\tau_{F_\nu}\,d_\nu}{B(0)}; \quad \text{(C-20)}$$

$$\bar{\tau}_F(w,T) = \frac{\int_0^\infty \frac{dB_\nu}{dT}\,\tau_{F_\nu}\,d\nu}{\frac{dB(T)}{dT}}. \quad \text{(C-21)}$$

$\bar{\tau}(w,T)$ is relatively independent of temperature, so that Eq. (C-17) may be approximated:

$$F(w) = B(w) - \bar{\tau}_F(w,T_0)\,B_0 - \int_0^w \bar{\tau}_F(w-w')\,dB(w'). \quad \text{(C-22)}$$

The subscript 0 refers to the position w = 0, which has arbitrarily been taken as the top of the atmosphere. In the integration it is more accurate and practical to evaluate the correction terms outside the integral at a reference temperature near the mean temperature of the atmosphere. In the following development such a temperature, T_r, is introduced along with a corresponding blackbody flux intensity, B_r. Again, integrating by parts,

$$F(w) = B(w) - \bar{\tau}_F(w,T_0)\,B_0 - [\bar{\tau}_F(w-w')\,B(w')]\Big|_0^w + \int_{\bar{\tau}_F(w)}^1 B(w')\,d\bar{\tau}_F(w-w'); \quad \text{(C-23)}$$

$$F(w) = -[\bar{\tau}_F(w,T_0) - \bar{\tau}_F(w,T_0)]\,B_0 + \int_{\bar{\tau}_F(w)}^1 B(w')\,d\bar{\tau}_F(w-w'). \quad \text{(C-24)}$$

From Eq. (C-22),

$$F(w) = B(w) - \bar{\tau}_F(w,T_0)\,B_0 - \int_0^w \bar{\tau}(w-w',T)\,\frac{dB(T)}{dT}\,dT(w'). \quad \text{(C-25)}$$

For fixed w,

$$B(w)\,\bar{\tau}_F(w,T) = \int_0^\infty B_\nu(T)\,\tau_{F_\nu}(w)\,d\nu; \quad \text{(C-26)}$$

$$\frac{d}{dT}[B(w)\,\bar{\tau}_F(w,T)] = \int_0^\infty \tau_F\,\frac{dB_\nu(T)}{dT}\,d\nu = \bar{\tau}_F(w,T)\,\frac{dB}{dT}; \quad \text{(C-27)}$$

$$d[B(w)\,\bar{\tau}_F(w,T)] = \bar{\tau}_F(w,T)\,dB; \quad \text{(C-28)}$$

$$B(w)\,\bar{\tau}_F(w,T)\Big|_{T_0}^{T_r} = \int_{B_0}^{B_r} \bar{\tau}_F(w,T)\,dB. \quad \text{(C-29)}$$

From Eq. (C-22),

$$F(w) = B(w) - B_r\,\bar{\tau}_F(w,T) + \int_{B_0}^{B_r} \bar{\tau}_F(w,T)\,dB - \int_0^w \bar{\tau}_F(w-w')\,dB(w'). \quad \text{(C-30)}$$

Since

$$\int_{B_0}^{B_r} \bar{\tau}_F(w,T)\,dB = (B_r - B_0)\,\bar{\tau}_F(w) \quad \text{(C-31)}$$

and

$$-\int_0^w \bar{\tau}_F(w-w',T)\,dB(w') = -B(w) + \bar{\tau}_F(w)\,B_0 + \int_{\bar{\tau}_F(w)}^1 B(w')\,d\tau_F(w-w'), \quad \text{(C-32)}$$

$$F(w) = [\bar{\tau}_F(w) - \bar{\tau}_F(w,T_r)]\,B_r - \int_1^{\bar{\tau}_F(w)} B(w')\,d\bar{\tau}_F(w-w'). \quad \text{(C-33)}$$

This is the form of the equation for downward flux of long-wave radiation at level w and involves integration upward from w' = w to w' = 0.

This derivation is due to Leith. The approach is similar to that used by Manabe and Möller [32] and Manabe and Strickler [22].

DISCUSSION

WUEBBLES: What do you think can be concluded from these studies, given the CIAP time frame of another year and a half?

MacCRACKEN: I think we'll be able to do some tracer experiments, which would be part of the validation study. We'll probably be able to try some significantly perturbed stratospheric-species distributions, to see what kind of effect occurs at the surface. It is not yet clear how much of a change in stratospheric ozone is needed to produce a surface-temperature change. It is also not obvious how altered stratospheric absorption will affect the troposphere, or the dynamics involved. Nor am I sure that the model will be sensitive enough to reproduce the very small perturbations we may have to deal with in CIAP.

With the Texas Instruments computer GFDL is going to get, it may be possible to achieve a good three-dimensional climatic simulation in a little less than the ten years Professor London predicted. The pressing problem is that we don't yet understand the causes of major climatic changes, over years or millions of years, or even of the Little Ice Age 400 years ago. The effects of an SST fleet will be like a perturbation in the noise in a signal. We don't know what causes the signal, and we're not sure what causes the noise; all we can look at is the perturbation. I hope that with the two-dimensional parameterized transport models we'll get some information in the next year or two which will at least let us ask the right questions.

McCLATCHEY: How long does it take you to run this two-dimensional model, and have you had a chance to run it for any length of time?

MacCRACKEN: The original model takes about a half-hour to run a year on the CDC 7600. We once ran two and a half years on a CDC 3400, and it has been run for a year and a half quite a few times. The present, expanded model is going to need at least twice that much computer time before we even try to include the kinetics, but we should still be able to compute for several years of model time. Of course, tens or hundreds of years are out of the question, given the computer time involved. The results are still reasonable as far as numerical error goes after a year or two; the question is what additional information would be gained from a longer run. During the earlier runs we wanted to see whether the atmosphere was in near-equilibrium with the different postulated surface conditions – for example, if you changed the solar constant, would the model reach a new cyclic-equilibrium state, and how long would it take? It turns out that it doesn't take long; if you run for a year and a half, the change from season to season is either small or quite large.

WOFSY: What about the chemical kinetics?

MacCRACKEN: I don't think we know enough about what kinetics to include at this point. Their effect on the model will depend on how simple the set of equations treated is.

PRELIMINARY RESULTS FROM A THREE-DIMENSIONAL, GENERAL-CIRCULATION/TRACER MODEL

J.D.MAHLMAN
NOAA Geophysical Fluid Dynamics Laboratory
Princeton University
Princeton, New Jersey

ABSTRACT: Some initial results from a three-dimensional tracer model are presented. The tracer model uses time-evolving, three-dimensional output from the general-circulation model described by Mahlman and Manabe [1]. In the tracer integrations, three-dimensional advection and horizontal sub-grid-scale diffusion are calculated. Arbitrary parameterizations of sources and sinks can be included. The advective terms and time differencing are formulated so as to suppress artificial numerical damping.

Currently, two major experiments are being conducted. The first is a diffuse point-source injection into the Northern-Hemisphere, mid-latitude winter stratosphere. The other is a vertically stratified tracer with a crudely simulated photochemical equilibrium at the upper level and a precipitation-dependent sink at the lowest levels.

The results of both experiments show many similarities to the behavior of analogous stratospheric trace substances. The first experiment shows features close to those of radioactive debris from recent Chinese bomb tests. The second experiment exhibits many features common with those of observed ozone.

INTRODUCTION

At the DOT CIAP Survey Conference (February 1972), the design and behavior of a recent GFDL global general-circulation model with seasonal variation were described briefly [1]. Some discussion was presented on current efforts to develop a three-dimensional model with the capability of running passive tracer experiments using time-dependent results from the general-circulation model.

At present, two lengthy tracer experiments are being numerically computed. Although not yet completed, they have progressed far enough for some conclusions to be reached. This paper presents some aspects of the model structure and some pertinent initial results.

MODEL STRUCTURE

The general-circulation model which provides input for the tracer model contains 11 basic levels, the highest at about 30 km. The average horizontal grid spacing is about 265 km. It is global in character and includes effects of topography, water vapor, and seasonally varying radiation. Ozone, cloudiness, and sea-surface temperatures are not "free" variables, because they are specified according to their observed seasonally varying values. (For a more complete description of the general-circulation model, see references 1-3.)

The general-circulation model used here is similar in structure to that of Manabe and Hunt [4] (which was used for their tracer study [5]). Some important differences, however, are that the previous model is only hemispheric, and lacks surface topography. The effects of water vapor were neglected and the radiation was fixed, rather than being allowed to vary seasonally as in the present model.

Because the tracer model must utilize the results of the general-circulation model, some special provisions are necessary. In the previous experiment of this nature [5, 6], the tracer integration was performed by including an additional dependent variable during the course of integrating the general-circulation model itself. The present tracer model utilizes general-circulation model data which has been time-averaged over 6-hour periods. This procedure allows for a much longer time step to be employed and also eliminates the spurious effects of the very short-period fluctuations. Because the tracer model can now be run independently of the general-circulation model, this leads to a

considerable improvement in computer efficiency and flexibility of experimental design. This approach, however, allows only for experiments in which the evolution of the tracer has no influence upon the dynamics. This is not a difficulty at present, because in most cases dynamic feedbacks should not be allowed until the model itself has demonstrated the capability of simulating the behavior of passive tracers properly. If this capability is lacking, dynamic feedbacks from some "free" tracers could be seriously distorted.

The continuity equation for a trace substance written in the sigma coordinate system ($\sigma = P/P_*$, where P is pressure and P_* is pressure at the earth's surface) [7] is

$$\frac{\partial}{\partial t} RP_* = -\nabla_\sigma \cdot \vec{V}_2 P_* R - \frac{\partial}{\partial \sigma} \dot{\sigma} P_* R \qquad (1)$$

+ "Diffusion" + "Filling" + "Sources" − "Sinks".

Here, R is the tracer mixing ratio (expressed in arbitrary units), ∇_σ the two-dimensional gradient operator on a sigma surface, $\vec{V}_2$ the horizontal velocity, and $\dot{\sigma} = d\sigma/dt$ the "vertical velocity" expressed in this coordinate system.

The three-dimensional tracer flux convergence, as determined by the first two terms on the right-hand side of (1), is calculated using a quadratic-preserving finite-difference scheme of approximately second-order accuracy in the horizontal. In order to reduce truncation error as much as possible, a fourth-order scheme is employed in the vertical.

"Diffusion" represents for these experiments only the sub-grid-scale horizontal diffusive transfer on a constant-height surface, as transformed to the sigma coordinate [8]. No explicit sub-grid-scale diffusive transfer is calculated in the vertical. Part of the purpose of this experiment is to examine whether the large-scale winds generated in the general-circulation model can properly simulate observed tracer behavior. Insofar as this objective allows, the integrated effect of sub-grid-scale diffusion is made as small as is physically and numerically consistent. This is accomplished by employing a horizontal coefficient which is locally dependent on the relative variability of the tracer as well as on the velocity deformation field. This has the effect of leaving the largest scales virtually undamped by diffusion while acting quite strongly on fluctuations whose scale is near the model's resolution limits. Indirectly this insures that virtually all of the simulated tracer transfer will be due to the model-generated winds and not partly to a somewhat arbitrary sub-grid-scale diffusion hypothesis.

"Filling" represents a correction to the advective terms when the effect of truncation error leads to a computed negative tracer mixing ratio. Since such a value is physically impossible, the negative number is not allowed to remain. This situation tends to occur locally when the upstream tracer mixing ratios are much smaller than the downstream ones. In the tracer model such negative values are corrected by "borrowing" tracer from the grid box downstream (in either x, y, or σ directions) from the most responsible advection component. If the box chosen for "borrowing" also does not contain an adequate amount of tracer, a more complicated search is employed. In any event, the "borrowing" is always done so that the total mass of the tracer (in the absence of sources and sinks) is conserved to within the roundoff accuracy of the computer. However, the introduction of "borrowing" always acts to produce a decrease in the global integral of R^2 ($\partial/\partial t \int_G R^2 dm < 0$, where m = mass), thus tending to act rather like sub-grid-scale diffusion. In the experiments described here, the decrease of $\int_G R^2 dm$ due to "diffusion" always dominates that due to "filling".

The modeling of sources and sinks is flexible, and depends upon the nature of the tracer being investigated. In these two experiments the sources differ, and consequently will be described later as part of the experiment explanation. In both experiments, the "sink" is modeled to simulate a removal process in the lower levels, given by

$$\text{"Sink"} = P_*(C_{dry} + C_{wet})R, \qquad (2)$$

where C_{dry} and C_{wet} are coefficients for dry and rainfall-dependent removal processes, respectively. C_{dry} has a non-zero value at the bottom two levels only. Expressed as an effective removal time, the values used in these calculations are C_{dry}^{-1} (990 mb) = 20 days and C_{dry}^{-1} (940 mb) = 30 days. These choices are based on removal rates estimated from the behavior of radioactive tracers in dry surface air.

On the other hand, the wet removal processes are assumed to be zero above 315 mb and dependent upon the rainfall rate below. The removal coefficient is modeled as

$$C_{wet} = B \times \frac{RAIN}{RAIN_G} \qquad (3)$$

where RAIN is the total precipitation calculated at the grid point over a 6-hour period, and $RAIN_G$ is the global average precipitation rate in terms of deposition per 6 hours. B is then the effective removal coefficient if it is raining locally at the global average rate. The reciprocal values of B employed in these two experiments are as follows: B^{-1}(990 mb) = 20 days; B^{-1}(940 mb) = 25 days; B^{-1}(835 mb) = 30 days; B^{-1}(685 mb) = 40 days; B^{-1}(315 mb) = 60 days. These choices are thought to be roughly compatible with observed residence times of particulate tracers. The model results are thought not to be critically sensitive to these choices.

MODEL RESULTS

At present, two major experiments are being performed. Due to the large amount of computer time involved, neither experiment was completed at the time of the Second Conference on CIAP. Because of this, certain aspects of the description of results and implications must be regarded as tentative until the analysis phase has been completed.

1. Mid-latitude Point-Source Tracer

The first experiment to be described is somewhat analogous to a megaton-range nuclear detonation. The only source acting is a large injection of tracer into the mid-latitude Northern-Hemisphere winter stratosphere. To reduce the very large space truncation error that occurs when all of the tracer is concentrated within a very few grid points, a somewhat diffuse initial condition is employed. The center of the initial tracer is at 65 mb, with tracer values 2/3 and 1/3 of the central mixing ratio at the first and second adjacent vertical levels, respectively. The horizontal distribution is diffused so that the concentrations decrease by about a factor of two every horizontal distance of 600 km away from the center. This type of distribution insures that effectively all of the initial tracer is contained within a single stratospheric quarter-wavelength, while drastically reducing the transport and damping due to "filling" in the initial stages.

This pseudo-point-source begins at model date January 1 with the center at 36°N and 180°E. Figures 1 and 2 show vector-streamline combinations at this date for the levels 10 mb and 65 mb. These figures show the very strong presence of the so-called Aleutian anticyclone; it can be seen that most of the initial tracer is located on the anticyclonic-shear side of the polar-night jet stream.

For the purposes of basic discussion in experiments of this complexity, it is quite useful to present the mechanisms leading to the evolution of the zonal mean of the tracer, even though the integration itself includes zonally asymmetric effects. This allows for a more direct comparison with the usual general-circulation statistics, observed tracer behavior, and simplified two-dimensional models. Such an approach also permits a more straightforward discussion of the various transport mechanisms. By transforming Eq. (1) to pressure coordinates and averaging with respect to longitude ($\overline{(\ )}^{\lambda}$), one obtains

$$\frac{\partial \overline{R}^{\lambda}}{\partial t} = \underbrace{-\frac{1}{a}\frac{1}{\cos\phi}\frac{\partial}{\partial\phi}\overline{v'R'}^{\lambda}\cos\phi}_{(a)} \underbrace{-\frac{\partial}{\partial P}\overline{\omega'R'}^{\lambda}}_{(b)} \underbrace{-\frac{\overline{v}^{\lambda}}{a}\frac{\partial R^{\lambda}}{\partial\phi}}_{(c)} \underbrace{-\overline{\omega}^{\lambda}\frac{\partial \overline{R}^{\lambda}}{\partial P}}_{(d)} + \overline{\text{“DIFFUSION”}}^{\lambda} + \overline{\text{“FILLING”}}^{\lambda} - \overline{\text{“SOURCES”}}^{\lambda} - \overline{\text{“SINKS”}}^{\lambda} + \overline{\text{“RESIDUAL”}}^{\lambda} \qquad (4)$$

where a is the radius of the earth, ϕ the latitude, P the pressure, and $\omega = dP/dt$ (vertical motion in pressure coordinates). Terms (a), (b), (c), and (d), along with $\overline{\text{“FILLING”}}^{\lambda}$, represent the effect of the large-scale dynamics. These terms have the following physical interpretations in terms of their influence on the net tendency of $\overline{R}^{\lambda}$:

(a) horizontal convergence of eddy tracer flux;
(b) vertical convergence of eddy tracer flux;
(c) horizontal advection of $\overline{R}^{\lambda}$ by the mean meridional circulation;

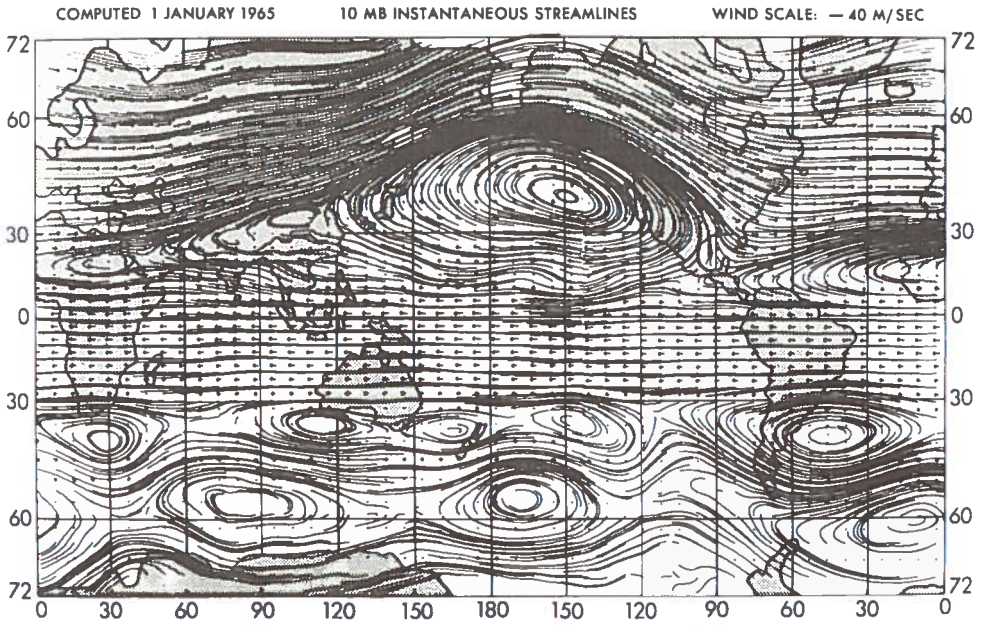

Figure 1. Mercator projection of calculated instantaneous streamlines for 10 mb at model date 1 January 1965. The arrows show local wind vectors with length proportional to speed as indicated at the upper right.

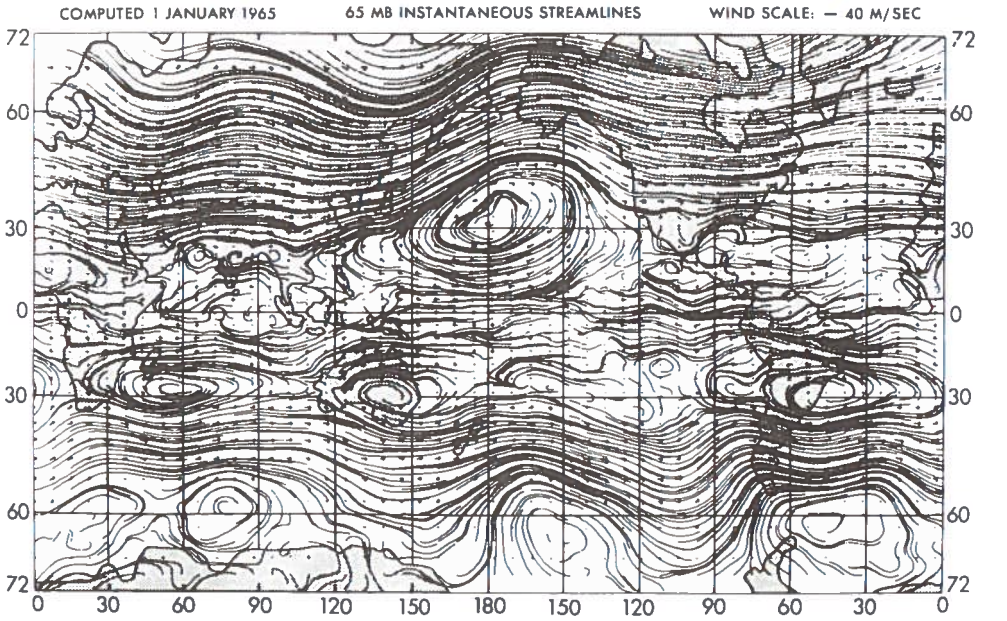

Figure 2. Mercator projection of calculated instantaneous streamlines for 65 mb at model date 1 January 1965. The arrows show local wind vectors with length proportional to speed as indicated at the upper right.

(d) vertical advection of $\overline{R}^{\lambda}$ by the mean meridional circulation.

The term $\overline{\text{"RESIDUAL"}}^{\lambda}$ represents the computational discrepancy which can occur in the balances because of sampling error, coordinate transformation, and numerical inconsistencies. If great care is not taken in the analysis formulation, the $\overline{\text{"RESIDUAL"}}^{\lambda}$ can be of the same order as the leading terms, thus drastically reducing the effectiveness of the analysis.

The zonally-averaged initial condition for this experiment is shown in Figure 3. In the initial adjustment phase (the first 15 days of the experiment), the tendencies were almost entirely due to horizontal eddy flux convergence, which produced large increases south of the center of the initial tracer. Within the first month the effects of the mid-winter stratospheric mean meridional circulation become important. This is particularly true in mid-latitudes, where strong downward transfer into the troposphere occurs. This model phenomenon is stronger than reality, and seems to be accentuated in part by limitations in the vertical resolution relative to the initial conditions. By April the protrusion into the troposphere has weakened somewhat, but is still a pronounced feature (see Figure 4). Figure 4 also shows the beginning of a significant poleward-downward slope of the axis of maximum tracer concentrations, in agreement with observation. Note that the total tracer amount transported into the Southern Hemisphere is relatively small, but that the largest amounts transported are in the lower stratosphere. At this point in the experiment, the rate of evolution of the tracer was quite slow.

One clear feature of observed behavior of radioactive tracers is the existence of a spring peak in mid-latitude surface air. The ability of a tracer model to successfully simulate this phenomenon serves as an important necessary condition for testing the basic validity of such a calculation. Figure 5 shows a time series of monthly-zonally-averaged tracer at 990 mb for various latitudes compared against observed surface radioactivity over the contiguous United States. The May peak appears to be well simulated in this experiment. A detailed description of this model phenomenon is somewhat beyond the intended scope of this presentation; more thorough analysis will be presented in a future publication.

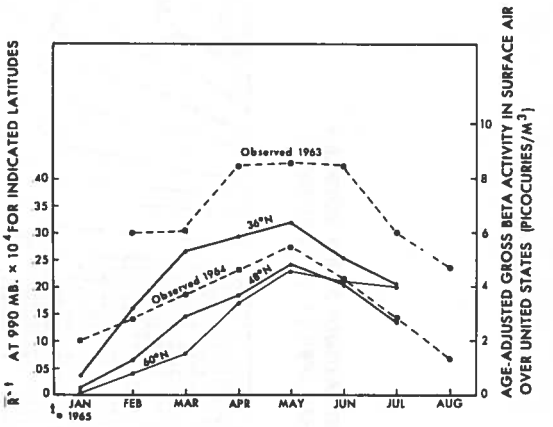

Figure 5. Comparison of time-series of monthly-mean, zonally-averaged tracer concentrations at the surface between the mid-latitude point-source experiment and observation. The calculated values (solid lines) are given for the three indicated latitudes according to the ordinate values on the left. The observed surface-air values (dashed lines) are taken from the U.S. Public Health Service Radiation Surveillance Network for the two years following the mid-latitude U.S. and Russian test series of 1962. The data cover the area of the contiguous United States with values given by the ordinate on the right.

Although this general-circulation model does not successfully simulate a mid-winter stratospheric sudden warming, there is a pronounced seasonal transition in mid-May which is quite similar to that of the actual atmosphere. During this time the tracer undergoes a marked adjustment, leading to large tracer increases in the high-latitude lower stratosphere in the Northern Hemisphere. For a typical vector-streamline chart at 10 mb during this adjustment period, see Figure 6. During this period the intensity of the flow is quite weak, but the meridional meandering of the Northern-Hemispheric disturbances is large.

The effect of this adjustment period on the redistribution of the tracer can be seen in Figure 7, which shows the zonal-mean concentration of the tracer for the month of July. A pronounced poleward-downward slope of the isolines is now seen in the Northern as well as the Southern

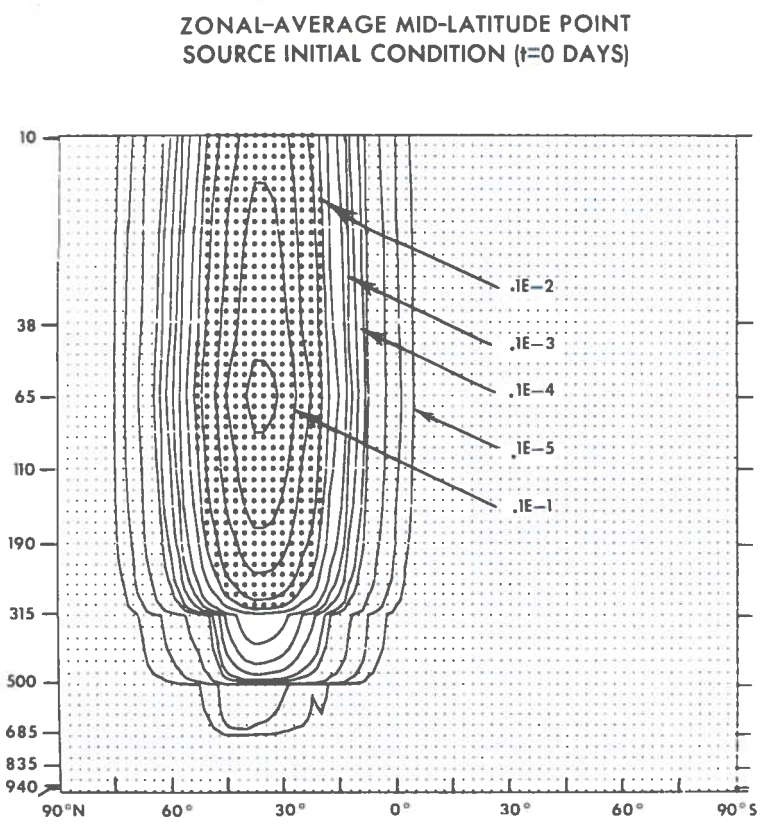

Figure 3. Latitude-height cross-section of the zonally-averaged mixing ratio (arbitrary units) for mid-latitude point-source initial conditions. Logarithmic contours are employed as indicated. Values greater than $.1 \times 10^{-2}$ are shaded with stars; values less than $.1 \times 10^{-4}$ are shaded with dots.

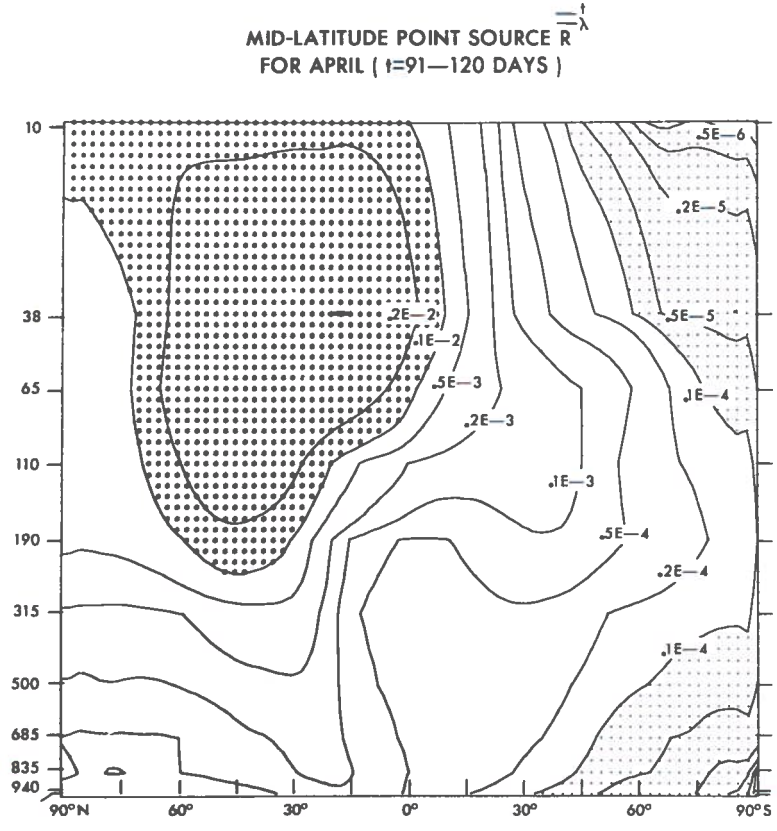

Figure 4. Latitude-height cross-section of zonally-averaged mixing ratio (arbitrary units) from the mid-latitude point-source experiment for the month of April. Logarithmic contours are employed as indicated. Values greater than $.1 \times 10^{-2}$ are shaded with stars; values less than $.1 \times 10^{-4}$ are shaded with dots.

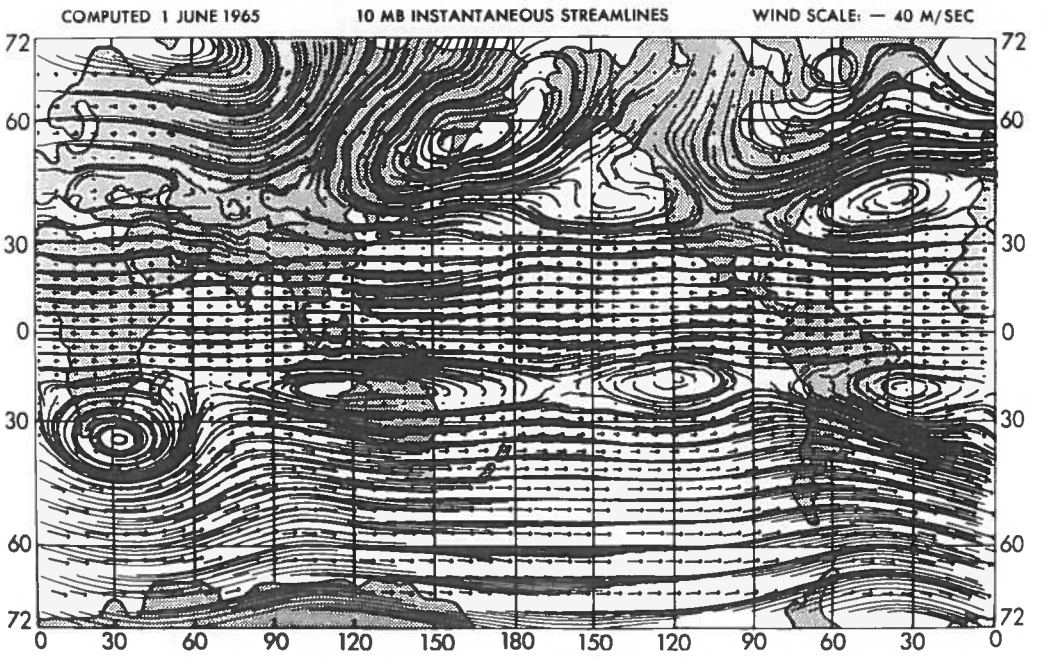

Figure 6. Mercator projection of calculated instantaneous streamlines for 10 mb at model date 1 June 1965. The arrows show local wind vectors with length proportional to speed as indicated at the upper right.

Hemisphere. The figure also reveals that comparatively little further buildup has occurred in the Southern Hemisphere except at 10 mb in the lower latitudes. For a comparison of this behavior with that of analogous radioactive tracers, see Machta and Telegadas' paper in this volume [9].

Prior to this spring-breakdown-type period the net tracer tendencies in the Northern-Hemisphere lower stratosphere tend to be rather small, as the result of a nearly total compensation between flux convergences by eddies and the mean meridional circulation. Once the adjustment period in late May begins, however, the net tendencies in the high-latitude Northern Hemisphere are accomplished mainly by horizontal eddy flux convergence.

This effect is found to operate considerably into the summer season, as is shown by the balances of Figure 8 at 65 mb for July. At this level no sources and sinks are operating. Also, the effects due to $\overline{\text{"DIFFUSION"}}^{\lambda}$, $\overline{\text{"FILLING"}}^{\lambda}$, and $\overline{\text{"RESIDUAL"}}^{\lambda}$ are so small that they cannot be plotted on the scale given here. Figure 8 shows that for this period in the Northern-Hemisphere high latitudes the positive net tendency is almost completely produced by horizontal eddy flux convergence. This is in marked contrast to the more usual case, in which the net tendency tends to be a small difference between nearly compensating dynamical processes. This figure shows a considerably different structure at lower Northern-Hemisphere latitudes. In mid-latitudes the strong negative net tendency is very nearly balanced by vertical eddy flux convergence. Yet at about 24°N the negative net tendency is balanced almost solely by transport by the mean meridional circulation, with dominance by the vertical part. The figure shows a nearly-zero net contribution in that region from the large-scale eddies. An interesting result from a more detailed analysis is that this nearly-zero eddy effect is actually the result of a nearly complete cancellation between the vertical and horizontal eddy flux convergences. On the other hand, between 0° and about 15°N the negative net tendencies are the result of a nearly-zero mean meridional circulation effect and mutually reinforcing horizontal and vertical eddy flux processes.

Figure 9 shows tracer balances for the same time period (July) but for the 10-mb level. This figure shows a totally different structure from that of Figure 8. The net tendencies and intensities of the transport mechanisms are very weak

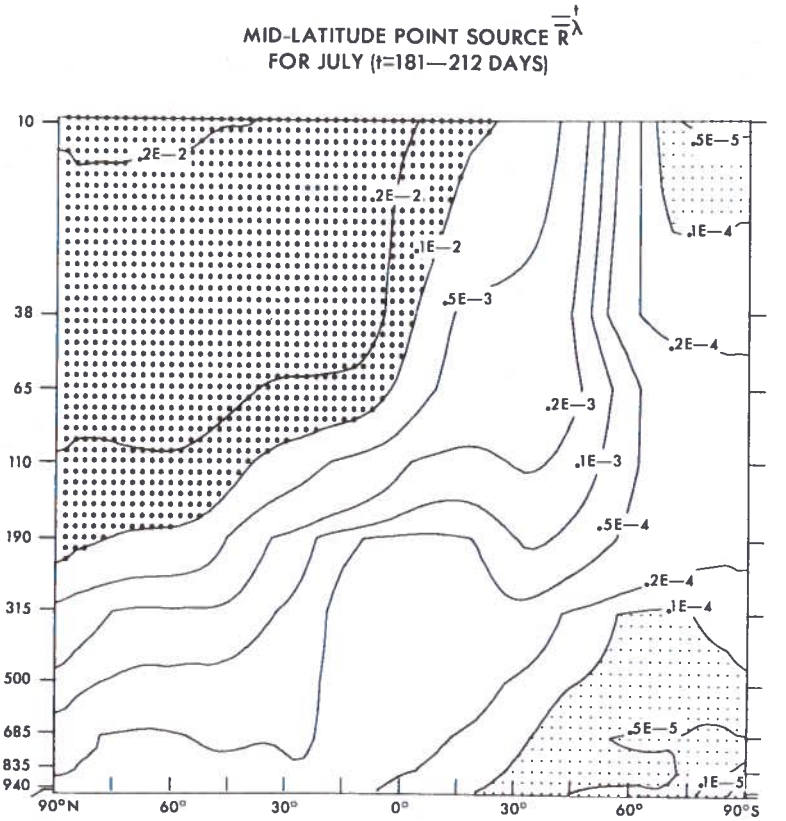

Figure 7. Latitude-height cross-section of zonally-averaged mixing ratio (arbitrary units) from the mid-latitude point-source experiment for the month of July. Logarithmic contours are employed as indicated. Values greater than .1 x 10^{-2} are shaded with stars; values less than .1 x 10^{-4} are shaded with dots.

at latitudes north of 24°N. Throughout the equatorial region a strong positive effect due to horizontal advection by the mean cell is present. This results from a pronounced change in structure of the 10-mb mean meridional circulation at this time of year. During the Northern-Hemisphere winter, $\overline{v}^{\lambda}$ at 10 mb is positive in low latitudes (flow toward the winter pole). As summer approaches, $\overline{v}^{\lambda}$ weakens and becomes negative, with the strongest southward flow occurring during June. It is this effect which allows the tracer in the Northern subtropics at 10 mb to be carried into the Southern Hemisphere. Past about 12°S the meridional circulation begins to weaken somewhat, but at this point the subtropical anticyclones act to evacuate the region and move the tracer further southward. The largest positive net tendency thus appears at about 24°S as a result of combined mean-cell and eddy processes.

Figure 10 gives the instantaneous vector-streamlines for 10 mb on July 31. The figure reveals that the region of negative $\overline{v}^{\lambda}$ in the tropics (described above) is almost totally devoid of longitudinal variations in the meridional wind component until about 15°S, thus allowing only the calculated simple, axially-symmetric transport to occur.

Figure 11 gives instantaneous vector-streamlines at 65 mb from the model on July 31. This gives conditions typical for the period of analysis shown in Figure 8. In the Northern Hemisphere the disturbances are quite weak, but contain significant meridional meandering. They are thus potentially effective in redistributing tracers, particularly because the strong negative coupling between the mean cell and eddies is not present as it is during the intense mid-winter months.

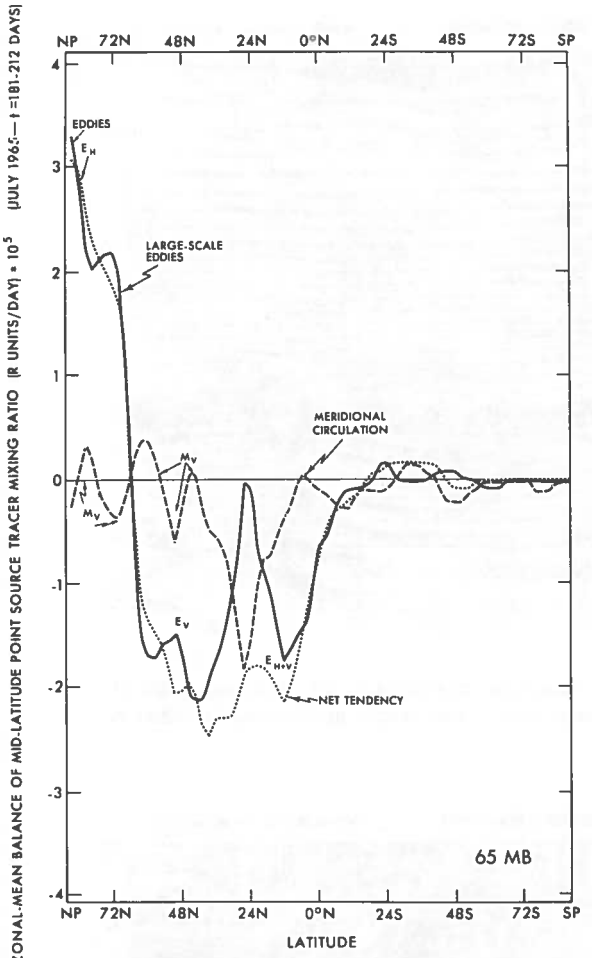

Figure 8. Mechanisms leading to changes in the zonal-mean mixing ratio (R units/day) for the mid-latitude point-source experiment as a function of latitude for July at 65 mb. The notations E_H, E_V, M_H, or M_V mean that for the given mean (M) or eddy (E) contribution to the net tendency, either the vertical (V) or horizontal (H) part dominates there as indicated.

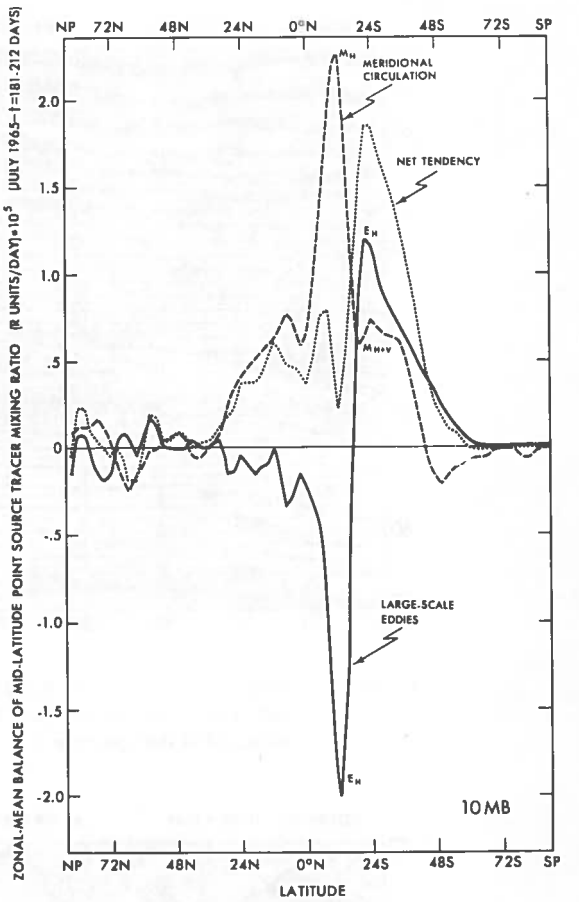

Figure 9. Mechanisms leading to changes in the zonal-mean mixing ratio (R units/day) for the mid-latitude point-source experiment as a function of latitude for July at 10 mb. (See Figure 8 for notation.)

In Figure 12 the zonal-mean balances for 940 mb in July are given. The figure shows a general, small negative net tendency. Much larger in magnitude is the $\overline{\text{"SINK"}}^{\lambda}$ term. In the Northern Hemisphere the $\overline{\text{"SINK"}}^{\lambda}$ is balanced largely by downward eddy flux. A considerable amount of tracer is transported equatorward through the subtropics by a reinforcing mean cell and eddies. In the intertropical convergence zone (about 10°N here) a large horizontal eddy flux convergence results, which is balanced by a combined horizontal and vertical mean-cell flux divergence and a strong local sink due to the large model-calculated precipitation there.

This experiment is still under way. A more detailed analysis of a number of aspects of the experimental behavior is in progress and will be discussed in more detail at some future date.

2. *Vertically Stratified Tracer*

This second experiment is not intended to exactly reproduce the behavior of any atmospheric trace constituent. Rather, it is designed to simulate the effect of the large-scale dynamics upon a tracer which should tend to be highly stratified in the vertical by virtue of a photochemically maintained source in the middle stratosphere and a sink at the ground. It may thus be

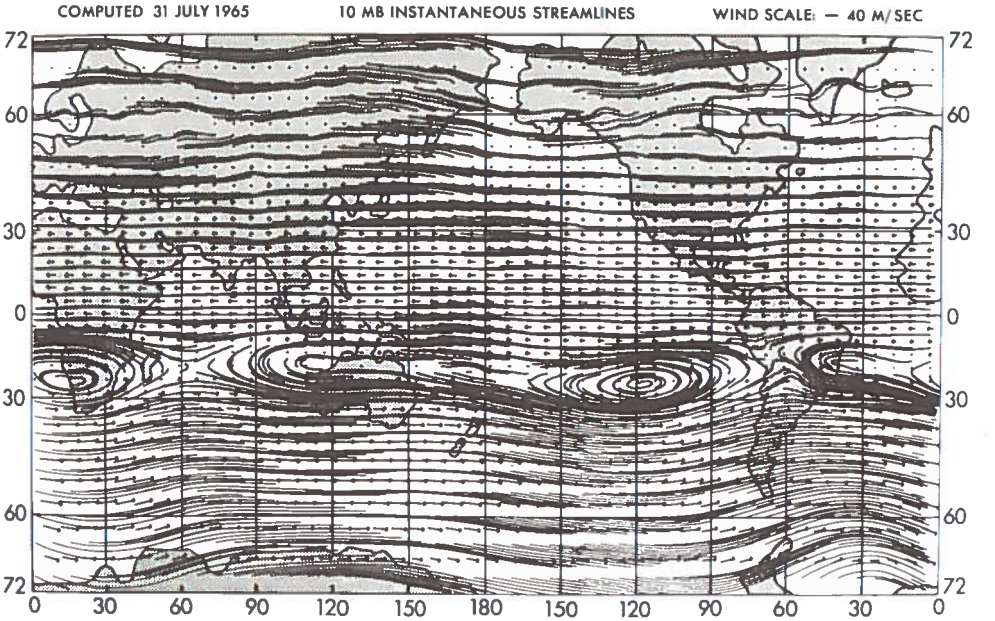

Figure 10. Mercator projection of calculated instantaneous streamlines for 10 mb at model date 31 July 1965. The arrows show local wind vectors with length proportional to speed as indicated at the upper right.

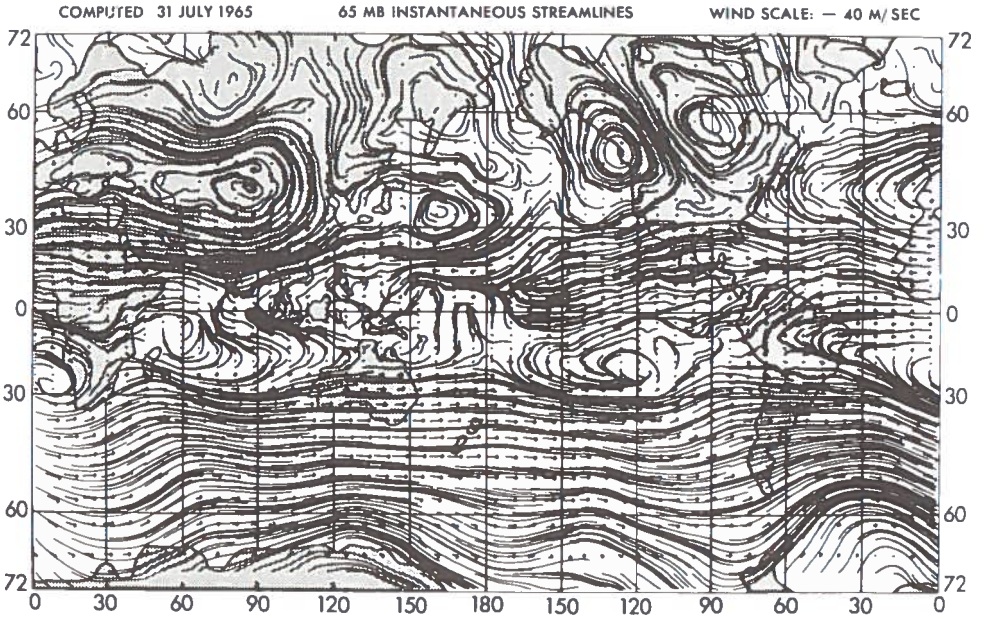

Figure 11. Mercator projection of calculated instantaneous streamlines for 65 mb at model date 31 July 1965. The arrows show local wind vectors with length proportional to speed as indicated at the upper right.

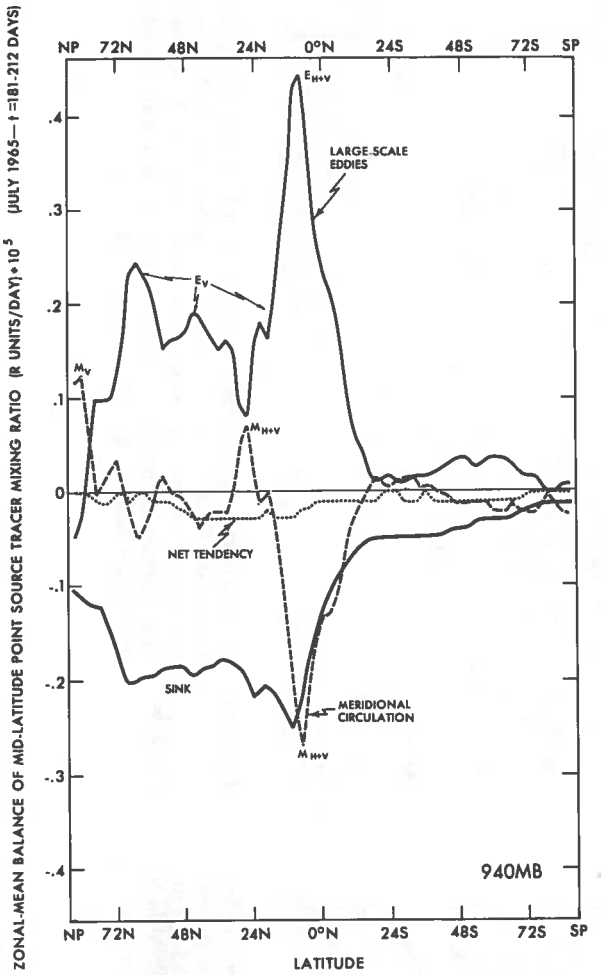

Figure 12. Mechanisms leading to changes in the zonal-mean mixing ratio (R units/day) for the mid-latitude point-source experiment as a function of latitude for July at 940 mb. (See Figure 8 for notation.)

thought of as being at least crudely similar to ozone.

The sink at the lower levels is modeled in exactly the same manner as in the previous experiment. The initial condition is specified according to the simple quadratic function

$$R(K) = \frac{(12-K)^2}{121}, \qquad (5)$$

where K is a model index ranging from 1 at the top sigma level to 11 at the lowest sigma level, next to the ground. This represents the value of the initial tracer at a given K level when $P_* = 1000$ mb. When P_* is not 1000 mb, the initial value is interpolated according to Eq. (5) so that initially *no* horizontal R gradients exist on isobaric surfaces.

The upper boundary condition is fixed at a constant value of 1.0 (the initial condition) for the entire length of the experiment. Physically, this may be pictured as a very rapid transition from an advection-dominated region to a photochemical-equilibrium region. The model-calculated flux of tracer out of or into this region is balanced exactly by a tracer source or sink. Thus, at the upper level the tracer may be physically thought of as damping back to its simple photochemical-equilibrium value (1.0) very rapidly after being disturbed by a vertical-transport process.

The model starting time for this experiment was August 1. The adjustment of the tracer to the initial condition is very rapid. Within 3 days the horizontal advection has the same magnitude as the vertical advection. A very large flux divergence of tracer (strongest in the tropics) takes place in the tropopause region. As a result, large amounts of tracer are transported to the lowest model levels and begin to be removed by the sink. Also, significant poleward gradients of zonal-mean tracer are beginning to form in the lower stratosphere. This can be seen in the zonal-mean cross-section for the month of August given in Figure 13. By November (see Figure 14) a distinct minimum in $\overline{R}^{\lambda}$ has appeared in the tropical troposphere near the intertropical convergence zone. The buildup in the higher latitudes relative to the tropics has continued. One interesting feature in Figure 14 is the appearance of a local maximum in $\overline{R}^{\lambda}$ at the equator at 38 mb. This appears to be related to a seemingly realistic equatorial-wave phenomenon which is simulated in the model stratosphere. Suffice it to say at this time that the maximum appears to be maintained by a convergence of a countergradient upward eddy tracer flux.

Some of the effects of the tracer's adjustment to both the seasonal transition and the initial condition can be seen in Figure 15. This figure shows the presence of negative tendencies in the tropical stratosphere and the entire troposphere for the month of November. On the other hand, higher latitudes of the Northern-Hemisphere stratosphere are experiencing positive net tendencies. The process continues into the winter season.

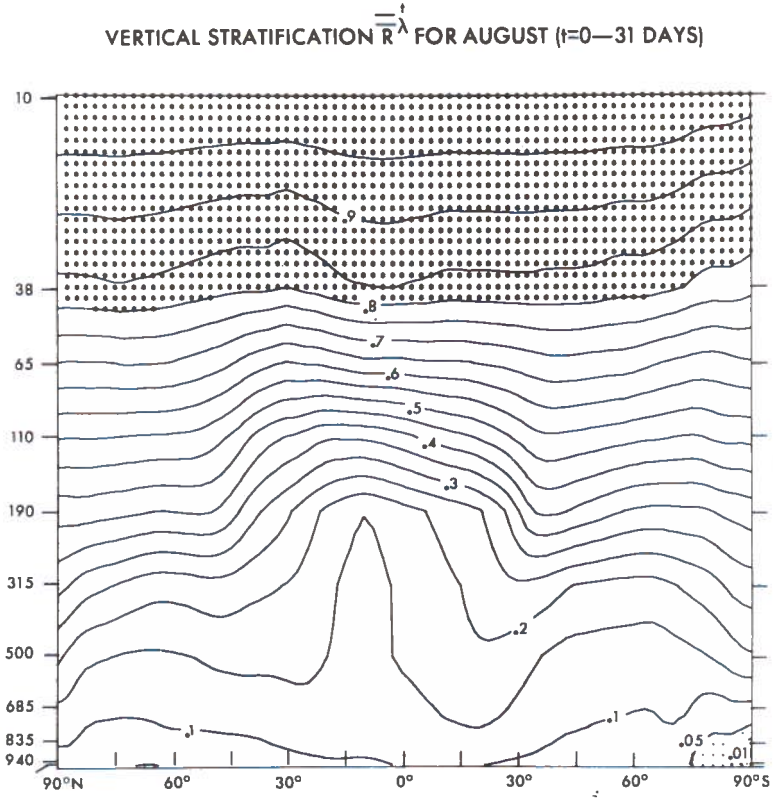

Figure 13. Latitude-height cross-section of zonally-averaged mixing ratio (arbitrary units) from the vertical-stratification experiment for August (first month of experiment). Linear contours are employed down to a value of .05. Below that, logarithmic contours are used. Values greater than .8 are shaded with stars; values less than .05 are shaded with dots.

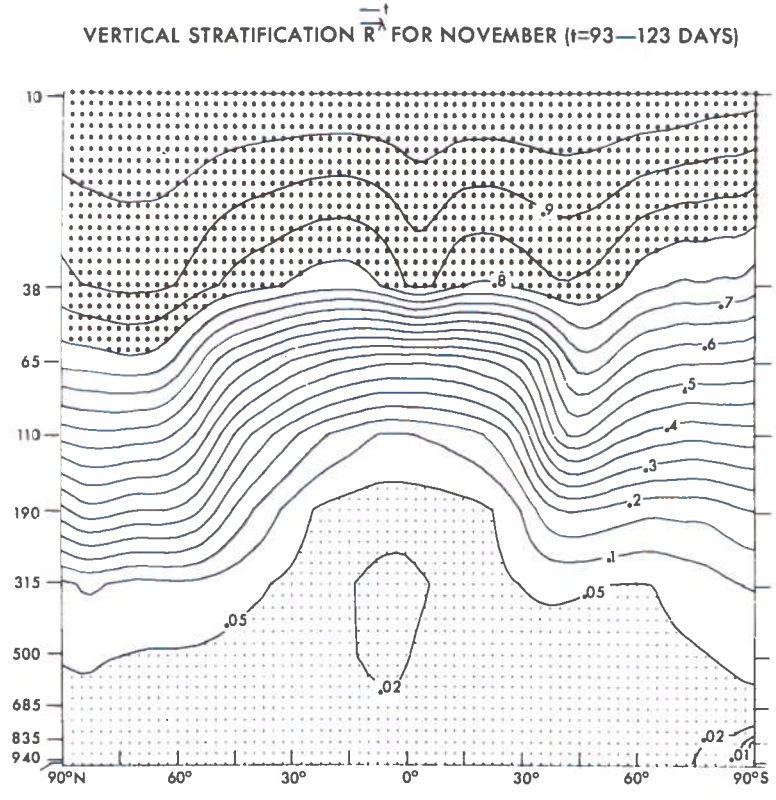

Figure 14. Latitude-height cross-section of zonally-averaged mixing ratio (arbitrary units) from the vertical-stratification experiment for November. Linear contours are employed down to a value of .05. Below that logarithmic contours are used. Values greater than .8 are shaded with stars; values less than .05 are shaded with dots.

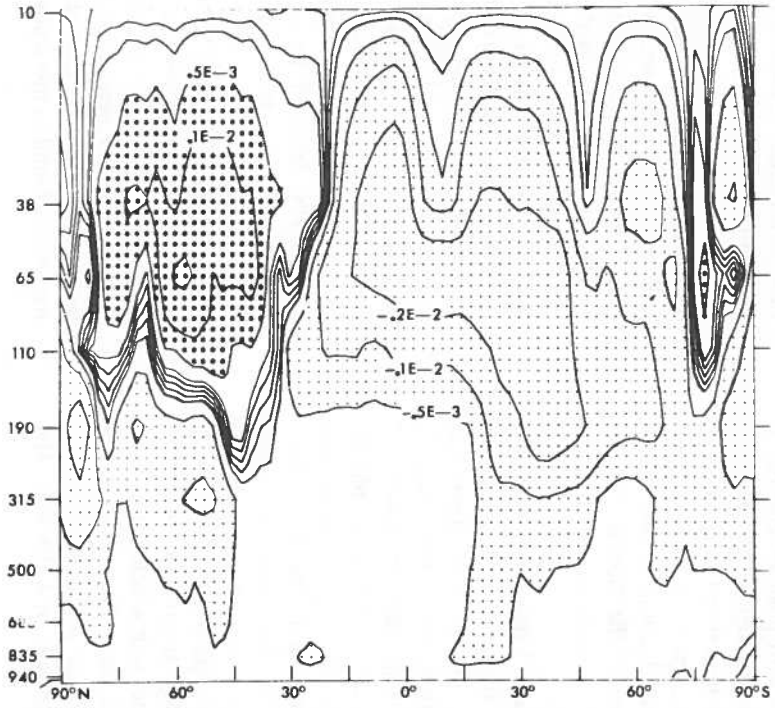

Figure 15. Latitude-height cross-section of the net tendency of the zonally-averaged mixing ratio from the vertical-stratification experiment for November (R units/day). Logarithmic contour intervals are employed as indicated. Values greater than .5 x 10^{-3} are shaded with stars; values less than -.5 x 10^{-3} are shaded with dots.

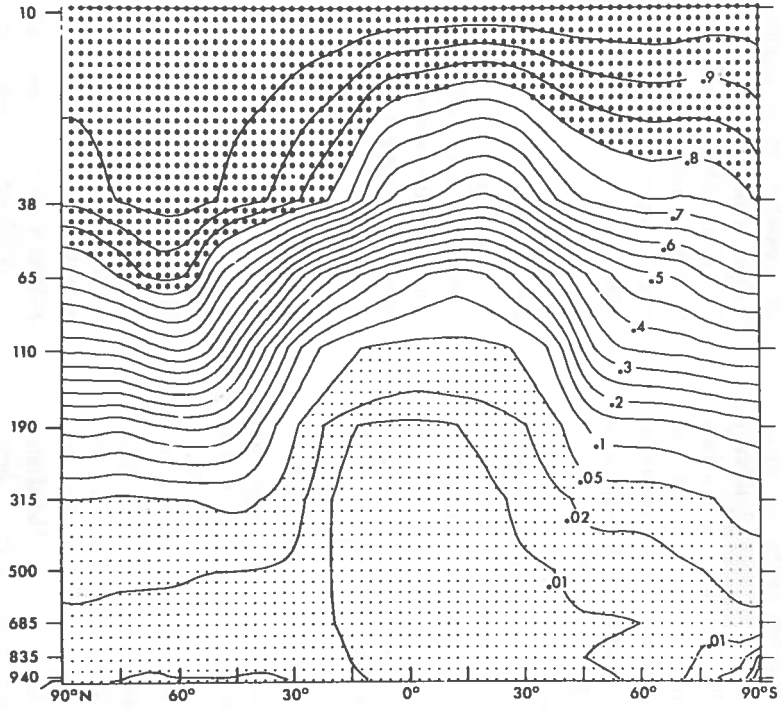

Figure 16. Latitude-height cross-section of zonally-averaged mixing ratio (arbitrary units) from the vertical-stratification experiment for February. Linear contours are employed down to a value of .05. Below that, logarithmic contours are used. Values greater than .8 are shaded with stars; values less than .05 are shaded with dots.

By February, the buildup in the Northern-Hemisphere stratosphere has led to a significant asymmetry between the two hemispheres (see Figure 16). Figure 16 also shows that the evacuation of the troposphere has progressed to such a point that there is almost a discontinuity in the vertical tracer gradient at the tropopause. Note that logarithmic contours are now necessary to resolve the tropospheric tracer structure relative to that of the stratosphere. For comparisons with the structure of ozone, see Hering [10] and Dütsch [11].

A rather typical view of the zonal-mean tracer balances of the Northern-Hemisphere mid-winter stratosphere for this experiment is given in Figure 17. Here, a significant hemispheric difference in the magnitude of the large-scale dynamic processes is shown. Contrary to some of the rather special behavior shown for the other experiment in Figures 8 and 9, the net tendency in the winter hemisphere is a rather small difference between very large opposing horizontal eddy-flux convergence and vertical advection by the mean meridional circulation. The degree of compensation between mean cell and eddies is so large that the linear correlation coefficient between them is -.98 for Figure 17. On the other hand, a small but significant positive tendency is formed in favor of eddies at highest latitudes, but in favor of the mean meridional circulation in mid-latitudes. It is this process which is producing the very gradual buildup of the model tracer in high latitudes of the Northern Hemisphere during winter, as typified by the net tendencies in Figure 15.

The zonal-mean tracer balance at 940 mb for January is given in Figure 18. A somewhat different structure is present here from that shown in Figure 12. Here, most of the tracer is supplied to the lower troposphere by downward eddy flux in mid-latitudes of both hemispheres. It is interesting to note that a significant amount of tracer is carried southward; this results from horizontal advection by the mean meridional circulation. Once it gets into the tropics, it is inserted into the intertropical convergence zone by convergence of eddy tracer flux. It is then balanced by a large local sink which results from the larger precipitation there. Note that in this figure the essential balance is that between the total dynamical mechanisms and the sink. The sink exhibits three separate peaks. The mid-latitude sinks are balanced directly by downward flux from above, while the tropical sink is kept large by horizontal transport from higher latitudes. Figure 18 shows the presence of a rather consistent negative net tendency at all latitudes. This is because the tracer amount has not quite reached a quasi-equilibrium value at this stage of the experiment.

This experiment is also still in progress. More complete results will be presented later when both the integration and the analysis of results have been completed.

SUMMARY

Preliminary results from two separate three-dimensional tracer experiments are presented. The first experiment shows results similar in many respects to the behavior of radioactive debris from Chinese bomb tests. The second experiment shows structure which is closely analogous to that of atmospheric ozone.

Analyses of various balances for most cases show that in the regions devoid of sources and sinks a strong compensation exists between the flux convergences caused by the mean meridional circulation and those produced by the large-scale eddies. However, very important exceptions occur during seasonal transitions of the large-scale circulation in the stratosphere. Such periods show significant decoupling of the more usual compensation between the meridional circulation and the eddies, thus allowing strong changes in the tracer distributions during such times.

The largest transport of tracer from the stratosphere into the troposphere for both experiments occurs in mid-latitudes, where a significant portion is removed locally. The remaining tracer is then transported predominantly equatorward by both mean and eddy processes, where it is finally removed by a strong sink in the intertropical convergence zone.

The results of these experiments are qualitatively similar to those of Hunt and Manabe [5]. Those experiments showed the strong compensations between meridional circulation and eddy transports found here. However, the significant decoupling of this compensation during seasonal transitions found in this study could not occur in

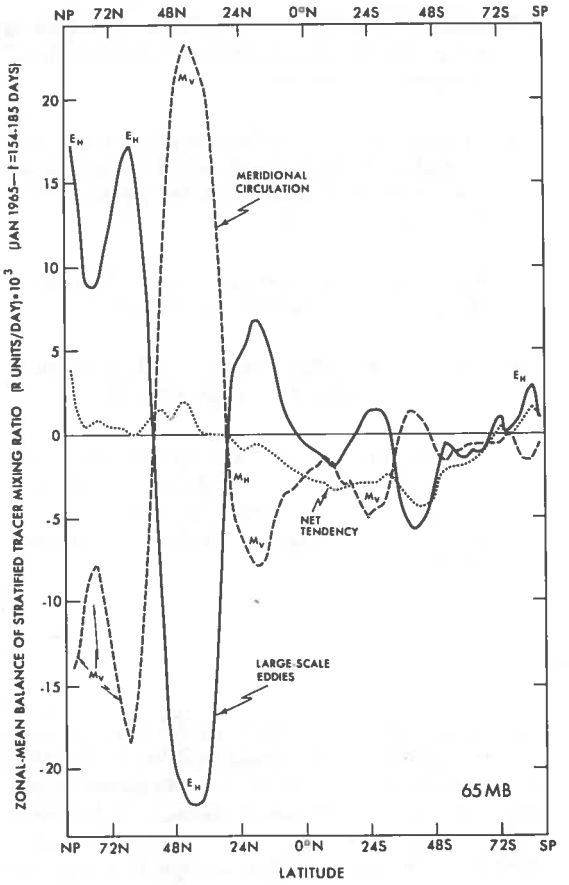

Figure 17. Mechanisms leading to changes in the zonal-mean mixing ratio (R units/day) for the vertical-stratification experiment as a function of latitude for February at 65 mb. (See Figure 8 for notation.)

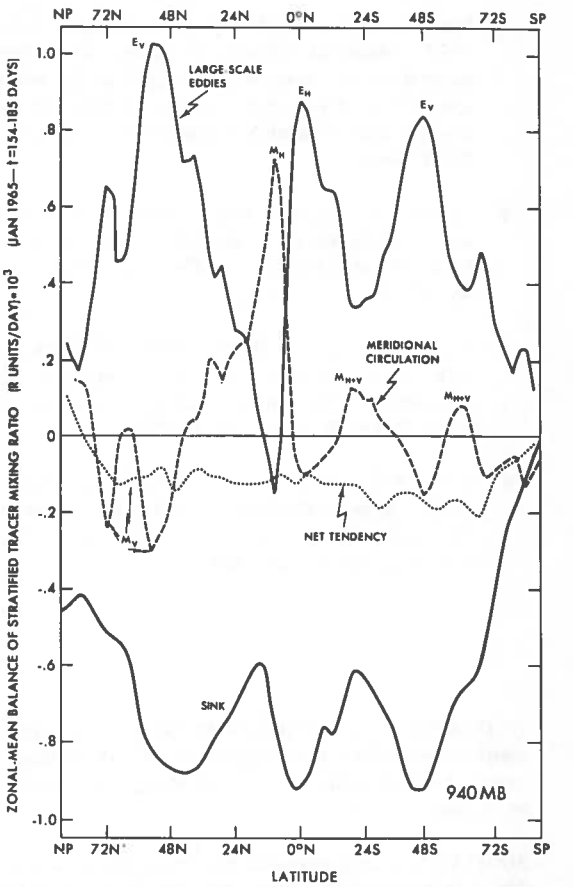

Figure 18. Mechanisms leading to changes in the zonal-mean mixing ratio (R units/day) for the vertical-stratification experiment as a function of latitude for February at 940 mb. (See Figure 8 for notation.)

that previous experiment because of the lack of seasonal variation in that model.

ACKNOWLEDGMENTS

The author is particularly grateful to W.J. Moxim, without whose invaluable assistance this project could not have been completed, and to Dr. S. Manabe, who formulated the original concept, designed the general-circulation model, and contributed many hours of valuable discussion.

In a project of this scope, one is dependent upon a successful interaction with a large number of persons. The results given here depend to a great extent upon the support given by the administration, technical staff, systems analysts, and computer operators, and the numerous technical discussions with colleagues at GFDL.

A portion of this work was supported by the Division of Biology and Medicine, U.S. Atomic Energy Commission.

REFERENCES

1. Mahlman, J.D., and S. Manabe, 1972: "Numerical simulation of the stratosphere: Implications for related climate change problems," in *Proceedings of the Survey Conference*, Feb. 15-16, 1972, Climatic Impact Assessment Program (A.E. Barrington, Editor), U.S. Department of Transportation (DOT-TSC-OST-72-13), 186-193.

2. Holloway, J.L., and S. Manabe, 1971: "Simulation of climate by a global general circulation model. I. Hydrologic cycle and heat balance," Mon. Wea. Rev. *99*, 335-370.

3. Manabe, S., J.L. Holloway, Jr., and D.G. Hahn, 1972: "Seasonal variation of climate in a time-integration of a mathematical model of the atmosphere," in *Proceedings of the Symposium of Physical and Dynamical Climatology* (Leningrad), WMO, Geneva.

4. Manabe, S., and B.G. Hunt, 1968: "Experiments with a stratospheric general-circulation model. I: Radiative and dynamic effects," Mon. Wea. Rev. *96*, 477-502.

5. Hunt, B.G., and S. Manabe, 1968: "Experiments with a stratospheric general circulation model. II. Large-scale diffusion of tracers in the stratosphere," Mon. Wea. Rev. *96*, 503-539.

6. Hunt, B.G., 1969: "Experiments with a stratospheric general circulation model. III. Large-scale diffusion of ozone including photochemistry," Mon. Wea. Rev. *97*, 287-306.

7. Phillips, N.A., 1957: "A coordinate system having some special advantages for numerical forecasting," J. Meteor. *14*, 184-185.

8. Kurihara, Y., and J.L. Holloway, Jr., 1967: "Numerical integration of a nine-level primitive equations model formulated by the box method," Mon. Wea. Rev. *95*, 509-530.

9. Machta, L. and K. Telegadas, 1972: "Examples of stratospheric transport," in this volume.

10. Hering, W.S., 1966: "Ozone and atmospheric transport processes," Tellus *28*, 329-336.

11. Dütsch, H.U., 1969: "Atmospheric ozone and ultraviolet radiation," in Climate of the Free Atmosphere, *World Survey of Climatology*, D.F. Rex (editor), Elsevier Publishing Company, 383-432.

DISCUSSION

ANDERSON: You find in your stratified tracer experiment a distribution that happens to be very similar to ozone. Logically, this says nothing about ozone's being inert, does it?

MAHLMAN: I didn't say that the ozone would be inert. My interpretation is rather that the mechanisms for shaping the observed structure of the lower stratosphere must be essentially of a dynamic nature. The quantitative details can be highly dependent upon photochemistry.

ANDERSON: I don't see how you can draw that conclusion. The correlation between your experiment and observed ozone could be strictly academic.

MAHLMAN: I am just saying that the observed distributions of ozone must necessarily be changed by stratospheric transport processes, and my experiment indicates that the simulated model dynamics can accomplish that.

ZIMMERMAN: In what way is the experiment set-up you describe here similar to or different from the GFDL experiments of Hunt?

MAHLMAN: There are some important differences. Hunt's experiment was performed concurrently with the general-circulation model as an extra variable, although the tracer had no effect on the model dynamics. The experiments described here are run independently of the general-circulation model integration, by using specially-prepared model-generated data tapes. The general-circulation model used for Hunt's experiments was somewhat simpler in structure. First, the domain was hemispheric rather than global. The incoming radiation was fixed at the annual mean value rather than marching through the seasons as in the present experiment. Water vapor was not included as a dependent variable, and no mountains were included at the lower boundary. The current model contains both effects.

PHILLIPS: In the vertical-stratification experiment, I was impressed with the slope of the mixing-ratio lines. In the first experiment, I thought I detected a buildup of tracer in the winter lower stratosphere to a spring maximum. However, I don't recall seeing the decrease from the spring maximum to the fall minimum in either experiment. On any graph of the seasonal variation of total ozone, the decrease from April to October is just as impressive as the buildup from October to April.

MAHLMAN: Actually, neither integration has proceeded far enough to be able to apply such a check. I agree that this is a feature of the behavior of ozone which provides a valid test for the model, both in the lower stratosphere and at the ground.

PHILLIPS: I think this might be an important point with respect to the conservation of ozone in the lower stratosphere. Photochemical losses may also be necessary to reduce the spring maximum to a fall minimum.

MAHLMAN: That is possible. However, you must consider that the fall minimum in radioactivity in the lower stratosphere and at the ground is just as pronounced. Clearly, no photochemistry is involved in that process.

BELMONT: Did you include the quasi-biennial oscillation in your computation?

MAHLMAN: The quasi-biennial oscillation is a process which cannot be "added" to such a calculation; it is a phenomenon which must appear naturally out of the governing physics of the model. This model does not simulate it. I am afraid that there is little hope of simulating it with the present vertical resolution. Your question is valid, however, because the features of ozone which relate to the quasi-biennial oscillation cannot be simulated in these experiments.

Unscheduled papers were presented by Dr. Chang and Dr. Johnston because of their direct relevance to some of the areas of CIAP's investigation. Both papers consider the recent report "Stratospheric Nitric Oxide Production from Past Nuclear Explosions and its Relevance to Projected SST Pollution", by H.M. Foley and M.A. Ruderman. Dr. Ruderman was unable to attend the presentations, but has supplied a reply to the papers at the editor's request.

COMMENTS ON THE POSSIBLE EFFECT OF NO_x INJECTION INTO THE STRATOSPHERE BY ATMOSPHERIC NUCLEAR WEAPONS TESTS

JULIUS S. CHANG
Lawrence Livermore Laboratory
University of California
Livermore, California

Recently it has been pointed out [1,2] that the atmospheric nuclear-weapons tests in the 50's and early 60's injected significant amounts of NO_x into the stratosphere. Therefore the same authors suggested that past ozone measurements be examined to determine whether the hypothesized NO_x catalytic cycle [3,4] had produced a detectable effect on stratospheric ozone content. From such an examination it was claimed that past ozone data showed "no evidence of ozone decrease in the months following the test explosions" (Reference 1, page 15). We believe that interpretation of this result as invalidation of the NO_x catalytic destruction of O_3 is premature and unjustified. We feel that Foley and Ruderman were misled by several often-misquoted numbers, and were too simplistic in their consideration of the physical process involved. Finally, these unfortunate errors were compounded by their very cursory examination of the available ozone data.

We shall not go into the details of the NO production rate from nuclear weapons. It is sufficient to note that the total yield estimate as given by Foley and Ruderman is really an upper bound, and that the net NO production per explosion should be reduced from their overestimate by a factor of between 2 and 10 [5]. Even accepting the numbers from [1] one should first establish the effects to be expected in the O_3 distribution, and then seek corroboration or refutation in the observational data. Foley and Ruderman failed to make clear the type and magnitude of change in O_3 they expected to find, and yet they concluded they did not see a change. One may assume that they used the *estimates* of [3] as their basis for comparison, since these are the most widely circulated. But a careful reading of [3] will reveal that the estimated NO_x catalytic effect on O_3 ranges from 3% to 50% reduction, depending on the equilibrium (fixed) NO distribution *and* concentration (Reference 3, pages 87-92). It should be pointed out that these results are steady-state calculations, i.e., made after the system has fully reacted. The highly important downward transport of O_3 from the chemically active upper stratosphere has been neglected completely. This is a crucial omission, in that the highly perturbed O_3 profiles in [3] are not in dynamic equilibrium. Indeed, the fact that dynamic interaction between the transport mechanism and chemical kinetics results in a large reduction in the observable effect of the NO_x catalytic process has already been pointed out [6]. One should also recognize the differences between the solutions calculated from continuous injection of NO due to SST's and those computed from the "delta function" injections of nuclear tests. In the former case a steady-state calculation is possible, while in the latter case one *must* deal with a time-dependent problem. Foley and Ruderman seem to have treated none of these considerations. This may have led them to expect an unrealistically large perturbation in the O_3 observations.

We have made some preliminary computations with a one-dimensional model combining diffusion and the NO_x catalytic cycle. These indicated that the maximum reduction in O_3 would occur approximately 250 days after NO injection, and would amount to <15% reduction in total O_3. If these effects of the NO injection are valid, one would not expect the cursory examination of the O_3 observations reported by Foley and Ruderman to have detected them. They reported no analysis of the O_3 data other than a visual examination of the reproduced curves of total O_3 at selected stations. Superpositions of O_3 annual curves (traced from [1]) for 1960-1964 for the stations reported by Foley and Ruderman appear in Figure 1. These make it clear that year-to-year random variations in mean monthly total O_3 are of the order of 10-20%. Yet for Kodaikanal and Marcus Island, Foley and Ruderman claimed "Even a five percent effect would be apparent in this very reproducible data" (Reference 1, page 16). (In fact, the diameter of their plotted data points exceeded 5% of the mean ordinate values.)

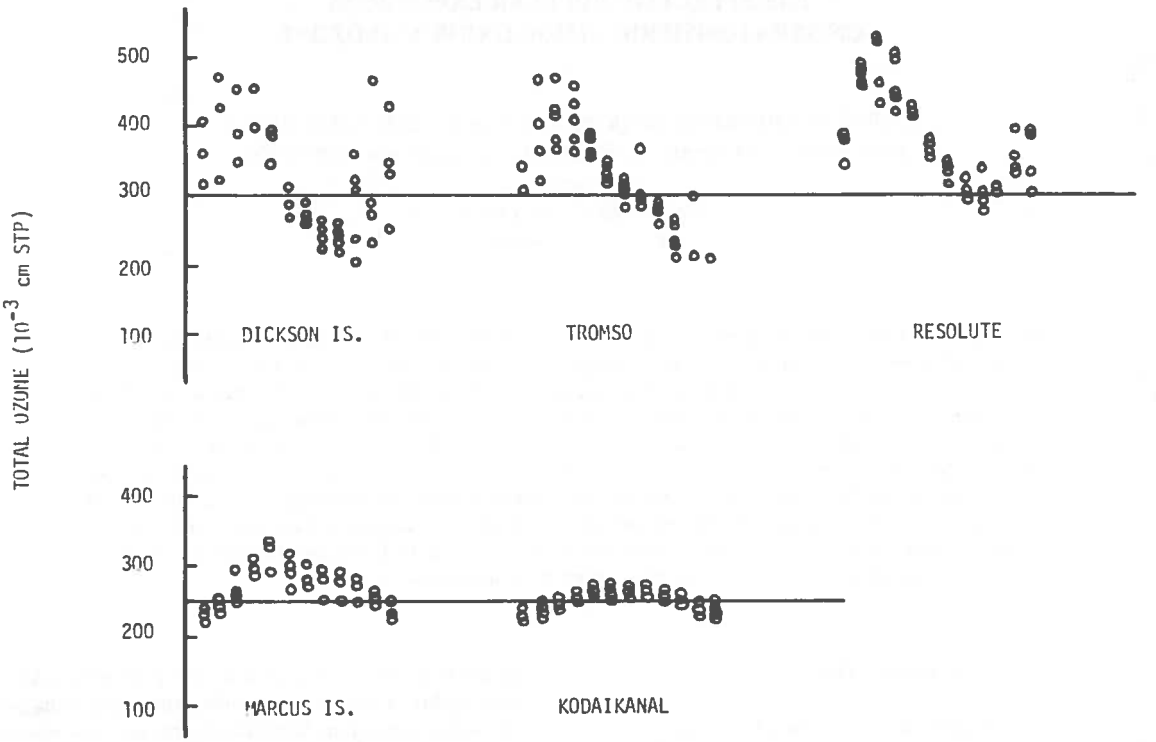

Figure 1. Five-year superposition of monthly ozone measurements (1960-1964).

We feel at present that the Foley and Ruderman study [1] is very inconclusive. It does not establish that NO injected into the stratosphere by nuclear weapons tests had no detectable effect on O_3 observations. We urge that a more careful study be carried out.

ACKNOWLEDGMENT

This work was in part performed under the auspices of the U.S. Atomic Energy Commission, and in part supported by the Climatic Impact Assessment Program, U.S. Department of Transportation.

REFERENCES

1. Foley, H.M. and M.A. Ruderman, "Stratospheric Nitric Oxide Production from Past Nuclear Explosions and its Relevance to Projected SST Pollution," JASON paper P894, Institute for Defense Analyses, 400 Army-Navy Drive, Arlington, Va. 22202 (1972).

2. Stein, K.J., "Ozone appears unaltered by NO", Aviation Week and Space Technology, November 6, 1972, page 28.

3. Johnston, H., "Catalytic reduction of stratospheric ozone by nitrogen oxides", Lawrence Berkeley Laboratory Report UCRL-20568, Berkeley, California (June 1971).

4. Crutzen, P.J., "On some photochemical and meteorological factors determining the distribution of ozone in the stratosphere: effects of contamination by NO_x emitted from aircraft", Report AP-6, Institute of Meteorology, University of Stockholm (October 1971).

5. Private communication from H. Johnston.

6. Chang, J.S., in "Summary Proceedings of the CIAP Joint Atmospheric Modeling and Chemical Dynamics Workshop," ed. R. Greenstone and R. Underwood, Report No. DOT-TST-90-2 (November 1972), p. 3-15.

THE EFFECT OF NUCLEAR EXPLOSIONS ON STRATOSPHERIC NITRIC OXIDE AND OZONE

HAROLD JOHNSTON, GARRY WHITTEN, AND JOHN BIRKS
Department of Chemistry, University of California at Berkeley
and
Lawrence Berkeley Laboratory
Berkeley, California

ABSTRACT: Foley and Ruderman have proposed that atmospheric nuclear-bomb tests have introduced significant quantities of nitric oxide into the stratosphere. To further explore this hypothesis, we have carried out a detailed examination of the total-ozone data for the world. These data appear to show a statistically significant decrease of stratospheric ozone during the period of intense nuclear-bomb testing, 1960-62, and a larger, statistically significant increase of total ozone, 1963-70, after cessation of large-scale atmospheric nuclear testing. Although these trends may have other explanations, their location and timing are consistent with the distribution of carbon-14 and strontium-90 in the stratosphere. The magnitude of the ozone decreases and increases, about 5%, is consistent with what one might expect from injections according to Foley and Ruderman's model, if consideration is given to the uncertainty with which those quantities are known.

INTRODUCTION

Foley and Ruderman [1] examined the question of the formation of nitric oxide from the air heated by nuclear explosions during the period of large-scale atmospheric testing, 1952-1962. They evaluated the upper limit of the rate of NO injection into the stratosphere and compared it to the rate of production of NO by supersonic transports (SST's).

They considered data from 29 ozone-observing stations, including graphs (their Figures 4 and 5) pertaining to 300 monthly averages, and a short table (their Table 6) averaging 216 monthly-average data points from *Ozone Data for the World* [2] (1960-70). They said that "large catalytic ozone reduction from such NO injection was not observed". However, the total set of *Ozone Data for the World* (ODW) involves over 90 different stations, over 8000 monthly averages, and over 178,000 observation-days. In this report we utilize all of these data, and we find a statistically significant decrease of global ozone in the period 1960-62 and a larger, statistically significant increase in ozone over the period 1963-70, after bomb tests stopped in 1962. The location and timing of these changes are consistent with the stratospheric distribution of strontium-90 and carbon-14, products of nuclear explosions. Of course, changes in atmospheric quantities can arise from many sources, and there may be other causes for these decreases and increases of ozone.

The calculation by Foley and Ruderman is carried out to one significant figure, neglecting a 15 percent term, taking γ to be 1.4 for air at 2000°K whereas it is 1.3, and rounding up to the next whole number. These approximations cause their final formula for the number of molecules of NO to be a factor of 2 too high. As they explain, uncertainty about the detailed mechanism of the entrainment-cooling of the rising fireball gives an uncertainty of a factor of 6 in the final result. All of their yields of nitric oxide employ the upper limit, and the values quoted are between a factor of 2 and a factor of 12 too high. The observed decrease in ozone (1960-62) and later increase (1963-70) are of about the magnitude that would be expected from a mid-value within the uncertainty in Foley and Ruderman's calculation.

This article reviews what we regard as the error in Foley and Ruderman's thermodynamic data, the uncertainty arising from the detailed chemical kinetics of forming nitric oxide in the fireball, and a consideration of possible short-term and long-term changes in ozone from nuclear explosions.

THERMODYNAMICS

Foley and Ruderman assumed that one-third of the energy of nuclear bombs went to heat air to 2000°K; they implicitly assumed that the temperature was held at 2000°K long enough (tens of seconds) to attain equilibrium for nitric-oxide formation

$$N_2 + O_2 \rightleftharpoons 2NO$$

They neglected adiabatic cooling of the fireball, since it was merely 15 percent of the cooling process. The number of nitric-oxide molecules formed from nuclear bombs was found by combining their Equations 2, 3, and 4 to give

$$N_{NO} = \frac{\left(\frac{4}{3} \times 10^{22}\, y_{MT}\right)(8 \times 10^{-3})(\gamma - 1)}{(1.38 \times 10^{-16})(2000)}$$

$$= 3.86 \times 10^{32}\, y_{MT}\,(\gamma - 1)$$

They took γ to be 1.4, so that $\gamma-1$ is 0.4, and the number of nitric-oxide molecules is $1.55 \times 10^{32}\, y_{MT}$, which they rounded up to 2 to give Equation 5

$$N_{NO} = 2 \times 10^{32}\, y_{MT}$$

The quantity γ is the ratio of heat capacity at constant pressure C_P to the heat capacity at constant volume C_v, which is C_P minus the gas constant R. According to the JANAF tables [3], the heat capacities of nitrogen and oxygen at 2000°K are

	C_P	C_v	γ
N_2	8.601	6.614	1.300
O_2	9.029	7.042	1.282
Average for air			1.295

The value of γ is 1.30, not 1.40. This might be a small matter, except for the rounding-up process. With γ = 1.30, the number of nitric-oxide molecules produced is

$$N_{NO} = 3.86 \times 10^{32}\, y_{MT}\,(0.30)$$
$$= 1.16 \times 10^{32}\, y_{MT}$$

If the 15% effect of adiabatic cooling is acknowledged, this number is reduced to $1.01 \times 10^{32}\, y_{MT}$, which is a factor of 2 less than Foley and Ruderman's figure. Thus it is necessary to rewrite their Equation 5 as

$$N_{NO} = 1.0 \times 10^{32}\, y_{MT}$$

A better method of calculating the energy required to heat air to 2000°K involves the integral of the heat capacity at constant pressure between 298° and 2000°K. Tabulated values of $H^0_T - H^0_{298}$ make this calculation easy to carry out. For air, the average value of $H^0_{2000} - H^0_{298}$ is 13.56 kcal mole^{-1}. Glasstone [4] gives the energy of a nuclear bomb as

$$E_{total} = 10^{12}\ \text{kcal}\ y_{MT}$$

If one-third goes to form hot air, its value is

$$E_{HA} = 33 \times 10^{10}\ \text{kcal}\ y_{MT}$$

If there is a 15% cooling by adiabatic expansion of the rising fireball, the residual energy is

$$E'_{HA} = 28.4 \times 10^{10}\ \text{kcal}\ y_{MT}$$

Dividing this energy by the enthalpy function for air at 2000°K, one finds

$$\text{moles of hot air} = 2.09 \times 10^{10}\, y_{MT}$$

$$\text{molecules of hot air} = 12.6 \times 10^{33}\, y_{MT}$$

$$\text{molecules of NO at 0.8\%} = 1.01 \times 10^{32}\, y_{MT} = N_{NO}$$

CHEMICAL KINETICS

The initial nuclear explosion is at temperatures far above 10^{5}°K, and the blackbody emission of radiation is largely in the region of soft X-rays, which are strongly absorbed by air to produce high temperatures. The fireball grows by emission and absorption of short-wavelength radiation, and it cools by emission of radiation transparent to air, of wavelength longer than about 185 nm. Within a few seconds a strong shock wave has carried away about one-third of the bomb energy, and radiation transmitted by air has carried away another one-third of the energy. The residual fireball, at an average temperature of about 6000°K, contains one-third of the energy, largely as dissociated oxygen and as thermal energies of the molecules and atoms; there are also about 1% nitric oxide and smaller quantities of nitrogen atoms, ions, and electrons. This residual fireball undergoes further cooling by rising and mixing with low-temperature ambient air.

There are two mechanisms whereby nitric oxide is formed from hot air. If air is held at a high temperature long enough for it to attain chemical equilibrium and is then cooled down, there will come a point at which the cooling rate is faster than the nitric-oxide relaxation rate, and at that temperature the equilibrium concentration of nitric oxide will be "frozen in". This mechanism applies to internal-combustion automobile engines, to the furnaces of power plants, and to the fireball at 6000°K which later rises, mixes, and cools. The volume of air in the original 6000°K fireball is sure to have a frozen-in nitric-oxide concentration corresponding to that at about 2000°K, regardless of the mechanism of cooling, if the time of cooling is a matter of about 10 seconds. The amount of nitric oxide formed changes slowly with freeze-out temperature, as Foley and Ruderman pointed out, and thus it is relatively insensitive to the cooling rate and cooling mechanism.

The other mechanism involves heating cold air up to a high temperature for a time short compared to attainment of chemical equilibrium with nitric oxide, and then cooling it to a lower temperature. This mechanism operates in jet aircraft engines, where chemical equilibrium is not reached. This mechanism also operates in the coolant air entrained into the rising fireball following a nuclear explosion. The amount of nitric oxide produced is kinetically controlled by a process with a very high activation energy, and it is enormously sensitive to the precise history of temperature and time. A sample of gas heated to 2000°K and cooled to 1900°K within a second would form very little nitric oxide. A sample of gas heated up to 1500°K while it cooled a portion of the original fireball would form no additional nitric oxide beyond the frozen-equilibrium amount in the original fireball. The first sample of gas entrained in the 6000°K fireball might very well attain chemical equilibrium above 2000°K, but a sample of gas entrained by the 3000°K fireball probably never attains 2000°K. A jet of hot air injected into the surrounding cold air could be cooled below

2000° K without any coolant air's attaining a temperature high enough to form additional NO. The situation will be the same if 6000°K air is rapidly mixed with a six-fold or more excess of coolant air. Foley and Ruderman assumed that the maximum possible amount of entrained air that could be heated to 2000° K was indeed brought to that temperature and held there or higher long enough to attain chemical equilibrium. This model produces five times as much nitric oxide in the entrained coolant air as in the air of the original fireball. They acknowledge that this effect creates a factor-of-6 uncertainty in the amount of nitric oxide formed by nuclear bombs (the paragraph after their equation 5).

Thermodynamics requires Foley and Ruderman's estimate of the NO production from nuclear bombs to be reduced by a factor of 2.0. The chemical kinetics of the detailed temperature history of the mixing process in the rising fireball gives a further factor-of-6 uncertainty in Foley and Ruderman's estimate. Their Equation 5 should read

$$N_{NO} \approx (0.17 - 1.0) \times 10^{32}\, y_{MT}$$

In addition, another factor acts to reduce the amount of NO_x introduced into the stratosphere by nuclear bombs. The rising bomb cloud, containing entrained moist tropospheric air, eventually cools to stratospheric temperatures. In general the bomb cloud acts like a thunderstorm cloud; copious quantities of water condense out, and much of it precipitates out of the lower stratosphere back into the troposphere. The oxides of nitrogen, especially NO_2, coprecipitated NO and NO_2, and HNO_3, are highly soluble in water and would be washed out of the stratosphere to some extent. Surface-level bomb tests mix large quantities of soil or water with the bomb cloud, and such material should also remove some oxides of nitrogen from the bomb cloud.

SHORT-TERM LOCAL EFFECTS

Foley and Ruderman give equations for calculating the expected height and size of the cloud following nuclear-bomb tests. At 30 minutes after detonation, the cloud sizes for 0.5, 5.0, and 50 megaton (MT) explosions are as indicated by Figure 1, which includes a standard ozone profile at 45° latitude. The overlap of the ozone profile and the stabilized bomb cloud is strongly dependent on the yield of the bomb. For a standard ozone profile at the equator, this overlap is indicated by cross-hatching in Figure 2. A bomb of 0.2 MT remains essentially within the tropical troposphere. A 1-MT bomb overlaps the ozone profile in the lower stratosphere, but it does not reach the level of maximum ozone concentration. A 10-MT bomb overlaps the maximum ozone. A 58-MT bomb, on the other hand, goes far above the ozone maximum, and it overlaps only a relatively small band of ozone. Table 1 gives the percentage of ozone vertical columns overlapped by bombs of various sizes. For short-term effects in the equatorial band, the maximum ozone reduction should result from a 10-MT bomb, for which a 65% overlap of

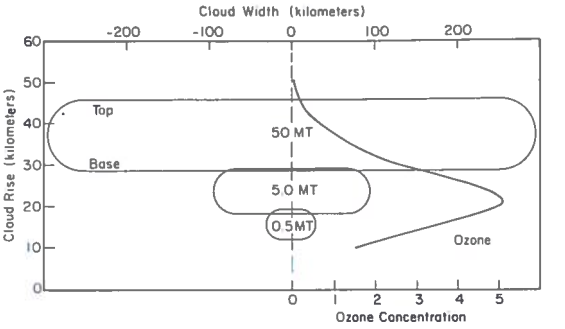

Figure 1. Elevation and dimensions of nuclear-bomb clouds 30 minutes after detonation, according to formulas by Foley and Ruderman [1]. A standard ozone profile at 45° latitude is shown.

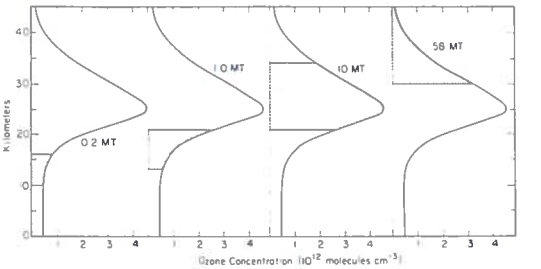

Figure 2. Overlap of standard tropical ozone profile with bomb clouds 30 minutes after detonation.

the ozone column is indicated. Considering the finite rate of the catalytic destruction of ozone by NO_x, one could expect approximately a 30 to 50% reduction of ozone within the bomb cloud during the first week or two of its existence. The effect would be less for both larger and smaller bombs.

As the fireball cooled by radiation emission, the radiation between 185 and 242 nm would dissociate oxygen to make ozone in a broad region surrounding the point of detonation. For bombs fired well above the ground, this mechanism would form some ozone directly in the stratosphere, and for large bombs the artificial ozone layer would lie under the stabilized cloud. This layer of ozone would act to invalidate the information obtained on the ground directly under a bomb cloud during its first few days of existence. We carried out a numerical integration of the distribution of radiation from the cooling fireball of a 20-kT bomb, and the energy emitted as radiation between 186 and 242 nm was about 1% of the total energy of the bomb. We assume that this quantity scales linearly with bomb yield. In that case, the amount of ozone generated from ultraviolet radiation in the Herzberg continuum would be

$$N_{ozone} \approx 3 \times 10^{31}\, y_{MT}$$

Table 1. Percent Overlap of Vertical Ozone Columns by Nuclear-Bomb Clouds of Various Sizes

		Bomb Yield (MT)								
Latitude	Season	0.2	0.5	1	2	5	10	20	30	58
0°	Spring	5	8	12	25	52	65	60	50	31
45°	Spring	16	25	33	41	46	42	33	27	16
45°	Fall	9	18	26	39	52	62	43	35	21
75°	Spring	26	37	44	47	41	30	28	16	10
75°	Fall	24	35	41	43	40	32	25	20	13

Thus about one-third as many molecules of ozone are produced as the kinetically-possible upper-limit estimate of nitric-oxide production. This ozone would not make a significant contribution to the total global amount, but it is 40 percent of the ozone column subtended by a 30-minute-old bomb cloud.

The principal USSR atmospheric tests were at Novaya Zemlya at 75°N. The largest tests were in late fall and winter, so there was little or no sunlight to support the photochemical reactions that destroy ozone. Ozone in the polar regions is formed in tropical and temperate zones and brought there by transport. Thus the ozone reductions from the big USSR tests are expected to be delayed until high-elevation NO has time to be moved into the temperate zones and the ozone formed there moved back to the polar regions at a lower elevation.

The size of a 30-minute-old bomb cloud is only about 10^{-4} the area of the earth. Thus the chance of a given ozone station's observing a young cloud is small. The ozone collar photochemically produced by the bomb itself would confuse the information anyway. Winds would shear the bomb cloud and move sheets of it in different directions at different elevations. Once the cloud has been sheared and spread around the world at one latitude, the concentration of NO is reduced so much that the effect of NO reduction of ozone is slow (months). Thus one should look for long-term global effects of the nuclear-bomb tests on stratospheric ozone, not for short-term local effects.

LONG-TERM GLOBAL EFFECTS

At a given total-ozone observing station, there is a substantial variation from day to day, as illustrated by data from Aspendale, Australia in Figure 3. There are systematic, rather-well-understood annual trends with a peak in the spring and a minimum in the fall, illustrated for the southern hemisphere by data from Aspendale in Figure 3 and illustrated for the northern hemisphere by data from Messina and Moscow in Figure 4. With the day-to-day fluctuations and the large seasonal cycle, it is difficult to detect a systematic trend in total ozone at any one station or on a global basis. Pittock [5] analyzed the detailed data at Aspendale, and by using the two-sided Student's t-test he calculated how many years (N) of observation would be required to establish or disprove (at the 95% confidence level) the occurrence

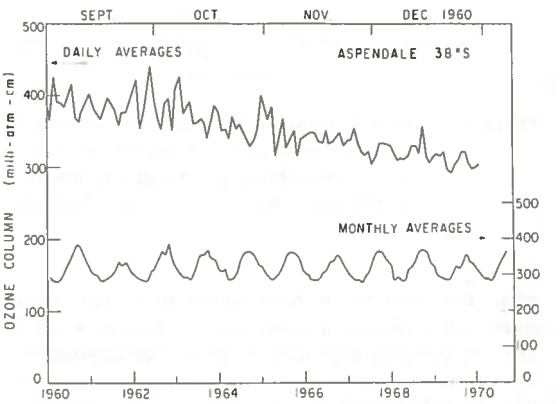

Figure 3. Total ozone columns at Aspendale, showing daily fluctuations and seasonal variations.

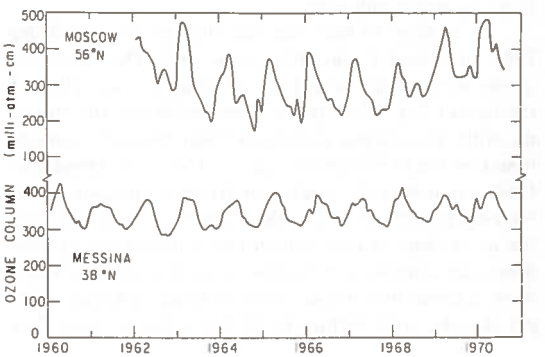

Figure 4. Total ozone columns at Moscow and at Messina.

of a real trend of magnitude b% per decade. His results are reproduced as Figure 5. Note that if there were a real increase or decrease of ozone at the rate of 30% per decade, it would require three years of observation to establish the trend with a 95% confidence level if one had the noise spectrum given by the observed ozone data at Aspendale. An extrapolation of Pittock's curve indicates that it would take almost two years to establish the presence of a real trend of 10% per year.

Foley and Ruderman [1] presented graphs of total ozone from five stations for the period 1960 to 1964

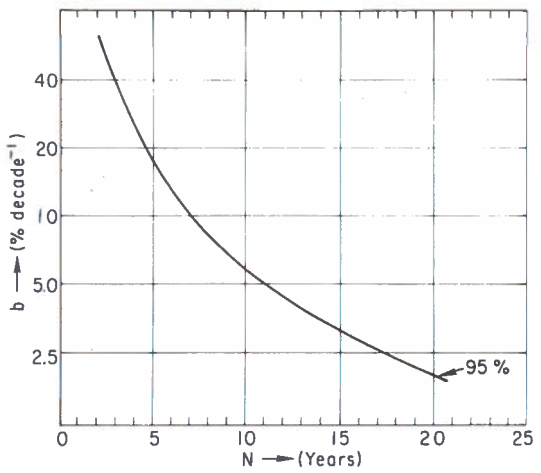

Figure 5. Graph showing the number of years N of observation required to determine a trend *b* (% ozone change per decade) to the 95% confidence level at Aspendale, Australia [5].

using data from *Ozone Data for the World* [2]. These graphs are analogous to those given in Figures 3 and 4, and any possible systematic trend is superimposed on the strong seasonal variations. For five years of observation, Pittock showed that it requires a careful statistical analysis to establish a trend of 20% per decade to the 95% confidence level. It is necessary to factor out the seasonal variations in order to detect real long-term global trends of the expected size from the NO_x input from nuclear-bomb tests.

A method of factoring out the seasonal trends has been presented by Komhyr et al. [6]. They analyzed ozone data of the world for the time interval 1961-70 (inclusive) for 10 stations. They evaluated the "mean monthly total-ozone deviations from monthly normals, based on the periods of record . . . The ozone trend lines [linear change with time] were fitted to the data by the least-squares method". Table 2 reproduces their results; the error range is two standard deviations (2σ), or three times the computed probable error. The seven stations show a linear increase in ozone between 2.4 and 10.0% per decade, well within the 95% confidence level (2σ).

We have adopted the method of Komhyr et al. [6], with one extension, to examine all the total ozone data in the published volumes of *Ozone Data for the World* [2]. For the stations considered by Komhyr et al., ozone was observed at least 25 days per month in almost every case. When we consider all the data from all stations, we find some cases where ozone was observed only once or twice a month. In our extension of Komhyr's method, we weighted the monthly means by the number of observations made that month. In agreement with Komhyr et al. [6], we find a statistically significant (5.1 ± 1.2%) increase in ozone during the period 1961-70 for 93 stations with 169,000 observation-days. We considered the increase of all stations for various time spans, 1960-70, 1961-70, 1962-70, etc. These are listed in Table 3. A comparison of one interval with another is complicated by the different number of stations in the various periods.

Table 3. Global Changes of Ozone for Various Time Intervals

Time Period	Years	Stations	Observation Days	b*	2σ	b yr. / 10
1960-70	11	93	178,000	4.5	1.2	4.9
1961-70	10	93	169,000	5.1	1.2	5.1
1962-70	9	92	159,000	4.8	1.3	4.3
1963-70	8	89	147,000	4.6	1.4	3.7
1964-70	7	89	132,000	4.9	1.6	3.4
1965-70	6	86	111,000	4.6	2.0	2.8

*b is rate of increase of ozone percent per decade

Foley and Ruderman [1] plotted the total-ozone data for Marcus Island, and they stated that this data showed no effect from nuclear bombs. The data for Marcus Island are presented both as monthly means and as deviations of the monthly mean from the ten-year norms in Figure 6. They start in February 1960 and end in June 1963. When analyzed by the method of Reference 6, these data show a *decrease* in ozone of 18 ± 16 percent per decade, contrary to Foley and Ruderman's statement. Also shown on Figure 6 is a set of data from a station that started observations in

Table 2. Summary of Data Analyses by Komhyr et al. [6]

Station	Mean O_3 m-atm-cm	% Increase per Decade (1961-70)
Huancayo, Peru	262	6.0 ± 1.2
Kodaikanal, India	257	10.0 ± 1.2
Mauna Loa, Hawaii	276	2.4 ± 1.8
Brisbane, Australia	289	6.6 ± 1.8
Nashville, USA	332	8.8 ± 2.1
Arosa, Switzerland	333	4.1 ± 3.0
Oxford, England	354	8.9 ± 3.0

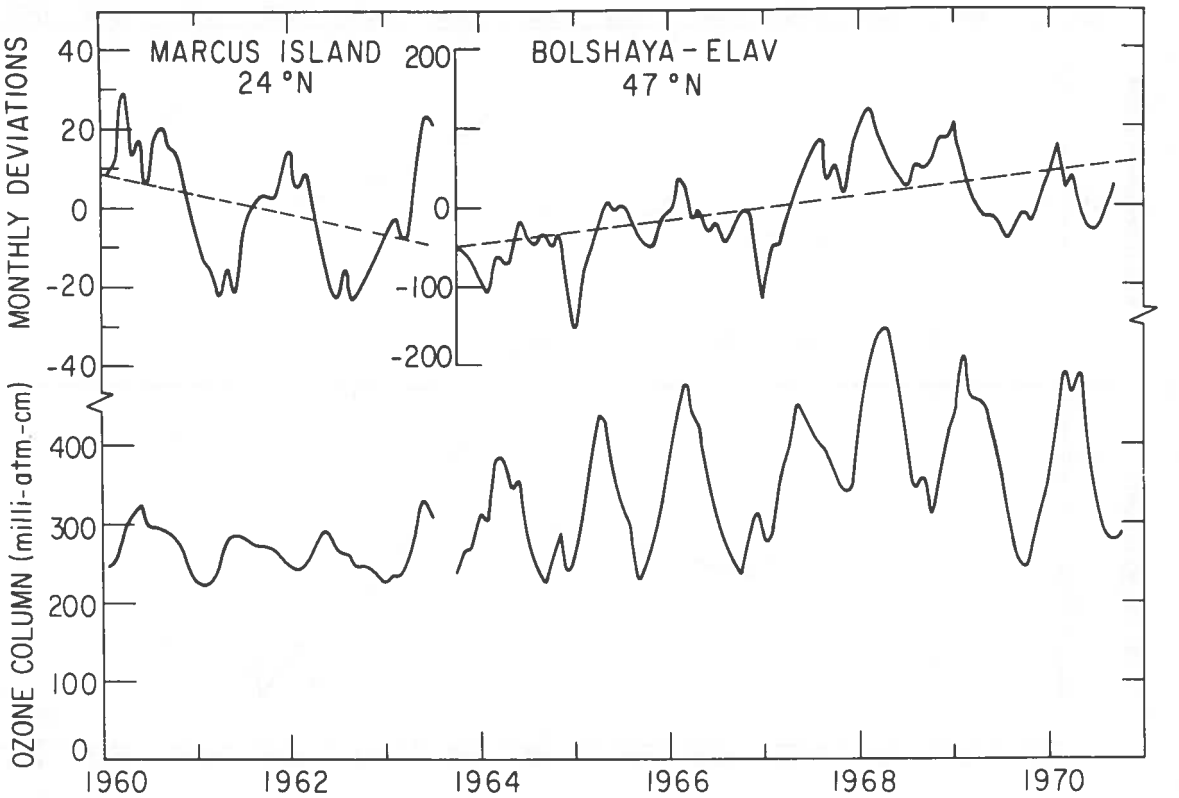

Figure 6. Total ozone column and monthly deviations (method of Komhyr et al. [6]) for Marcus Island and for Bolshaya-Elav.

September 1963, after the bomb testing had stopped. The total ozone data and the monthly deviations show a strong *increase* in ozone over the next several years. Large-nuclear-bomb testing extended from 1952 through 1962, and then stopped. Komhyr et al. found ozone from seven stations to increase from 1961-70. One plausible explanation of Komhyr's trend is that it represents the ozone of the world returning to normal after the perturbation (1952-62) of nitric-oxide injections from nuclear-bomb tests. To test the reasonableness of this hypothesis, one must look in detail at the history and magnitude of the bomb debris in the stratosphere.

Foley and Ruderman have demonstrated that nuclear bombs probably inserted significant quantities of nitric oxide into the stratosphere. Although nitric oxide from the bombs was not analyzed, very extensive analyses were made of strontium-90, excess carbon-14, and other radioactive products from the bombs. The fission yield of nuclear bombs is proportional to Sr-90 production, and Sr-90 was extensively sampled in the stratopshere. However, over the period 1952-62 there was a variation in the ratio of total yield to fission yield; also, Sr-90 is lodged in particulate matter, and may be subject to faster removal from the stratosphere than gaseous substances such as NO. Excess C-14 is in the form of a gas, and is proportional to total yield from nuclear bombs. However, as the level of C-14 drops to a low value, there is feedback from the troposphere, the ocean, and the biosphere. As tracers for probable duration and location of bomb-produced nitric oxide in the stratosphere, the advantages and disadvantages of Sr-90 and C-14 are complementary. The total global stratospheric burdens of Sr-90 and C-14 are given as a function of time between 1951 and 1971 in Figure 7. The data were from Glasstone [4], Telegadas [7,8], and Krey and Kajewski [9].

The trends in Figure 7 refer to global stratospheric bomb debris. The detailed distribution of artificial nitric oxide in the stratosphere is as important as the absolute amount [10]. The distribution of C-14 with latitude and elevation is given by Figure 8. Figure 8a gives the distribution of excess C-14 in March-May 1960, the beginning of the observed ozone series in ODW. Figure 8b gives C-14 just before the 1961-62 bomb series started. Figure 8c (March-May 1962) shows a large quantity of C-14 in the north polar region, and Figure 8d (March-May 1963) is just past the peak of C-14 for the globe. The amount of C-14 has decreased notably by May 1964 (Figure 8f), and the distribution of May 1966 (Figure 8g) is close to that of 1960 (Figure 8a). Figure 8 shows that relatively little C-14 entered the stratosphere in the southern hemisphere.

The data of Figure 7 show the carry-over of nuclear debris in the stratosphere from the 1952-58 tests into the period of ozone observations after 1960,

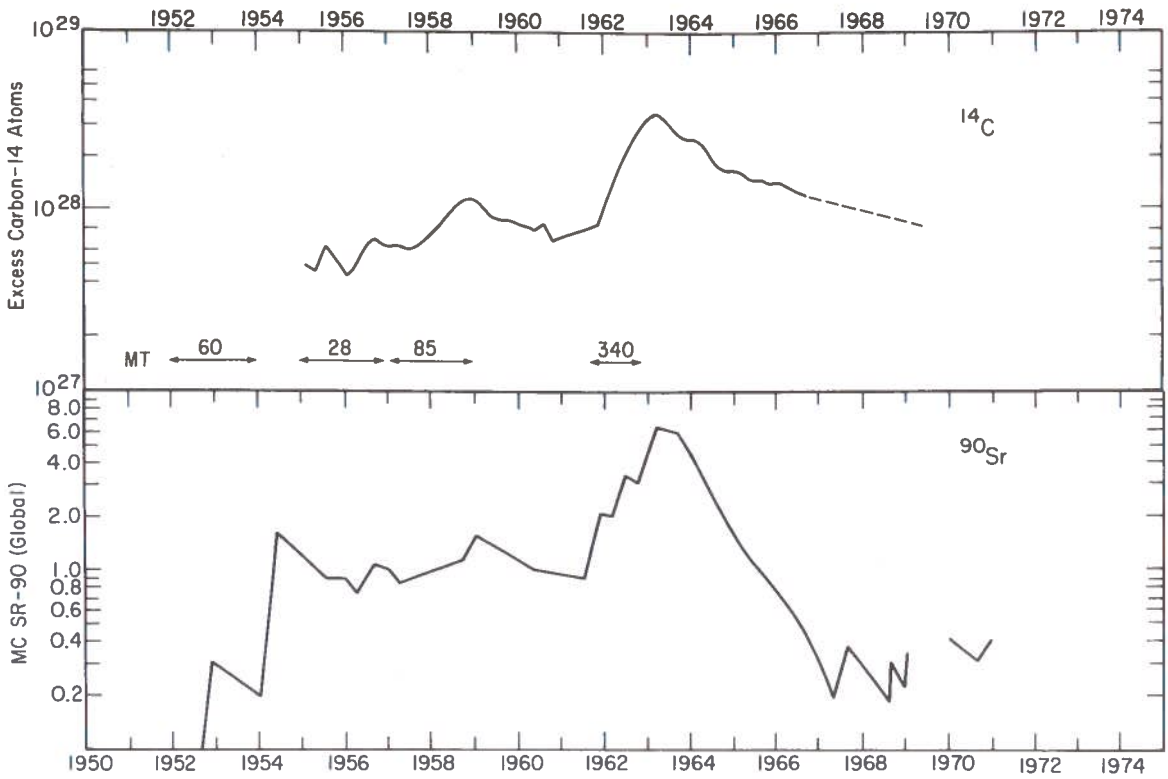

Figure 7. The variation with time of total stratospheric inventory of strontium-90 and carbon-14, with periods and yields (MT) of nuclear explosives.

and before the major series of tests in 1961-62. The peak of C-14 at February was about four times the value of C-14 on January 1960. The peak of Sr-90 (also February 1963) is six times the residual value of Sr-90 in the stratosphere in January 1960. The 1963 peak of Sr-90 fell to the January 1960 value by July 1965, but the gaseous C-14 did not return to its 1960 value until 1970. If artificial nitric oxide from nuclear bombs is correlated with Sr-90 and C-14, one might expect ozone to decrease between 1960 and early 1963 and to increase from 1963 to the late 1960's. These trends would be superimposed on the daily noise pattern (Figure 3) and the seasonal trends (Figures 3, 4, and 6). They should be much more pronounced in the northern hemisphere than in the southern hemisphere (Figure 8).

During the years 1960-62, 30 ozone-observing stations measured total ozone during at least 30 out of 36 months. These stations are listed in Table 4. At 23 out of 30 stations, ozone decreased during the years 1960-1962; it increased at only 7 stations. The average change per decade is -10.8%. Of the 30 stations in Table 4, 27 of them had at least 30 months of observations (20 had over 80 months of observations) between 1963 and 1970. Of these 27 stations, 22 showed an increase in ozone, and two-thirds of them showed both a decrease during 1960-62 and an increase during 1963-70. The average increase for these 27 stations is 7.2% per decade.

A close examination of the Komhyr plots for all stations shows a number of stations with positive deviations in the early 1960's, a minimum in the middle 1960's, and high values again in the late 1960's, e.g.: Aarhus, Alma-Ata, Moscow, Murmansk, Riga, Kuibyshev, Mont-Louis, Messina, Yakutsk, Port-aux-Français, Resolute. This conspicuous minimum of ozone in the middle 1960's is a recurring pattern.

The average change in ozone as a function of time interval and latitude is given in Table 5. In combining different stations involving widely different numbers of observations and widely different standard errors in estimating the linear-change function, we used the reciprocal of the square of the standard deviation as a weighting factor. This method suppresses the contribution from stations that covered only a short time span, that had relatively few observations, or that had large scatter of points. Table 5 should be studied in comparison with Figure 8. These figures (and other data from the HASL reports [7,8]) show relatively little change of C-14 in the southern hemisphere. Table 5 shows no significant change in stratospheric ozone in the southern hemisphere. In the northern hemisphere there was a significant decrease in ozone during the period 1960-62, followed by an increase in 1963-70. Figure 8 shows the largest concentration and persistence of carbon-14 in the northern part of the northern hemisphere. Table 5 shows a much larger decrease in total ozone for stations

Table 4. Stations with at Least 30 Months of Observation in the Period 1960-62, with Observations in 1963-70 (b, ozone increase per decade, percent)

Station	1960-62 Mos. of obs.	1960-62 b	1960-62 2σ	1963-70 Mos. of obs.	1963-70 b	1963-70 2σ
Aarhus, Denmark	36	-12.7	14.9	92	-8.9	7.6
Abastumani, USSR	35	-36.1	34.0	29		
Ahmadabad, India	36	+12.3	11.3	82	+8.0	3.7
Alma-Ata, USSR	30	-9.1	23.5	91	+25.9	11.5
Arosa, Switzerland	36	-5.8	18.4	90	+4.6	5.0
Aspendale, Australia	36	-3.7	17.7	92	-4.3	2.4
Brisbane, Australia	36	-4.3	11.7	92	+1.2	2.4
Cagliari-Elmas, Italy	36	-3.4	12.5	92	+13.5	4.2
Camborne, UK	36	-11.8	19.2	38	+17.2	9.2
Edmonton, Canada	36	-16.0	13.6	92	+3.3	4.3
Eskdalemuir, UK	36	-32.8	23.3	7		
Fort Collins, USA	31	-5.8	9.6	36	+18.0	12.8
Kagoshima, Japan	36	+55.9	19.3	92	0.0	4.8
Karadag, USSR	31	-89.3	22.6	36	+6.9	37.4
Kiev, USSR	31	-11.4	29.8	92	+9.5	8.4
Kodaikanal, India	36	-0.6	8.4	90	+12.4	1.9
Leningrad, USSR	30	-7.0	29.3	84	+12.8	8.4
Lerwick, UK	36	-26.7	15.9	79	+7.5	4.7
Marcus Is., Japan	36	-38.8	16.1	6		
Messina, Italy	36	-32.5	11.3	92	+8.2	3.2
New Delhi, India	36	+15.0	16.1	92	-5.6	3.3
Oxford, UK	36	-18.2	17.9	92	+6.8	4.5
Port-Aux-Français (Indian Ocean)	30	+2.0	24.8	70	+29.0	19.0
Quetta, Pakistan	36	-7.0	17.0	37	+4.5	10.1
Resolute, Canada	35	-32.1	19.1	83	+4.1	6.2
Sapporo, Japan	36	+1.0	16.6	92	+4.1	3.2
Tateno, Japan	36	+10.7	16.7	92	-0.9	4.2
Toronto, Canada	36	-11.6	18.8	88	+1.7	4.4
Tromsø, Norway	30	+11.1	31.0	64	+10.6	7.8
Vigna di Valle, Italy	36	-15.2	14.6	90	+4.1	4.4
Average per decade %		-10.8			+7.2	
% in interval		-3.3			+5.8	

Table 5. Geographical Variation of Ozone Changes for the Two Time Intervals 1960-62, 1963-70

Latitude (degrees)	Time Period	% Increase per Decade	2σ	No. of Stations	No. of Meas. Days
50N-90N	1960-62	-12.6	10.6	20	11,000
	1963-70	+7.6	3.2	28	47,000
	1960-70	+6.5	2.4	29	57,000
0-90N	1960-62	-7.6	7.0	42	28,000
	1963-70	+5.6	1.5	74	129,000
	1960-70	+5.3	1.2	76	156,000
0-90S	1960-62	-3.6	18.8	9	4,200
	1963-70	-1.2	3.1	15	19,000
	1960-70	+0.2	2.3	17	23,000
All Stations	1960-62	-7.1	6.5	51	32,000
	1963-70	+4.6	1.4	89	147,000
	1960-70	+4.5	1.2	93	178,000

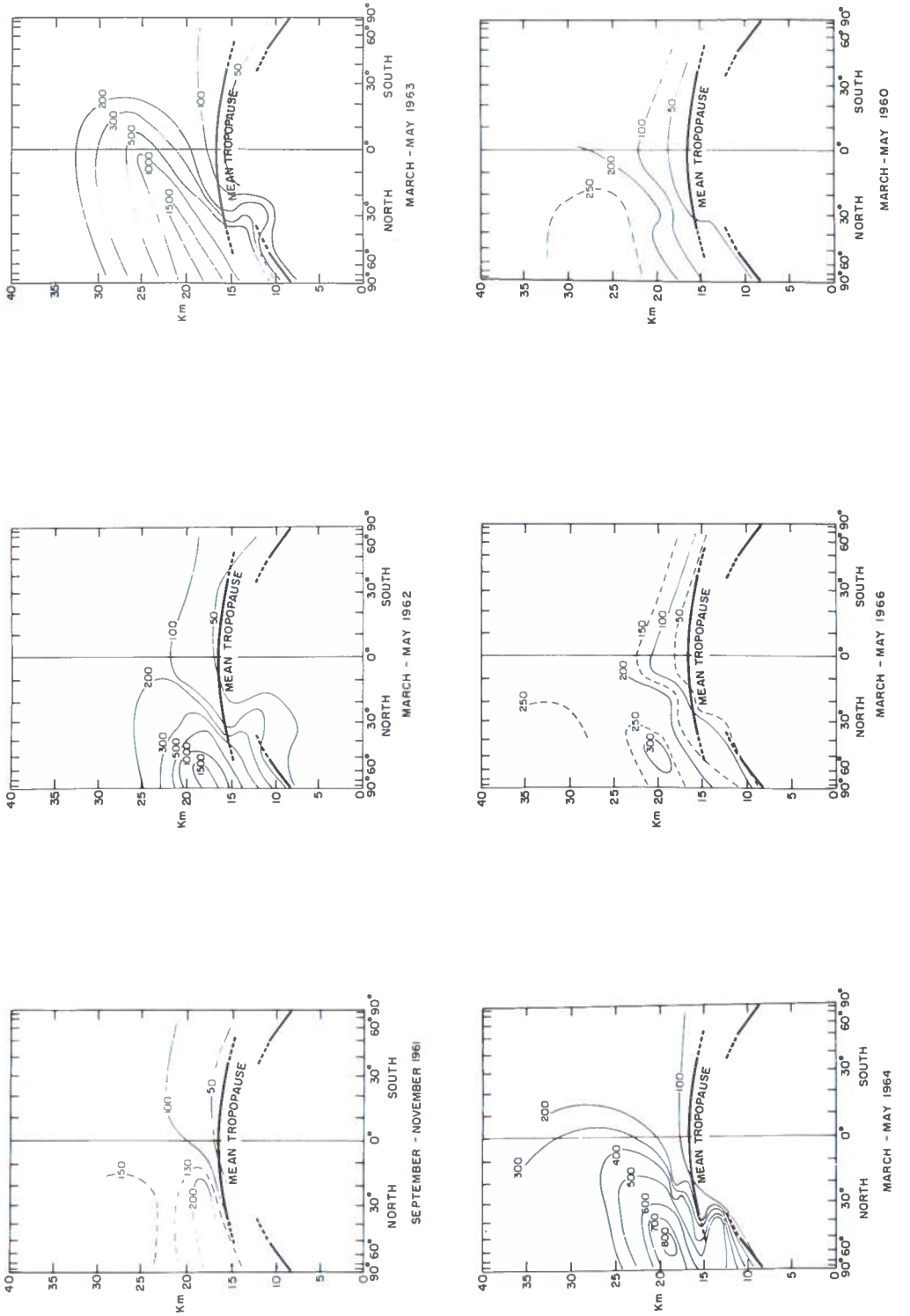

Figure 8. Contour maps of zonally averaged excess carbon-14 in the stratosphere, in units of 10^5 atoms of carbon-14 per gram of air.

north of 50°N than for the entire hemisphere or for the globe. The geographical pattern of ozone changes (decreasing 1960-62, increasing 1963-70) shown in Table 5 are consistent with the temporal and geographical trends shown by carbon-14 in Figures 7 and 8.

Correcting Foley and Ruderman's thermodynamics by a factor of 2 and showing the factor-of-6 uncertainty range arising from considerations of chemical kinetics in the rising fireball, one obtains for the production of nitric oxide from nuclear bombs

$$N_{NO} = (0.17 - 1.0) \times 10^{32} y_{MT}$$

According to tables given by Foley and Ruderman, the total nuclear-bomb yield from 1952 to 1962 was 513 MT. Thus the total number of molecules of nitric oxide produced by nuclear bombs between 1952 and 1962 is expected to be between the limits

$$N_{NO} = (0.8 - 5.1) \times 10^{34} \text{ molecules}$$

One American SST operating normally for 10 years produces 4.8×10^{32} molecules of NO. Thus the decade of bomb testing had an average effect equivalent to the number of SST's

$$N_{SST} \text{ (10-year average)} = 18 \text{ to } 103$$

Alternatively, it is as if SST flights had started in 1952 and increased linearly until 1962 to reach the total

$$N_{SST} \text{ (1962 max.)} = 36 \text{ to } 206$$

and then all flights stopped. The ozone data of the world then showed a significant increase of about 5% after the cessation of tests in 1962. If ramping up from 0 to 36 SST's caused the ozone of the world to decrease by 5% (the magnitude of the later rebound), then the effect of NO on the stratospheric ozone is *greater* than that previously predicted [10], which was about 3 or 4%. If ramping up from 0 to 206 SST's caused the ozone of the world to decrease by only 5 percent, then the effect is somewhat smaller than the central value predicted in Reference 10. Such a ramp model for the introduction of 200 SST's was expected to reduce ozone by about 10 percent in terms of the previous model, although a wide range of effect was regarded as possible. It may be that the oxides of nitrogen from nuclear-bomb tests of 1952-62 constituted a measurable injection experiment, and the consequent reductions of ozone may be ascribable (perhaps only in part) to this injection experiment.

CONCLUDING REMARKS

This is not to say that we accept at face value the explanation of the trends shown in Tables 4 and 5 in terms of the effect of nuclear bombs. There are a large number of reasons for meteorological and climatological changes. *Ozone Data of the World* may be unreliable because of instrumental or operational difficulties. The points we should like to make here are three: (1) The expected reduction in ozone from the nuclear tests of 1952-62 is a matter of a few percent. (2) There was a significant decrease in total ozone between 1960-62 and a significant increase in total ozone between 1963-70. (3) These trends are consistent with the predicted effect of nuclear bombs, but there may also be other explanations.

Foley and Ruderman's examination of the statistics of ozone changes in the period before and after the bomb tests was inadequate. They looked at too few data, and they did not use a sensitive method to analyze for long-term trends. There are long-term trends, and these trends may be due to the injection of NO by nuclear bombs.

ACKNOWLEDGMENT

This work was supported under the Climatic Impact Assessment Program, by means of an interagency agreement between the Department of Transportation and the Atomic Energy Commission. We thank the many students who contributed their services in transcribing *Ozone Data for the World* from the red books to tables suitable for computer processing.

REFERENCES

1. Foley, H.M., and M.A. Ruderman, "Stratospheric nitric oxide production from past nuclear explosions and its relevance to projected SST pollution," JASON paper P894, Institute for Defense Analyses, Arlington, Virginia (1972).

2. *Ozone Data for the World*, Canadian Department of Transport, Meteorological Branch, in cooperation with the World Meteorological Organization, (1960-70).

3. Stull, Prophet, et al., *JANAF Thermochemical Tables* (Second Edition), National Bureau of Standards, NSRDS-NBS-37 (1971).

4. Glasstone, S., *The Effects of Nuclear Weapons*, U.S. Atomic Energy Commission, U.S. Government Printing Office, p. 486 (1964).

5. Pittock, A.B., "Evaluating the risk to society from the SST," Search *3*, 285-289 (1972).

6. Komhyr, W.D., E.W. Barrett, G. Slocum, and H.K. Weickmann, "Atmospheric ozone increase during the 1960s," Nature *232*, 390-391 (1971).

7. Telegadas, K., "The Seasonal Stratospheric Distribution of Cadmium-109, Plutonium-238, and Strontium-90," Health and Science Laboratory Report 184, U.S. Atomic Energy Commission, 53-118 (1967).

8. Telegadas, K., "The Seasonal Stratospheric Distribution and Inventories of Excess Carbon-14 from March 1955 to July 1969," Health and Safety

Laboratory Report 243, U.S. Atomic Energy Commission, 3-86 (1971).

9. Krey, P.W. and B.T. Kajewski, "Updating Stratospheric Inventories to February 1971," Health and Safety Laboratory Report 245, 103-124 (1971).

10. *a.* Johnston, H.S., "Catalytic reduction of stratospheric ozone by nitrogen oxides," UCRL-20568, 1-114 (1971).

b. Johnston, H.S., "Reduction of stratospheric ozone by nitrogen oxide catalysts from supersonic transport exhaust," Science *173*, 517-522 (1971).

REPLY TO PAPERS OF DR. CHANG AND DR. JOHNSTON

Malvin A. Ruderman

The 6×10^{34} molecules of NO which Foley and I originally estimated to have been injected into the stratosphere by the 1961-62 explosions approximated or exceeded the normal NO abundance in various stratospheric models. The equilibrium of NO with ozone is expected to be achieved at most stratospheric altitudes within a few months, which is much less than the NO residence time. Thus we anticipated that the injected NO, initially widely distributed in altitude, would have an effect on ozone comparable to that of an approximately doubled natural stratospheric NO abundance. And while our presentation of data was not designed to display a small ozone suppression, it was adequate to reveal the large one (greater than 10%) we expected to find.

I accept Professor Johnston's reduction of our original NO estimate by about a factor of 2. But discarding the conventional cooling model for a rising hot-air cloud could give an additional reduction of a factor of 3 at most, not a factor of 6. The Marcus Island data in Dr. Johnston's Figure 6 is discussed as a possible example of bomb-initiated ozone decrease we had overlooked. However, his calculated ozone-abundance slope would be even more negative if all post-explosion data were ignored (An effect of the same magnitude could have been obtained from an ozone drop of slightly less than 5% after the fall of 1961, if analyzed in the same way.)

Contrary to Dr. Chang's assertion, we do not state that past ozone data showed "no evidence of ozone decrease," only that certain tabulated data (our Table 6, JGR, in press) do not. His assumption that we used the estimates of his reference 3 is incorrect. (The lowest part of the range of NO_x effects he quotes from that reference comes from models quite inappropriate for the altitude distribution of explosion-injected NO.) I do not agree with Dr. Chang's judgment that one would not expect our "cursory examination" to detect a 15% reduction in total ozone; it seems to me that a consistent lowering by that amount in the given tabulated data or our own graphs would be quite apparent.

Because of the particular applicability of some recent work done at ARAP, the following unscheduled paper was presented.

SOLUTIONS OF THE CHEMICAL KINETIC EQUATIONS FOR INITIALLY INHOMOGENEOUS MIXTURES

GLENN R. HILST
Aeronautical Research Associates of Princeton, Inc.
Princeton, New Jersey

ABSTRACT: O'Brien [1] and Donaldson and Hilst [2] have recently discussed the effects of inhomogeneous mixing and turbulent diffusion on simple chemical reaction rates. This report is a more extensive analysis of when inhomogeneous mixing has a significant effect on chemical reaction rates.

INTRODUCTION

Since the publication of earlier analyses of the effects of inhomogeneous mixing on chemical reaction rates [1,2], there has been concern about whether or not *real* situations exist in which these effects are significant, particularly with regard to chemical reactions in the free atmosphere. It therefore seems desirable to examine more closely the conditions under which these effects *can* be significant and to relate these conditions to real-world situations and problems. Such an analysis is provided in the next section.

As is noted below, there are indeed important real-world situations, including atmospheric reactions, in which the inhomogeneous nature of the reactant mixtures not only is significant but completely dominates the reaction rate. To summarize these situations briefly, the *potential* for significant effects exists when the values of the products of the variance-to-mean-squared ratio of the concentrations exceed 0.25. This potential is *realized* only if there is a nonzero correlation of the joint fluctuations of the reactant concentrations. When a correlation does exist, however, two classes of problems emerge: 1) reaction rates are significantly accelerated when this correlation is positive, and 2) reaction rates are significantly depressed if this correlation is negative. The first case is directly associated with the injection of relatively high concentrations of the reactants into a clean background or one of more-or-less uniformly-mixed low concentrations of the reactants. More generally, this is the multiple- or intermittent-source problem. The second case is directly associated with those situations where the chemical rate is fast in comparison with the local diffusive mixing rate and has been discussed by O'Brien [1], Donaldson [3], and Donaldson and Hilst [2].

Failure to account for the inhomogeneous nature of the reactant mixture in the use of chemical kinetic models under these circumstances can readily lead to orders-of-magnitude errors in the prediction of chemical reaction rates.

THE BASIC CHEMICAL KINETIC EQUATIONS FOR INHOMOGENEOUS MIXTURES

Following Donaldson and Hilst [2], we assume an isothermal, irreversible, two-body reaction between chemical species α and β to form γ and δ.

$$\alpha + \beta \rightarrow \gamma + \delta \tag{1}$$

We further assume that the reaction rates for any joint values of the concentrations of the reacting chemical species are correctly specified by

$$\frac{\partial C_\alpha}{\partial t} = -k_1 C_\alpha C_\beta \tag{2}$$

$$\frac{\partial C_\beta}{\partial t} = -k_2 C_\alpha C_\beta \tag{3}$$

and

$$\frac{\partial}{\partial t}(C_\gamma + C_\delta) = -\frac{\partial}{\partial t}(C_\alpha + C_\beta) \tag{4}$$

where C_i denotes the concentration of the ith chemical species (expressed as a mass fraction), and k_1 and k_2 are the reaction rate constants.

Equations (2) and (3) specify the *local* instantaneous rate of change of the concentration of the reactants. In order to determine the average rate of change, we assume that the local history of the joint values of C_α and C_β comprises a stationary time series, and that each may be dissected into its mean and fluctuating components

$$C_\alpha = \overline{C}_\alpha + C'_\alpha \tag{5}$$

and

$$C_\beta = \overline{C}_\beta + C'_\beta \tag{6}$$

and, by definition, $\overline{C'_\alpha} = \overline{C'_\beta} = 0$. Under these assumptions the chemical kinetic equations for the average rates

of change of the concentrations of α and β are readily shown to be

$$\frac{\partial \bar{C}_\alpha}{\partial t} = -k_1 (\bar{C}_\alpha \bar{C}_\beta + \overline{C'_\alpha C'_\beta}) \tag{7}$$

and

$$\frac{\partial \bar{C}_\beta}{\partial t} = -k_2 (\bar{C}_\alpha \bar{C}_\beta + \overline{C'_\alpha C'_\beta}) \tag{8}$$

In order to solve equations (7) and (8) we need a prediction equation for $\overline{C'_\alpha C'_\beta}$. This is readily derived (cf. Ref. 2) as

$$\begin{aligned}\frac{\partial \overline{C'_\alpha C'_\beta}}{\partial t} = &-k_1 (\bar{C}_\alpha \overline{C'^2_\beta} + \bar{C}_\beta \overline{C'_\alpha C'_\beta} + \overline{C'_\alpha C'^2_\beta}) \\ &-k_2 (\bar{C}_\beta \overline{C'^2_\alpha} + \bar{C}_\alpha \overline{C'_\alpha C'_\beta} + \overline{C'^2_\alpha C'_\beta})\end{aligned} \tag{9}$$

which introduces four new terms, $\overline{C'^2_\alpha}$, $\overline{C'^2_\beta}$, $\overline{C'_\alpha C'^2_\beta}$, and $\overline{C'^2_\alpha C'_\beta}$. The prediction equations for $\overline{C'^2_\alpha}$ and $\overline{C'^2_\beta}$ are

$$\frac{\partial \overline{C'^2_\alpha}}{\partial t} = -2k_1 (\bar{C}_\beta \overline{C'^2_\alpha} + \bar{C}_\alpha \overline{C'_\alpha C'_\beta} + \overline{C'^2_\alpha C'_\beta}) \tag{10}$$

and

$$\frac{\partial \overline{C'^2_\beta}}{\partial t} = -2k_2 (\bar{C}_\alpha \overline{C'^2_\beta} + \bar{C}_\beta \overline{C'_\alpha C'_\beta} + \overline{C'_\alpha C'^2_\beta}) \tag{11}$$

They do not introduce any more new terms. In order to close equations (7) through (11), and thereby achieve a chemical sub-model for reactions in inhomogeneous mixtures, we require prediction equations for the third-order correlations $\overline{C'^2_\alpha C'_\beta}$ and $\overline{C'_\alpha C'^2_\beta}$.

Before proceeding to the closure problem, however, it is instructive to examine more closely the limits of the effects of concentration fluctuations on chemical reaction rates, and the conditions under which these effects become significant. This examination may be made in two steps: 1) when are the fluctuations of concentration negligible (i.e., when are the reaction rates predicted satisfactorily by the mean values of concentration alone?), and 2) when may the third-order correlations be neglected? For the latter cases, equations (7) through (11) comprise the closed set discussed by Donaldson and Hilst [2].

The Limits of Errors in Reaction Rate Predictions if Concentration Fluctuations are Neglected

The neglect of concentration fluctuations in determining reaction rates is equivalent to the assumption that the local values of C_α and C_β are constant in time. Under this assumption, $C'_\alpha = C'_\beta \equiv 0$ and the predicted reaction rates are simply

$$\left(\frac{\partial \bar{C}_\alpha}{\partial t}\right)_s = -k_1 \bar{C}_\alpha \bar{C}_\beta \tag{12}$$

and

$$\left(\frac{\partial \bar{C}_\beta}{\partial t}\right)_s = -k_2 \bar{C}_\alpha \bar{C}_\beta \tag{13}$$

where the subscript s denotes the steady-state assumption. Then the ratio of reaction rates predicted from the inclusion of concentration fluctuations to those predicted neglecting these terms is

$$\frac{\partial \bar{C}_\alpha/\partial t}{(\partial \bar{C}_\alpha/\partial t)_s} = 1 + \frac{\overline{C'_\alpha C'_\beta}}{\bar{C}_\alpha \bar{C}_\beta} \tag{14}$$

An identical equation gives the relative rates of depletion of the β species.

The limits on equation (14) are readily determined from equation (7) or (8) and elementary statistics. First, we note from equation (7) that for irreversible reactions $\partial \bar{C}_\alpha/\partial t \leq 0$, and therefore

$$\frac{\overline{C'_\alpha C'_\beta}}{\bar{C}_\alpha \bar{C}_\beta} \geq -1 \tag{C1}$$

Further, from elementary statistics we note that

$$-1 \leq \frac{\overline{C'_\alpha C'_\beta}}{(\overline{C'^2_\alpha C'^2_\beta})^{1/2}} \leq +1 \tag{C2}$$

and therefore

$$\begin{aligned}-\left(\frac{\overline{C'^2_\alpha}}{\bar{C}^2_\alpha}\frac{\overline{C'^2_\beta}}{\bar{C}^2_\beta}\right)^{1/2} \leq \frac{\overline{C'_\alpha C'_\beta}}{\bar{C}_\alpha \bar{C}_\beta} \\ \leq \left(\frac{\overline{C'^2_\alpha}}{\bar{C}^2_\alpha}\frac{\overline{C'^2_\beta}}{\bar{C}^2_\beta}\right)^{1/2}\end{aligned} \tag{C3}$$

Substituting conditions (C1) and (C3) into Equation (14), we establish the limits

$$\begin{aligned}0 \leq 1 - \left(\frac{\overline{C'^2_\alpha}}{\bar{C}^2_\alpha}\frac{\overline{C'^2_\beta}}{\bar{C}^2_\beta}\right)^{1/2} \leq \frac{\partial \bar{C}_\alpha/\partial t}{(\partial \bar{C}_\alpha/\partial t)_s} \\ \leq 1 + \left(\frac{\overline{C'^2_\alpha}}{\bar{C}^2_\alpha}\frac{\overline{C'^2_\beta}}{\bar{C}^2_\beta}\right)^{1/2}\end{aligned} \tag{C4}$$

Conditions (C4) set the *maximum* errors in the prediction of reaction rates which the neglect of concentration fluctuations can produce. These limits are set by the individual variance-to-mean-squared ratios of C_α and C_β, and are therefore functions of the *marginal* frequency distributions of C_α and C_β.

The limits established by conditions (C4) are shown graphically in Figure 1. We note immediately that the limiting errors in reaction predictions occasioned by neglect of concentration fluctuations are small for $\left(\frac{\overline{C'^2_\alpha}}{\bar{C}^2_\alpha}\frac{\overline{C'^2_\beta}}{\bar{C}^2_\beta}\right)^{1/2} < 0.5$, but increase to

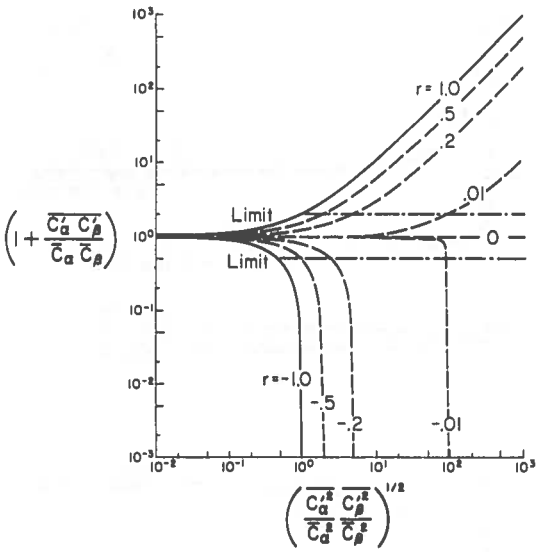

Figure 1. The limits of errors of prediction of chemical reaction rates incurred by the neglect of concentration fluctuations. (See text for explanation of terms.)

highly significant values as this ratio exceeds 1.0. The *potential* for order-of-magnitude errors in the prediction of the reaction rate exists whenever the product of the variance-to-mean-squared ratios greatly exceeds 1.0.

The actual error depends, of course, on $\overline{C'_\alpha C'_\beta}/\bar{C}_\alpha \bar{C}_\beta$. This actual error may be examined by forming the ratio

$$r = \frac{\overline{C'_\alpha C'_\beta}}{\bar{C}_\alpha \bar{C}_\beta} \Bigg/ \left(\frac{\overline{C'^2_\alpha}}{\bar{C}^2_\alpha} \frac{\overline{C'^2_\beta}}{\bar{C}^2_\beta} \right)^{1/2} = \frac{C'_\alpha C'_\beta}{(\overline{C'^2_\alpha}\,\overline{C'^2_\beta})^{1/2}} \tag{15}$$

where r is the ordinary correlation coefficient, and in this usage expresses the ratio of the actual error in reaction-rate predictions to the maximum possible error for any given joint distribution of C_α and C_β. Selected values of r are also graphed in Figure 1. In the limit of r = 0 no error in reaction-rate predictions is occasioned by the neglect of concentration fluctuations. This is, of course, the situation when C'_α and C_β are randomly distributed and $\overline{C'_\alpha C'_\beta} = 0$. However, it is clear from Figure 1 that even modest values of r produce significant errors in the reaction rate prediction when $\left(\frac{\overline{C'^2_\alpha}}{\bar{C}^2_\alpha} \frac{\overline{C'^2_\beta}}{\bar{C}^2_\beta} \right)^{1/2} > 1$, particularly when $r < 0$.

We shall return to this analysis, and identify joint distributions of C_α and C_β for which the fluctuations of concentration must be included later. We now turn to the importance of the third-order correlations in the chemical-kinetics equations.

The Role of the Third-Order Correlation Terms

Going back to equations (9) to (11), it is evident that the primary role of the third-order correlations is to be found in their control of the rate of change of $\overline{C'_\alpha C'_\beta}$, both directly and through the rates of change of the variances, $\overline{C'^2_\alpha}$ and $\overline{C'^2_\beta}$. The effects of the third-order correlations on the reaction rates will therefore appear primarily as a *time-integrated effect* on $\overline{C'_\alpha C'_\beta}$, and any cumulative error in the estimates of $\overline{C'^2_\alpha C'_\beta}$ and $\overline{C'_\alpha C'^2_\beta}$ will produce a cumulative error in $\overline{C'_\alpha C'_\beta}$.

We may deduce immediately from equations (9) through (11) that if

$$\left.\begin{aligned} &\overline{C'^2_\alpha C'_\beta} \ll \bar{C}_\beta \overline{C'^2_\alpha} + \bar{C}_\alpha \overline{C'_\alpha C'_\beta} \\ \text{and} \quad &\overline{C'_\alpha C'^2_\beta} \ll \bar{C}_\alpha \overline{C'^2_\beta} + \bar{C}_\beta \overline{C'_\alpha C'_\beta} \end{aligned}\right\} \tag{C5}$$

their effect on $\overline{C'_\alpha C'_\beta}$ is negligible and we may close the model equations by setting $\overline{C'^2_\alpha C'_\beta} = \overline{C'_\alpha C'^2_\beta} = 0$. To illustrate that conditions (C5) are met under any given circumstance, we must evaluate the joint distributions of C_α and C_β from which these moments are derived, since there are now no limiting conditions on their marginal distributions. In other words, we must turn attention to the *distribution functions* from which the means and moments have been derived if we are to determine the importance of third- or higher-order correlations in chemical reaction rates. Ideally, we would examine simultaneous experimental measurements of $C_{\alpha i}$ and $C_{\beta i}$ to make this assessment; unfortunately, very few such data exist. However, as long as we assume that the basic chemical kinetic equations are correct (and our whole theory is based on this assumption) we can proceed by solving these basic equations for various initial distributions of $C_{\alpha i}$ and $C_{\beta i}$, determining in the process the time histories of all of the relevant moments of these distributions.

THE MOMENT-GENERATING MODEL

Under the assumption that only chemical reactions are operative in changing the concentrations of α and β, the chemical kinetic equations can be written as total derivatives and integrated directly as a function of reaction time.

$$\frac{dC_{\alpha i}}{dt} = k_1 C_{\alpha i} C_{\beta i} \tag{16}$$

$$\frac{dC_{\beta i}}{dt} = k_2 C_{\alpha i} C_{\beta i} \tag{17}$$

and

$$C_{\alpha i}(t) - C_{\alpha i}(O) = \frac{k_1}{k_2} (C_{\beta i}(t) - C_{\beta i}(O)) \tag{18}$$

while

$$C_{\beta i}(t) = \frac{C_{\beta i}(O) - \frac{k_2}{k_1} C_{\alpha i}(O)}{1 - \frac{k_2}{k_1} \frac{C_{\alpha i}(O)}{C_{\beta i}(O)} \exp\left\{ - \left(C_{\beta i}(O) - \frac{k_2}{k_1} C_{\alpha i}(O) \right) k_1 t \right\}} \tag{19}$$

Equations (18) and (19) specify the joint values of $C_{\alpha i}$ and $C_{\beta i}$ at time t, given their initial values and the reaction rate constants. They may be used to specify the frequency distribution of ($C_{\alpha i}$, $C_{\beta i}$) at any time t, given their initial frequency distribution $n_i(0)$, since, in the absence of mixing, n_i is conserved as $C_{\alpha i}$ and $C_{\beta i}$ change value due to chemical reaction. Equations (18) and (19) provide the information necessary to calculate all of the relevant moments of $n_i(C\alpha_i, C_{\beta i})$ and their rates of change. We may introduce any arbitrary initial distribution $n_i(C_{\alpha i}, C_{\beta i})$, subject only to the constraints

$$\left.\begin{aligned} 0 \leq C_{\alpha i} \leq 1 \\ 0 \leq C_{\beta i} \leq 1 \end{aligned}\right\} \quad \text{and} \quad 0 \leq C_{\alpha i} + C_{\beta i} \leq 1 \tag{C6}$$

In order to illustrate the general behavior of the distribution of C_α and C_β and the associated first-, second-, and third-order moments, we have chosen a simple distribution of points along the line $C_\alpha = 1 - C_\beta$ and weighted each point equally ($n_i = 1/N$). The time history of n_i ($C_{\alpha i}$, $C_{\beta i}$) is shown in Figure 2 and the moments of these distributions are plotted in Figure 3.

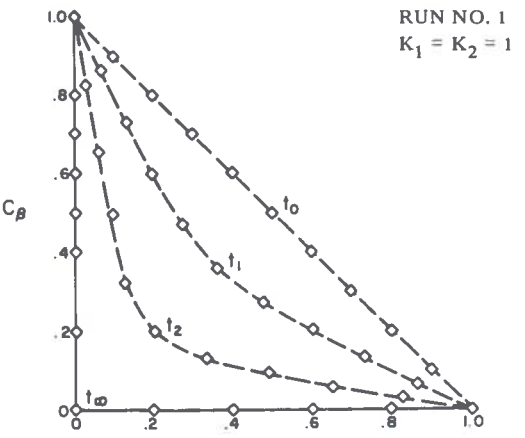

Figure 2. Example of the time history of the joint frequency distribution of ($C_{\alpha i}$, $C_{\beta i}$) given the initial distribution shown for t_0 and $k_1 = k_2 = 1$. Each point was weighted equally ($n_i = 1$) for calculation of the moments of these distributions (shown in Figure 3).

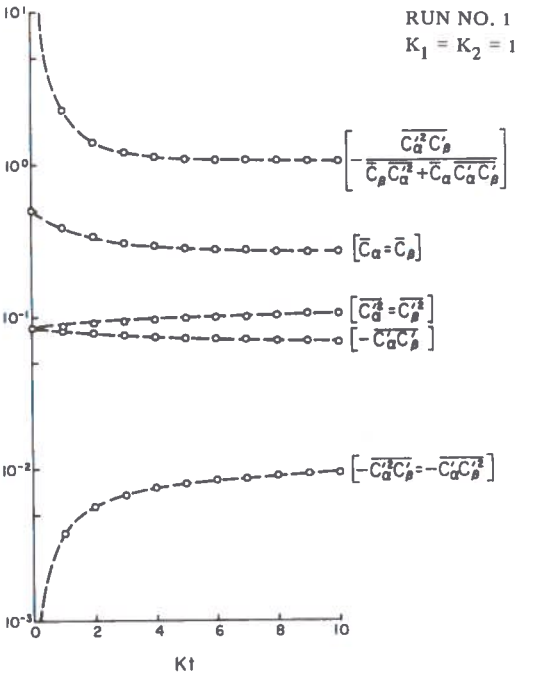

Figure 3. Time history of the first-, second-, and third-order moments of $n_i(C_{\alpha i}, C_{\beta i})$ for the distributions shown in Figure 2.

Note particularly the distortion of the originally linear distribution of (C_α, C_β) and the associated decrease (from zero) of the third-order moments. The relative magnitudes of $\overline{C_\alpha'^2 C_\beta'}$ and $\overline{C}_\beta \overline{C_\alpha'^2} + \overline{C}_\alpha \overline{C_\alpha' C_\beta'}$ are also plotted in Figure 3; as can be seen there, $\overline{C_\alpha'^2 C_\beta'}$ and $\overline{C_\alpha' C_\beta'^2}$ completely dominate the initial change of $\overline{C_\alpha' C_\beta'}$. However, this latter effect is too short-lived to be significant in the prediction of the time history of mean concentrations. This fact is shown in Figure 4, where the predictions of C_α and C_β as a function of time, first neglecting the fluctuations completely and then neglecting only the third-order moments, are compared with the exact solution. The latter assumption produces an error of approximately 10% at kt = 10, while the total neglect of the fluctuations produces an error of 300% at that time.

As a further example, one which illustrates the importance of the third-order correlations, we have constructed the distribution functions which simulate the case of intermittent sources. For physical perspective, imagine a crosswind freeway on which the automobile traffic ranges from a steady, bumper-to-bumper stream to only an occasional vehicle. We assume that each vehicle emits approximately the same amount of pollutants per unit time, but that the ratio of the α and β species emitted is slightly variable from one vehicle to another. Now we ask, "What is the average reaction rate for these exhaust materials immediately downwind from the roadway as a function of the intermittency of the traffic?"

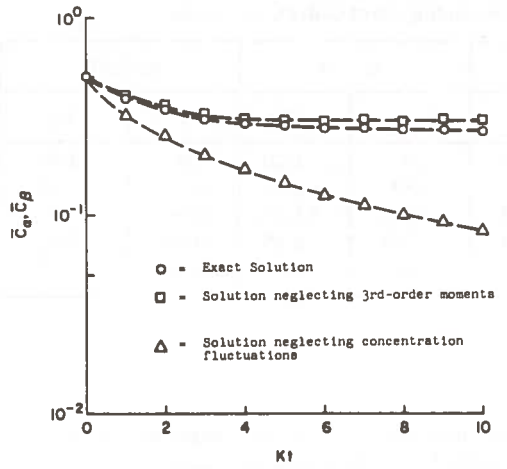

Figure 4. Comparison of the predictions of $\bar{C}_\alpha$ and $\bar{C}_\beta$, under assumptions listed, with exact values from the moment-generating model using the distributions shown in Figure 3.

We simulate this situation by the frequency distribution for (C_α, C_β) shown in Figure 5. The variability of C_α and C_β due to variable exhaust emissions is portrayed as a circularly symmetric distribution, and we take $C_\alpha = C_\beta = 0$ when there is no traffic upwind of our observation line. (Small background concentrations have been assumed in another calculation but produce no significant effect.) We assume further that the pairs of nonzero values of (C_α, C_β) occur with equal frequency, and we measure the intermittency of the traffic as the fraction of time there is a vehicle upwind of the observation line, t_i. The moment-generating model has

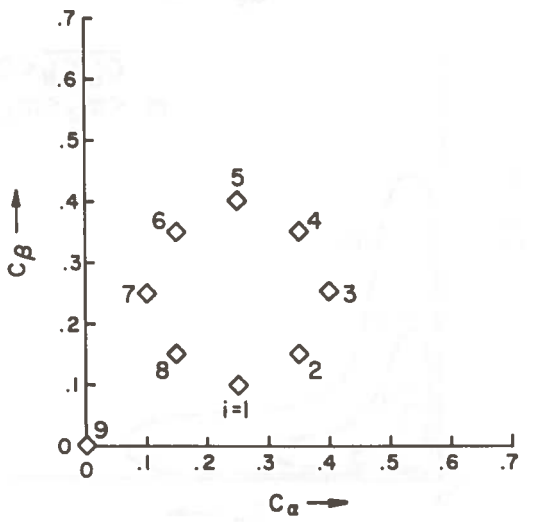

Figure 5. Joint distributions of (C_α, C_β) chosen to simulate chemical reaction rates immediately downwind of a roadway on which traffic is variably intermittent.

been used to determine the chemical reaction rates as a function of kt for t_i = 1.0, 0.5, 0.33, 0.2, 0.1 (t_i = 1.0 corresponds to a steady, bumper-to-bumper stream of traffic).

Table 1 shows the values of $A_1 = \left(\frac{\overline{C'^2_\alpha}}{\bar{C}^2_\alpha}\,\frac{\overline{C'^2_\beta}}{\bar{C}^2_\beta}\right)^{1/2}$, $r = \frac{\overline{C'_\alpha C'_\beta}}{(\overline{C'^2_\alpha}\,\overline{C'^2_\beta})^{1/2}}$, and $A_2 = \frac{\overline{C'^2_\alpha C'_\beta}}{\bar{C}_\beta \overline{C'^2_\alpha} + \bar{C}_\alpha \overline{C'_\alpha C'_\beta}}$ at kt = 1

and for each value of t_i, along with the observed ratios of $\partial\bar{C}_\alpha/\partial t$ to the reaction rates predicted assuming steady values of C_α and C_β, $(\partial\bar{C}_\alpha/\partial t)_s$, and to the rates predicted neglecting the third-order correlations, $(\partial\bar{C}_\alpha/\partial t)_I$. These results, which are now firmly grounded in reality, show clearly that the potential errors in predicting reaction rates while neglecting the concentration fluctuations can be realized. Although the effects of concentration fluctuations are negligible for a steady stream of traffic, t_i = 1, chemical kinetics based on this assumption underestimate the initial depletion rate of $\bar{C}_\alpha$ and $\bar{C}_\beta$ by a factor of 9 when t_i = 0.1!

Table 1. Comparison of Reaction Rates With and Without Third-Order Correlations, for kt = 1

t_i	A_1	r	A_2	$\frac{(\partial\bar{C}_\alpha/\partial t)}{(\partial\bar{C}_\alpha/\partial t)_s}$	$\frac{(\partial\bar{C}_\alpha/\partial C)}{(\partial\bar{C}\alpha/\partial t)_I}$
1.0	0.19	-0.41	-0.04	0.92	1.0
0.50	1.40	0.61	0.02	1.86	1.0
0.33	2.7	0.67	0.50	2.80	1.0
0.20	5.0	0.74	1.48	4.70	1.0
0.10	11.0	0.75	4.00	9.25	1.0

The effect of neglecting the third-order moments is not evident at kt = 1, however, since we started with the correct value of $\overline{C'_\alpha C'_\beta}$, and the integral effect of neglecting $\overline{C'^2_\alpha C'_\beta}$ and $\overline{C'_\alpha C'^2_\beta}$ is not yet large at kt = 1. Their integral effect on the predictions of $\bar{C}_\alpha$ and $\partial\bar{C}_\alpha/\partial t$ can be seen, however, in the time histories of these quantities when the third-order correlations are neglected. Values of $B_1 = \bar{C}_\alpha/\bar{C}_{\alpha I}$ and $B_2 = (\partial\bar{C}_\alpha/\partial t)/(\partial\bar{C}_\alpha/\partial t)_I$ for each value of t_i and kt = 1, 5, 10, 16, and 20 are listed in Table 2.

An inspection of this table shows that the first effect of neglecting the third-order correlations, while retaining the first- and second-order moments, is to produce significant errors in the reaction rate. This is, of course, the first integral effect on $\overline{C'_\alpha C'_\beta}$. The second effect is on the mean values predicted for the concentrations, an error which depends upon the time integral of $\overline{C'_\alpha C'_\beta}$. We also note that not only can the errors be large (for example, the reaction rate is overpredicted by a factor of 100 when t_i = 0.1 and kt = 20) but we get the totally erroneous results of positive values of $\partial\bar{C}_\alpha/\partial t$ and negative values of $\bar{C}_\alpha$!

Table 2. Time History of Reaction Rates Predicted Neglecting Third-Order Correlations

t_i	kt = 1		kt = 5		kt = 10		kt = 16		kt = 20	
	B_1	B_2	B_1	B_2	B_1	B_2	B_1	B_2	B_1	B_2
1.0	1.0	1.01	1.0	1.33	1.0	1.25	1.0	1.40	1.0	1.60
0.50	1.0	1.00	1.05	1.60	0.92	2.60	0.83	(-6.80)	0.77	(-2.35)
0.33	1.0	1.00	1.21	1.17	1.24	1.50	1.08	(-1.50)	0.96	(-0.50)
0.20	1.0	1.00	1.67	0.54	7.20	0.30	(-1.33)	0.09	(-0.50)	0.02
0.10	1.0	1.00	2.31	0.40	(-1.42)	0.41	(-0.30)	0.03	(-0.14)	0.01

Note: ( ) indicates $\overline{C}_{\alpha I}$ or $\left(\frac{\partial \overline{C}_\alpha}{\partial t}\right)_I$ has the wrong sign.

From these results we conclude that a generally useful chemical kinetic model must include the representation of the moments of the concentration fluctuations through the third-order.

SUMMARY

The various considerations and examples of the effects of concentration fluctuations on chemical reaction rates discussed above may be summarized as follows:

- The effects of concentration fluctuations can be significant, to the point of dominating chemical reaction rates. The situations under which they are significant are characterized by joint distributions of the reactant concentrations which are skewed toward large values of these concentrations, since this is the condition under which the variance-to-mean-squared ratios can be large with respect to 1.
- The chemical reaction rate is significantly accelerated when the concentration fluctuations are positively correlated and is depressed when these fluctuations are negatively correlated. Combining these two requirements for significant effects of concentration fluctuations, we may sketch the general character of the joint distributions of C_α and C_β which require the inclusion of concentration fluctuations in chemical kinetic models. These are shown in Figure 6. The first, when $\overline{C'_\alpha C'_\beta} > 0$, is essentially the distribution of concentrations used for the intermittent traffic situation described above. The second, when $\overline{C'_\alpha C'_\beta} < 0$, may be quickly identified with the situation when the chemical reaction is retarded or stopped by local depletion of one of the reactants. This latter case depends strongly upon the relative rates of chemical reaction and of local diffusive mixing. Further study of this situation requires an appropriate coupling of the chemical and diffusion equations.
- For strongly skewed distributions of C_α and C_β, which are the case when concentration fluctuations become dominant in the determination of the chemical reaction rate, the third-order correlations of these distributions *must* be included in the generalized chemical kinetic model. The neglect of these terms leads to the highly erroneous result that either the reactants are produced (rather than depleted) or the mean concentrations go to negative values.

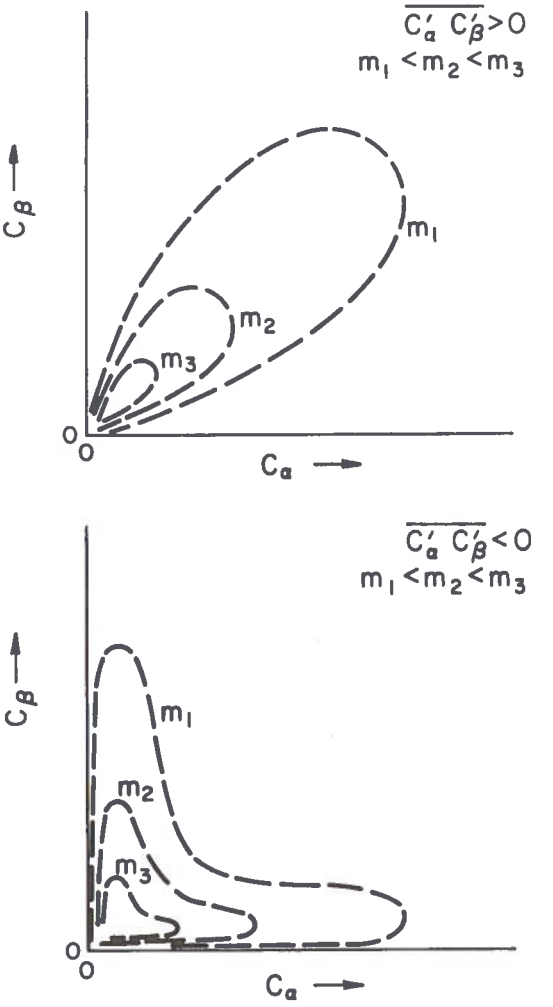

Figure 6. General types of joint frequency distributions of C_α and C_β for which concentration fluctuations are significant in determining chemical reaction rates.

ACKNOWLEDGMENT

This research was supported by NASA Contracts No. NAS1-11433 and NAS1-11873, and by EPA Contract 68-02-0014.

REFERENCES

1. O'Brien, E.E., "Turbulent mixing of two rapidly reacting chemical species," Physics of Fluids *14*, No. 7, 1326-9 (1971).

2. *a.* Donaldson, Coleman duP., and Hilst, Glenn R., "The effects of inhomogeneous mixing of atmospheric photochemical reactions," Environ. Sci. & Tech. *6*, 812-816 (1972).

b. Donaldson, Coleman duP., and Hilst, Glenn R., "Chemical reactions in inhomogeneous mixtures: The effect of the scale of turbulent mixing," Proc. 1972 Heat Transfer and Fluid Mechanics Institute, Stanford University Press (1972).

3. Donaldson, Coleman DuP., "A progress report on an attempt to construct an invariant model of turbulent shear flows," AGARD Conf. Proc. No. 93, London (1971).

DEVELOPMENT OF A THREE-DIMENSIONAL STRATOSPHERIC GLOBAL CIRCULATION MODEL AT THE NATIONAL CENTER FOR ATMOSPHERIC RESEARCH

WARREN M. WASHINGTON
*National Center for Atmospheric Research**
Boulder, Colorado

ABSTRACT: The NCAR global circulation model has recently been used to investigate the effects of orography on the general circulation of the stratosphere. To simulate the observed stratospheric features, such as the Aleutian stratospheric anticyclone in January, we need to include the effect of orography. We arrived at this conclusion by performing numerical experiments with and without orography. Without mountains, we find that the stratospheric patterns are nearly zonal, whereas in the more realistic mountain experiment we obtain very good agreement with observed stratospheric geographical distribution.

INTRODUCTION

Numerical experiments with the 12-layer NCAR model were performed and compared to the observed January climate. The principal objective of these experiments was to see the effect of the earth's orography on simulation. As we will point out in more detail, this effect is very important in simulating the proper geographical distribution in the stratosphere.

The stratospheric model developed at NCAR is a logical sequel to the earlier tropospheric version. To compare our stratospheric model with the earlier version, we added six 3-km layers to the top of the previous model [1-3], which extended it from 18 km to 36 km. This addition required changing the radiation treatment so that we now account for ozone heating within the lower stratosphere. The remaining physical processes in the model were left unchanged.

BRIEF DESCRIPTION OF MODEL

A complete description of the tropospheric model can be found in the references cited in the Introduction. We mention only briefly some of the features of the model not covered in these references.

Figure 1 shows the vertical cross-section of the model. We now have 12 layers of 3 km each, which extends the model atmosphere vertically to 36 km. Surface pressure P_s and vertical velocity w_s are computed along the earth's surface, and within the troposphere and stratosphere pressure p and vertical velocity w are computed at 3-km intervals from 3 to 36 km. Zonal and meridional wind components u and v, respectively, temperature T, specific humidity q, and density ρ are computed at 3-km intervals from 1.5 to 34.5 km. The enlarged section in Figure 1 shows the boundary variables within the Prandtl and Ekman layers. On the left side of the figure, we indicate the approximate pressure levels.

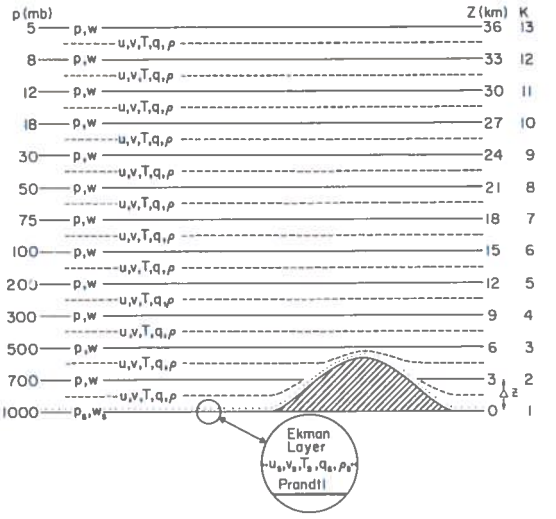

Figure 1. Vertical cross-section of the 12-layer NCAR stratospheric model.

* The National Center for Atmospheric Research is sponsored by the National Science Foundation.

The horizontal grid is subdivided into 5° intervals of latitude and longitude. To prevent the geographical distances from becoming too short in the polar region, we interpolate values longitudinally. The methods of interpolation, as well as other numerical procedures used for the model, are discussed in Oliger et al. [4].

For this January simulation, we specify the sun's declination and the observed January mean ocean surface temperature. Over land and snow-ice regions, we compute the surface temperature from an energy equation based on a balance of solar flux, net infrared flux, latent heat flux, and sensible heat flux between the surface and both the atmosphere and the subsurface layer. The tropospheric cloudiness at 3 and 9 km is computed from the moisture amounts in the hydrological cycle. The method of dealing with orography and the subgrid-scale horizontal and vertical transports of momentum, sensible heat, and moisture can also be found in the previously mentioned model references.

A detailed comparison between observations and our computations is now in progress; however, we will show a few results of the latest experiments. In Figure 2, we depict the 30-day mean distribution of kinetic energy with wavenumbers (1-5) for different levels (4.5, 19.5, and 31.5 km) and latitudes (60°N, 30°N, 0°, 30°S, and 60°S). The solid and dashed lines represent the mountain and non-mountain experiments, respectively. Since most of the energy is in the lowest wavenumbers, we shall discuss them only. As Dickinson [5] and others have shown from theoretical studies, only the planetary waves of lowest wavenumbers transmit energy upward from the troposphere to the stratosphere. For waves with higher wavenumbers, the energy is generally trapped in the troposphere. As we see in Figure 2, most of the kinetic energy in the winter stratosphere (31.5 km) is in wavenumbers 0-3, whereas in the summer hemisphere the energy amounts are much less and proportionally more in the zonal component. One point of special interest is that for the mountain case we see a dominance of wavenumber 1 at 31.5 km. We also note that there is more energy available in the troposphere for transmission to the stratosphere in the winter hemisphere. We will be able to see how hemispheric-dependent this result is when we complete our July experiment.

Figures 3 and 4 show the meridional transports of westerly momentum $\overline{u'v'}$ by large-scale eddies and sensible heat flux $\overline{v'T'}$. We can easily see that the addition of mountains enhances the eddy transports of both quantities. Although we have not completed the analysis of the experiments, we expect that most of this additional transport in the stratosphere will be in relatively low wavenumbers. In the troposphere, we see that the eddy sensible heat transport is less in the higher northerly latitudes in the mountain experiment compared to the non-mountain case. This is also found to a lesser extent in the tropospheric simulation of Kasahara and Washington [3]. The agreement of both quantities with the observed data is quite reasonable.

The geographical distribution of the pressure at fixed heights for the model is compared with the observed heights at fixed pressure. The correspondence is not exactly one-to-one. The important point here is to see whether the 30-day mean geographical distribution is close to the observed pattern. In Figure 5, we see that the mountain experiment M is much closer to the observed than the non-mountain experiment NM. We believe the main reason for this improvement is that the tropospheric simulation is better in the mountain experiment. We will discuss the details of this improvement in our forthcoming paper. One failure of this and other general-circulation models (see References 6 and 7) is that they do not reproduce the stratospheric sudden warming. The reason for the failure of the models has not yet been fully explored.

ACKNOWLEDGMENTS

I acknowledge my two collaborators on the stratospheric model – T. Sasamori and A. Kasahara. We are also grateful to G. Williamson for running the experiments.

REFERENCES

1. Kasahara, A., and W.M. Washington, 1967: "NCAR global general circulation model of the atmosphere," Mon. Wea. Rev. *95*, 389-402.
2. Washington, W.M., and A. Kasahara, 1970: "A January simulation experiment with the two-layer version of the NCAR global circulation model," Mon. Wea. Rev., *98*, 559-580.

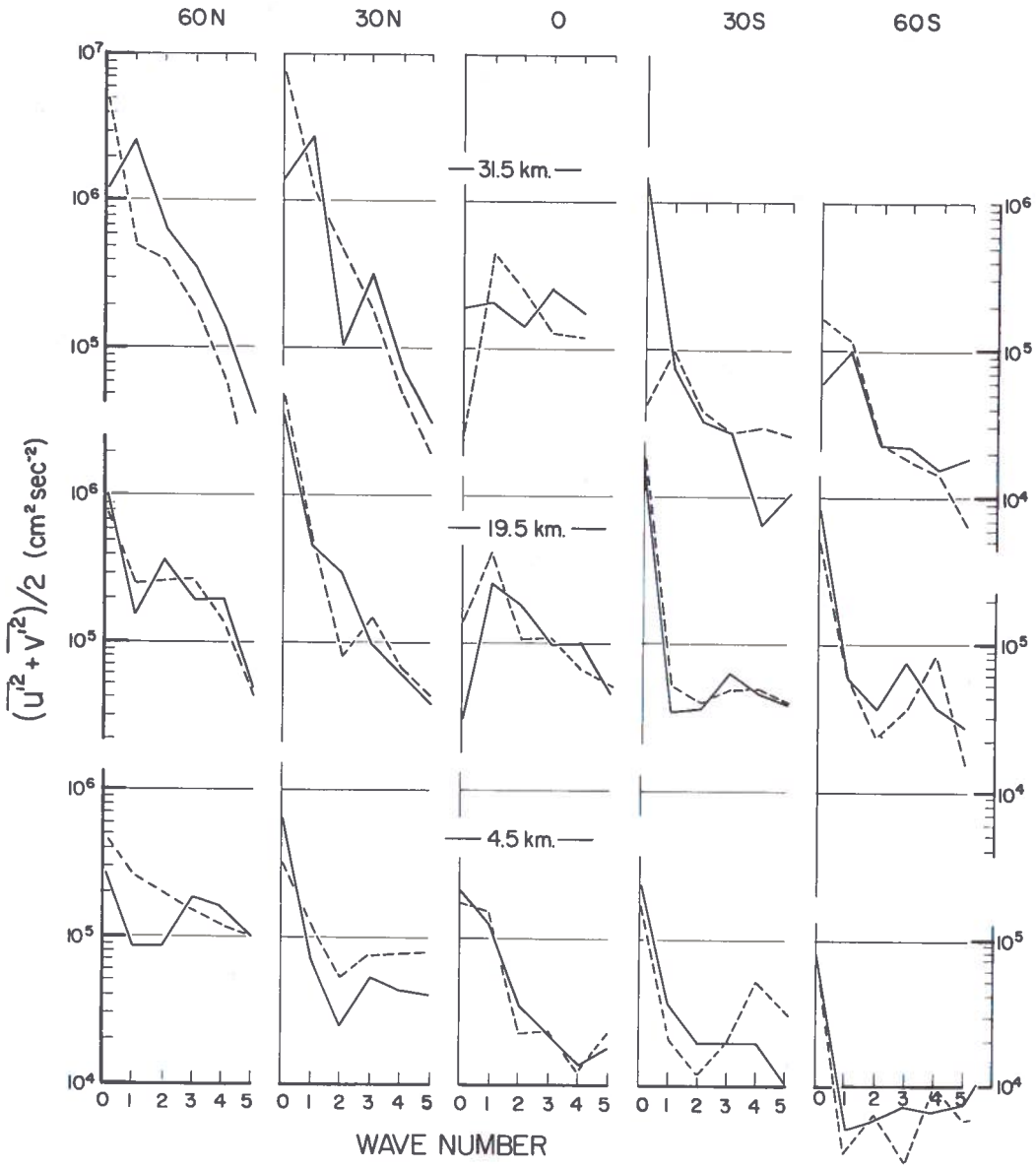

Figure 2. Distribution of eddy kinetic energy vs. wavenumber for various levels and latitudes.

3. Kasahara, A., and W.M. Washington, 1971: "General circulation experiments with a six-layer NCAR model, including orography, cloudiness and surface temperature calculations," J. Atmos. Sci. *28*, 657-701.

4. Oliger, J.E., R.E. Wellck, A. Kasahara, and W.M. Washington, 1970: *Description of NCAR Global Circulation Model*, NCAR TN-56, National Center for Atmospheric Research, Boulder, Colo., 94 pp.

5. Dickinson, R.E., 1968: "Planetary Rossby waves propagating vertically through weak westerly wind wave guides," J. Atmos. Sci. *25*, 984-1002.

6. Mahlman, J.D., and S. Manabe, 1972: "Numerical simulation of the stratosphere: Implications for relative climate change problems," in *Proceedings of the Survey Conference*, Feb. 15-16, 1972, Climatic Impact Assessment Program, A.E. Barrington, ed., Department of Transportation, DOT-TSC-OST-72-13, 186-193.

7. Miyakoda, K., R.F. Strickler, and G.D. Hembree, 1970: "Numerical simulation of the breakdown of the polar night vortex in the stratosphere," J. Atmos. Sci. *27*, 139-154.

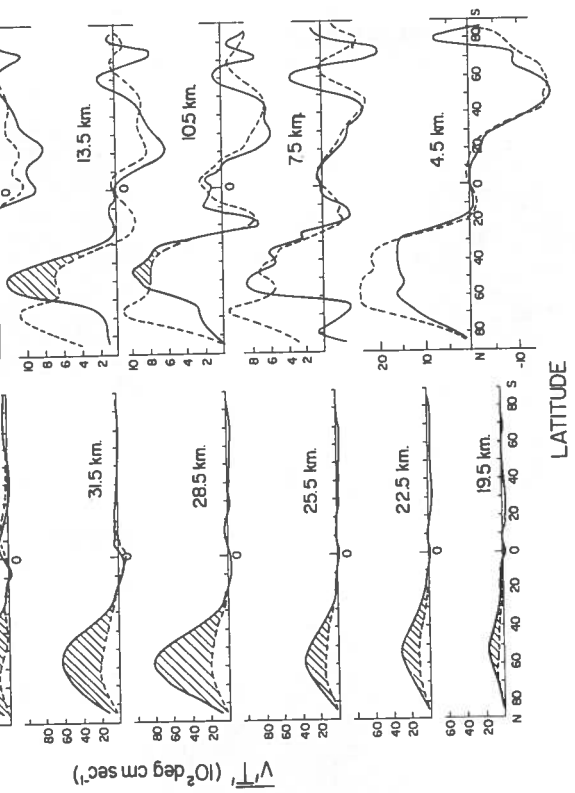

Figure 4. Latitudinal distribution of $\overline{v'T'}$ for different levels.

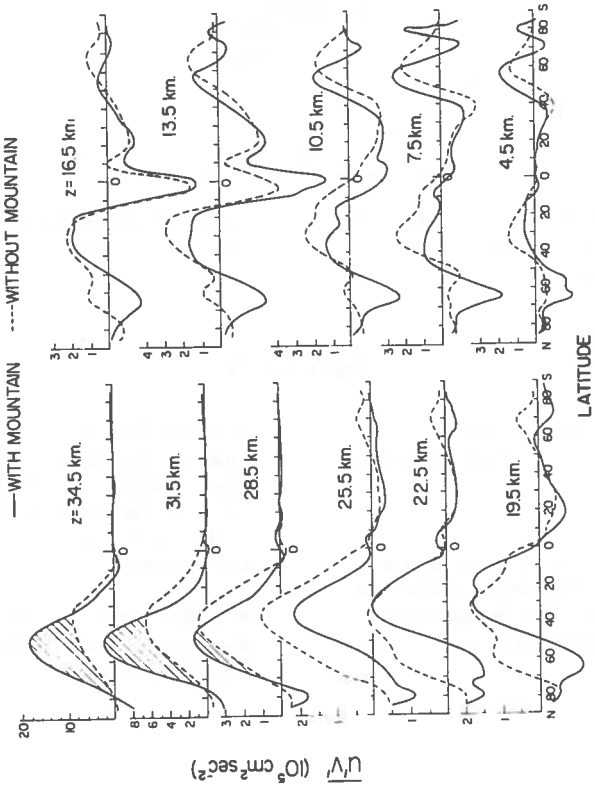

Figure 3. Latitudinal distribution of $\overline{u'v'}$ for different levels.

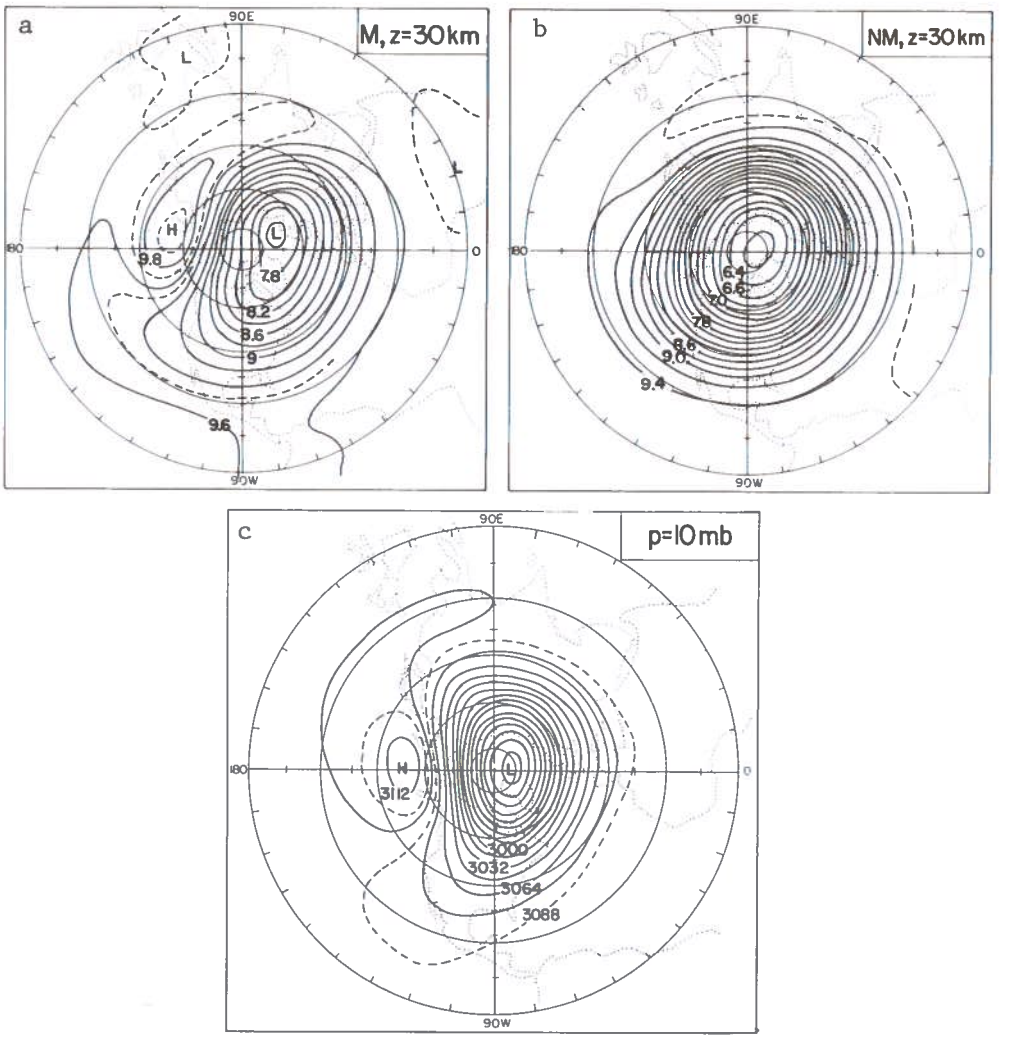

Figure 5. Comparison of computed and observed geographical distribution for January: (a) mountain experiment M at 30 km, (b) non-mountain experiment NM at 30 km, (c) observed heights at 10 mb.

DISCUSSION

(UNIDENTIFIED): Is the effect of mountains on the stratosphere a direct one, or a coupling mechanism through the hydrologic cycle?

WASHINGTON: I can't give you a simple answer to that. The mountains must be included to simulate the troposphere properly; we suspect that this improvement in tropospheric circulation is reflected by proper stratospheric circulation.

(UNIDENTIFIED): It seems to me that if you take a ratio of eddy kinetic energy to total energy or zonal kinetic energy, you should get numbers lower than those of the actual atmosphere. If this is how your model works, why do you get larger horizontal eddy heat transfer?

WASHINGTON: The contours aren't quite the same in the diagrams, but the computed and observed values are about the same.

THE SENSITIVITY AND COMPARISON OF GENERAL ATMOSPHERIC CIRCULATION MODELS

MICHAEL WARSHAW
The Rand Corporation
Santa Monica, California

ABSTRACT: A series of statistical tests on the data produced by simulations of the global atmosphere should be performed to ensure that observed changes in climatological variables are attributable to systematic differences in the state of the atmosphere – not merely to random excursions of the same atmospheric system.

Erroneous conclusions could result from improper testing. For example, it is difficult at present to compare two different simulations with each other, or to compare a simulation with the real climate.

INTRODUCTION

The use of a computer simulation of the global atmospheric circulation is the most promising way of answering the climatological questions posed by the Climatic Impact Assessment Program. Among the many problems inherent in the use of such models, we have chosen to investigate the following three:

- How sensitive is the model to changes in boundary conditions? That is, can an observable change in a predicted atmosphere be causally related to the boundary condition change or is it just an acceptable random state resulting from a slight perturbation or uncertainty in initial conditions?
- Models claiming to predict the same physical phenomena should agree if they begin with identical boundary and initial conditions. What is meant by "agreement" in the presence of small differences in initial conditions, and do existing models, in fact, agree?
- A model, ideally, should predict the real atmosphere. Does this happen? Or, alternatively, what actual comparisons are possible between a model and a very large file of real climatological data?

The eventual purpose of this study is to formulate statistical models, testing procedures, and data retrieval programs which will help answer these questions. This paper will describe some of our past and present approaches and experience with the first of the three tasks, model sensitivity, and then briefly describe some future plans for tasks two and three. With regard to present work, it is too soon for conclusive results. For this reason, this paper is informal and discursive. We will save formalism for the time when definitive results are available.

THE ORIGINAL EXPERIMENT

In all the discussion to follow, the word "model" refers to the Mintz-Arakawa 2-level general circulation model [1,2]. For some time, the almost canonical question (or scapegoat problem) was, "What would be the effect on the climate if all the Arctic sea ice were replaced by water at -1°C?" (Water temperatures in the M-A model are not permitted to vary.) We entered the arena early in 1972 [3] with the experiment described below.

The initial conditions were chosen to simulate the state of the atmosphere for December 31, and the model run to simulate the next 60 days. This run is called the "control" run. Next, the initial global temperature fields at both the 400-mb and 800-mb levels were perturbed with an additive random temperature. These random "noise" temperatures were drawn from a normal distribution having zero mean and 1°C standard deviation. The model was re-run for the same 60 days as the control run. Following this, the original temperature field was again perturbed by

new random additive noise drawn from the same distribution, and the model run again for the same 60 days. This gave us 3 runs, identical in all respects except for very small changes in the initial temperature field.

The experiment is completed by re-running each of the above 60-day simulations, *except* with the Arctic sea ice removed and replaced with sea water. The initial temperature fields are, however, kept identical to those of runs 1-3.

Using these 6 runs, we formulate an analysis-of-variance model and proceed to test the hypothesis that removing the Arctic ice had no effect on the climatological variables of interest. The 2 X 3 layout is illustrated in Table 1, where Y_{ij} for the original experiment was the zonal average of the variable, averaged also over the last 30 days of the run. The procedure has since been extended to a multivariant test, so that the Y_{ij} may now be vector-valued, but Y_{ij} was only univariate in the work reported here.

Table 1. Array of Scalar Variables

	Unperturbed ($Y_{.1}$)	Perturbation No. 1 ($Y_{.2}$)	Perturbation No. 2 ($Y_{.3}$)
Ice In ($Y_{1.}$)	Y_{11}	Y_{12}	Y_{13}
Ice Out ($Y_{2.}$)	Y_{11}	Y_{22}	Y_{23}

We may interpret differences in variables in the same row as "noise" in the experiment, and differences in variables in the same column as useful "signal." An analysis-of-variance procedure provides a sharp procedure for testing whether the row means, $Y_{i.}$, are significantly different by eliminating the effects of differences in the column means, $Y_{.j}$. Table 2 reproduces the results given in [3]; we see that many changes in temperature, geopotential height, zonal wind, and heat transport may be statistically attributed to the removal of the Arctic sea ice.

Some important points remain to be made relative to this original experiment. First, it is readily apparent that the economics of this procedure are totally unacceptable. The cost of simulating a single day by use of the Mintz-Arakawa model is approximately \$230,* so the cost of replicating each run at least three times in order to provide adequate sampling is not likely to be the way of the future. An intermediate approach might be to run n (≥ 3) replications of the control case, each with some initial condition perturbation, but make only one run of the experiment which embodies the change in boundary conditions. For scalar variates, this is the standard t-test, which gives less sharp results than the F-test while reducing the computing by only 30 percent. Ideally, we'd like to make only one control run and one experimental run. Below is an example of how to get into trouble with this approach, followed by a discussion of methods under study to extract more needed information from the sample provided by only one control and one experimental run.

THE CASE OF THE ALEUTIAN LOW

Figure 1 shows the location (latitude and longitude) and pressure of a local minimum in the North Pacific called the Aleutian low. There are six data points, 3 for the ice-in simulations and 3 for ice-out. Originally it was claimed that the removal of the Arctic ice *caused* a significant lowering of the pressure and westward shift of the low pressure center, as inferred from the two nonperturbed data points [4]. Upon running the simulation four more times with the already

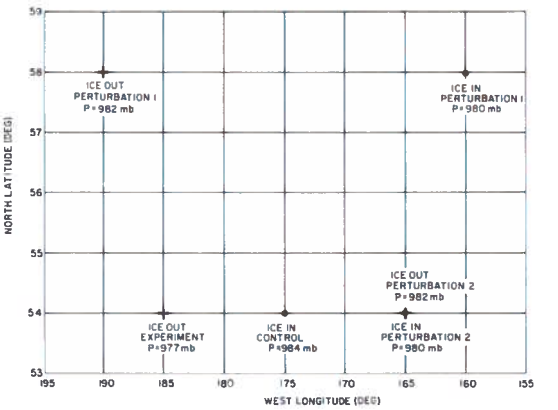

Figure 1. Location and pressure of the Aleutian low. 30-day mean, Arctic ice-in vs ice-out (3 samples of each).

* Using the IBM 360/91 computer at UCLA.

Table 2. Data and Statistics for Temperature, Geopotential Height, Zonal Wind, Polar Heat Transport, and Polar Momentum Transport

Variable	Region	Altitude (mb)	Ice-In			Ice-Out			Mean Ice-In/Out Difference	F-Statistic (1,2) Deg Freedom	Significance
			Control	Pert. 1	Pert. 2	Control	Pert. 1	Pert. 2			
Temperature, T, °C	70-90°N	1000	-21.681	-23.188	-19.987	-6.044	-5.382	-6.145	-15.765	189	Reject @ .005
		800	-26.432	-26.624	-24.63	-17.284	-16.155	-17.342	-8.970	95	Reject @ .01
		400	-48.884	-50.279	-47.277	-53.084	-49.974	-52.166	2.929	3.23	Accept
	54-70°N	1000	-11.823	-11.121	-11.034	-6.561	-6.021	-6.086	-5.104	3169	Reject @ << .005
		800	-19.101	-18.916	-18.214	-14.218	-14.034	-14.008	-4.658	432	Reject @ << .005
		400	-45.866	-47.449	-45.835	-46.185	-46.142	-45.809	-0.339	4.67	Accept
	30-54°N	1000	4.184	4.703	4.072	4.525	4.606	4.84	-0.338	1.82	Accept
		800	-5.230	-4.745	-5.229	-1.703	-4.762	-4.472	-1.423	1.74	Accept
		400	-32.261	-32.172	-32.583	-33.353	-32.746	-32.785	0.622	5.82	Accept
Temperature Gradient ΔT, °C	86°N	T(1000) - T(400)	25.949	25.893	27.448	52.368	48.892	52.621	-24.869	619	Reject @ << .005
Geopotential Height H, Hectometers	70-90°N	1000	4.705	4.667	4.731	4.404	4.473	4.322	0.302	23.5	Reject @ .05
		800	20.951	20.944	21.126	21.441	21.532	21.445	-0.466	35.3	Reject @ .025
		400	68.647	68.491	69.202	69.393	69.840	69.472	-0.788	6.38	Accept
	54-70°N	1000	6.304	6.243	6.296	6.220	6.213	6.221	0.06	14.5	Accept
		800	22.970	22.937	23.039	23.279	23.291	23.285	-0.303	110	Reject @ .01
		400	71.008	70.765	71.195	71.739	71.737	71.771	-0.760	43.5	Reject @ .025
Geopotential Height Gradient, ΔH	H(86) - H(66)	800	-3.756	-3.592	-3.58	-3.492	-3.470	-3.565	-0.134	3.43	Accept
		400	-3.370	-2.814	-2.775	-3.230	-2.900	-3.481	0.217	0.74	Accept
	H(66) - H(46)	800	-1.322	-1.456	-1.199	-0.948	-0.990	-0.981	-0.353	23.7	Reject @ .05
		400	-3.517	-4.047	-3.110	-2.404	-2.669	-2.545	-1.019	18.1	Reject @ .05
Zonal Wind Velocity V, m sec^{-1}	74-82°N	800	-0.171	-1.937	0.220	0.805	1.347	1.576	-1.872	6.86	Accept
		400	3.708	0.896	2.673	5.580	4.697	6.794	-3.265	21.6	Reject @ .05
	46-62°N	800	7.789	9.790	7.434	5.911	7.278	6.816	1.670	9.0	Accept
		400	18.639	21.458	17.508	14.177	16.282	15.580	3.856	15.3	Reject @ .05
Polar Heat Transport F, cal sec^{-1}	70°N	800	2.308×10^{14}	2.668×10^{14}	3.164×10^{14}	1.306×10^{14}	1.324×10^{14}	1.055×10^{14}	1.485×10^{14}	20.6	Reject @ .05
		400	1.012×10^{14}	-1.346×10^{14}	-1.146×10^{14}	0.190×10^{14}	0.770×10^{14}	-5.484×10^{14}	1.015×10^{14}	0.53	Accept
Polar Momentum Transport, M g cm^2 sec^{-2}	70°N	Total	1.265×10^{26}	1.443×10^{26}	1.246×10^{26}	0.771×10^{26}	0.639×10^{26}	0.977×10^{26}	0.522×10^{26}	11.3	Accept

described perturbations, it became clear (and you needn't be a statistician to see it) that the shift and lowering of the pressure was well within the random variation of the triple of numbers (latitude, longitude, pressure).

This is exactly the sort of problem which will have to be faced over and over again when searching simulation results for significant change in the presence of the very high cost of additional samples.

PRESENT WORK IN HYPOTHESIS TESTING USING TWO SIMULATION RUNS

The central problem in assessing the sensitivity of a climatic simulation is simply how to get enough *independent* samples of both the control and the experiment to permit some reasonably sharp form of hypothesis testing. Instead of making independent runs as described above, we are trying to extract equivalent information from the temporal sequence of data generated by a single run.

Remembering that this is not a report on final results, but only an interim statement, we'll outline procedures which are now undergoing tests with both simulated and real data.

Assume the model produces a sequence of data, i.e., a variable of meteorological interest, possibly vector-valued, $X_1, X_2, \ldots, X_n$. For example, X_i might be the array representing the 800-mb temperatures at every grid point over North America, and the subscript indexes time. For the Mintz-Arakawa model, X_i and X_{i+1} are separated by 6 hours. One procedure is to take all the available data (if the simulation were 60 days long we'd have $X_1, X_2, \ldots, X_{240}$) and find the smallest k such that the subsequence X_1, $X_{1+k}, X_{1+2k}, \ldots, X_{1+nk}$ $(1 + nk \leqslant 240)$ has the following properties:

- The subsequence has a sufficiently small estimated first-order correlation coefficient, $\hat{r}_1$. We expect the Durbin-Watson test for absence of first-order correlation to provide the appropriate testing procedure. That is, if we accept the null hypothesis from the Durbin-Watson test, we claim the subsequence is uncorrelated.
- The subsequence has no significant cyclical component. The turning-point test [5] provides a convenient test of this property. The turning-point test counts the number of "peaks" and "troughs" in the time series and tests the hypothesis that this number came from a distribution of independent random variables.
- Last, the sequence should have no significant linear trend. To test for this property, we apply the Kendall rank correlation test [5]. This test takes the sequence $X_1, X_2, \ldots, X_n$ and counts the number of pairs in which $X_j > X_i$, $j > i$. This number, N, is compared with the expected number in a random series, and the excess (or deficiency) over the expected number indicates a tendency toward a positive (or negative) trend.

If we fail to reject the null hypothesis of all three tests, we have an adequate demonstration that the random variables in the subsequence X_1, $X_{1+k}, \ldots$ are uncorrelated and we'll treat them as independent samples. Assuming that there exists a sufficiently small k (or, equivalently, a sufficiently large sample) which still satisfies the above requirements for both the control and the experiment runs, we proceed as follows:

- Using the independent samples from each run, we estimate the covariance matrix, G, for the vector variables, X_i – that is, the covariance between the same meteorological variables at different spatial locations (say, for instance, over the grid points covering North America).
- We ask that the sample size be large enough to permit the inversion of the covariance matrix. Too few samples, while permitting a rough estimation of G, leaves G singular, and we require G^{-1} to formulate a test statistic.

The investigator, and let's assume he (or she) is a meteorologist, is now faced with the first of several interesting questions. They concern the assumptions he's willing to make about the behavior of the real atmosphere in order to achieve a sharper test in discriminating between the control and experimental run. For instance, should he *assume*, a priori, that nature would generate identical covariance matrices for identical regions independently of whether the control

or experimental condition is being observed? If so, we may proceed directly to the final hypothesis-testing stage. If not, the investigator may call for an equality-of-covariance test [6]. If this test *rejects* the hypothesis of equality, we have the classical Behrens-Fisher problem (that of testing for the equality of means when the variances are unknown and unequal) for which the hypothesis tests are just not as good as for the case of equal covariances. Remember here that a-priori knowledge is better than blindly testing for equality, because there is always the non-zero probability of rejecting the hypothesis of equality when, in fact, it is true. Moreover, the equality-of-covariance test is not very good for large covariance matrices.

In any event, we're finally prepared to use Hotelling's T^2-test [6] to test the hypothesis that the control and experimental runs have the same mean value, where, again, we mean a vector of mean values of the geographical area of interest.

FILTERING THE DATA AND COVARIANCE MATRIX

In order for us to be able to use the T^2-test for equality of two mean vectors, the original data had to meet quite a few criteria. Highly correlated data can do this only at the cost of decreasing sample size. In other words, the more we separate the samples in time trying to achieve independence, the fewer samples we'll have left. There are two procedures which promise to save the really difficult cases.

First, if we have any reason to believe that the data $\{X_i\}$ are generated by a process which is primarily a Markov process, so that successive values of X are represented by the equation

$$X_i = \rho_1 X_{i-1} + U \tag{1}$$

where U is a random variable and ρ_1 is the first-order correlation coefficient, then $\{X_i\}$ is transformed to the uncorrelated sequence $\{Y_i\}$ by the relationship [7]

$$Y_i = X_i - \hat{\rho}_i X_{i-1} \tag{2}$$

where $\hat{\rho}_1$ is the first-order correlation coefficient *estimated* from the sample $\{X_i\}$.

Now, the closer the sequence $\{X_i\}$ comes to behaving as if it were generated by Eq. (1), the closer $\{Y_i\}$ comes to being an uncorrelated sequence. This is all well and good – except when we examine what effect the transformation has had on the moments. Assume now that we actually have two vector sequences $\{X_i\}$ and $\{Z_i\}$ represented in the sample data from the control and experimental runs. To demonstrate this argument, assume both X_i and Z_j have *identical* mean values, μ, and variance, σ^2. Hence we would expect to *accept* an hypothesis made about the equality of means, since by definition they're equal. Now, transform $\{X_i\}$ and $\{Z_i\}$ according to

$$Y_i = X_i - \hat{\rho}_x X_{i-1} \tag{3}$$

$$W_i = Z_i - \hat{\rho}_y Z_{i-1} \tag{4}$$

where $\hat{\rho}_x$ and $\hat{\rho}_y$ are the estimated first-order correlation coefficients and themselves random variables. The sequences $\{Y_i\}$ and $\{W_i\}$ have the following moments:

$$E[Y_i] = (1 - \hat{\rho}_x)\,\mu \tag{5}$$

$$E[W_i] = (1 - \hat{\rho}_y)\,\mu \tag{6}$$

$$\text{var}\,(Y_i) = (1 - \hat{\rho}^2)\,\sigma^2 \tag{7}$$

$$\text{var}\,(W_i) = (1 - \hat{\rho}^2)\,\sigma^2 \tag{8}$$

Notice that the transformation has the favorable property of reducing the variance of each sample, but unfortunately, since $\hat{\rho}_x$ and $\hat{\rho}_y$ are random variables, there is no reason why $E[Y_i]$ and $E[W_i]$ should be equal. In practice, for very large $\hat{\rho}_x$ and $\hat{\rho}_y$, the transformation introduces such a large bias in the means that, even with the variance-reducing property, the transformation is not of much value. However, if by testing for the equality of $\hat{\rho}_x$ and $\hat{\rho}_y$ (say, using the Fisher Z-transformation, [8]) and finding them equal (or by arguing from the physics that one would *expect* them to be equal – a risky proposal) we could define a mean correlation coefficient, $\hat{\rho} = 1/2\,(\hat{\rho}_x + \hat{\rho}_y)$, the Markov process transformation could be of great value since it introduces no extra uncertainty into the problem.

Note that even with all these ancillary tests and assumptions, the Markov process transformation doesn't make for sharper discrimination in the final testing of mean values, since the new means are closer together in a way that is not

compensated for by the reduction of variance. What we might get, however, is a sufficiently large uncorrelated sample, so at least some hypothesis-testing about the equality of means can be done.

Another, even more ad-hoc, procedure might be adopted if the sample size is so small that the covariance matrix is singular. If G is an $n \times n$ covariance matrix, then G is non-singular if $T \geqslant n + 1$ where T is the sample size. In cases where this inequality is not satisfied, we might try formulating the matrix of correlation coefficients, R, associated with G. Then, whenever $r_{ij} < r^*$ set $g_{ij} = 0$, where r^* is some small number. In other words, choose an r^*, say $r^* = 0.1$. Then if the estimated correlation coefficient is less than r^* we arbitrarily set the corresponding covariance $g_{ij} = 0$. This tends to eliminate small values of g_{ij} which contribute very little to the structure of the problem, but do influence the singularity of G. If this is at all acceptable, the trick will be to find an approximation to the smallest r^* which makes G non-singular. Trial and error might suffice.

MODEL COMPARISONS

Rather less progress has been made on the problem of comparing two models or comparing one model to the real atmosphere. A trial comparison has been made between the 3-D Mintz-Arakawa model and the zonally averaged model (ZAM) of MacCracken. This was done to test algorithms which produce compatible initial conditions, and the actual comparison of predicted results wasn't completed.

The comparison is done by computing the zonal averages of M-A results *after* the run has been made, and then comparing these zonal averages with those produced directly by ZAM. Work will be accelerated on the comparison task, but we foresee the problems of what constitutes model agreement and the requisite physical explanation should they fail to agree.

The availability of real climatological data should help here. We are preparing a 5-year data base using NCAR raw data. This consists of temperature, geopotential height, wind, and relative humidity every 12 hours. We stress the importance of obtaining the sequential data at least daily and of insuring that these data are readily accessible to the investigator, and we are implementing a data retrieval system which permits easy comparison between the real climate and the M-A results. The same should be true of ZAM data if we make minor variations in our retrieval program, so there's a lot that can and will be done in the realm of three-way comparisons.

REFERENCES

1. Gates, W.L., E.S. Batten, A.B. Kahle, and A.B. Nelson (1971), *A Documentation of the Mintz-Arakawa Two-Level Atmospheric General Circulation Model*, R-877-ARPA, The Rand Corporation, Santa Monica, Calif., 408 pp.

2. Arakawa, A., (1972), "Design of the UCLA general circulation model," in *Numerical Simulation of Weather and Climate*, Technical Report No. 7, Department of Meteorology, University of California, Los Angeles, 122 pp.

3. Warshaw, M., and R.R. Rapp (1972), *An Experiment on the Sensitivity of a Global Circulation Model: Studies in Climate Dynamics for Environmental Security*, R-908-ARPA, The Rand Corporation, Santa Monica, Calif., 26 pp.

4. Fletcher, J.O. (1971), *Numerical Simulation of the Influence of Arctic Sea Ice on Climate*, International Symposium on Physical and Dynamical Climatology, Leningrad, USSR, 16-20 August 1971.

5. Kendall, M.G. (1963), *The Advanced Theory of Statistics, Vol. III: Design and Analysis, and Time Series*, Hofner Publishing Company, New York, 552 pp.

6. Anderson, T.W. (1958), *An Introduction to Multivariate Statistical Analysis*, John Wiley & Sons, New York, 373 pp.

7. Dyer, R.M. (1971), "Method for filtering meteorological data." Mon. Wea. Rev. *99*, 435-438.

8. Hoel, P.G. (1956), *Introduction to Mathematical Statistics*, John Wiley & Sons, New York, 331 pp.

STATUS OF THE CIAP BIOLOGICAL IMPACT PROJECT

DONALD R. SHELDON
Institute for Defense Analyses
Arlington, Virginia

ABSTRACT: This paper describes the scope of the CIAP BIP, and presents the recommendations which grew out of the Biological Impact Workshop of September 1972.

Let me begin with a brief reading from an ecology book: "Biological components must be combined with sunlight and chemicals in definite proportions according to very definite principles if the environment is to function in a way that makes the continued development of life possible."*

While this conference has been laboring mightily with the questions of "sunlight and chemicals", this session will concentrate on the "proportions and principles".

On September 14 and 15, 1972, a Biological Impact Workshop was conducted here at the Transportation Systems Center. To the biologists, the most interesting possible results of high-altitude aircraft operations were catalytic destruction of ozone by nitrogen oxides injected into the stratosphere, and the consequent increase in intensity of middle UV irradiance in the biosphere. Also of interest, though extremely unlikely, were those energy-coupling interactions whose effects might be felt in terms of climate modification (wind, precipitation, temperature changes). While such effects are far more difficult to quantify than ozone depletion, particularly at the local level, they could have major biological impact.

My objective here is not to detail what is known about the biological impact of these changes, but rather to outline what studies are presently being initiated on behalf of CIAP and to enlist your advice and counsel on their content. Subsequent papers review much of our present knowledge about biological interactions and illustrate the complexity of studies in these areas.

Table 1 lists the various successive levels of biological organization. Many of you, I suspect, generally deal with the components toward the bottom of the list (I prefer the lower middle myself). Each segment interacts with every other one, however, and all influence, and are influenced by, their physical and chemical surroundings.

Table 1. Levels of Biological Organization

Biosphere
Ecosystems
Communities
Populations
Individuals (Organisms)
Cellular Aggregates (Organs)
Cells
Organelles
Macromolecular Aggregates
Macromolecules
Molecules
Atoms

To illustrate the complications involved in designing a biological study program, consider weather response for each of the four seasons. Limit the variables to temperature (hotter, unchanged, or colder) and precipitation (wetter, unchanged, or drier), neglecting differing magnitudes of change and any interactions, and you quickly generate $(3 \times 3)^4$, or some 6,561 different possible climatic years – a situation which exemplifies the complexity of the problem and the need for some simplification.

The biology panel felt that parametric range limitation was a reasonable first step in this simplification. We therefore addressed the question of what and how intense are the impacting forces. Table 2 illustrates the preliminary estimate of the range of changes in climate parameters against which the biological program has been designed.

The lower limit for temperature change is based on work by Rasool which indicated that

* Odum, E.P., *Ecology*, Holt, Rinehart and Winston, New York, 1963.

Table 2. Summary Table of Climatic Parameter Ranges *

Surface Temperature	$-2 < \Delta T < 0.2°C$
Winds	$-0.12 < \frac{\Delta V}{V} < 0.06$
Precipitation	$-0.12 < \frac{\Delta P}{P} < 0.06$
Radiation	$0.07 < \frac{\Delta \Phi_E}{\Delta \Phi} < 2$ ($\lambda = 307.5$)
	$0.40 < \frac{\Delta \Phi_E}{\Delta \Phi} < 30$ ($\lambda = 295$)

* Assumes a fleet of 500 SST's by 1985. Courtesy H. Hidalgo, IDA.

the surface temperature is very sensitive to the aerosol content of the atmosphere. (I should point out, though, as a measure of its uncertainty, that this theory is not supported by volcanic data.) The upper limit was defined by the "greenhouse effect" of increased water content in the stratosphere. Wind and precipitation ranges are derived from the temperature assumptions. The radiative flux was calculated from the ozone absorption coefficient and sun angle at mid-latitudes at equinox, assuming values of 5 and 50 percent ozone depletion by NO_x catalysis. Of course, these are only estimates, and will be modified as we receive results from CIAP investigations into the perturbed troposphere. They were generated just to provide upper and lower limits on these parameters so that biological tests and experiments could be designed with some assurance that final estimates would fall somewhere within the range over which our experiments were conducted.

Biologically speaking, I certainly hope they do, since, for example, a 2°C decrease in global temperature accompanied by a 12 percent decrease in precipitation (which I assume would then fall predominately as a crystalline solid rather than as a liquid) would need little study to document its significant biological effects.

One further comment relative to this table concerns the changes in ultraviolet irradiance. The upper and lower bounds for each wavelength here are predicated upon 50 percent and 5 percent decreases in stratospheric ozone respectively. As you all know, the effect of such changes on radiative flux increases by orders of magnitude with decreasing wavelength. Unfortunately, as subsequent papers show, the efficiency with which UV radiation causes deleterious biological effects also increases at the shorter wavelengths. We have yet to resolve whether large irradiance changes below about 2900 Å, which still result in extremely low dose rates ($< 1 \times 10^{-6}$ W/m^2/nm), have any biological significance.

Recent examination of nuclear test data† apparently reopens the whole question of the significance of stratospheric NO_x injection. It may be we are seeking solutions to a non-problem.

At the September organizational meeting, the biology panel divided into two working groups, one for botanical problems and a second for animal and human health problems. Each was charged with:

- Defining the need for state-of-knowledge review papers
- Outlining the test and experiment programs needed
- Making recommendations for action, ranked in the light of CIAP goals

A final joint session of the two groups resulted in the problem breakdown shown in Table 3. You can see from the list of investigators which areas CIAP is already looking at and which new areas the panel felt should be addressed.

The botanical group made the following recommendations:

1. Initiate field experiments to see how changes in ultraviolet irradiation affect photosynthesis, crop yield, pollination, seed germination, and growth. Since past experiments have rarely had UV flux as the sole variable, screening experiments encompassing a wide range of species are most desirable. The effects on corn, tomatoes, alfalfa, soy beans, grains, selected tree seedlings, and brushy plants would be particularly interesting. (These studies will soon be initiated at Utah State University, University of Florida, and USDA, Beltsville.)

†Foley, H.M., and M.A. Ruderman, IDA Research Paper 894, August 1972.

Table 3. Biological Impact Program

Problem Area	Investigator(s)
• The Effects of Enhanced UV Irradiance	NCI, FDA } Lead Roles
– On Skin Cancer and Human Health	Temple University University of Queensland
– On Terrestrial Plants	USDA University of Florida Utah State University
– On the Aquatic Biome	(to be determined)
– On Insect Populations	(to be determined)
• Agricultural Response to Climatic Change	USDA
• Measurements and Systems Evaluation	NOAA Smithsonian Institute Temple University University of Queensland IDA

2. Initiate similar studies of the effects of UV radiation on shallow-water aquatic plants and planktonic or other free-floating species. (Not yet implemented.)
3. Institute field experiments on ecosystem response to enhanced UV radiation. Of particular interest would be tundra and alpine ecosystems, tree seedling areas, and tropical rain forest. (This is partially covered by experimentation under 1.)
4. Review in depth the literature dealing with the effects of ultraviolet radiation on plants, including pertinent foreign publications, for inclusion in the CIAP Monograph. (Similar reviews are required of all CIAP biological project contractors.)
5. Assemble and critically evaluate the data relating to the effects of climatic change (other than UV irradiance) upon agricultural productivity and related food-availability interactions. Large changes (e.g., ±12%) would certainly have significant, undesirable consequences; what will be interesting is the projection of effects of small changes (e.g., ±1-2%). (The USDA is working on this area.)

As Table 3 showed, the Department of Agriculture has already organized studies in areas germane to its interests. Similarly, the National Cancer Institute has undertaken the task of implementing and monitoring those studies dealing with human cancer problems associated with changes in atmospheric ozone content discussed in the following section. (The results of a recent NCI planning workshop on CIAP problems have been incorporated into the following section.)

The panel group which dealt with animal and human health made the following recommendations:

1. Update and evaluate the epidemiological data with regard to the correlation of latitude of residence, genetic makeup, and life style with the incidence and prevalence of skin cancer in man. An instrument network is badly needed for evaluating the variance in ultraviolet radiation reaching the various populations. For this purpose Robertson-type meters, although admittedly imperfect, might offer the best compromise between cost, availability, and utility of operation. Their use in past studies, which might then be directly correlated with CIAP data, also speaks in their favor. Other devices and methodologies are still being evaluated. (A coordinated effort by NOAA, The Smithsonian Institute, Temple University and Dr. Robertson and his colleagues will be focused upon this instrumentation question. NCI will address the epidemiology of skin cancer.)

2. Initiate experiments and review data on the effects of enhanced UV radiation on insect species and their behavior patterns. (Not yet implemented.)
3. Initiate experiments to evaluate the response of shallow-water animal species (e.g., coral, shallow breeding fish) to enhanced UV radiation. (This has not yet been begun; see paragraph 2 in the botanical group's recommendations.)
4. Initiate experiments employing the hairless mouse and a suitably filtered solar simulator to quantify the magnitude of skin cancer production as a function of increased radiation in this model system, and to investigate the molecular basis of the changes observed. (The likelihood that continuity-of-effort and time requirements for such studies will exceed those available to CIAP has resulted in their being addressed in more definitive terms within the NCI program.)
5. Assemble and analyze data relating to: maximum permissible exposure times for prevention of disabling sunburn as a function of UV flux; the availability and suitability of sunscreen compounds; and changes in life-style patterns which help prevent acute and chronic effects of UV radiation exposure. This effort was viewed as a worthwhile public information/education effort even for current radiation levels, aside from any increase in radiation which might result from stratospheric modification. (Professor Blum's paper in this volume covers the subject in greater detail. At present, however, CIAP does not plan to undertake such studies.)

terms of CIAP predictions of climatic change, and the results compiled and documented. In the area of systems integration, the program will take into account the effects predicted by studies of the perturbed troposphere panel. It will be responsible to the Economic Consequences group for estimates and projections of biological effects. Finally, it is to meetings such as this, of course, that we all look for critical review and comment.

In sum, the biological impact studies of CIAP have been oriented toward the documentation of the causal relationships between the described environmental changes and known problem areas in the biosphere (e.g., the skin cancer problem), as well as towards broader-range surveys of less well understood phenomena (e.g., plant and insect response to UV flux changes). Those interactions which are better understood (e.g., the effects of climate changes on agriculture productivity) will be reassessed in

DISCUSSION

GOLDBURG: I don't think we should ignore the possibility that after all this study we may find that a fleet of SST's might actually increase stratospheric ozone.

ELLSAESSER: I think we should also remember that a climatic change may have deleterious effects in one area and beneficial ones in another, particularly in the case of something like UV, which already varies with latitude. I do have one question I hope someone here can answer: How can snow blindness be due to UV damage, when the regions in which it occurs have the greatest ozone depth and the longest path length?

URBACH: That's easy. Snow and ice are almost perfect reflectors, so that although the sun angle is not high the extremely long exposure times of the Arctic summer result in about double the UV dose you might expect, ten or twelve hours a day. This is more than sufficient to cause serious sunburn and, in part, snow blindness. In fact, it was a North Pole expedition in about 1840 that made the observation that it was ultraviolet light that caused sunburn, back when nobody knew much more about UV than that it existed.

ULTRAVIOLET RADIATION OF SUNLIGHT AND SKIN CANCER

HAROLD F. BLUM
Department of Biological Sciences
State University of New York at Albany

ABSTRACT: At present we are in no position to predict the effects of increased ultraviolet radiation in sunlight, resulting from decreased ozone cover, on the incidence of skin cancer in man. For example, erythema, whose optical sensitivity spectrum is currently used as the measure of UV effects on skin, is not closely enough related to cancer growth to serve as an index. But more important, only recently have ultraviolet irradiance and skin-cancer incidence been studied simultaneously in the same geographical area. Many more such measurements are needed, preferably with instrumentation which takes into account scattered radiation. Even when accurate data on UV radiation, skin cancer, and the ozone cover are available, however, it will be difficult to make sound predictions.

Laboratory experiments indicate that only wavelengths between about 0.29μ and 0.32μ normally cause cancer, but that large doses at longer wavelengths may also be effective. It has also been shown in the laboratory that the cumulative effects of successive doses result in accelerated cancer growth. If this holds true for man, the incidence of skin cancer should be a function of the square root of annual UV radiation in sunlight. The varied characteristics of the human population complicate any estimates.

The physiological effects of reducing the ozone cover are very difficult to estimate, and education in the matter of exposure could mitigate them considerably. The greater dangers may be those which affect the ecological balance of the earth.

In the course of the thirty years or so that I have been concerned with ultraviolet radiation and cancer, many people have asked me how to avoid getting skin cancer from sunlight. For a long time my answer was "avoid excessive exposure", after which I made my getaway before being pinned down as to details. But in the last two years I have had a number of inquiries – some of them from high places – regarding the danger that an increase in ultraviolet radiation, resulting from diminished ozone in the stratosphere, might increase the incidence of skin cancer in our population. I have replied that I should expect the incidence to increase, but that I could not estimate to what extent (although I have been confronted with various estimates made by others). Now it seems I can no longer escape giving reasons for my reticence on those occasions, which stems from a healthy respect for the complexity of the problem.

It would seem that if we knew enough about geographical distribution of the ultraviolet radiation of sunlight, of the incidence of skin cancer, and of the ozone cover, we ought to be able to predict the effect of changes in the last by comparison of figures for different regions of the earth. But even if enough measurements of these three aspects of the problem were available, correlating them so as to make sound predictions would not be a simple matter. I shall try, in the limited time available, to anticipate some of the difficulties and uncertainties that would be encountered, in hopes of giving you a better idea of the kinds of measurement that might be needed and the compromises that would have to be made.

Let us examine some factors and conditions that make estimating the relationship of sunlight and skin cancer so difficult and uncertain. Figure 1 represents spectral relationships that need to be taken into account. The curves drawn there, however, are only approximate, and some of them are no more than sophisticated guesses. Indeed, it might be well to think that each curve asks a question rather than answers one. For example, what are the wavelengths of sunlight that cause cancer? Here we must depend upon measurements made with experimental animals (mice and rats), since direct experiments cannot be made on human beings. Using mice, mercury arc radiation, and spectral filters, we have been able to set a long wavelength limit at about 0.32μ, since longer wavelengths do not induce cancers under these conditions [1]. But does this limit apply to men and sunlight?

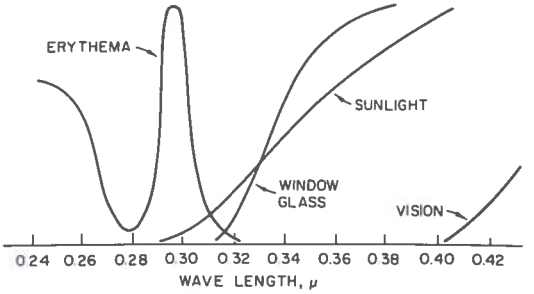

Figure 1. Spectral relationships (reproduced with permission of Geographical Reviews [9]). The ordinate units are arbitrary, so the curves show only approximate spectral relationships. The ERYTHEMA curve shows relative response to different wavelengths. As wavelength increases, SUNLIGHT increases in intensity, WINDOW GLASS transmission increases, and sensitivity of VISION increases.

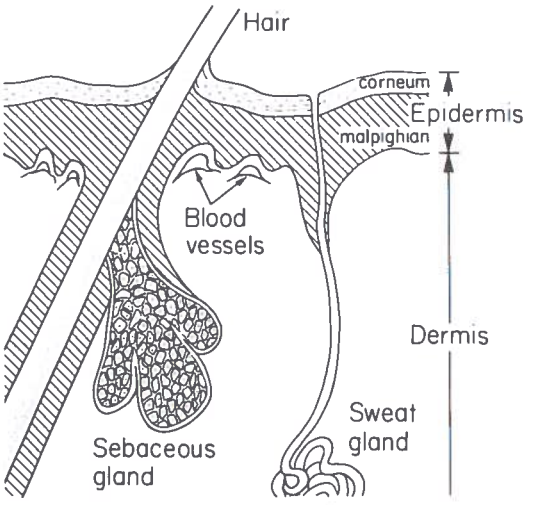

Figure 2. Schematic cross-section of human skin (reproduced with permission of Geographical Reviews [9]).

The generally adopted measure of the action of ultraviolet radiation on human skin is a curve of the kind labelled *erythema* in Figure 1, which has a long-wavelength limit at about 0.32μ. This curve is based on observations of the erythema (red color) that develops locally after skin has been dosed with monochromatic ultraviolet radiation. Aside from inaccuracies that may enter into such determinations [2], how well does this curve correspond to the spectrum of cancer induction? Figure 2 is a diagrammatic cross-section of human skin; it is oversimplified, but illustrates the kind of optical situation with which we must deal. The erythema results from dilation of small blood vessels that lie just beneath the epidermis, permitting increased blood flow in them. The dilation results from photochemical action in the epidermis, however, rather than in the vessels themselves. (Here again I am giving an oversimplified outline of things that may add to the uncertainty of the problem at hand [3].)

Skin cancer is a manifestation of abnormal growth in the population of living cells of the epidermis. It is not closely related to the dilation of the underlying vessels, and cannot be measured accurately in terms of the erythema spectrum. The corneum (Figure 2) is composed of remains of dead cells that were once part of the live layer beneath. The corneum absorbs spectrally (the absorption being enhanced by scattering), and so acts as a filter that modifies the shape of the erythema spectrum, as can be seen by comparing the curves in the upper part of Figure 3. The situation is no doubt further

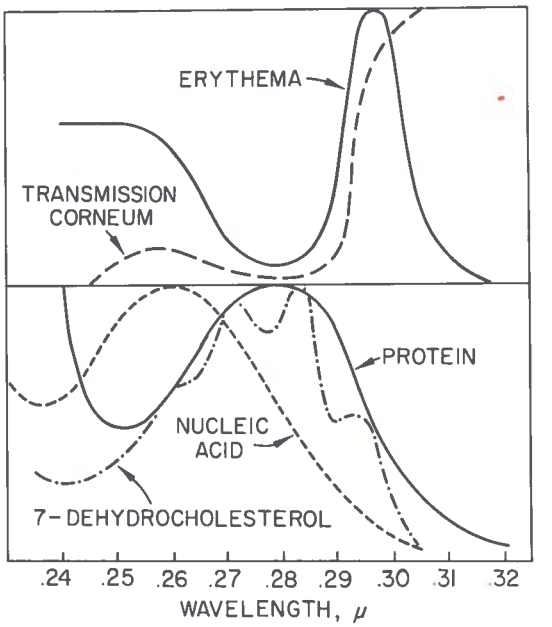

Figure 3. Spectral relationships between erythemal response and other factors (reproduced with permission of Geographical Reviews [9]). Ordinate units are arbitrary. Above, TRANSMISSION CORNEUM represents measured transmission of a sample of human corneum. Below, absorption spectra of three photoreactive substances in skin (7-dehydrocholesterol is the percursor of vitamin D.)

complicated by inner filter effects, including absorption and scattering by particles of the melanin pigment which gives dark color to skin.

In the lower part of Figure 3 are shown absorption spectra for three substances: nucleic acid, protein, and the precursor of vitamin D. All of them may be light-absorbers for photochemical reactions in the epidermis, and could conceivably play this role in cancer induction, but the complex optics of the skin do not permit us to tell which. All these photobiologically active substances have limits of absorption not far from 0.32μ, which may give us confidence in this value as a long-wavelength limit for cancer induction. All the curves fall off asymptotically, though, as does the erythema curve, so any limit has to be chosen somewhat arbitrarily and cannot be considered exact. Forbes [4] has shown recently that radiation of wavelengths longer than 0.32μ can induce cancers if the doses are large enough. The intensity of sunlight rises rapidly in this region; it can be seen from Figure 1 that such an effect, whatever its explanation, could shift the effectiveness of sunlight toward longer wavelengths. Laboratory experiments such as those projected by Fred Urbach, using simulated sunlight and hairless mice to simulate human skin more closely, may give us better information in this regard. But in the meantime, at least, we are making a guess when we use the erythema spectrum as a measure of cancer induction, the sophistication of the guess depending on how well we understand the uncertainties involved.

Under outdoor conditions the short-wavelength limit of sunlight reaching the earth's surface sets a limit for cancer induction around 0.29μ, although radiation of wavelengths as short as 0.2537μ induces cancer under laboratory conditions. Because of the high absorption coefficient of ozone, however, the shorter-wavelength region of sunlight varies greatly with solar angle (both in amount and shape of the spectrum) and, of course, with the amount of ozone cover. Such variation may be measured with a flat-surfaced instrument; we are concerned with an integration of the ultraviolet radiation that impinges on odd-shaped surfaces, however, such as a man's face, and here other factors enter. Rayleigh scattering makes scattered radiation probably more important than direct sunlight as regards our problem. We cannot see ultraviolet radiation (see Figure 1), but if we could the sun might appear as only a bright spot in a blazing heaven. Another factor is reflection from the terrain, which is much greater from a snow field than from greensward or forest. With ultraviolet radiation coming from all directions, estimation of the amount absorbed by the skin has to take into account the pattern in which this radiation reaches the exposed skin, which Urbach [5] has shown to vary widely with sky, terrain, and solar angle. When we add these uncertainties to the biological ones, the possibility of making exact measurements that would be meaningful with regard to our problem appear overwhelming. Can we make some compromise?

Studies of incidence of skin cancer have not as a rule been accompanied by attempts to measure ultraviolet radiation in the geographical areas concerned; a latitude distribution similar to that of total or visible sunlight has all too often been assumed. Recently, however, studies have been made which measured ultraviolet radiation and skin cancer in the same geographical areas. These began in Australia, where physicists and epidemiologists teamed together [6,7], and have been extended to New Guinea, Philadelphia, and Ireland [5]. As a result, we have much better evidence than heretofore that the ultraviolet radiation in sunlight causes cancer of the skin of man. The studies are not sufficient for the kind of estimates we would like to make, however, and should be extended.

After what I have said about uncertainties, you are no doubt curious as to how ultraviolet radiation was measured in these studies. Here we come to a compromise. The instrument designed for the purpose by Don Robertson [7] presents a flat horizontal surface to sun and sky, and so neglects radiation reflected from the terrain. The photosensitive element is a magnesium tungstate phosphor which has a spectral range similar to that of the erythema spectrum – but, as has been pointed out, this may not correspond exactly to the spectrum for cancer induction. The instrument measures total ultraviolet radiation reaching the phosphor, but cannot distinguish spectral variations. These are weaknesses, but they would enter to some extent with any instrument that might be devised. On the advantage side, this instrument has been field-tested for stability, and it can give a continuous record of its measurements in absence of an operator. At the moment

we are concerned with getting measurements as rapidly as possible, and this instrument provides a uniform standard for comparison. The same uniformity is needed in epidemiological measurements, and we might save time by following the methods adopted by the Australians. Then if a better instrument is devised for measuring ultraviolet radiation (which does not seem very likely, considering the uncertainties), and if epidemiological methods better adapted to the particular purpose become available, we may make the necessary adjustments without losing the value of those measurements already made. In any case, it seems unlikely that enough data can be gathered to make the kinds of estimates that are desired before the deadline that has been set. But it is important to get data now from as many places as feasible if we are to have a datum plane from which to measure changes, if and when the ozone cover in the stratosphere is altered.

Once measurements of cancer-inducing radiation have been obtained, the problems of comparison and interpretation arise; here laboratory experiments can again give needed insight. Cancer is a growth process based upon duplication of cells, in which the overall growth rate depends upon both rate of duplication and the size of the participating cell population. These things determine whether cancer will appear before an animal dies of old age or other causes. To induce cancers with ultraviolet radiation the dose must be repeated many times. This gives an all-important clue, since it suggests that each successive dose accelerates growth of the cancer. If the doses have equal accelerating effect, the following series rule should be obeyed:

$$1+2+3+...n = (n^2+n)/2 \cong n^2/2\,, \qquad (1)$$

where n is the number of doses.

The last member of (1) is a close approximation when n is large, and assuming that equal-sized doses are given, and that each dose increases growth rate in proportion to its energy, the following proportionality should be observed:

$$n_c^2/2 \propto 1/D\,, \qquad (2)$$

where D is the amount of ultraviolet radiation in a single dose, and n_c the number of doses that must be given before a cancer appears.

Experiments with equally spaced doses and varied dose size conform to this proportionality. But n_c also varies with the interval, and here a more complex relationship obtains. In a recent reanalysis of our data [8] I have found a theoretical explanation which quantitatively fits the wide variety of dosage conditions studied, heretofore unrecognized indeterminacy being taken into account: the rate of cell duplication and the size of the population of duplicating cells cannot be measured simultaneously. I will not go into the theory, but only point out that its success in explaining results of experiments on mice lends confidence that the proportionality represented in (2) applies to man.

Returning to outdoor conditions, and again oversimplifying, let us treat each year's total ultraviolet radiation from sunlight as a single dose (A), and assume that these are equal for all years. The incidence of tumors (S) among a population of persons subjected to similar sunlight exposure should on this basis be inversely proportional to the average number of years required to induce cancers (Y),

$$S \propto 1/Y \propto A\ 1/2. \qquad (3)$$

Thus the incidence of skin cancer would be related to the square root of the annual ultraviolet radiation of sunlight, and estimates based on an assumed linear relationship could be subject to wide error. Variations in annual radiation would be summed into the total accumulated effect, thus adding one more uncertainty to our estimates.

There is a general desire to set tolerance limits for any noxious agent, but it should be clear by now that this cannot be done with any assurance for ultraviolet radiation and skin cancer. We have to depend on laboratory measurements again. All animals that have received a number of doses of ultraviolet radiation presumably have cancers [8], but these may not grow fast enough in some animals to be observed before death. Thus, the life span of the animal also enters into any tolerance limit that might be set.

Up to this point no mention has been made of the effect of variation in intensity of ultraviolet radiation. It was found in the laboratory that n_c increases as an exponential die-away function of intensity (dose-rate) without abrupt break, down to the point at which death of the

animals prevents further measurements [8]. Thus no intensity threshold can be set – instead we have one more uncertainty, since intensity is one of the variables in natural sunlight.

Given all these uncertainties, one may surely hesitate to apply "common-sense" physical criteria to this problem without taking into account the biology of the system dealt with. Here we have more uncertainties, including one that is very serious. The animals used in laboratory experiments are genetically homogeneous, whereas genetic inheritance in the human population is quite mixed. This has a bearing on skin cancer incidence; for example, blacks in the United States have much less skin cancer than whites. This is no doubt related to protection afforded by the melanin pigment that colors the negro skin, but thickness of the corneum and perhaps other factors also enter [9]. We do not have adequate information to judge how close a parallel should be drawn between skin color and response to ultraviolet radiation. If we are to estimate the effect of change of ozone cover on the incidence of skin cancer in human populations, we need to take into account the distribution of hereditary characteristics, and this may be complicated (to say the least).

I fear I have not indicated great confidence in predictions as to the increase in skin cancer which might be expected if the ozone cover is reduced, except to agree that there should be some effect. Even with more adequate measurements of outdoor conditions we might still be at a loss as to how to interpret them. Laboratory studies more nearly simulating the problem may be helpful, but they will take several years to carry out.

Up to now I have stressed the problem of skin cancer, since this is one that seems uppermost in people's minds at moment. But sunburn and the production of vitamin D in the skin are more directly related to the ultraviolet of sunlight (spectral relationships are indicated in Figure 3), and both should be affected by changes in ozone cover. Acute sunburn may be a considerable hazard; it is probably responsible for loss of many work-hours, to say nothing of the fact that persistent exposure may have detrimental cosmetic effects later on. (Of course, one of the things that needs to be combatted is the uncritical notion that "sunlight is good for you", and that a well-tanned skin is a sign of good health and a life of leisure.) Vitamin D is formed in skin by ultraviolet radiation, but is also available in adequate amounts from any well-balanced diet. More convenient sources exist for treatment and prevention of rickets. Some of the recent speculations about the injurious effects of excess production of vitamin D by sunlight, are misleading, however [9], and the evidence for hypervitaminosis in man needs more thorough examination.

One more thing should be mentioned. The general public is poorly informed with regard to these problems, and an educational campaign may be in order. Many would be reassured to know that they do not have to stay out of the sun during all daylight hours in order to avoid sunburn and cancer of the skin, but only for a few hours during the middle of the day. The hours depend, of course, upon which end of a time zone one is in, and whether daylight saving time is in effect; a general rule might be that when the sun is more than 60° from zenith (four hours) there is little or no danger with the present ozone cover. Window glass gives sufficient protection even at midday. A public educated in this regard would be better prepared to take care of themselves should a reduction in the ozone cover lead to a pronounced increase in ultraviolet radiation.

People are likely to be overly frightened, these days, by the word "cancer". It should be pointed out to them that the kinds of cancers that can be attributed to sunlight (basal-cell and squamous-cell cancers) are not terribly dangerous, since if caught in time they may be successfully treated. There are much more dangerous cancers of the skin, the melanomas, but these are rare, and usually occur on parts of the body that are not exposed to sunlight (whether sunlight has an exacerbating effect when they do occur on exposed parts is not clear).

I hope I have not given you the impression that the effects of reducing the ozone cover would be trivial. Direct injury to man's skin could be largely avoided, however, unless the resultant increase in ultraviolet radiation were quite large. In that case our social habits might have to be changed somewhat, and our hectic days be ameliorated by long lunch hours and siestas. On the other hand, the *indirect* effects on man that might result from changes in the

environment caused by increased ultraviolet radiation could be very much more important. We know little about these, but we should remember that one component of the environment cannot be changed without altering others. In this regard, I suggest a reading of Garrett Hardin's latest book, one title of which is "The Voyage of the Space Ship Beagle" [10].

REFERENCES

1. Blum, H.F., "Sunlight as a causal factor in cancer of the skin of Man," J. Nat. Cancer Inst. *9*, 247-50, 1948.

2. Urbach, F., D. Berger, and R.E. Davies, *Proc. XIII Congr. Internatl. Dermatol.*, 1112-17, 1968.

3. The reader interested in going further into the subject may wish to consult Urbach, F. (ed.) *The Biologic Effects of Ultraviolet Radiation*, Pergamon Press, 1969; and Blum, H.F., *Carcinogenesis by Ultraviolet Light*, Princeton Univ. Press, 1959.

4. Forbes, P.D., "Effects of long wave ultraviolet light on the skin of mice," *VI Internatl. Cong. Photobiol., Abstracts*, 1972.

5. Urbach, F., "Geographical Pathology of Skin Cancer," pp. 635-653, Urbach, *op. cit.*

6. Gordon, G. and H. Silverstone, "Deaths from skin cancer in Queensland, Australia," pp. 625-634, Urbach, *op. cit.*

7. Robertson, D.F., "Correlation of observed ultraviolet exposure and skin-cancer incidence in Queensland and New Guinea," pp. 619-623, Urbach, *op. cit.*

8. Blum, H.F., "Indeterminacy of cell population growth in cancers." Not yet published.

9. Blum, H.F., "Is sunlight a factor in the geographical distribution of human skin color?" Geographical Rev. *54*, 557-81, 1969.

10. Hardin, G., *Exploring New Ethics for Survival. The Voyage of the Space Ship Beagle*, Viking Press, 1972.

DISCUSSION

(UNIDENTIFIED): To get some idea of what change SST's would produce, we need to know what the present variability in incidence of skin cancer is.

BLUM: At present, we have that kind of statistics from only a few parts of the earth. We need a much broader set of UV measurements and skin-cancer statistics before we can make estimates.

SHELDON: The National Cancer Institute is just completing an exhaustive survey of six U.S. cities as to incidence of skin cancer, life style, genetic background, and so on. A number of European studies have been made, and Dr. Robertson's work in Australia seems to indicate latitudinal variation of the incidence and prevalence of skin cancer. Generally, however, these data need to be correlated with studies of the change in UV flux, temperature, and so on with latitude.

(UNIDENTIFIED): Do we know the variability for a city such as Philadelphia, where we might hope that climatic conditions are fairly well known?

URBACH: For Philadelphia, no. We do have twenty years' worth of data for at least ten places in Texas, and for the whole of Texas by county. The variation from year to year is minimal, less than 2%, with a general upward trend. I think there is a general increase in all kinds of cancer, probably just because people are getting out into the sun more, wearing less.

BLUM: Remember that skin cancer is the result of years of exposure, so the incidence in any given year represents twenty or forty years of past history, depending on the area. Even if we make measurements now, it would probably take five years of an SST fleet's flying before we could see results.

SHELDON: I think the original question involved variation in ultraviolet irradiation with latitude. The intensity of 280- to 320-nm radiation in summer at 60° latitude is about 70% of that at the equator. At 60°, however, people generally receive exposure during only three months of the year, so the *yearly* total is considerably less than 70% of the equatorial value; if I remember correctly, the difference is actually about fourfold, depending on the specific sites compared.

BLUM: Even at the equator, if you spent all your time in the jungle, your exposure would not be very great. This is why I think we need a variety of measurements under different conditions, rather than latitudinal averages.

GOLDBURG: I'm a little confused. I thought I heard that a latitudinal dependence had been shown for melanoma, but that Dr. Blum had said that it was not yet certain that melanoma was directly attributable to exposure to sunlight.

URBACH: That is true. The established skin-cancer incidence data is for cancers other than melanoma. The melanoma data, including the latitude gradient, is rather recent; Dr. Fitzpatrick, whom I see in the audience, could give you more information on it.

ULTRAVIOLET RADIATION AND PHOTOSYNTHESIS

EDWARD B. KNIPLING
Agricultural Research Service
U.S. Department of Agriculture
Stoneville, Mississippi

ABSTRACT: Because stratospheric flights of supersonic transport (SST) aircraft may increase the flux of solar ultraviolet (UV) radiation reaching the earth's surface, this paper reviews the literature on the adverse effects of UV on photosynthesis. UV radiation damages biological systems primarily through destruction of specific cellular constituents rather than alteration of broad physiological processes. Photosynthesis is affected soon after absorption of UV radiation because of its general dependence on cellular integrity and specific dependence on UV-vulnerable enzymes and other proteins. Most of the research on UV effects on photosynthesis has been conducted with high-intensity radiation at 254 nm, which is shorter than the waveband of concern, 280 to 320 nm. However, limited data from the unnaturally high intensities of this waveband indicate a small reduction in photosynthesis of single-celled algae. Considerable additional research is needed in this waveband using solar UV energy levels and intact higher plants to define better the effects on photosynthesis and the potential changes in agricultural productivity. Recommendations are made in this paper for specific experimental approaches to this problem.

INTRODUCTION

Aircraft exhaust effluents released into the stratosphere could catalyze the photochemical destruction of ozone. This in turn may allow more ultraviolet (UV) radiation within the 280- to 320-nm waveband to reach the earth's surface [1,2]. Current best estimates of the magnitude of such effects from a worldwide fleet of 500 SST aircraft projected for the years 1985 to 1990 indicate a 3 to 50% depletion of stratospheric ozone and a 10 to 200% increase in UV flux from present natural levels [3]. Present UV levels at the earth's surface vary considerably because of latitude, altitude, diurnal, and seasonal changes, but the total energy of solar UV within the 280- to 320-nm waveband is of the order of 10^{-4} watts/cm^2 or 10^3 ergs/cm^2/sec [4]. Spectrally, the present intensities are zero at 280 nm and range from about 0.1 ergs/cm^2/sec at 295 nm to 10 ergs/cm^2/sec at 320 nm [4].

A principal objective of the U.S. Department of Transportation's 1971 to 1974 Climatic Impact Assessment Program (CIAP) is to evaluate the potential effects of the increased UV flux on biological systems [1,2]. This paper considers the potential effects of UV on the primary energy-fixation process of photosynthesis. A discussion of the significance of photosynthesis to man, and salient features of the process, will be followed by a summary of the limited literature on the adverse effects of UV on photosynthesis, and recommendations for meaningful research into potential UV-vulnerable areas.

PHOTOSYNTHESIS

A photosynthesis symposium held in 1966 was entitled "Harvesting the Sun" [5]. In a sense this is literally the principal business of chlorophyll-bearing plant tissues: that is, the harnessing of energy from solar radiation and its transformation to and storage as organic carbon compounds that can be utilized by living systems. This capture and storage of energy through photosynthesis provides the foundation of all life. We depend on green plants not only for food and much of our clothing and shelter, but also for much of our physical surroundings and environment, including the oxygen we breathe. Furthermore, the technological and industrial advancement of civilization is dependent on the photosynthesis and subsequent formation of fossil fuels which occurred in previous geologic times.

Thus, because of the fundamental significance of photosynthesis, it is quite appropriate that one of the major concerns of CIAP be the assessment of the effect of ultraviolet radiation on this primary energy-fixation process. Assessment of the UV effects in these terms, and in terms of subsequent changes in plant growth and

environment, is perhaps the most meaningful way to make the impact of the UV factor comprehensible to man.

Photosynthesis is a complex process consisting of many physical and chemical reactions and events. A highly generalized chemical equation for the process is:

$$CO_2 + H_2O \xrightarrow[\text{green plant}]{\text{light}} \text{glucose} + O_2 \qquad (1)$$

Although equation (1) lists some of the principal reactants (CO_2 and H_2O) and products (sugar and O_2), it is grossly oversimplified and even misleading. A more correct expression (but still much simplified) is:

$$CO_2 + 2H_2O \xrightarrow[\text{green plant}]{\text{light}} (CH_2O) + H_2O + O_2 \qquad (2)$$

An important point of this equation is that the principal product is not indicated as glucose; instead it is a carbon skeleton, signified by CH_2O in parentheses. Although much of this carbon skeleton is synthesized into glucose and subsequently to other carbohydrates, a good deal of it is channeled directly into amino acids and fatty acids, which are the building blocks of proteins and lipids respectively. Another point is that for each CO_2 molecule reduced or C atom fixed in the process, two H_2O molecules enter into the reaction and one H_2O molecule is regenerated. The water molecule regenerated, however, is not one of the molecules that enters into the reaction; it arises from two of the hydrogen atoms of the reactant water and one of the oxygen atoms of CO_2. The two oxygen atoms of the reactant water are the source of the diatomic O_2 which is given off in gaseous form as a primary product in photosynthesis.

Thus, in photosynthesis, water is split to form O_2 and hydrogen ions which are used to reduce CO_2 and regenerate H_2O. I am dwelling on the path of water molecules in this reaction because the splitting of H_2O to form O_2, chemical energy, and reducing power in the form of H^+ and e^- is the principal use of light energy in photosynthesis, and appears to be one of the UV-vulnerable reactions.

Although the entire photosynthesis process generally is carried out in the presence of light, the reduction of CO_2 to the carbon skeleton and its subsequent synthesis into organic forms of carbohydrates, fats, and proteins can be carried out in the dark. These parts of photosynthesis are often called the dark reactions.

The breakdown of photosynthesis into the light reactions and dark reactions can be summarized as:

Light Reactions: (3)

$$2H_2O \rightarrow 4H^+ + 4e^- + O_2$$

Dark Reactions: (4)

$$CO_2 + 4H^+ + 4e^- \rightarrow (CH_2O) + H_2O$$

Sum:

$$CO_2 + 2H_2O \xrightarrow[\text{green plant}]{\text{light}} (CH_2O) + H_2O + O_2$$

The sum of the light and dark reactions is, as can be readily seen, the same as equation (2).

The light and dark reactions can be further broken down and described as a series of physical and chemical events involving numerous intermediate and catalyst compounds. Let's first consider the light reactions.

The green pigment chlorophyll is the chromophore for the light energy used in photosynthesis. Photons absorbed by the pigment excite its electrons to unstable higher energy levels. This energy then passes through a series of protein acceptors and donors. The electron-deficient chlorophyll accepts electrons from a water molecule, which causes the molecule to split. The light energy absorbed in photosynthesis pumps electrons uphill against a free energy gradient from a potential of about +0.8 volt to -0.4 volt, a total of 1.2 electron-volts per electron transferred. Four electrons or hydrogen equivalents are moved for each molecule of CO_2 reduced or O_2 produced; thus, a total of 4.8 electron-volts is required. This is equivalent to about 112 kcal per mole of CO_2 [6].

In the electron-transport system, electrons are first transported from chlorophyll to plastoquinone, resulting in the splitting of H_2O. The excited electrons then fall from plastoquinone to cytochrome f, plastocyanin, and P700, in that order, with a net loss of energy. This energy, however, is not entirely lost as heat, but is incorporated into high-energy chemical bonds of

adenosine triphosphate (ATP), which are used later in the chemical reduction of CO_2. The substance P700 that sustains this fall in energy is a special form of chlorophyll which was made electron-deficient by a second photo-event that transported an excited electron to ferrodoxin and then to nicotinamide adenine dinucleotide phosphate (NADP) to produce the reduced pyridine nucleotide (NADPH). The latter is a strong reductant and, along with ATP, is a principal product of the light reactions in photosynthesis. The chemical energy and reducing power of ATP and NADPH should be regarded only as intermediate products of photosynthesis, because they are consumed later in the CO_2 fixation or dark reactions of photosynthesis.

In the dark reactions the primary event is the fixation or acceptance of a CO_2 molecule by carbon compounds. This carboxylation reaction, like all subsequent reactions, is catalyzed by specific enzymes and cofactors. Carboxylation may occur by means of two major mechanisms. In most plants, including nearly all those in temperate latitudes, a 5-carbon sugar, ribulose diphosphate, accepts a CO_2 molecule and forms two 3-carbon molecules of phosphoglyceric acid. This compound is immediately energized and reduced by the ATP and NADPH produced in the light reactions of photosynthesis to produce the stable intermediate glyceraldehyde phosphate. A pool of the compound is the primary carbon product of this CO_2 fixation and reduction process; this mechanism is therefore termed the C3 pathway of photosynthesis. The 3-carbon compound has a number of important roles in photosynthesis. One is a regenerative phase which reproduces the 5-carbon acceptor molecules. Another is production of the simple sugars fructose and glucose, which in turn form sucrose and more complex carbohydrates such as starch and cellulose. Glyceraldehyde phosphate also can be channeled directly into fatty-acid and lipid synthesis, or into amino-acid and protein synthesis. Yet another fate is incorporation through intermediate compounds into various respiration mechanisms, the process by which chemical energy is yielded to biological systems.

The other major mechanism by which CO_2 fixation or carboxylation occurs is of special importance because it occurs in some of our most productive crop plants – for example, corn, sugar cane, and some other tropical grasses. In this mechanism the 3-carbon compound pyruvate is energized by ATP to form phosphoenolpyruvate, which is the CO_2 acceptor. Thus, a 4-carbon intermediate compound is the primary product of photosynthesis from this carboxylation process, and this mechanism is called the C4 pathway.

In a description of photosynthesis it is important to consider the physical plant structures involved in the process and how closely these are coupled to the photo and chemical events. A chlorophyll-bearing plant cell is a highly organized membranous structure consisting of numerous sub-units or organelles that carry out discrete metabolic functions. Chlorophyll and photosynthesis occur in organelles called chloroplasts, which are disc-shaped structures generally about $5 \times 2 \times 1$ μm in size. A chloroplast is highly structured, with a lamellar system made up of protein-lipoid membranes. Concentrated stacks of these membranes are called grana, and are the principal sites of the chlorophyll pigments; they are where the light reactions of photosynthesis occur. The embedding matrix, called the stroma, houses the enzyme systems and pool of intermediates involved in the dark reactions. The stroma also contains nucleic acids, both DNA and RNA, which are involved in chloroplast reproduction and synthesis of chloroplast proteins. Around the periphery of the chloroplast is a reticulum which is thought to provide a route for transport of photosynthetic reactants and products in and out of the chloroplast.

The system of delivering gaseous CO_2 from the air around a plant to the interior of a leaf and to the chloroplasts is another important aspect of photosynthesis that should be considered. This is largely a physical diffusion process, and thus is greatly influenced by both environmental and physiological factors. The outside covering of leaves consists of a waxy cuticle which is nearly impervious to diffusing CO_2 and water vapor. However, the cuticle and underlying epidermal layer of leaf cells contain pores called stomata which permit the passage of these gases.

Stomata are valve-like structures that open and close according to a complex and poorly understood physiological process. However, it is clear that the light reactions of photosynthesis in

the two surrounding cells, called guard cells, are required to initiate opening. The high-energy compound ATP appears to increase the ionic and osmotic concentrations of the cells, resulting in an influx of water. This hydraulic system is known to be the actual force that causes the stomatal pore to open. CO_2 then enters the interior of the leaf and photosynthesis proceeds. Stomatal opening and closing is highly sensitive to drought or plant-water deficits, low temperatures, radiation intensity, and wind shock. It seems likely that the stomatal mechanism would be sensitive to changes in ultraviolet radiation flux as well.

EFFECTS OF ULTRAVIOLET RADIATION

Having reviewed various aspects of the photosynthesis process, I would now like to discuss the effects of UV radiation on biological systems and photosynthesis. A number of workers in the field of UV research have shown that in biological systems UV primarily affects not physiological processes such as photosynthesis *per se*, but specific cellular constituents. Although many substances absorb UV, the two main classes of compounds thought to be the chromophores of UV radiation damage are nucleic acids and proteins [7]. Although it is not completely clear what specifically occurs chemically when molecules of these substances absorb UV, in effect they are "denatured" and rendered ineffective in their normal action and cellular role. A host of secondary changes and physiological consequences results, including disturbances to photosynthesis.

Much of the early work on the UV effects on photosynthesis is summarized in reviews by Rabinowitch [8]. One of the first studies was conducted by an American investigator named Arnold in 1933 [9]. He irradiated cultures of the unicellular alga *Chlorella* with a germicidal lamp, a nearly monochromatic source at 254 nm, and observed a rapid, linear decrease in photosynthesis to a zero value between 0 and 20 minutes. Because respiration was unaffected, Arnold concluded that the UV effect was specific to photosynthesis and did not represent a general killing of the cells. In 1951, Holt et al. [10] observed similar adverse effects of UV on *Chlorella* and another species of algae. The UV effects on some enzyme activities and on some of the specific reactions of photosynthesis were also determined. They concluded that the action of UV radiation was associated with the Hill reaction – that is, the splitting of water and the electron-transport system of the light reactions. Studies by various people within the last 10 years [11,12] with spinach chloroplasts showed that UV radiation destroyed plastoquinone, the initial protein electron acceptor after chlorophyll is excited and water is split, but other investigators [13-16] concluded that this was not the exclusive or major cause of UV inhibition of photosynthesis. Yamashita and Butler [17] found experimental evidence that the site of inhibition was chlorophyll and its mechanism of light excitation and splitting of water. One of the most recent works [16] concluded that the inhibition at this site was due to the physical disruption of the integrity of the chloroplast lamellar membranes.

With the exception of one study, all of the UV research on photosynthesis described above was done with germicidal lamps at 254 nm. Jones and Kok [13], however, irradiated their samples with the broad spectral band of a xenon arc lamp. In addition they isolated specific, narrow wavebands with various filters and determined the spectral response of UV inhibition of photosynthesis in isolated spinach chloroplasts. Inhibition by UV was greatest at about 250 nm, but there also was a significant effect in the 280 to 320 nm waveband, about 20% of that at 250 nm. Similarly, Haldall [18], working with two algae species, observed up to 10 to 15% inhibition of photosynthesis by UV of 280 to 300 nm for one species, and UV of 280 to 310 nm for the other species. There was no inhibition at wavelengths longer than about 310 nm. The inhibition at the shorter wavelengths was attributed to a general protein denaturation, rather than to denaturation at a specific reaction site in the light reactions of photosynthesis. These data suggest that UV radiation in the waveband of 280 to 320 nm does inhibit photosynthesis to some extent. Thus, the concerns about the potential impact of routine commercial stratospheric aircraft flight on plants are justifiable.

From this review, however, I do not feel firm conclusions can be drawn about the effects of UV of 280 to 320 nm on photosynthesis, and

I will not attempt to estimate the limits of the potential effects. As I pointed out earlier, most of the research reviewed was conducted with germicidal lamps radiating at 254 nm. Also, the radiation intensities used in this work were either unstated or much higher than those expected to occur with stratospheric perturbation. The value of this research to CIAP is further limited because it was done with unicellular algae or isolated chloroplasts. Although this research approach provides good model systems and yields fundamental information on mechanisms of injury, it does not necessarily reveal what will happen to intact plants in their natural environment. Plants are able to avoid some UV injury to internal parts by physical or chemical shielding by outer tissues [7]. Also, damage to nucleic acids is partially reversed when tissues are simultaneously exposed to longer-wave solar irradiation [7].

RECOMMENDATIONS

Although I cannot estimate the UV effects on photosynthesis, I feel that I can make recommendations for some meaningful immediate research in this area. In all experiments, UV irradiation sources of known spectral distributions and energy levels must be used. The energy levels used in these experiments should include the range of UV intensities expected to occur at the earth's surface as a result of the stratospheric reduction of ozone. It is also important that intact plants and leaf tissues be used as test materials, in addition to single-celled systems and isolated chloroplasts.

On the basis of the potential vulnerability of photosynthesis and related processes to UV, I recommend that these experiments include the following:

1. Effect of UV on gaseous CO_2 uptake by plants as a gross measure of the effect of UV on net photosynthesis. Although such data will not reveal *why* photosynthesis is affected, it will show *how much* it is affected. CO_2 fixation is perhaps the best measure of photosynthesis that agriculturists and ecologists can use to relate to plant productivity.
2. Measurement of incorporation of radioactive CO_2 (C^{14}) into plants, with particular emphasis on the effect of UV on the distribution patterns of the radioactive label in different intermediates and ultimately in the different main classes of food products – carbohydrates, lipids, and proteins. Changes in the distribution pattern may reveal changes in enzyme activities and kinetics which might be responsible for changes in food quality.
3. Effect of UV radiation on some of the specific reactions and protein, electron donor-acceptor compounds in the light reactions of photosynthesis. This research would be similar to the studies reviewed above except that UV in the 280 to 320 nm waveband would be used.
4. Effect of UV radiation of 280 to 320 nm on the activity of the carboxylation enzymes, that is, the enzymes that are responsible for the initial fixation of CO_2 into an organic form. These studies should be made for both the C3 and C4 photosynthetic mechanisms previously described.
5. Effect of UV on cellular ultrastructure, particularly on the integrity of the chloroplast lamellar and reticulum systems. These studies will involve electron-microscope work.
6. Effect of UV radiation on epidermal guard cells and on the stomatal opening and closing mechanism. Since the stomata of many non-woody plant species, including most agricultural crops, are located on the upper leaf surfaces, the guard cells may be the most vulnerable of all photosynthetic units in the entire leaf. Even if radiation of 280 to 320 nm does not directly affect the photosynthetic process, the overall efficiency of photosynthesis in terms of the amount of gaseous CO_2 taken up into the leaf could be significantly reduced if UV in some other way, perhaps through changes in membrane permeability or potassium-ion flux, promotes stomatal closing or interferes with stomatal opening.

7. Measurements of the UV optical properties (reflection, transmission, absorption) of intact leaves and isolated leaf parts such as the cuticle and epidermal cell layer. Studies should be made to determine to what extent plants can adapt over time to sublethal UV intensities through changes in their optical properties that increase the shielding of their internal parts.

Considerable research is needed immediately to define the effects of UV of 280 to 320 nm on photosynthesis and to make the findings relevant to the Climatic Impact Assessment Program.

REFERENCES

1. Barrington, A.E., ed., 1972: *Proceedings of the Survey Conference*, February 15-16, 1972, Cambridge, Mass., Climatic Impact Assessment Program, Department of Transportation Report No. DOT-TSC-OST-72-13, 281 pp.

2. Grobecker, A.J., 1972: "Assessment of climatic changes due to flights in the stratosphere," American Institute of Aeronautics and Astronautics Fifth Fluid and Plasma Dynamics Conference, June 26-28, 1972, Boston, Mass. AIAA Paper No. 72-658, 16 pp.

3. Sheldon, Donald R., 1972: "Status of the Biological Impact Project," in this volume.

4. Green, A.E., 1972: Personal communication, unpublished data, Astronomy Department, University of Florida.

5. San Pietro, A., F.A. Greer, and T.J. Army, eds., 1967: *Harvesting the Sun: Photosynthesis in Plant Life*, Academic Press, New York, 342 pp.

6. Zelitch, I., 1971: *Photosynthesis, Photorespiration, and Plant Productivity*, Academic Press, New York, 347 pp.

13. Jones, L.W. and B. Kok, 1966: "Photoinhibition of chloroplast reactions. I. Kinetics and action spectra," Plant Physiol. *41*, 1037-1043.

7. Caldwell, M.M., 1971: "Solar UV irradiation and the growth and development of higher plants," Photophysiology *6*, 131-177.

8. Rabinowitch, E.I., 1956: *Photosynthesis and Related Processes*, 2 vols., Interscience Publ., New York.

9. Arnold, W., 1933: "The effect of UV on photosynthesis," J. Gen. Physiol. *17*, 135-143.

10. Holt, A., I. Brooks, and W. Arnold, 1951: "Some effects of 2537 Å on green algae and chloroplast preparation," J. Gen. Physiol. *34*, 627-645.

11. Bishop, N.I., 1961: "The possible role of plastoquinone (Q-254) in the electron transport system of photosynthesis," in *CIBA Foundation Symposium on Quinones in Electron Transport*, G.E.W. Wolstenholme and C.M. O'Connor, eds., Churchill Press, 385-404.

12. Shavit, N. and M. Avron, 1963: "The effect of ultraviolet light on photophosphorylation and the Hill reaction," Biochim. Biophys. Acta *66*, 187-195.

14. Jones, L.W. and B. Kok, 1966: "Photoinhibition of chloroplast reactions. II. Multiple effects," Plant Physiol. *41*, 1044-1049.

15. Mantai, K.E., J. Wong, and N.I. Bishop, 1967: "Studies on the effects of ultraviolet irradiation on photosynthesis and on the 520 nm light-dark difference spectra in green algae and isolated chloroplasts," Biochim. Biophys. Acta *131*, 350-356.

16. Mantai, K.E., J. Wong, and N.I. Bishop, 1970: "Comparison studies on the effects of ultraviolet irradiation on photosynthesis." Biochim. Biophys. Acta *197*, 257-266.

17. Yamashita, T. and W.L. Butler, 1968: "Inhibition of chloroplasts by UV-irradiation and heat treatment," Plant Physiol. *43*, 2037-2040.

18. Haldall, P., 1964: "Ultraviolet action spectra of photosynthesis and photosynthetic inhibition in a green and red alga," Physiol. Plantarum *17*, 414-421.

DISCUSSION

ELLSAESSER: Let us be careful that our viewpoint is not too simplistic. I should like to make three points: First, life apparently originated on this earth during a time of much greater UV exposure than what we now have. Second, the reason radiological treatment is used for cancer is that radiation has different effects on healthy and unhealthy tissues. Third, the detrimental effects of radiation on some aspects of organism growth might have beneficial effects in the long term or on other aspects.

LIN: What organic compounds have their primary absorption in the 280-to-320-nm waveband?

KNIPLING: I am not sure that any have their primary absorption in this region. Those with absorption peaks elsewhere have some absorption in this region, however, including nucleic acids and proteins. And all enzymes are protein molecules, as are the compounds involved in the electron-transport system and the light reaction of photosynthesis.

LIN: What component of proteins is responsible for absorption at 280 to 320 nm?

KNIPLING: The proteins can be broken down into amino-acid components, and some of the ring-structure amino acids absorb principally in this region.

ECOLOGIC CONSIDERATIONS OF SOLAR RADIATION CHANGE

MARTYN M. CALDWELL
Ecology Center
Utah State University
Logan, Utah

ABSTRACT: The biological implications of increased solar ultraviolet radiation on the earth's surface, which would result from decreased stratospheric ozone concentrations, are discussed. The UV wavelengths which are most influenced by changes in ozone concentration are also those most effectively absorbed by nucleic acids and proteins, the critical components of all living cells. Since most UV-caused physiological alterations are deleterious, many organisms have developed avoidance mechanisms to minimize ultraviolet radiation exposure. These consist of behavioral traits in animals and shielding by body coverings and pigments in both plants and animals. Most organisms also have repair systems which are very effective in reversing damage at present ultraviolet radiation levels. The relevant question for CIAP is: at what level of increased UV radiation would the avoidance and repair mechanisms of organisms no longer be able to cope with the radiation exposure? This is of concern not only for man and his agriculture, but for all organisms in natural ecosystems. A complete evaluation of the biological impact of increased UV radiation must take into account subtle changes in genetic and physiologic properties of all organisms, including those which may appear to have little immediate economic value.

Although a very minute amount of UV solar energy reaches the earth's surface, the quantum energy levels in this portion of the spectrum are such that biological photochemical reactions are easily effected. Though a few of these biological responses to UV radiation may be beneficial to organisms, most are decidedly deleterious. At wavelengths shorter than 315 nm, ultraviolet radiation is effectively absorbed by proteins and nucleic acids (see Figure 1). Since proteins are important building blocks of cell membranes and enzymes, and nucleic acids are the genetic constituents which in essence direct all development and metabolism, it is not surprising that ultraviolet radiation absorbed by these compounds would have pronounced biological manifestations. Ultraviolet wavelengths shorter than 315 nm are known to result in a wide variety of physiological disruptions in bacteria, fungi, higher plants, and animals from protozoa to man [1,2,3]. For sufficiently high intensities of UV irradiation, these physiological disruptions can be lethal, or at least debilitating for the organism. Reduced photosynthetic rates, inhibition of various enzyme actions, induction of tumors or cancers, and reduced visual acuity are examples of the effects of sub-lethal UV radiation doses on organisms. In addition to these immediate responses, there are also more subtle ones such as genetic alterations, which may not be apparent for several generations. Altered mutation rates and chromosomal aberrations can be effected by UV irradiation in the laboratory. Furthermore, even for the levels of UV radiation presently reaching the earth's surface, mutations in the molds *Aspergillus* and *Penicillium* have been documented [4]. Therefore, the question is not whether ultraviolet radiation can be harmful to organisms, but instead, at what radiation thresholds this damage becomes apparent in most organisms.

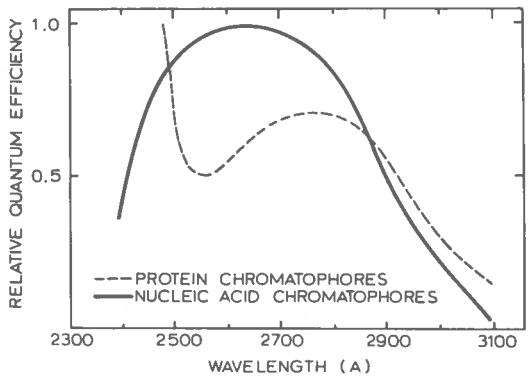

Figure 1. Generalized absorption spectra for proteins and nucleic acids. Adapted from Giese [1].

Currently, most ultraviolet radiation below 315 nm is absorbed by the stratospheric ozone layer before it reaches the earth's surface. A certain amount does penetrate to the earth's surface, however, and has demonstrable effects on man and other organisms. It is also apparent that most organisms possess avoidance and repair mechanisms to mitigate damage from UV at present levels.

AVOIDANCE MECHANISMS

Avoidance mechanisms include radiation shielding by external coverings such as feathers, fur, and cuticular waxes, and by internal filters such as melanin pigment in human skin and flavonoids in plant tissues. Although external body coverings and pigments serve other purposes as well, such as thermal insulation and camouflage, susceptibility to UV radiation damage is often negatively correlated with the development of these shielding mechanisms. For example, in Hereford cattle the high incidence of eye cancer appears to be correlated with the absence of skin pigment around the eye [5], and the degree of UV radiation damage to plants can often be negatively correlated with the development of certain plant pigments [6,7]. Behavioral responses to solar radiation also undoubtedly play a role in avoidance of UV radiation damage. Diel migrations of certain plankton seem to occur in response to the diel solar-radiation cycle. These plankton may migrate to great depths during the day, and then rise toward the surface at night.

Many terrestrial animals are active only in the evening or at night, and seek shade or other cover during the daytime. Although this behavior is primarily designed to escape the heat of day or predators, it also provides a mechanism for escaping the most intense ultraviolet radiation during the midday hours. Many of these behavioral responses to sunlight would probably continue to provide protection for many animal species even if solar UV radiation intensities on the earth's surface increased. For some animal species, though, this might not be the case. For example, vertebrates such as the desert iguana seek shade when air temperatures become too high. The behavioral response is to heat, not ultraviolet radiation. However, since heat and UV radiation are highly correlated, the avoidance of one does serve as a mechanism for avoiding the other. The increase in UV radiation intensities on the earth's surface which would result from a decrease in stratospheric ozone would be disproportionately large in relation to the total solar radiant-heat load. Animals would thus be exposed to longer periods of greater UV irradiation while temperatures were still relatively cool. The effects of this increased UV exposure on populations of different animal species is difficult to evaluate. However, it would not be unreasonable to predict a higher incidence of cancers and increased mortality in some animal species.

Animal species which are active only in the evening or during the night develop melanin pigments and other shielding devices to a lesser extent than animals which are active during the daytime hours [8]. It has been shown that penetration of UV radiation through the body walls and various tissues of reptiles which are normally active only in the evening or night hours is much greater than that for reptiles which are active during the day. Therefore, it is apparent that shielding against ultraviolet radiation and behavioral responses to sunlight are complementary adaptations which together serve to protect many animal species.

Since plants do not enjoy mobility, ultraviolet radiation can be avoided only through protective shielding by waxes and flavonoid pigments, or by changes in the orientation of leaves to minimize solar radiation exposure.

It should be emphasized, by the way, that water, which comprises a significant proportion of plant and animal tissues, is not an effective absorber of ultraviolet radiation [8].

REPAIR MECHANISMS

In addition to avoiding ultraviolet radiation, most plants and animals can repair ultraviolet radiation damage by several elaborate mechanisms. For example, photoreactivation is a reversal of ultraviolet radiation damage to DNA molecules (the basic genetic constituent of most cells). This process operates in a wide variety of organisms ranging from bacteria to higher plants and most animal species, except for placental

mammals. Photoreactivation is energized by radiation of longer wavelengths of sufficient intensity. Since longer-wave radiation is always present when animals or plants are exposed to UV radiation, energy is always available for this repair process. Also, there are several repair functions that are independent of light, generally referred to as "dark repair" systems. Several of these were outlined by Smith at the CIAP Survey Conference [9]. In all, six different repair processes exist in the plant and animal kingdoms, each requiring a series of highly specific enzymes. Although it is possible to speculate on the course of evolution only in retrospect, it would certainly be reasonable to hypothesize that the multiplicity and specificity of these reasonably elaborate repair systems so widespread in the plant and animal kingdoms is the result of the need of these organisms to survive ultraviolet radiation exposure.

The importance of repair mechanisms is dramatically revealed when they are absent. For example, some alpine plants, when exposed to UV radiation of intensities and wavelengths simulating that received in the natural environment during the course of a 9.5-hour day, exhibited damage if this irradiation was carried out in the absence of radiation of longer wavelengths [7]. In this situation the plants were deprived of photoreactivation because of the absence of longer wavelengths, and therefore damage became apparent which would not have otherwise. Organisms which lack repair systems because of mutated genes which block the action of certain enzymes are very susceptible to UV radiation damage. A strain of the common colonic bacteria (*Escherichia coli* K-12 *uvrA recA*) which is deficient in two UV-radiation repair mechanisms was found to be very susceptible to solar UV irradiation. In one minute of midday exposure in Texas, 99.9% of the population was killed [10]. In humans, the hereditary condition known as Xeroderma pigmentosum is evidenced by a syndrome of multiple-skin-cancer development following extremely brief exposures to sunlight. This condition has been shown to result from absence of a dark-repair mechanism for UV injury to DNA in these individuals. These examples illustrate the importance of UV-radiation repair processes which appear to exist in a wide variety of plants and animals to protect them from the intensities of solar UV radiation that currently reach the earth's surface.

THE RELEVANT QUESTION FOR CIAP

There is little doubt that the current UV radiation level at the surface of the earth is sufficient to cause biological damage, and that avoidance and repair mechanisms adequately mitigate this UV-induced damage under current conditions. The critical question for the CIAP program in the ecologic context is: In the case of increased solar ultraviolet intensities, would the present avoidance and repair capabilities of organisms be able to cope with the increased exposure? From laboratory investigations it is already known that repair systems have only limited effectiveness. If doses and dose rates of UV radiation are excessive, repair systems are not capable of preventing or completely reversing damage. At what threshold of increased UV radiation intensities would the repair systems of most organisms lose their effectiveness? Similarly, though shielding and behavioral avoidance may be presently effective for many organisms, will they continue to be sufficiently protective if UV radiation intensities increase?

Answers to these questions are not available at present. Most of the photobiological work to date has dealt with UV radiation of wavelengths and intensities not representative of the current terrestrial solar UV spectrum. Since biological reactions are highly wavelength-specific, a quantitative evaluation of the biological effects resulting from increased UV irradiance is further complicated.

BIOLOGICAL EFFECTIVENESS OF UV RADIATION

Most of the strikingly detrimental biological UV radiation effects result from UV absorption by proteins and nucleic acids [1,2]. Certain pigments, hormones, and other organic substances can absorb UV radiation and result in physiological alterations in plants and animals. However, for most detrimental responses caused by UV radiation of wavelengths shorter than 315 nm, proteins and nucleic acids are the responsible UV-absorbing agents. It is not surprising, for example, to find that the biological action

spectrum for UV damage in protozoans closely matches the absorption spectra of proteins and nucleic acids as determined by Giese [1]. At wavelengths longer than 285 nm, the absorption spectra of proteins and nucleic acids are essentially identical and can be approximated by a single curve (see Figure 2). Since wavelengths between 280 and 315 nm are those which would increase most with reductions in stratospheric ozone, it would seem most appropriate to direct attention to this waveband. Action spectra for UV irradiation responses in a variety of lower and higher plants are represented in Figure 3. For most of these phenomena, the biological action spectra do correlate reasonably well with the generalized curve for protein and nucleic-acid absorption. Considering wavelength-dependent absorption and scattering by plant tissues which would alter the apparent biological action spectra, this correspondence is surprisingly close. The one exception, where the action spectrum does not correspond with the protein and nucleic-acid absorption spectra, is Figure 3I, for which a plant hormone was the responsible UV-absorbing agent.

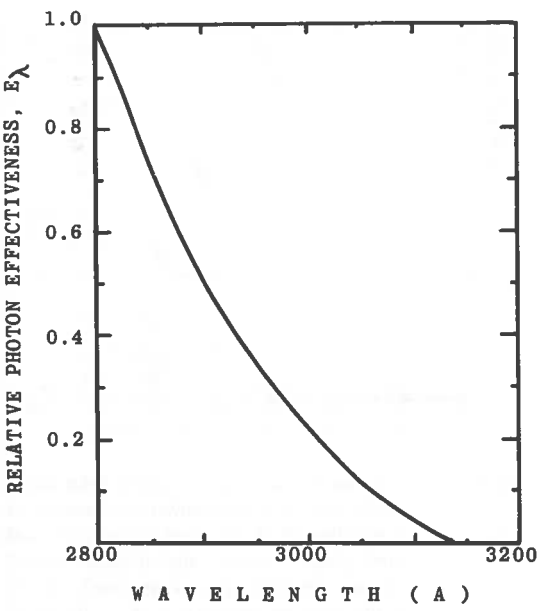

Figure 2. A generalized curve to represent the relative photon effectiveness of UV radiation in inducing biological response when protein or nucleic-acid chromatophores are involved. From Caldwell [2].

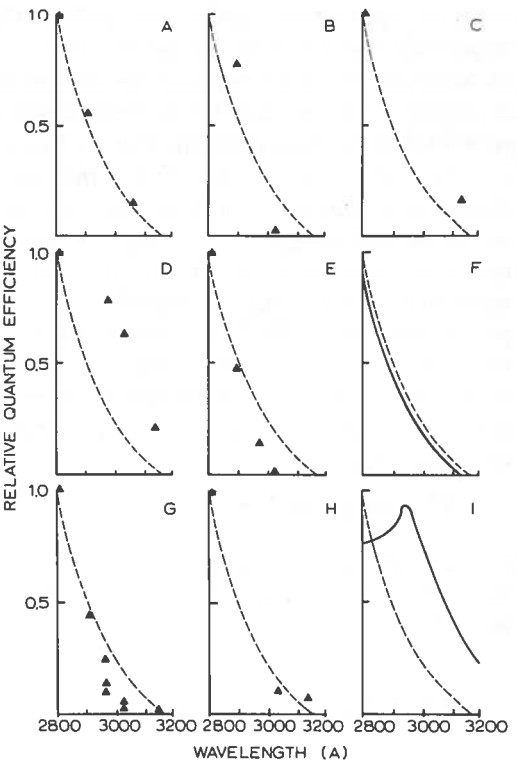

Figure 3. Plant UV action spectra relative to 2800 A. A. mutation of liverwort spores, *Sphaerocarpus donnellii* [11]; B. mutation in the fungus *Trichophyton mentagrophytes* [12]; C. inhibition of photosynthesis in *Chlorella pyrenoidosa* [13]; D. cessation of cytoplasmic streaming in epidermal cells of *Allium cepa* [14]; E. frequency of "endosperm deficiencies" in corn due to chromosomal deletion or mutation [15]; F. germicidal action spectrum [16]; G. epidermal cell damage in *Oxyria digyna* leaves [7]; H. induction of chromosomal aberrations in *Tradescantia paludosa* [17]; I. base curvature of *Avena coleoptiles* [18]. Intermittent lines represent biological action spectra for UV effects on plant cells [7]. All of the action spectra have been expressed in terms of relative quantum efficiency which denotes either relative quantum effectiveness (spectra A, B, E. F, H, and I) or relative quantum sensitivity (spectra C, D, and G). From Caldwell [2].

For the portion of the UV spectrum between 280 and 315 nm, Caldwell [7] has used these biological action spectra to define a generalized curve of biological effectiveness of UV

radiation when proteins and nucleic acids are the responsible UV-absorbing substances (see Figure 2). Since photochemical reactions are effected by absorption of whole quanta, it is conventional in photobiology to express radiation on the basis of photons rather than energy. Using this curve (Figure 2), a convenient unit of photon irradiance can be defined, weighted for biological effectiveness. For monochromatic UV irradiation in this wavelength range, the biologically effective photon irradiance, $EIP(UV\text{-}B)_\lambda$, can be defined as the product of the relative photon effectiveness of that wavelength, E_λ, as defined by Figure 2 and the number of quanta cm^{-2} sec^{-1} $Å^{-1}$ at that wavelength, Q_λ.

$$EPI(UV\text{-}B)_\lambda = Q_\lambda \cdot E_\lambda \qquad (1)$$

For polychromatic radiation, as received from the sun, the effective UV photon irradiance would be

$$EPI(UV\text{-}B) = \int_{280}^{315} Q_\lambda \, E_\lambda \, d\lambda \qquad (2)$$

This unit would be appropriate for many destructive UV effects of radiation on biological organisms. However, other effects (such as erythema of human skin) possess different action spectra, and therefore cannot be defined by these particular radiation units.

CHANGES IN BIOLOGICALLY EFFECTIVE UV RADIATION WITH CHANGES IN STRATOSPHERIC OZONE

The increase in UV radiation intensities penetrating to the earth's surface in the event of partial stratospheric ozone destruction can be estimated using the unit of biologically effective UV irradiance. Since ozone UV transmittance decreases exponentially with decreasing wavelengths in the wavelength range 280 to 315 nm (see Figure 4), changes in stratospheric ozone would have a disproportionate influence at different wavelengths. In Figure 5 are shown the calculations of Cutchis [19], predicting the percentage of increase in UV radiation at different wavelengths for various percentages of change in total ozone concentration. On the basis of these data, for a 50% decrease in stratospheric ozone (which is the extreme estimate of

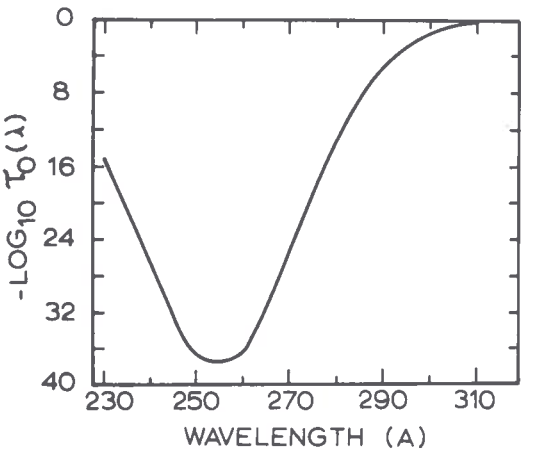

Figure 4. Logarithm of the transmittance for 0.280 atm-cm of atmospheric ozone at various wavelengths. Adapted from Barker [21].

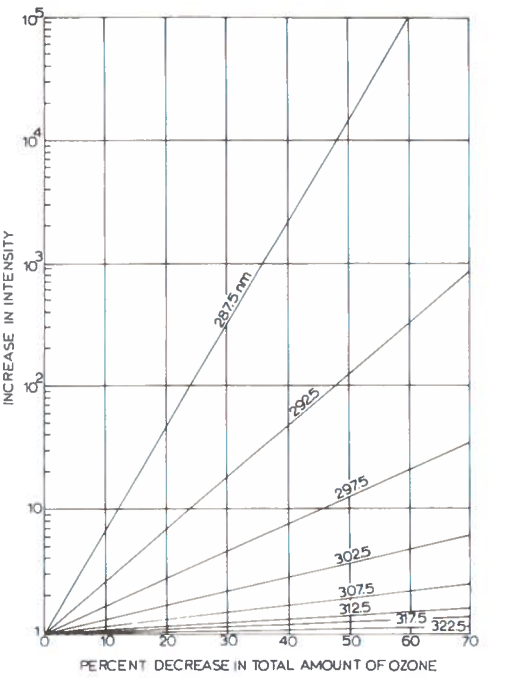

Figure 5. Increase in intensity of direct solar ultraviolet radiation at different wavelengths as a function of the percent decrease in total atmospheric ozone concentration. Initial ozone concentration is assumed to be 0.341 atm-cm; the solar angle is 30° from the zenith. From Cutchis [19].

Johnston [20]), total ultraviolet radiation in the waveband 290 to 312.5 nm would increase to 195% of the original intensities (assuming an

original ozone concentration of 0.341 atm-cm and a solar angle of 30° from the zenith). If these data are recalculated to integrate biological effectiveness as defined in Equation 2, this 50% decrease in stratospheric ozone would yield an estimated biologically-effective photon irradiance of 270% of the original irradiance values. This greater-percentage increase reflects the greater biological effectiveness of shorter wavelengths, which are also the wavelengths most influenced by changes in ozone concentrations. In a similar manner, Cutchis [19] weighted irradiance values for effectiveness in producing erythema of human skin, and found that this 50% decrease in stratospheric ozone would result in an effective irradiance 300% higher for this erythemal response.

Although many organisms may be able to withstand a threefold increase in biologically effective UV irradiation, others may not. Naturally, species of agricultural importance are those of immediate concern to man, aside from himself. Many broadleaf agricultural plant species are quite susceptible to UV irradiation [22]. Even if these plant species are able to survive the increased irradiance, their productivity may be decreased. Certainly, decreased agricultural productivity on a large scale in the face of an increasing human population would be an unacceptable consequence of stratospheric ozone reduction.

Of less immediate concern to man are the more subtle influences of UV radiation on plants, animals, and microbes of natural ecosystems. Over extended time periods these may be quite crucial, however. Even if only a very few species were actually eliminated or greatly reduced in numbers by increased UV irradiation of natural systems, the absence of these seemingly insignificant members might seriously alter the functioning of entire ecosystems. Also, sublethal effects on organisms in natural systems could have far-reaching consequences. For example, though the green plants of terrestrial ecosystems and the phytoplankton of aquatic systems may not be killed by increased UV irradiance, reduced photosynthesis on the part of these organisms which form the basis of the food chain would lead to an energy shortage for all other organisms in these ecosystems. Other disruptions in growth patterns and forms of various organisms could also have subtle but decisive effects on ecosystems in the long term.

Even though most insects are reasonably well shielded from UV radiation, many insects have vision in the ultraviolet portion of the spectrum, and depend on this part of the spectrum for orientation. If this orientation were disturbed by alterations in ultraviolet intensities, principal insect pollinators and important predatory insects might be less effective. This could have far-ranging consequences in many ecosystems. Subtle alterations in the genetic material of plants and animals of little importance to the present generation could be significant in subsequent generations.

INTERACTIONS OF UV RADIATION WITH OTHER STRESSES

The direct effects of increased UV radiation on organisms, whether dramatic or subtle, also interact with other factors of the environment. For example, temperature stress or increased UV irradiation alone may be tolerated by many organisms, but the simultaneous occurrence of both stresses may have synergistic consequences with which the organism cannot cope. Similarly, interactions of increased UV intensity and air pollutants such as fluorides may result in damage to some sensitive plant or animal species. The interaction of increased UV intensities and plant and animal pathogens should also be considered. Increased UV irradiation may cause host organisms to be more susceptible and sensitive to various pathogens. On the other hand, there is also the prospect that increased UV irradiation would *decrease* the susceptibility to pathogens, as has been suggested in experiments showing reduced virus susceptibility of bean plants [23]. These and many other reactions of physical and biotic factors to increased UV irradiation must be taken into account before all consequences of the ecologic effects of a change in solar radiation can be ultimately evaluated.

CONCLUSIONS

As a first approximation, it is appropriate to investigate the most obvious direct biological consequences of increased solar UV irradiation, such as decreased productivity of agricultural

crops or increased mortality of economically important plants and animals. However, before intentional alterations of stratospheric ozone can be contemplated, all the ramifications and interactions of both agricultural and natural ecosystems must be thoroughly evaluated. Even the most subtle biological impacts on organisms of little immediate economic value need to be seriously explored.

SUMMARY

This discussion considers the biological implications of the increase in solar ultraviolet radiation on the earth's surface which would result from a decrease in stratospheric ozone concentrations. Below 315 nm, the biological effectiveness of reactions involving absorption of radiation by nucleic acids and proteins increases exponentially with decreasing wavelength. Since UV absorption by ozone also increases exponentially with decreasing wavelength, any decrease in ozone concentration would be most pronounced at the wavelengths which are also most biologically effective.

Although a few biological responses to ultraviolet radiation may be interpreted as beneficial, most UV radiation effects are decidedly deleterious. Ultraviolet radiation is effectively absorbed by proteins, the important building blocks of cell membranes and enzymes, and nucleic acids, the genetic constituents of cells which essentially direct all development and metabolism.

Most organisms have evolved so as to effectively cope with the UV radiation intensities currently striking the earth's surface. Often they protect themselves from UV radiation simply by shielding, such as feathers, fur, waxes, or pigments. In the case of animals, behavioral adaptations such as avoiding intense sunlight can be quite effective. However, this behavior is usually not a direct response to UV radiation, but is a response to other factors, such as visible light or heat. Finally, most organisms possess a variety of molecular repair systems, which are extremely effective in reversing disruptions of nucleic acids caused by present levels of ultraviolet radiation, thereby preventing manifestations of this genetic disarrangement in the form of cell damage.

The question for CIAP then becomes: At what level of UV irradiation would the avoidance and repair mechanisms of organisms no longer be able to cope with the increased UV radiation exposure? This is of prime concern not only for man and his agriculture, but for all organisms in natural ecosystems as well. The functioning of an entire ecosystem is often dependent on involved interrelationships between different species. Thus, even subtle biological responses to UV radiation must be taken into account. For example, though green plants and plankton may not be killed by slightly increased UV irradiation intensities, reduced photosynthesis would be, in the long run, just as important to the functioning of our natural ecosystems. Although most insects are reasonably well shielded from UV radiation, many insects depend on the ultraviolet portion of the spectrum for orientation. If this orientation were disturbed, principal insect pollinators might be much less effective. Also, subtle alterations in the genetic material of plants and animals which are of little importance to the present generation could be significant in subsequent generations.

Although any evaluation of the biological impacts of increased solar UV radiation intensities naturally centers on the most obvious possible consequences, such as decreased productivity of agricultural crops, increased mortality of economically important plants and animals, or increased risk to man, a complete evaluation must ultimately include the more subtle biological impacts on *all* organisms.

REFERENCES

1. Giese, A.C., "Studies on ultraviolet radiation action upon animal cells," in *Photophysiology*, ed. A.C. Giese, Vol. 2, p. 203-245. Academic Press, New York (1964).

2. Caldwell, M.M., "Solar UV irradiation and the growth and development of higher plants," in *Photophysiology*, Vol. 6, p. 131. Academic Press, New York (1971).

3. Smith, K.C., et al. "Biological Impacts of Increased Intensities of Solar Ultraviolet Radiation," Nat. Acad. Sci. Special Report (1973).

4. Hollaender, A., and Emmons, C.W., "Induced mutation and speciation in fungi," Cold Spring Symp. Quant. Biol. *11*, 78 (1946).

5. Anderson, D.F., "Cancer eye in cattle," Mod. Vet. Pract. *3*, 43-47 (1970).

6. Biebl, R., "Beobachtungen über UV-Strahlenresistenz anthokyanhaltiger Zwiebelepidermiszellen," Protoplasma *37*, 566 (1943).

7. Caldwell, M.M., "Solar ultraviolet radiation as an ecological factor for alpine plants," Ecol. Monogr. *38*, 243 (1968).

8. Porter, W.P., "Solar radiation through the living body walls of vertebrates with emphasis on desert reptiles," Ecological Monogr. *37*, 273 (1967).

9. Smith, K.C., "The biological effects of ultraviolet radiation on man, animals, and plants," in *Proceedings of the Survey Conference*, Feb. 15-16, 1972, ed. A.E. Barrington, Climatic Impact Assessment Program, U.S. Dept. of Transportation, DOT-TSC-OST-72-13 (1972).

10. Harm, W., "Biological determination of the germicidal activity of sunlight," Radiat. Res. *40*, 63 (1969).

11. Knapp, E., Reuss, A., Risse, O., and Schreiber, H., "Quantitative Analyse der mutationsauslösenden Wirkung monochromatischen UV-Lichtes," Naturwiss. *27*, 304 (1939).

12. Hollaender, A., and Emmons, C.W., "Wavelength dependence of mutation production in the ultraviolet with special emphasis on fungi," Cold Spring Harbor Symp. Quant. Biol. *9*, 179 (1941).

13. Bell, L.N., and Merinova, G.L., "Effect of dosage and wavelength of ultraviolet radiation on photosynthesis of *Chlorella*," Biofizika [Russian transl.] *6*, 21 (1961).

14. Glubrecht, H. von, "Über die Wirkung von UV-Strahlen in somatischen Zellen," Z. Naturforsch. *8b*, 17 (1953).

15. Stadler, L.J., and Uber, F.M., "Genetic effects of ultraviolet radiation in maize. IV: Comparison of monochromatic radiations," Genetics *27*, 84 (1942).

16. Luckiesh, M., *Applications of Germicidal, Erythemal, and Infrared Energy*, D. Van Nostrand, New York (1946).

17. Kirby-Smith, J.S., and Craig, D.L., "The induction of chromosome aberrations in *Tradescantia* in ultraviolet radiation," Genetics *42*, 176 (1957).

18. Curry, G.M., Thimann, K.V., and Ray, P.M., "The base curvature response of *Avena* seedlings to the ultraviolet," Physiol. Plant. *9*, 429 (1956).

19. Cutchis, P., presentation to Biological Impact Workshop, Sept. 16, 1972, Cambridge, Mass. (1972).

20. Johnston, H., "Reduction of stratospheric ozone by nitrogen oxide catalysts from supersonic transport exhaust," Science *173*, 517 (1971).

21. Barker, R.E., Jr., "The availability of solar radiation below 290 nm and its importance in photomodification of polymers," Photochem. and Photobiol. *7*, 275 (1968).

22. Cline, M.G., and Salisbury, F.B., "Effects of ultraviolet radiation on the leaves of higher plants," Rad. Bot. *6*, 151 (1966).

23. Benda, G.T., "Some effects of ultraviolet radiation on leaves of French bean (*Phaseolus vulgaris* L.)," Ann. Appl. Biol. *43*, 71 (1955).

AGRONOMIC EFFECTS OF CLIMATIC CHANGE

R.H. BIGGS AND J.F. BARTHOLIC
Institute for Food and Agricultural Sciences
University of Florida
Gainesville, Florida

ABSTRACT: The first part of this report is directed at the possible effects on cultivated plants of an increase in UV-B radiation (280-315 nm) in the biosphere. It focuses on UV damage to plants' cellular processes, and on their adaptive mechanisms for utilizing certain photochemical reactions while protecting themselves against damaging ones. Additional research is recommended.

The second part of the paper deals with the consequences of climatic changes. The effects of temperature, precipitation, and weather patterns on crop yield in any given area are explored.

Part 1: Effects of Ultraviolet Irradiation on Cultivated Plants

R.H. Biggs

INTRODUCTION

Measurements of solar radiation flux at various points from the top of the atmosphere to the surface of the earth have demonstrated the atmosphere's filtering and scattering properties, and illustrated its dynamic nature. Changes in any component of this system, whether by natural or human agency, affect some other portion of the biosphere. This is the basic concept of the ecosystem. The change may be as simple as lighting a lamp to extend the day-length for a plant so as to initiate flowering, or as complex as the establishment of an environment on a space vehicle which will sustain life. The Climatic Impact Assessment Program's objective of evaluating by 1974 the potential effects on the biosphere of an increase in the UV-B portion (280-315 nm) of solar radiation [1,2] is one of tremendous magnitude.

The direct effects of UV-B radiation on biological systems can be studied by relating the frequency and intensity of irradiance to time and total solar flux, and then evaluating the plant responses: tolerance, lethal levels, sensitivity factors, and mechanisms of damage and natural protection. Our present knowledge in many of these areas has been reviewed recently by Caldwell [3] and Smith [4]. This report focuses on plants' responses to UV-B radiation, and the mechanisms by which they protect themselves from it.

UV CHEMISTRY AND BIOLOGICAL RESPONSE

This discussion has two basic themes. First, the biochemistry and physiology associated with the UV portion of the spectrum may be as varied as that associated with the visible portion. Second, plant responses are all based on primary processes, but their number and interactions vary.

Primary photochemical processes which occur on excitation of polyatomic molecules are dissociation into free radicals, decomposition into separate molecules, intramolecular rearrangement, photoisomerization, hydrogen-atom abstraction, photodimerization, photosensitized reactions, photoionization, and "internal" or "external" electron transfer [5]. With simple molecules in a rarefied gas phase, as in the stratosphere, only four of these primary photochemical processes generally occur. Quantitative prediction of the nature and efficiency of the primary processes which may occur as a result of irradiation for even very simple molecules in a gaseous state is not yet possible. Our knowledge

of polyatomic systems is based on noting various systematic patterns and correlations that exist between chemical structure and photochemical reaction modes. From these correlations, predictions are made as to the nature and extent of primary processes to be expected in related compounds [5]. When it comes to complicated biological systems, we are not at the "reasonable prediction" stage for any class of compounds. The only plant response we can measure in relation to photochemistry is photosynthesis [6]. With other systems (e.g., photoperiodism, photo-sensitive germination, respiration, tropism, pigment formation, and stomatal closure) the effects of radiant energy on biochemistry are still hypotheses. Phytochrome is likely to be the receptor for the radiant energy in some of the processes, but the primary photochemical reaction and the immediate coupling reaction are not known for any of them. It is significant, however, that even without knowing this, we can still predict with reasonable accuracy the responses of plants to radiation in the 400- to 1000-nm range [6]. This has been made possible by observations of plant growth and development as related to alteration in light regimes – experiments similar to those with polyatomic molecules, differing only in complexity due to the increased number of variables. Where a primary, overriding physiological process is strongly linked to a particular energy level and frequency of irradiation, predictions can be made with considerable accuracy – for example, in triggering soybeans to pass from a vegetative to a flowering state.

Previous work has provided us with some general understanding of the effects of increased UV radiation on crops. An increase in intensity or frequency of UV irradiation of cytoplasmic and nuclear constituents is generally held to be damaging to cellular processes. Second, the constituents of plant cells are decreasingly selective in their absorption of energy at shorter wavelengths. The concomitant photochemistry is quite different for reactions associated with decreasing the wavelength or increasing the intensity of radiation within the UV spectrum. The biologically damaging reactions, such as molecular decomposition or photodimerization [7], override biologically beneficial ones, such as electron transfer [6]. Third, plants vary widely in the extent of their response to radiation, depending on morphological, biochemical, and physiological variables. Adaptive mechanisms, to utilize certain beneficial photochemical reactions and to protect against others, have evolved to a high degree in vascular plants.

Plants vary greatly in their responses to ultraviolet light [3]. This variation is, logically, greatest for UV-B irradiation, since it lies at the short-wavelength side of the atmospheric window for UV-visible solar radiation. Plants have evolved in an environment where small amounts of UV-B radiation normally occur. UV-B irradiation may vary throughout the season due to atmospheric changes [1]. Measurements of the magnitude of normal diurnal, seasonal and annual changes are a part of CIAP [1,2] and will help biologists in their predictions.

Constituents of plant cells are decreasingly selective in absorption of radiation as wavelength decreases, particularly in capture and dissipation of a quantum of energy without the constituents' being irreversibly changed [7]. Proteins and nucleic acids, which are very basic to cellular functions, are photochemically altered by UV-B irradiation [3,4,8]. Irreversible changes in DNA, RNA, protein, and other critical cellular regulatory chemicals have been interpreted as damaging reactions [3,4,8]; reactions which synthesize or restore key molecules to the original state have been characterized as repair mechanisms [4].

Investigators agree that UV irradiation of certain key cytoplasmic and nuclear constituents is damaging to cellular processes. It is reasonable to assume that these potentially lethal reactions were responsible for elaboration of different mechanisms in plants to compensate for biologically damaging reactions from UV-B irradiation. Mechanisms to dissipate UV-B radiation before it causes damage are absorption and reflection by extra-cellular compounds, such as cuticular waxes and oils [3], and by cell-wall materials.

An example of the variation in UV-transmission properties of cuticles can be found in Figure 1, together with the UV-transmission characteristics of cell-wall material. The cuticles were isolated from epidermal tissue using an enzymic mixture of cellulase, hemicellulase, and pectinase [9]. Cell-wall material was isolated from oat seedlings (*Avena sativa*) using methods described by Cleland [10], and was primarily a mixture of

pectic and cellulosic substances. The UV-transmission curves were obtained using a grating spectrophotometer (Beckman, model DBG). Cuticular membrane samples were compared to an air reference; the cell-wall material (1%) was compared to a H_2O standard, since it was homogenized in distilled H_2O. Thus, in both cases, only relative values can be obtained. However, it is evident that cuticles do vary in UV-B optical properties, and that cell-wall material also has to be considered as an absorbing substance. These data support those obtained by measuring the optical properties of mechanically removed epidermal strips [3]. The latter technique permits the examination of components of the system, as has been done with solvent extraction of certain waxes, and oils and pigments from epidermal tissues [3].

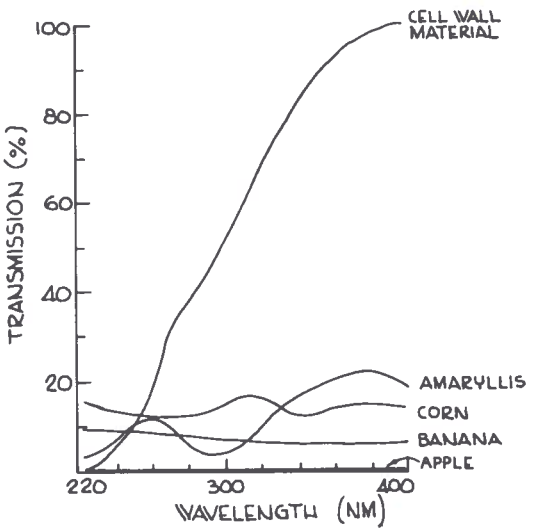

Figure 1. UV transmission of isolated cuticles from leaves of amaryllis and corn, fruits of apple and banana, and cell-wall material from oat seedlings. Cuticle transmission is measured relative to air, cell-wall transmission relative to water.

Survival has been a major molding force for the myriad of present-day organisms. The degrees of complexity evident at a macrobiotic level are a result of molecular diversity. Thus, it is not surprising that deposition of extra-cellular material by plants varies considerably, and that this material has functional properties.

In addition to the absorption properties of extra-cellular material, the location of protoplasm in relation to these materials is important to survival. The meristemiatic, regenerative tissues of many higher plants are located several cell layers below the surface. Thus, electromagnetic energy must filter through several cell layers. From an engineering aspect this is also advantageous, since the tissues are protected against stresses such as water deficits, thermal changes, pests, and so on. The most susceptible tissues are young, vegetatively growing buds, where only embryonic leaves afford a cover. Even these tissues may be protected, however, if growth takes place during darkness, or in periods of light when the UV portion of the spectrum is low or missing, or in the shade of other parts of the plant or another plant.

Basic to this concept of avoidance would be plant processes altered in a positive manner by UV irradiation. That plants can respond to UV to alter physiological processes is demonstrated by the data of Curry et al. [11]. As shown in Figure 2, the action spectra for base-curvature of *Avena* seedlings is in the UV-B portion of the spectrum, with a maximal response at about 295 nm. This might be linked to survival by avoidance. We need to keep in mind, however, that many plant processes may be influenced by UV radiation, and that such an overall action spectrum is only a reference point. The "m-shaped" curve of Figure 2 evidences a very complex system.

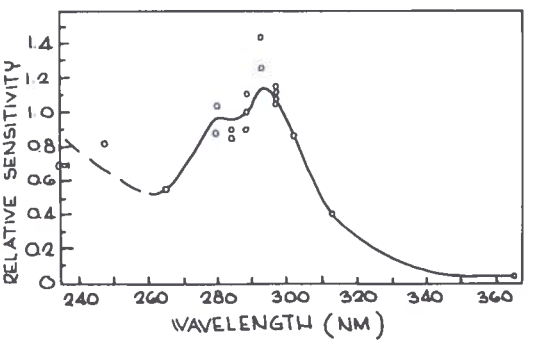

Figure 2. Action spectrum for base curvature of *Avena* seedlings (circles and solid line). The ordinates give the reciprocal of the number of quanta needed for 8.6° curvature, relative to that at 289 nm (data from reference 11).

CONCLUSIONS

Examination of our present knowledge of the reactions of plants to UV-B radiation clearly shows that not enough data is available to allow a reasonable prediction of plant responses to an environment with enriched UV-B radiation, particularly the interrelated responses in an ecosystem. At present, much of our understanding is based on experiments with lamps emitting in the UV portion of the spectrum at low intensities. Frequently the detailed spectra of these lamps were not specified, but they were probably rich in UV-C (<280 nm). The critical experiments of increasing or decreasing only the UV-B portion of solar irradiation and determining the response of organisms is the direct method of testing the overall response of a higher plant, or of an ecosystem that may have many processes that could be influenced by other-than-natural amounts of UV radiation. These should be top-priority experiments. Yet even they will have limited value in predicting plant responses until they are coupled with a better understanding of primary processes.

RECOMMENDATIONS

If the objectives of the Climatic Impact Assessment program are to be realized, the following areas need additional research for predicting the effects on plants – beneficial, harmful, or nonexistent – of increased levels of UV-B radiation:

1. The relative sensitivity of a range of plants to UV-B radiation, particularly cultivated plants and those in vital food chains.

2. The influence of UV-B radiation on the productivity of several critical crop plants. Experiments in this area should take into account as broad a network of interaction between organisms as possible; e.g., an increase in productivity might result if UV-B depressed the activity of an organism that was limiting production.

3. The natural defense mechanisms elaborated by plants (morphological, biochemical, or physiological) to guard against UV-B radiation's reaching UV-sensitive materials in the cytoplasm and nucleus. Such measurements will be extremely important as indicators for predicting plant responses.
4. The action spectra of several recognized, critical physiological processes subjected to UV-B irradiation – e.g., cell division, germination, leaf production, photosynthesis, respiration, water balance in guard cells, flowering, and fruiting.
5. Finally (to re-emphasize an early recommendation [4]) a network of monitoring stations to assess the spectral quality and quantity of UV radiation entering the biosphere. It is important that these measurements be related to calibrated energy standards and provide narrow-band spectral data, particularly in the 280 to 315 nm region of the spectrum.

REFERENCES

1. Grobecker, A.J., "Assessment of climatic changes due to flights in the stratosphere," presented at American Institute of Aeronautics and Astronautics Fifth Fluid and Plasma Dynamics Conference, June 26-28, 1972, Boston, Mass., AIAA Paper No. 72-658 (1972).

2. Sheldon, D.R., Institute for Defense Analyses, personal communication (1972).

3. Caldwell, M.M., "Solar UV irradiation and the growth and development of higher plants," Photophysiology *6*, 131-177 (1971).

4. Smith, K.C., "The biological effects of ultraviolet radiation on man, animals, and plants," in *Proceedings of the Survey Conference*, Feb. 15-16, 1972, Climatic Impact Assessment Program, Department of Transportation, A.E. Barrington, ed., DOT-TSC-OST-72-13, 243-250 (1972).

5. Calvert, J.G. and J.N. Pitts, Jr., *Photochemistry*, John Wiley, New York (1966).

6. Zelitch, I., *Photosynthesis, Photorespiration, and Plant Productivity*, Academic Press, New York (1971).

7. Jagger, J., *Introduction to Research in Ultraviolet Photobiology*, Prentice-Hall, Inc., Englewood Cliffs, New Jersey (1967).

8. Erixon, K. and W.L. Butler, "Destruction of C^{550} by ultraviolet radiation," Biochim. Biophys. Acta *253*(2), 483-486 (1972).

9. Barmore, C.R. and R.H. Biggs, "Ethylene diffusion through citrus leaf and fruit tissue," J. Amer. Soc. Hort. Sci. *97*, 24-27 (1972).

10. Cleland, Robert, "Auxin and the mechanical properties of the cell wall," in *Plant Growth Regulators*, E.M. Weyer, ed., Ann. of N.Y. Acad. Sci. *144*, 3-18 (1967).

11. Curry, G.M., K.V. Thimann, and P.M. Ray, "The base curvature response of *Avena* seedlings to the ultraviolet," Physiol. Plantarum *9*, 429-440 (1956).

DISCUSSION

ELLSAESSER: It is my impression that the most productive areas of the world are the low-latitude deserts, when we supply them with sufficient water. Have you any indication that ultraviolet damage occurs in plants in that situation? If it does not, doesn't that suggest that plants can tolerate considerable variation in UV exposure?

BIGGS: We have not examined those plants with UV in mind, nor has any experimental work been done. The first plants, or plant strains, placed in the desert did not do well, in most instances. But through careful selection of the plants and selective breeding, plants of high productivity can be grown in areas whose UV irradiation is as high as that which might result from the estimated possible ozone-shield reduction.

FITZPATRICK: What is the chemical nature of the absorbers in the banana or apple – the cuticle and the waxes on the surface?

BIGGS: The cuticle contains cutin. Cutin refers to a diverse group of complex polymers, composed principally of esters of monocarboxylic acids which contain two or three hydroxyl groups. The physical characteristics of this group of polymers vary considerably, particularly upon weathering.

Part 2: Changes in Crop Productivity and Cropping Patterns

J.F. Bartholic

INTRODUCTION

Climate is an integration of many environmental factors. These factors include variation with time (both diurnal and annual) of temperature, humidity, wind characteristics, and solar and thermal radiation-flux densities. Average climatic changes with time are important, but it is the extreme ones which are critical when it comes to effects on ecosystems. To evaluate the effect of a climatic change on crop productivity, both the scope of the change and the specific crop of interest must be clearly defined; each crop has its unique response to climatic variations.

For centuries man has been adapting plants to specific areas and climatic conditions. Recently, with the extensive breeding programs in most countries and the advances in genetics and hybridization, the breeding of plants for specific areas has progressed rapidly. Also, agriculturists have developed a better understanding of the importance of climate to agricultural practices such as planting, spraying, and the like. Thus, scientific evaluation of the effects of climatic change on crop productivity must also consider the effects on agriculture management.

It has been suggested that increased stratospheric flight would principally affect UV irradiation, and have only minor effects on other climatic factors. Since UV irradiation is covered by other authors, I should like to speculate on the other possible climatic effects: a temperature change at the earth's surface of between -2°C and +1°C, a change in precipitation, and an alteration in general weather patterns.

POSSIBLE EFFECTS OF CHANGE IN CLIMATE

Temperature Effects

The relationship between climatic factors and yield of corn over a 20-year period has been extensively analyzed [1,2,3]. Figure 1, taken from this data, shows that during June temperatures were near-optimum for corn growth; any change in temperature would have caused some reduction in yield. In July or August, a slight increase in temperature would also depress the yield. For example, a 1°C (≈2°F) increase during August would depress yields 1.5 to 2 bushels per acre, a 2% reduction in yield. Thus, even small changes in temperature can have a significant effect on yield of corn. However, such changes may have different effects during different stages of growth, and are also different for each crop. Analysis of the effects of temperature change must be referred to a specific crop if meaningful conclusions are to be drawn.

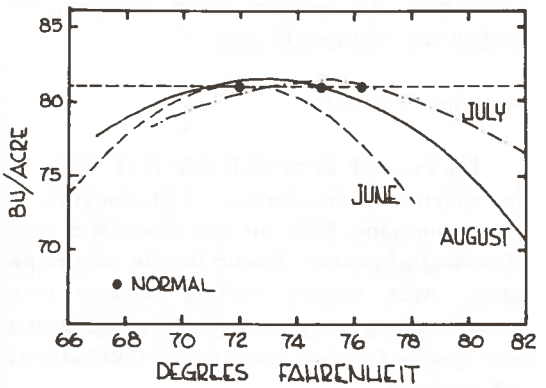

Figure 1. Response of corn yields to temperature in the corn belt of the United States [2].

Although some generalizations can be made for agricultural crops concerning the effect of temperature on productivity, each type of crop has a unique response to temperature. These response patterns for three important vegetable crops are shown in Figure 2, which gives the assimilation of CO_2 (sometimes referred to as dry-matter accumulation) vs. temperature. This experiment was done under controlled conditions with elevated CO_2 concentrations, so the data should not be considered as absolute; the relative patterns should be valid, however. Those patterns show that increases in temperature result in increased assimilation until an optimum is reached, after which the rate decreases. For potatoes growing at 28°F, an increase in temperature of 1 to 2°F would increase productivity. For potatoes growing at their optimum temperature of 30°, though, any increase or decrease in temperature would reduce productivity. The rate of change is less pronounced for tomatoes and cucumbers. (This data reemphasizes the importance of relating climatic change to a specific crop.)

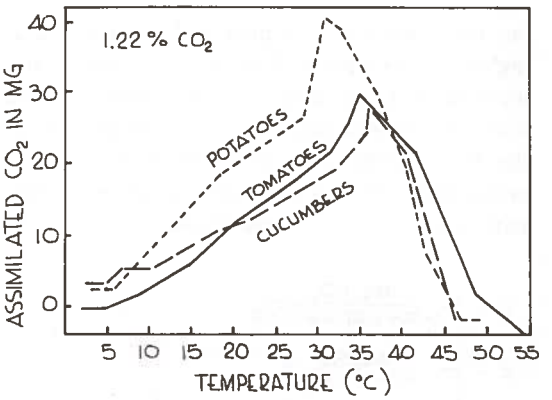

Figure 2. Relation between assimilated CO_2 and leaf temperature for some vegetable crops [4].

Plant respiration rates are also affected by temperature. Figure 3 shows respiration rates vs. temperature for alfalfa. Alfalfa is similar to most crops in that its respiration rate increases with temperature. Since respiration reduces net photosynthesis (dry-matter accumulation) the result can then be considered as a loss of net product. Generally, respiration occurs throughout the day, so information on the alteration of the diurnal temperature pattern is necessary to evaluate potential changes in respiration. Although changes in respiration rates during a specific night might have little effect on the dry-matter accumulation, the cumulative effect is significant over an entire growth season.

Figure 4 relates the gross assimilation, respiration, and net assimilation discussed separately in Figures 2 and 3. Figure 4 shows that for pine grown under cool conditions net assimilation is optimum at 15°C. The optimum temperature for pine is lower than that for vegetable crops (Figure 2) because of pine's rapid increase in respiration with temperature. Gross assimilation,

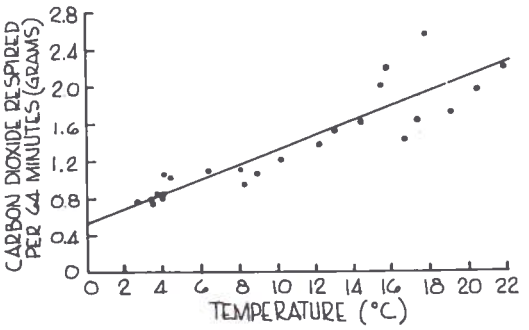

Figure 3. Effect of temperature on respiration of alfalfa [5].

on the other hand, is predicted to level off at higher temperatures. For a pine forest, any increase in temperature over the optimum would decrease net assimilation over the entire life of the timber crop. Thus, it would be necessary to evaluate the effect of climatic change on productivity over a 30- to 50-year period.

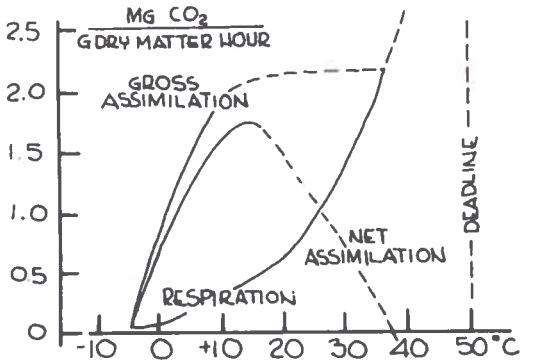

Figure 4. Relationship of gross assimilation, respiration, and net assimilation of cembra pine in the sun to temperature of the needles [6].

Small annual temperature changes could affect the length of the growing season for crops. The growing season is generally defined as the number of frost-free days, i.e., the length of time between the average last freeze in the spring and the average first freeze in the fall. Figure 5 is a composite portrait of the annual average number of frost-free days and average January temperatures for Mississippi. If temperatures increased, the isotherms would be shifted northward. For a 1°C increase, the number of frost-free days might be expected to increase 5 to 8 days during the months of the last spring freeze and the first fall freeze. Such a decrease in the growing season seems to be typical for the postulated temperature change.

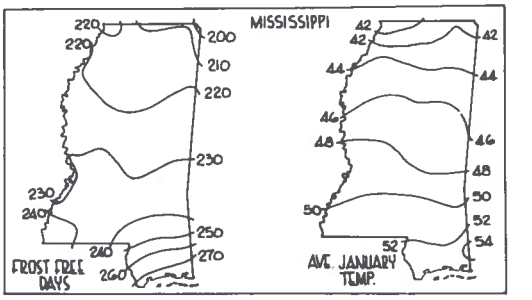

Figure 5. Annual average number of frost-free days and average January temperatures for Mississippi [7].

The implications of such a shift are agronomically important. Generally, the longer the growing seasons, the more solar radiation captured by photosynthesis, the greater the dry-matter accumulation, and the greater the yield of marketable product. A temperature decrease would have the opposite effect, lowering the productivity of a specific area.

Precipitation Effects

The network of possible effects of change in the amount or distribution of precipitation is all-encompassing. Both our agricultural and natural ecological systems depend heavily on precipitation. Also, natural drainage systems have evolved and our entire structure of reservoirs has been designed around expected rainfall patterns and extremes.

Crop productivity is affected by the availability of water from the soil. Soils vary greatly in their water-holding capacities; sands frequently hold as little as 1 to 2 inches of available water in the root zone, while clay loam may hold four times that amount. Figure 6 shows the response of corn yields to preseason precipitation in the corn belt. A close correlation exists between preseason precipitation stored in the soil and the ultimate yield for crops such as corn and wheat, which grow in soils with a higher water-holding capacity. It is possible to predict wheat yield in North Dakota simply by knowing preseason soil moisture. The effect of variations in

rainfall during a growing season on a short-term crop which gets most of its water from preseason soil moisture is much less than that on a crop with a long growing season, or a crop grown on a soil with low water-holding capacity.

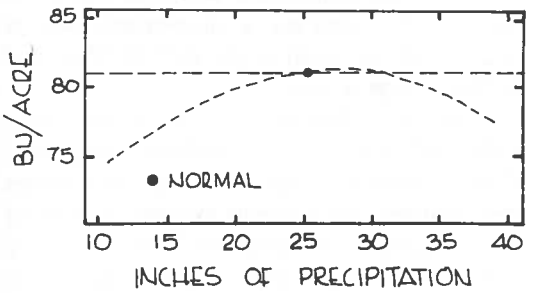

Figure 6. Influence of preseason precipitation on corn yields in the corn belt of the United States [2].

Since corn has a relatively long growing season, precipitation later in the year is also of importance. Figure 7 shows the relationship between yield and inches of rainfall during the months of June, July, and August. During June and August small changes in rainfall are not significant. During the month of July, however, changes in rainfall greatly affect yield. July is a critical month for corn, since it is during this period that tasseling and silking occur, and these processes are very dependent on soil moisture and temperature. A 1-inch decrease in rainfall during July could depress yields by 5 bushels per acre, a 6 to 7% reduction. Such a change could have drastic economic implications.

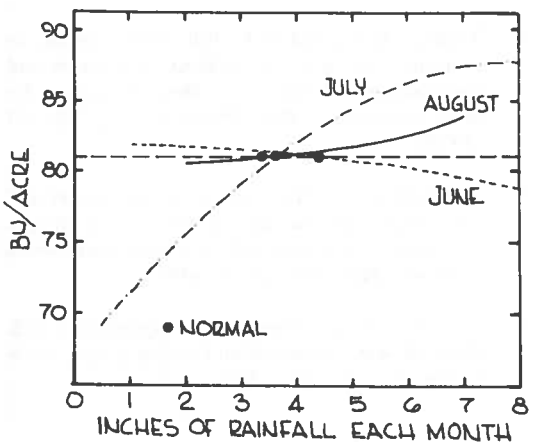

Figure 7. Response of corn yield to rainfall during different stages of growth [2].

Climatic factors interact to influence yield. Figure 8 shows the interaction of temperature and rainfall during the critical month of July. It can be seen that high rainfall (6 inches) coupled with rising temperature increased yield. However, with low rainfall (1 inch) any temperature increase tended to decrease yields. With an intermediate rainfall (3.5 inches) yields fell off to either side of the 77°F optimum. Thus, changes in one climatic factor cannot be evaluated independently of other factors. Crop productivity results from an integration of the total environment.

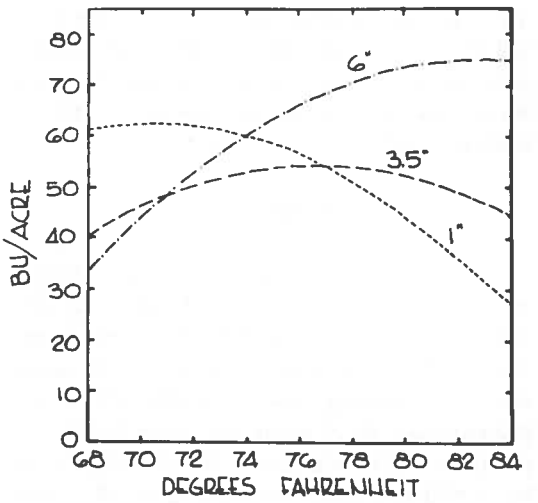

Figure 8. Yield of corn in July as influenced by temperature at differing levels of precipitation in Iowa [1].

Modifications to Weather Patterns

Some possible effects of modifications to weather patterns have already been discussed. Conditions detrimental to plant growth could result from even minor shifts in weather patterns, because of the change in the climatic extremes involved. Whenever plants, or individual plant organs, reach an extreme beyond which they cannot function, death in part or in total occurs. This effect is perhaps most pronounced at low temperatures; temperatures below 40°F can be harmful to plant growth, and for temperature-sensitive crops temperatures below 32° can be lethal. (This minimum temperature extreme generally regulates the length of the growing season for cold-sensitive crops.) The detrimental effects

of high-temperature extremes can also cause death.

If weather patterns are shifted, so that unseasonable changes occur, or lower-than-usual minimum temperatures are reached, entire plant communities could be destroyed. A case in point is the citrus industry of the Florida peninsula, with nearly a million acres. The fruit can sustain temperatures to 28°F for only a few hours. The leaves and twigs have a freezing point several degrees lower, depending on prior hardening. However, unseasonably low temperatures early in the season, or extremely low temperatures during the winter months, can kill them too. A freeze 10 years ago resulted in the loss to the citrus industry of a half-billion dollars. If weather patterns were shifted in such a way that more severe freezes occurred, the loss in just this one industry could exceed a billion dollars.

SUMMARY

If the agronomic effects of climatic changes are to be properly evaluated, each climatic change must be defined in both magnitude and time. This information was shown to be necessary for evaluating changes in temperature and precipitation. In addition, soil water-holding capacity should be considered. No single factor can be considered independently, since all factors interact to affect the final yield, as was shown for corn in Figure 7. The effects of climatic change must be considered for a specific crop, or at least for a category of crops with similar physiological behavior.

Changes of extremes in marginal growing areas, whether caused by modification of weather patterns or by minor climatic shift, can wipe out these areas for the production of a specific crop. Fortunately, from the standpoint of agricultural productivity, a wide selection of varieties of each crop is available, varying greatly in their length of growing season and their tolerance of drought and high temperatures. Thus, if climate were modified the agricultural productivity of annuals could in many cases be maintained at a relatively high level by means of the available agricultural technology, except in marginal areas.

In the case of perennial crops, shifts in agricultural practices would be more difficult. For instance, some fruit trees live 50 years or more. A similar length of time is needed before a forest crop can be harvested. For perennials, the effects of low-temperature extremes cannot be overcome by planting a short-growing-season variety, and the result might well be death and the loss of large acreages of fruit crops.

The earth's climate has gone through many cycles, and natural ecosystems have been able to adapt to them. Generally, however, these cycles have occurred over relatively extended periods of time, frequently centuries or longer. Climatic changes that might result from stratospheric flight would be much more rapid. Ecosystems would not necessarily be completely lost, but certainly geographic shifts of plants and animals could be expected with even very minor changes in climate.

REFERENCES

1. Thompson, L.M., "Weather and technology in the production of corn and soybeans," C.A.E.D. Report 17, Iowa State University (1963).

2. Thompson, L.M., "Weather variability and the need for a food reserve," C.A.E.D. Report 26, Iowa State University (1966).

3. Colville, W.L., "Environment and maximum yield of corn," in *Maximum Crop Yields – The Challenge*, ASA Special Publication No. 9, 677 S. Segoe Road, Madison, Wisconsin, 21-36 (1967).

4. Molga, M., *Agricultural Meteorology*, Warsaw (1962).

5. Thomas, M.D., and G.R. Hill, "The continuous measurements of photosynthesis, respiration and transpiration of alfalfa, and wheat growing under field conditions," Plant Physiology *12*, 285-307 (1937).

6. Tranquillini, W., "Die bedeutung des lichtes and the temperature für die kohlensaureassimilation von pinus ambra-jungwuchs an einem hochalpinen standort", Planta *46*, 154-78 (1955).

7. *Climate and man*. Yearbook of Agriculture. U.S. Dept. of Agr., Government Printing Office, Washington, D.C., 942-943 (1941).

DISCUSSION

MacCRACKEN: Are there any historical records of how plants react to major climatic changes? Do they migrate further north or south, or do they try to adapt where they are? And if it took 30 years for a climatic change of the magnitude being considered by CIAP to occur, would the plants be able to cope with it over that time?

BARTHOLIC: There is some record of species adaptation; there is a wide variety of genetic material within any plant community, so the capacity for change exists. We know that through time vegetation has changed drastically, both by migration and by genetic evolution. 30 years is very short relative to the time span of naturally occurring changes, though. Of course, where man is in control, we can modify agricultural practices to accommodate the change. We have available the genetic material and the breeding programs to minimize detrimental effects, or even take advantage of climatic change.

(UNIDENTIFIED): Is there some way to normalize all the plant components of the average American's diet so that we could see more directly how people would be affected by the possible increases or decreases in the yield of various crops?

BARTHOLIC: That would be a good idea. The information presently available for specific crops could be compiled and organized into categories, such as legumes and fruits, and all graphed together as a function of temperature or precipitation change.

SCHAINKER: Also, it seems to me that a lot of crops are presently grown at near-optimum climatic conditions. If so, it might be worthwhile to examine the slopes of their relative production curves as conditions vary from that optimum.

BARTHOLIC: That's a good suggestion too. I imagine that, like crops, most plants in ecosystems do operate near their optima.

REITER: The biological-impact studies must take into account the tremendous natural variability of climate. There are long, slow climatic cycles, and there are abrupt, catastrophic ones. I seem to remember that somewhere in the sixteenth century summer weather in the Alps got so bad so suddenly that mining tools were abandoned before the advance of the glaciers, and only in the last decade or so has it been possible to retrieve them. It seems to me that this kind of change would hit the marginal growing areas you referred to, rather than the crop heartlands. I think this was true in the recent wheat failures in Russia; I would be interested to know whether this pattern is in evidence historically, and how important such marginal areas are to a country's economy.

REMARKS ON DETERMINING SOCIAL AND COST MEASURES OF CLIMATIC CHANGES

HENRY M. PESKIN
National Bureau of Economic Research
The Urban Institute
Washington, D.C.

ABSTRACT: The stratosphere can be treated as a social asset that provides valuable services, some of which may be degraded by the effects of high-altitude flight. Efforts to measure these services in dollars have been based on a "willingness-to-pay" principle. A number of problems arise in applying this theory, however; other measures may have to be found.

Why are we concerned with cost measures? As scientists, our concerns are often closely linked to our individual perspectives. Thus, the chemist and physicist might model the stratosphere as a mixture of molecules. Their concern is with difficult problems of how these molecules interact in the presence of solar energy. The meteorologist, on the other hand, may see the stratosphere as a collection of streams of compressible fluids. His view suggests its own set of difficult fluid-flow problems. Indeed, it is a herculean and complex task for the CIAP organizers to focus the divergent points of view of the physicist, meteorologist, chemist, and biologist together.

Those of us with a scientific interest in policy also have a special point of view – our own model of the stratosphere. We see the stratosphere as a social asset that provides valuable services. Of special importance are the well-established ultraviolet-shielding function and the less-well-understood contribution the stratosphere makes to our meteorological environment – services rendered to those of us on the earth. In addition, there are the existing and potential services rendered to those of us traveling at high altitude – an uncongested travel medium, a source of oxidizing agents for the aircraft fuel, and a place to dispose of engine wastes. It is, of course, this last service that is of special concern to CIAP.

Specifically, if this disposal service conflicts or competes with the other services, the problem immediately arises of whether all the services will be allocated among the competitive users efficiently – whether, for example, too much or too little will be allocated to aircraft.

Economic theory teaches that a requirement for an efficient allocation of these services is that the gain in value to society associated with increased use of the stratosphere by aircraft must cover any associated increases in social costs. These social costs have two components: first, the cost in fuel, manpower, etc., necessary for the flight; and second, the cost to society in general of any adverse alteration due to the allocation of stratospheric services. Estimating and measuring this second cost component is the main concern of the sixth phase of the CIAP program.

Estimating this cost component requires two steps. First, the physical implications of changes in stratospheric services must be determined. Of special interest may be the effects of such changes on human health, crop yields, days of nice weather, etc. As economists, we acknowledge our ignorance of such matters and gladly pass the buck to our colleagues in the "hard" sciences.

However, the second step is our responsibility: namely, converting these physical effects to some value measure that will permit the comparison of social gains and losses necessary to assure the efficient allocation of stratospheric services. This is no easy task.

The approach that has been tried for similar problems – for example, determining how valuable unpolluted air is for a city – is based on a "willingness-to-pay" principle. Employing this principle requires us to pose the following

hypothetical question: If the services of the stratosphere could be bought and sold, how much would people be willing to pay for them? If, for example, a given reduction in the ultra-violet-shielding service leads to an increase in the probability of contracting skin cancer, how much would people be willing to pay to have the former skin cancer probability restored? Or, if the stratosphere provides a service that helps maintain a given mean surface temperature, so that a reduction in this service changes this temperature and consequently lowers agricultural crop yields, how much would farmers be willing to pay to have the former yields restored?

Because such questions are hypothetical, posing them directly often does not yield reliable responses. Those who have worked on these problems attempt to provide better information by posing less hypothetical, but more indirect questions, the answers to which may provide clues. For example, one might ask himself what people *should* be willing to pay to avoid disease, assuming that whatever they are willing to pay, it will, at least, cover the demonstrable economic costs, if not the psychic costs. Ron Ridker used this approach when he estimated the health losses due to air pollution in the U.S. in 1958 at $360-400 million*.

As another example, one might estimate how much a farmer might be willing to pay for reversal of a change in agricultural production by asking what is the value to him of current production. Any estimates of the physical change in production could then be valued at the current market price. Indeed, this procedure was followed by Maunder in his estimates of the value of climatic variations in agriculture in New Zealand**. For example, he calculated that a two-inch increase in the mean October rainfall would be worth about $260,000 per New Zealand county, due to an expected increase in butterfat yield of nine pounds per cow.

The ability of these auxiliary questions to provide answers that are approximately correct for the hypothetical questions depends on fairly complex economic considerations. Economic theory does provide guidance that permits some assessment. For example, we have reason to believe that Maunder's valuation of agricultural yield changes is probably more accurate than Ridker's valuation of health changes.

However, both Ridker's and Maunder's procedures, like others used in similar investigations, suffer from certain serious defects. One implicit assumption is that either a person's willingness-to-pay is the same for all individuals or that the distribution of effects among individuals does not matter. Another assumption is that the quantitative estimate of willingness-to-pay is independent of the location where the estimate is made. While such considerations may not be important if the interest in stratospheric effects is confined to a single geographical region, it is quite important if the effects are to be assessed internationally. An example of the problem could be illustrated by attempting to value a human life by its economic contribution to society. With this procedure, the estimated dollar value of an English worker's life would be about half that of an American's. Such a valuation would raise a few international eyebrows. Consequently, if CIAP is to maintain its international flavor, it may be necessary to find measures of social cost other than the often-used dollar or money measure.

I only raise these problems. I have no ready-made answers. I feel, however, that their difficulties justify bringing together experts who are at least as qualified in the area of social cost determination as those assembled here are in their respective scientific disciplines. To this end, the Department of Transportation is assembling such a group of outstanding experts on December 11 in Washington. Although various disciplines are represented – meteorologists, zoologists, and economists – they all share a common interest in converting physical impacts into social cost measures. It is impossible to be specific about methods of analysis at this time. However, given the possibility that our colleagues in the physical and biological sciences may not come up with specific results in the near term, they are prepared to conduct their analyses on an "as-if", parametric basis – using hypothetical data to formulate the hypothetical questions.

Our hope is that this group will be able to apply the techniques of the "soft" sciences to the CIAP problem as effectively as their colleagues gathered here have applied the techniques of the "hard" sciences.

---

* Ronald G. Ridker, *Economics of Air Pollution*, Praeger, 1967.

**W.J. Maunder, "Effect of Significant Climatic Factors on Agricultural Production and Incomes," Monthly Weather Review *96*, No. 1, January 1968, pp. 39-46.

DISCUSSION

(UNIDENTIFIED): You mentioned posing hypothetical questions for determining the cost of taking care of SST wastes. Don't we have good SST cost figures for two categories – the cost of making the plane, and the cost of time saved in flight?

PESKIN: Yes, we have some idea of the cost to build and of the marginal benefits of the use of the stratosphere by aircraft. What we are concerned with in the sixth CIAP volume is the *marginal cost*. The key policy issue is whether the marginal benefit exceeds this marginal cost; if it does not, we should question the use of the stratosphere by any sort of aircraft. Now, the marginal cost can be divided into an external and an internal component. Your question refers to the internal one. The external one is the costs to society, such as the fact that the engine exhausts may reduce the ultraviolet shielding.

The benefits can also be broken down into an external and an internal component. The internal benefits are those to the traveler, usually measured in terms of how much he is willing to pay to travel. The external benefits are more vague, such as enhancement of national prestige.

(UNIDENTIFIED): How do you measure these external effects? For example, if one of the effects of exhaust in the stratosphere is a change in longevity, how do you attach a societal value to it?

PESKIN: It is especially difficult to get valid willingness-to-pay responses in the areas of health and longevity. Economists such as Ron Ridker and Lester Lave attempt to answer the question on the basis of the economic value of life. They do look at things like the horizon of life and retirement factors, but we have not yet found a way to take the psychic values into account.

GOLDBURG: Your benefit-cost equation must determine a different need for each country. How do you set it up for the world? Does the balance of trade enter into it?

PESKIN: This equation is actually a condition for efficiency – that is, if this condition does *not* hold, it is possible to make some people in the world better off without making anyone else worse off. You are talking about the distributional aspect, which I think is outside the realm of economics. That problem is a political one.

THE CLIMATIC IMPACT OF POLLUTANTS INJECTED INTO THE STRATOSPHERE

PANEL DISCUSSION

ALAN J. GROBECKER
U.S. Department of Transportation
Chairman

GIICHI YAMAMOTO	*Tohoku University, Japan*
JACQUES BLAMONT	*CNES, France*
A.J. DYER	*CSIRO, Australia*
HAROLD JOHNSTON	*University of California at Berkeley*
ELMAR REITER	*Colorado State University*
WILLIAM KELLOGG	*National Center for Atmospheric Research*

GROBECKER: For this final panel, I have gathered here representatives of four nations. Each has been asked to summarize our progress on CIAP and indicate areas still needing investigation if we are to meet the CIAP objective of a coherent, thorough report in 1974.

YAMAMOTO: The panel discussion on aerosols gave me the impression that the theory of the formation of stratospheric aerosols may be very important to CIAP. The subject is a very complex one, involving the mechanisms of aerosol formation and fallout and diffusion of aerosols in both vertical and lateral directions. We know that there are injections due to volcanic eruptions under natural conditions; for CIAP we need to know the effect of injections from aircraft. I think that quantitative estimates of the aerosol budgets of both the natural and the perturbed stratospheres are needed, since without them we cannot estimate the climatic impact of aerosols.

At present I am studying the effect on atmospheric heating rate of the absorption of solar radiation by aerosols. This absorption also decreases the amount of solar radiation reaching the earth. While both these effects might influence the climate, we cannot estimate the magnitude of their influence until we know the amount, the spatial distribution, and the size distribution of aerosols in the stratosphere.

I should like to show you the results of extending some of my earlier calculations to the aerosols produced by the Mt. Agung volcanic eruption*. I first estimated the amount of aerosols injected into the stratosphere from the decrease in direct solar radiation observed at Mauna Loa, Hawaii (slide 1). Next I estimated

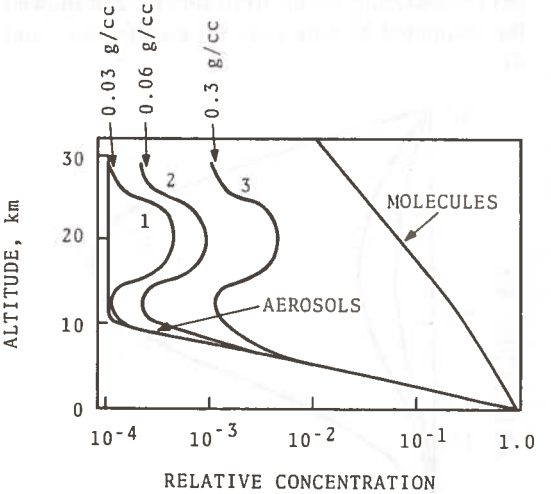

Slide 1. Calculated aerosol vertical distributions resulting from the eruption of Mt. Agung.

the heating rate in the stratosphere as a function of the imaginary part of the average refractive index of aerosols (slide 2). It is important that

*Dr. Yamamoto's earlier work on atmospheric radiative transfer, which considered the range of possible effects of absorption and scattering by aerosols, appeared in J. Atmos. Sci. *24*, 1405 (Nov. 1972).

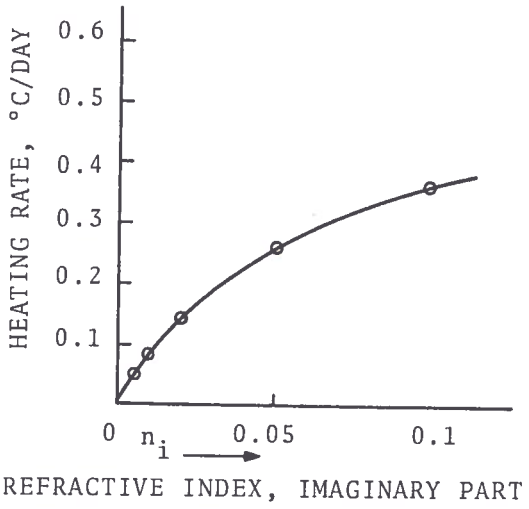

Slide 2. Calculated stratospheric heating rate vs. the imaginary part of the aerosols' refractive index, for the Mt. Agung eruption. $\beta = 0.01$, $p \leq 100$ mb, sunlit hemisphere.

we determine the latter quantity more accurately, because the heating rate is strongly affected by it. Last, I assumed several aerosol amounts which might result from an aircraft fleet's operating in the stratosphere, and showed the estimated heating rates for each (slides 3 and 4).

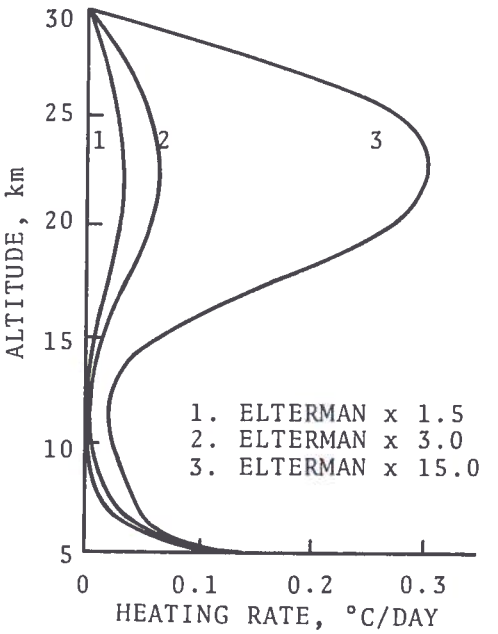

Slide 3. Heating rate vs. altitude for $n_i = 0.10$, given three aerosol distributions resulting from SST-fleet operation.

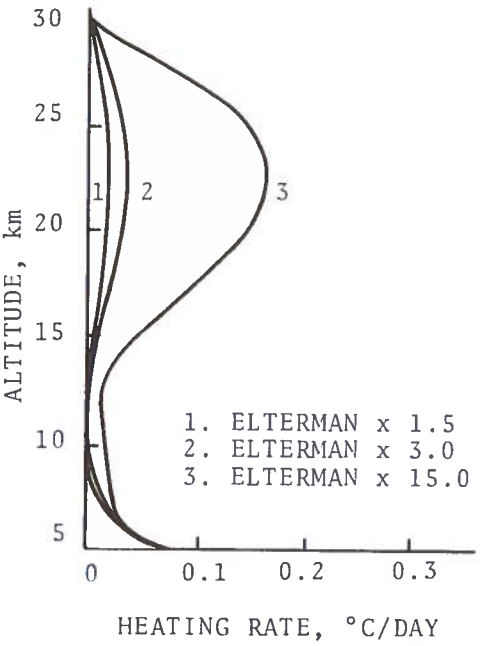

Slide 4. Heating rate vs. altitude for $n_i = 0.03$, given three aerosol distributions resulting from SST-fleet operation.

DYER: Last year the Australian Academy of Sciences set up a committee to make the same sort of investigation as CIAP, though in a far shorter time. This group found that "we would not expect significant adverse climatic effects to derive from aircraft assumed by us to be flying in 1985". Its next sentence caused distress in some quarters: "However, the possibility of deleterious changes cannot be completely dismissed, and accordingly any Australian decision on supersonic aircraft should be taken in light of all the qualifications embodied in this report."

Three of the committee's recommendations are important and generally applicable, I think. First, stratospheric flight should be restricted to below about 18 kilometers. Second, the aircraft industry should take all possible steps to reduce emissions of oxides of nitrogen. Third, a continuing program of stratospheric monitoring should be begun.

The areas investigated by the Australian group were almost identical with those we have been discussing at this conference. They were better off in having a good idea of the position of the stratospheric particulate material, so that they could relate emissions, water vapor, particulates, and so on to it. They identified the oxides

of nitrogen as a major problem area, however, just as we have done here. They concluded that the warnings of the photochemists should be heeded, even though their detailed conclusions might not be accurate, and I agree.

Another area of interest to us on the Australian committee was the possibility that cloud formation might be increased. It is very difficult to monitor clouds, however, and to detect any changes in cloudiness. It may be that we have a choice between flying in the stratosphere and decreasing the ozone cover, or flying in the troposphere and increasing the cloud cover.

A number of ongoing activities in Australia are relevant to CIAP. Several groups are working in atmospheric physics. One group is working on general-circulation modeling, though of course with special reference to the southern hemisphere. Another group is investigating the nature and quantity of stratospheric particles. A group in my own laboratory is studying the radiative properties and radiation balance of clouds; this includes making radiation observations all day, every day, and documenting them, as part of a radiation network.

Analysis of this radiation data made it possible to show in 1967 that quite a lot of volcanic dust from the 1963 Agung eruption entered the stratosphere. In September 1963 the average reduction in direct radiation at Melbourne was 25%. The next wave of dust came through in July 1964, reducing the direct reading by about 15%; the following year the reduction was about 8%. This pattern matches that of the global spread of fission products from nuclear tests.

Our ozone program has a network of seven Dobson spectrophotometers scattered around Australia, from Darwin (12°S) to Macquarie (52°S). The one at Melbourne was put in in 1956, and the last one in 1968, so we have as much as 17 years of data in some places. We also have a program to measure ozone directly, by means of balloon-borne sensors. We have been sending up a balloon once a week for the last six years, so we have quite a body of well-documented ozone profiles.

I think there is still a good deal of work to be done in the area of photochemistry. It seems to me that new species are being added at the rate of one per five minutes of discussion, and I have the greatest admiration for those who are attacking this incredibly complex problem. The Australian report suggested that the answer to the problem CIAP is investigating would probably come ultimately from linking this very detailed photochemistry with the general-circulation models in such a way as to include the feedback between the two. I think this is true; I feel that shortcut methods do not include enough of the elements needed to accurately describe the physical situation, particularly where climatic modification is concerned, and it would be very easy to modify a trend into a disaster.

I have a plea to make in closing: Avoid ambiguous phrases like "the winter of 1970". Remember that when it's springtime in the Rockies, it's autumn in Australia!

BLAMONT: I was impressed by the University of Wyoming findings that aerosol residence time was of the order of seven to nine months. They agree well with Dr. Machta's data on the zirconium-cerium ratio, from which he deduced that residence halftime was a small number of months. In the northern hemisphere, the ozone distribution does not follow isentropic patterns; a large transport toward the lower altitudes is definitely present. The transport phenomena are the main factors determining the concentration of minor constituents in the stratosphere. For instance, in the case of ozone, there is a source at high altitude, and ozone goes down through the stratosphere. The important point is what is lost in the lower altitudes. We once thought that something injected into the stratosphere would stay there forever. This is not true if the time constant is a few months. Unfortunately, we do not have enough accurate data on the transport phenomena to be able to understand them. I am sorry that more programs in CIAP are not devoted to experimental study of these important phenomena; the AFCRL proposal and its program for next year are the type of study that should be encouraged. Transport phenomena should be studied from two points of view: first, the *local*, which would be essentially measuring the parameters of the turbulence and winds at and above the tropopause; and second, the *global*, in particular the stratospheric wind systems around the world.

In connection with the ozone question, I should like to show you a few slides from Dobson's 1965 book. The first slide shows the ozone distribution as a function of time during one year. At 50°N you can see that the ozone maximum is in March and the minimum in August-September, with a difference of a factor of 2. The summer ozone maximum is due to transport from the equator to the poles and back; here we find a time constant of just a few months. This suggests that the global-scale time constants in the stratosphere are shorter than we had thought.

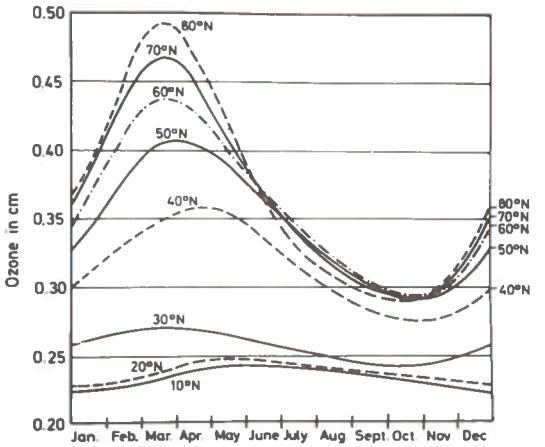

Slide 1. Annual variation of ozone at each 10° of north latitude.

The second slide, which uses 1957 data, shows a correlation of the total integrated ozone content with tropopause altitude. This indicates that the ozone concentration is largely controlled by the loss at the tropopause, not by what happens in the stratosphere.

The third slide shows day-to-day ozone variations over Europe. Note that on the first day the value over London is 342; two days later it is 265. Compare this large variation with a predicted SST-induced change of a few percent over two years. If the time constants have a value of a few months, I don't see how such a phenomenon could even be detected.

Of course, this argument depends on the quality of our present ozone data. I am not at all sure that we have a satisfactory description of the ozone problem, since we know so little about

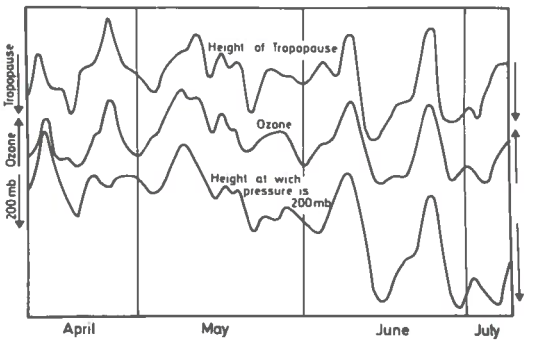

Slide 2. Correlation of ozone content and tropopause altitude, April-July 1957.

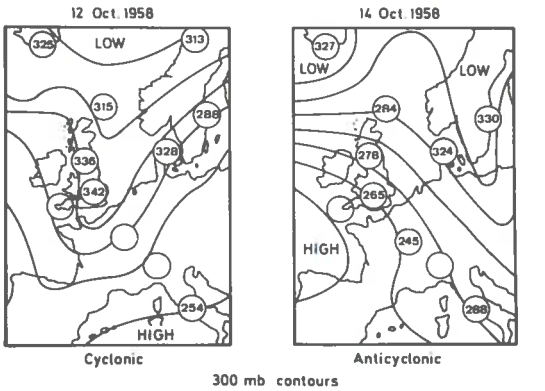

Slide 3. Ozone column over Europe, 12 and 14 October 1958.

the transport. A complete analysis of the Nimbus ozone data has not yet been made. Important though the photochemistry is, it may be the transport which controls the evolution of the ozone profile.

Now I should like to say a few words about nitric oxide. It reminds me of a play by Pirandello, "Così è, se vi pare" – however you see it, is right. The central character shows up only for one minute, at the very end. The same is true of nitric oxide; no one has seen it, so we can talk about how important it is; but when it does appear, such as after a nuclear test, it doesn't do anything. Strictly speaking, Foley and Ruderman's data and other data discussed yesterday have no meaning. Even if Foley and Ruderman are wrong by a factor of 2 or 12, they do point out something no one had been thinking of, which is that there is a lot of NO in a nuclear bomb; a comparison of the production rate of

NO to some spotty ozone data should be done *very* carefully, however.

People who have made Dobson ozone measurements know how difficult they are; with a careful experimenter, data may be good for two years, but they often deteriorate. You could take 135,000 data points, weight them according to the quality of the data, and end up with a negative number. We have no good global measurements of ozone, and no measurements of nitric oxide at all.

In summary, we don't know much. The first priority of CIAP should be to collect good data; there is no point in spending a lot of money on models if we are going to feed them with data of dubious value. We need really *good* measurements of the transport phenomena, of ozone, and of nitric oxide. I am not convinced that the workhorse of this program, the RB-57, will get them for us. I should like to see CIAP look seriously into the possibility of using superpressurized balloons. Such a balloon, with a payload of a few pounds, will stay in the stratosphere for six months to a year, giving a really useful accumulation of data. We need such significant measurements before we start feeding large computers.

JOHNSTON: I want to give you a quick history of our knowledge of the photochemistry of the stratosphere. The first big step forward was taken by Sydney Chapman in 1930; with a series of five chemical reactions, he got a better-than-zero-order approximation. Considering the other uncertainties of the time, it was a good start. During the next 30 to 35 years, the laboratory data on light-absorption cross-section and rate constants in these five reactions, coupled with atmospheric motions, seemed to give about the correct amount of ozone for the world. Everybody realized quite early, however, that this theory didn't give the correct distribution over latitude.

Ever since the late 1940's Marcel Nicolet has been concerned about the other things in the stratosphere. There are a number of minor species interacting in various ways. He pointed out the effects of free radicals based on water, oxides of nitrogen, and other trace species.

In 1961, Hans Dütsch made what I think was the first statement on the probable inadequacy of the Chapman reactions. He noted that there were discrepancies between the new rate constants found in the laboratories and those Chapman had used, which were based on experimental data of the 1920's and 1930's. The actual observed ozone in the stratosphere was much less than that calculated from the Chapman model with the new constants, including motions. Dütsch felt that we should wait and see whether more changes would come out of the laboratories; if the new values were substantiated, we would have to revise much of our thinking on the stratospheric photochemistry.

The data continued to improve. By 1965, Barrie Hunt felt that some explanation of the ozone deficit had to be made. He tried one model based on excited oxygen atoms and molecules, and showed that it didn't work. He then tried the so-called "water reaction" model. He postulated two reactions, and showed that if they proceeded at a certain rate the deficit – a factor of two or three globally – could be accounted for by the water reactions.

People have tried to measure the rates of these reactions in the laboratory. They are elusive and very difficult to measure, and are still not accurately known. It does seem, however, that they are substantially slower in the stratosphere than Hunt assumed.

In 1970, Paul Crutzen pointed out that reactions of the oxides of nitrogen could explain the ozone deficit. In the last two or three years, laboratory scientists have begun to agree as to the values of the rate constants of the Chapman mechanism and the basic oxides-of-nitrogen cycle. We now have rate constants from studies made at stratospheric temperatures and pressures which agree pretty well with each other. The Chapman reactions appear to be insufficient by about a factor of five to explain what is going on in the stratosphere.

During any second, global ozone is being made five times faster than it is being transferred to the troposphere or destroyed by the Chapman reactions. To the best of our present knowledge, the only thing sufficient to account for this discrepancy is chain reactions of the oxides of nitrogen. Water reactions are probably important too in the upper stratosphere. Other unknown trace reactants may also be engaged in fast cyclic reactions, thus having a disproportionately large effect. One-way reactions could not account for such a large discrepancy.

Now, what effect will the SST have on all this? Before 1971, the ozone deficit was ascribed to the water reactions. If the water now in the stratosphere reduced ozone by about a factor of two or three, and if SST's would increase this water by about 10% world-wide, adverse effects due to increased water would merit serious consideration. When it was found that water reactions were not fast enough to account for the ozone deficit, however, they no longer seemed to be a problem.

If it is the oxides of nitrogen in the stratosphere which cause the ozone to be two or three times less than it would otherwise be, we need to know how much they would be increased by a fleet of SST's. Our best estimate at present – omitting the ammonia source discussed earlier at this conference – is that 500 American SST's would inject oxides of nitrogen by a factor of between one and five faster than nature does. So, the best current information suggests that the SST would approximately double the quantity of this very active natural ingredient.

Hesstvedt said yesterday that, using his model, which includes atmospheric motions and photochemistry, he found that doubling the oxides of nitrogen decreased the ozone by 10%. While this number does not seem large, remember the point I made in my 1971 paper: the *distribution* of the nitrogen oxides is important. In that paper I assumed a background distribution of NO_x which averaged about 7 parts per billion. For a given artificial increment to this natural background, I found that for a very highly constrained vertical distribution, the column ozone reduction would be 3%. If the same increment of NO_x over the same assumed natural background had a highly constrained horizontal distribution, there would be a 50% reduction of the local ozone column. With the numbers as we knew them then, somewhere between a 3% and a 50% reduction of ozone from NO_x could be expected, depending on the distribution of the NO_x in the stratosphere.

This brings us to one of the most important aspects of CIAP: the establishment of the amount and distribution of oxides of nitrogen, in both the natural stratosphere and the stratosphere as perturbed by SST operation. Modelers in particular need some idea of where aircraft exhausts will go, and how long they will dwell in various locations. Questions about layers, local maxima, and hemispheric seasonal maxima need to be answered.

Photochemists have not reached the detailed conclusions the Australian report attributes to them. We have only been able to identify important variables and establish a broad range of uncertainty – 3 to 50% – for the effects on ozone of aircraft-emitted oxides of nitrogen. I fully agree that detailed measurements of present levels and careful calculations of future levels and distributions are needed.

REITER: Just to prove that this panel has not been brainwashed, I'd like to take issue with some of my colleagues' statements. I don't think we're really groping in the dark when we talk about the vertical ozone distribution in the atmosphere. Admittedly the Dobson observations are crude, and biased with respect to fair weather, but we also have the results of a large sampling program run here in the U.S. several years ago. Balloons were sent up with a chemical sensor that measured the oxidation rate produced by ozone, and they turned out to be capable of measuring detailed layering effects. When the layers were integrated, the results came fairly close to concurrent Dobson measurements, which lent credence to previous ground-based measurements of total ozone. In addition, sensing equipment flown on satellites agrees within a very few percent with concurrent Dobson measurements. So, I think our knowledge of stratospheric ozone distribution is in better shape than has been suggested.

We also know quite a bit about how ozone is moved around in the atmosphere by transport processes. The effect of tropospheric-stratospheric exchange processes, especially in temperate latitudes, has been identified almost to the order of magnitude of tonnage. We know quite well that the average residence time of stratospheric air in mean latitudes is of the order of about a year, thanks to radioactive-debris transport calculations made with trajectory techniques and the like.

The problem I would like to address myself to is the variability of the natural stratosphere. We would like to think of climatology as giving us nice mean values, like the average annual temperature in Timbuktu or rainfall in Poughkeepsie. Unfortunately, that is statistics, not

climatology, and is very little help in understanding the atmosphere. In trying to include some allowance for variability, you immediately run into two problems. A dynamicist will tell you that at any given moment the atmosphere is on the brink of disaster, with cyclones growing, anticyclones blocking, circulation systems breaking down, and the like. A climatologist, on the other hand, will tell you that the atmosphere is basically stable, with just minor changes in temperature which produce ice ages and tropical periods. We have to find our perspective somewhere between these two viewpoints.

We do know that there are climatic variations, but we have not yet pinpointed their causes. There are a dozen or so theories around, from ice-age ones to those that "explain" smaller variations, but we still cannot identify precisely the cause of any of the earth's climatic shifts. "Climate" is a spectrum, starting from the interannual variability of a parameter like temperature, and continuing with its gradual variation over a few years, or the eleven-year sunspot cycle, or 30 years, or 100 years, and so on.

The effects of this variability must be carefully estimated – for example, its impact on the Junge layer, which has been mentioned before. The best physical model for the origin of the Junge layer we have at present is one of ascending motions in the atmosphere of the tropics, which impinge upon the tropopause and then spread out more or less horizontally along isentropic surfaces. This is how tropical air moves into higher latitudes. There is some evidence that this spreading out occurs relatively rapidly along quasi-horizontal surfaces, but considerably more slowly vertically.

Curiously, the Junge layer coincides with an atmospheric region that is extremely dry. The explanation is that the tropopause region, with temperatures in the neighborhood of -80°C, acts like a dehumidifier and freezes out almost all water vapor.

A student at the Geophysical Institute in Alaska recently presented evidence on the long-term trend in tropopause heights at various equatorial stations which suggests that the equatorial tropopause was relatively low (and hence warm) in 1963. Some observers attributed this to the Mount Agung eruption; however, the trend continued for several years, which might suggest a certain periodicity. In any case, such a trend should have a significant effect on the amount of moisture which seeps into the stratosphere, and perhaps even on the oxides of nitrogen transported into the stratosphere.

In the middle 1960's, the scientific literature was full of remarks on noctilucent clouds. Almost everyone north of the Canadian border seemed to have seen them. There was apparently a marked reduction in such observations in the late 1960's. Could noctilucent cloud formation possibly be tied in with the long-term behavior of the tropical tropopause? Certainly tropopause behavior can significantly affect the water-vapor content of those parts of the stratosphere in which SST's would fly.

The ozone variability also merits investigation. We pretty well know the kinds of transport processes involved, I think, but we need to fill in some details. For instance, at one point we thought the biennial variation of the tropical-wind regimes affected the ozone transport, because ozone exhibited a matching "biennial variation" for several years. There was a variation of more than 10% during the spring maximum between an ozone-rich year and the subsequent ozone-poor year, as measured in Tateno, Japan, or Arosa, Switzerland. Unfortunately, though, the biennial tropical-wind variation has continued, and the "biennial" ozone variation has not. This opens the question of whether it is really the wind system in the tropics that modulates ozone behavior, or whether it is the circulation in extratropical latitudes. In any case, the ozone level for a given month will vary considerably from one year to the next. The variation includes the effects of a long-term trend, and of shorter-term ones, such as the influence of local synoptic systems, which we discovered from satellite measurements.

Transport processes in the higher latitudes change greatly from year to year. In the northern hemisphere, the vortex breaks down in December in some years, while in others it remains well developed until March. Also, the northern and southern hemispheres act quite differently; the large-scale circulation system of the southern hemisphere is by no means a simple symmetric counterpart of the northern one.

The problem with atmospheric variability lies in the fact that the atmosphere has many

degrees of freedom when it comes to performing the simple task of moving heat from the equator to the pole. Planetary waves account for a large part of the transport in the northern hemisphere. Unfortunately, when the atmosphere transports heat it must also transport momentum of rotation, which makes things rather complicated. There are also smaller perturbations caused by cyclone waves, and on top of that smaller-scale diffusion. This variability of the atmosphere on different scales makes each month completely different from the same one in the preceding year, in terms of temperature, precipitation, energetics, or whatever, and also makes the hemispheres differ significantly from one another in the same month – though admittedly the data base in the southern hemisphere is restricted at present to the results of radiosondes in Australia, and some satellite and French EOLE data which we hope will tell us something about circulation patterns in the oceanic regions. This is one of the greatest challenges of the atmosphere: when we talk about climatology, and the climatic impact of stratospheric flight, we must remember that the natural atmosphere's patterns do not repeat themselves year after year. And until we understand why these wide variations in behavior occur, and why they somehow even out in the long run, we cannot claim to know much about the atmosphere.

KELLOGG: Since so much has already been said, I am just going to quickly summarize my personal views on what the most important questions for CIAP are. Since we can't concentrate on everything, these are the topics I would give priority.

First, if we compare the two main issues – that is, climate as Elmar Reiter has been talking about it, and the ozone question – it seems to me that the ozone question is more important, for a very simple reason. I think that the climatic effect of a fleet of SST's would be small relative to other things man is doing to the atmosphere. The possibility of affecting the ozone shield is nearly unique, however, and seems more and more important as we begin to understand it.

Concentrating on the ozone question, then: The quality of ozone is determined by both photochemistry and dynamics, as we have heard over and over. I feel that we can answer the ozone question only by combining the dynamics and photochemistry in a single model. While we have heard several papers here on the subject, none of the models can do this yet. I hope that by 1974 at least one will be able to. The test of whether a model is a good combined dynamic-photochemical one will be whether it can reproduce the ozone distribution as it is now, with all its variations, and also reproduce the distributions of the other significant minor constituents that react with ozone. Once we have such a model, we can get an almost immediate answer on the effects of SST exhaust emissions.

To determine how well a model reproduces the real stratosphere, we need to know what the stratosphere is really like. We should know the ozone distribution, and how oxides of nitrogen and water vapor behave. We also need a better knowledge of the motions in the atmosphere.

Of course, we don't yet know what the NO distribution of the atmosphere is. This is obviously a crucial measurement; it should be monitored, along with ozone, which we can already measure pretty well. We barely know how to measure water vapor; aerosols we know how to measure somewhat better, and are doing so. All of these species must be measured well enough to define their distribution in the real stratosphere.

One other physical aspect we need to know more about is how fast things mix in the stratosphere. I think Glenn Hilst came closest to being quantitative about this matter, when he pointed out the need to understand the mixing in the stratosphere because the photochemistry is affected by the speed of the mixing processes.

It is curious that so little is known about the mixing processes in the stratosphere. In 1954 I was in charge of a series of smoke-puff experiments over Holloman Air Force Base, New Mexico. It was very simple; each puff was made by sending up a balloon carrying a homemade smoke bomb, which was detonated at a predetermined pressure. The puffs were then tracked by Askania phototheodolites. We studied 22 smoke puffs in the stratosphere over one place in summer. But as far as I know, no one has ever repeated this experiment at other latitudes and at other times of year. So we still know very little about the diffusion processes on this scale, a few meters to a few hundred meters – or, for that matter, on larger scales either.

My impression is – to change the subject a little – that we are not very well informed on the

biological effects of a change in ultraviolet radiation at ground level due to a change in the stratospheric ozone. It seems to me that we have not yet done our homework in this area; I think we already know the flux of solar UV radiation and its variations well enough to give the biologists the information they need to calculate possible effects. I don't think we need a big new program of UV measurement; no doubt the results would be interesting, but I think our present information is good enough for all practical biological purposes.

I should like to turn briefly to one other subject: the testimony I gave before Congress in the spring of 1971, which I felt was not properly reported. Like Harold Johnston, I'd like to give a little bit of history. As you probably remember, that SST hearing had to do with building two prototypes. The *Study of Critical Environmental Problems*, made at MIT the preceding summer, had discussed the question of stratospheric modifications; since I had led the working group that wrote that portion, I was asked to testify on the possible environmental effects of a fleet of SST's.

In SCEP, we had identified the possibility of a change in ozone – not correctly, as Johnston pointed out, since we had not included oxides of nitrogen in our calculations, but nonetheless an ozone decrease of about one percent. We had also pointed out the possibility of climatic variations. It seemed important to tell Congress directly what the SCEP study had concluded, and to explain the uncertainties along with the findings. The message was, essentially, that 500 SST's probably would cause global changes in ozone and in climate, but that such changes would probably be less than natural fluctuations due to volcanic eruptions and the like, and they would be very much less than the normal variations with time or location. There was also another point to be made, which was that two prototypes couldn't possibly have a global effect. Also, in Mr. Peskin's terms, the internal costs and benefits were a great deal larger than the external ones in the case of the two prototypes.

That, in essence, was the message I gave the House and Senate Appropriations Committees. It didn't come out quite that way in the newspapers, though, and I am grateful for this chance to tell my colleagues what it really was.

CONFERENCE SUMMARY

ALAN J. GROBECKER
U.S. Department of Transportation
Washington, D.C.

So much information is presented at a four-day meeting like this that it is no small task to try to summarize it. I hardly know where to start, and I can't possibly do justice to all the material we have heard and discussed. This conference represents a major milestone in the Climatic Impact Assessment Program, however, and I think it will be worthwhile to review a few of the points we noted.

In the session covering the natural stratosphere, both the University of Wyoming and NOAA's Atmospheric Physics and Chemistry Laboratory reported finding positive correlation of water vapor, ozone, and particulates. This is a change from our previous conceptions. The NOAA group determined transport and dispersion by measuring the radioactive tracers injected by various atomic-bomb tests. The gradient of tracer concentration along a given normal trajectory indicated that mixing was rapid laterally and very slow vertically; the horizontal diffusivity was on the order of 3×10^{10} cm^2 sec^{-1}, and the vertical diffusivity about one-millionth of that.

Harries and Stone's trace-gas measurements from the Concorde indicate mixing ratios of 2×10^{-8} for NO_2, 2×10^{-7} for N_2O, and an upper limit of 3.4×10^{-9} for SO_2. These measurements are especially significant on two counts: they were some of the first measurements of the oxides of nitrogen, and they were made in the stratosphere. They are preliminary, however; we expect soon to have nitric-oxide measurements made with instruments employing the principle of chemiluminescence detection, whose sensitivity is adequate for accurate measurement of ambient concentrations. Also, Murcray, Goldman, et al. have obtained new vertical profiles for nitric acid, carbon monoxide, and water vapor, using an infrared spectrometer. Léna et al. of Meudon have obtained far-infrared spectra for O_2, O_3, and H_2O, in a flight experiment on the Caravelle in the upper troposphere.

Given all these measurements, as well as some others I haven't mentioned, I think we need a catalog of infrared-spectral data, like the one for the visible region which the National Bureau of Standards has been publishing for a number of years. The data are available in various libraries, and CIAP will try to find someone willing to accept the responsibility for compiling it.

The panel discussion on aerosols covered both their heterogeneous chemistry and their effect on radiation, and made it clear that we need more intensive study of the physics and chemistry of aerosol formation and reaction with gaseous material. More data on the size distribution of aerosols is necessary, particularly on Aitken nuclei, which are below the optical scattering range. The possible role of hydrocarbons in aerosol formation should be clarified, and the effects of aerosols on the global radiation balance should be pursued along the lines Yamamoto described. At present, both Japan and Europe are working on these problems more than the U.S.

In the sessions particularly concerned with chemistry. Garvin identified 100 to 125 reactions in the stratosphere which are important to CIAP; they involve 42 constituents, some of which are sensitive to wavelengths between 180 and 400 nm. Davis reported recent results of measurements of the rate constant for $O(^3P) + NO_2 \rightarrow NO + O_2$ and its temperature dependence; he also gave preliminary results on $O + H_2O_2$, $SO_2 + HO_2$, and $HO_2 + NO$, which are crucial reactions in CIAP's study of the stratosphere. Slanger confirmed Davis' results for $O + NO_2$ by an independent method. While there are still many reactions whose rate constants are not adequately known, I think we are starting to zero in on them.

Schiff and Megill developed the nitric-oxide detector based on chemiluminescence I mentioned earlier. The instrument is expected to give

a signal of 1000 counts per second for 3 ppb of NO at stratospheric ambient pressure, with a detection limit of about 1% of that. We hope that this sensitivity will be adequate to reveal the natural altitude distribution of nitric oxide, which has eluded us to date.

The panel chaired by Professor Nicolet drew a number of conclusions. Kaufman suggested that our knowledge of stratospheric chemical reactions is in good shape; others feel that it would be safer to say that it's improving. Nicolet believes that intensive research is still needed on certain reactions, especially those involving methane and OH, since – as McElroy suggested – they lead to the production of water vapor. He favors studying them in the laboratory at stratospheric temperatures.

In the discussion of engine emissions, we got a foretaste of the large amount of data that is being analyzed for trace contaminants with which engine developers have recently become concerned. Exhaust data are being compiled for the Olympus 593 (the Concorde engine) and the J85 and J93, two existing U.S.-developed supersonic engines. Of course, we can expect new developments in engine technology in the next decade or so; NASA will be making projections of these new directions for CIAP.

The emissions data presented clearly demonstrate that manufacturers can accurately predict actual engine-emission levels at conditions other than sea-level static, on the basis of laboratory combustor-rig tests. This detailed knowledge of what engines will introduce into the atmosphere, and the explanation of the subtleties involved, are very important contributions to CIAP. I was disappointed that so few people attended that session, since much of the past confusion about emission levels has been due simply to lack of communication. The Concorde data is particularly valuable, and I want to give special thanks to the Rolls-Royce/SNECMA team for their efforts on our behalf.

In the first of the perturbed-atmosphere sessions, Hoshizaki spoke on the behavior of engine exhaust in the immediate wake of the airplane. He has developed models, based on wake data in the high troposphere, which give us an idea of how the wake would diffuse from the central line of the cruise path in the first 1000 seconds. Hudson presented some ideas on chemical-release experiments – both approaches and objectives – and emphasized the need for experimental as well as mathematical simulation.

In the modeling session, Mahlman reviewed the preliminary results of his three-dimensional tracer experiments. I found his presentation particularly interesting, because under simple boundary conditions, using motions without any chemistry, his model approximated the observed distribution of ozone reasonably well. This points up the tremendous importance of dynamics, especially when it comes to reconciling the distribution of ozone in the stratosphere with the rate at which it is photochemically generated.

Chang and Johnston both commented on Foley and Ruderman's very recent paper, which explored the possibility that past nuclear-weapons testing constituted a stratospheric perturbation analogous to those we are investigating, and analyzed ozone data to see the effects on stratospheric chemistry and dynamics.

Moving to a different perspective, we looked at the possible biological effects of climatic changes. It is these biological considerations that most people wonder about: What would these changes do to me, to the food I eat, to the world I live in? Ultimately, it is these questions that CIAP must answer. Certainly we know that an increase in the ultraviolet portion of sunlight can have adverse effects – sunburn, wrinkling, photosensitivity to medication – and UV levels seem to correlate with skin-cancer incidence. Increased UV can also damage plants, by inhibition of photosynthesis, mutation, direct burning of leaves or growth tissue, and other effects. Other changes in climate, such as temperature and precipitation, can have a very large effect on plants; we need to find out the consequences of these alterations, particularly on crops, and especially in marginal growing areas, where changes in extreme conditions could render them unsuitable for the crop in question. Peskin's paper showed how social costs such as these biological effects can be used in a quantitative assessment of questions such as the SST one.

The last panel brought out, I felt, several of the areas we need to do some more work in. Dyer noted the extreme complexity of the photochemistry, and suggested that models should include feedback between the circulation and chemistry. Blamont expressed particular

concern about the quality of transport, ozone, and nitric-oxide measurements. Reiter discussed the extremely wide variability of the atmosphere – and climate – and pointed out that we don't yet know what causes it.

I'd like to take this opportunity to say that I think the modeling we are doing is important. Congress set an engineering objective for the CIAP study: Find out as best you can by 1974 what will happen in the stratosphere in 1990 if we have a fleet of supersonic aircraft. In trying to find the answer to that question, we must develop a scientific description of the stratosphere, but the only way we can project the consequences of an artificial perturbation is by modeling. Since we have no single model which can exactly simulate all the complexities of the stratosphere, we must of necessity rely on simpler ones which will give us approximations. Even these may take four or five years to reach maturity, since no one was interested in modeling the stratosphere until fairly recently, but we must make all possible use of the partial answers they can provide within the CIAP time frame. We need to get the modelers as much good data as we can – especially data on stratospheric diffusion coefficients on various scales – since a model is only as good as its parameters.

I hope that all of you have found this conference as interesting as I have, though I know I feel rather overwhelmed by the barrage of information I am trying to assimilate. Thank you for coming.

LIST OF PARTICIPANTS

Marcel Ackerman
Institut d'Aéronomie Spatiale de Belgique
Avenue Circulaire 3
B-1180 Bruxelles, Belgium

Stanley I. Adelfang
Lockheed California Company
P.O. Box 551
Burbank, CA 91503

I.E. Alber
TRW Systems
One Space Park
Redondo Beach, CA 90278

George Alyea
Meteorological Laboratory
Massachusetts Institute of Technology
Cambridge, MA 02139

Larry Anderson
Lockheed Palo Alto Research Laboratory
3251 Hanover Street
Palo Alto, CA 94304

Akio Arakawa
Department of Meteorology
University of California, Los Angeles
Los Angeles, CA 90024

T.E. Ashenfelter
NOAA Air Resources Laboratory
8060 13th St.
Silver Spring, MD 20910

Donald W. Bahr
Aircraft Engine Group
General Electric Company
Cincinnati, OH 45215

J.P. Baluteau
Section d'Astrophysique
Observatoire de Paris
92 Meudon, France

John L. Barnes
Department of Engineering
University of California, Los Angeles
Los Angeles, CA 90024

Earl W. Barrett
Atmospheric Physics and Chemistry Laboratory
NOAA Environmental Research Laboratories
Boulder, CO 80302

A.E. Barrington
DOT Transportation Systems Center
55 Broadway
Cambridge, MA 02142

Jon Bartholic
Institute of Food and Agricultural Sciences
University of Florida
Gainesville, FL 32601

William C. Bartley
National Academy of Sciences
2101 Constitution Avenue
Washington, D.C. 21418

Arnold M. Bass
National Bureau of Standards
Washington, D.C. 21234

Ernest Bauer
Institute for Defense Analyses
400 Army-Navy Drive
Arlington, VA 22202

LTC Gordon A. Beals
Headquarters, Air Weather Service
Scott Air Force Base, IL 62225

A.D. Belmont
Research Division
Control Data Corporation
Box 1249
Minneapolis, MN 55440

Sidney Benson
Stanford Research Institute
Menlo Park, CA 94025

Abraham L. Berlad
State University of New York
Stony Brook, NY 11790

R.H. Biggs
Institute of Food and Agricultural Sciences
University of Florida
Gainesville, FL 32601

Jacques Blamont
Centre National d'Etudes Spatiales
129 Rue de l'Université
75 Paris VII, France

Wayne Bloch
Environmental Protection Agency
4th and M Streets, SW
Washington, D.C. 20460

Harold F. Blum
Department of Biological Sciences
State University of New York at Albany
1400 Washington Ave.
Albany, NY 12222

M.H. Bortner
Building 100
GE Valley Forge Space Center
P.O. Box 8555
Philadelphia, PA 19101

Guy Brasseur
Institut d'Aéronomie Spatiale de Belgique
3 Avenue Circulaire
1180 Brussels, Belgium

Alan W. Brewer
Department of Physics
University of Toronto
Toronto, Ontario, Canada

A.J. Broderick
DOT Transportation Systems Center
55 Broadway
Cambridge, MA 02142

William J. Burroughs
British Embassy
3100 Massachusetts Avenue, NW
Washington, D.C. 20008

Ezio Bussoletti
Section d'Astrophysique
Observatoire de Paris
92 Meudon, France

John Busterud
Council on Environmental Quality
722 Jackson Place, NW
Washington, D.C. 20006

Richard Cadle
National Center for Atmospheric Research
P.O. Box 1470
Boulder, CO 80302

Martyn Caldwell
Ecology Center
Utah State University
Logan, UT 84321

Lin Callis
NASA Langley Research Center (419A)
Hampton, VA 01730

Capt. J.M. Calo
Air Force Cambridge Research Laboratories
Hanscom Field
Bedford, MA 01730

Morton Camac
Aerodyne Research Inc.
Tech/Ops Building
South Avenue
Burlington, MA 01803

Lawrence S. Caretto
School of Engineering
San Fernando Valley State College
Northridge, CA 91324

Robert Cavalleri
Science Applications, Inc.
1701 N. Fort Meyer Drive
Arlington, VA 22209

K.S.W. Champion
Air Force Cambridge Research Laboratories
Hanscom Field
Bedford, MA 01730

Julius Chang
Lawrence Livermore Laboratory
P.O. Box 808
Livermore, CA 94550

Seville Chapman
94 Harper Road
Buffalo, NY 14226

David Chleck
Panametrics, Inc.
221 Crescent St.
Waltham, MA 02154

Dr. Alistair Christie
Atmospheric Environment Service
4905 Dufferin St.
Downsview, Ontario, Canada

R.J. Cicerone
University of Michigan
2455 Hayward Ave.
Ann Arbor, MI 48105

Roderick Clayton
Department of Genetic Development
Cornell University
Ithaca, NY 14850

Marcel G. Compagna
DOT Transportation Systems Center
55 Broadway
Cambridge, MA 02142

R.J. Conti
Lockheed Palo Alto Research Laboratory
3251 Hanover Street
Palo Alto, CA 94004

Samuel C. Coroniti
Deputy Manager, CIAP
Department of Transportation
400 7th St., SW
Washington, D.C. 20590

Myron Corrin
Science Department
Colorado State University
Fort Collins, CO 80521

Richard Craig
Department of Meteorology
Florida State University
Tallahassee, FL 32306

Paul J. Crutzen
Institute of Meteorology
University of Stockholm
Tulegatan 41
10432 Stockholm, Sweden

Derek Cunnold
Department of Meteorology
Massachusetts Institute of Technology
Cambridge, MA 02139

Pythagoras Cutchis
Institute for Defense Analyses
400 Army-Navy Drive
Arlington, VA 22212

R.J. Cvetanović
National Research Council of Canada
Ottawa, Ontario, Canada

John D'Atre
General Electric Ordnance Systems
100 Plastics Ave.
Pittsfield, MA 01201

Eric Davies
Rolls-Royce Aero Engines, Inc.
551 Fifth Avenue
New York, NY 10017

Douglas Davis
Department of Chemistry
University of Maryland
College Park, MD 90406

Roger DeBar
Lawrence Livermore Laboratory
P.O. Box 808
Livermore, CA 94550

Thomas Degges
Visidyne Inc.
19 3rd Avenue
Burlington, MA 01803

E.C. DeLand
R & D Associates
525 Wilshire St.
Santa Monica, CA 90403

Frank Del Greco
Air Force Cambridge Research Laboratories
Hanscom Field
Bedford, MA 01730

Robert Dickinson
National Center for Atmospheric Research
P.O. Box 1470
Boulder, CO 80302

Basil Dimitriades
EPA National Environmental Research Center
Research Triangle Park, NC 27711

Marcia Dodge
Division of Chemistry & Physics
EPA National Environmental Research Center
Research Triangle Park, NC 27711

Leonard A. Donadio
Dynatrend
131 Middlesex Turnpike
Burlington, MA 01803

C.S. Downie
1007 Priscilla Lane
Alexandria, VA 22308

S. Roland Drayson
Atmospheric and Oceanic Service Department
University of Michigan
Ann Arbor, MI 48104

William H. Duewer
Lawrence Livermore Laboratory
P.O. Box 808
Livermore, CA 94550

M.W. Dumais
DOT Transportation Systems Center
55 Broadway
Cambridge, MA 02142

W.C. Dunlap
DOT Transportation Systems Center
55 Broadway
Cambridge, MA 02142

A.J. Dyer
Division of Atmospheric Physics
CSIRO
P.O. Box 77
Mordialloc, Victoria 3195, Australia

H. Frank Eden
Aeronomy & Meteorology Programs
National Science Foundation
Washington, D.C. 20550

Theodore R. Ellis
Dynatrend, Inc.
131 Middlesex Turnpike
Burlington, MA 01803

Hugh Ellsaesser
Lawrence Livermore Laboratory
P.O. Box 808
Livermore, CA 94550

James C. Elms, Director
DOT Transportation Systems Center
55 Broadway
Cambridge, MA 02142

Louis Elterman
Air Force Cambridge Research Laboratories
Hanscom Field
Bedford, MA 01730

James Elwood
Pratt & Whitney Aircraft Division
United Aircraft Corporation
400 Main Street
East Hartford, CT 06118

David Escoe
Department of Transportation
400 7th St., SW
Washington, D.C. 20590

W. Evans
Atmospheric Environment Service
Department of Environment
Downsview, Ontario, Canada

C.B. Farmer
Jet Propulsion Laboratory
California Institute of Technology
4800 Oak Grove Drive
Pasadena, CA 91103

R.W. Fenn
Air Force Cambridge Research Laboratories
Hanscom Field
Bedford, MA 01730

J.P. Few
ARO, Inc.
Arnold Engineering Development Center
Arnold Air Force Station, TN 37389

Donald E. Findley
Department of Transportation
400 7th St., SW
Washington, D.C. 20590

Thomas Fitzpatrick
Massachusetts General Hospital
Fruit Street
Boston, MA 02114

Edward Flynn
Department of Transportation
400 7th St., SW
Washington, D.C. 20590

A.K. Forney
DOT Federal Aviation Administration
800 Independence Avenue, SW
Washington, D.C. 20591

James P. Friend
Department of Meteorology & Oceanography
New York University
Bronx, NY 10453

Bruce H. Frisch
Aeronautics and Astronautics
1290 6th Avenue
New York, NY 10019

John S. Garing
Atmospheric Optics Laboratory
Air Force Cambridge Research Laboratories
Hanscom Field
Bedford, MA 01730

David Garvin
Chemistry Building
National Bureau of Standards
Gaithersburg, MD 20234

Norman E. Gaut
Environmental Research and Technology
429 Marrett Road
Lexington, MA 02173

Robert Gelinas
Lawrence Livermore Laboratory
P.O. Box 808
Livermore, CA 94550

Steven Georgiev
Dynatrend, Inc.
131 Middlesex Turnpike
Burlington, MA 01803

Forrest Gilmore
R & D Associates
P.O. Box 3580
Santa Monica, CA 90403

Arnold Goldburg
The Boeing Company
Seattle, WA 98124

Harold Goldstein
Building 100
GE Valley Forge Space Center
P.O. Box 8555
Philadelphia, PA 19101

Daniel Golomb
Air Force Cambridge Research Laboratories
Hanscom Field
Bedford, MA 01730

R.E. Good
Air Force Cambridge Research Laboratories
Hanscom Field
Bedford, MA 01730

Philip Goodman
Panametrics, Inc.
221 Crescent Street
Waltham, MA 02154

Robert Gould
AeroChem Research Laboratories, Inc.
P.O. Box 12
Princeton, NJ 08540

Donald Grantham
Air Force Cambridge Research Laboratories
Hanscom Field
Bedford, MA 01730

Carlton Gray
Draper Laboratory
Massachusetts Institute of Technology
Cambridge, MA 02139

Paul Graystone
Meteorological Office
Bracknell, Berkshire, England

Alex Green
Department of Physics and Astronomy
University of Florida
Gainesville, FL 32601

Lewis Greenspan
National Bureau of Standards
Washington, D.C. 20234

Reynold Greenstone
Department of Transportation
400 7th St., SW
Washington, D.C. 20590

Lloyd Grissom
ARO, Inc.
Arnold Engineering Development Center
Arnold Air Force Station, TN 37387

A.J. Grobecker
Manager, CIAP
Department of Transportation
400 7th St., SW
Washington, D.C. 20590

Jack Grobman
NASA Lewis Research Center
2100 Brookpark Road
Cleveland, OH 44135

Richard Grojean
Department of Electrical Engineering
Northeastern University
360 Huntington Ave.
Boston, MA 02115

Paul Guthals
Los Alamos Scientific Laboratory
P.O. Box 1663
Los Alamos, NM 87544

Joe Gwiazdowski
Department of Transportation
400 7th St., SW
Washington, D.C. 20590

J. Brooks Haberl
General Electric Ordnance Systems
100 Plastics Ave.
Pittsfield, MA 02101

Robert Hampson
National Bureau of Standards
Washington, D.C. 20234

Frederick Hanser
Panametrics, Inc.
221 Crescent St.
Waltham, MA 02154

Thomas M. Hard
DOT Transportation Systems Center
55 Broadway
Cambridge, MA 02142

Edwin Hart
Argonne National Laboratory
9700 South Cass Avenue
Argonne, IL 64039

James J. Hartford
American Institute of Aeronautics and Astronautics
1290 Avenue of the Americas
New York, NY 10019

Donald F. Heath
NASA Goddard Space Flight Center
Greenbelt, MD 20771

Kenneth Heinze
Institute for Defense Analyses
400 Army-Navy Drive
Arlington, VA 22202

William Heiser
USAF Aero Propulsion Laboratories
Wright-Patterson AFB, OH 45433

R.E. Henderson
USAF Aero Propulsion Laboratories
Wright-Patterson AFB, OH 45433

Wayne S. Hering
Upper Atmospheric Branch
Air Force Cambridge Research Laboratories
Hanscom Field
Bedford, MA 01730

John T. Herron
National Bureau of Standards
Washington, D.C. 20234

Eigil Hesstvedt
Institute of Geophysics
University of Oslo
P.O. Box 1022, Blindern
Oslo 3, Norway

John B. Heywood
Mechanical Engineering Department
Massachusetts Institute of Technology
Cambridge, MA 02139

Henry Hidalgo
Institute for Defense Analyses
400 Army-Navy Drive
Arlington, VA 22202

Ernest Hilsenrath
NASA Goddard Space Flight Center
Greenbelt, MD 20771

Arthur Hilsenrod
DOT Federal Aviation Administration
800 Independence Ave., SW
Washington, D.C. 20591

Glenn R. Hilst
Aeronautical Research Associates of Princeton, Inc.
50 Washington Road
Princeton, NJ 08540

E.D. Hinkley
Massachusetts Institute of Technology
Cambridge, MA 02139

D.J. Hofmann
Department of Physics and Astronomy
University of Wyoming
Laramie, WY 82070

K.M. Hopkins
USAF Aero Propulsion Laboratories (TBC)
Wright-Patterson Air Force Base, OH 45433

Hiroshi Hoshizaki
Lockheed Palo Alto Research Laboratory
3251 Hanover St.
Palo Alto, CA 94304

Frank Hudson
Sandia Laboratories
P.O. Box 5800
Albuquerque, NM 87115

R.D. Hudson
NASA Manned Spacecraft Center
Houston, TX 77058

Robert E. Huffman
Air Force Cambridge Research Laboratories
Hanscom Field
Bedford, MA 01730

Richard W. Hurn
U.S. Bureau of Mines
Energy Research Center
Bartlesville, OK 74003

H. Ishikawa
Institute of Atmospherics
University of Nagoya
Nagoya, Japan

René Joatton
Société Nationale Industrielle Aérospatiale
37 Boulevard de Montmorency
Paris XVI, France

Harold S. Johnston
Department of Chemistry
University of California, Berkeley
Berkeley, CA 94720

T.H. Jones
General Electric Co.
P.O. Box 2500
Daytona Beach, FL 32015

H. Kamiyama
Geophysical Institute
Tohoku University
Sendai, Japan

James Kassner
Cloud Physics Department
University of Missouri
Rolla, MO 65401

Frederick Kaufman
Department of Chemistry
University of Pittsburgh
Pittsburgh, PA 15213

Ryuma Kawamura
Faculty of Science
University of Tokyo
6-1, Komaba-4, Meguro-ku
Tokyo, Japan

William Kellogg
National Center for Atmospheric Research
P.O. Box 1470
Boulder, CO 80302

Thomas J. Keneshea
Air Force Cambridge Research Laboratories
Hanscom Field
Bedford, MA 01730

William Kirchhoff
Physics Building
National Bureau of Standards
Washington, D.C. 20234

Bennett Kivel
AVCO-Everett Research Laboratory
2385 Revere Beach Pkwy.
Everett, MA 02149

Anthony Klarman
Naval Air Propulsion Test Center
Trenton, NJ

E.B. Knipling
USDA Agricultural Research Service
P.O. Box 225
Stoneville, Mississippi 38776

Joseph B. Knox
Lawrence Livermore Laboratory
P.O. Box 808
Livermore, CA 94550

Charles Kolb
Aerodyne Research Inc.
Tech/Ops Bldg.
South Avenue
Burlington, MA 01803

Professor Kopcewicz
University of Warsaw
Warsaw, Poland

Donald Koppel
Riverside Research Institute
80 West End Ave.
New York, NY 10023

Philip W. Krey
Health and Safety Laboratory
U.S. Atomic Energy Commission
376 Hudson Street
New York, NY 10010

A.J. Krueger
NASA Goddard Space Flight Center
Greenbelt, MD 20771

Dr. Emanuel Landau
HEW Public Environmental Health Service
Rockville, MD 20852

James D. Lawrence
NASA Langley Research Center (401A)
Hampton, VA 23365

Steven Lawrence
Institute of Geophysics and Planetary Physics
University of California, Los Angeles
Los Angeles, CA 90024

Allan Lazrus
National Center for Atmospheric Research
P.O. Box 1470
Boulder, CO 80302

J.F. Leach
British Aircraft Corp.
P.O. Box 77
Filton, Bristol, England

Dr. William M. Leach
Bureau of Radiological Health
HEW Public Environmental Health Service
Rockville, MD 20852

W.Z. Leavitt
DOT Transportation Systems Center
55 Broadway
Cambridge, MA 02142

Pierre Léna
Section d'Astrophysique
Observatoire de Paris
92 Meudon, France

Hiram Levy II
Smithsonian Astrophysical Observatory
60 Garden St.
Cambridge, MA 02138

Robert Lin
GTE Laboratories
40 Sylvan Road
Waltham, MA 02154

Lt. Lawrence H. Linden
Headquarters, U.S. Air Force (PREV)
Washington, D.C. 20330

Harold Lindenhofen
Headquarters, U.S. Air Force (PREV)
Washington, D.C. 20330

Bernard Lippman
New York University
Bronx, NY 10453

Julius London
Department of Astro-Geophysics
University of Colorado
Boulder, CO 80302

Hylan B. Lyon, Jr.
Office of Science and Technology
Executive Office of the President
Washington, D.C. 20506

Michael MacCracken
Lawrence Livermore Laboratory
P.O. Box 808
Livermore, CA 95440

Lester Machta
Director, Air Resources Laboratory
National Oceanic and Atmospheric Administration
8060 Thirteenth Street
Silver Spring, MD 20910

Donald I. MacLean, S.J.
Boston College
Chestnut Hill, MA 02167

Jerry Mahlman
NOAA ERL Geophysical Fluid Dynamics Laboratory
Princeton University
P.O. Box 308
Princeton, NJ 08540

Donald W. Male
Arnold Engineering Development Center
Arnold Air Force Station, TN 37389

Carroll Maninger
Lawrence Livermore Laboratory
P.O. Box 808
Livermore, CA 94550

George L. Manire
Environmental Protection Agency
Research Triangle Park
Durham, NC 27711

Oscar Manley
Visidyne, Inc.
19 3rd Avenue
Burlington, MA 01830

Howard Margolis
Institute for Defense Analyses
400 Army-Navy Drive
Arlington, VA 22202

Ronald Massa
Dynatrend, Inc.
131 Middlesex Turnpike
Burlington, MA 01803

John Mastenbrook
Naval Research Laboratory
1555 Overlook Ave., SW
Washington, D.C. 20390

Charles H. McCellan
NASA Langley Research Center
Hampton, VA 23365

Robert McClatchey
Air Force Cambridge Research Laboratories
Hanscom Field
Bedford, MA 01730

Billy M. McCormac
Lockheed Palo Alto Research Laboratory
3251 Hanover Street
Palo Alto, CA 94304

Michael B. McElroy
Center for Earth and Planetary Physics
Harvard University
Cambridge, MA 02138

W.K. McGregor, Jr.
ARO, Inc.
Arnold Engineering Development Center
Arnold Air Force Station, TN 37389

William J. McKechney
USAF Aero Propulsion Laboratories
Wright Patterson AFB, OH 45433

James R. McNesby
National Bureau of Standards
Washington, D.C. 20234

Douglas Meadowcroft
European Aerospace Corporation
605 Third Avenue
New York, NY 10016

L.R. Megill
Center for Research in Aeronomy
Utah State University
Logan, UT 84321

Cdr. Edward C. Melton, Jr.
Office of Naval Research
Arlington, VA 22217

S. Michinowski
Academy of Science
Institute of Geophysics
Warsaw 3, Poland

Thomas Mikus
Department of Mechanical Engineering
Massachusetts Institute of Technology
Cambridge, MA 02139

Alvin J. Miller
National Oceanic and Atmospheric Administration
8060 13th Street
Silver Spring, MD 20910

R.H. Miller
Department of Aeronautics
Massachusetts Institute of Technology
Cambridge, MA 02139

John B. Minkoff
Riverside Research Institute
80 West End Avenue
New York, NY 10023

Masao Misaki
Meteorological Research Institute
4-35-8 Koenji-kita, Suginami-ku
Tokyo, Japan

O. Kenneth Moe
McDonnell-Douglas Astronautics
5301 Bolsa Avenue
Huntington Beach, CA 92647

Volker A. Mohnen
State University of New York at Albany
1400 Washington Avenue
Albany, NY 12222

James M. Morris
DOT Transportation Systems Center
55 Broadway
Cambridge, MA 02142

Peter Muecke
Australian Embassy
1601 Massachusetts Avenue
Washington, D.C. 20036

David G. Murcray
Department of Physics
University of Denver
Denver, CO 80210

Rocco Narcisi
Air Force Cambridge Research Laboratories
Hanscom Field
Bedford, MA 01730

James Neely
ARO, Inc.
Arnold Engineering Development Center
Arnold Air Force Station, TN 37389

Arthur W. Nelson
Pratt & Whitney Aircraft Division
United Aircraft Corporation
400 Main Street
East Hartford, CT 06108

Marcel Nicolet
Institut d'Aéronomie Spatiale de Belgique
3 Avenue Circulaire
B-1180 Brussels, Belgium

Franklin E. Niles
Ballistics Research Laboratory
Aberdeen Proving Ground, MD 21005

Hugh Odishaw
National Research Council
2101 Constitution Ave.
Washington, D.C. 20418

Toshio Ogawa
Geophysics Institute
Kyoto University
Kyoto, Japan

Robert Oliver
Institute for Defense Analyses
400 Army-Navy Drive
Arlington, VA 22202

Fritz Ostherr
Dynatrend
131 Middlesex Turnpike
Burlington, MA 01803

Yih-Ho Pao
Flow Research, Inc.
1819 South Central Avenue
Kent, WA 98031

John Paulson
Air Force Cambridge Research Laboratories
Hanscom Field
Bedford, MA 01730

Rudolf Penndorf
AVCO Corporation
201 Lowell Street
Wilmington, MA 01887

J. Penner
Harvard University
Cambridge, MA 02138

T.J. Pepin
Department of Physics and Astronomy
University of Wyoming
Laramie, WY 82070

Porter Perkins
NASA Lewis Research Center
31000 Brook Park Road
Cleveland, OH 44135

Henry M. Peskin
The Urban Institute
2100 M Street, NW
Washington, D.C. 20037

Norman Phillips
Department of Meteorology
Massachusetts Institute of Technology
Cambridge, MA 02139

Steve Piacsek
Naval Research Laboratory
Washington, D.C. 20390

E.T. Pierce
Stanford Research Institute
Menlo Park, CA 94025

Robert W. Pinnes
Department of Transportation
400 Seventh St., SW
Washington, D.C. 20590

Walter G. Planet
NOAA National Environmental Satellite Service
Suitland, MD 20235

Josef Podzimek
Cloud Physics Research Center
University of Missouri
Rolla, MO 65401

John Polutchko
Dynatrend, Inc.
131 Middlesex Turnpike
Burlington, MA 01803

Jerome Pressman
Pressman Enterprises
4 Fessenden Way
Lexington, MA 02173

Ronald Prima
Meteorology Department
Massachusetts Institute of Technology
Cambridge, MA 02139

Alain Quillévérré
SNECMA
Villaroche
77 Moissy, France

Elliot Raisen
Illinois Institute of Technology Research Institute
10 W. 35th St.
Chicago, IL 60637

Robert Rapp
RAND Corporation
1700 Main Street
Santa Monica, CA 90406

Elmar Reiter
Department of Atmospheric Science
Colorado State University
Fort Collins, CO 80521

Brian Ridley
Centre for Research in Experimental Space Science
York University
Downsview, Ontario, Canada

L.W. Roberts
DOT Transportation Systems Center
55 Broadway
Cambridge, MA 02142

P.D. Rogers
British Air Corporation (USA), Inc.
399 Jefferson Davis Highway
Arlington, VA 22202

James M. Rosen
Department of Physics and Astronomy
University of Wyoming
Laramie, WY 82070

N.W. Rosenberg
Air Force Cambridge Research Laboratories
Hanscom Field
Bedford, MA 01730

Donald Rote
Argonne National Laboratory
9700 South Cass Avenue
Argonne, IL 60439

Malvin A. Ruderman
Institute for Advanced Studies
Princeton, NJ 08450

Robert W. Rummel
Trans World Airlines
605 Third Avenue
New York, NY 10016

Robert E. Sampson
Environmental Protection Agency
2565 Plymouth Rd.
Ann Arbor, MI 48105

Edward S. Sarachik
Department of Meteorology
Massachusetts Institute of Technology
Cambridge, MA 02139

Robert F. Sawyer
Department of Mechanical Engineering
University of California, Berkeley
Berkeley, CA 94720

Robert B. Schainker
Systems Control, Inc.
260 Sheridan Avenue
Palo Alto, CA 94306

Harold I. Schiff
Centre for Research in Experimental Space Science
York University
Downsview, Ontario, Canada

R. Schoen
Aeronomy & Meteorology Programs
National Science Foundation
Washington, D.C. 20550

M.J. Scotto
DOT Transportation Systems Center
55 Broadway
Cambridge, MA 02142

William A. Sedlacek
Los Alamos Scientific Laboratories
Box 1663
Los Alamos, NM 87544

Daniel J. Seery
United Aircraft Corporation Research Laboratories
400 Main St.
East Hartford, CT 06108

Michael Seibert
GTE Laboratories
40 Sylvan Road
Waltham, MA 02154

Donald Sheldon
Institute for Defense Analyses
400 Army-Navy Drive
Arlington, VA 22209

Tatsuo Shimazaki
Aeronomy Laboratory
NOAA Environmental Research Laboratories
Boulder, CO 80302

Itsuro Shimizu
Chief, Aerological Division
Japan Meteorological Agency
Otemachi, Chiyodaku
Tokyo, Japan

Alexis Shlanta
Atmospheric Physics and Chemistry Laboratory
NOAA Environmental Research Laboratories
Boulder, CO 80302

R.V. Simonaitis
Ionospheric Research Laboratory
Pennsylvania State University
University Park, PA 16902

Colin G. Simpson
DOT Federal Aviation Administration
800 Independence Ave., SW
Washington, D.C. 20591

Norman Sissenwine
Aeronomy Laboratory
Air Force Cambridge Research Laboratories
Hanscom Field
Bedford, MA 01730

Tom G. Slanger
Stanford Research Institute
Menlo Park, CA 94025

H. Prescott Sleeper, Jr.
Northrop Services, Inc.
6025 Technology Drive
P.O. Box 1484
Huntsville, AL 35807

Al Snelson
Illinois Institute of Technology Research Institute
10 W. 35th St.
Chicago, IL 60637

Donald E. Snider
Concepts Analysis Laboratory
U.S. Army Ballistic Research Laboratories
Aberdeen Proving Ground, MD 21005

Kenneth Spengler
American Meteorological Society
45 Beacon Street
Boston, MA 02108

William C. Steber
Department of Transportation
400 7th Street, SW
Washington, D.C. 20591

C.G. Stergis
Air Force Cambridge Research Laboratories
Hanscom Field
Bedford, MA 01730

Charles B. Stewart
Commercial Airplane Group
The Boeing Company
Seattle, WA 98124

Richard W. Stewart
NASA Goddard Institute for Space Studies
2880 Broadway
New York, NY 10025

Richard L. Strombotne
Department of Transportation
400 7th St., SW
Washington, D.C. 20590

Fred Stuhl
Ford Motor Company
P.O. Box 2053
Dearborn, MI 48121

J.C. Sturm
DOT Transportation Systems Center
55 Broadway
Cambridge, MA 02142

Jack A. Suddreth
National Aeronautics and Space Administration
600 Independence Ave., SW
Washington, D.C. 20546

Walter Sullivan
The New York Times Company
229 West 43rd Street
New York, NY 10036

N. Sundararaman
Department of Meteorology
University of California, Los Angeles
Los Angeles, CA 90024

William Swider, Jr.
Air Force Cambridge Research Laboratories
Hanscom Field
Bedford, MA 01730

Raymond L. Taylor
AVCO Everett Research Laboratory
2385 Revere Beach Parkway
Everett, MA 02149

Thomas Taylor
The Aerospace Corporation
2350 E. El Segundo Blvd.
El Segundo, CA 90245

Kosta Telegadas
NOAA Air Resources Laboratory
8060 Thirteenth Street
Silver Spring, MD 20910

Shelby Tilford
Naval Research Laboratory
4555 Overlook Avenue, SW
Washington, D.C. 20390

Takao Tohmatsu
Geophysics Research Laboratory
Faculty of Science
University of Tokyo
Yayoi 2-11-16, Bunkyo-Ku
Tokyo 113, Japan

Robert Toth
Jet Propulsion Laboratory
California Institute of Technology
4800 Oak Grove Drive
Pasadena, CA 91103

C.N. Touart
Air Force Cambridge Research Laboratories
Hanscom Field
Bedford, MA 01730

Steve Traugott
Martin Marietta, RIAS
1450 S. Rolling Road
Baltimore, MD 21227

N.P. Trentacoste
Science Applications, Inc.
1701 N. Fort Meyer Drive
Arlington, VA 22209

Richard Turco
R & D Associates
P.O. Box 3580
Santa Monica, CA 90403

Robert L. Underwood
Department of Transportation
400 Seventh St., SW
Washington, D.C. 20590

Fred Urbach
Skin & Cancer Hospital
3322 North Broad St.
Philadelphia, PA 19140

S.V. Venkateswaran
Department of Meteorology
University of California, Los Angeles
405 Hilgard Avenue
Los Angeles, CA 90024

Sidney Verner
Environmental Protection Agency
4th & M Streets, SW
Washington, D.C. 20460

Douglas Vickery
British Aircraft Corp.
Filton, Bristol, England

William Viezee
Stanford Research Institute
Menlo Park, CA 94021

F.E. Volz
Air Force Cambridge Research Laboratories
Hanscom Field
Bedford, MA 01730

Dr. Alexander Vranos
Pratt & Whitney Division
United Aircraft Corp.
400 Main St.
E. Hartford, CT 06108

John Walton
Lawrence Livermore Laboratory
P.O. Box 808
Livermore, CA 94550

Raymond Wanta
Air Force Cambridge Research Laboratories
Hanscom Field
Bedford, MA 01730

Peter Wardman
British Aircraft Corporation
Filton, Bristol, England

Michael Warshaw
RAND Corporation
1700 Main St.
Santa Monica, CA 90406

Warren Washington
National Center for Atmospheric Research
P.O. Box 1470
Boulder, CO 80302

Michael P. Weinreb
NOAA National Environmental Satellite Service
Suitland, MD 20233

J.A. Weinman
University of Wisconsin
Madison, WI 53706

Robert F. Weiss
AVCO Everett Research Labs
2385 Revere Beach Parkway
Everett, MA 02149

Arnold Wexler
National Bureau of Standards
Washington, D.C. 20234

Raymond Wexler
NASA Goddard Space Flight Center
Greenbelt, MD 20771

Robert C. Whitten
NASA Ames Research Center (245-4)
Moffett Field, CA 94040

Gerry Wijntjes
Block Engineering, Inc.
19 Blackstone Street
Cambridge, MA 02139

Beatrice Willard
Council on Environmental Quality
722 Jackson Place, NW
Washington, D.C. 20006

M.R. Williams
Bristol Engine Division
Rolls Royce Ltd.
P.O. Box 3
Filton, Bristol, England

S.C. Wofsy
Smithsonian Astrophysical Observatory
60 Garden St.
Cambridge, MA 02138

David Wu
Environmental Research and Technology, Inc.
429 Marrett Road
Lexington, MA 02173

Donald Wuebbles
Aeronomy Laboratory
NOAA Environmental Research Laboratories
Boulder, CO 80302

Giichi Yamamoto
Geophysical Institute
Tohoku University
Sendai, Japan

Alex S. Zachor
Honeywell Radiation Center
2 Forbes Road
Lexington, MA 02173

Martin Zelbrielski
United Aircraft Corp. Research Laboratories
400 Main Street
E. Hartford, CT 06108

Samuel Zimmerman
Air Force Cambridge Research Laboratories
Hanscom Field
Bedford, MA 01730